Analysis of the Influence of Different Manufacturing Methods on the Thermal Aspects of Permanent Magnet Electrical Machines

Mehmet Çağlar Kulan

School of Engineering

Electrical and Electronic Engineering

Newcastle University

A thesis submitted for the degree of

Doctor of Philosophy

May, 2018

Analysis of the Influence of Different Manufacturing Methods on the Thermal Aspects of Permanent Magnet Electrical Machines

Ph.D. Thesis **M. C. Kulan** **May, 2018**

Abstract

Accurate thermal modelling of permanent magnet (PM) electrical machines is of primary importance for improving the overall design in terms of efficiency, torque/power density and over-load time capability. The investigation of crucial thermal parameters leads to achieve a more homogenous temperature distribution and avoid hot spots in electrical machines.

This doctoral research employs different manufacturing methods for improving machine thermal performance such as coil pressing and stator end windings encapsulation for PM machines. A number of thermal modelling approaches including analytical and computational finite element (FEA) methods are utilised to identify the machine thermal parameters within an acceptable accuracy and the results are validated experimentally. The effect of uncertainty and sensitivity of important thermal parameters have also been studied thoroughly.

Coil pressing improves the thermal characteristic of PM machines by packing the conductors in a smaller slot volume but could lead to a degradation of winding insulation, affecting machine reliability. A first step for investigating the coil pressing is to ensure that the proposed method does not deteriorate the mechanical integrity and electrical durability. Then, attention is focused on the estimation of the effective thermal conductivity of compressed coils. Lastly, a set of accelerated life tests, when the acceleration variable is temperature have also been conducted to investigate the life expectancy of the on-tooth compressed stator windings.

Encapsulation of the stator end windings by adding thermal paste into the machine end region is another method having potential for the thermal improvement of PM machines. This method aims to enhance the cooling capability of the machines, which do not have dedicated cooling instruments. A permanent magnet alternator (PMA) with and without thermal paste for an aerospace application has been investigated thermally in this case. Analytical and computational temperature estimation techniques have been employed simultaneously to analyse the thermal improvement of the machine quantitatively. The mechanism of heat flow through a flange mounted PMA is also described by developing an equivalent thermal lumped parameter model.

Index Terms – Accelerated life tests, coil pressing, end windings encapsulation, electrical machines manufacturing, finite element analysis, permanent magnet machines, thermal analysis

Acknowledgements

Looking back over four years of studying and doing research, I find it difficult to capture the influence that the experience has had on me in few words…

A doctoral dissertation is usually considered to be a personal accomplishment. However, it would not have been possible for me to finish this work without the inspiration, encouragement, and support from many people.

First of all, I would like to express my most sincere thanks to Dr. Nick J. Baker. He has been a wise and trusted supervisor throughout the entire process. It is due to his constant inspiration and encouragement that I have gained a deeper understanding of engineering and made progress toward solving problems and improving my communication skills as a researcher. Had it not been for his vision, encouragement, and his confidence in my ability, much of this work would not have been completed. I am deeply grateful for his guidance.

I am also indebted to all the technicians within the department for their help and assistance to my experimental work.

I would also like to acknowledge Dr. James D. Widmer and Dr. Sana Ullah for the times we had discussions when trying to solve certain problems.

I would also like to thank my friend Adem Aydin and my PhD colleague Mohamed Alsadie Mohamed who made my stay here pleasurable while I was miles away from home.

Lastly, however mostly, I wish to thank my parents in Turkey. They introduced me to science, taught me the value of the hard work and gave endless support along the way. They have always offered me so much and asked me for so little. Thanks also go to my sister, Dr. Pinar Kulan Yildiz who was always heartening and encouraging throughout my education life.

This thesis is dedicated to my mother. Her love and support has made it possible for me to get it done.

Newcastle Upon Tyne, England

May, 2018

Mehmet Caglar Kulan

CONTENTS

LIST OF FIGURES

LIST OF TABLES

ACRONYMS AND SYMBOLS

AWG	American Wire Gauge
CAD	Computer Aided Design
CFD	Computational Fluid Dynamics
CFL	Courant-Friedrich-Lewy
CCVS	Current Controlled Voltage Source
DOF	Degree of Freedom
EMF	Electromotive Force
EV	Electric Vehicle
FEA	Finite Element Analysis
FSCW	Fractional Slot Concentrated Winding
GA	Genetic Algorithm
HEV	Hybrid Electric Vehicle
HTC	Heat Transfer Coefficient
HiPot	High Potential
IEC	The International Electro technical Commission
IM	Induction Motor
IPM	Interior Permanent Magnet
ISG	Integrated Starter Generator
IR	Insulation Resistance
LP	Lumped Parameter
MMF	Magneto-motive Force
MPC	Multi-Point Constraint
NEMA	National Electrical Manufacturers Association
PMA	Permanent Magnet Alternator
PM	Permanent Magnet
PMSM	Permanent Magnet Synchronous Motor
pp EAR	Pulse to Pulse Error Area Ratio
PI	Polarization Index
SMC	Soft Magnetic Composite
Sm Co	Samarium Cobalt
SPM	Surface Permanent Magnet
SRM	Switched Reluctance Motor
TCC	Thermal Contact Conductance
TEFC	Totally Enclosed Fan Cooling
TFM	Transverse Flux Machine
TLPM	Tubular Linear Permanent Magnet
TSSF	Temperature Sensitive Ferro Fluids
VCVS	Voltage Controlled Voltage Source

A	Surface area
α_m	Taylor number
B	Arrhenius Model Parameter
B_g	Airgap Flux Density
β	Weibull Shape Parameter
β_t	Thermal expansion coefficient
c_p	Specific Heat
c_w	Wave Speed
C	Arrhenius Model Parameter
C_p	Specific Heat Capacity
D	Displacement
D_h	Hydraulic Diameter
E	Young's Modulus
ε	Strain
ε_c	Emissivity Coefficient
F	Force
F_l	Lowest Mode Frequency
f	Electrical Frequency
f_s	Safety Factor
G_{th}	Thermal Conductance
h	Heat Transfer Coefficient
h_s	Smallest Element Size
I	Current
J	Current Density
K_m	Motor Constant
K_{wb}	Slot Fill Factor
k	Thermal Conductivity
k_{normal}	Normal Stiffness
k_s	Stiffness
L	Length
m	Mass
N	Number of Turns
N_m	Number of Magnets
N_s	Number of Slots
n_{rad}	Radial Static Force
P	Power
Q	Heat Flux Density
q	Heat
R	Thermal Resistance
R_{DC}	Electrical Resistance
R_{ro}	Rotor Outer Radius
S_y	Yield Strength
σ	Stress
σ_c	Stefan-Boltzman Constant
δ	Airgap Length
T	Temperature/Torque
t	Time
ΔT	Temperature Difference
Δt	Integration Time Step
τ^{max}	Maximum Shear Stress
u_r	Rotor Peripheral Velocity
η	Fan Efficiency

$\boldsymbol{\mu}$	Dynamic Viscosity	$\boldsymbol{\omega}$	Angular Frequency
$\boldsymbol{\vartheta}$	Kinematic Viscosity	$\boldsymbol{\theta}$	Temperature Rise
$\boldsymbol{V}$	Volume	$\boldsymbol{\rho}$	Mass Density
$\boldsymbol{g_v}$	Volumetric Heat Generation		

Chapter 1. Introduction

1.1 Developments in Electrical Machines

Electric machines are one of the most popular machines of everyday life and their number of types increase with developments in science, engineering and technology [1]. There are many reasons why electrical machines have been growing and evolving recently. Some of those reasons are [1]:

- Development in material engineering: rare-earth permanent magnets (NdFeB, SmCo), high temperature superconductors, amorphous laminations, cobalt alloy laminations, high temperature insulation materials etc.
- New application fields: electric vehicles (EVs), hybrid electric vehicles (HEVs), robotics, aerospace applications, weapon systems, magnetic levitation systems, microelectromechanical systems (MEMs), marine vessels and submarines, harsh environment applications etc.
- Impact of power electronics: variable speed drives (VSD), switched reluctance motor (SRM) drives
- New control schemes: intelligent drives, fuzzy control, sensor-less control etc.
- New topologies: transverse flux machines (TFMs), superconducting motors, bearing less motors, rotary-linear motors, magnetically geared machines etc.
- Impact of numerical modelling and computing: the finite element analysis (FEA), multi-objective optimization methods (neural networks, genetic algorithm etc.)
- Demand on high torque motor drives, e.g. EVs and HEVs, traction applications etc.
- Reliability demands: fault tolerant machines, elimination of brushes and reduction of maintenance etc.
- Need for energy savings and environmental protection

All these reasons imply that electric machines and associated drive systems are one of the most important research fields of electrical and electronic engineering and advances in electronics, material science, control systems and computation contributes the development of modern electrical machines significantly.

Electromechanical systems have the biggest share in electric and electronic market. According to [2], electric motors consume 46.2% of all global electricity generation, leading to almost 6040 Megatons of CO_2 emissions annually. It is also estimated that 300 million motors are being used in industry.

Energy efficiency of machines is a crucial issue to achieve sustainable development of the world to ensure environmental protection and natural resources saving.

There are numerous types of electrical machines used for different applications. Comparison of most popular and researched electric machines such as cage induction motors (IMs), permanent magnet brushless motors (PMBMs) and switched reluctance motors (SRMs) is performed in [1]. It is tabulated in Table 1.1.

Table 1.1 Comparison of popular electrical machine topologies [1]

	Cage IMs	**PMBMs**	**SRMs**
Power density	Lower than PMBM	Highest	Lower than PMBM
Efficiency	Lower than PMBM	Over 90%	About 1% more than equivalent IMs
Power factor	0.8-0.9	High (up to 1)	Switched d.c. motor
Performance at low speed	Poor	Good	High torque, low efficiency
Torque ripple	Less than 5%	Up to 10%	15-20 %
Power electronics converter	Not necessary for constant speed	Necessary	Necessary
Cost	Cost effective motor	More expensive than IMs and SRMs	Cost effective motor

As given in Table 1.1, permanent magnet (PM) electrical machines are superior in terms of machine efficiency and power density although they are not very cost effective compared to cage induction machines and switched reluctance machines.

Recent advances in permanent magnet materials, power semiconductor switching devices and modern control techniques mean PM machines are now being used in a wide range of applications which include actuators, robotics, machine tools, electric vehicles, aerospace generators and renewable energy generation. From this standpoint, PM brushless machines have become more attractive than other types of electrical machines.

There are a lot of proposed methods to build high performance PM electric machines based on analytical approaches and finite element analysis (FEA). The aim is to increase machine performance without degrading other aspects of the electrical machines.

Briefly, the main advantages of the use of permanent magnets in construction of electrical machines can be described as follows:

- High power and torque density
- Simplification of construction and maintenance
- No field excitation losses on the system which means higher efficiency
- Better dynamic performance
- Reduction of prices for particular applications

Based on all these advantages, PM machine drives are the best in terms of torque and power density but there is still room for the improvement of these machines in terms of torque/power density by considering different manufacturing methods. Since the efficiency of PM machines has a strong relationship with the manufacturing process, it should be further studied by taking advantage of innovative manufacturing methods to improve the total machine performance regarding electrical, mechanical and thermal aspects.

The thermal limits set the constraints of an electrical machine. Therefore, the performance improvement of PM electrical machines requires a multi-disciplinary approach and the thermal constraints should be taken into account at an early stage in the optimization process of the machine design.

Heat transfer in electric machines is equally important as electromagnetic and mechanical design. Thermal analysis of the electric machines, however, is more complex and more non-linear than the electromagnetic behaviour. Electric machine designers usually prefer more approximate methods for determining the thermal behaviour of the machines, while exact methods are pursued for electromagnetic design. Electromagnetic design of the machine determines the machine geometry, winding design and power semiconductors for drive systems. All these items affect the manufacturing cost. However, as long as increase in temperatures of electric machines is at nominal values, thermal condition of the machine will only affect how long the motor will last due to insulation degradation [3]. There might be a little effect of machine thermal behaviour on the machine torque delivered. Therefore, knowing more about the behaviour and effects of the heat generated in the machine during operation is of great importance regarding reliability issues of electrical machines.

1.2 Objectives

This research investigates the influence of a number of manufacturing approaches such as coil pressing and stator end windings encapsulation on the thermal performance of permanent magnet electrical machines for traction and aerospace applications. The research tackles the following issues:

- Coil pressing has potentials for improving the thermal characteristic of PM machines by packing the conductors in a smaller slot volume yet the reliability of compressed stator windings is of great concern to machine designers and an electrical machine with compressed windings must have acceptable electrical and thermal performance parameters. Therefore, this thesis proposes a number of numerical and experimental methods including structural FEA simulations and accelerated life tests to quantitatively determine the mechanical durability and electrical integrity of the compressed windings.
- The important thermal parameters (i.e. slot thermal conductivity) might be affected by the compression of coils as the average slot thermal conductivity is a complex function of the conductor packing factor. As formerly no concise relationship was set between the slot average thermal conductivity and the coil pressing, a number of thermal modelling approaches including analytical and computational methods have been developed in this thesis to identify the machine thermal parameters within acceptable accuracy.
- Deformation of the conductors and enhanced thermal behaviour in the windings are the conditions that occur when coils are compressed at high pressures. The pros and cons of coil pressing regarding the machine electrical and thermal performance have been revealed by conducting a case study: a PM electrical machine design for the application of an Integrated Starter Generator (ISG) in recent hybrid electric vehicles (HEVs).
- This research also proposes a thermal improvement method, a part of manufacturing process, for a flange mounted permanent magnet alternator (PMA) for aerospace. Due to cooling system limitations in aerospace applications, a thermally conductive silicon based encapsulation material has been utilised in the stator housing to investigate the possible thermal improvements in the PMA. The mechanism of heat flow, when thermal paste is present, has been analysed by developing a theoretical thermal lumped parameter model and by performing thermal FEA simulations.

The research described in this thesis aims to enlighten the reader about the influence of some recent manufacturing methods (i.e. coil pressing and machine end windings potting) on the machine thermal aspects, having potential for the thermal improvement of permanent magnet

electrical machines. Moreover, advantages and disadvantages of the proposed machine design methods regarding electrical, mechanical and thermal aspects are discussed thoroughly.

1.3 Contribution to Knowledge

This thesis is designed to contribute to the knowledge base regarding the thermal analysis of recent manufacturing methods including coil pressing and stator end windings encapsulation. The outcome of the research regarding contribution to knowledge is summarised as follows:

- Quasi-static explicit dynamics analysis of the coil pressing in FEA is explained and the methodology of the structural analysis of coil pressing is described in the thesis.
- The effective slot thermal conductivity of the compressed windings is estimated and a new approach to perform thermal FEA simulations for the deformed magnet wires has been demonstrated.
- The influence of stator end windings encapsulation on the thermal aspects of a PM machine has been researched quantitatively and a lumped parameter model has been developed to compute the heat flow through the thermal paste added into the stator housing.
- The life expectancy of the on-tooth compressed windings has been revealed by conducting a set of accelerated life tests employing Arrhenius-Weibull life model.

1.4 Published Work

The followings are conference and journal papers peer-reviewed and published during the course of this doctoral research:

- M. C. Kulan; N. J. Baker; J. D. Widmer, "Design and Analysis of Compressed Windings for a Permanent Magnet Integrated Starter Generator," in IEEE Transactions on Industry Applications, vol. 53, no.4. pp. 3371-3378, July-Aug. 2017.
- M. C. Kulan and N. J. Baker, "A thermal equivalent circuit to quantify the effect of thermal paste on heat flow through a PM machine," *2017 IEEE International Electric Machines and Drives Conference (IEMDC)*, Miami, FL, 2017, pp. 1-7.
- M. C. Kulan, N. J. Baker and J. D. Widmer, "Design of a high fill factor permanent magnet integrated starter generator with compressed stator windings," 2016 XXII International Conference on Electrical Machines (ICEM), Lausanne, 2016, pp. 1513-1519
- M. C. Kulan, N. J. Baker, J. D. Widmer and S. M. Lambert, "Modelling the mechanical and thermal properties of compressed stator windings," 8th IET International Conference on Power Electronics, Machines and Drives (PEMD 2016), Glasgow, 2016, pp. 1-6.
- N. J. Baker, D. J. Smith, M. C. Kulan and S. Turvey, "Design and performance of a Segmented Stator Permanent Magnet Alternator for Aerospace," in IEEE Transactions on Energy Conversion, vol. 33, no. 1, pp. 40-48, March 2018.
- N. J. Baker, D. J. Smith, M. C. Kulan and S. Turvey, "Design and performance of a segmented stator permanent magnet alternator for aerospace," 8th IET International Conference on Power Electronics, Machines and Drives (PEMD 2016), Glasgow, 2016, pp. 1-6.
- M. C. Kulan, N. J. Baker, "Thermal Aging Investigation of Random Wound Compressed Stator Windings," 9th IET International Conference on Power Electronics, Machines and Drives (PEMD 2018), Liverpool, 2018, pp. 1-6.

A journal manuscript, submitted as of December 2017 for peer review is listed as follows:

- M. C. Kulan; N. J. Baker, " Development of a Thermal Equivalent Circuit to Quantify the Effect of Thermal Paste on Heat Flow through a Permanent Magnet Alternator," in IEEE Transactions on Industry Applications (Submitted)

1.5 Overview of the Thesis

Chapter 1: Introduction

A brief introduction of the thesis is given in this chapter. The thesis objectives and contribution to knowledge are also included here.

Chapter 2: Literature Review

This chapter includes extensive literature research on thermal improvement and analysis of permanent magnet electrical machines by comparing existing methods. The potentials of different manufacturing methods on the machine thermal performance are described.

Chapter 3: Structural Analysis of Coil Pressing

A thorough description of quasi static modelling has been introduced as it is required to understand the dynamic FEA modelling of complex geometries such as electric bobbins. Finite element analysis is used to achieve the closest prediction of the deformation during coil pressing by employing a number of techniques, such as mass scaling, mesh optimisation, prevention of contact penetration etc. Some case studies are included to demonstrate how an accurate structural modelling of coil pressing is achieved.

Chapter 4: Integrated Starter Generator (ISG) Design

In order to implement on-tooth coil pressing, a case study which employs an Integrated Starter Generator (ISG) is conducted by performing electromagnetic FEA simulations. The best candidate ISG machine in terms of a user defined multi-objective optimisation function is selected to further study the effect of coil pressing on the machine electrical and thermal performances.

Chapter 5: Thermal Modelling of Stator Windings

A number of analytical and FEA approaches have been developed to estimate the slot thermal conductivity in this chapter. The accuracy of the proposed thermal conductivity prediction methods has been presented. Several case studies are employed to demonstrate how the slot thermal properties are being affected by the slot fill factor.

Chapter 6: Thermal Investigation of Integrated Starter Generator with Compressed Stator Windings

The experimental methodology of on–tooth coil pressing is described in this chapter. The effective thermal conductivity of the ISG coils is determined using different methods: steady state thermal FEA simulations and short time transient thermal tests. Thermal performance of the ISG machine with compressed windings is discussed in detail.

Chapter 7: Thermal Aging Investigation of Compressed Stator Windings

On–tooth pressed ISG coils have been aged by conducting high temperature oven tests. Accelerated life test results are provided to investigate the life expectancy of the compressed magnet wires at nominal operating conditions.

Chapter 8: Development of a Thermal Equivalent Circuit to Quantify the Effect of Thermal Paste on Heat Flow through a Permanent Magnet Alternator

The mechanism of heat flow when the end windings of a flange mounted permanent magnet alternator are encapsulated, has been analysed by developing a thermal lumped parameter model and by performing thermal FEA simulations. Detailed steady state and transient thermal results of the permanent magnet alternator along with experimental results are presented in this chapter.

Chapter 9: Conclusion and Future Work

Conclusions of the research are given at the end of the thesis along with future work.

Chapter 2. Literature Review

2.1 Thermal Improvement of Electric Machines

With the increasing requirements for miniaturization, energy efficiency and cost reduction [4], it is necessary to apply optimal Multiphysics models to the design of highly constrained PM electrical machines [5]. Design of modern electrical machines is a Multiphysics problem which requires electromagnetic, thermal and mechanical investigations since constraints of electric machines might be dictated by mechanical and/or thermal limits depending on applications. The mechanical and thermal analysis of electric machines have received less attention than electromagnetic analysis. This is quite clear from the number of papers published on the design and analysis of electrical machines as shown in Figure 2.1.

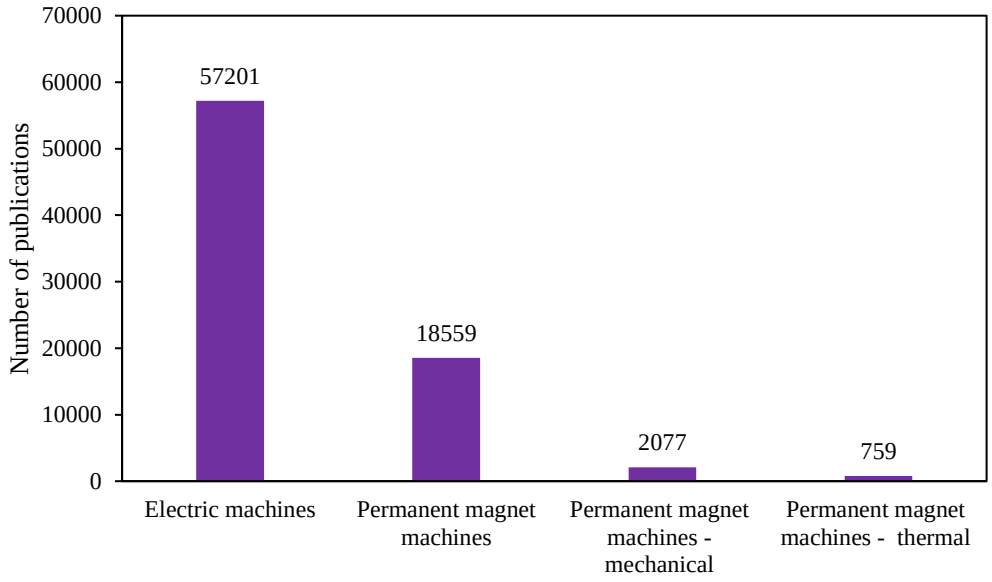

Figure 2.1 Number of papers published in IEEE Xplore Digital Library between 1932-2017 for the selected keywords

Mechanical and thermal characteristics affect reliability and durability of electric machines and are therefore as important as electrical performance during the machine operation to provide a continuous operation and better life expectancy. Hence, modern electric machines require a multi-disciplinary approach.

Due to increasing kW/kg of electric motors as shown in Figure 2.2 [6], electric motors replace piston engines or turbine engines. According to Hendershot [6], cooling and efficiency are very important for electric propulsion as high power density electric machines are only possible with enhanced cooling systems. This shows that an efficient cooling system is crucial for electric propulsion.

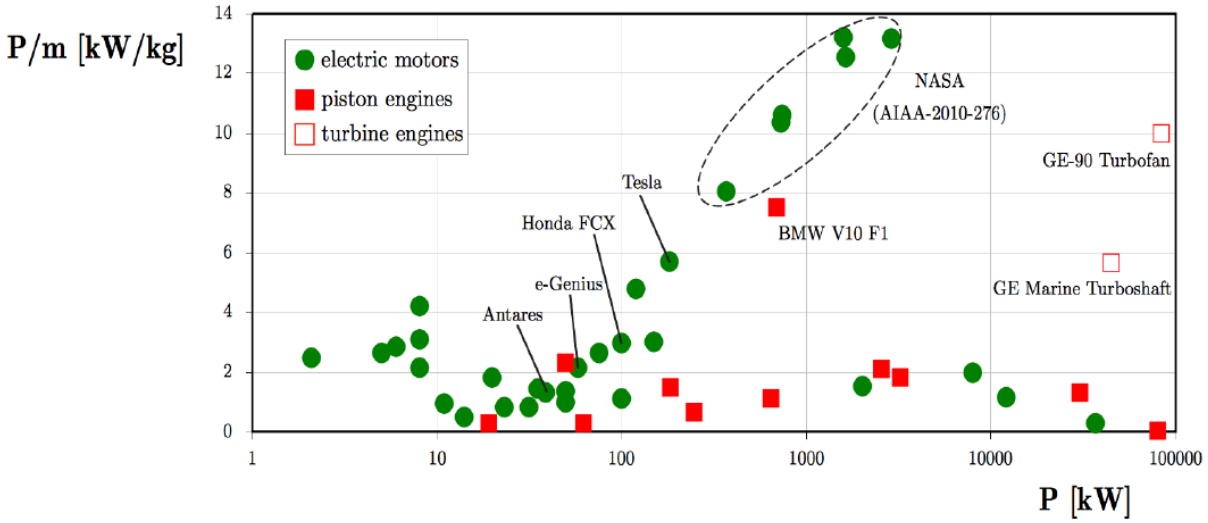

Figure 2.2 Specific power density of current propulsion systems: electric, piston and turbine[6]

Since there is a physical relationship between the machine losses and temperature, it is impossible to accurately analyse one without the other [4]. Therefore, electro-thermally coupled machine design approach is necessary for high performance electric machines. Either analytical or computational methods can be used to evaluate machine performance electrically and thermally in order to obtain high performance and high durability electric machines.

Thermal degradation is inevitable for electric machines. According to Huang et al. [7], every component of the electrical machine is subjected to degradation since the first day in service. Rotor/stator winding insulation failures and bearing failures are two of the most common observed failures for electric machines. These are due to combined mechanical, thermal and electrical stresses. However, thermal life characteristics of the machine windings are vital with regards to service life as thermal stress harshly affects the machine life expectancy. Furthermore, it is well known that a 10°C increase in temperature reduces insulation life by approximately 50% [3]. This means that thermal aspects of electric machines are crucial during the operation.

Power loss analysis is a key to perform accurate thermal design of permanent magnet machines. According to Wrobel et al [8], in the literature, there are two research themes on design of electrical machines: ‘complete design optimization methods’ and ‘design for application methods’. In the first theme, there are numerous published literatures as given in [9-12]. The complete design optimization approach is all based on multi-physics optimization tools and the common point of all those papers is to use simplified power loss components during multi-objective optimization procedure. Nonetheless, Wrobel et al. emphasises that the second method, design for application method, leads to more accurate power loss investigation for the

proposed permanent magnet machines. Unlike the first theme, ‘design for application’ methods look in detail into various power loss components. Therefore, the unforeseen effects such as excessive heat generation and/ or power loss could be detected at early stage [8]. There are a substantial number of technical papers on ‘design for application’ method as given in [13-25]. The power loss components on magnets, rotor - stator iron cores and machine windings due to magneto-motive force (MMF) space and time harmonics, air friction and winding configuration etc. have been investigated in detail and a number of analytical and computational methods have been proposed in those papers. The main advantage of the ‘design for application’ method in comparison to ‘multi-physics optimization methods’ is that the power loss components of electrical machines can be calculated with very low error. In terms of thermal design and analysis of PM electrical machines, accuracy and location of electrical and mechanical power losses are crucial as it leads to estimate machine temperature distribution with a higher accuracy and possible thermal design methods or cooling systems can be applied for the machine under investigation to provide better thermal characteristics.

Thermal performance of a PM electrical machine can be improved by implementing cooling techniques such as water or oil cooling jackets, totally enclosed fan cooling (TEFC), air cooling with appropriate casing fin design and direct rotor cooling etc. All these cooling methods are dependent on machine size, speed, power density, over-load use, loss distribution and application.

In the literature, there are many new cooling approaches for PM electrical machines. All the proposed cooling methods are chosen exclusively for the machine under investigation. Several previous research outcomes with regards to the thermal aspects of electrical machines will be discussed in this chapter.

In [26], a combined electromagnetic and thermal optimisation method was proposed for an aerospace application. Overall design process targets minimum mass with improved thermal performance. It is offered natural convection since force convection is not more reliable compared to natural convection. As a result, a housing type with radial longitudinal fins was proposed as it was lighter choice regarding overall mass of the PM machine. Through the multi-objective optimisation, a 16.3% reduction in the total motor mass has been achieved. The geometry based considerations for the housing type was illustrated in Figure 2.3 [26].

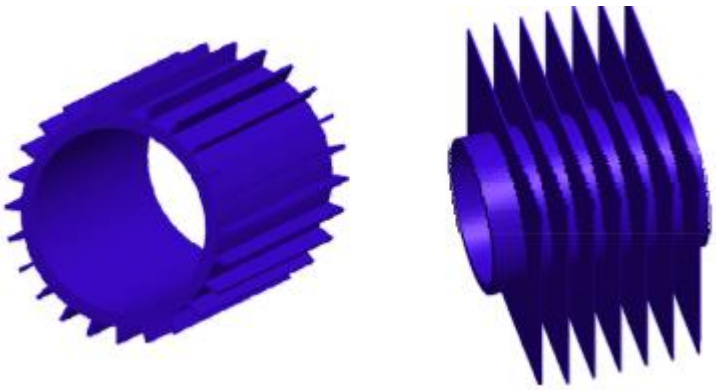

Figure 2.3 Axial longitudinal fins (left), radial fins (right) [26]

According to Galea et al, a simple and novel cooling technique can be implemented in machine phase windings [27]. This research is based on a higher thermal conductivity path between the centre of the slot and the cooling arrangement. The main purpose is to reduce machine hot spot temperature usually located in the end windings. The reported work was implemented on the water cooled 12 slot/10 pole double layer wound tubular linear PM machine (TLPM). The proposed method as depicted in Figure 2.4, was analysed using FEA and thermal lumped parameter (LP) network and also the results are validated experimentally. A reduction of approximately 40% in the slot hot-spot temperature is achieved for the same current loading [27].

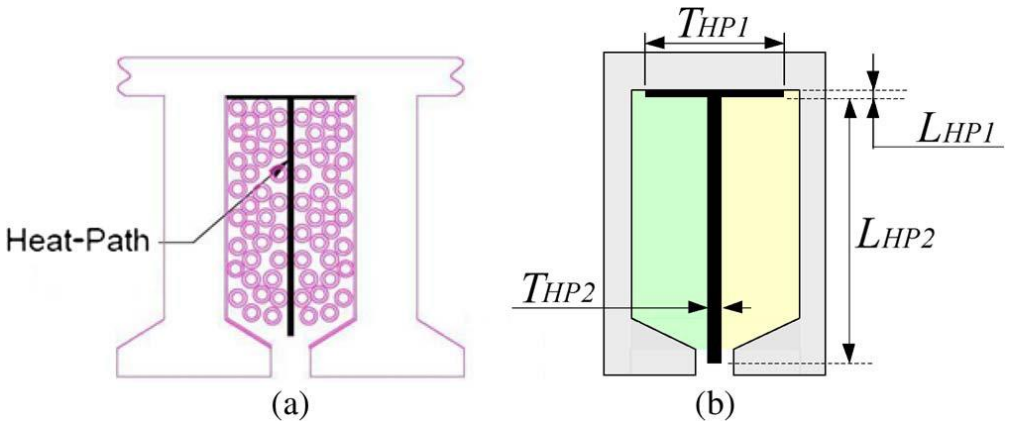

Figure 2.4 (a) Slot with heat path and (b) structure of the proposed heat path [27]

Similarly, indirect slot cooling for high power density PM machines with concentrated winding is proposed in [28]. This can be considered as a new cooling technique for the machines with flat wires. According to Schiefer et al, there remains unused space inside the slots when flat wires are used for the machines with concentrated windings which can be used for water cooling channels. Due to the small thermal resistance between the winding and cooling channels, the proposed cooling approach delivers outstanding cooling performance compared to cooling jackets [28]. 3D printable cooling channels were implemented for a traction motor. For the same current density, FEA results show about 140°C hot spot temperature reduction in the prototype

in comparison to conventional cooling jackets. The proposed geometry is shown in Figure 2.5 [28].

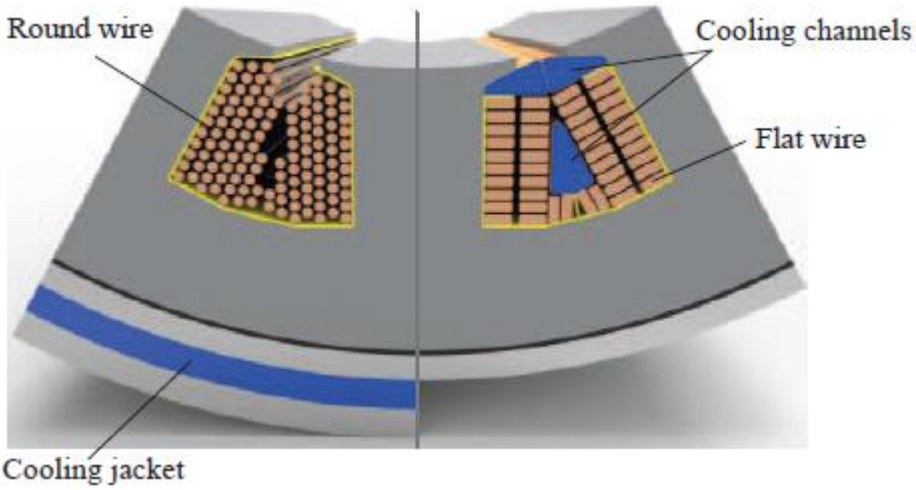

Figure 2.5 Conventional round winding (left), new cooling system with flat wires (right) [28]

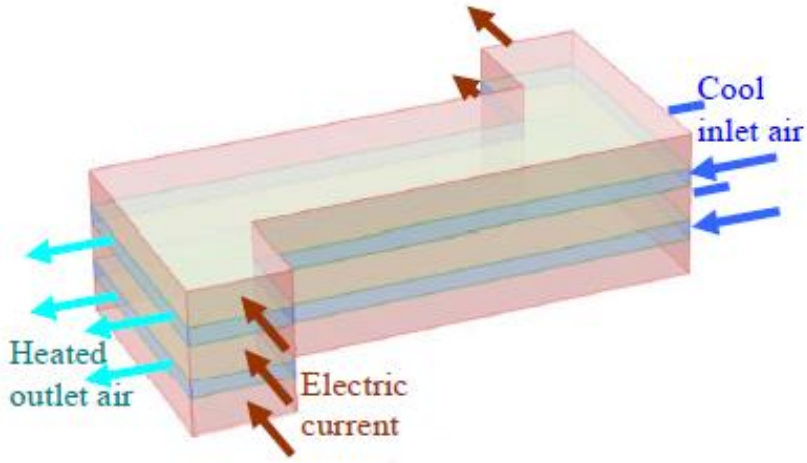

Figure 2.6 A section of laminated wave winding with air cooling channels [29]

Similarly, in [29], a traction machine with directly cooled laminated wave windings is proposed. One section of a three-phase axially stacked machine was used for the thermal improvement. This research mainly shows the potential of direct forced cooling of laminated stator windings with very high current density (up to 22.5 A/mm^2). Although FEA and computational fluid dynamics (CFD) results show great thermal improvement in the machine, experimentally, air leakage of force cooling did not exhibit the same performance as computational methods. A section of the laminated wave winding with air channels is depicted in Figure 2.6, above [29].

A very interesting thermal improvement method is proposed in [30]. Temperature sensitive ferro-fluids (TSSF) are circulated over the end windings of an electrical machine. Since magnetic leakage field of end windings are used to energise the circulation, the proposed cooling system requires no additional moving mechanical parts, pumps or sensors [30]. It was

investigated using CFD simulations yet no experimental validation of the effect of thermomagnetic cooling was included. In the proposed system, hot spot temperature reduction is about 25% compared to air cooled system as given in Figure 2.7 [30].

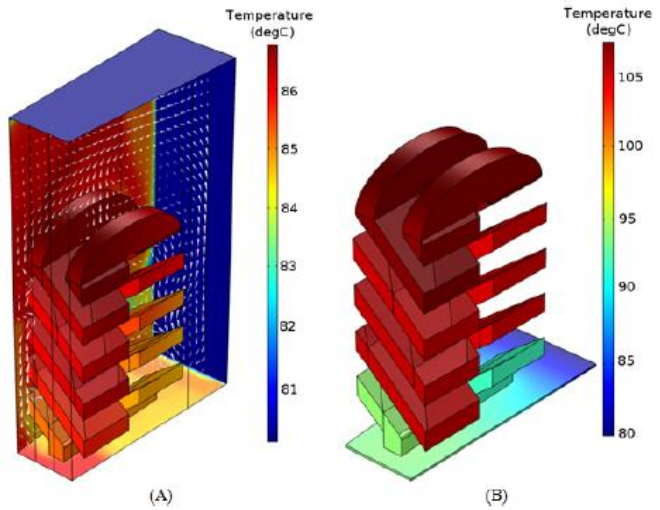

Figure 2.7 End winding temperature distribution: (A) TSSF cooled, (B) air cooled [30]

According to Festa et al [31], circumferential cooling is highly effective cooling technique for machines with high torque density. In this method, laminations are divided into sub-laminations and some canals occurring due to sub-stacks are cooled by a forced convection system [31]. The effectiveness of the proposed method was compared to conventional water jacket cooling. It was demonstrated that it is possible to design an air cooled motor with the same torque density as a water jacket cooled machine. The efficiency might even be slightly increased. Thermal models are illustrated in Figure 2.8, below [31].

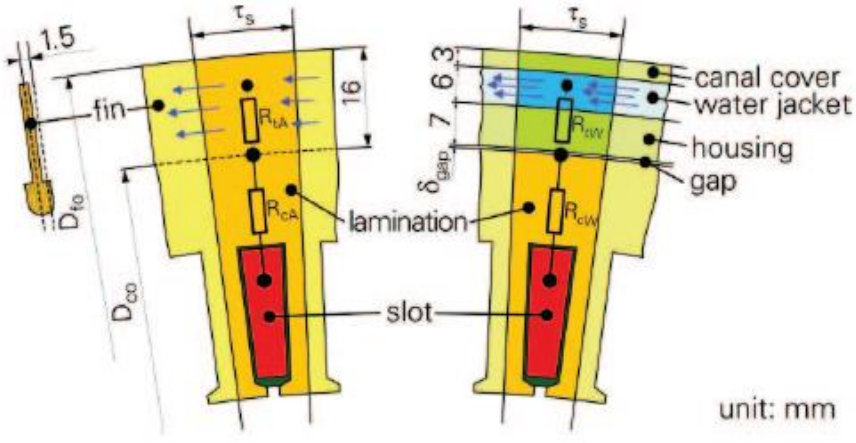

Figure 2.8 Thermal models of circumferential forced air cooling (left), water jacket cooling (right) [31]

It is also important to see what type of cooling systems are common in commercial HEVs. Comparison of HEV design features and published specifications are given in Table 2.2 [6]. It was tabulated that the commercial HEVs usually utilise forced cooling systems such as spray

cooling for stator windings, oil circulation and water/glycol heat exchangers. This shows that complex cooling systems are required for high torque/power density traction applications.

For rotor cooling in HEVs, Toyota Prius 2010 rotor punching has mass reduction pockets which facilitate efficient cooling for an inner PM synchronous electric machine [6]. Also, combination of the external convection systems are common to provide better cooling for high power HEVs. For example, 2014 Porsche Panamera E-Hybrid, as illustrated in Figure 2.9, facilitates two separate forced cooling systems: water jacket with oil and forced air flow through the rotor assembly [32].

Oil spray cooling with or without use of nozzles requires a motor partially filled with oil [32]. Toyota Prius traction electric motor used such a method recently. In this case, the level of oil is very important parameter as excessive amount of oil might increase windage loss due to wet air-gap in the machine.

Table 2.2 The published specifactions of HEVs [6]

Design Feature	2008 LS 600h	Hybrid Camry	2004 Prius	2010 Prius
Motor peak power rating	165 kW @ 5250 revolutions per minute (rpm) (disputed)	105 kW @ 4500 rpm (disputed)	50 kW @ 1200–1540 rpm	60 kW
Motor peak torque rating	300 Nm	270 Nm	400 Nm	207 Nm
Rotational speed rating	10,230 rpm	14,000 rpm	6,000 rpm	13,500 rpm
Separate generator used?	Yes	Yes	Yes	Yes
Generator specifications	Not published	Not published	33 kW	42 kW
Source of power to MG2	Battery and/or ICE via generator	Battery and/or ICE via generator	Battery and/or ICE via generator	Battery and/or ICE via generator
PMSM rotor design	Interior PMs with triangular configuration	Interior PMs with "V" configuration	Similar to Camry	Similar to Camry
Motor winding configuration	Parallel	Parallel	Series	Series
Number of rotor poles	8	8	8	8
Bi-directional dc-dc converter output voltage	~288-650 Vdc	250-650 Vdc	200-500 Vdc	200-650 Vdc
Bi-directional dc-dc converter power rating	36.5 kW	30 kW	20 kW	27 kW
PMSM cooling	Same as Camry, yet with oil squirters for stator	Oil circulation and water/glycol heat exchanger	Same as Camry	Same as Camry, yet no direct heat exchanger

Figure 2.9 2014 Porsche Panamera E-Hybrid 416 horsepower – water jacket with oil and air induction system (dual cooling system) [32]

Heat extraction systems through conduction is as important as natural or forced convection systems. If a material typically has high electrical conductivity, it usually has good thermal conductivity. The development of material science enables high thermal conductivity insulation materials. The thermal conductivity of air is 0.026 $W/m.K$ at 27°C and it is important to know the value of air thermal conductivity for comparison purposes. The standardisation of electrical insulations is provided by The International Electrotechnical Commission (IEC) and National Electrical Manufacturers Association (NEMA). The insulation classes (i.e. maximum allowed hot spot temperature) of typical insulation materials are given in Table 2.3 [32].

Table 2.3 Standard insulation classes [32, 33]

IEC 60085 Thermal Class	NEMA Class	NEMA (Letter class)	Typical materials
90	-	-	Un-impregnated paper, silk cotton and vulcanized natural rubber
105	105	A	Silk, paper, cotton
120	-	-	Epoxy resins, polyurethane
130	130	B	Mica, glass fibre, asbestos
155	155	F	Class 130 materials
180	180	H	Silicone elastomers

200	-	N	Teflon
220	220	R	IEC Class 200 materials
-	240	S	Polyimide enamels and films (Kapton™ and Alconex GOLD)
-	-	-	Newly developed NeoTem™ up to 300°C

Some of the latest high thermal conductivity insulation materials from different manufacturers are reported in Table 2.4 [32].

Table 2.4 High thermal conductivity insulation materials [32]

Insulation material	Thermal conductivity ($Wm^{-1}K^{-1}$)	Electric Resistivity (Ohm × cm)	Manufacturer
MC4260	0.6 – 0.7	8×10^{14}	Elantas
Kapton FN	0.12	$1.5 - 2.3 \times 10^{17}$	DuPont
Nomex Paper	0.12 – 0.15	$8 \times 10^{11} - 8\times10^{16}$	DuPont
PEEK 450G	0.25	4.9×10^{16}	Victrex
Circalok 6006	1.1	1×10^{16}	Lord
ECCTreme ECEA 3000	0.18	$> 10^{18}$	DuPont
Teflon PTFE	0.221	$>10^{18}$	DuPont

The importance of the tabulated thermal conductivities is that modern cooling systems are not only dependent on the sophisticated external cooling systems and primarily, heat transfer by conduction in electrical machine should be designed to provide efficient and optimal cooling. Therefore, the selection of insulation material is a part of thermal design of any electrical machine since the improvement of average thermal conductivity of electric machines results in significant temperature reduction on machine hot spot.

In the literature, efforts have been made to improve heat transfer by conduction for particular applications. Electrical windings are exposed to more attention for thermal conductivity improvement in electrical machines as temperature distribution inside the winding profoundly

affects machine reliability. Novel measurement techniques and the use of high thermal conductivity insulation materials draw interest in machine thermal design.

In [34, 35], the authors present analytical and experimental methods to measure equivalent thermal conductivity of impregnated (Epoxylite EIP 4260 and varnish) windings. The rectangular winding samples are selected in terms of conductor fill factor, material, aspect ratio and impregnation material. Some important thermal parameter results are derived. The windings samples being used in experimental work are shown in Figure 2.10.

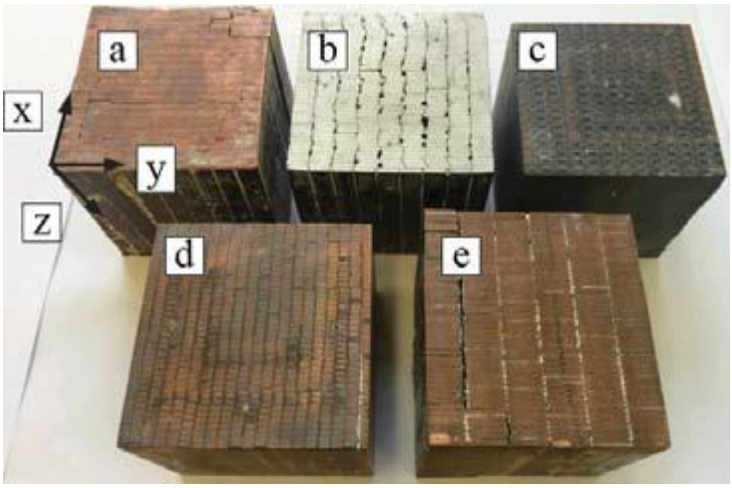

Figure 2.10 Impregnated winding samples with rectangular profiled aluminium and copper conductors with different conductor fill factors [34]

It is shown that thermal conductivity on xy-plane varies between 1.9 and 4.3 $W/(mK)$ for different winding samples [34]. In this study, it is also demonstrated that the highest fill factor winding segment has the highest equivalent thermal conductivity value. The importance of this study is that thermal conductivity is enhanced by high thermal conductivity insulation materials which are Epoxylite EIP 4260 and Elmotherm 073-1010 resins in this case.

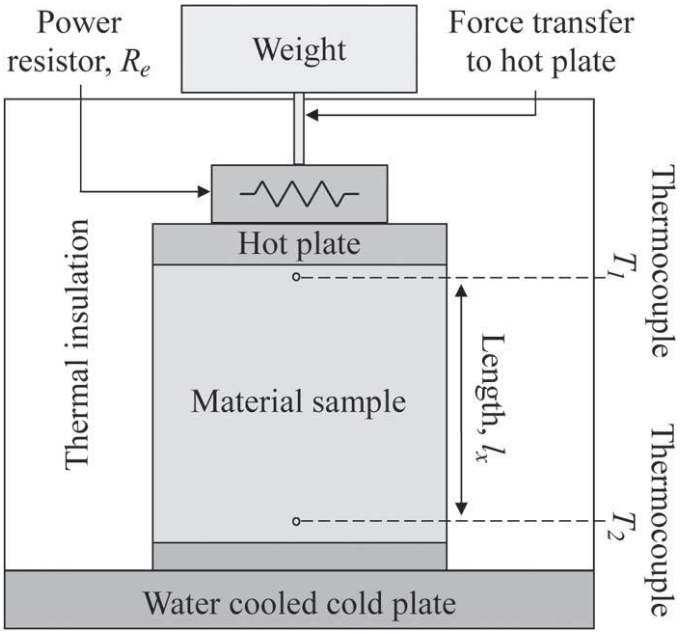

Figure 2.11 Schematic of an experimental setup for thermal parameters estimation [35]

Similarly, an experimental thermal conductivity measurement technique has been proposed for the impregnated winding samples in [35] as given in Figure 2.11. The winding samples comprise aluminium conductors with polyamide-imide insulations and aluminium oxide insulation and copper conductors with only polyimide-imide insulations. In all cases, an epoxy impregnation is used. Experimentally, thermal conductivity values ranging between 2.3 $W/(mK)$ and 6.5 $W/(mK)$ are obtained. This research is also a comparative study of magnet wires with different coating, insulation and conductor materials.

As a result, it is shown that direct liquid cooling, spray cooling, dual cooling, fin design and forced air cooling methods are all examples of heat extraction (by convection) methods in modern electrical machines. It should be also emphasised that the selection of high thermal conductivity insulation materials and application of those materials into electrical machines are also crucial for heat extraction (by conduction). All the proposed cooling methods in the literature are based on particular application and some methods are more attractive for modern electrical machines in terms of cost effectiveness, weight and reliability.

The common point of all these published work reviewed in Section 2.1 is that they are examples of new or recent cooling methods. This is a part of electrical machine thermal investigations. In addition to new methods, thermal 'analysis' methods such as analytical approaches, FEA simulations, CFD modelling methods and experimental measurement techniques are of also primary importance as it is always required to estimate the machine thermal behaviour at early stage of the design optimisation. Therefore, in Section 2.2, the recent thermal 'analysis' and investigation methods are introduced.

2.2 Recent Thermal Analysis Methods

2.2.1 Analytical Thermal Analysis Methods

Electric machine thermal analysis can be divided into two types: analytical lumped circuit and computational methods [4]. The analytical approaches are known for fast thermal calculations. However, in order to develop an accurate models, the developer of the network must define the equivalent circuit accurately with main heat flow paths [36, 37]. In the analytical lumped parameter approach, electrical analogy of heat flow inside the machine is estimated by taking conduction, convection and radiation into account for heat transfer. For a machine lumped parameter model, simple resistive circuits for steady state thermal models and/or higher order RC circuits might be utilised for transient thermal models. The most important thing in the development of lumped thermal circuit is that heat flow across the machine geometry must be estimated within a high accuracy by calculating thermal parameters. This leads to development of lumped thermal modelling in the literature by proposing different analytical methods.

According to Kuehbacher et al [38], different lumped thermal network approaches can be used for thermal modelling of electrical machines. Classical, T-equivalent and k-shift models are given in Figure 2.12. In order to eliminate possible invalid heat flow direction at initial time with T-equivalent circuit, Kuehbacher et al proposes k-shift method which might be useful for transient lumped thermal modelling of electrical machines. K-shift method is based on defining boundary resistances and a centre resistance between the nodes [38]. The main purpose is to distribute thermal capacitances into small pieces as it might affect initial temperature response in transient circuit.

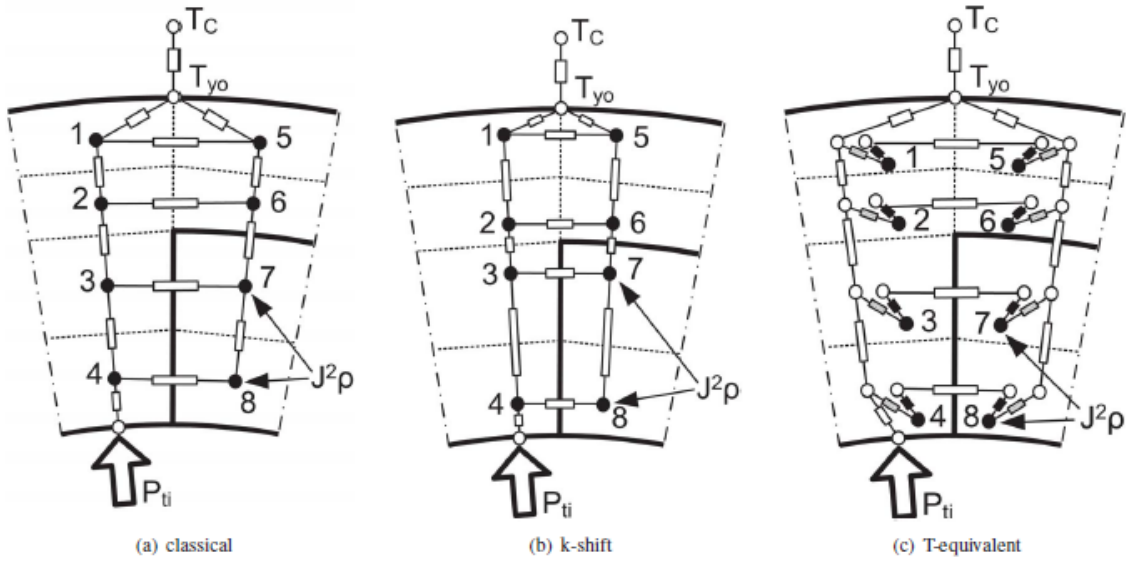

Figure 2.12 Different thermal lumped parameter approaches [38]

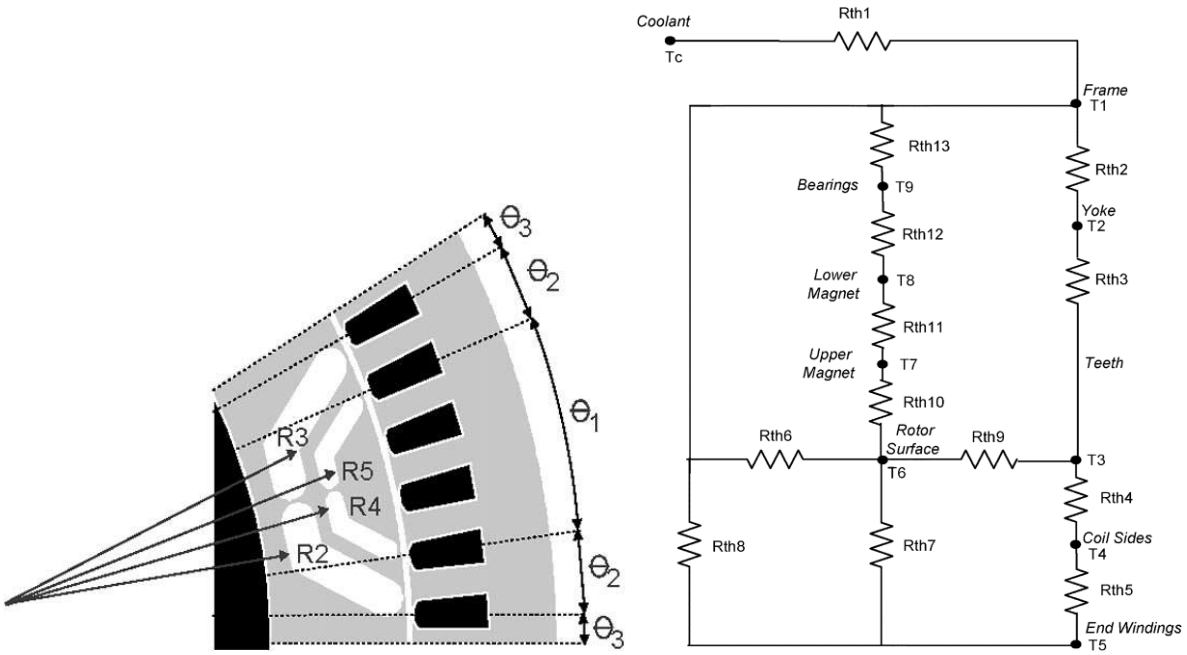

Figure 2.13 Cross- section of the IPM (left), 10-node thermal network model (right) [39]

Node reduction in the thermal lumped models is also an important issue if a sufficient accuracy is obtained with the proposed thermal model. This allows the developer to quickly implement a thermal network into a machine optimisation process. El-Refaie et al [39] proposes a 10-node thermal network model for 6 kW – 12 pole interior PM multi-barrier (IPM) starter /alternator machine. It is illustrated in Figure 2.13 [39].

Similarly, a 10-node equivalent circuit for a surface PM synchronous machine (SPMSM) for a HEV powertrain application is proposed in [40]. The circuit also considers ohmic losses due to magnet eddy currents. This research is also based on simplified lumped parameter thermal model of an electric machine. This is an important study as magnet demagnetisation due to temperature variation inside the rare-earth permanent magnets can be detected by simple thermal lumped models during the machine optimization. The proposed electrical analogy circuit is depicted in Figure 2.14 [40].

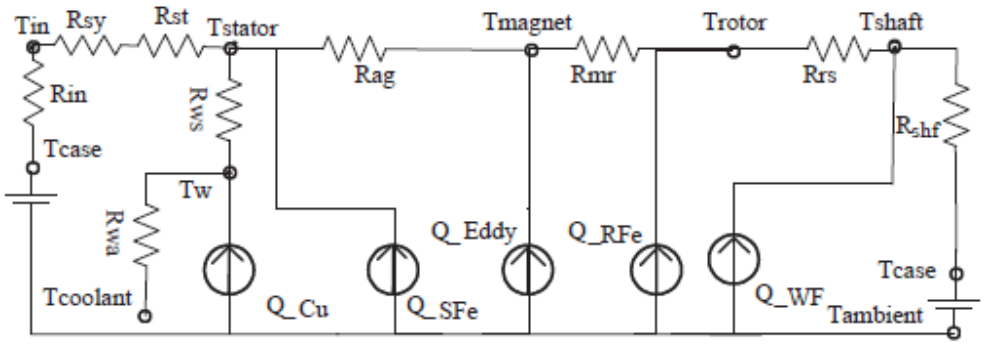

Figure 2.14 Equivalent 10-node thermal circuit for a SPMSM [40]

2.2.2 Computational Thermal Analysis Methods

In addition to thermal lumped models, FEA and CFD analysis are very demanding regarding model setup and computational time [4]. The principal strength of the computational methods is that any machine geometry can be modelled. CFD is usually used for the prediction of flow in complex regions. FEA is usually used for heat transfer by conduction in solid models [4].

One of the popular commercial software packages based on thermal lumped circuit analysis is Motor-CAD [41]. It is a fast solution for any machine with external natural convection, TEFC or liquid cooling etc. All conduction and convection thermal resistances are calculated by the software and then temperature variation around the machine is obtained. Many different housing types for natural convection or forced convection systems can be utilised in the software as shown in Figure 2.15 [41].

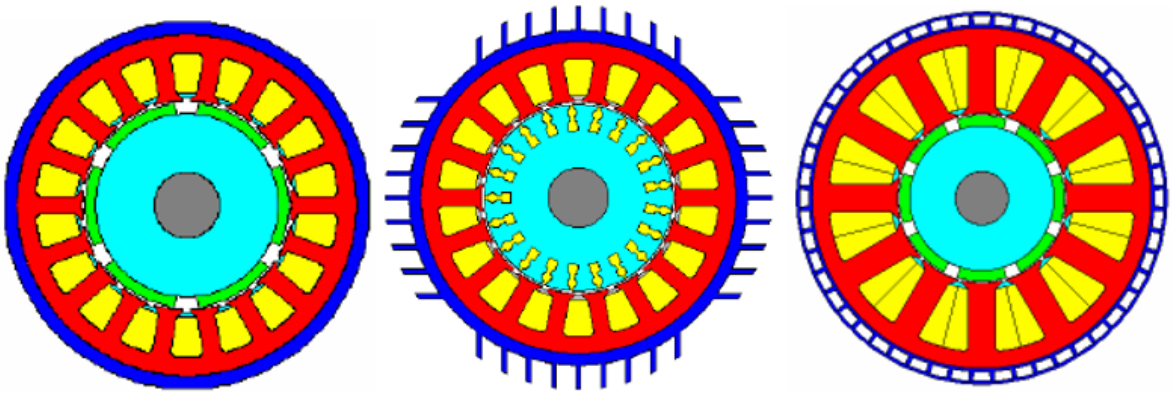

Figure 2.15 Examples of housing types: natural convection (left), forced convection (middle), water jacket (right) [41]

There are various roles of FEA thermal analysis of electric machines. Sensitivity analysis and model calibration can be done using commercial thermal FEA software such as ThermNet by Infolytica, Ansys Steady State or Transient Thermal, JMAG, Flux by Cedrat or Opera FEA. The principal role of FEA for thermal analysis is to model complex geometric shapes [4]. The heat transfer through machine windings is one of the complex thermal model and FEA analysis can be used to calculate equivalent thermal conductivity and then can be used in thermal equivalent circuits [42].

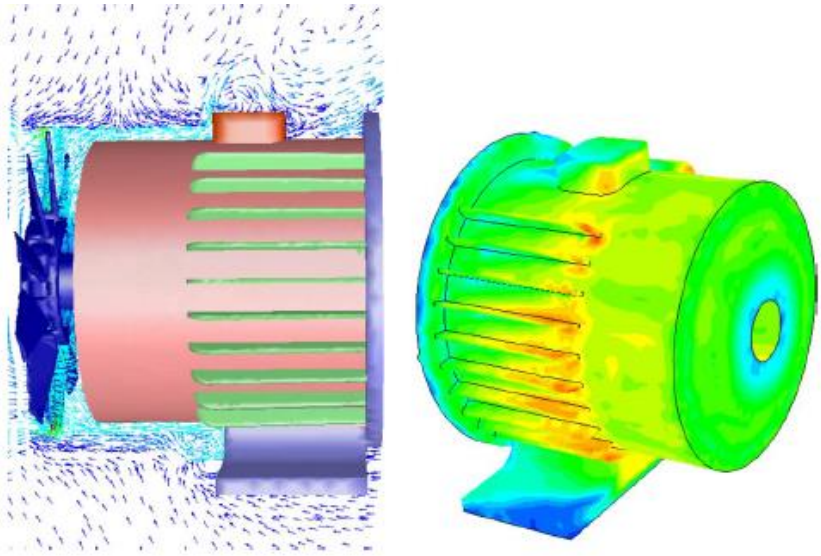

Figure 2.16 Fluid flow vectors around a TEFC machine (left), temperature distribution (right) [4]

With the recent development in computing, the proper understanding of fluid flow is attained using computational fluid dynamics instruments. The modern CFD codes are mostly based on finite volume technique solving Navier-Stokes equations [4]. CFD simulations require more in-depth knowledge in fundamental physics and the complexity of meshing process also needs advanced computational skills. In electrical machines, CFD is a tool for determining coolant flow rate, velocity and pressure distribution in the cooling passages, machine closed regions or around the machine [4]. Furthermore, it is essential for designing efficient fan cooling and water jackets in thermal design of electrical machines. An example to TEFC machine thermal design with fluid velocity vectors and resulting temperature variation is shown in Figure 2.16 [4].

2.2.3 Experimental Thermal Analysis Methods

Thermal analysis can also be conducted by solely experimental methods. They are based on temperature and heat flux measurements. The important thermal parameters such as convection heat transfer coefficients can be obtained by performing steady state thermal experiments. One of the most commonly used heat transfer measurement method is to use thin film heat flux sensor [43]. This sensor measures the temperature differences between two or several locations within a thermal insulation material with a known thickness and other thermal parameters to determine the local heat flux via Fourier's one dimensional law of conduction equation. This method was first reported by Martinelli et al [44]. The use of heat flux sensor in electrical machines thermal analysis is reported in [43, 45]. It is also illustrated in Figure 2.17 [46].

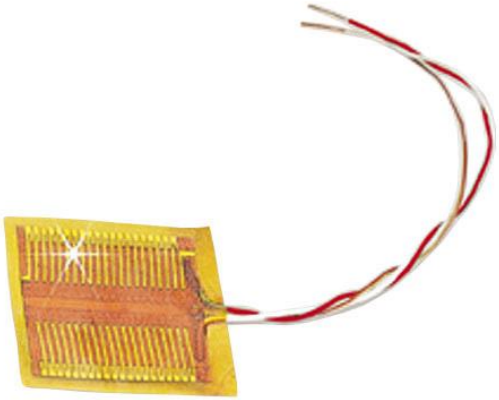

Figure 2.17 Thin film heat flux sensor [46]

The calibration of heat flux sensor is essential and disruption of geometric surface profile and thermal conditions with the presence of the sensor might lead to experimental error. Flanders reports that the overall error due to surface profile disruption is the order of 10 per cent [47]. Also, thermal boundary condition modifications could be required due to the presence of heat flux sensor. This was stated by Dunn et al [48]. Danielsson [49] reports that when the heat flux sensor is attached to a surface with low thermal conductivity, the effect of wind on the calibration is significantly reduced as the calibration process is strongly influenced by wind or moving fluid around the sensor.

Capacitance calorimeters are also used for measuring instantaneous heat transfer rate into a surface by measuring the rate of change in thermal energy of an element inside the solid surface [43]. A capacitance calorimeter consists of thermally insulated cylindrical slab manufactured from high thermal conductivity metals such as copper or aluminium etc. A thermocouple is attached to the bottom of the slab to measure heat flux into the sensor. In order to measure convective heat flow from a surface with known thermal properties, the capacitance calorimeter can be used and heat transfer coefficient is determined by equation (1.1).

$$\frac{T - T_\infty}{T_0 - T_\infty} = e^{\frac{t\,(hA)}{mc_p}} \tag{1.1}$$

where T_∞ = cylindrical slab temperature at steady state, K

T_0 = cylindrical slab temperature at initial state, K

t = time spent, s

A = surface area, m^2

m = mass of the slab, kg

C_p = specific heat capacity $J/(kg.K)$

h = heat transfer coefficient, W/m^2K

There is a standard method for operating the capacitance calorimeters and their design parameters and limitations are documented at ASTM E457-96 [50].

Experimental heat transfer coefficients can be also evaluated by measuring the one dimensional thermal pulse penetration [43]. In this transient method, only surface temperature data is required to evaluate the heat transfer coefficients. This form of heat flux measurement is common in short time duration hypersonic facilities and blow down turbomachinery experiments [51, 52]. In this method, the experimental convection heat transfer coefficients are determined by using the equation given in (1.2).

$$\frac{T_s(t) - T_{initial}}{T_{aw} - T_{initial}} = 1 - e^{\beta^2}.erfc(\beta) \quad (1.2)$$

where $\beta = \frac{h\sqrt{t}}{\sqrt{\rho c_p k}}$

T_s = surface temperature, K

T_{aw} = adiabatic wall temperature, K

ρ = density of the solid surface, kg/m^3

k = Thermal conductivity of the solid surface, $W/(mK)$

Nonetheless, it is not easy to determine wall surface heat transfer coefficient by equation (1.2), as the adiabatic wall temperatures, T_{aw}, in most thermal experiments are unknown. If adiabatic wall temperature is determined theoretically as proposed in [53], the heat transfer coefficients can be calculated by selecting correct combination of heat transfer coefficient and adiabatic wall temperature. In order to reduce error between recorded temperature history and theoretical temperature data, minimal root mean square regression method is introduced [53].

Alternatively, the use of the infrared camera to measure the surface temperature and to evaluate heat transfer coefficients on a surface of interest are introduced by Harmand et al. [54] and Mori [55]. The principal working principle of infrared camera is based on electromagnetic waves absorbed and emitted from materials continuously as their molecular energy levels rise or lower by heating or cooling the material. In other words, the infrared camera measures the intensity and wavelengths of emission from a surface to detect the surface temperatures [43]. One of the most important advantages of using the infrared camera is its capability to image global temperature distribution which is quite useful in electrical machines. If there is optical access

on the surface of interest, the infrared camera can be used to monitor temperature variation. However, surface emissivity values of the materials must be found out to obtain thermally accurate infrared images.

2.3 Stator Manufacturing Methods and Thermal Improvement Potentials

The electrical and thermal efficiency of permanent magnet machines have a strong relationship with the manufacturing process. Since energy losses directly affect machine thermal performance, it is convenient to investigate major loss components and how they are affected by the manufacturing process. It should be noted that thermal investigations are not only based on selection of appropriate cooling systems as a post-design process. The principal aim of the machine designers should be rather the reduction of energy losses and thermal management of the inevitable machine losses through in-depth investigation of heat removal in an efficient way. In this context, manufacturing methods have quite significant effects on machine overall electrical and thermal performance. Therefore, manufacturing methods are shown a particular importance in the literature.

2.3.1 Slot Fill Factor

Copper losses can be reduced by reducing the coil electrical resistance. To reduce coil resistance, the coil length should be minimized and the coil fill factor ($Total\ coil\ sectional\ area/Slot\ area$) should be improved [56]. Electrical machine designers aim for slot factors that are as large as possible to increase efficiency. The improvement of slot fill factor is both dependent on stator manufacturing method and winding configuration.

The selection of winding configuration has some consequences on the machine thermal performance as majority of internal heat generation inside electrical machines occurs in stator windings as a result of stator current which generates ac and dc ohmic losses. The heat removal from the machine windings is dependent on slot fill factor since heat removal by conduction would be more significant for densely packed conductors in a smaller stator slots volume. If better heat transfer is achieved for the stator windings, the outcome of this improvement for an electric machine is as follows:

- Thermal degradation of magnet wire insulation becomes slower and so lifetime of the electric machine would be longer. This results in enhanced machine reliability.
- Due to higher effective thermal conductivity of stator windings, more armature current could be injected into the stator windings without operating machine over temperature or over temperature time duration for critical applications with a particular duty cycle could be extended.

2.3.2 Fractional Slot Concentrated Windings

In general, the stator core manufacturing methods determine the suitable winding methods. Therefore, each stator manufacturing method might have corresponding winding methods [57]. The most commonly employed winding configurations for three phase radial flux PM machines are classified as follows [58]:

1) Overlapping configuration: Traditional distributed or concentrated
2) Non-overlapping configuration: Concentrated or alternate teeth wound

Non-overlapping winding configurations in PM machines are referred to as fractional slot concentrated winding (FSCW). FSCW is a winding type that the number of slots per pole per phase is fractional. If number of slots per pole per phase is one, it is traditionally called concentrated windings [59]. In distributed windings, number of slots per pole per phase is an integer number. It might be two or higher. The distributed winding configurations are either fully pitched – single layer (i.e one pole pitch is 180° electrical and pole pitch is equal to coil span) or short pitched – double layer (i.e pole pitch is greater than coil span).

In the literature, the opportunities and challenges of FSCW PM machines are greatly discussed [14, 20, 24, 58, 60-63]. Although FSCW configuration ensures many advantages over distributed windings, some concerns such as high MMF space harmonics, high rotor eddy current losses, unbalanced winding configurations, lower winding factors, unbalanced rotor pull-up forces, noise and vibration are still under investigation for the PM machines with FSCW windings. Some of those drawbacks could be mitigated by analytically proper selection of both pole-slot combination and magnet position on the rotor (i.e. surface or buried PMs) for certain applications.

FSCW started gaining more attention since FSCW PM machines achieve significantly higher copper slot fill factor when coupled with segmented structures [58]. This type of winding also provides high power density, high efficiency, short end turns, fault tolerance etc. [58]. The selection of segmental core structure with fractional slot concentrated windings reduces the demanded size of lamination sheets. Hereby, the waste of material and capability of the punching machine could be greatly reduced. According to [57], the best segmental case is with a single tooth as the waste factor is significantly reduced with the smaller angle of segments.

These opportunities of FSCW PM machines demonstrate that they could be more appropriate candidates as compared to the machines with traditional distributed windings, for high power density (W/kg) applications and also FSCW PM machines might have great potentials for further thermal improvement of electrical machines due to shorter end turns and better slot fill

factors. FSCW PM machines are paid more attention with regards to thermal aspects as their electrical and thermal performance could be enhanced significantly by recent manufacturing methods.

2.3.3 Stator Manufacturing Methods

The important thermal parameters of an electrical machine such as effective slot thermal conductivity, stator core thermal conductivity and thermal contact conductance between the stator segments are always dependent on manufacturing process. However, in many cases, improvements in stator manufacturing process require a trade-off in productivity and different manufacturing processes should be compared in terms of cost, mass production, practicality etc [56].

There are some innovative manufacturing methods which are still under investigation to increase slot fill factor and thereby machine electro-thermal performance. These include segmented core, spiral laminated core, joint lapped core and plugged in teeth manufacturing for stator of an electrical machine. It is useful to give a brief explanation of these manufacturing processes as a part of literature survey:

2.3.3.1 Joint Lapped Core

In this method, stator segments are connected using convex and concave joints. As the manufacturing technique is not conventional, it requires special tools. Nevertheless, it increases the slot fill factor significantly (75%). An illustration is provided in Figure 2.18.

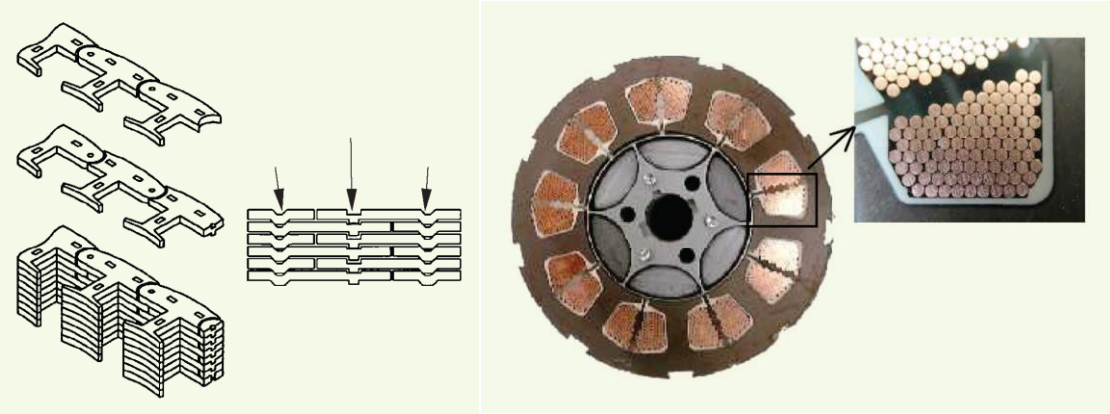

Figure 2.18 The proposed joint lapped core structure to achieve high fill factor by Akita et al. [56]

2.3.3.2 Segmented Core

In this method, stator iron is split into segments as shown in Figure 2.19 [64]. This is similar to conventional stator manufacturing. It reduces the wasted iron during the production by up to

60%. [65] Also, it can help improve the slot fill factor due to modular stator use. However, the segments need to be welded together that increases the cost and production time.

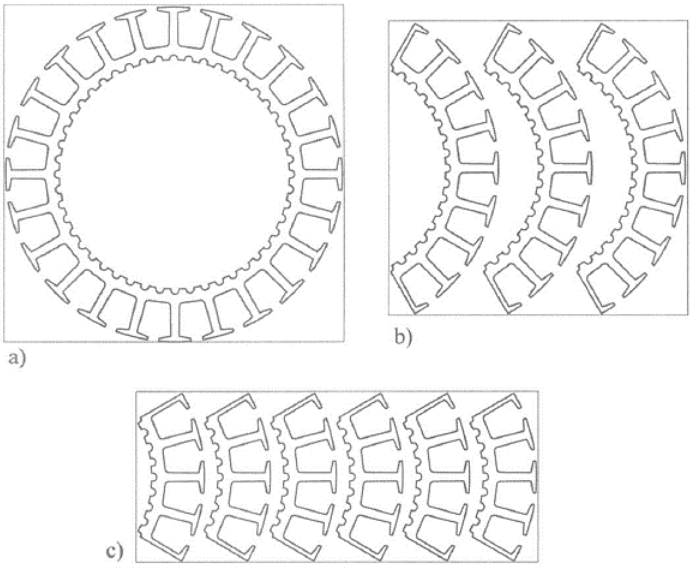

Figure 2.19 Stator laminations: a) entire section, b) 120° segments and c) 60° segments [64, 65]

2.3.3.3 Spiral Laminated Core

In this method, the core is manufactured from a long iron band which reduces amount of wasted iron up to 56%. However, thickness of the stator back is a limiting factor for this manufacturing method. This method requires special manufacturing tools and production machines. In Figure 2.20, spiral stator core is illustrated [64].

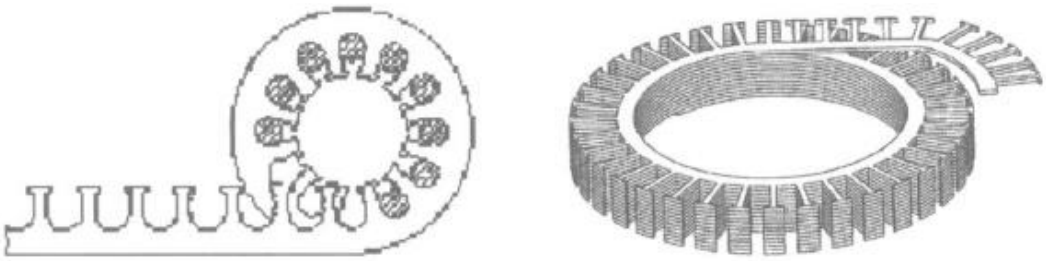

Figure 2.20 Spiral laminated cores from Mitsuhiro [66] (left), and inner stator from Lee [67] (right)

2.3.3.4 Plug-in-tooth Stator Core

Stator yoke and teeth are segmented in such a way that the wound stator teeth are then plugged in the laminated stator core back. This is not a conventional way of manufacturing for the stator of an electrical machine. This method aims to increase the slot fill factor up to 60-65% by possibly degrading the machine rigidity due to the segmented back iron. It is depicted in Figure 2.21 [58].

Figure 2.21 Stator structure with laminated plug-in tooth technique [58, 68]

2.3.3.5 Modular Stator Core with Segmental Teeth and Solid Back Iron

Jianxin et al [57] proposes a stator manufacturing method for high slot fill factor non-overlapping winding configurations. In this method, soft magnetic composites (SMCs) are utilised in the stator back iron and laminated teeth are assembled to the SMC iron core. This method is more cost effective and ensures easier assembly compared to fully laminated and segmented stator structures [57]. Although the use of SMCs increases iron losses (20 Watts in this case), slot fill factor is greatly improved due to pre-wound coils. The proposed segmentation is shown in Figure 2.22 [57].

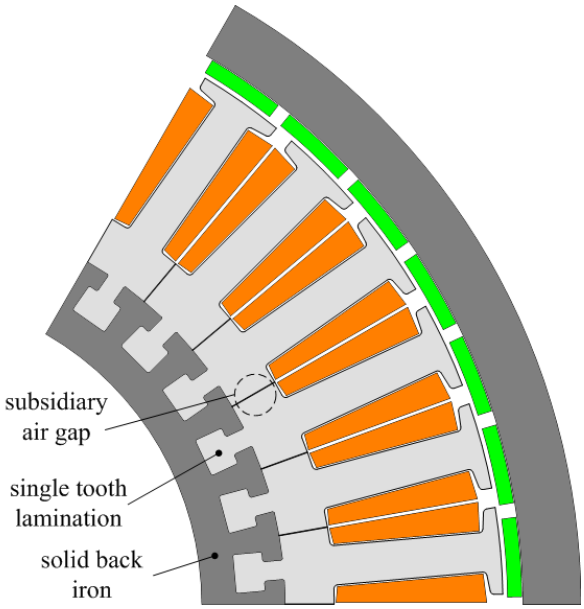

Figure 2.22 Jianxin's proposed single tooth segmentation method with the use of SMCs in the stator core back [57]

2.3.3.6 Casting Production of Stator Coils

According to Gröninger et al [69, 70], the coils can be produced by a casting process. In this method, a stator coil is formed by moulding copper or aluminium to achieve a bobbin. This allows to produce flat conductors with very high slot fill factor. This type of manufacturing offers significant advantages over conventional production methods in terms of performance, torque density and cost. The geometry of the casting production was displayed in Figure 2.23 [69, 70].

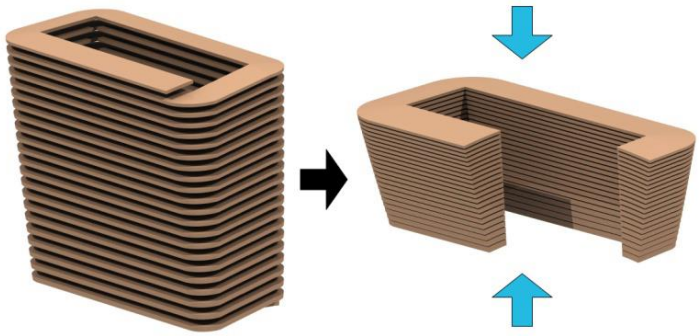

Figure 2.23 General coil geometry for casting production [70]

The flat alignment of the conductors increase the slot fill factor up to 90% [70]. This increases the power density of the machine significantly. However, this way of production changes the conventional machine manufacturing and requires special tools. In terms of thermal improvement, the measured thermal resistance from coil to lamination stack has been reduced by about 6 times when round wire and cast coils are compared [69].

2.3.3.7 Modular 3-phase Machines with Laminated Windings for HEVs

Andersson et al [71] proposes a machine designed with axially distributed single layer winding segments with a core that builds a modular three phase machine. The laminated winding benefits from implementing buried end windings. Due to higher slot fill factor (60%) in laminated windings, a higher thermal conductivity is achieved in the slot area. The thermal conductivity along the along the copper laminations can be increased up to 300 W/ mK which is slightly lower than bulk copper thermal conductivity [71]. When airflow is provided into the winding layers, the laminated windings work as heat sinks in the machine. The axially separated modular machine with laminated windings is illustrated in Figure 2.24 [71].

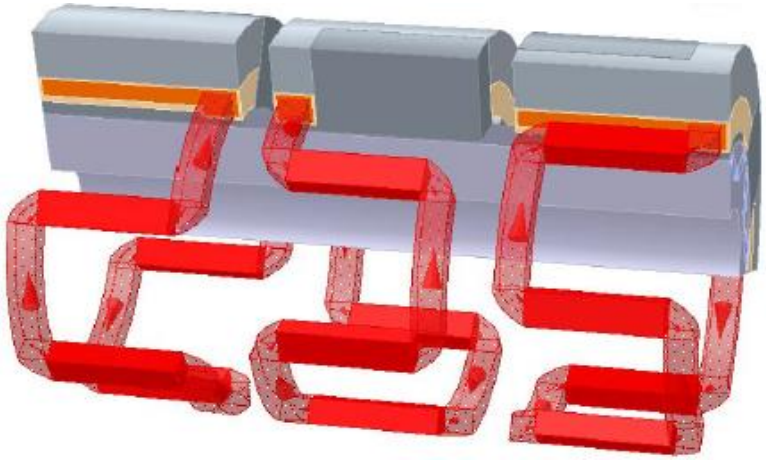

Figure 2.24 Axially separated 3-phase machine with laminated windings [71]

2.3.3.8 Electric Vehicle Traction Motor with Hairpin winding

Jung et al [72] applied hairpin winding to an electric vehicle traction motor to achieve high efficiency and power density. Hairpin windings decrease unnecessary spaces between windings. It comprises of square coils of the hairpin shape which are inserted into slots and end turns are welded together. It is reported that it reduces heat generated by coils due to lower current density and improves efficiency of the motor by reducing the copper loss [72]. Also, stator teeth width can be increased according to high space factor and iron loss, vibration and noise can be reduced [72]. It is also claimed that hairpin windings might have some advantages over toroidal windings such as increasing number of turns leading to improve the power density or to reduce the size of motor.

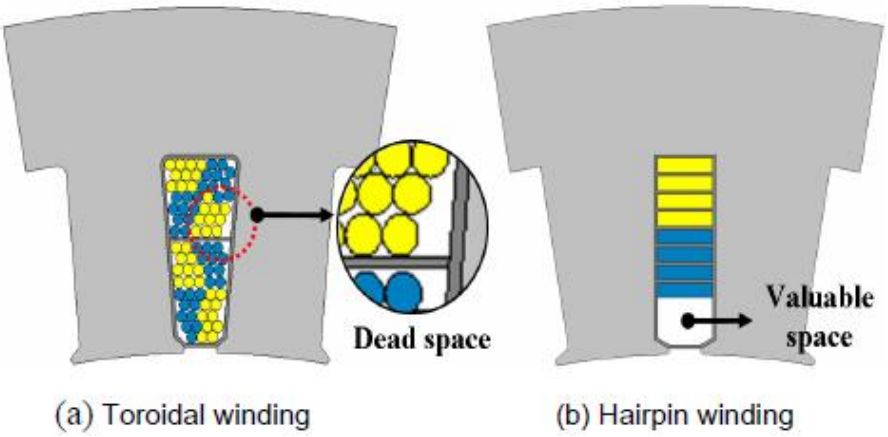

Figure 2.25 Toroidal winding vs. hairpin winding reported by Jung et al. [72]

An illustration for the comparison purpose is depicted in Figure 2.25 [72]. Similarly, the advantages of axially inserted rectangular coils on space fill factor and machine performance is also demonstrated in [73] for a golf cart. The developed motor achieved 120% greater power density per volume compared to a commercial machine with round wires [73]. The use of rectangular coils allows for reduction of slot opening further due to axially inserted coils as

opposed to round copper windings requiring a particular slot opening gap for automated or semi-automated winding systems.

The prominent previous studies on the stator manufacturing methods with different winding configurations have been reported above. Although the proposed design methods targets higher machine performance, it is convenient to express that some of the proposed manufacturing method is quite complex and far from mass production. Nevertheless, a number of previous research attain practical and cost effective design methodology with innovative approaches. In other words, the proposed stator and winding manufacturing methods have pros and cons because improvements in machine design usually require trade-off between productivity and boosted electro-thermal performance.

2.3.3.9 Stator Materials

According to Hayashi et al [74], the use of the high silicon steel is more practical at improving the efficiency opposed to use of increased slot fill factor. Hayashi et al claims that the use of high performance iron cores such as 10JNEX900 and Amorphous alloy in electric machines is much more influential than slot fill factor improvement as this was demonstrated on switched reluctance machines (SRMs) in their published work [74]. It is reported that about 5% fill factor improvement in slot fill factor increased the machine efficiency 1%. Nonetheless, the use of amorphous iron with a thickness of 0.025 mm improves the machine efficiency 5% [74]. Thus, it is claimed that the adaptation of high silicon steel is more practical solution for efficiency improvement. It should be noted that amorphous iron is quite expensive material compared to more common silicon electric steels.

2.3.3.10 Compression of Coils

Development of the powder metallurgy offers great advantages in the manufacturing of stator components. Soft magnetic composites (SMC) provide unique advantages like 3-dimensional flux paths. SMC consists of iron powder particles coated with insulated films. The iron particles are electrically insulated from each other, yet lower permeability can be considered as a problem in SMC materials. This reduces the saturation flux density of the machine. Even though SMC materials are considered as not effective as conventional laminated steel, some prototypes using SMC have showed superior performance than that of conventional laminated steels. According to Jack et al [75], high performance machines can be obtained using SMC to build a stator core. Furthermore, they achieved exceptionally high fill factor (78%) using pre-pressed windings with powdered iron stator core [75]. Figure 2.26 illustrates a cross-sectional view of a pre-pressed windings.

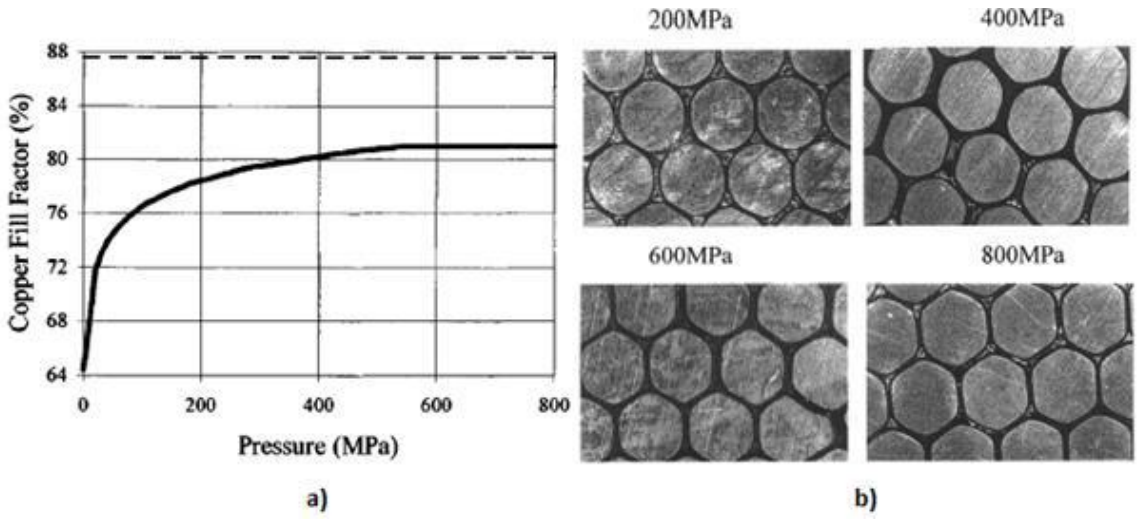

Figure 2.26 a) Variation of copper fill factor for varying applied pressures, b) Coil cross-sectional view at different pressures [75]

The opportunities of pre-pressed windings have been also investigated in [76-78]. Widmer et al proposes the use of aluminium windings for pre-pressed motor coils due to the fact that aluminium can provide a number of potential benefits such as lower mass density compared to copper, low cost, high thermal capacity which is important in overload conditions and improved recyclability. It is also reported that more than 75% fill factor can be achieved by pressing of the coils with aluminium windings.

Since the slot fill factor mainly affects phase resistance, conductor current density and slot heat density, it is an important design parameter from the machine performance point of view. Due to the significant increase in slot fill factors (up to 78%) in compressed coils, a number of advantages can be obtained regarding machine performance: number of turns for a phase winding might be increased; DC winding losses might be reduced if relatively thicker conductor diameters are chosen for the same slot area; winding slot area might be reduced due to densely packed conductors, allowing for increase in teeth width leading to iron loss reduction in stator.

A thermal performance comparison has been performed in [75] for pre-pressed copper windings coupled with segmented SMC stator. It is shown that the effective thermal resistance of the coil was improved by about 60%. (i.e. thermal resistance of: winding plus laminated core in commercial machine: 0.34 $°C/W$; pre-pressed winding plus SMC core is 0.2 $°C/W$.)

Although thermal conductivity of aluminium (230 $Wm^{-1}K^{-1}$) is lower than copper thermal conductivity (387 $Wm^{-1}K^{-1}$), Widmer et al achieved a significant improvement in slot thermal conductivity of 2.14 $Wm^{-1}K^{-1}$ in thermal tests of compressed aluminium conductors [78]. It has also been shown that for the same tests conditions (i.e. same rms phase current), the motor coil temperature for compressed aluminium gives 26% lower rise in temperature when

compared to random wound copper coils [79]. A compressed aluminium coil at 250 MPa is given in Figure 2.27 with the coil temperature variation.

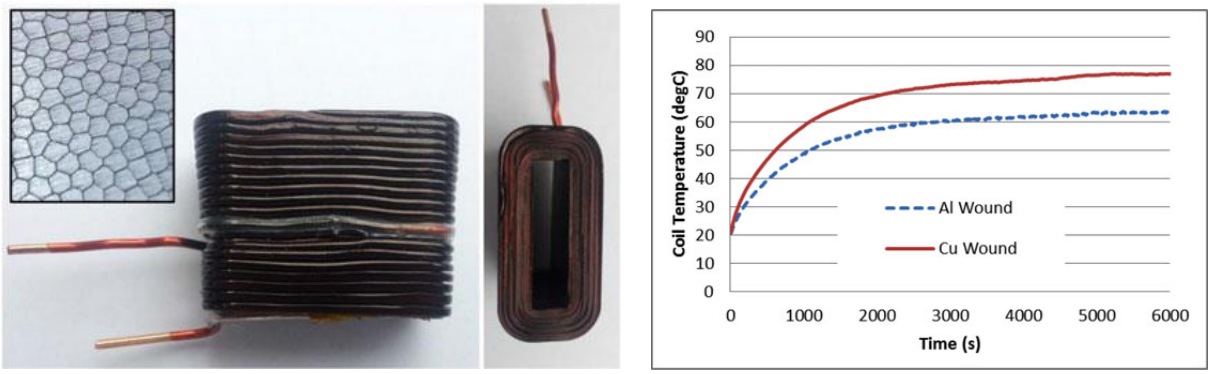

Figure 2.27 Compressed coil at 0.75 fill factor (left), temperature variation for Al wound and Cu wound windings (right) [79]

It is clear that there are many advantages to using compressed windings as electrical and thermal performance of the PM machines can be significantly improved. Nonetheless, in terms of reliability of electrical windings, the authors [75, 76, 78] have not reached a certain conclusion as deformation of magnet wire enamels is likely during the compression of coils at high pressures varying between 200 MPa and 800 MPa. In other words, coil pressing process needs to be monitored regarding deterioration of wire insulation.

2.4 Literature Survey Conclusions

The thermal aspects of PM electrical machines have been thoroughly investigated in the literature survey. Some important points should be extracted from this deep thermal design, analysis and measurement techniques proposed in the literature so as to demonstrate the significance of this research regarding thermal improvements of PM electrical machine coupled with recent manufacturing methods. Therefore, the outcome of literature survey is summarised as follows:

- Mechanical and thermal aspects of PM electrical machines are paid less attention compared to electromagnetic aspects.
- Due to increasing kW/kg of electric machines, high power density electric machines are only possible with enhanced cooling systems.
- Power loss analysis is a key to perform accurate thermal design of permanent magnet machines. Multi-physics optimization and machine-specific loss analysis are two important themes of recent machine design publications. In ‘multi-physics optimization’ process, more general electrical, mechanical and thermal aspects are combined to design optimum PM machines for different applications. However, in

'design for application' process detailed energy loss analysis are conduced to be able to perform more accurate electrical and thermal modelling afterwards.

- Thermal aspects of electrical machines are divided into two themes: cooling methods (i.e. TEFC, liquid, direct, spray cooling etc.) and thermal analysis methods (i.e. thermal FEA, CFD, lumped thermal model and experimental measurement techniques etc.). In other words, the majority of thermal investigations are either concentrated on novel cooling 'methods' resulting thermal improvement of electric machines, or accurate thermal 'analysis' of electrical machines with the proposed analytical, computational and experimental techniques.
- Recent manufacturing methods have been also investigated in detail as they might have potentials to enhance thermal characteristics of PM electric machines by changing or modifying conventional stator and/or winding manufacture methods for PM electrical machines.
- It has also been described that all proposed thermal improvement methods come with some drawbacks such as complicated manufacturing issues, more weight in the overall drive system and higher costs etc. Therefore, some cooling methods are solely exclusive to machines for certain purposes. It is not easy to compare many different cooling techniques in terms of thermal performance since some of them could be more appropriate than others in different application fields including domestic, traction, aerospace and military etc.

2.5 Outline of the Thesis regarding Literature Survey

There are a number of manufacturing methods such as the machines with laminated windings, plug-in-tooth, pressed coils etc., having a potential for thermal improvement of PM electrical machines in the literature. Among these proposed methods, pre-pressed windings at very high slot fill factors (about 75%) can benefit from high thermal conductivity due to reduction of air between compressed coil strands. The coil pressing method does not change conventional manufacturing methods which is an advantage for machine designers and it only adds a further stage to get the coils ready for PM electrical machines.

The coil pressing method can be applied any segmented stator electric machines with single tooth winding configuration. Joule losses of stator windings can be decreased with compressed windings. This in turn increases efficiency merits of electrical machines. Also, the heat generated inside compressed windings might be easily removed from the coils. This improves thermal performance of the machines.

The previous research [75, 76, 78, 79] on coil pressing demonstrated many advantages of coil pressing in electrical machines. However, electrical and mechanical coil integrities are still not clear due to high pressures applied during the compression. This might cause further questions on machine reliability as deformation of insulation is likely during compression of coils.

The first part of this research will therefore focus on mechanical and electrical integrities of compressed coils and maximum achievable fill factors for different conductor diameters. After that, the electrical and thermal advantages of coil pressing on an Integrated Starter Generator (ISG) machine will be thoroughly investigated and the important thermal parameters of compressed windings will be determined.

In the second part of the research, another thermal improvement technique that is high thermal conductivity thermal paste potting into machine end region will be investigated thoroughly. A permanent magnet alternator (PMA) for aerospace application will be used to investigate the effect of thermal paste on heat flow through the machine.

Finally, a set of accelerated life tests when the accelerating variable is temperature will be conducted to determine the thermal endurance (i.e. durability) of the on-tooth compressed windings.

The pros and cons of the proposed methods in terms of thermal aspects of electrical machines will be discussed in detail and a set of results from the research will be presented.

Chapter 3. Structural Analysis of Coil Pressing

3.1 Introduction and Objectives

In this chapter, mechanical stress analysis of the compressed coils has been investigated by performing structural FEA simulations. A thorough description of quasi static structural modelling has been introduced as it is required to understand the response of complex geometries such as electric bobbins under dynamic loads. Although pressing coils at high pressures increases slot fill factor dramatically, the conductor wire deformation during this process is still unclear. The finite element method has been used to achieve the closest prediction of the deformation process using a number of techniques, such as mass scaling, loading rate determination, prevention of contact penetration and mesh optimisation etc.

The main objective of coil pressing simulations is to inspect if there is material fracture in magnet wire insulation which would lead to a turn to turn short circuit in the stator windings, known as a fault condition. Equivalent von-Mises stress results and equivalent plastic strain results in the magnet wire insulation of thermoset based polymers have been investigated by solving quasi-static non-linear coil pressing simulations.

3.2 Modern Magnet Wires

Magnet wire or enamelled wire is a copper or aluminium wire which is coated with a very thin layer of insulation. There are many application fields of magnet wire including transformers, inductors, motors, electromagnets and so on. The insulation on the magnet wire ensures separate individual turns with only one conduction path. Magnet wire insulation is major source of the heat accumulation in electrical machines. In a given electrical machine, it is therefore the hottest temperature spot occurs inside the winding due to I^2R losses. As standard magnet wire is available in three different types of materials, general material properties are shown in Table 3.1 [80].

Table 3.1 Magnet wires with different types of materials

Magnet Wire Material Properties						
Material	*Symbol*	*Density* $g/cm3$	*Resistivity* $\mu\Omega/cm$	*Weight Factor*	*Resistance Factor*	*Temperature Coefficient*
Copper	Cu	8.89	1.72	1	1	0.00393
Silver	Ag	10.49	1.59	1.18	0.95	0.00380
Aluminium	Al	2.703	2.83	0.3	1.64	0.00410

Modern magnet wires use one to four layers of polymer film insulations to withstand the applied voltage and generated heat in current carrying conductors. Film insulation thickness usually varies from 0.05 to about 0.1 mm [81]. Although the most common magnet wire for random-wound electric machines is a round copper wire insulated with polyimide-imide insulation, there are many different types of polymer based magnet wire insulations as given below [82]:

- Poly-vinyl-formal Enamels
- Polyurethane Enamels
- Polyester-imide Solderable Enamels
- Polyester-imide Enamels
- Polyester Enamels
- Polyamide-imide Enamels
- Polyimide Enamels
- Nylon Enamels
- Bondable Enamel

Magnet wires are classified by diameter, insulation class (grades) and temperature class. AWG (American Wire Gauge) is a standardised wire gauge system that increasing gauges number symbolise decreasing wire diameters when magnet wires are classified by their diameter. It varies between 0 to 40 AWG. Magnet wires are also classified by their temperature class from 105°C to 220°C. Since the insulation films are the most sensitive to thermal overloads, the selection of the insulation film is critical for long service life. If magnet wires are subjected to higher temperature overloads, life expectancy will be greatly reduced. Therefore, the design engineer should consider environmental conditions and overall temperature increase for an electrical machine. In Table 3.2, temperature class of magnet wires with different insulation types is tabulated [80]. Temperature class usually indicates the temperature of the magnet wire at which it has a 20,000 hour service life.

Table 3.2 Temperature class of magnet wires

Magnet Wire Temperature Class		
Temperature Class	**Insulation Type**	**Dielectric Constant**
105°C	Polyurethane*	6.20
105°C	Formvar	3.71

130°C	Polyurethane-Nylon*	6.20
155°C	Polyurethane-155	6.20
180°C	Polyester Solderable*	3.95
200°C	Polyester-amid-imide	4.55
220°C	Polyimide	3.90

*Solderable insulations

In addition to diameter and temperature classifications, magnet wires can be also classified by breakdown voltages. A magnet wire could be a type of Grade 1, Grade 2 or Grade 3. Thicker insulation means higher grade thereby higher breakdown voltage. Higher ambient temperatures might lead to a reduction in insulation breakdown voltage.

3.3 Thermosetting Polymers

A polymer can be defined as a large molecule composed of repeated sub-units. Polymers range from common synthetic plastics including nylon, rubber, resins etc. to some biomolecules. The classification scheme could be fulfilled according to behaviour of polymers with rising temperature. In this context, polymers can be studied under two titles: thermoplastic and thermosetting polymers. If a polymer becomes permanently hard and does not soften upon heating, which is called irreversibly cured, it is called a thermosetting polymer [83].

Each type of thermosetting material has a unique set of mechanical properties including elasticity, ductility, brittleness etc. Since magnet wire enamels are thermosetting polymers, it is convenient to describe mechanical properties of thermosetting polymers which in fact explain macroscopic behaviour of the thermosets.

3.3.1 Material Behaviour of Thermosetting Polymers

A material is elastic if its deformation is constant and instantaneous upon applied force and recovers it original shape upon removal of the force applied. The elastic behaviour of materials can be explained using the relationship:

$$\sigma = E\epsilon \tag{3.1}$$

where $\sigma = Force/area$, $\epsilon = \Delta l/l_0$ denotes stress and strain of the material respectively. This equation is known as Hooke's law and E is the modulus of elasticity or Young's modulus ($N/mm^2 = MPa$), a material dependent property equals to the slope of the stress-strain curve. The solid materials which exhibit such behaviour are called linear. Almost all materials exhibit linear behaviour to some degree. Metals, ceramics, polymers at sufficiently low stress values

act as linear materials. Typical stress-strain curve of a ductile material is given in Figure 3.1 [84].

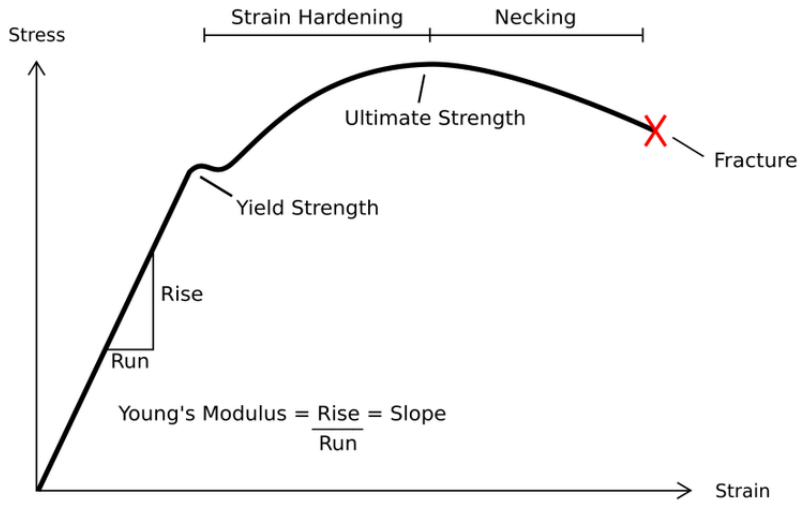

Figure 3.1 Typical stress- strain curve for metals [84]

The yield strength is an indication at which elastic deformation ends and plastic deformation begins. Moreover, the tensile strength is the maximum point of stress-strain curve that demonstrates the maximum tensile stress which might be sustained by a material specimen [85]. A certain amount of plastic deformation due to increasing strain rate causes material failure which is known as a material fracture.

The modulus of elasticity of polymers is highly relevant in their applications and dependent on temperature. With the increasing temperature, values of elastic modulus, tensile strength and yield strength decrease, whereas ductility of the material decreases [85]. For the certain types of applications, material properties of the polymers are very important because they determine the mechanical behaviour of the material under certain load conditions. In order to understand to what extend polymers are stiff, Figure 3.2 is illustrated [86]. It can be noted that modulus of elasticity of polymers can be maximum about 10 GPa. This shows that polymers are relatively not stiff and could be considered as more flexible materials compared to metals and alloys. For this reason, flexibility and stiffness of components composed of both metals and polymers are dominated by the weaker one which is polymers in this case. Therefore, the strength of magnet wires are dependent upon polymer based wire coatings.

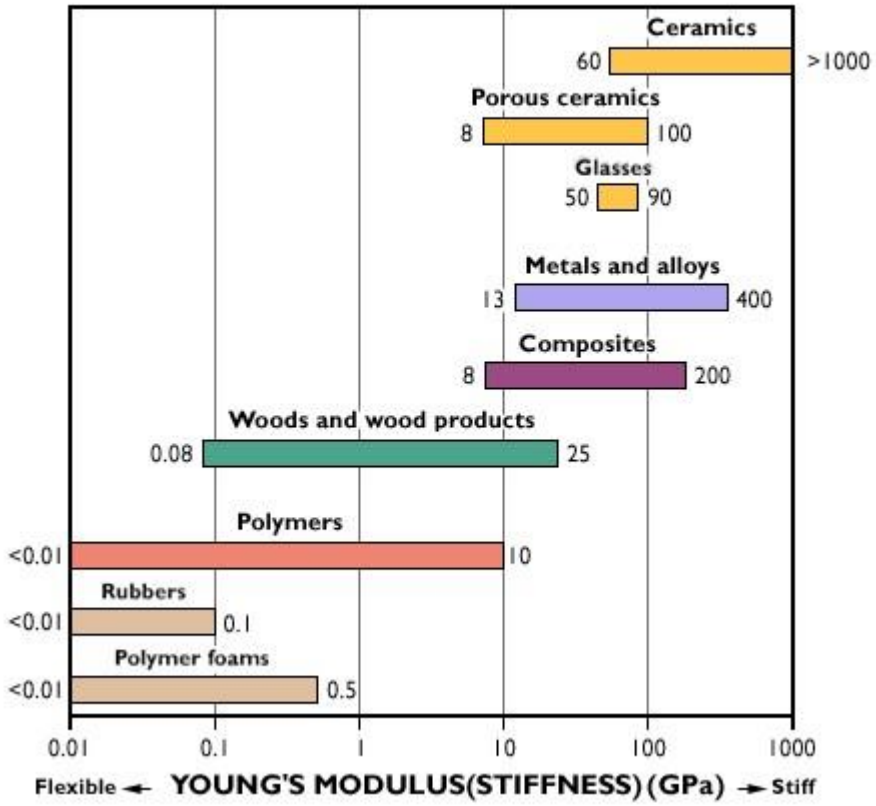

Figure 3.2 Modulus of elasticity of materials [86]

3.4 Structural FEA Analysis of Coil Pressing

During the compression of coils, a high pressure is applied to the coils carefully without forming any macroscopic material failure. Since tensile modulus of thermosetting polymers such as polyester-imide or polyimide, is lower compared to metals such as copper, aluminium etc., deformation after a certain pressure value is likely. Therefore, deformation mechanisms of the magnet wires will be investigated using computational methods.

3.4.1 Explicit Dynamics (FEA) Simulations

Finite Element Analysis (FEA) involves building a complicated geometry with simple blocks, or dividing a complicated geometry into smaller pieces. FEA can be applied to many engineering problems to solve the mathematical model of complicated physical phenomenon including stress analysis of machines, dynamic responses of trains, airplanes under different mechanical, thermal or electromagnetic loading [87]. These applications can also be extended to material science, biomedical engineering or geophysics and many other modern engineering fields emerging in recent years. A general procedure of a finite element method to solve complex models is as follows:

- Divide the geometry into elements to create a mesh consisting of nodes
- Describe the physical quantities of each element

- Assemble the elements to form a mathematical system equation for the entire model
- Apply external loads (force, velocity, pressure, displacement etc.) and define boundary conditions
- Solve the system equations and calculate unknown quantities (stress, strain etc.) at the nodes

If the relationship between the response of a structure and the load applied is linear, the structure is linear and the simulation is also called linear simulation [88]. Otherwise, the simulation is a nonlinear simulation. In real world, all structures exhibit nonlinearity in some degree. However, if nonlinearities are negligible and they do not affect the response of a structure, nonlinear simulations are not needed. However, pressing coils by applying high pressure and deforming the structure permanently cannot be considered as a linear simulation. There are many sources of nonlinearity in FEA simulations. These might be large deformation due to applied loads, change of connectivity between the separate bodies and stress-strain behaviour of the material presented in simulations.

Usually nonlinear simulations are much more challenging in comparison to linear simulations in terms of computing time and accuracy of system response for different load conditions applied to the system. Therefore, solution parameters (i.e. FE analysis settings and boundary conditions) are crucial to obtain a simulation result similar to real world phenomena occurring due to complex physical interactions of materials under different load conditions.

Due to the fact that large deformation occurs in compression of bobbins by applying high pressures, it is clear that coil pressing simulations are highly nonlinear. In addition to geometry nonlinearity, material nonlinearity exists because of stress-strain relation. In other words, FEA coil pressing simulations will be non-linear due to geometry and material non-linearity.

Topology nonlinearity in FEA simulations is because stiffness matrix changes due to changes of contact status of the different bodies [88]. Contact nonlinearity itself is challenging and it is usually accompanied by large deformation. Due to existence of contact faces between individual copper conductors in a winding, deformation due to non-linear contact is likely in FEA modelling of the coil pressing.

In order to solve a highly non-linear engineering problem, special types of FEA packages could be utilised. Explicit Dynamics analysis system which is available in Ansys CAE package is the most appropriate choice for coil pressing simulations in comparison to transient structural simulation tools.

If an engineering problem is dynamic rather than static, transient dynamic simulation packages will be preferred using FEA tools. Transient dynamic simulations usually require extremely small time steps to converge an accurate solution. [88] There are two types of time integration methods: implicit and explicit methods. Since explicit methods are very efficient for each time step, it will allow calculation of very large number of time steps within the duration of simulation time. Although explicit methods are appropriate in order to obtain very accurate simulation results, it is not suitable for long duration engineering problems [88]. As an example, if the dynamic response of a system takes a few seconds rather than a few milliseconds, then many millions of time steps will be required so as to observe the complete dynamic behaviour of the system. This type of FEA analysis might be required for certain physical problems. In these situations, high performance computing facilities such as parallel computing could be utilised to make the total simulation run time acceptable.

As transient structural simulations often fail due to convergence issues for long duration simulations such as quasi static compression or high speed impact problems, the integration time should be small enough to obtain accurate results. The main difference between implicit and explicit simulations is that explicit methods do not require iterations within a time step. This was described using the following difference equations:

$$D'_{n+\frac{1}{2}} = D'_{n-\frac{1}{2}} + D''_n \Delta t \tag{3.2}$$

$$D_{n+1} = D_n + D'_{n+\frac{1}{2}} \Delta t \tag{3.3}$$

where D_n , D'_n and D''_n are displacement, velocity and nodal acceleration, respectively. $D'_{n+\frac{1}{2}}$ and D_{n+1} requires historical information only. This means that no iteration required for each cycle. Since D_n and D'_n values are known for the last cycle, strain and strain rate can be calculated. As an example, for a 2D 4-node quadrilateral element, nodal displacement vector will have 8 components as shown in equation (3.4).

$$\{d\} = \{d_1 \ d_2 \ d_3 \ d_4 \ d_5 \ d_6 \ d_7 \ d_8\} \tag{3.4}$$

Using a shape function $[N]$, displacement field $\{u\}$ can be written in the form:

$$\{u\} = [N]\{d\} \tag{3.5}$$

For small deformation, relation between displacement and strain can be written as

$$\epsilon_X = \frac{\partial u_X}{\partial X}, \quad \epsilon_Y = \frac{\partial u_Y}{\partial Y}, \ \epsilon_Z = \frac{\partial u_Z}{\partial Z} \tag{3.6}$$

where ϵ_X, ϵ_Y and ϵ_Z are strain rates for x, y and z- axis respectively. Using the relations such as equations (3.2) and (3.3), nodal strain rate and strain value will be updated for each explicit cycle. For the calculations of stress, volumetric information is needed. The volume change at each element will allow us to update mass density. Using the relation between stress and strain given in equations (3.7 – 3.9), stress is integrated over the elements and external loads are added to the calculations in order to form nodal forces [88].

$$\epsilon_X = \frac{\sigma_X}{E} - v\frac{\sigma_Y}{E} - v\frac{\sigma_Z}{E}$$
$$\epsilon_Y = \frac{\sigma_Y}{E} - v\frac{\sigma_Z}{E} - v\frac{\sigma_X}{E} \qquad (3.7) – (3.9)$$
$$\epsilon_Z = \frac{\sigma_Z}{E} - v\frac{\sigma_X}{E} - v\frac{\sigma_Y}{E}$$

where E is Young's modulus and v is Poisson's ratio. After obtaining all required parameters, nodal acceleration which is denoted as D''_n is calculated for each cycle using the formula given in equation (3.10).

$$D''_n = \frac{F_n}{m} + \frac{b}{\rho} \qquad (3.10)$$

where b is the body force, m is nodal mass and ρ is the mass density. In each cycle D_n , D'_n and D''_n are calculated and updated on order to obtain the response of a problem using explicit methods. Solution algorithm for explicit dynamics is schematically illustrated in Figure 3.3 as shown below.

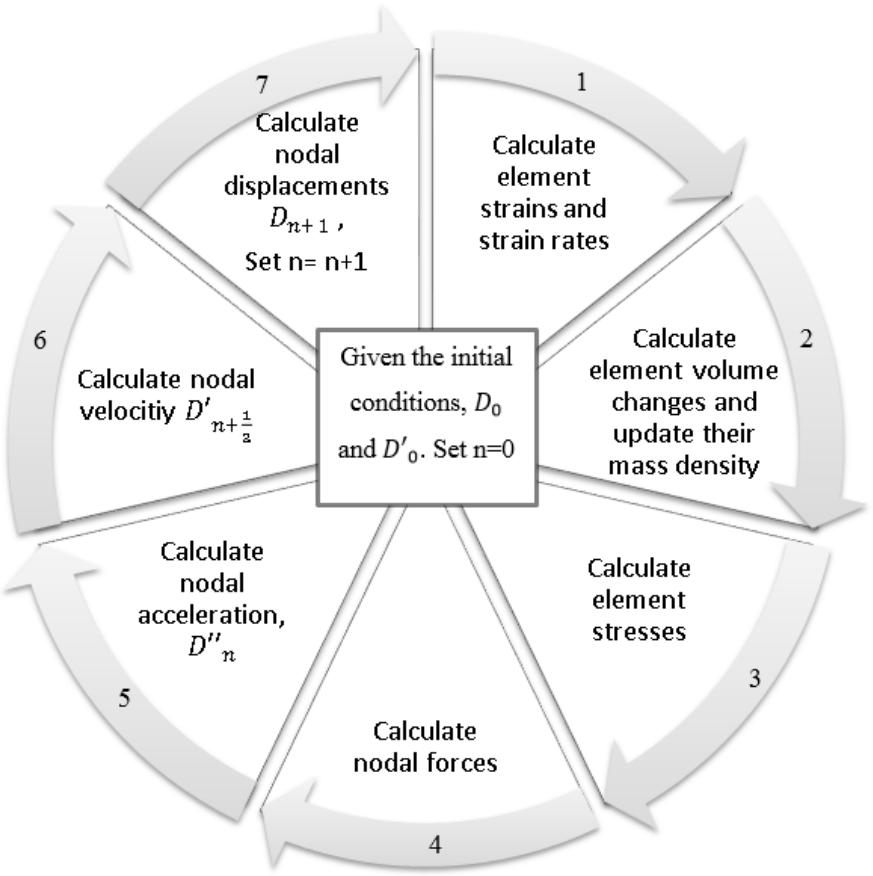

Figure 3.3 Solution algorithm for explicit FEA methods

Explicit methods are usually suitable for high speed collision tests and blast problems due to very small time durations. For low speed problems, explicit dynamics are not very useful due to enormous simulation duration. Nevertheless, explicit method is still useful for low speed or quasi static problems due to more accurate results while high deformation is the case for the simulation geometry. As compression of coils is considered to be quasi static low speed phenomena in real life, explicit methods will result in better accuracy in terms of nodal stress-strain calculations. A typical time integration time step is about 1 nanosecond to 1 microsecond for explicit dynamics simulations. Simulation end time that is dependent on duration of problem and in reality is usually about 1 millisecond to 1 second. If the physical problem occurs over more than one second in real life, explicit methods are not appropriate choice to solve a problem due to extremely long computer CPU time. Since the main objective of coil compression simulations is to inspect wire enamel integrity during the pressing operation, explicit dynamics FEA with quasi static solvers is an appropriate choice to obtain sufficiently accurate deformation results.

3.5 Quasi- Static Explicit Dynamic Analysis of Coil Pressing

If a non-linear problem involves very complex contact conditions and very large deformations, quasi static simulations are applicable using particular finite element methods. Quasi static

simulations are usually suitable for metal forming applications such as drawing, strain hardening, rolling etc. Coil pressing operation could be considered in this class of problems due to complex contact conditions and large deformations. As explicit methods are originally developed for high speed impact events such as collision tests, application of explicit dynamics methods to quasi static events requires special consideration. There is an important factor that should be considered when low speed problems are analysed using explicit solvers [89]:

- As natural time period of a quasi-static problem is relatively too long compared to high speed impact problems, quasi-static problems with long time duration are usually impractical to model. Millions of time increments would be required.

In order to solve this problem, there are some methods which might be applied during the solution setup of quasi-static explicit dynamics solvers. These are summarised as described below [89]:

1. Artificially increasing the speed of the process in the simulation is often required to obtain an economical solution.
2. Artificially reducing the time scale of the process by increasing loading rate. The disadvantage is that it will cause higher strain rates during the calculation of nodal stress and strain.
3. Artificially increasing the material density by a factor of $f2$, increases the stable time increment by a factor of f. This allows us to reduce CPU execution time of an explicit simulation.

Increasing the loading rate and increasing the material density, which is also called mass scaling, have similar effects on the quasi-static simulations. They aim to reduce total simulation end time. These are very important for simulation setup parameters that significantly affect the results (i.e. shape and equivalent stress/strain values of a simulation). The important question here is how much loading rates or material density can be increased without changing the response of a problem. For this reason, artificial modifications in the simulation setup should be investigated in detail in order to understand effects of these methods in quasi-static non-linear coil pressing simulations.

3.5.1 Loading Rates

All structures undergo several modes of vibration. The dominant response of a quasi-static analysis will be the first structural model. Any complex mechanical structure can vibrate in many different ways. Fundamental period or first mode of vibration is important in order to

choose reasonable loading rate for the analysis of a quasi-static coil pressing simulation. As mode of vibration is required to estimate the impact velocity, a simple structure with first, second and third mode of vibration is illustrated in Figure 3.4 [90].

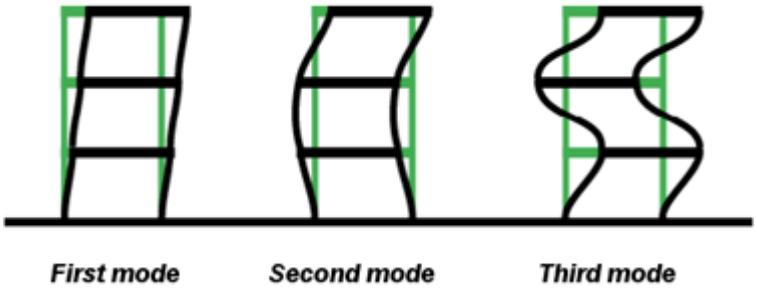

Figure 3.4 A mechanical structure at different vibration modes [90]

As the natural frequency of a first mode vibration is required to choose a loading rate, corresponding time period for first natural frequency should be estimated. Angular natural frequency, ω of a first order degree of freedom (DOF) model can be written as:

$$\omega = \sqrt{\frac{k_s}{m}} \tag{3.11}$$

In the equation (3.11), the natural frequency of a structure is proportional to the square root of the stiffness of the structure and inversely proportional to the square root of the total mass of the body. First natural frequency of the model can be estimated using modal vibration analysis FEA software tools for complex mechanical structures. From the point of view of coil pressing simulations, obtaining a natural frequency for a piece of stator winding would be very difficult to estimate due to physical structure of a stator coil.

If the global deflection or total displacement is estimated in the direction of impact, then impact velocity can be calculated by using the formula given in equation (3.12):

$$Velocity = [Global\ Deflection] \times [Time\ period\ of\ first\ natural\ frequency\ of\ a\ model] \tag{3.12}$$

The principal aim to calculate impact velocity here is to limit the impact velocity to 1% of the wave speed of the material. Typically, wave speed in metals is 5000 m/ sec [89]. Since the wave speed for an electrical bobbin is not known, a method has been suggested in [89]. This is given in the following order:

- A series of simulations can be run in the order from fastest load rate to the slowest. As load rate decreases, analysis time will be greater. This in turn increases the solution accuracy.

- After conducting a series of simulations, results such as deformed shapes, stress, strain values are examined to have an understanding for the effects of varying loading rates.
- Excessive speeds will result in unrealistic mesh deformation with localized stress and strain rates.
- In quasi static simulations, if excessive loading is used, a steep initial slope in the load versus displacement curve might occur. This means that response of a simulation during the solution process should be examined. As explicit dynamics simulations generate time dependent simulation results such as equivalent von-Mises Stress versus time or equivalent plastic strain versus time, sudden changes in these plots should be observed to have an idea about solution accuracy.

In order to understand the effect of loading rate, a bulk forming process has been shown in [89]. The aim there is to investigate the accuracy of a deformed shape with respect to speed of the process.

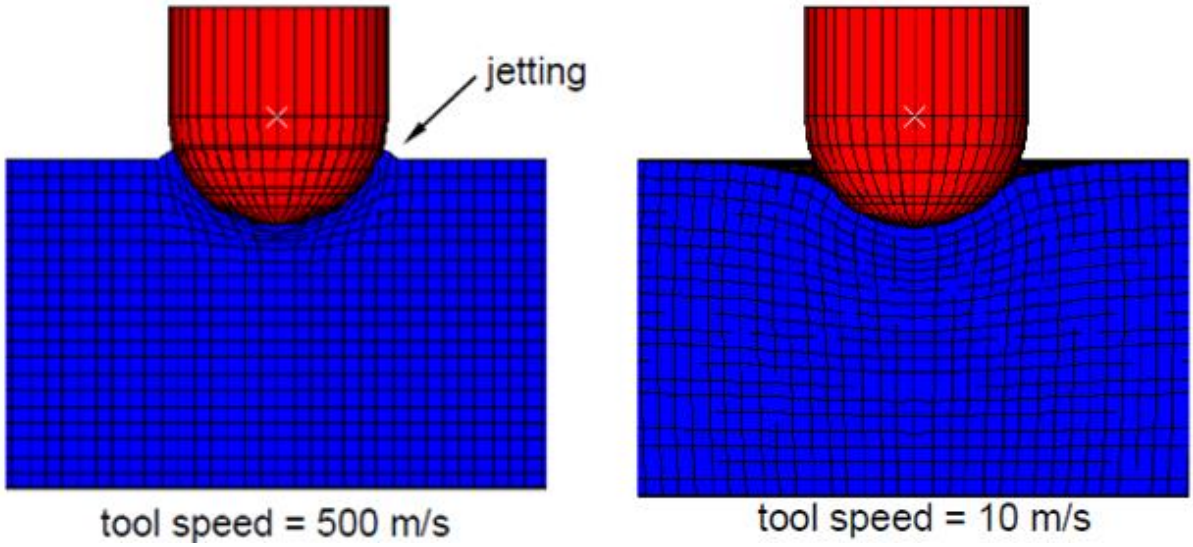

Figure 3.5 Effect of loading rate on the material deformation [89]

As seen in Figure 3.5, 180° axisymmetric model of a bulk forming process has been illustrated. When the tool speed is very high, highly localized deformation occurs during the high speed impact. This impact is called jetting as shown in the left picture above. In order not to obtain inaccurate localized mesh deformation during the process, the loading speed must be chosen correctly. As the nature of coil pressing simulations is quite close the bulk forming process, this type of inaccurate simulation response might be encountered for very large loading rates. In order to demonstrate this process, a coil pressing simulation with very large loading rates was investigated.

3.5.1.1 Case Study: Loading Rate in Coil Pressing Modelling

Figure 3.6 shows a 3D cross-section of copper magnet wires. In order to compress the model with a pressure boundary condition, a ramp function reaching 270 MPa in 0.1 milliseconds was applied to the model to see the effect of very high loading over a short time. During this coil pressing simulation, no plastic region has been enforced to see only elastic deformation in the simulation geometry. Material data for polyimide based copper magnet wire is provided, including Young's modulus, Poisson's ratio and isotropic material density.

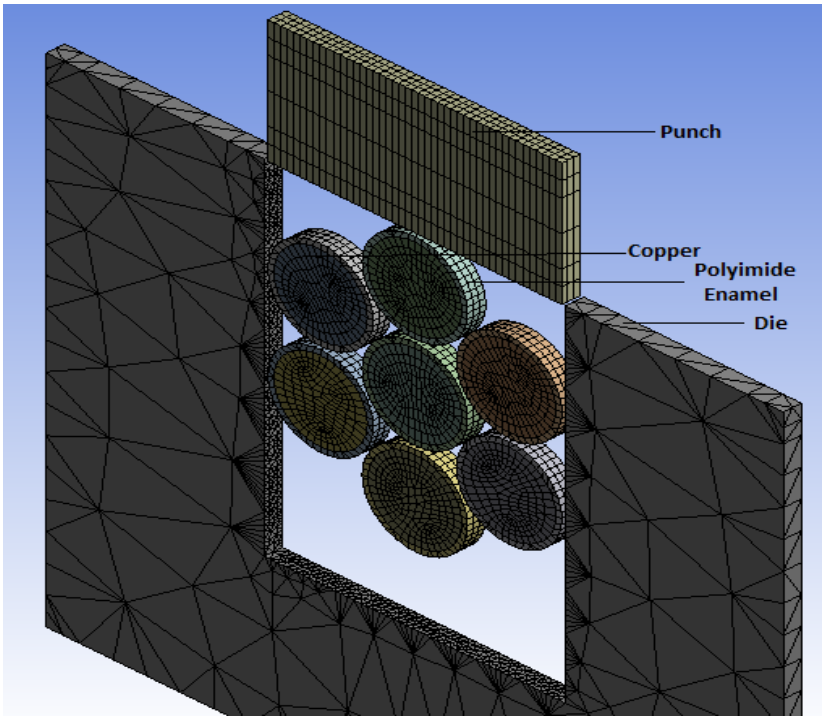

Figure 3.6 A segment of winding to be compressed at high loading rates

Since this simulation is considered to be an artificially accelerated simulation due to very high impact load at very small time duration, obviously, the results obtained from this simulation will not be accurate. A deformation is obtained similar to that shown in Figure 3.5 due to increased loading rate. The plot of equivalent von-Mises stress varying with time and 3D deformed model are given as seen in Figure 3.7 and Figure 3.8, respectively. As shown in Figure 3.7, equivalent von-Mises stress vs. time plot shows high rate of change of pressure in a transient response. Moreover, although applied pressure is a ramp function with highest value of 270 MPa, simulation results give very high stress concentration regions in the deformed body. Equivalent stress result of the deformed body exceeds 2500 MPa which is not possible in real life as it is far beyond the magnet wire ultimate tensile and fracture strengths (345 MPa). Inspecting simulation results such as stress versus time plot and mesh deformation during the pressing will help follow more reasonable simulation methodology to obtain more accurate deformation results.

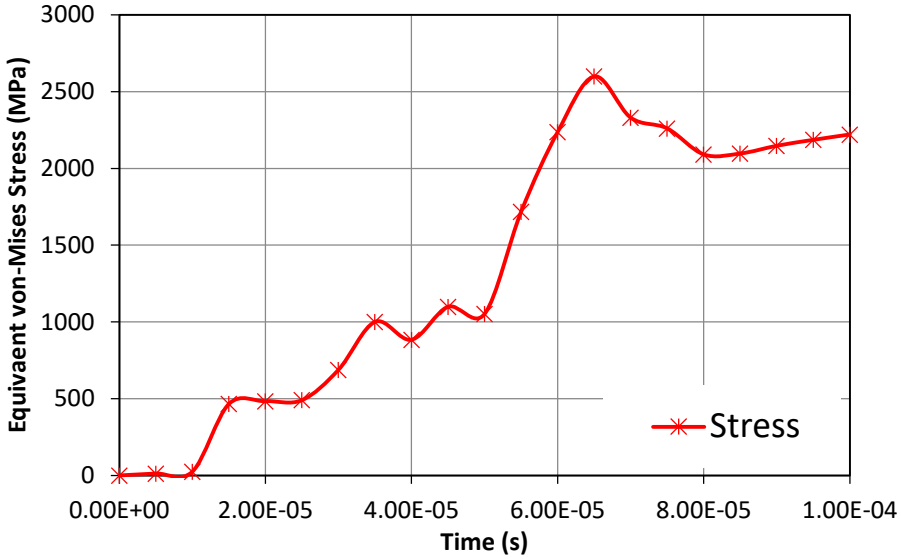

Figure 3.7 Equivalent von-Mises stress on the deformed model

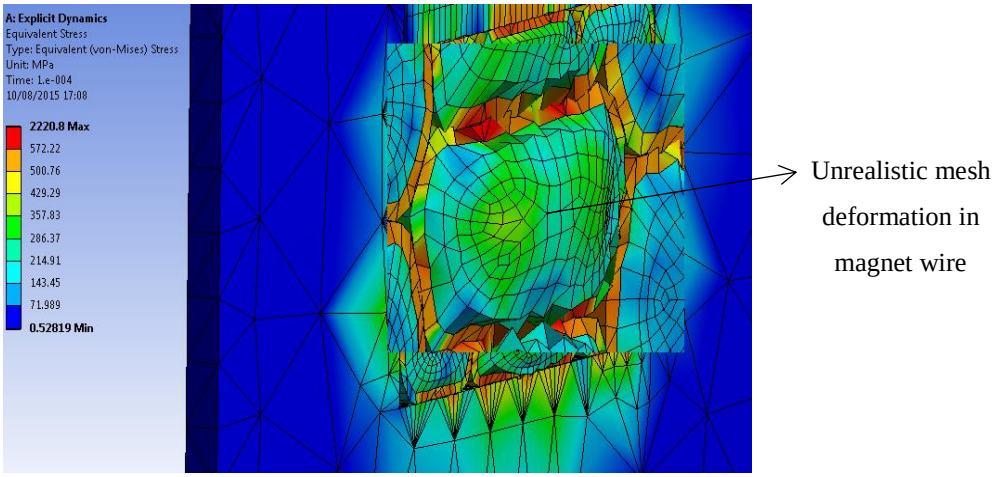

Figure 3.8 Deformed copper magnet wires under high loading

In Figure 3.8, stress on the copper magnet wire is absorbed by the material which is prone to bounce under high pressure effect. Ideally, this is not the case in quasi-static simulations, because quasi-static simulations are long time duration events. Very small simulation end time with high pressure loads cannot be considered to be quasi-static. These simulations are rather high speed impact problems which are easier to model using explicit methods. For this reason, loading rates in the simulation must be minimised as much as possible to obtain accurate response of the material under high pressure, speed or force.

3.5.2 Energy Balance in Quasi-Static FEA Simulations

Energy balance is an important parameter to evaluate whether a simulation is yielding an appropriate quasi-static simulation response. For any physical problem, the work applied by external forces must be equal to internal energy absorbed by the simulation geometry. Therefore, energy history for a quasi-static test must be monitored by:

- The ‘work done’ energy should be first inspected. This shows us how external force is in use during the simulation history. If the external loads do not generate a work done energy, then solution will not converge and the simulation will give an error. This is principally due to energy balance that must be under control for each solution cycle.
- It is expected that internal energy and work done energy should vary in a similar fashion. Thus, energy created due to external forces will be consumed by internal energy of the system. This is an important balance between the external loads and generated deformation in the simulation geometry.
- Since only quasi-static simulations are considered here, kinetic energy should be sufficiently small to obtain more accurate quasi-static simulation response. Higher kinetic energy means that response of the system is dynamic rather than static. A balance between static and dynamic responses should be achieved for accuracy reasons.
- Contact energy should be also checked during the simulation. Ideally, contact energy is expected very close to zero if contact penetration is not presented in the system. However, if contact interfaces interpenetrate due to lower penetration stiffness, this will cause negative energy [91]. Nevertheless, negative contact energy at certain level might be accepted if relatively small contact penetration occurs during the simulation.
- The effect of hourglass deformation in the deformed mesh is illustrated in Figure 3.9. If a quasi-static system includes hourglass modes (oscillatory), non-physical modes of deformation occur without producing a stress [92]. This depends on simulation geometry, material and meshing applied to the whole model. Mesh refining will significantly reduce the effects of hour glassing. As a general guideline, hour glassing energy should not exceed 10% of the internal energy. Hour glassing modes cause inaccurate deformation especially when mesh elements are not fully integrated to each other. Adding linear and quadratic bulk viscosity coefficients to the system might reduce this effect but it is not recommended as they influence global deformation response of the overall model [92].

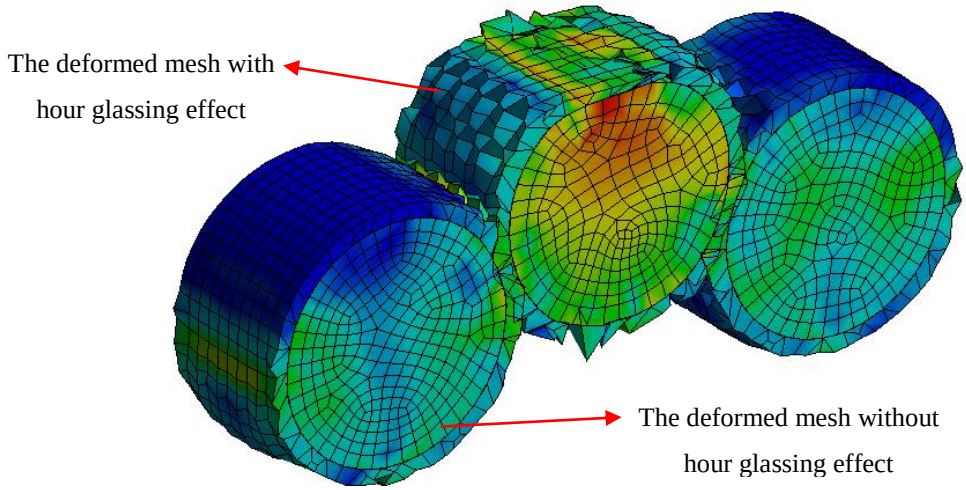

Figure 3.9 Deformed mesh with and without hour glassing effect

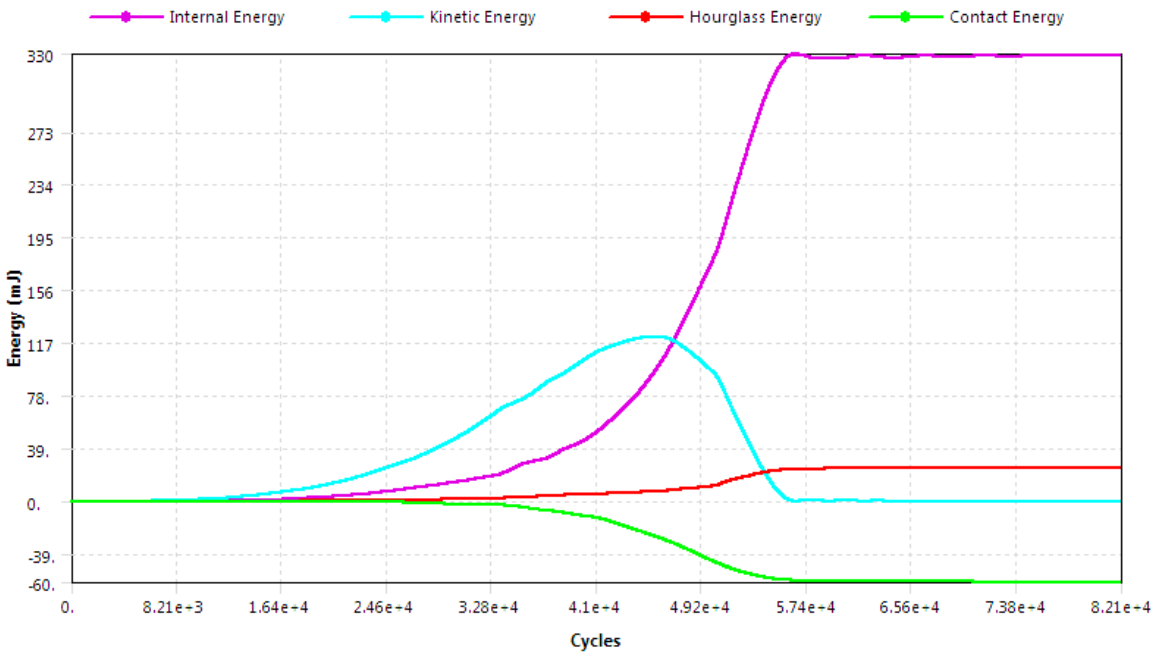

Figure 3.10 Energy summary at high loading rate for the compressed model

An energy summary plot of the simulation given in Figure 3.8 is demonstrated in Figure 3.10. As discussed above, in this simulation the loading rate was too large and unrealistic deformation and stress results had been obtained. As shown in Figure 3.10, negative contact energy occurs due to very high penetration between the contact interfaces. Although hourglass energy is presented, it is still acceptable when compared to internal energy of the model. Ideally, kinetic energy is expected to be close to zero in order to obtain quasi-static modelling behaviour. However, kinetic energy is almost 36 % of the energy due to work done. Therefore, this simulation result is mostly dynamic rather than static or quasi-static due to the fact that a very large loading rate has been exerted to the system for a short time, only 0.1 milliseconds in this case.

Examination of the energy content in energy summary windows will help understand if explicit dynamics simulation results reflect quasi-static solution rather than dynamic high speed impact solution. Although increasing loading rate brings some advantages such as reduction of CPU time, after a certain loading rate value, simulation results will be more dynamic which is not desired for very low speed quasi-static simulations. This states that simulation setup methodology is crucial for non-linear quasi-static simulations.

3.5.3 Mass Scaling

When the loading rates are increased to efficiently model a quasi-static pressing simulation, the material strain rates calculated in the simulation are artificially high by the same factor applied to increase the loading rate [89]. Importance of material strain rate is dependent on the application. If the material is strain rate insensitive, this is irrelevant. However, if material strain rate is an important parameter to observe deformation, material strain rate should be considered for failure criteria of the material.

For coil pressing simulations, material strain rate is an important parameter because if the simulation is not analysed in its natural time period, which is usually longer time durations for quasi-static experiments, material strain rate will be calculated incorrectly. In order to increase time duration which is very costly computationally, mass scaling can be adapted to the system to obtain more accurate results for longer time period simulations.

Although mass scaling is a method to achieve quasi-static solutions, inaccurate material deformation might accompany non-linear simulation results. Therefore, a factor which is used for mass scaling must be selected by performing several quasi-static simulations with different amounts of mass scaling factors. After obtaining several simulation results with different numbers of mass scaling factors, the results are compared to each other to understand if deformed body is accurate enough in comparison to experimental results.

There are several important topics which should be considered to understand the mass scaling concept thoroughly. Therefore, explicit dynamics integration time steps and effect of material density to the integration time steps have been explained in detail.

3.5.3.1 Integration Time Steps

According to the mathematicians, Courant, Friedrich, Lewy, a single time step, Δt should be chosen such that a wave should not travel further than the smallest element size [88]. This is written in equation (3.13):

$$\Delta t \leq \frac{h_s}{c_w} \tag{3.13}$$

where h_s is the smallest element size, dependent upon model meshing, c_w is the wave speed in the element and Δt is an integration time step. Equation (3.13) is known as Courant- Friedrich-Lewy (*CFL*) condition. In explicit dynamics simulations, a safety factor f_s, is used to further ensure the solution stability. For this case, the equation is rewritten as below:

$$\Delta t \leq f_s \frac{h_s}{c_w} \tag{3.14}$$

The smallest time step is dependent on smallest element size. For this reason, it should be ensured that one or two very small elements do not control the whole simulation time steps to obtain a converged solution. This states that uniform mesh size is always desirable for explicit dynamics solutions.

3.5.3.2 Automatic Mass Scaling

The principal idea of mass scaling is to artificially increase the mass of small elements so that stability time steps can be increased [88]. The wave speed in an element is written:

$$c_w = \sqrt{\frac{E}{\rho}} \tag{3.15}$$

where E is the Young's Modulus and ρ is the mass density of the element. Furthermore, $\rho = m / V$, where m is the mass and V is the volume of the element. Substitution of equation (3.15) into equation (3.14) gives:

$$\Delta t \leq f_s h_s \sqrt{\frac{m}{VE}} \tag{3.16}$$

Time step is thus directly proportional to mass density. By increasing the mass of small elements of the material, the integration time step is improved. Increasing the material density by a factor of ${f_s}^2$ increases the stable time increment by a factor of f_s. The default value of *CFL* time step is 10e-20 seconds in the explicit dynamics design tool. As this is too low for a *CFL* time step value, mass scaling is not applied to the system, if there is no smaller element size causing lower time step than default value. Therefore, the default value of the *CFL* time step should be reduced so as to obtain a model with artificially increased material mass density. However, it should be noted that further increasing material mass density will result in erroneous solution due to variation in material inertia, rigidity and bulk viscosity. This is the reason that mass scaling might be applied to several problems to see the effect of it on the material deformation. Then, a suitable factor for mass scaling value could be chosen.

In explicit dynamic simulations, mass scaling is achieved either automatically by predicting a CFL time step or manually by increasing the mass density of the material during the material properties definition. In addition, mass scaling would be achieved by varying Young's modulus of the material. However, this is not recommended as varying the material leads to inaccurate stress and strain values on the deformed shapes.

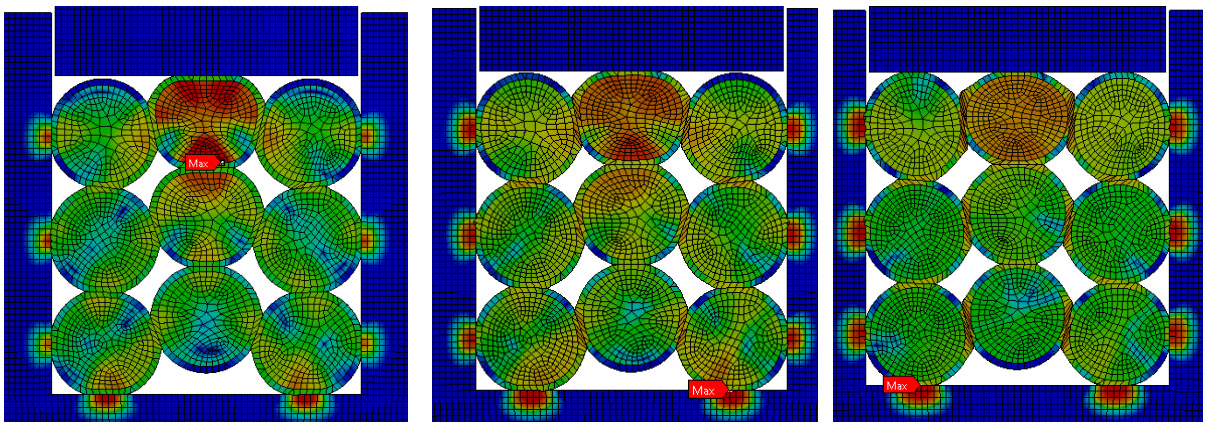

(a) 1 (b) 10 (c) 100

mass scaling factor

Figure 3.11 Deformed coil models with varying mass scaling factor

Several mass scaling factors have been applied to a coil pressing problem as shown in Figure 3.11 given above. If the scaling factor is 1 which demonstrates the original problem without mass scaling, a more accurate non-linear deformation model is obtained. When mass scaling factor f_s is scaled by 10 and 100, the deformed body is getting far from the original deformation of the model. This demonstrates that mass scaling with higher scaling factor is not suitable for obtaining accurate modelling of the simulation. Therefore, mass scaling factor should be selected by conducting several FEA simulations with different scaling factors. This is important to have a model with correct deformation model.

3.5.4 Static Damping

Since explicit dynamic simulations are mainly designed for transient dynamic problems rather than quasi-static problems, static damping might be also utilised to damp the lowest mode of oscillation. This will provide a solution with lower amount oscillation content to reach steady state. The value of dimensionless static damping for critical damping of lowest mode of vibration is defined as:

$$Static\ Damping = \frac{2F_l\Delta t}{1 + 2\pi F_l\Delta t} \tag{3.17}$$

where F_l is the lowest frequency of the system. In order to achieve critically damped system, static damping value should be chosen such that static damping value will not be higher than critical damping value and static damping value will not be below the critical damping value. This means that it should be exactly same as critical damping value to mitigate unnecessary oscillations in the system to reach steady state without any transient oscillation effect.

For highly non-linear quasi-static systems such as coil pressing simulations, predicting a convenient static damping value for the solution will help model more static simulations without seeing any transient response in the systems response. However, prediction of lowest frequency of the system due to damping is very difficult for composite geometry like electric bobbins. Some FEA packages provide frequency contents of different mode of vibrations for complicated geometry. This might be utilised to see the frequency content of the lowest mode of vibration.

If the static damping is set correctly, more static simulations could be obtained due to reduction of unnecessary transient oscillations in the system. For high speed impact simulations, static damping is not needed as the solution is rather dynamic.

3.5.5 Solution Accuracy in Quasi-Static FEA Modelling

Solution of transient structural systems is achieved by implicit methods as explained in the previous section. Accuracy control of the implicit solutions is similar to what Newton-Raphson method follows for solution convergence criteria. Nonetheless, solution accuracy is not based on iterations for explicit methods. Instead, explicit methods use the principle of conservation of energy to monitor solution accuracy during the simulation. At each explicit cycle, the current energy of the system is calculated including kinetic energy and strain energy and reference energy which could be defined as total energy at start cycle. This can be written as shown below:

$$Reference\ Energy + Work\ Done_{reference \rightarrow current} = Current\ Energy \tag{3.18}$$

As energy error might occur during the solution due to contact penetration, hour glassing effect or low mesh density, it must be monitored during the solution of explicit simulations. Usually, an energy error up to 10 % is considered to be accurate explicit solution. This value might be altered for certain non-linear modelling. That is, energy error for any explicit solution can be described as [88]:

$$Energy\ Error = \frac{\left|(Current\ Energy) - (Reference\ Energy) - (Work\ Done)_{reference \rightarrow current}\right|}{\text{Max}\ (|Current\ Energy|, |Reference\ Energy|, |Kinetic\ Energy|)} \tag{3.19}$$

According to equation (3.19), the source of error is difference between the current energy and sum of reference energy and work done. In other words, if the system uses principle of conservation of energy effectively, the solution will converge without any energy error. Therefore, principal reasons of energy error such as low mesh density, contact problems etc. should be evaluated for certain explicit simulations. Moreover, a certain material might add or subtract energy from the system, causing energy unbalance.

3.5.6 Solid Body Contact in Non-linear Simulations

When two separate bodies touch each other, they become mutually tangential and said to be in contact in structural finite element simulations. There are three principal features that should be provided in contact regions [93]:

1. Contact regions do not inter-penetrate.
2. Contact surfaces can transmit compressive normal forces and tangential frictional forces.
3. Tensile normal forces are usually not transmitted by contact regions.

Contact regions can change simulation non-linearity. In other words, stiffness of the system is dependent upon the contact status if separate bodies are touching or separated. Since physical contact regions in reality do not interpenetrate. The FEA software must satisfy this condition for bodies in contact with each other in order to prevent contact penetration. The concept behind contact penetration can be explained by simple spring system, known as Hooke's law as given in Figure 3.12 [93].

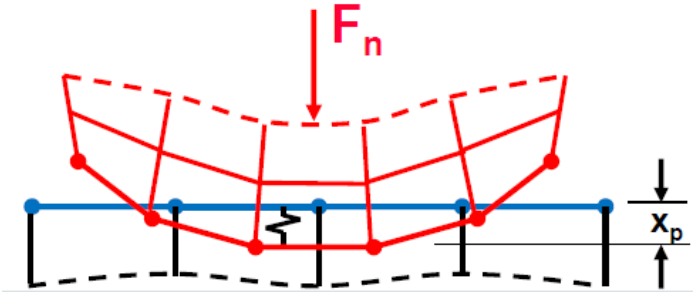

Figure 3.12 Contact interpenetration with simple spring modelling [93]

Since all contact surfaces transmit normal forces between separate solid bodies, first of all a force normal to contact plane can be defined. A spring with a constant is used to model contact stiffness with maximum penetration x_p. Using the Hooke's law:

$$F_{normal} = k_{normal}\, x_{penetration} \tag{3.20}$$

In equation (3.20), for finite contact force, there is contact stiffness between the contact faces with a constant k. The higher contact stiffness means the lower penetration according to equation (3.20). Ideally, for infinite contact stiffness, one would get zero contact penetration between two separate bodies. However, as long as contact penetration is small, the solution results will be accurate.

For non-linear solid body contact, FEA benefits from Pure Penalty and Augmented Lagrange contact formulations [93]. They are quite similar to each other to prevent contact interpenetration, but Augment Lagrange method is a bit different due to an extra term λ. This extra term makes the magnitude of contact stiffness less sensitive for varying contact forces. It is given in equation (3.21).

$$F_{normal} = k_{normal}\, x_{penetration} + \lambda \tag{3.21}$$

The detection of contact is another issue that should be taken into consideration for highly non-linear explicit dynamic simulations. For specific case of contact such as no separation or bonded, multi-point constraint (MPC) contact formulation is also available. This formulation is not similar to Augmented Lagrange and Pure Penalty methods because it adds constraint equations for different displacements between contact surfaces. This contact algorithm is efficient if the bodies are bonded to each other. Default contact formulation for explicit methods is Pure Penalty method which is quite efficient to prevent high interpenetrations between separate bodies. Moreover, Pure Penalty contact formulation uses integration point detection to detect contact points between the parts. Another method is nodal detection so that it detects contact points only at contact nodes. This method is efficient for bonded contacts with MPC formulation.

Since prevention of contact interpenetration is very important to obtain accurate results for coil pressing simulations, several factors which lead to interpenetration should be considered for simulation results with high accuracy. These are listed as follows:

- Increasing the loading rate will increase contact interpenetration between the wire enamels. Therefore, several simulations with the different amounts of loading rate should be tried to obtain models with less contact penetration.
- Increasing the mass too much via mass scaling will cause severe penetration problem. Then, the result may not be acceptable. Therefore, mass scaling might be applied with small scaling factors for higher accuracy.
- Higher static friction coefficients between the bodies might cause a higher contact interpenetration due to effect of frictional coefficient on the contact stiffness.

- Increasing the body interaction friction between the separate turns would lead to less contact penetration. This has been observed during the coil pressing simulations.
- Altering solution precision from single to double in the explicit methods will reduce contact interpenetration considerably. Therefore, if a contact interpenetration is not preventable, single precision might be used. This will in turn result in less solution accuracy in non-linear simulations.

In order to see how contact interpenetration occurs in the coil pressing simulations, cross-section of a bobbin has been illustrated with severe interpenetration and without penetration as shown in Figure 3.13.

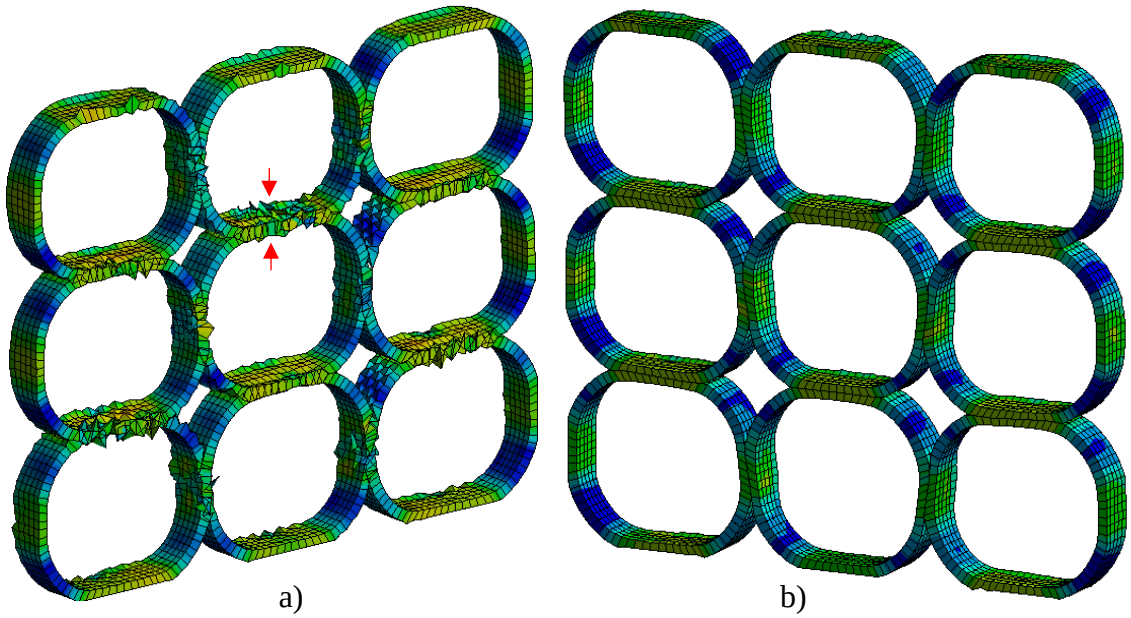

a) b)

Figure 3.13 Contact interpenetration in wire enamels (a) presented, (b) not presented

3.5.7 Meshing

One of the most important factors that influences the material response for highly non-linear explicit simulations is meshing. FEA software provides many different types of meshing methods for different analysis. Generating default mesh on the model will not give accurate simulation results. Therefore, fine meshing with high relevance should be satisfied for explicit dynamics simulations.

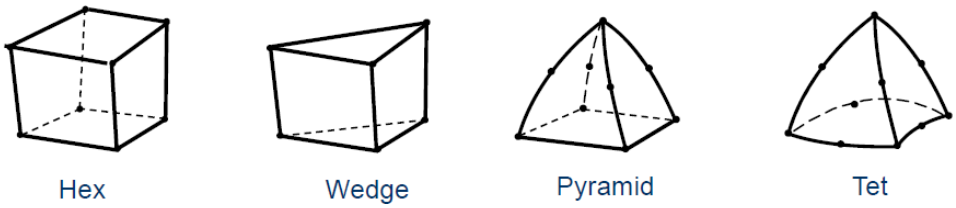

Figure 3.14 Different types of mesh elements [94]

As shown in Figure 3.14, hexahedrons can fill a given volume more efficiently in comparison to other mesh elements such as wedge, pyramid or tetrahedron [94]. For highly non-linear problems, more uniform meshing is desired to have a model with more homogeneous element distribution. Also, filling the model volume with lower number of elements is important to reduce total solution cycles in explicit simulations. This implies that hexahedrons dominant meshing is always preferable for the solutions with high deformations. In order to realize the effect of different mesh elements on the high deformation problems, a tetrahedron dominant model has been simulated for the coil pressing problem. This is given in Figure 3.15.

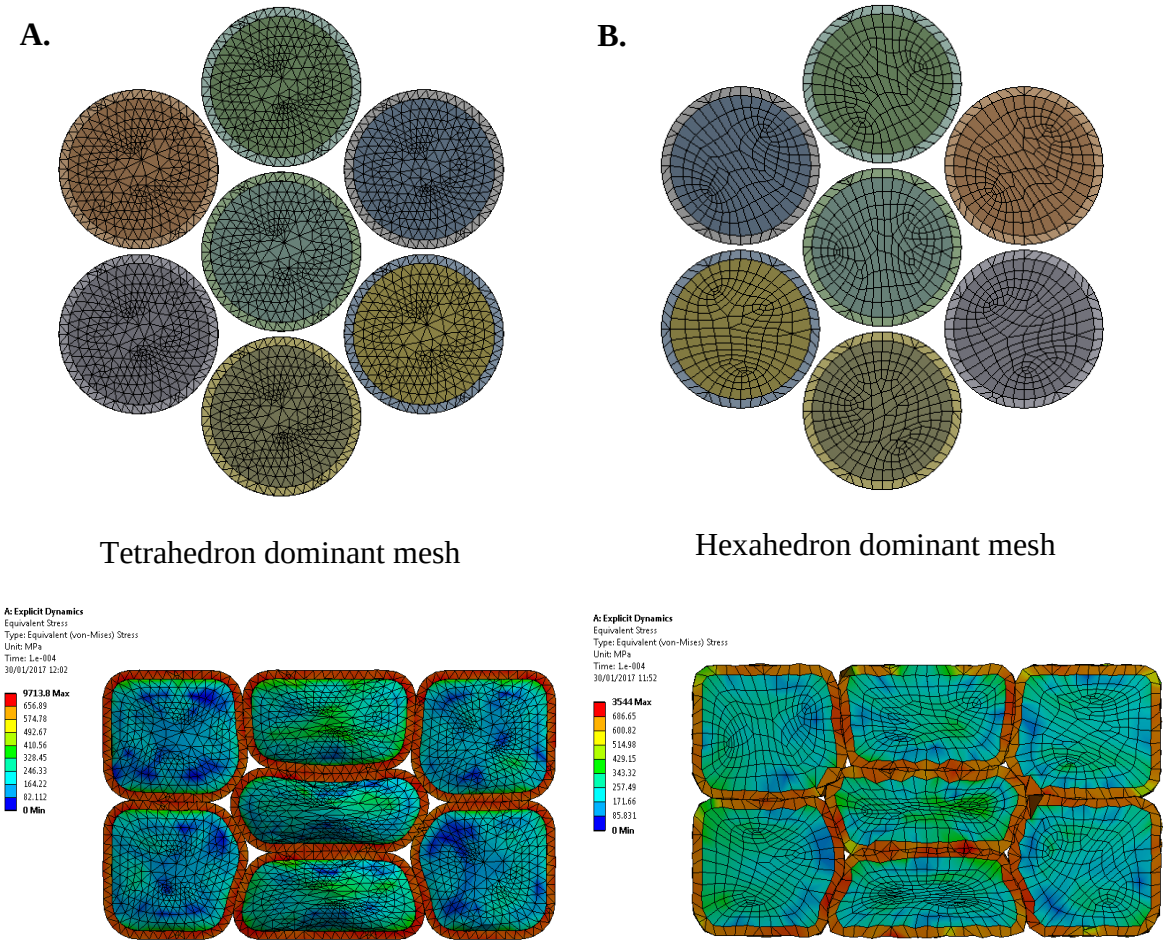

Figure 3.15 (A) Tetrahedron dominant meshing **(B)** hexahedron dominant meshing

In Figure 3.15, two high speed impact response of 7-turn coils have been demonstrated. In the first case, predominant element type is tetrahedrons. On the other hand, predominant element type is hexahedrons in the second case. If the solution with deformed bodies are investigated, it can be noted that more realistic deformation occurs for the simulation with hexahedron meshing, because hexahedron elements are prone to deform uniformly. This will lead to reduce air voids between the turns as shown in Figure 3.15 (B). That is, although element selection is not always dependent on the user for very complex geometries, hexahedron dominant meshing

should be preferred if it is applicable. This will lead to higher deformation capacity of the geometry with higher relevance meshing.

3.6 Case Study: Modelling of Coil Pressing

In Section 3.5, a thorough explanation of quasi-static non-linear simulations by using explicit methods has been performed. Since all physical aspects of non-linear quasi-static simulations are investigated in the previous section, a quasi-static coil pressing simulation will be investigated mechanically by proposing an appropriate way for this type of FEA modelling.

3.6.1 Material Properties of Polyimide for FEA

For the FEA modelling, Grade 2 enamelled copper magnet wire with overall diameter 0.566 mm has been chosen with 0.045 mm enamel thickness. Polyimide based enamel has been considered for modelling because polyimides are mechanically and chemically more stable and operate at temperatures in excess of 240°C [95]. It is possible to see the mechanical limits of high quality modern copper magnet wires for coil pressing simulations. General material properties is tabulated in Table 3.3.

Table 3.3 Mechanical, thermal and electrical properties of polyimide

Mechanical, Thermal and Electrical Properties of Polyimide		
Density	$1.3\,x10^3$ – $1.8x\ 10^3$	$kg/m3$
Young's Modulus	$2.44\ -\ 4$	GPa
Compressive Modulus	$2.82\ -\ 2.97$	GPa
Shear Modulus	0.91 – 0.955	GPa
Poisson's Ratio	0.33 – 0.35	-
Yield Strength	72 – 158	MPa
Compressive Strength	133 – 227	MPa
Elongation	2 – 3	mm/mm
Minimum Service Temperature	-248	$°C$
Maximum Service Temperature	271	$°C$
Thermal Conductivity	0.23 – 0.502	$W/m.°C$
Electrical Resistivity	$5.39E20$ – $4.85E21$	$\mu ohm.cm$

Dielectric Breakdown	18.9 – 20	MV/m

The yield strength of polyimide is 158 MPa after which plastic deformation occurs. Below this stress value, only elastic deformation will be presented. Elongation which might be described as strain rate during the material failure will be included for FEA modelling to investigate whether material fracture occurs. Although thermal and electrical properties are presented in Table 3.3, these are not important for the point of view of mechanical FEA simulations.

Since one of the reasons of non-linearity in coil pressing simulations is the material non-linearity, plasticity should be defined for polyimide enamels for FEA modelling. Prediction of stress-strain curve can be achieved using either bilinear or multilinear isotropic hardening as the material is isotropic. As the yield strength and maximum fracture strength of the polyimide is known, the stress-strain data for polyimide is given in Table 3.4

Table 3.4 Engineering stress-strain data for polyimide

Plastic Strain (mm/mm)	Stress (MPa)
0	158
3	345

In Table 3.4, the first data row determines the yielding point of the material. After this value, the material strain will increase up to a maximum 300 % until it reaches a 345 MPa fracture strength. It can be noted that 300 % elongation is not realistic for material elongation, however, due to the artificially increased loading rate which was discussed in Section 3.5.1, this value in fact corresponds to a 3 % material elongation for polyimide based enamel. The data given in Table 3.4 is linearized and so does not precisely demonstrate a true stress-strain curve of the material.

3.6.2 Material properties of Copper for FEA

For FEA simulations, mechanical material properties of pure copper are given in Table 3.5. As plastic deformation will occur under high stress during the compression of magnet wires, multilinear isotropic hardening data has been also provided for copper.

Table 3.5 Mechanical properties of copper

Mechanical Properties of Copper		
Density	8900	$kg\ m^{-3}$
Shear Modulus	47700	MPa

Multilinear isotropic hardening stress-strain data points which are a default for explicit dynamics simulations are tabulated in Table 3.6. As shown in stress-strain data table, copper deforms elastically until stress reaches 120 MPa. Until 450 MPa, copper experiences significant plastic deformation. Since Young's modulus of copper is very high compared to that of polyimide, high compressive and tensile stress deform copper at relatively lower amounts.

Table 3.6 Engineering stress-strain data for copper

Plastic Strain (mm/mm)	Stress (MPa)
0	120
0.3	450
1E+20	450

3.6.3 Material properties of the pressing tools (Steel 4340) for FEA

Steel 4340 is a 1.8% nickel –chromium- molybdenum high hardenability high tensile steel [96]. Typical applications are heavy duty shafts, gears, couplings, pins etc. As the focus is not on this material, a default material as defined in material library has been used for the FEA modelling. Punch and die modelled for the simulations are of a type hard steel that is Steel 4340. The mechanical properties are given in Table 3.7.

Table 3.7 Mechanical properties of Steel 4340

Mechanical Properties of Steel 4340		
Density	7830	$Kg\ m^{-3}$
Yield Stress	7.92E+0.8	Pa
Hardening Constant	5.1E+08	Pa
Hardening Exponent	0.26	-
Strain Rate Constant	0.014	-
Bulk Modulus	1.59E+11	Pa
Shear Modulus	8.18E+10	Pa

3.6.4 3-D FEA Modelling of Coil Pressing

A coil cross-section with 9-turn copper magnet wire with Grade 2 polyimide coating has been modelled with 0.1 mm extrusion which makes the geometry 3-D. The extrusion length is kept small due to computational cost of quasi-static problems. The simulation geometry is illustrated in Figure 3.16.

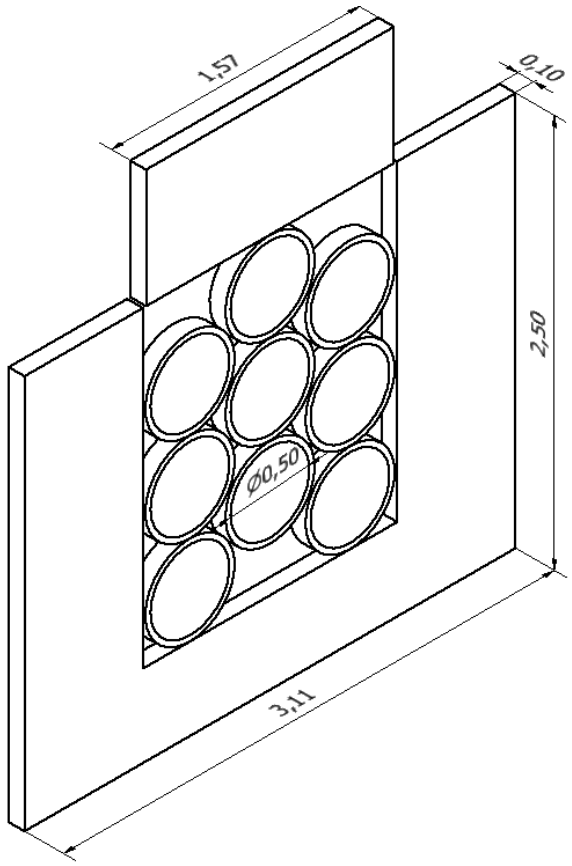

Figure 3.16 3-D cross sectional view of a 9 turn coil

As seen in Figure 3.16, a coil with 3-layers has been modelled with the highest fill factor achievable for 9 turns. The distance between each vertical layer is 0.015 mm and the distance between turns in each layer was set to zero which will minimize the effect of relatively high speed collision between the turns. If a distance is left between the coil and bottom of the die, this will cause high speed impact which in turn results in large unrealistic deformation. That is, dimensioning of the whole model will affect the quasi-static simulation results. Therefore, 3-D geometry has been optimised to reduce the effect of collision between the separate bodies during the compression at certain velocity.

The fill factor for the original slot area is calculated to be 0.55. The principal aim is to enhance the slot fill factor by varying the original slot area for the same amount of copper. Thus, a high fill factor stator winding could be obtained without observing any insulation failure.

3.6.5 Contact Regions and Body Interactions

In order to provide accurate contact regions, the following methodology has been tracked for quasi–static coil pressing problems:

- A bonded solid contact has been set between each copper wire and its polyimide coating. It was also set to unbreakable. It is shown in Figure 3.17.

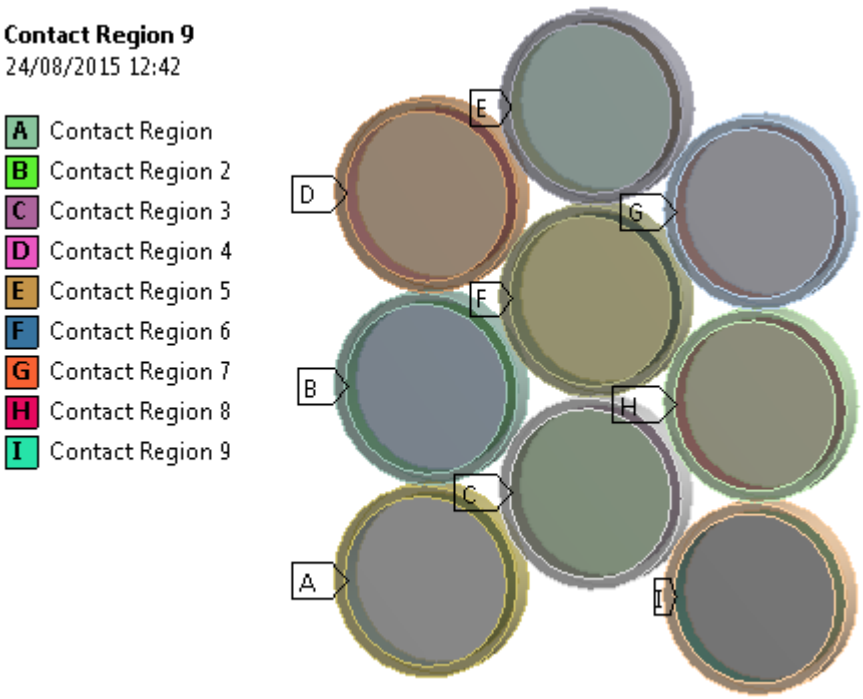

Figure 3.17 Unbreakable bonded contact faces between copper and its insulation

- Static frictional contact with a friction coefficient of 0.1 is assumed between the turns as the sliding frictional contact becomes more important during the body interactions.
- Body interaction is not exactly same as contacts. Its main purpose is to establish a relation between separate parts that could be in contact or not during the compression of the coil. For instance, two separate bodies might not be initially in contact and they do not share any impact due to boundary conditions, but during the process of coil pressing they might share some physical boundary conditions including stress and strain rate. In this case, FEA should understand that they will interact with each other during the solution. This is provided by setting up body interactions between all bodies if an interaction will be the case throughout the problem solution.
- A frictional body interaction between the turns has been set with a coefficient of 0.3. This is relatively higher frictional interaction between the separate bodies to reduce the contact interpenetration.

3.6.6 Initial Boundary Conditions

A punch and die are required for the purpose of compression and the geometry should be fixed from the bottom by introducing a fixed support at the bottom. Instead of applying fixed support for the whole die, only bottom surface has been applied a fixed support. This gives a higher order degree of freedom for the die under load which is pressure.

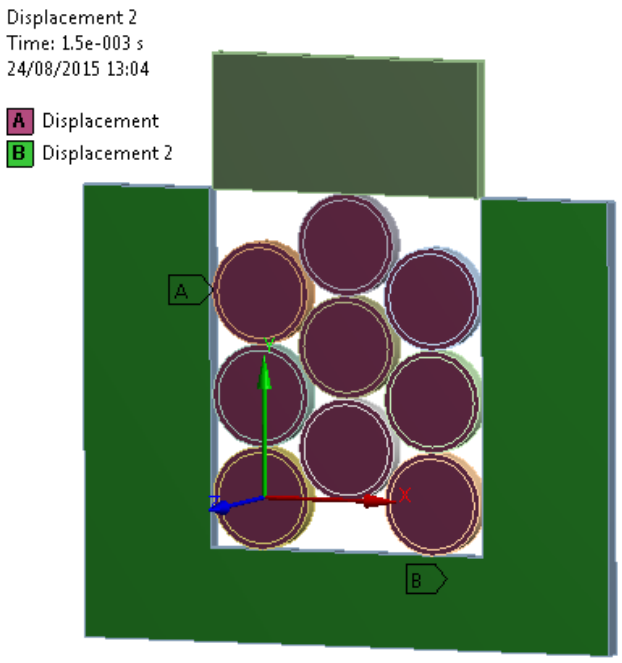

Figure 3.18 Displacement supports applied to the coil and die

The initial coordinates of the magnet wires will change due to an applied load, so a free displacement support only in the x-y plane has been provided for all turns of the coil. This must be provided for all moving bodies in certain directions. Furthermore, a displacement support is also applied to die to let it move at certain degree to absorb a part of kinetic energy generated during the impact. The applied displacement supports are illustrated in Figure 3.18.

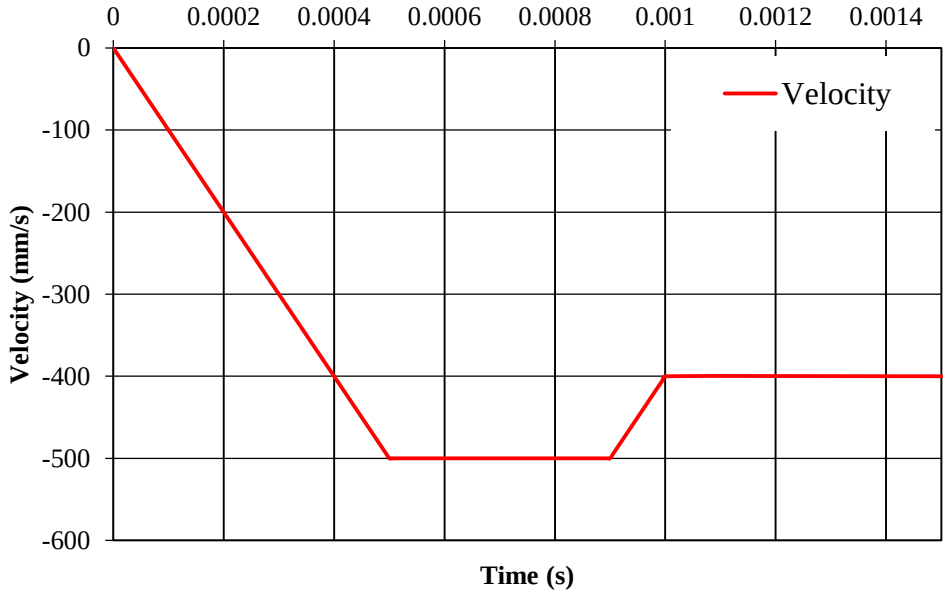

Figure 3.19 The applied velocity boundary condition as a function of time

The velocity load has been used in the simulation. In reality, coils are pressed with pressing tools that apply a high pressure. Although pressure load is applicable to coil pressing simulations, this was not preferred, because a pressure boundary condition cannot control the

amount of displacement with respect to time. This is very important for quasi-static analysis methods which must provide a low speed collision for the model by considering natural time duration of the event. Therefore, a velocity load is very convenient to press the coil at certain amount of time duration by preventing high speed collision. The velocity boundary on the punch is plotted in Figure 3.19.

The speed of the punch increases up to 500 mm/s (or 0.5 m/s) in 0.5 milliseconds (i.e. ramp increase), then the speed of the punch is kept fixed at 500 mm/s for the next 0.4 milliseconds. To reduce the effect of high speed collision, after a certain time, the speed of punch is reduced to 400mm/sec as shown in Figure 3.19. The velocity load compresses the coil in a controlled manner with a certain amount of displacement. The time integration of velocity function gives the total displacement of the punch. In this case, the total displacement is 0.57 mm.

3.6.7 Solver Control

Solver control settings are the most important part of the explicit dynamic simulations. Some parameters including maximum energy error, time step, CFL time step and damping controls should be defined accurately.

Mass scaling has been enabled for coil pressing simulations. Automatic mass scaling requires CFL time step that is a number where if a single time step is too small, it will be accelerated by applying artificial mass to each nodal element to improve time step throughout the simulation. CFL time step was selected as 1e-6 seconds which means that if a single time step is a smaller value than CFL time step, the solver will automatically add artificial mass to each element to increase time step thereby reduce the simulation time.

The simulation end time chosen for this quasi-static simulation is 1.5 milliseconds. The speed of punch does not reflect natural time of the event as coil pressing cannot be achieved in a few milliseconds in reality. The actual speed of the press is assumed to be at least 100 times slower than this. Therefore, simulated results of the compression process need to be scaled down a hundred times. This model has been solved in about 18 hours with 4- core, 24 GB memory PC to see the total dynamic response of the system. Note that if natural time of the coil pressing event was used for the models to obtain the original plastic strain results, converging to a solution would take about 1800 hours when the same time step is used for the solution.

Energy error might occur during the explicit dynamics simulations, but this must be kept within a limit which was chosen 20% for pressing simulations. If energy error exceeds 20%, solver will stop automatically as it shows simulation will be far from the accurate results.

3.6.8 Simulation Results and Discussion

Since there are different types of material failure criterions to make a decision whether a fracture occurs or not in the material, one should be chosen to justify if material fracture has occurred. It is very difficult to analyse the solution in terms of material fracture. In order to understand failure analysis, very common ductile failure model has been explained in detail.

- **Maximum Shear Stress Theory (Tresca Criterion)**

  According to maximum shear stress theory, ductile failure occurs when the maximum shear stress τ^{max} exceeds one half of the material yield strength S_y [87]. If a factor of safety n has been determined for the structure, the failure design equation can be written as:

$$\tau^{max} < \frac{S_y}{2n} \tag{3.22}$$

- **Distortion Energy Theory (von-Mises Criterion)**

  According to distortion energy theory, ductile failure occurs when maximum von Mises stress ${\sigma_e}^{max}$ exceeds the material yield strength S_y [87]. Applying a factor of safety n to the structural model, the design equation is in the form:

$${\sigma_e}^{max} < \frac{S_y}{n} \tag{3.23}$$

As the compression of coils causes a significant plastic deformation in the magnet wires, the criterions given above are not appropriate choices to inspect material fracture in the simulation results, because according to these criterions, the failure occurs just after exceeding the material yield strength. Since the plastic deformation is predominant in the compression of bobbins, it is clear that stress and strain results are far from the elastic region of the material. This shows that the failure conditions given above will not be able to justify the compression of coils by applying high pressures.

The total displacement is 1.57 mm that provides reduction in slot depth. The equivalent von-Mises stress results with respect to varying simulation time are given in Figure 3.20.

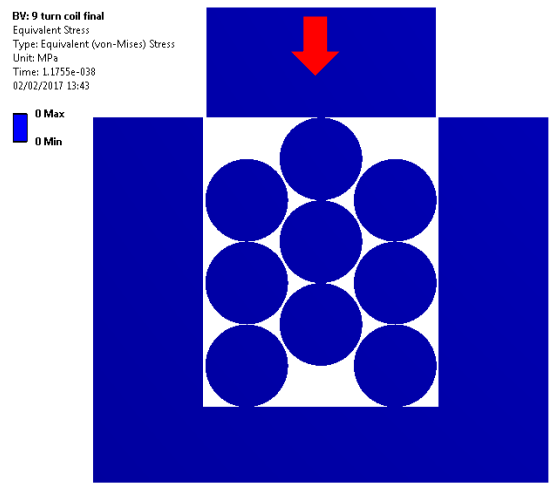

At t=0 sec

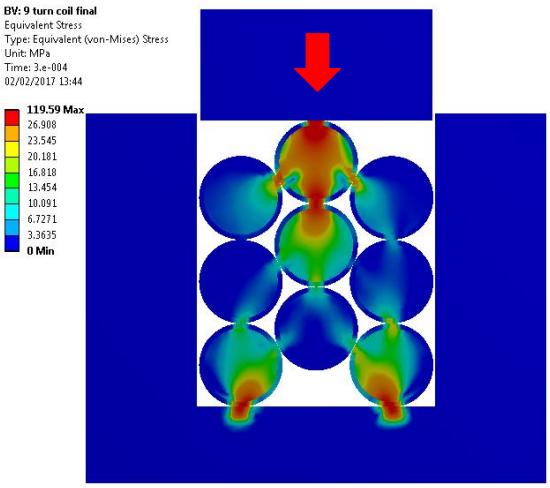

At t = 3e-4 sec

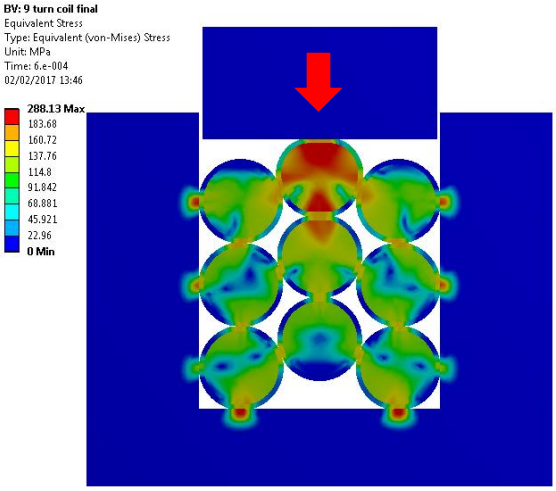

At t= 6e-4 sec

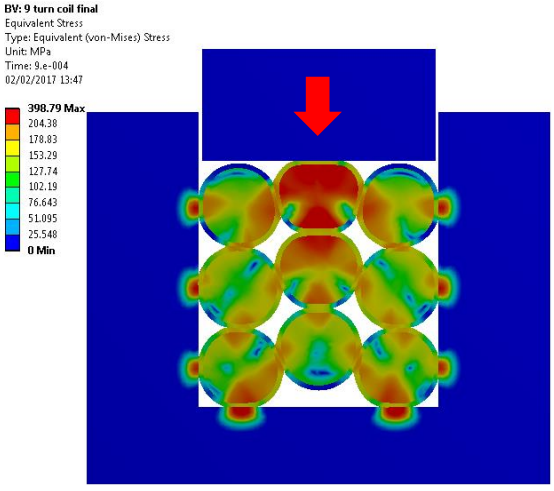

At t= 9e-4 sec

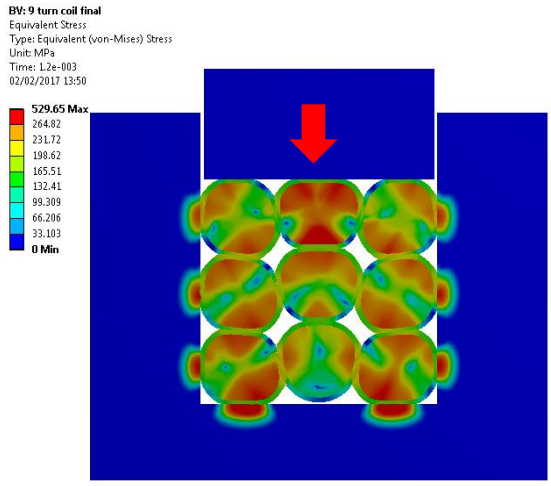

At t= 1.2e-3 sec

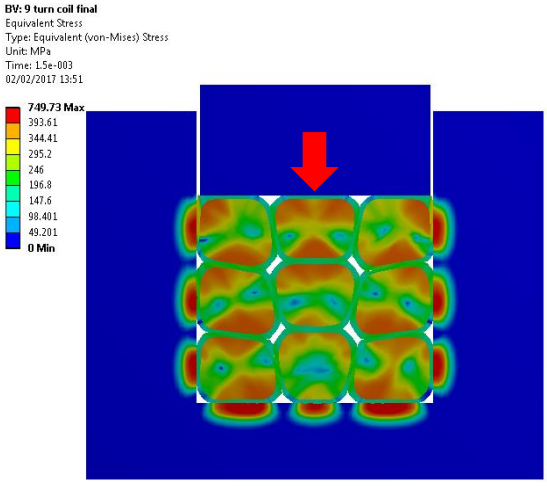

At t = 1.5e-3 sec (End Time)

Figure 3.20 Equivalent von-Mises stress at different time instants

During pressing of the coil, air gaps between the turns have been reduced and the entire coil was packed in a smaller volume. This results in higher slot fill factor, however, the greater reduction in the coil area might cause higher von-Mises stress points in the deformed model.

In Figure 3.20, equivalent von-Mises stress of the deformed model at different time instants is given. All conductors experience a significant plastic deformation. As an example, stress-strain relationship for wire enamel in the middle conductor is given in Figure 3.21A. The exerted velocity load in Figure 3.21B on a single turn shows relatively higher speed collision between conductors resulting larger momentum calculations within the solver, although it is not desired for a quasi-static FEA approach.

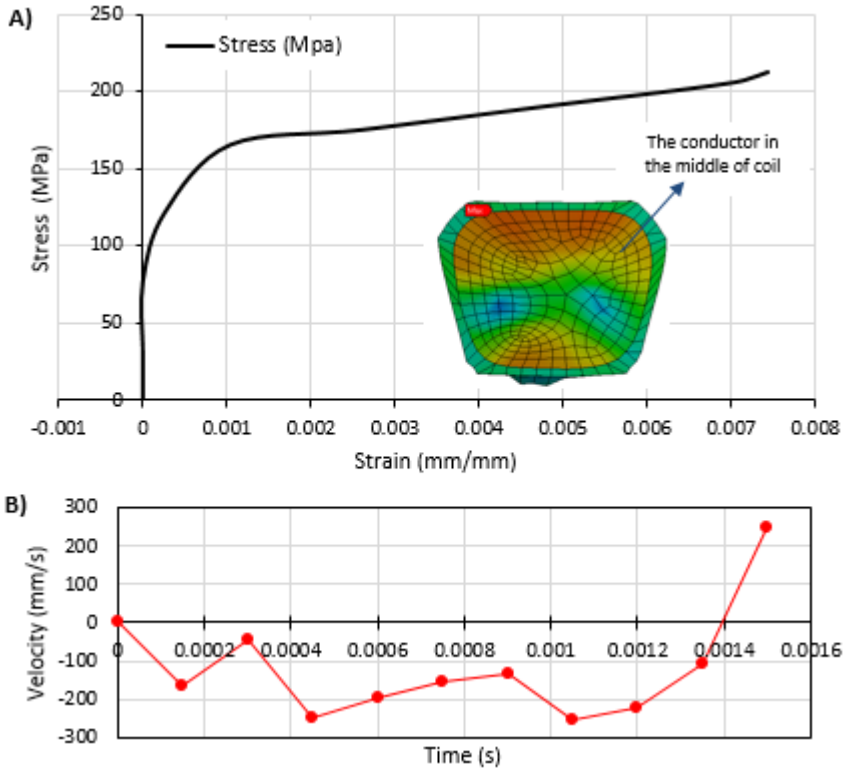

Figure 3.21 (A) Plasticity on a single pressed conductor, (B) Velocity load on the conductor

Each conductor of the coil might have certain stress and strain rates as deformation in some turns is more significant. Therefore, equivalent plastic strain on all magnet wire enamels is illustrated in Figure 3.22 to clarify whether material fracture occurs due to higher plastic strain rates.

In Figure 3.22, the maximum plastic strain occurs between the die wall and magnet wire enamel due to relatively higher friction between the steel part and magnet wire enamel. On the contrary, it can be observed that the plastic strain rate is quite lower in the regions where only magnet enamels are in contact with each other. This shows that the difficulty in the coil pressing is higher sliding friction coefficient between the magnet wire surface and steel wall.

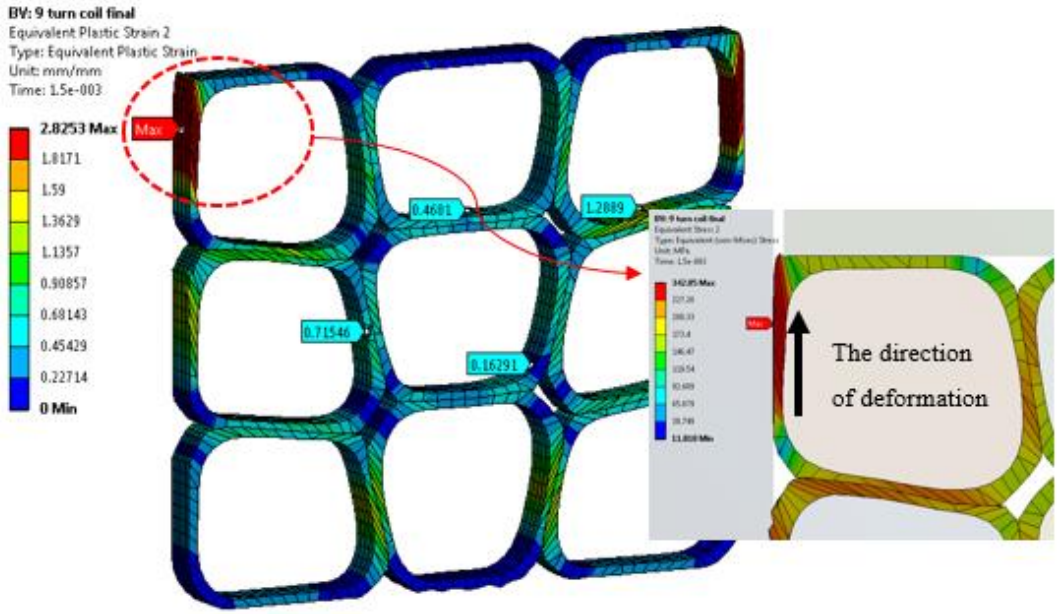

Figure 3.22 Equivalent plastic strain in polyimide magnet wire coating

The highest strain rate of 0.028 mm/mm (down scaled due to loading rate) occurs at 342.8 MPa. Maximum strain rate of 0.03 mm/mm, which is equivalent to 3% elongation is usually applicable for polyimide thermosets. Although plastic deformation is significant especially on the external surface of the steel, no material fracture has been observed in the quasi-static modelling of the coil as the equivalent plastic strain is less than maximum allowed plastic strain. If the coil is compressed more to reduce the slot volume, magnet wire insulation failure is likely.

Pressing the coil has improved the slot fill factor. Before the compression, slot fill factor was calculated to be 0.55. After the compression, it was calculated to be 0.77. In relatively thinner conductors with diameters ranging between 0.2 to 1 mm, the slot fill factor can be as high as 0.77-0.8.

The total equivalent von-Mises stress in the coil including copper wire and its insulations can be examined to observe how much stress has been generated on the compressed bobbin. This is shown in Figure 3.23.

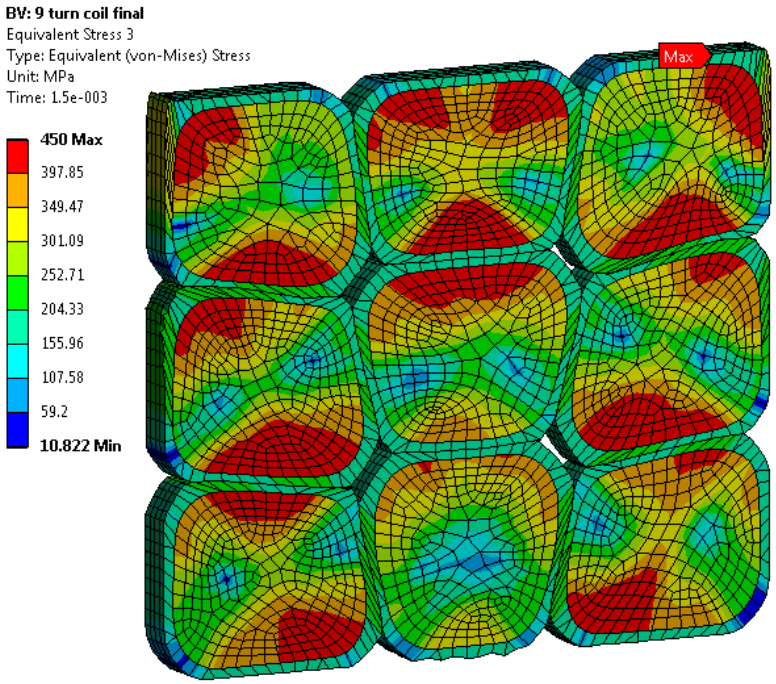

Figure 3.23 Equivalent von-Mises stress in the coil

There is no direct way to understand if the compression of the coil is static rather than dynamic. However, the kinetic energy produced during the compression of the coil could be examined. It is expected that kinetic energy of the compression should be sufficiently low in comparison to internal energy of the system as shown in Figure 3.24.

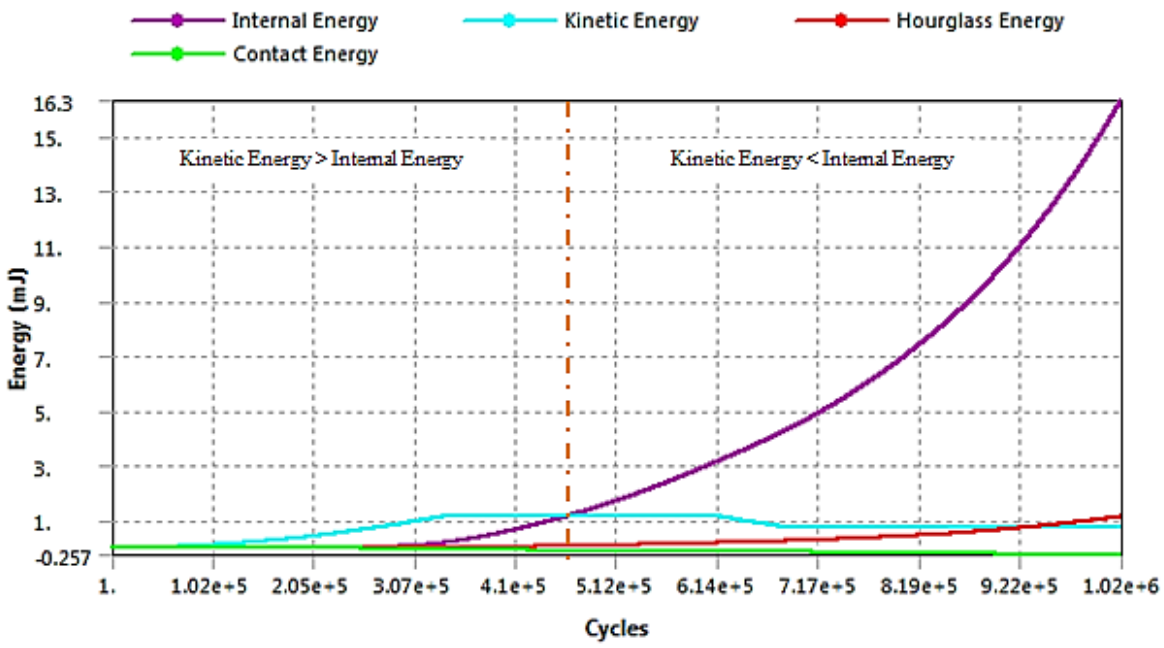

Figure 3.24 Energy summary of the simulated model

In Figure 3.24, solution cycles vs. energy content of the simulation is plotted. In the beginning of the simulation, kinetic energy increases and internal energy is lower. Also, the contact energy is close to zero and hour-glass energy is less than 10% of internal energy demonstrating that

conservation of energy for the deformed model satisfies the conditions regarding the simulation accuracy. The total amount of kinetic energy throughout the simulation is sufficiently small compared to internal energy (i.e. work done energy) deforming the coil.

It can be noted that in Figure 3.19, the velocity of punch is decreased at t=9e-4 sec. The effect of speed reduction is immediately reflected to the system kinetic energy as can be observed in Figure 3.24. Therefore, when quasi static modelling is performed, design engineers could monitor kinetic energy of the model and make a decision if the loading rate should be reduced. Moreover, a step change in the system loading should be minimized as much as possible to keep the system kinetic energy low enough. The solution for this case study is not the best case and this might be improved by accepting some computational costs. This is achieved by reducing loading rate which in turn decreases plastic strain rate. Hence, the deformed model would be closer to reality.

3.7 Case Study: On-tooth coil pressing

As emphasised in Figure 3.22 in Section 3.6.8, most of the deformation occurs in the interface between the magnet wire enamel and steel die cavity. This makes coil pressing quite delicate if the coil is pressed on a dummy tooth and placed into original laminated machine teeth. The material fracture is more likely on the external surfaces of the compressed coil in comparison to inter turn surfaces. In order to prevent material failure on magnet wire enamels, a method called on-tooth pressing could be adapted.

On-tooth coil pressing is a technique where a modular laminated stator tooth is pressed after it is wound with a required number of turns. The advantage of this method is that pressed bobbin will not be extracted from a dummy tooth as material fracture is more likely in that case. Even if the bobbin is taken off a dummy tooth shape safely, insertion of the compressed winding into the laminated teeth is still a problem regarding magnet wire enamel degradation. In order to prevent possible material failure problems, a bobbin can be therefore directly compressed on the original stator lamination.

The coil pressing could be quite critical at some circumstances when a machine is designed for a particular application with high slot fill factor. When conductor diameter is determined for a machine, the slot fill factor is taken into consideration and it is usually chosen around 0.4- 0.5 which means that a machine designer has to utilise relatively thinner conductors for a certain slot area. If relatively thicker magnet wires are chosen, the designer should make sure that those conductors can be fit into machine slots easily.

In order to demonstrate how fill factor can be a critical design parameter for a machine, a case study has been conducted. This study is based on a on a 72 slot/64 pole PM electric motor for in-wheel electric vehicle application as proposed in [97].

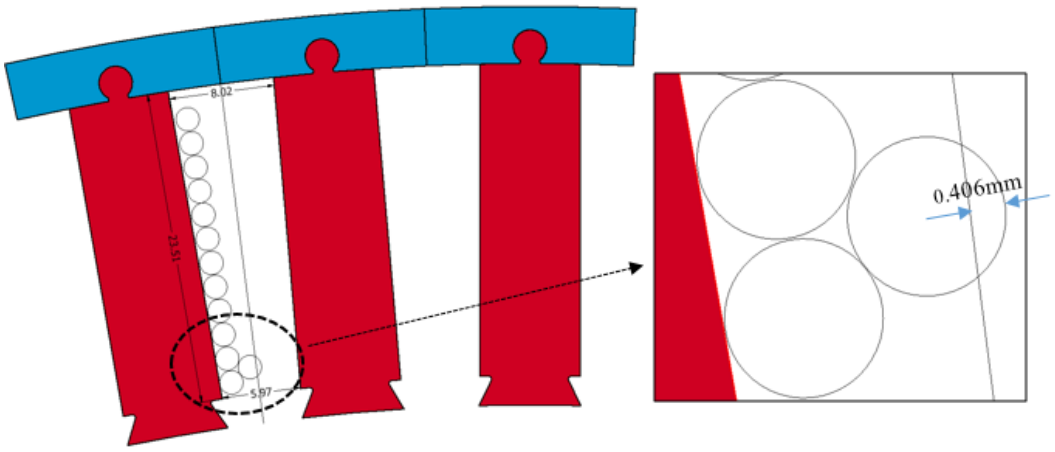

Figure 3.25 A stator segment of 72slot/64 pole PM machine with 23 turn single tooth windings

The stator segments given in Figure 3.25 utilise single tooth winding consisting of 2-layer 23 turn bobbin. The possible conductor diameters for this machine cannot be greater than 1.6 mm due to limited area of the slot. The thicker conductors with 1.8 mm diameter cannot be fit into the slot as some of the conductors would be out of the given slot area in the bottom layer of winding as shown in Figure 3.25. Coil pressing can be quite useful to fit those conductors into the original slot area. If a bobbin with 1.8 mm conductor diameter is compressed about 0.4 mm, the machine can be designed with magnet wires with 1.8 mm conductor diameter. This condition can be simulated by quasi-static FEA to investigate whether the machine bobbin consisting of magnet wires with 1.9 mm overall diameter can be compressed at least 0.4 mm without observing any insulation failure.

3.7.1 FEA Simulation Results

Quasi-static FEA simulations have been performed to investigate what could be the maximum fill factor improvement for the magnet wires with 1.9 mm diameter, as illustrated in Figure 3.26. In Figure 3.26C, displacement on the punch is 0.455 mm demonstrating that 2-layer winding with 1.9 mm wires can be compressed more than 0.406 mm. This shows the machine segments given in Figure 3.25 can be built with magnet wires with 1.9 mm overall diameter. In the simulations, the maximum achievable fill factor for the coil is 0.73 which is depicted in Figure 3.26E corresponding to 0.77 mm punch displacement. After certain displacement (0.793 mm) of the punch (Figure 3.26F), a material fracture is observed.

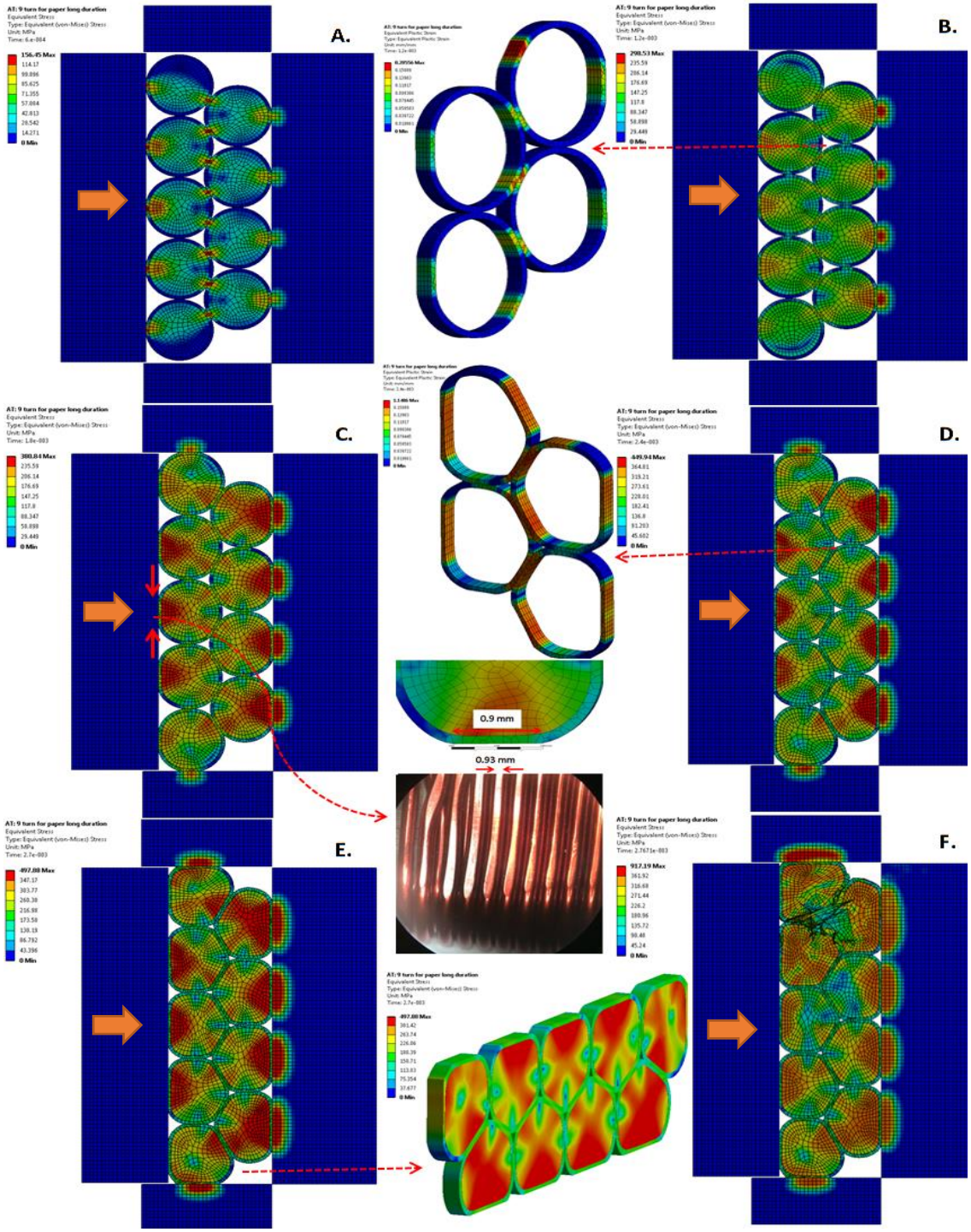

Figure 3.26 The deformation of a 2-layer winding at different time instants with 1.9 mm magnet wires

3.7.2 Experimental Results and Discussion

A 23-turn coil with 1.8 mm conductor diameter was compressed in a die cavity as shown in Figure 3.27. The initial slot fill factor for the coil is around 0.59. A very thin (0.075 mm) polyimide type slot liner has been used as an insulation material between the laminations and winding. Although, there are only 2 layer of wires in the bobbin, air gaps between the turns are quite significant since the conductors are thick. By squeezing the bobbin inside the cavity of

pressing tool, the air gaps has been reduced and the conductors have been packed in a smaller volume. The achieved fill factor is around 0.66. Hence, the magnet wires with a 1.8 mm conductor diameter can be utilised for the machine coils.

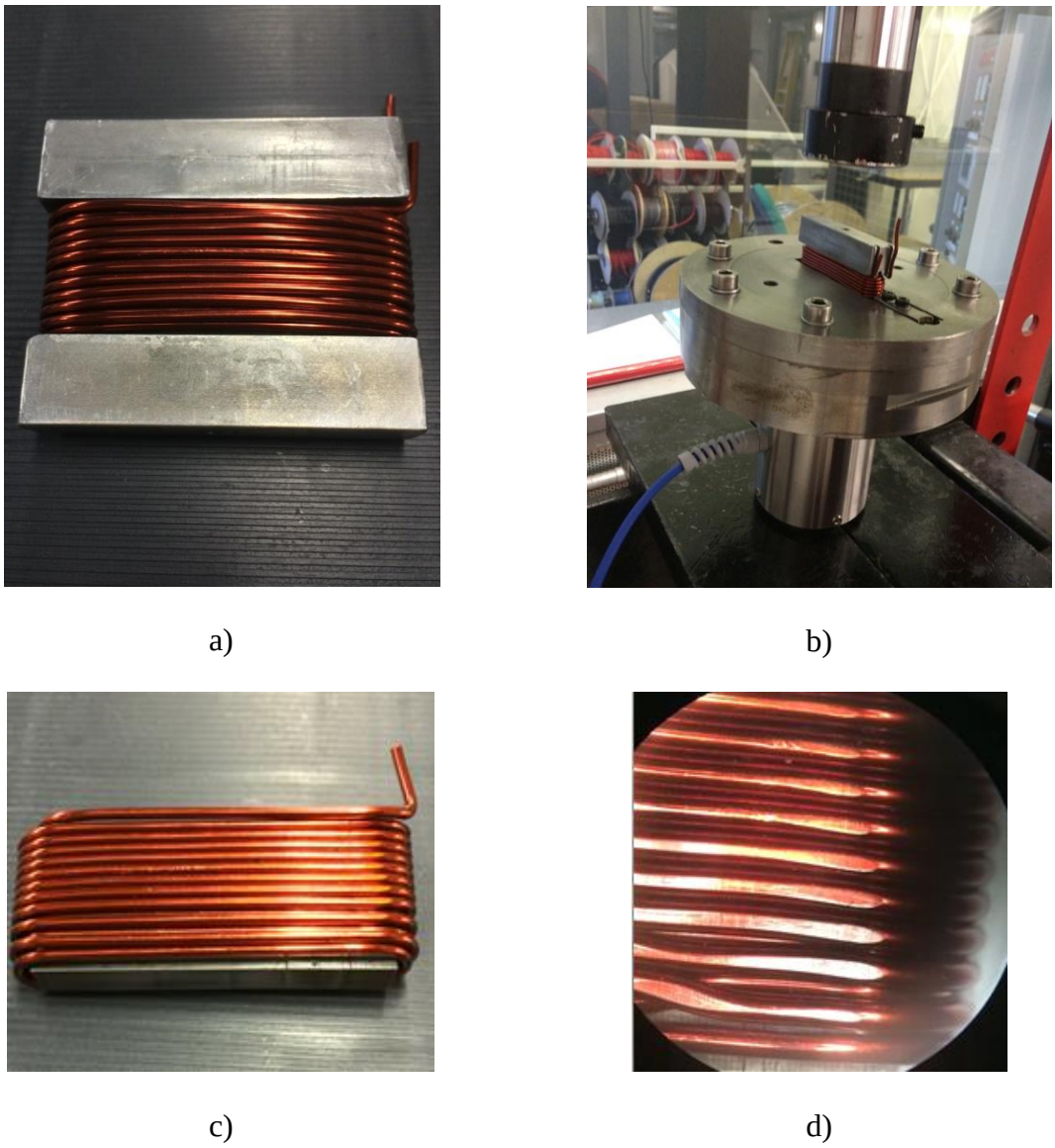

a) b)

c) d)

Figure 3.27 A coil pressing experimental approach on the laminated tooth

In Figure 3.27c, the compressed coil is shown. After compression, material failure was not observed macroscopically and insulation resistance tests have been also conducted to inspect turn to ground wall insulation resistance. There was no insulation problem (>100MΩ) regarding insulation resistance. The deformation on the magnet wires is not quite clear in macroscopic point of view. However, flattened surfaces of the wires is depicted in Figure 3.27d. The compressed coil in the experiment can be matched to Figure 3.26C as the calculated slot fill factor in FEA at the time instant 1.8e-3 sec is around 0.67. It can be seen that about 0.4 mm deformation on magnet wires is not very significant in both experiments and FEA simulations. Nevertheless, it is demonstrated that a slight improvement of slot fill factor might have

significant results on machine performance since relatively thicker conductors might be utilised by pre-pressing coils even in smaller amounts. Furthermore, thermal parameters of the coil such as the effective thermal conductivity might be improved in this case by pressing the coil because better thermal contact interfaces could be achieved between turns when the air voids between the turns are reduced.

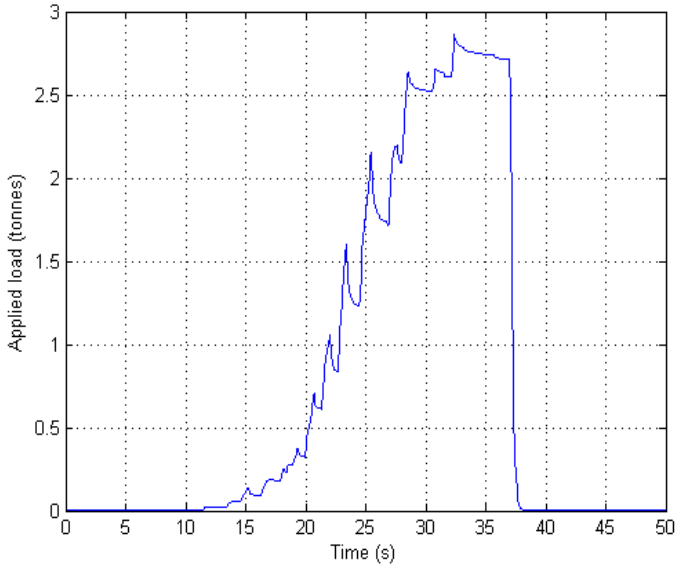

Figure 3.28 Applied loading with respect to time by a pressure transducer

Apart from the outcome of this case study, the natural time of the event in coil pressing (around 20 seconds) can be observed in Figure 3.28. As stated in Section 3.5, natural time of the event for coil pressing is not very suitable for explicit dynamic simulations requiring high speed events, but the event could be accelerated even if it is a low speed event in FEA by applying some analysis settings resulting artificially increased strain rates as discussed in this chapter thoroughly.

3.8 Multi-body Static Structural Simulations

Quasi-static coil pressing simulations are effectively based on dynamic phenomenon as it aims to deform the structure slowly and therefore the inertia force is small and can be ignored. A dynamic load might cause a structure to vibrate hence the inertia force is sufficiently big and must be considered in the simulations [98]. On the other hand, a static load is usually applied very slowly as the inertial forces need to be eliminated and the acceleration of the system is almost zero.

In this chapter, the performed FEA simulations do not use static structural approach since there are many sources of non-linearity such as contact, geometry and material and it is difficult to solve coil pressing simulations by applying static loads such as pressure or force etc.

Large strains and deformations in the model create convergence issue in static structural modelling and it is caused by several elements as follows [99]:

- Rigid body motion
- Force balance
- Material instability
- Element formulation error

These factors make the static structural modelling very challenging as rigid body motion, rapid loading rate and material plastic strain increment are all present in the coil pressing geometry. The main cause of a rigid body motion in the coil pressing geometry is that all conductors are held together only by contact and this results in a rigid body motion and a force convergence problem [99]. Also, high loading rates cause the same problem and it can be alleviated by reducing the time step (i.e. more number of steps) or loading rate. A very high number of time steps are very useful to solve non-linear FEA simulations yet this makes the problem computationally too costly. Furthermore, too large plastic strain is another difficulty, leading to a convergence issue. Finally, element formulation (i.e. meshing) is an important factor might cause a solver error. Higher order refined elements (i.e. hexahedrons) are required especially for curved surfaces to resolve the element formulation problems [99].

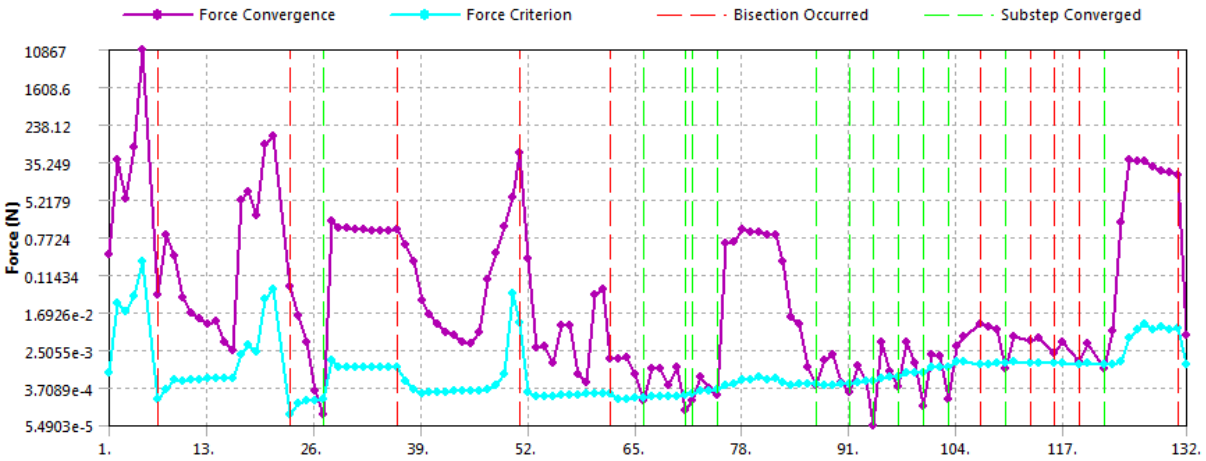

Figure 3.29 A force convergence problem obtained in static structural FEA of coil pressing

A number of static structural coil pressing simulations have been performed yet a force convergence problem was obtained as shown in Figure 3.29. If there is a significant difference between the applied load and the summation of internal forces of the equilibrium iteration, a sub-step does not converge [100]. The convergence usually is satisfied if the force residuals are less than the force convergence criterion. Although some sub-steps achieves force convergence in Figure 3.29, the overall problem does not satisfy the force criterion, meaning that the non-linearity is quite challenging when the solver is pure static. The convergence problem might be

alleviated by improving the boundary conditions, however this makes the coil pressing phenomena far from the reality.

The nature of coil pressing (i.e. problem definition in FEA) is more dynamic as the conductors have higher order degree of freedom (DOF) and they are free to move during the compression. A time dependent slow loading such as velocity boundary condition makes the coil pressing process inspect-able. Therefore, all the FEA simulations presented in this chapter is based on a dynamic modelling yet more specifically a quasi-static modelling.

3.9 Conclusion

In this chapter, the process of modelling material deformation in coil pressing has been described and demonstrated experimentally. It is shown that coil pressing simulations are challenging and require particular attention to get an accurate deformation. The simulation methodology of the coil pressing is stricter in terms of the boundary conditions compared to other FEA counterparts with implicit solvers. Non-linear material properties are also crucial for the closest prediction of the deformation in the compressed coils as the plasticity is significant in the compressed windings.

Chapter 4. Integrated Starter Generator (ISG) Design

4.1 Introduction and Objectives

The permanent magnet (PM) brushless machines are a strong candidate for EV and HEV applications. The torque density is high due to simple and light weight rotor structure. The efficiency merits of PM machines are very high compared to other type of machines such as cage IMs and SRMs [1].

As one of the principal objectives of this thesis is to investigate the pros and cons of compressed coils in terms of permanent magnet machine electro-thermal performance, this chapter mainly employs a case study which conducts a design of PM integrated starter generator for HEVs. After optimising the machine geometry, the slot dimensions have been fixed for the further investigation of on-tooth coil pressing regarding the machine electrical and thermal aspects.

Several PM machines with different pole-slot combinations and magnet topologies have been designed in this chapter based on multi-objective optimisation to select the most suitable candidate machine for the given application.

4.2 Integrated Starter Generator (ISG)

Electrification of the automotive sector has received great interest recently as it may represent a way of significantly reducing road traffic emissions. Electric vehicles can be classified as hybrid, fully electric, or range extended electric, each having its own unique requirements for the electric machine designer. Most automotive companies are working in at least one of these areas and some already have a marketable product.

Due to increase in electric power demand (usually 6 to 10 kW) in modern cars, the size of electric generator in modern vehicles has been increasing and the conventional generator systems located at the front of engine suffer from heavy weight and bulky size [101, 102]. In addition, the conventional starter motor located at the rear of the engine is coupled with the flywheel to provide starting torque demand of an internal combustion engine. In order to incorporate both functions in a single unit, integrated starter generator systems (ISGs) have been developed for micro and mild HEVs [102]. The ISG subsystem in vehicle system is outlined as in Figure 4.1.

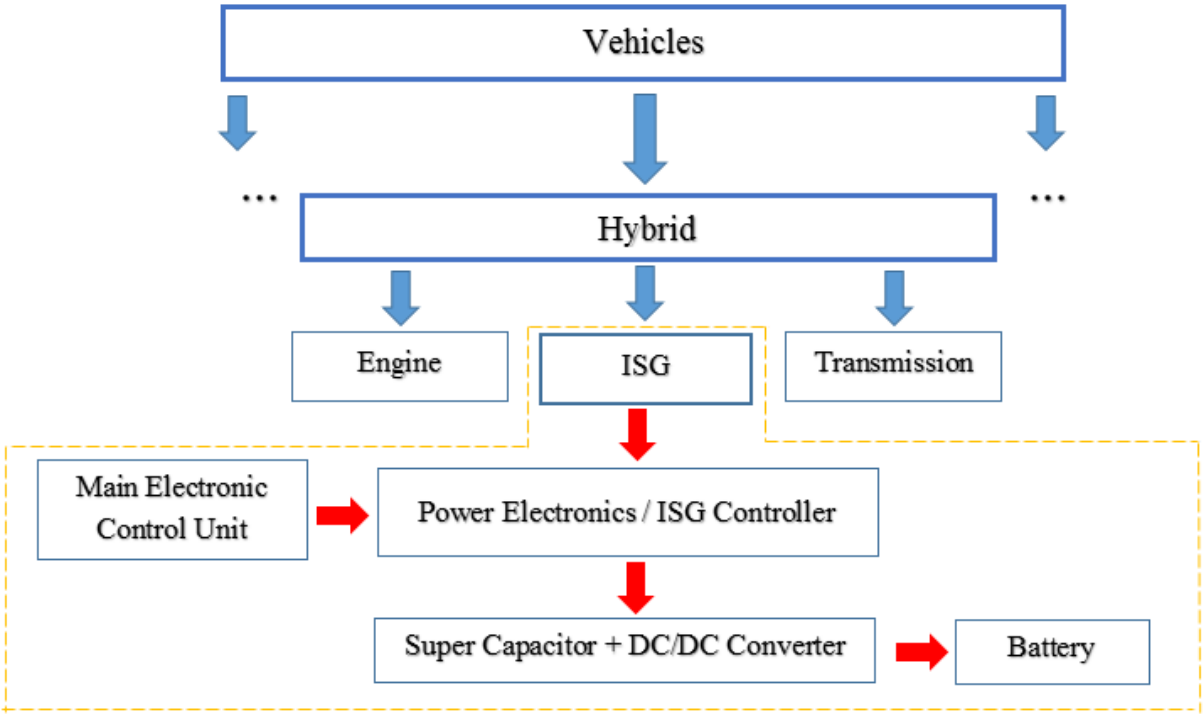

Figure 4.1 ISG subsystem in hybrid electric vehicles

The integrated starter generator (ISG) is an important device for hybrid electric vehicles (HEVs) replacing the conventional starter motor and the alternator. ISG is a part of electric vehicle system and its main functions are listed below [101-103]:

- To crank the engine (diesel or gasoline)
- To generate electric power
- Idle start-stop function, crucial at urban traffic jam and traffic lights
- Regenerative breaking during vehicle deceleration and power assistance

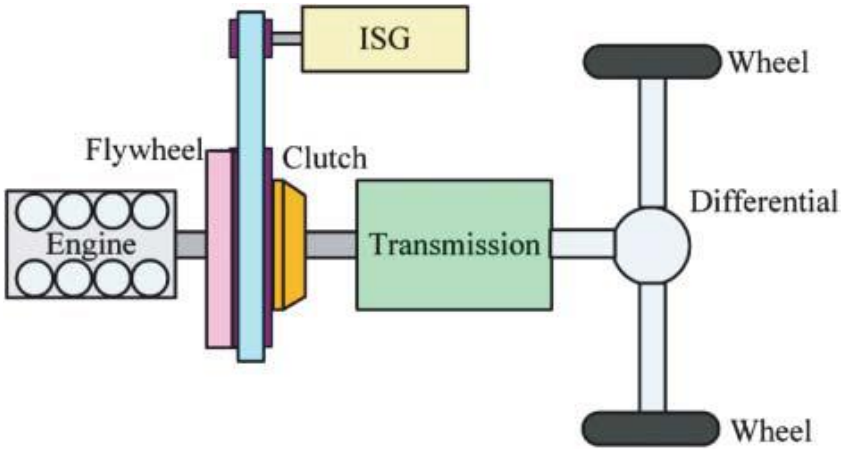

Figure 4.2 Belt-driven ISG system [102]

If the ISG is mounted the location of conventional generator or starter motor to couple with the flywheel and engine via the belt, it is called belt-driven ISG system as shown in Figure 4.2 [102].

The ISG system can be directly mounted onto the crankshaft by eliminating flywheel coupled with the engine. Although crankshaft ISG system reduces the construction cost and complexity, it should withstand severe vibration of the crankshaft that might be achieved by additional mass of iron. The crankshaft mounted ISG might require some changes on vehicle chassis to accommodate the ISG system. The crankshaft mounted ISG is depicted in Figure 4.3 [102].

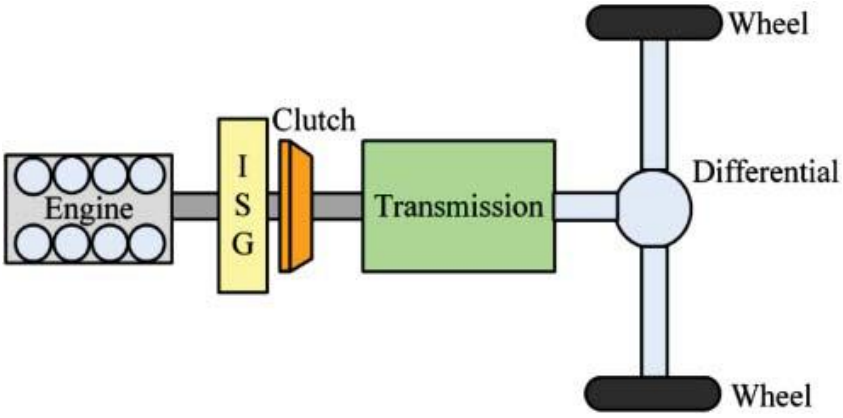

Figure 4.3 Crankshaft ISG system [102]

Unlike the machine in a pure electric vehicle, the ISG machine charges battery as it is powered by battery without stable voltage output and operates with electric loads almost at constant voltage at the speed range corresponding to engine start speed (200 to 600 rpm) to a rated speed at continuous generating power mode (6000 rpm) [103].

Induction, switched reluctance (with or without [104] permanent magnets), doubly salient and wound field brushless machines [105] have all been proposed for ISGs and a good summary of the relative merits is provided in [106]. The design and losses of brushless permanent magnet (PM) machines for ISGs have been investigated [107]. PM machines are paid more attention for this application due to their high efficiency and high torque density.

PM synchronous machine and induction machine are the main competitors for ISG system applications. As PM synchronous machines can be built with larger airgap compared to induction machines, they are better candidates for the ISGs mounted on crankshaft in which oscillations and vibration might be severe [102]. Nonetheless, the engine coupled rotor might be exposed to high temperatures that could trigger permanent magnet demagnetization for the PM ISG systems. Therefore, thermal improvement of PM ISGs is critical for crankshaft mounted systems. Better thermal characteristic should be provided to crankshaft mounted ISG

machines by further thermal investigations such as low thermal resistance machine design and advanced cooling systems.

4.3 Design of Synchronous PM Integrated Starter Generator

Typical ISGs have maximum low speed instantaneous torques of greater than 170 Nm, for a cold start, whilst being capable of delivering over 90% efficiency at high speed when operating as a generator. Size constraints imposed by the existing drive train require the use of high torque density machines to meet the maximum torque required in the available space. Key machine parameters are shown in Table 4.1 for a typical specification [108]. The machine specifications are based on a crankshaft mounted ISG system of a Volvo HEV. Note the large shaft diameter to accommodate existing shape of the vehicle clutch.

Table 4.1 Key machine parameters [108]

Stator outer diameter	290 mm
Shaft diameter	150 mm
Machine stack length	40 mm
Efficiency, 50 Nm torque at 1500 rpm	93%
Motor mode shaft torque at 200 rpm for 10 sec.	180 Nm
Maximum DC bus voltage	350 V
Generator mode power at 2000-5000 rpm	22 kW continuous
Surrounding temperature at generator mode	95°C
Surrounding temperature at motor mode	-30°C
Liquid Cooling system (Water jacket)	6 litre/min

From the efficiency point of view, PM machines with 8 to 12 poles are preferable for ISGs. Peculiarities of this ISG drive are its relatively large shaft (150 mm) and external diameters compared to traditional ISG systems as discussed in [101, 103]. For this reason, 18 slot/10 pole and 21 slot/16 pole ISG configurations are proposed for the given machine dimensions. Surface mounted and interior PM type machines were designed using FEA.

ISGs should provide continuous power at a wide speed range in generator mode. Surface mounted PM machines are not appropriate machine configurations as there is no significant salient effect due to negligible difference between d- and q- axis reluctance. However, surface PM machines have also been addressed as they represent traditional approach for the

synchronous PM machine design and also from the efficiency point of view, surface PM machines could give more insight about their inner PM counterparts.

The proposed ISGs employ concentrated single tooth windings and fractional number of slot per pole per phase which maximises the machine torque density. Although fractional slot concentrated winding (FSCW) PM machines generally have high contents of space harmonics in the airgap MMF leading to high rotor loss, cogging torque and torque ripple, they have several advantages including high power density, short end turns, high slot fill factor, flux weakening capability and fault tolerance [14, 20, 58, 97, 109]. Some unwanted effects could be mitigated by appropriate selection of pole slot combination and design optimisation.

For the given space limitations, the proposed ISGs must satisfy the following basic design constraints:

- An inner rotor directly coupled with engine crankshaft
- Single tooth windings with short end turns due to limited axial length so overlapping distributed windings are not suitable due to long end windings.
- DC bus voltage is limited and must be considered for the voltages across coils.
- A radially shallow rotor which limits the rotor magnet arrangement especially for multi-layer IPM configurations.

The optimisation of the ISGs have been achieved by using commercial FEA packages including Infolytica MagNet, Optinet and MotorSolve. After parametrisation of the initial designs with a script file, an evolutionary based optimisation with several design constraints has been carried out as outlined in a flowchart diagram in Figure 4.4.

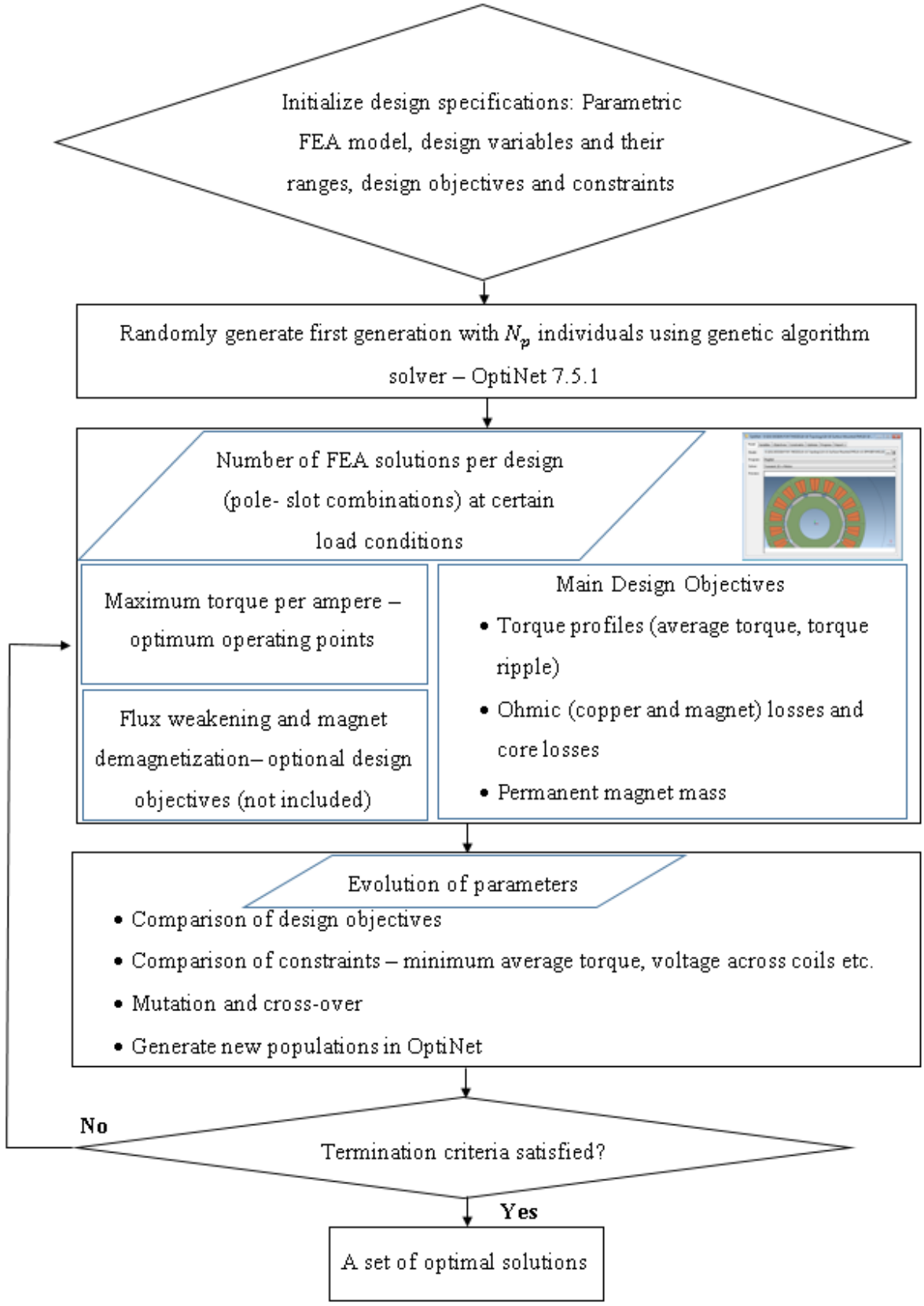

Figure 4.4 Flowchart of the ISG optimisation using genetic algorithm solver

As highlighted in Figure 4.4, a user defined multi-objective optimisation function is used to achieve the optimal ISGs. However, the proposed multi-objective function does not take into account some important parameters such as flux weakening, cogging torque and magnet

demagnetisation. These parameters, however, must be kept within acceptable limits. More sophisticated multi-objective functions or multi-physics optimizations could have been suggested but this is not the principal scope of the work in this thesis.

The fixed parameters for the optimisation process are as follows:

- Maximum outside diameter
- Maximum inside diameter
- Fixed air gap length (1 mm)
- Maximum lamination stack length

The following parameters were variables of the multi-objective function:

- Rotor outer diameter and stator inner diameter with 1 mm air-gap
- Stator core back
- Tooth width
- Tooth tip dimensions
- Slot opening
- Magnet span angle and magnet width

The objective function is targeted at reducing magnet mass, torque ripple and machine losses in generator mode at 1500 rpm. Efficiency requirement of the system at this operating condition must be greater than 93% as tabulated in Table 4.1. The proposed function is given in (4.1).

$$\{F(z)_{obj}\} = \left\{\lambda_1 \frac{M_{magnet}}{M_{magnet(max)}} + \lambda_2 \frac{T_{ripple}}{T_{ripple(max)}} + \lambda_3 \frac{Loss}{Loss(\max at\ 80\ \%\ eff)}\right\} \qquad (4.1)$$

$$0 < \{F_{obj}\} \leq 1$$

In (4.1), $F(z)$ is a vector of optimization variables including magnet dimensions and stator tooth-slot dimensions. λ_1, λ_2 and λ_3 are the penalty factors which were chosen as 0.3, 0.3 and 0.4 respectively. The optimised 18 slot – 10 pole and 21 slot – 16 pole radial flux ISGs are discussed and compared regarding their performance in the following sub-sections. Since the proposed objective function does not consider all the important design parameters, it is important to emphasise that a number of proposed ISG designs were inspected after GA optimisation and manual optimisation have also been conducted to satisfy some criterions such as material saturation, field weakening capability (selection of number of turns) and mechanical safety of buried magnets etc.

4.4 18 slot – 10 pole ISG Configurations

In PM machines, the number of magnet poles is often limited by power electronic switching capabilities as the number of magnet poles determines the fundamental electrical frequency. The higher the speed generally, the lower the number of magnet poles. Also, the number of magnet poles is limited by the rotor geometry and topology. If one increases number of magnet poles by narrowing magnets, the amount of magnet flux that leaks from magnet to magnet increases which does not contribute torque production.

18 slot-10 pole machine can be appropriate selection for the PM ISGs when the fundamental electrical frequency, magnet leakage for the given rotor dimensions, rotor radial forces and the least common multiple of pole slot combination influencing cogging torque were all taken into account for initial decision making. Some general features of 18 slot – 10 pole fractional slot PM machines are given in Table 4.2.

Table 4.2 General features of 18 slot-10 pole PM machine

18 slot – 10 pole radial flux PM synchronous machine	
Machine winding	concentrated – double layer
Reduction of coil span compared to full pitch in slot pitches	0.8
Fundamental winding factor (k_{w1})	0.735
Number of slot/pole/phase	0.6
Least common multiple of N_s and N_m	90
First static radial force harmonic (n_{rad}) if slot number is odd number	(No unbalanced magnetic pull- even slot number)
Number of symmetries	1

The number of stator slots also determines the index of the first static radial force harmonic as given in equation (4.2):

$$n_{rad} = \min\left(\frac{(2q-1)N_s \pm 1}{N_m}\right) \tag{4.2}$$

where q is any positive integer. N_s and N_m are number of stator slots and number of rotor poles, respectively. This is a valid equation if N_s is odd number. The greater n_{rad} is, the lower static radial force between the rotor and stator. Also, fractional slot windings, producing less back

EMF harmonic content, generally give more sinusoidal back EMF compared to integral slot motors where N_s/N_m is an integer.

The winding configuration (concentrated-single tooth) of 18 slot 10 pole machine is illustrated in Figure 4.5.

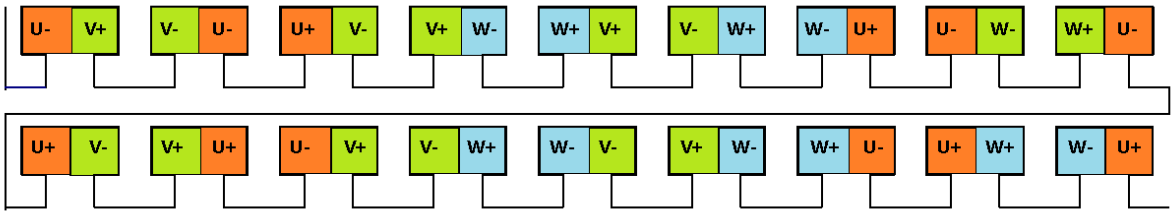

Figure 4.5 18 slot – 10 pole PM machine balanced winding layout

Based on the general features of 18 slot -10 pole PM synchronous machine, a number of magnet topologies including surface mounted and buried (both I-shape and V-shape) PM machines were designed and optimised using FEA. The performance of the proposed ISGs are thoroughly discussed in the following sub-sections.

4.4.1 18 slot-10 pole SPM ISG Machine

18 slot -10 pole surface mounted PM machine was optimised with regards to the proposed objective function given in equation (4.1). The multi-objective optimization aims to reduce magnet mass, machine losses and torque ripple in weighted factors at 1500 rpm generating mode. 93% minimum efficiency is the constraint of the optimization at this operating condition. The final dimensions of 18 slot-10 pole ISG is tabulated in Appendix – A.

Sintered Neodymium-Iron-Boron (NdFeB) magnets with a peak residual flux density of 1.29 Tesla at 20°C have been selected for the machine, which is a magnet grade of N40 family. The optimised machine has bread loaf type, radially magnetised permanent magnets achieving peak flux density of about 1.1 Tesla at no load in the machine airgap.

As given in Figure 4.6, the slotting effect in machine airgap leads to change magnetic flux density in SPM machines. This is also due to change in magnet operating point relative to the portion of the magnets exposed to stator teeth. Because of the localized flux density variations in airgap, this creates losses in magnets. Therefore, slot opening is an important parameter regarding magnet loss and machine inductance. The greater slot passage generally, the greater magnet losses in surface PM machines.

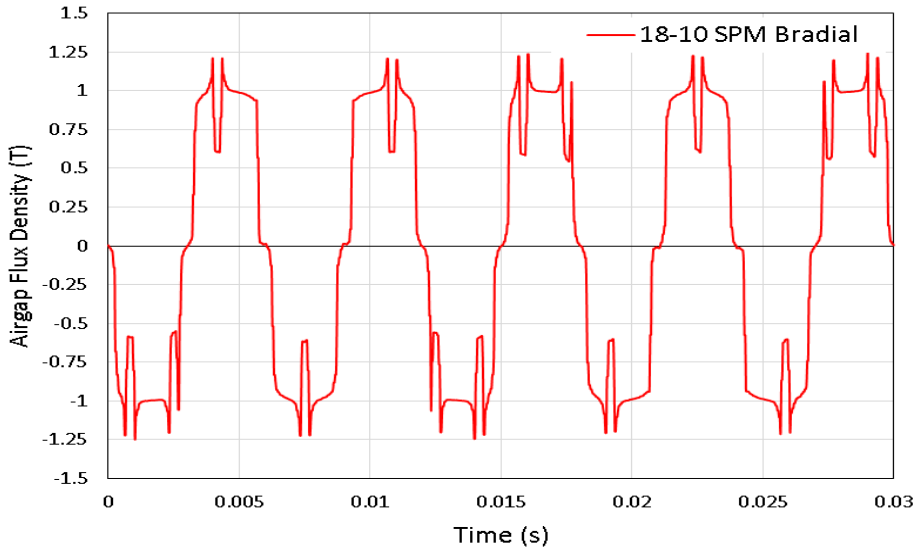

Figure 4.6 Air gap radial flux density for 18 slot – 10 pole SPM

Surface mounted PM machines might suffer from relatively greater magnet mass compared to inner PM machines as armature reaction due to machine electrical loading in the airgap tends reduce magnet flux density (i.e. operating point) leading to use more magnet material to achieve a similar amount of torque compared to accurately optimised inner PM machines. Therefore, magnet thickness in SPM machines is a critical optimisation variable that needs to be taken into account at different current loadings to achieve less-magnet material PM machines.

Permanent magnet demagnetization is also more critical in surface PM machines compared to buried PM counterparts since the magnets are directly exposed to magnetic field produced by stator coils, leading to the induction of more eddy current loss in permanent magnets that increases magnet temperature. This is not desirable as permanent magnets could be permanently demagnetised at very high temperatures because temperature increase causes higher demagnetization flux density (elevated knee point in magnet BH curve in the second quadrant).

Although it is not hardly constrained in the GA optimisation process, motor constant, K_m is the most important parameter in PM electrical machines to maximise the achievable machine torque. For 3-phase PM machines, it is given in equation (4.3) [110].

$$K_m = \frac{T}{\sqrt{P}} = B_g R_{ro} L_{st} \sqrt{\frac{3 N_m K_{wb} A_{sl}}{\rho (L_{st} + L_{end})}} \tag{4.3}$$

where T is torque, P is power, B_g, R_{ro} and L_{st} are airgap flux density, rotor outside radius and effective machine stack length respectively. N_m , K_{wb} and A_{sl} stands for number of poles, slot fill factor and slot area respectively. ρ and L_{end} are resistivity and end winding lengths respectively.

Based on equation (4.3), increasing the airgap flux density maximises torque, but this requires thicker tooth body width and stator yoke width, leading to smaller slot cross-sectional area. This is the principal equation to maximise torque for the given dimensions of the machine. It basically states the relationship between the electric and magnetic loading which can be optimised by selecting optimum δ_R which is defined as:

$$\delta_R = \frac{Rotor\ outer\ radius}{Stator\ outer\ radius} \tag{4.4}$$

δ_R is an optimisation variable that should be taken into account for the optimisation of PM machines. δ_R is found to be 0.66 for the optimised 18-10 PM ISG.

The final machine geometry for 18 slot/10 pole ISG is given in Figure 4.7 showing no load flux density distribution, refined mesh and machine schematic simultaneously.

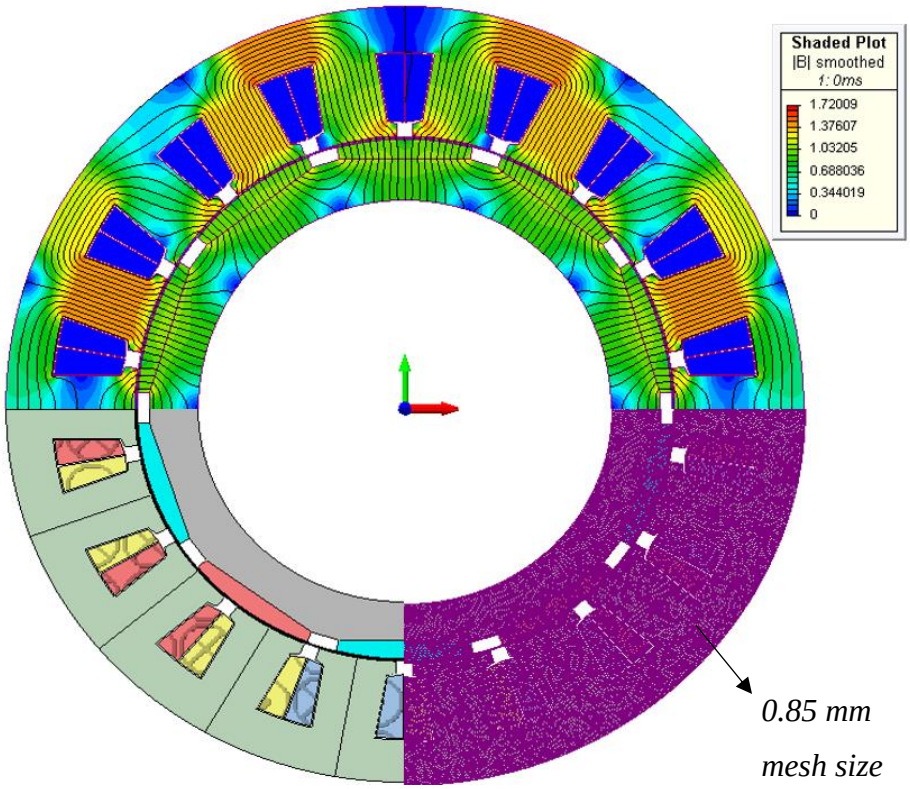

Figure 4.7 18 slot – 10 pole SPM ISG

The proposed SPM machine provides back EMF with low harmonic content, plotted in log-linear chart in Figure 4.8. Phase back EMFs and a line to line back EMF obtained from the FEA at 2000 rpm continuous generating mode are also shown in Figure 4.8.

Since the proposed ISGs must satisfy several operating conditions in motor and generator modes, the proposed SPM machine was investigated in terms of loss, efficiency, torque ripple and magnet mass.

The ISG machine has also a number of current loadings at different operating points. This results in varying current densities in phase windings that should be considered regarding the machine thermal constraints. A performance chart has been generated demonstrating different machine performance parameters at different operating conditions. The multi-objective optimization value is also determined by using the equation given in (4.1).

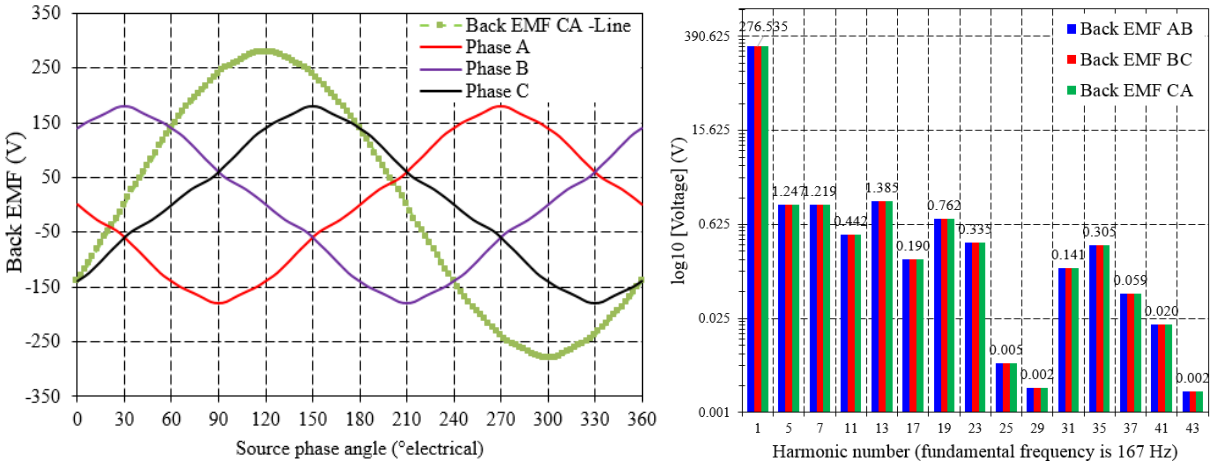

Figure 4.8 Phase and line back EMFs (left), harmonic content of line to line back EMFs (right) at 2000 rpm - FEA

Main performance parameters of 18-10 SPM ISG are tabulated at several operating points and d-q axis analysis of the machine was performed. The key results for the proposed ISG are given in Table 4.3. The detailed results of the machine at different operating conditions are given in Appendix – A.

Table 4.3 18 slot – 10 pole SPM ISG Key Results

1500 rpm Generator mode ($Efficiency_{min} = 93\%$)		
Torque:		
Mean torque	50.84	$N.m$
Torque ripple	5.056	% (in per cent)
Cogging torque (peak to peak)	1.8	$N.m$
Losses:		
Copper loss	229.01	$Watt$
Magnet ohmic loss	135.2	$Watt$
Iron loss (Hysteresis+Eddy current)	69.79	Watt
Efficiency:	94.56	%
2000 rpm continuous Generator mode – d-q axis analysis		
L_d , d-axis inductance	0.99	mH
L_q , q-axis inductance	1.04	mH
Saliency ratio (ξ)	1.05	–
Average reluctance torque	0.007	Nm

Power factor	0.85	–

In Figure 4.9, the torque-speed envelope of the machine at different advance angles are given showing that the machine torque drops quickly above the base speed.

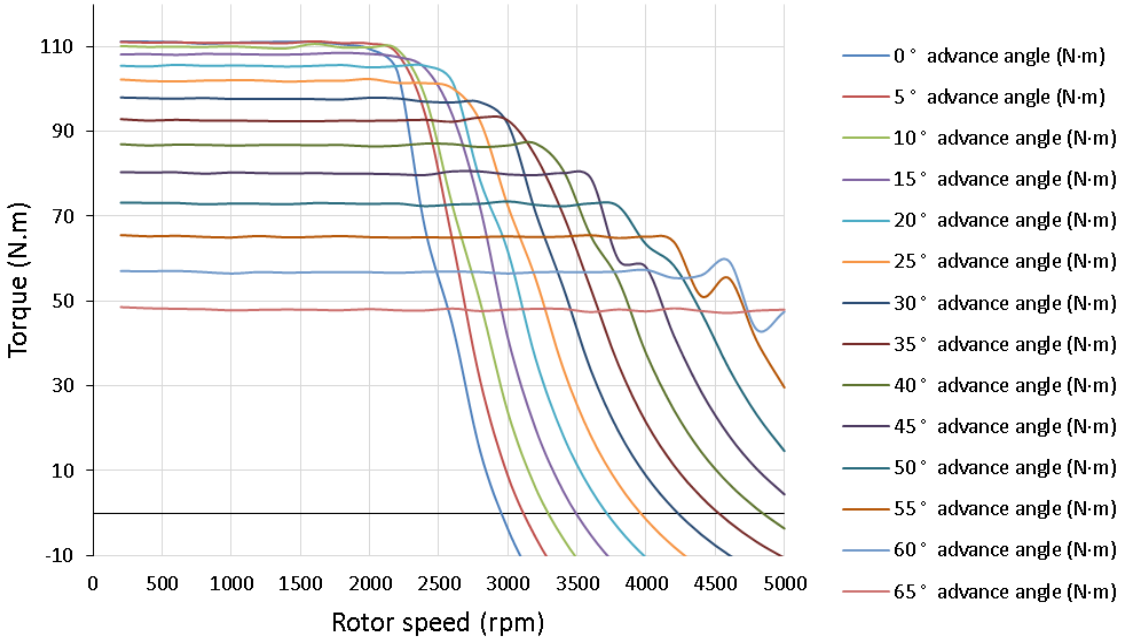

Figure 4.9 Torque-speed envelope of 18 slot – 10 pole SPM ISG

4.4.1.1 Brief Discussion

The important design results have been demonstrated for 18 slot-10 pole SPM ISG machine. The performance parameters are discussed as follows:

- The proposed ISG has 94.56% efficiency at 1500 rpm. The magnet losses (135.2 Watts) are quite significant as the magnets are surface mounted and machine current loading is relatively high to produce the rated torque. The magnet mass dependent upon the chosen magnet thickness is also significant as the proposed machine must be resistant to demagnetization at higher speeds whilst the armature current is shifted to -d-axis. Nonetheless, demagnetization on PMs was not observed for the worst case when the armature current is in the negative d-axis at higher speeds.
- It was shown that the SPM ISG can generate sinusoidal phase back EMFs with low harmonic contents.
- Current densities at different loadings were determined. The current density, J_{rms} equals to 25.5 A/mm^2 at motoring mode for 10 sec at -30°C surrounding temperature. The current density at motoring mode would not be a problem due to a short time loading.

- The machine core losses, dependent on electrical frequency are not very significant as it is not a high speed machine. Thin non-oriented electrical steel with 0.18 mm lamination thickness (NO18[1]) was chosen for the proposed ISGs.
- The rotor saliency, ($\xi = 1$) is not presented in the proposed SPM ISG and the machine field weakening or constant power region might not be sustained at higher speeds as Figure 4.9 demonstrates that at rated current, the machine torque after base speed drops quickly resulting in narrow constant power region. Moreover, it is shown that power factor of the surface mounted machines can be high enough that is 0.85 in this case.
- The machine does not provide reluctance torque as there is no difference between d-q axis inductances.
- The proposed ISG has about 5% torque ripple at 1500 rpm which is high as less torque ripple for traction applications is always desired. It could be further reduced by elimination of harmful PM flux density harmonics in the airgap or magnet skewing can be employed [111].

4.4.2 18 slot – 10 pole buried I-Shape ISG Machine

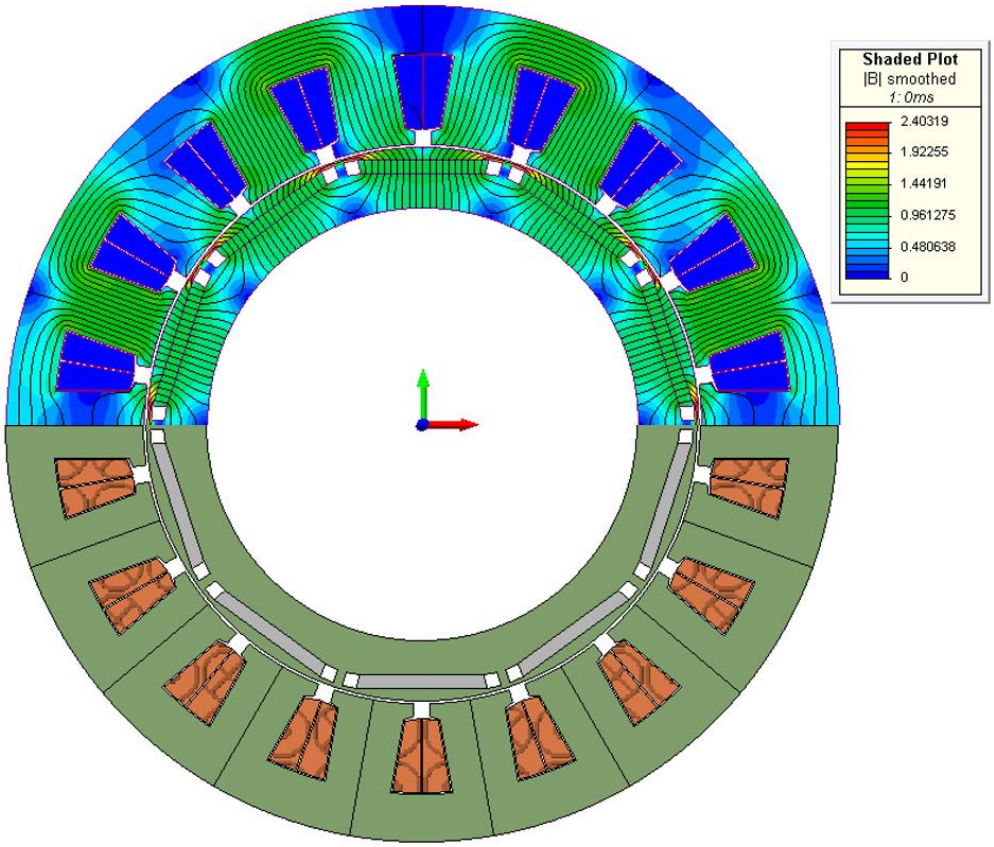

Figure 4.10 18 slot – 10 pole I-shape PM ISG at no load

[1] The mechanical properties NO18 electric steels can be found in Appendix – A.

The interior permanent magnet (IPM) machines combine magnetic and reluctance torque as they utilise the reluctance torque due to the difference between d- and q- axis inductances. IPM machines make the motor suitable for high speed applications. In order to see the performance merit of 18 slot- 10 pole ISG with interior magnet topology, a buried I-shape PM ISG with 18 slot and 10 pole was designed and optimised as illustrated in Figure 4.10 at no-load[2].

The phase back EMFs and a line to line back EMF are given in Figure 4.11 below with its harmonic content in log-linear chart. Only odd harmonics are shown since even harmonics are in phase with each other in Y-connected machines.

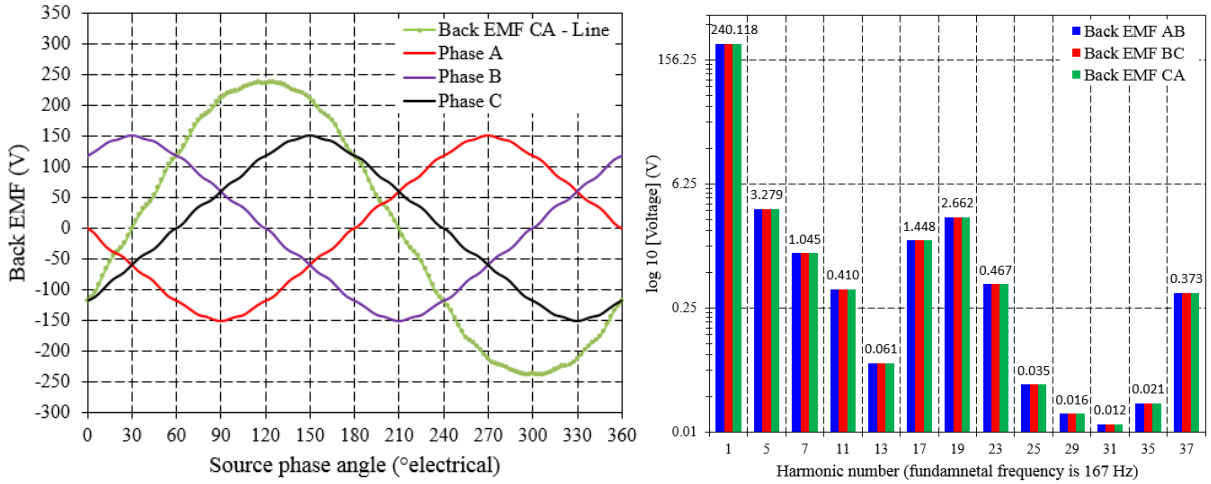

Figure 4.11 Phase and line back EMFs (left), harmonic content of line to line back EMFs (right) at 2000 rpm - FEA

As shown in Figure 4.11, the line to line back EMF is close to a sinusoidal waveform but the 5th, 7th, 17th and 19th harmonics exist in smaller amplitudes that might be distorting the fundamental component. The key results for the proposed ISG are given in Table 4.4[3] and Figure 4.12.

Table 4.4 18 slot – 10 pole buried I-shape PM ISG Key Results

1500 rpm Generator mode ($Efficiency_{min} = 93\%$)		
Torque:		
Mean torque	50.02	$N.m$
Torque ripple	4.94	% (in per cent)
Cogging torque (peak to peak)	0.51	$N.m$
Losses:		
Copper loss	270	$Watt$
Magnet ohmic loss	65.48	$Watt$
Iron loss (Hysteresis+Eddy current)	75.35	Watt

[2] The optimised machine dimensions are given in Appendix – A.
[3] The detailed results of the machine at different operating conditions are given in Appendix – A.

Efficiency:	94.77	%
2000 rpm continuous Generator mode – d-q axis analysis		
L_d , d-axis inductance	1.47	mH
L_q , q-axis inductance	1.87	mH
Saliency ratio (ξ)	1.272	–
Average reluctance torque	10.3	Nm
Power factor	0.75	–

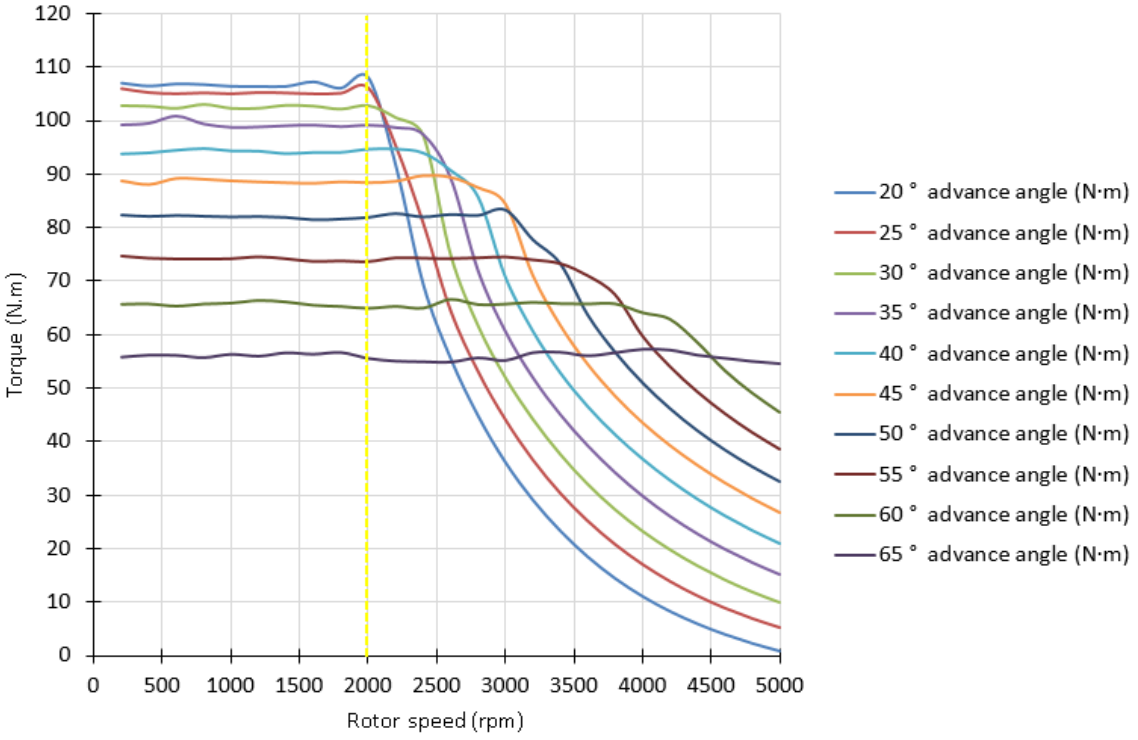

Figure 4.12 Torque-speed envelope of 18 slot – 10 pole buried I-shape PM ISG

4.4.2.1 Brief Discussion

For the ISG applications, the interior PM machines are usually preferred rather than surface mounted PM machines. A summary of the key performance parameters is given as follows:

- Since the magnets are embedded into the rotor core, they are less exposed to time and space harmonics of magnetic field in machine airgap. This shields the permanent magnets from eddy currents inducing loss on magnets. Therefore, the magnet loss (65.4 Watts) has been halved in the interior PM ISG in comparison to the SPM ISG design. It is also noted that the magnet mass has been reduced by about 28% for the interior PM machine compared to the SPM ISG design. The similar torque can be achieved with less magnet amount of magnet as the reluctance torque (10.3 Nm) is present.
- The I-shape buried PM ISG has a saliency of 1.27 which is low since the topology of the I-Shape buried PM machines does not quite differ from the surface mounted PM machines. By increasing the magnet layers in rotor core, the difference between d- and

q- axis inductances could be improved as it contributes to saliency to generate more reluctance torque.

- The proposed I-shape PM ISG has 94.7% efficiency at 1500 rpm which is higher than the SPM ISG machine. This improvement is mainly due to the reduction of magnet losses. However, rotor core losses increases in this case due to sub and superior harmonics of magnetic field in airgap inducing eddy current rotor losses in the rotor iron.
- It can be noted that at low speed motoring mode, the current density is very high which is 30.2 A_{rms}/mm^2. This shows that the effect of reluctance torque at 200 rpm is not significant and the machine requires more current to satisfy 180 Nm average torque value for 10 sec cold start. Another important condition is that the peak airgap flux density in inner PM machine is usually lower than surface PM machines because of magnet leakage is more significant in interior magnet PM machines. The peak airgap flux density, $\widehat{B_p}$ at no load condition was found to be 0.88 Tesla in this case.
- The proposed I-shape PM can provide continuous power between 2000- 5000 rpm. As shown in Figure 4.12, the torque requirement of the machine at higher speeds can be satisfied up to 5000 rpm. The machine will not have very large constant power to speed ratio, but by controlling d-axis current and load angle, 22 kW constant power can be achievable up to 5000 rpm.

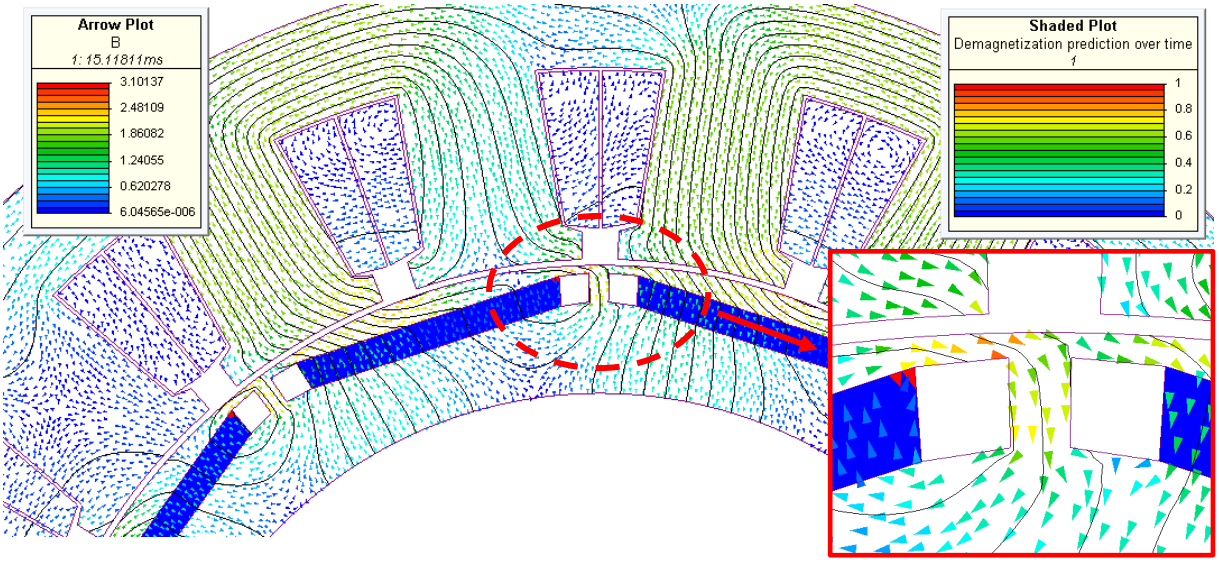

Figure 4.13 Demagnetization at high current loading in motor mode

- Magnet demagnetization needs to be evaluated for the optimised machine. At 200 rpm motoring mode when magnet temperature is 100°C, demagnetisation over time is obtained in FEA as shown in Figure 4.13. Upper corners of the magnets experience demagnetisation due to very high flux density (about $2.9 - 3\ T$) in iron bridges.

4.4.3 18 slot – 10 pole buried V-Shape ISG Machine

V-shape arrangement of the rotor structure can increase magnet excitation dosage effectively in comparison to straight type permanent magnets [112]. By arranging the magnets in a V-shape, magnet thickness can be reduced without risk of demagnetisation. The possible reasons of it are: either magnet leakage flux is increased hence improving the operating point of permanent magnets or magnet is being screened from the armature reaction flux [113, 114]. An appropriate angle between V-shape magnets under each pole reduces cogging torque and torque ripple significantly. Magnetic bridge is also an important parameter to maximise the torque characteristics with an optimal barrier shape [115]. It is also shown that the optimised V-shape machines might exhibit different performance in low speed region and field weakening regions [116]. Furthermore, segmentation of V-shape magnets provides wider field weakening region due to larger d-axis inductance and less PM flux linkage according to Duan et al [117].

18 slot-10 pole V-shape PM machine has been investigated for the ISG application. The optimisation variables including magnet thickness, V-angle, shaft distance, iron bridge thickness, flux barriers of the machine are shown in Figure 4.14.

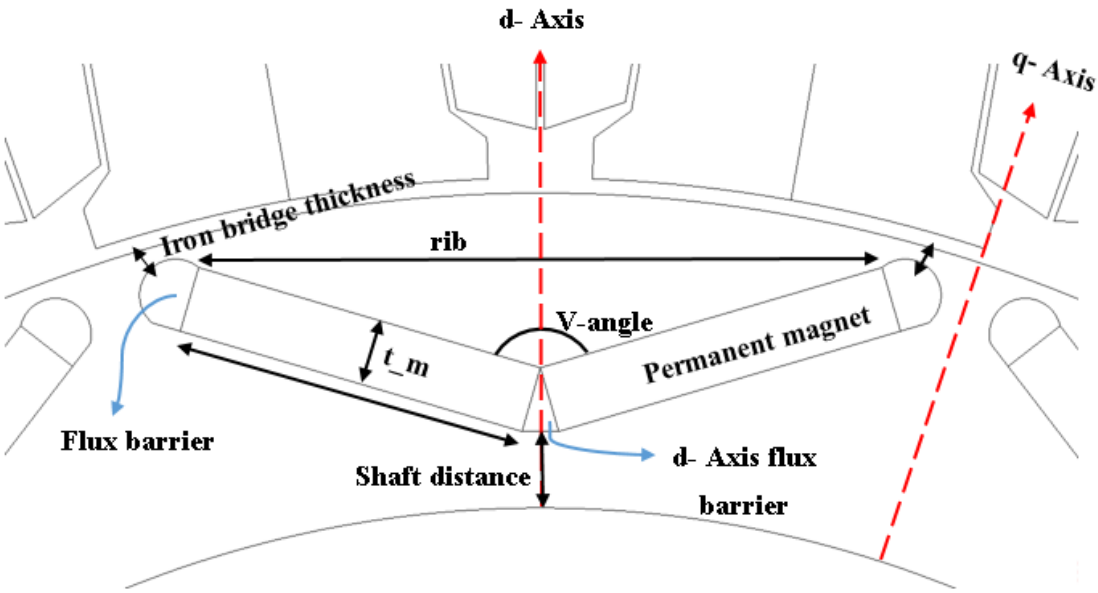

Figure 4.14 Key geometrical parameters of the V-shape PM ISG

No-load flux function and magnetic field plot are depicted in Figure 4.15 for the 10 pole – 18 slot V-shape PM ISG.

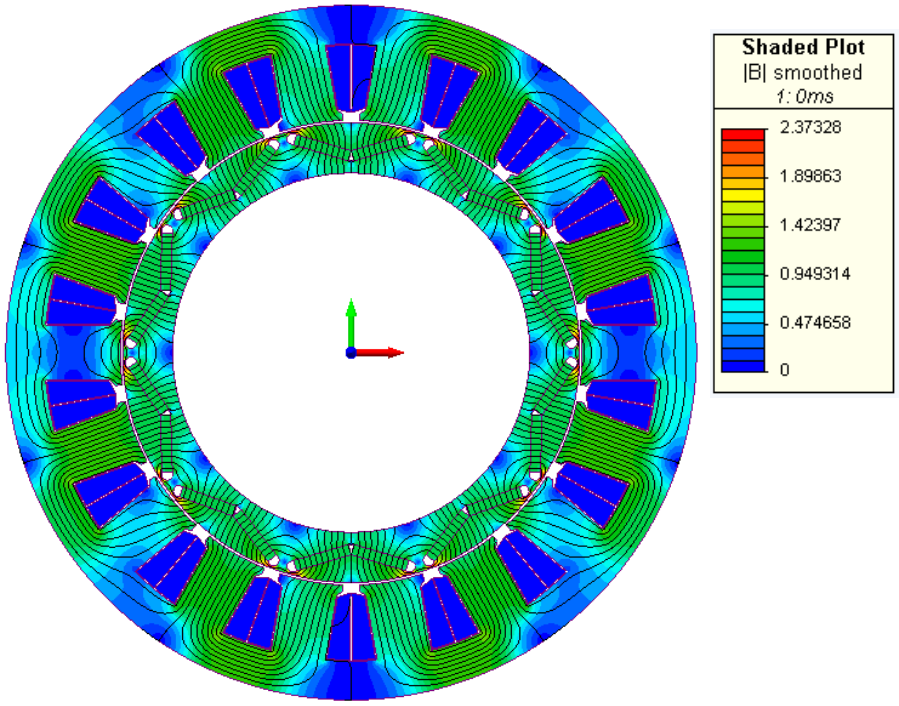

Figure 4.15 Magnetic flux density distribution in 18 slot – 10 pole V-shape ISG at no load

The phase back EMFs and a line to line back EMF are given in Figure 4.16 with its harmonic content, which is in log-linear scale to emphasise the low amplitude harmonics.

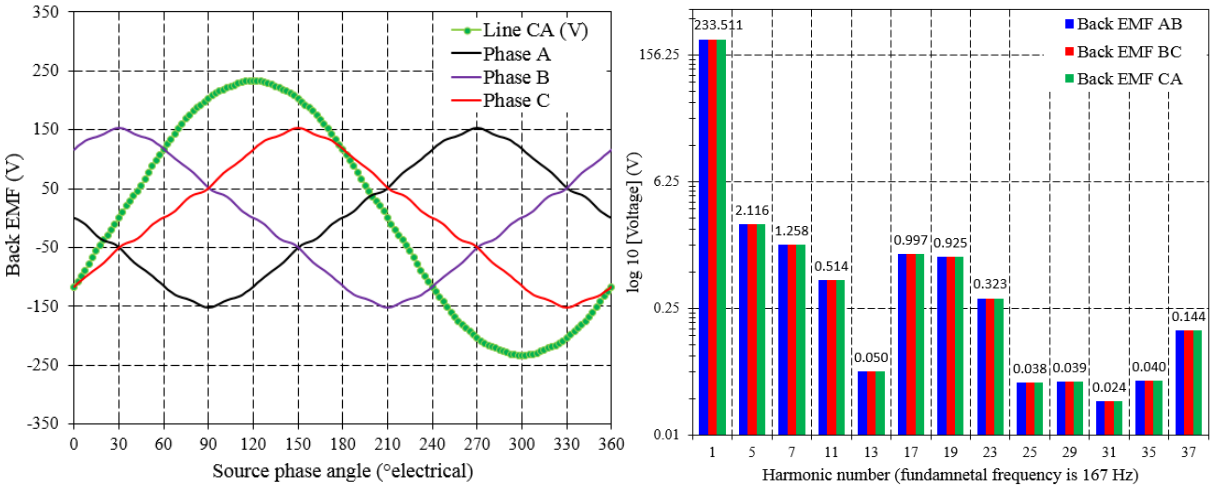

Figure 4.16 Phase and line back EMFs (left), harmonic content of line to line back EMFs (right) at 2000 rpm - FEA

The key results for the proposed ISG are given in Table 4.5 and Figure 4.17. The detailed results of the optimised V-shape ISG at different operating conditions are given in Appendix – A.

Table 4.5 18 slot – 10 pole interior V-shape PM ISG Key Results

1500 rpm Generator mode ($Efficiency_{min} = 93\%$)		
Torque:		
Mean torque	50.3	$N.m$
Torque ripple	3.35	% (in per cent)

Cogging torque (peak to peak)	0.86	$N.m$
Losses:		
Copper loss	266.8	$Watt$
Magnet ohmic loss	24.16	$Watt$
Iron loss (Hysteresis+Eddy current)	81.57	Watt
Efficiency:	95.29	%
2000 rpm continuous Generator mode – d-q axis analysis		
L_d , d-axis inductance	1.42	mH
L_q , q-axis inductance	2.01	mH
Saliency ratio (ξ)	1.415	–
Average reluctance torque	18.3	Nm
Power factor	0.754	–

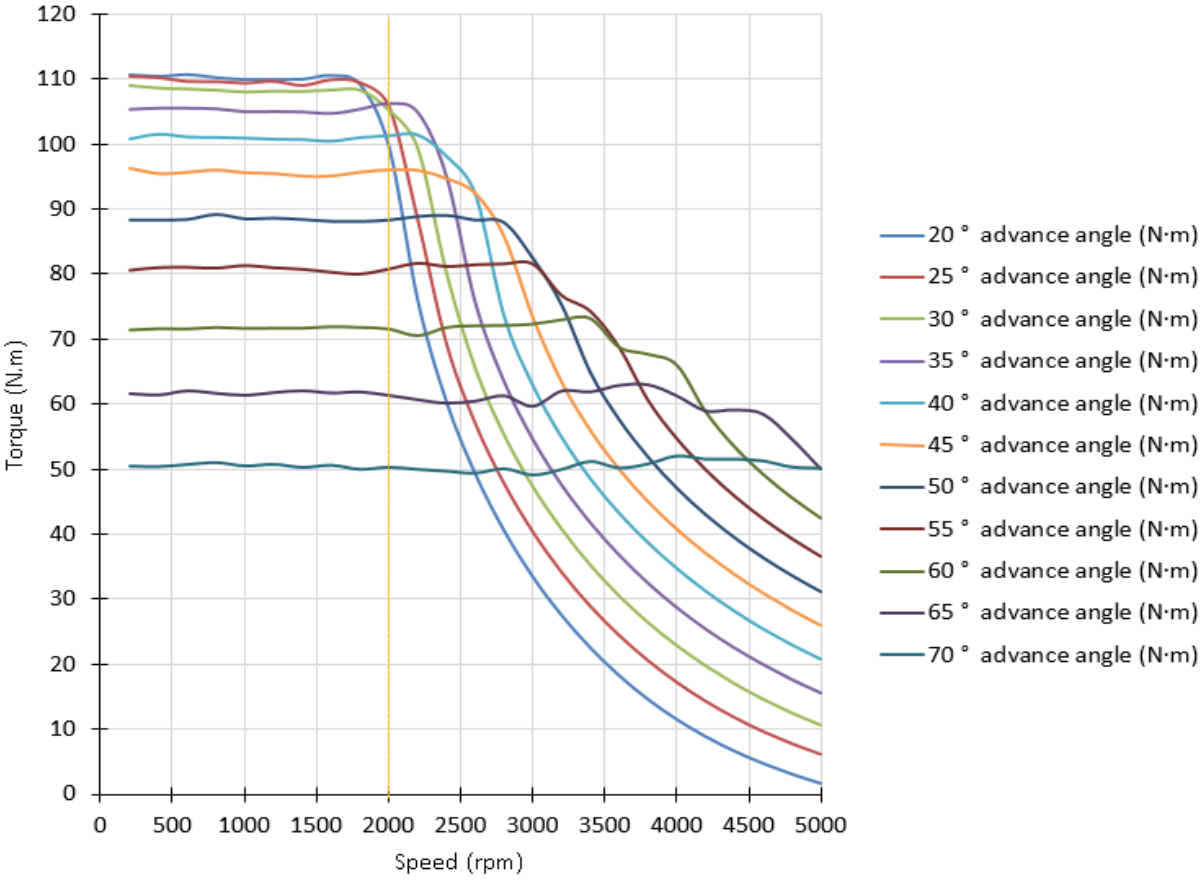

Figure 4.17 Torque-speed envelope of 18 slot – 10 pole V-shape PM ISG at rated current

4.4.3.1 Brief Discussion

18 slot – 10 pole V-shape PM machine has been designed to meet the requirements of ISG. The main features of the proposed ISG are as follows:

- It is shown that the V-shape PM ISG has higher efficiency merit (95.29%) in comparison to interior I-shape and SPM ISGs.

- V-shape PM ISG gives the lowest value of multi-objective optimization in 18 slot -10 pole machines. As the objective function should give the lower values in optimal solutions, V-shape PM ISG is better than interior I-shape and SPM machines proposed in Section 4.4.1 and 4.4.2.
- Due to improved saliency with V-shape arrangement of magnets resulting in higher reluctance torque, phase currents required for the rated torque is reduced leading to drop in current densities at different operating points. Although the surface PM machines give higher flux density in machine air gap, the V-shape machines can achieve high enough magnet flux density by accurate arrangement of magnetic bridges and the V-shape angle as given in Figure 4.18. Magnetic flux density is an important parameter to improve the motor constant and the maximum achievable torque.

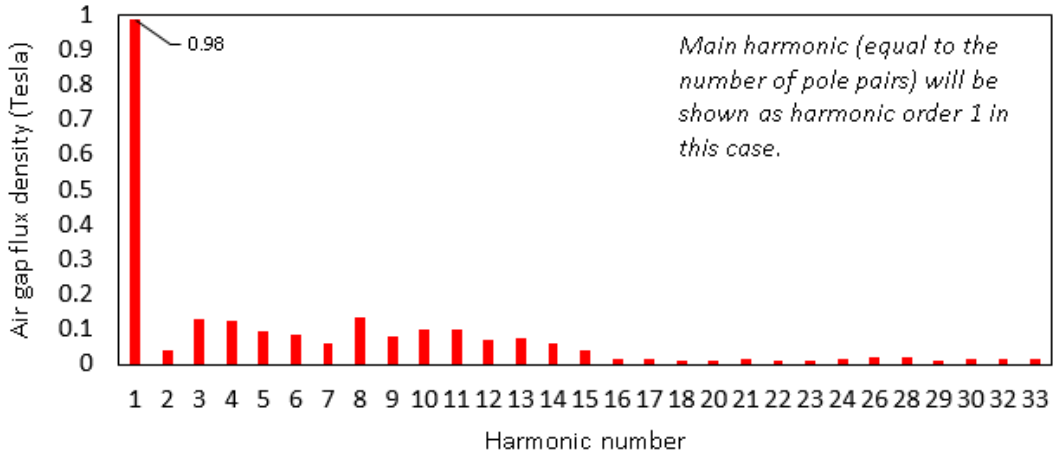

Figure 4.18 Air gap flux density harmonics at no load

- Magnet ohmic losses due to the induced eddy currents have been reduced significantly compared to interior I-shape and SPM ISG machines. It is found to be 24.1 watts at 1500 rpm which gives about 82% less magnet loss compared to SPM ISG machine. It should be noted that the magnet masses are not equal in this comparison.
- Total magnet mass for the optimised V-shape machine is only 0.64 kg which is about 0.25 kg less magnet mass compared to SPM ISG.
- 17.5 % total torque is obtained from the machine reluctance with 1.41 saliency ratio. The saliency is still not very high as it could be further improved by proposing multi-layer interior magnet layer with flux barriers. However, the rotor core is relatively shallow in the given machine dimensions making the machine not appropriate for multi barrier PM arrangements.
- As shown in Figure 4.17, the machine field weakening operating region is significantly improved compared to 18 slot – 10 pole SPM machine. The proposed ISG produce sufficient amount of torque in the field weakening region to be able satisfy constant

power operation up to 5000 rpm although Figure 4.17 shows only the rated current torque-speed envelope at different current advance angles.

- Magnet demagnetisation was not observed when the stator current in -d-axis and magnets are directly under the teeth at 2000 rpm continuous generator mode of operation at 100°C surrounding temperature because the magnets are screened from the armature reaction in the machine airgap.

4.5 21 slot – 16 pole ISG Configurations

A crankshaft integrated starter generator for HEV requires smooth operation with low cogging torque as it acts as a direct drive motor. It is undesirable to have high torque ripple, vibration and noise in electric vehicle applications. Also, high cogging torque and torque ripple deteriorates the characteristics of speed control at low speeds [118].

If N_s and $2p$ represent number of slots and pole pairs of a PMSM respectively, the greatest common factor of N_s and $2p$ is equal to 1 in asymmetric PM machines[118]. Otherwise, it is symmetric. 21 slot -16 pole PMSM is an asymmetric PM machine so that it can provide smooth operation if the rotor eccentricity is accurately positioned. Due to given dimensions of the ISG for design and optimisation, 21 slot – 16 pole PM machine can be a candidate for the ISG machine. Some general features of 21 slot – 16 pole PM machines are tabulated in Table 4.6.

Table 4.6 General features of 21 slot – 16 pole PM machine

21 slot – 16 pole radial flux PM synchronous machine	
Machine winding	concentrated – double layer
Reduction of coil span compared to full pitch in slot pitches	0.312
Fundamental winding factor (k_{w1})	0.890
Number of slot/pole/phase	0.438
Least common multiple of N_s and N_m	336
First static radial force harmonic (n_{rad}) if slot number is odd number	1.25 – asymmetric

The winding configuration for 21 slot -16 pole PMSM is illustrated in Figure 4.19 showing that the proposed machine cannot be divided into sub-machines due to asymmetric phase windings.

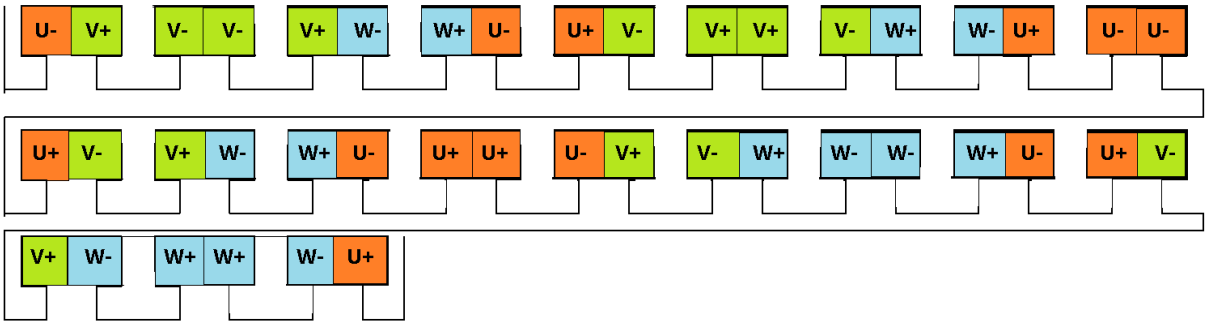

Figure 4.19 21 slot – 16 pole PM machine balanced winding layout

A number of 21 slot – 16 pole PM machine topologies regarding location of magnets in the rotor has been investigated. In other words, surface mounted PM, interior I-shape PM and interior V-shape PM ISGs are thoroughly investigated, that aims to achieve the highest performance in terms of multi-objective optimisation.

4.5.1 21 slot – 16 pole SPM ISG Machine

21 slot – 16 pole SPM machine is designed to be able to propose the most appropriate design for ISG application. The machine geometry with no load flux density is shown in Figure 4.20.

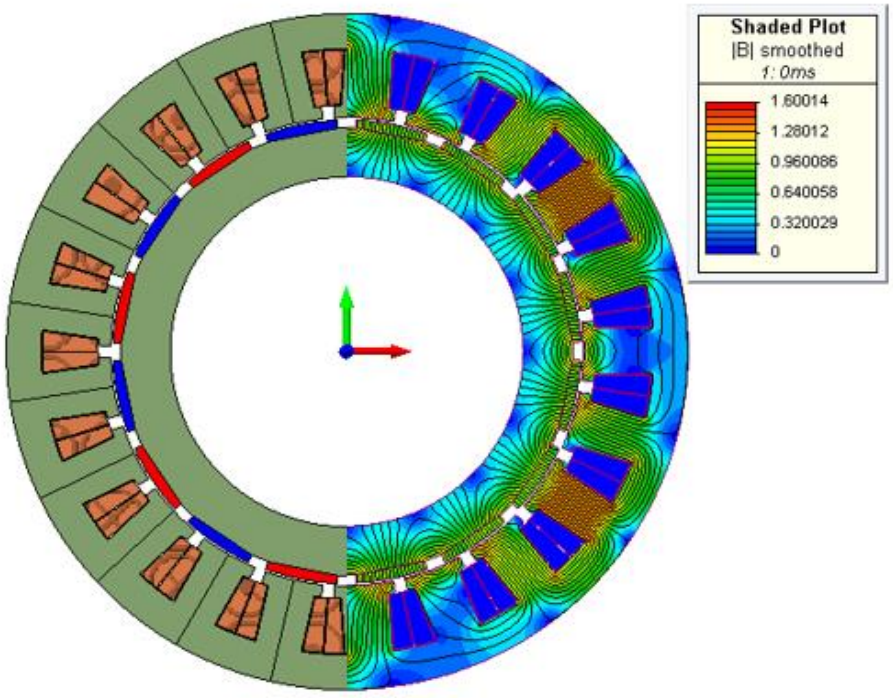

Figure 4.20 21 slot – 16 pole machine geometry with no load flux density

The FEA phase back EMFs and their line to line harmonic contents are given in Figure 4.21. The optimised machine dimensions for 21-16 SPM ISG are given in Appendix – A.

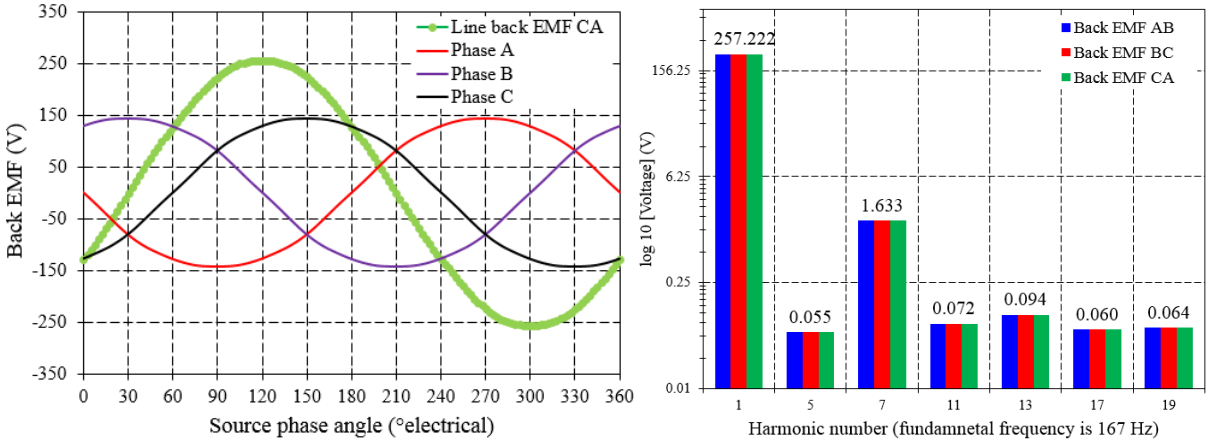

Figure 4.21 Phase and line back EMFs (left), harmonic content of line to line back EMFs (right) at 2000 rpm - FEA

As shown in Figure 4.21, line to line back EMF consists of fundamental + 7^{th} harmonic if harmonic content amplitudes less than 0.1 volt are neglected. This indicates that 21 slot – 16 pole SPM gives highly sinusoidal line back EMF at the Y-connected machine output.

The key results for the proposed ISG are given in Table 4.7 and Figure 4.22. The detailed results of the 21slot – 16 pole SPM ISG at different operating conditions are given in Appendix – A.

Table 4.7 21 slot – 16 pole SPM ISG Key Results

1500 rpm Generator mode ($Efficiency_{min} = 93\%$)		
Torque:		
Mean torque	50.6	$N.m$
Torque ripple	1.24	% (in per cent)
Cogging torque (peak to peak)	0.2	$N.m$
Losses:		
Copper loss	158.9	$Watt$
Magnet ohmic loss	150.3	$Watt$
Iron loss (Hysteresis+Eddy current)	79.66	Watt
Efficiency:	95.11	%
2000 rpm continuous Generator mode – d-q axis analysis		
L_d , d-axis inductance	0.74	mH
L_q , q-axis inductance	0.74	mH
Saliency ratio (ξ)	1	–
Average reluctance torque	0	Nm
Power factor	0.77	–

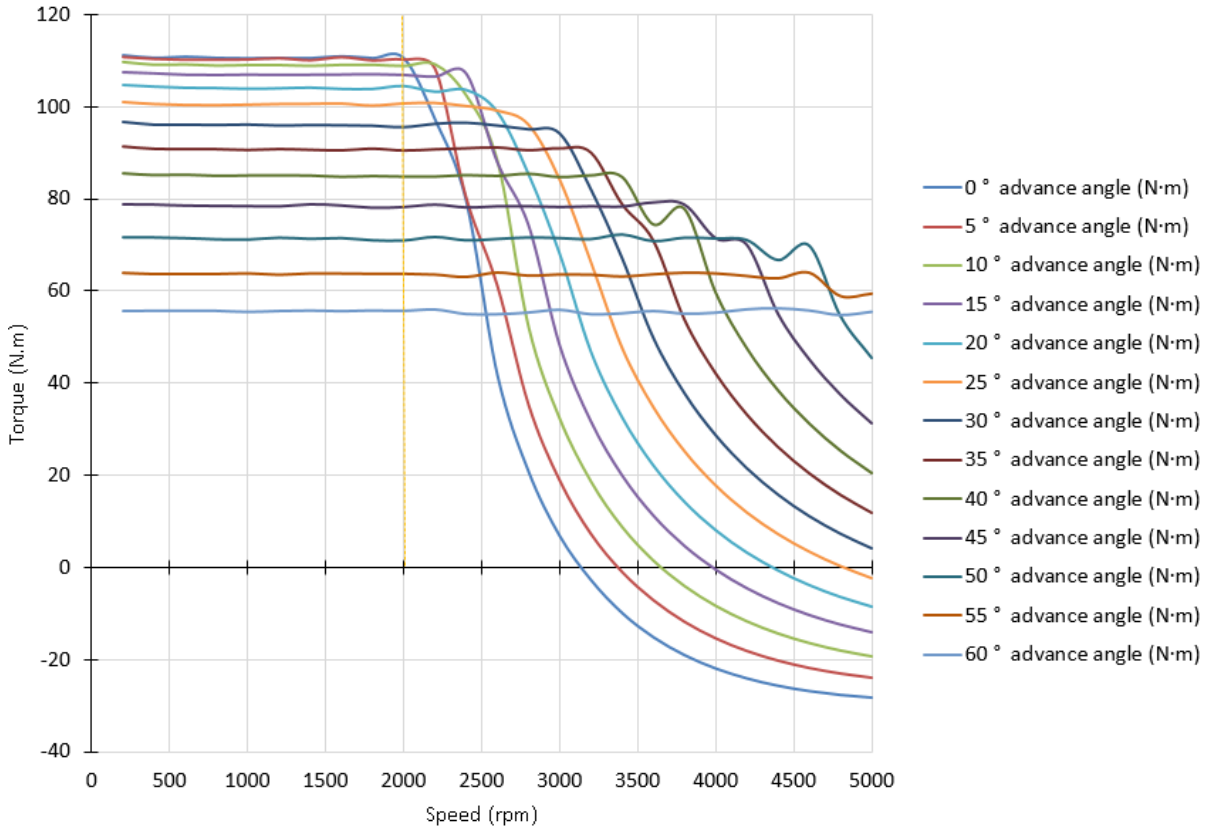

Figure 4.22 Torque – speed envelope of 21 slot – 16 pole SPM ISG at rated current

4.5.1.1 Brief Discussion

The analysis of 21 slot – 16 pole SPM ISG is discussed as follows:

- It is shown that 21 slot -16 pole machine topology can provide smooth torque with very low torque ripple (1.24% at 1500 rpm and 1.77% at 2000 rpm).
- The multi-objective function gives lower value when compared to 18 slot -10 pole ISG configurations proving that asymmetric 21 slot – 16 pole machine can be better choice in terms of torque ripple, machine loss and magnet mass.
- Magnet mass is calculated to be 0.607 kg which is the lowest magnet mass for the designed ISG configurations.
- The proposed SPM machine may not be suitable for the ISG applications when field weakening is considered. If the applied current is reduced and the machine current angle is altered in field weakening region, SPM ISG would not provide continuous power at very high speeds as the reluctance torque is not presented due to saliency ratio which is 1 in this case.
- Demagnetization proximity field for the permanent magnets is also investigated at 2000 rpm generating mode when the rated current is in negative d-axis and the surrounding temperature is 100°C. As shown in Figure 4.23, the higher the magnetic field (i.e. close

to zero or positive values), the more susceptible magnets for demagnetization, because the value of demagnetization proximity (T) is associated with magnetic field difference between stator and permanent magnets. Due to armature reaction magnetic field, magnet operating point varies. In order to prevent permanent demagnetization, the worst case scenario when stator field is directly opposite to magnet field should be investigated. In this case, the permanent magnets are safe and demagnetization is not observed.

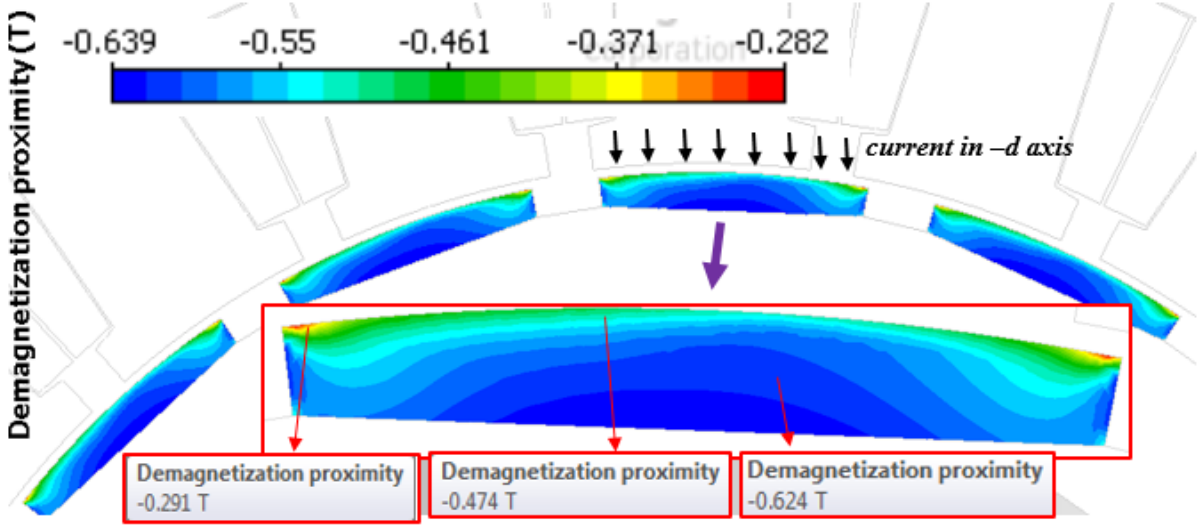

Figure 4.23 Demagnetization proximity field when negative d-axis current is applied at 2000 rpm generator mode at 100°C surrounding temperature

4.5.2 21 slot – 16 pole interior I-shape PM ISG Machine

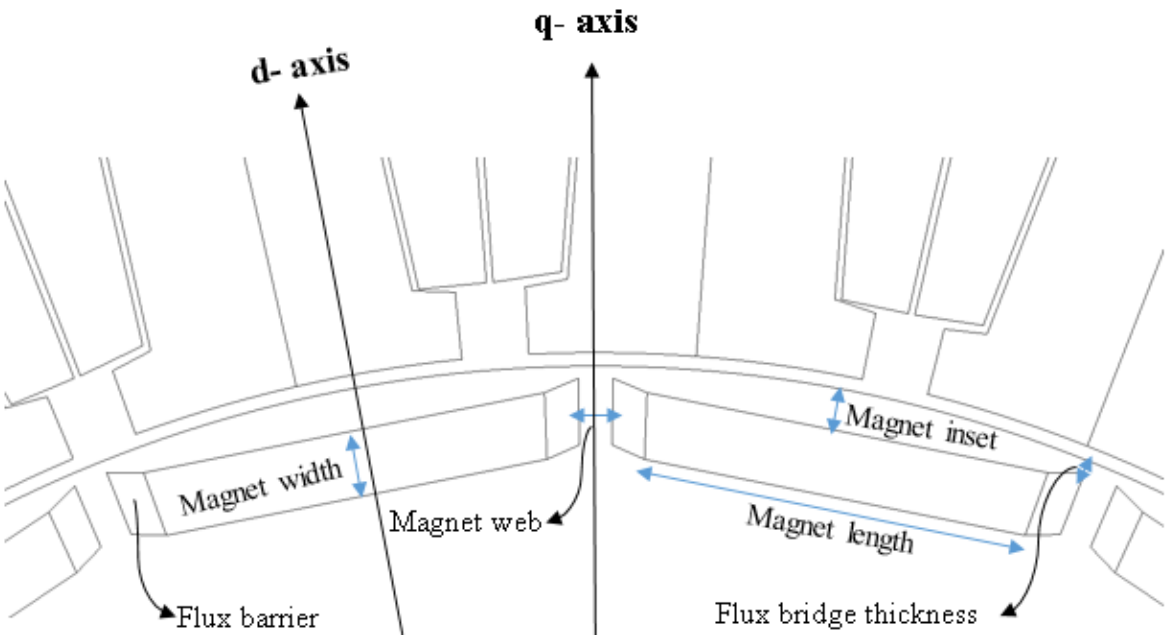

Figure 4.24 I-shape interior PM rotor geometry and dimensions

The interior I-shape PM ISG geometry is shown in Figure 4.24. Tangential I-shape PM machines offer saliency and reluctance torque. As permanent magnets are screened from airgap magnetic field, eddy current loss in electrically conductive permanent magnets becomes smaller than that in surface PM topologies. Magnet web is an important parameter to maximise the saliency ratio. However, air gap flux density and mechanical stress should be also considered while choosing magnet web length. Magnet width and length controls airgap flux density which is one of the most important performance parameter for PM machines. The flux bridge thickness can be chosen considering mechanical stress and peak air-gap flux density.

I-shape interior PM ISGs are offered for highly constrained ISG applications in the literature. Multi-physics modelling and comparison analyses for interior PM ISGs are investigated in [5, 107]. The performance parameters of the proposed interior I-shape PM ISG are tabulated in Table 4.8.

The detailed results of 21 slot – 16 pole buried I-shape PM ISG at different operating conditions are given in Appendix – A.

Table 4.8 21 slot – 16 pole buried I-shape PM ISG Key Results

1500 rpm Generator mode ($Efficiency_{min} = 93\%$)		
Torque:		
Mean torque	50.4	$N.m$
Torque ripple	2.94	% (in per cent)
Cogging torque (peak to peak)	0.065	$N.m$
Losses:		
Copper loss	202.5	$Watt$
Magnet ohmic loss	70.99	$Watt$
Iron loss (Hysteresis+Eddy current)	84.35	Watt
Efficiency:	95.48	%
2000 rpm continuous Generator mode – d-q axis analysis		
L_d , d-axis inductance	0.86	mH
L_q , q-axis inductance	1.05	mH
V_d , d-axis voltage	183	$volt$
V_q, q-axis voltage	68.5	$volt$
Saliency ratio ($\xi = {}^{L_q}/_{L_d}$)	1.23	–
Power factor	0.68	–

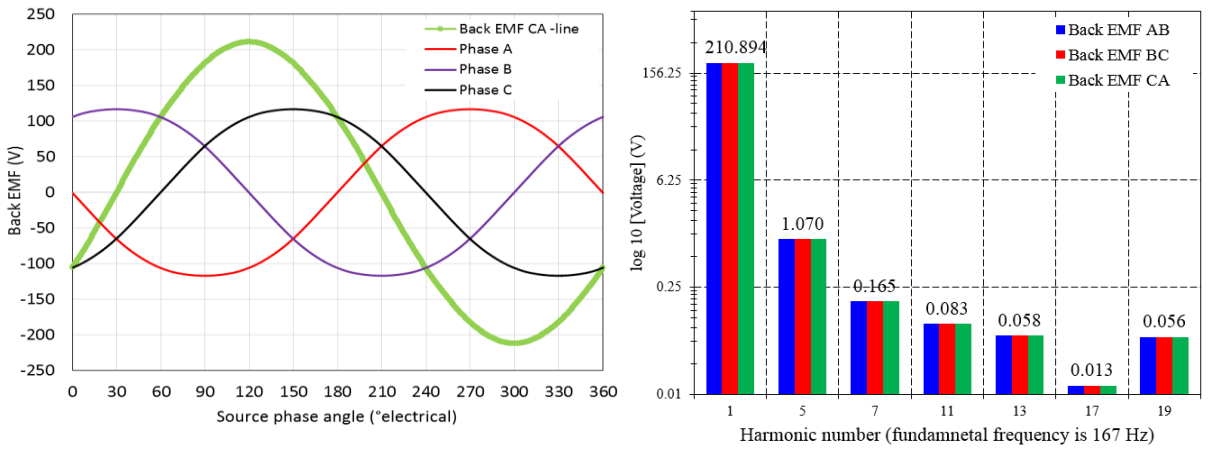

Figure 4.25 Phase and line back EMFs (left), harmonic content of line to line back EMFs (right) at 2000 rpm - FEA

As shown in Figure 4.25, the line to line back EMF contains only fundamental + 5th harmonic and other higher harmonics can be ignored due to very small amplitudes (less than 0.17 volt). Figure 4.26 below depicts torque–speed envelope of the proposed ISG at the rated current by varying the current angle.

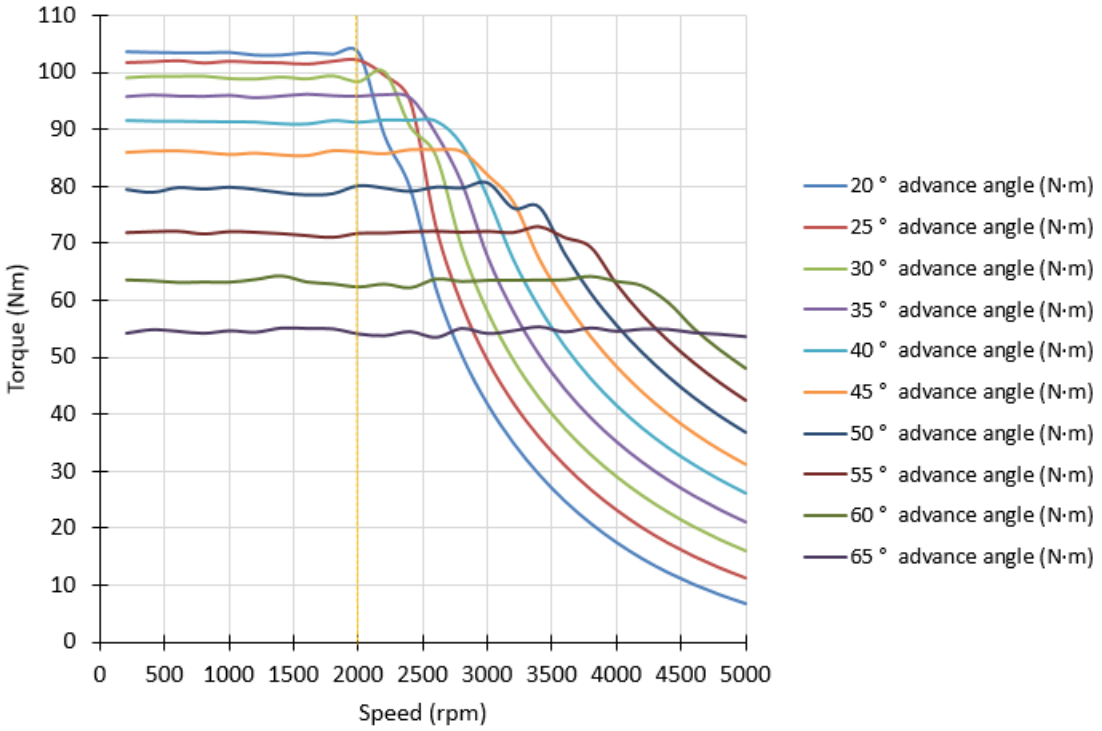

Figure 4.26 Torque – speed envelope of 21 slot – 16 pole interior I-shape PM ISG at rated current

4.5.2.1 Brief Discussion

After obtaining the performance parameters of the proposed interior I-shape PM ISG, some important results have been discussed as follows:

- It is shown that 21 slot – 16 pole PM machine topology can be a good choice to reduce the torque ripple as in this case torque ripple at 1500 rpm generator mode is 2.94%. Also, peak to peak cogging torque is only 0.065 Nm. The rotor eccentricity is very important for asymmetric machines to keep the cogging torque and torque ripple very small. Otherwise, undesired torque ripple might increase.
- Magnet ohmic loss is reduced by about 53% compared to surface PM ISG within the same pole slot combination. However, more magnet is required in this case as magnet leakage flux is higher than that in SPM ISG.
- Magnet demagnetisation was not observed as magnets are shielded inside the rotor core in this case.
- Compared to 21 slot – 16 pole SPM machine, the user defined optimization function weighted by torque ripple, magnet mass and machine losses gives less performance in this case as magnet mass and torque ripple increase in the proposed I-shape PM machine.
- The proposed I-shape PM ISG, however, provides higher efficiency (95.48%) at 1500 rpm generator mode when compared to the SPM machine efficiency (95.11%) due to lower amount of losses, especially due to reduction of magnet eddy current losses.

4.5.3 21 slot – 16 pole V-shape PM ISG Machine

V-shape magnet topology for interior PMSM machines could provide better performance since magnet flux can be concentrated in rotor core by positioning permanent magnets in V-shape with a certain V-angle. By proper design of V-shape, the air gap flux density can be kept high enough (i.e. 0.9 -1 T) as airgap flux density is an important performance parameter in PM machines. Furthermore, V-shape interior PM machine utilise reluctance torque due to inductance asymmetry between L_d and L_q. It is shown that flux concentrating PM machines such as spoke type interior PM motors can utilise higher air-gap flux density than magnet remanent flux density as most flux lines pass through machine airgap [119]. For the design of V-shape PM rotor, iron bridge thickness, V angle, flux barriers, magnet width and length are important optimisation parameters to obtain high reluctance torque and airgap flux density.

The main parameters of the proposed V-shape ISG are tabulated in Table 4.9. The proposed machine geometry and no load flux density distribution is shown in Figure 4.27. The quality of phase back EMFs and its line to line harmonic contents are also given in Figure 4.28.

Table 4.9 The main machine parameters for 21 slot – 16 pole V-shape PM ISG

Optimised Machine Dimensions	
Stator inner diameter	200.7 mm
Stator outer diameter	290 mm
Active stack length	40 mm
Rotor outer diameter	198.7 mm
Rotor inner diameter	150 mm
Distance of V angle from the shaft centre	84.25 mm
V angle	130°
Magnet bridge thickness	1.127 mm
Magnet thickness	4 mm
Tooth width	19.5 mm
Tooth tip thickness	2.5 mm
Slot opening	7 mm
Stator yoke thickness	15 mm
Slot area	388 mm^2
ISG mass without shaft	14.16 kg

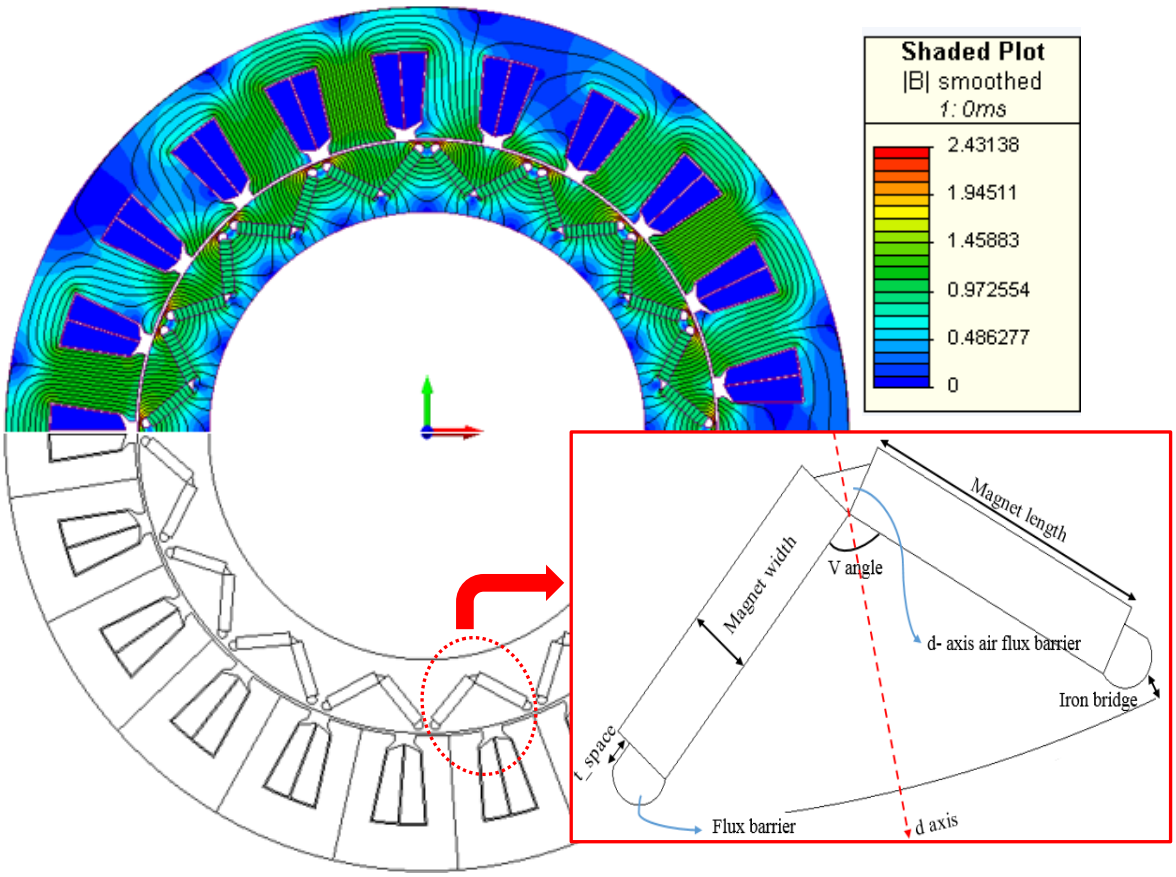

Figure 4.27 No-load flux density distribution of 21 slot -16 pole V-shape PM ISG and the optimised machine geometry

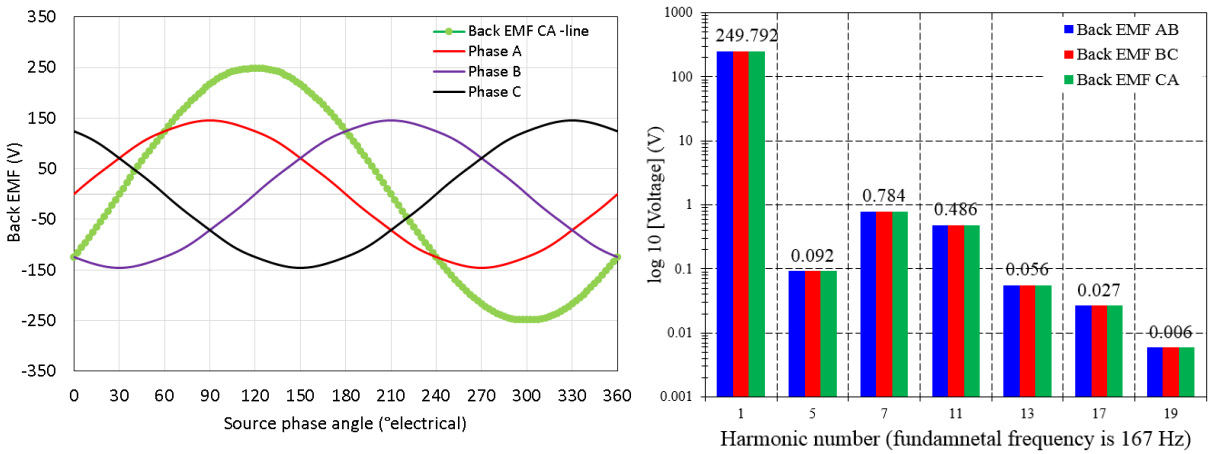

Figure 4.28 Phase and line back EMFs (left), harmonic content of line to line back EMFs (right) at 2000 rpm - FEA

The key results for the proposed ISG are given in Table 4.10[4].

Table 4.10 21 slot – 16 pole interior V-shape PM ISG Key Results

1500 rpm Generator mode ($Efficiency_{min} = 93\%$)		
Torque:		
Mean torque	50.5	$N.m$
Torque ripple	2.3	% (in per cent)
Cogging torque (peak to peak)	0.066	$N.m$
Losses:		
Copper loss	151.3	$Watt$
Magnet ohmic loss	23.38	$Watt$
Iron loss (Hysteresis+Eddy current)	92.46	Watt
Efficiency:	96.71	%
2000 rpm continuous Generator mode – d-q axis analysis		
L_d , d-axis inductance	0.62	mH
L_q , q-axis inductance	0.976	mH
Saliency ratio (ξ)	1.574	–
Average reluctance torque (time averaged)	16.3	Nm
Power factor	0.79	–

Figure 4.29 shows d-q axis inductance assymetry at different phase currents and torque components (i.e. reluctance + magnet torque) at varying current angles. The maximum reluctance torque due to rotor saliency is 21.25 Nm corresponding to 19% of the peak machine torque. In Figure 4.30, the torque-speed plot of the V-shape ISG at the rated current is shown by varying the current advance angle. It is shown that 21 slot -16 pole V-shape ISG can provide

[4] The detailed performance results of the machine at different operating conditions are given in Appendix – A.

sufficient amount of torque by current control in field weakning region to satisfy constant power up to 5000 rpm since the minimum torque must be higher than 42 Nm at the rated speed for continuous power.

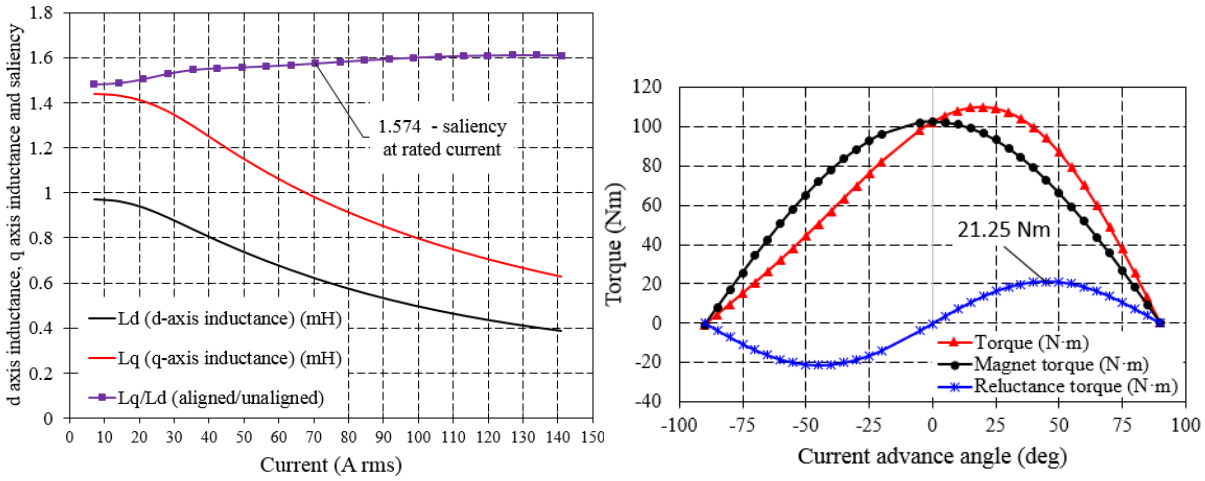

Figure 4.29 d-q axis inductance and generated saliency at different currents (left), torque components varying with respect to current advance angle (right)

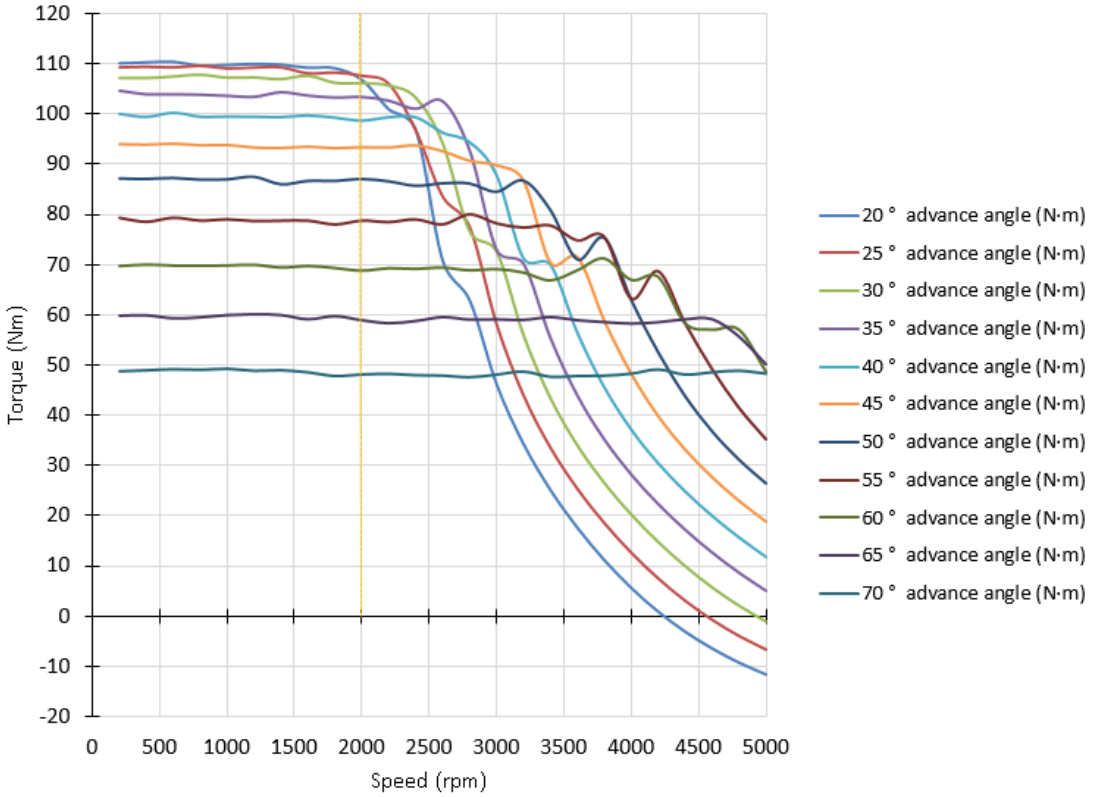

Figure 4.30 Torque – speed envelope of 21 slot – 16 pole interior V-shape PM ISG at rated current

4.5.3.1 Brief Discussion

After depicting the important performance parameters of 21 slot – 16 pole V-shape ISG, the significance of the optimised V-shape machine is discussed as follows:

- 21 slot – 16 pole V-shape ISG achieves the highest efficiency (96.7% at 1500 rpm) compared to all the other proposed ISG designs as the magnet loss (23.3 Watts) and the copper losses (151.3 Watts) are reduced significantly. Eddy current loss plot at 1500 rpm under load condition is shown in Figure 4.31 and it is clear that the magnets are mostly screened from rotor losses due to sub and superior harmonics of airgap magnetic field. This helps reduce the magnet losses in interior magnet rotor topologies. For further reduction of the magnet ohmic losses, PMs could be segmented which shortens eddy current flow paths inside the electrically conductive PMs.

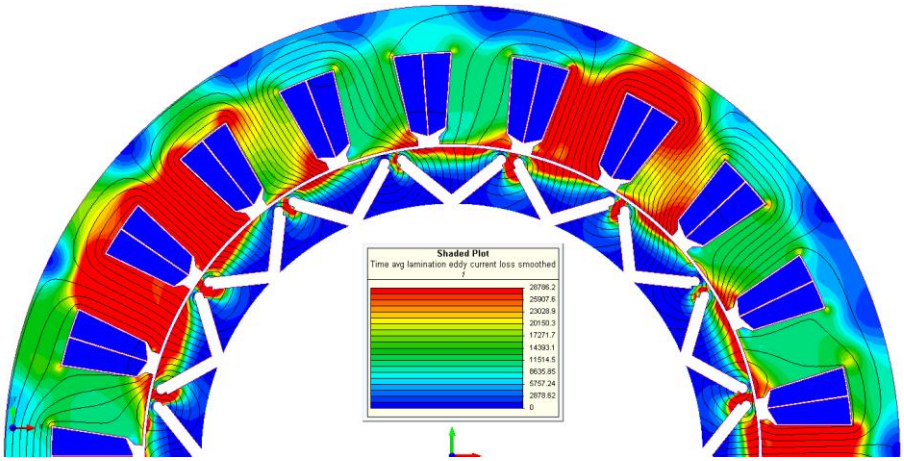

Figure 4.31 Lamination eddy current losses: legend interval 28786 – 0 W/m^3

- 21 slot -– 16 pole V-shape ISG provides the highest saliency (1.57) and reluctance torque (21.2 Nm) in comparison to other proposed ISGs showing that more suitable choice for crankshaft mounted ISG application.
- Although it is not considered in the overall design optimisation, 21 slot – 16 pole V-shape ISG is lighter (14.16 kg) than all other proposed ISG configurations when the lamination, winding and magnet masses are summed up.
- Magnet demagnetisation is not observed permanently, even for the worst case scenario when the magnets are at 100°C and all stator current is in –d axis when the machine at the rated current.
- Regarding the multi-objective optimisation function, 21 slot – 16 pole V-shape machine is the second best candidate. However, it is clear that surface mounted PM machines might not satisfy continuous power operation after the base speed as machine saliency is not applicable. Therefore, 21 slot-16 pole V-shape PM machine is the best candidate when all performance parameters are considered for ISG application.
- The interior PM machines usually facilitate very thin iron bridges to reduce magnet leakage and to improve air-gap flux density. However, there is a mechanical constraint that iron bridges must be resistant to centrifugal forces at higher speeds since magnets

embedded into the rotor produce mechanical stress on the rotor iron bridges which are the weakest parts of rotor core. A rotor structural analysis therefore is required to ensure that the rotor structure is safe at the machine rated speed. In Figure 4.32, a structural FEA analysis is performed and maximum deformation on the iron bridge thickness is obtained. There are two cases: bonded magnets and un-bonded magnets for the FEA investigation. The both results show that V-shape PM ISG with 1.127 mm iron bridge thickness is safe up to 5000 rpm.

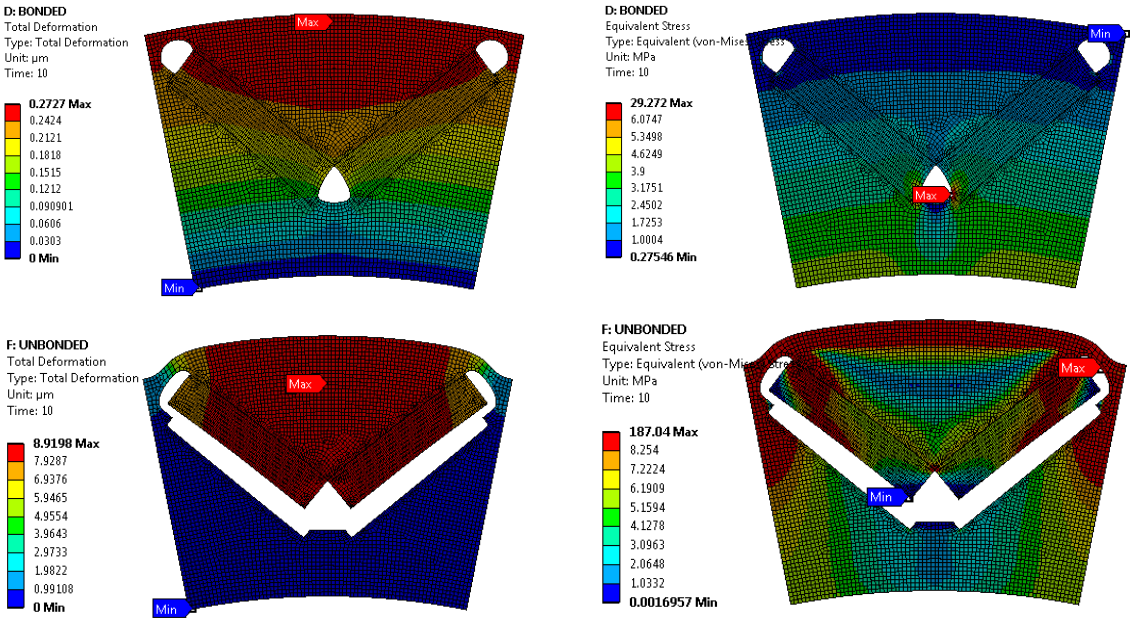

Figure 4.32 Deformation and Equivalent von-Mises Stress results on rotor structure when magnets are bonded (top); un-bonded (bottom)

Note that Figure 4.32 does not show the true scale of the deformation. In other words, it shows magnified deformation on the rotor core structure. The maximum deformation is 8.91 μm and equivalent von-Mises stress on the rotor structure when magnets are not bonded is 187 MPa showing that rotor iron core is safe as the yield strength of NO18 laminations is about 400 MPa.

4.6 Comparisons of the Proposed ISG Designs

After design and analysis of a number of PM ISG machines, efficiency, magnet mass, multi-objective design function and torque ripple have been compared in several histograms as given in Figure 4.33 below.

21 slot – 16 pole V-shape ISG presents a high reluctance torque (19% of the rated torque) and efficiency (≥ 96.5%). In terms of the multi-objective design function, 21 slot – 16 pole V-shape machine is the second best candidate after 21 slot- 16 pole SPM ISG. However, the most suitable candidate for the ISG application is V-shape ISG when the field weakening region and

constant power region are considered. 21 slot -16 pole V-shape ISG gives very low cogging torque – only 0.06 Nm.

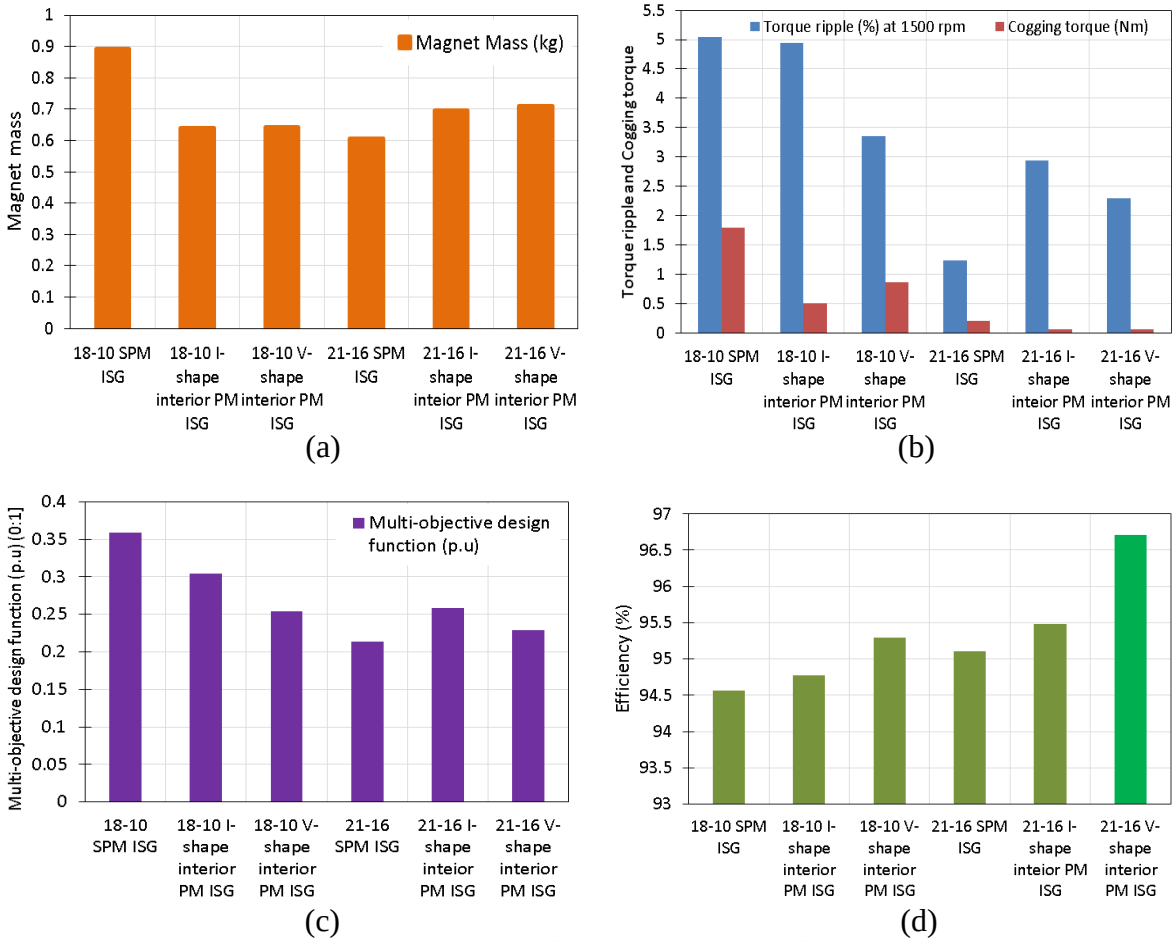

Figure 4.33 (a) Magnet mass comparison; (b) torque ripple and cogging torque comparison; (c) multi-objective design optimisation function comparison; (d) overall efficiency comparison

It is also demonstrated that 21 slot – 16 pole ISG is mechanically safe at the rated speed and does not present any permanent magnet demagnetization at 100°C surrounding temperature. Although saliency (≈ 1.6) is the highest in 21 slot -16 pole V-shape configuration, it is still low and it could be improved by offering more magnet layers and flux barriers in the rotor core.

4.7 Analysis of the Influence of Slot Fill Factor on the Performance of 21 slot – 16 pole V-shape PM ISG

Based on equation (4.3), increasing the stator slot area and slot fill factor improves motor constant and so the machine torque can be maximised. However, improving the slot fill factor and slot area affect tooth body width and stator yoke width adversely. If the slot fill factor can be improved without varying the other geometrical parameters, the machine torque is increased according to equation (4.3).

The critical mathematical equation in terms of machine electrical loading is given in equation (4.5) [120].

$$A_{sl} = \frac{N \times I_{RMS}}{J_{RMS} \times K_{wb}} \tag{4.5}$$

where N is a number of turns, J_{RMS} is stator current density and I_{RMS} is phase current. K_{wb} stands for slot fill factor. According to equation (4.5), when the slot area (A_{sl}) is fixed, improving slot fill factor helps to increase MMF or help reduce stator current density J_{RMS}.

Although the only theoretical relationship between electrical loading and slot fill factor is defined in equation (4.5), the implication of equation (4.5) on machine electrical and thermal performance is more comprehensive. The principal electrical and thermal advantages of the increased fill factor are as follows:

- The amount of copper in the slot can be increased hence a larger diameter wire can be used and for the same slot loss a higher current can be applied.
- A coil with an increased fill factor has a higher thermal conductivity and hence heat is removed from the slot more effectively and a higher current can be applied for this reason.
- There also exists a possibility that the fill factor can be used to increase the conductor area such that copper can be replaced by aluminium, meaning a lighter machine. If the fill factor can be increased sufficiently then an increase in torque could be achieved whilst also reducing mass [77].
- The outer diameter of the machine might be reduced by keeping the copper area the same but using the extra space gained from the higher fill factor to bring the stator core back in.

A high fill factor ISG prototype can be achieved by on-tooth pre-pressed coils in this case. A particular example is shown in Table 4.11 to state that the higher slot fill factor ISG designs result in better electrical performance and higher torque density. A fill factor of 0.73 is later shown to be achievable using on tooth pressing in Chapter 6.

Table 4.11 Improvement of slot fill factor

	Traditional stator	***Segmented stator***	***On-tooth pressed coil***
Slot Fill Factor	0.45	0.57	0.73
Number of turns	13	91	91
Copper cross-sectional area (mm^2)	162	180	226.8
Copper loss at 1500 rpm - generator mode (Watts)	151.3	136.2	108.1
Drive current; copper loss is kept at 151.3 watts maximum (A_{rms})	33.9	35.7	40.1
Average torque; copper loss is kept at 151.3 watts (N. m)	51.09	54.31	61.35

The reduction of copper losses in the segmented stator in Table 4.11 is due to parallel connection of the ISG teeth with a fill factor of 0.57. The further reduction of copper losses could be achieved by on-tooth pressing since relatively thicker conductors are densely packed in the slot area. In Table 4.11, increasing slot fill factor from 0.45 to 0.73 results in copper losses being reduced by almost 28.5%. This prediction is based on only fill factor and bulk copper area inside the slot. In the real prototype, copper loss reduction is also dependent on commercially available conductor sizes. Alternatively, the proposed ISG can be loaded with more current for the same copper losses, increasing machine torque density. As pressing the coil enhances thermal contact conductance between the conductors, the effective thermal conductivity of the slot would be improved in this case.

4.8 Loss Analysis of 21 slot – 16 pole V-shape PM ISG

4.8.1 Copper Losses

The copper losses are associated with power dissipation in the armature windings of the machine. Although DC losses are usually a significant source of total winding losses, high frequency and high current densities in stator windings lead to skin and proximity effects, causing additional loss in the windings [121]. The electrical frequency dependent ohmic losses (i.e. AC losses) are more significant at high speed, high power machine applications. However, AC losses due to high frequency proximity and skin effects of the currents in the conductors were not considered in the efficiency calculations.

AC losses at 1500 rpm generator mode is computed to be 30.34 Watts that is one fifth of the DC copper losses at 100°C. An FEA simulation was performed when the machine on load to investigate the frequency dependent AC copper losses as shown in Figure 4.34. The number of

turns in this case is 13 as the number of parallel paths in the machine is 1. In high speed machines, AC losses becomes more predominant and must be considered at early stages of the design. Litz wires (i.e. multi-strands) might be of importance to reduce the frequency dependent copper losses. This is however not the scope of the work.

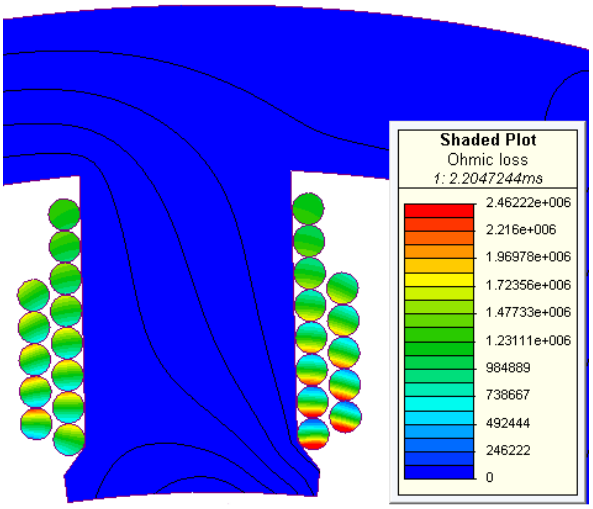

Figure 4.34 13–turn solid copper wires with a diameter of 2.92 mm to compute AC losses

The DC losses due to resistance and RMS current flow in the conductors are significant source of the machine losses in this case. The winding losses in a three phase machine fed with direct current is given by

$$P_{winding,DC} = 3R_{DC}I^2 \tag{4.6}$$

where R_{DC} is the DC resistance for one phase winding and I is the phase current (RMS). The DC resistance is given by

$$R_{DC} = \rho \frac{L_{winding}}{A_{winding}} \tag{4.7}$$

where ρ is the resistivity ($\rho = 2.26 \times 10^{-8}\ Ohms.m$ at 100°C), $L_{winding}$ and $A_{winding}$ are the length and cross-sectional area of the phase windings, respectively.

In order to calculate the DC winding resistance for a 3-phase machine including the machine end windings, equation (4.8) is derived using the ISG tooth dimensions:

$$\{Length_{single\ tooth\ winding} = Number\ of\ turns \times [2 \times (stack\ length) + 2 \times (tooth\ width) + 4 \times (average\ distance\ of\ single\ side\ of\ winding\ to\ tooth)]\}$$

$$\{Total\ Length_{3-phase\ winding} = Number\ of\ slots \times Length_{single\ tooth\ winding}\}$$

Then, the total machine resistance R_{DC} (Ω) at 100°C is given by

$$R_{DC} = 2.26 \times 10^{-8}\ Ohms.m \times \left[\frac{Total\ Length_{3-phase\ winding}}{Conductor\ cross-sectional\ area}\right] \quad (4.8)$$

Using equations (3.6) and (3.8), the DC copper losses for the machine calculated theoretically if the phase RMS current, I is known.

4.8.2 The ISG Machine Losses at 2000 rpm Continuous Generator Mode

2000 rpm generator mode is when the machine is at the rated torque. The machine losses including frequency dependent iron losses and DC copper losses are active in this operating condition. The end windings effect was also included in the calculation of DC ohmic losses. The machine suffers from significant magnet eddy current losses as electrical loading is relatively high at this operating point and the magnets are not segmented. The machine is divided into several pieces as shown in Figure 4.35.

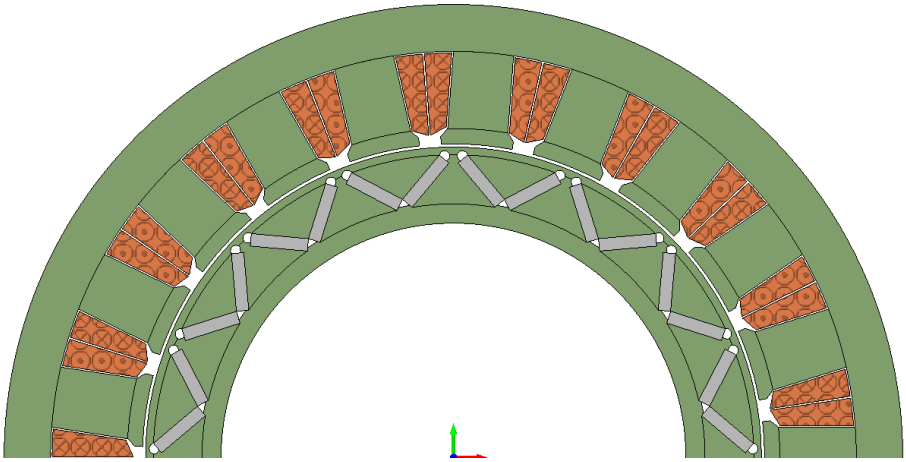

Figure 4.35 The machine geometry discretization to compute losses at certain regions

In Figure 4.36, the machine losses at 2000 rpm generator mode, obtained from the FEA are shown, required to investigate the machine thermally. The AC copper losses are not considered for the simplicity. The winding configuration has been altered from series to parallel as thinner conductors utilise higher fill factor. Thus, the conductor diameter is selected to be 1.25 mm and the number of parallel paths is 7. In series connection of the coils, the conductor diameter is 2.92 mm with a number of turns: 13 as tabulated in Appendix – A.

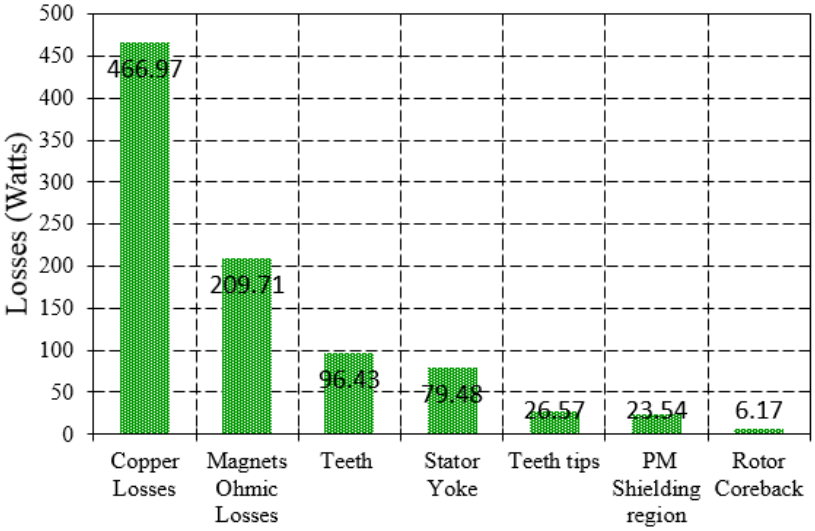

Figure 4.36 21 slot -16 pole V-shape PM ISG losses at 2000 rpm continuous generator mode

4.9 Conclusion

The aim of this chapter was to find the realistic tooth dimensions for coil pressing and thermal analysis. The final stator tooth geometry of 21 slot -16 pole V-shape ISG, which will be used in the thermal investigation of on-tooth compressed coils, is shown in Figure 4.37. Stator teeth segmentation will be also presented in Chapter 6 as it makes the on-tooth coil pressing possible for further thermal investigations of the stator windings.

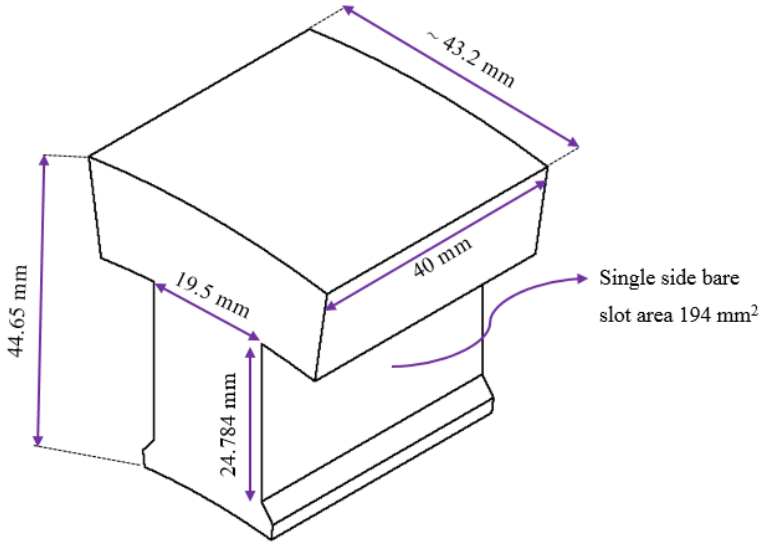

Figure 4.37 A single tooth geometry of 21 slot – 16 pole V-shape PM ISG

Chapter 5. Thermal Modelling of Stator Windings

5.1 Introduction and Objectives

In order to demonstrate how the effective thermal conductivity of a bobbin is improved by increasing the slot fill factor, steady state thermal FEA simulations have been carried out. After performing several FEA simulations, effective thermal conductivity has been predicted by using the one dimensional steady state Fourier law of heat.

In the literature, there is extensive research on the estimation of the effective thermal conductivity of stator windings. Most of the research gives a theoretical approach to predict the winding thermal conductivity. In this chapter, an alternative method that utilises steady state FEA simulations will be introduced. The accuracy of the proposed method will be investigated analytically and several case studies will be presented to demonstrate the effect of fill factor on the slot thermal conductivity.

5.2 Case Study: Slot Thermal Conductivity Investigation

In order to understand the importance of equivalent slot thermal conductivity, only heat generation inside copper windings is considered. Internal heat generation inside stator slots will be distributed inside the machine via thermal conduction as shown in Figure 5.1.

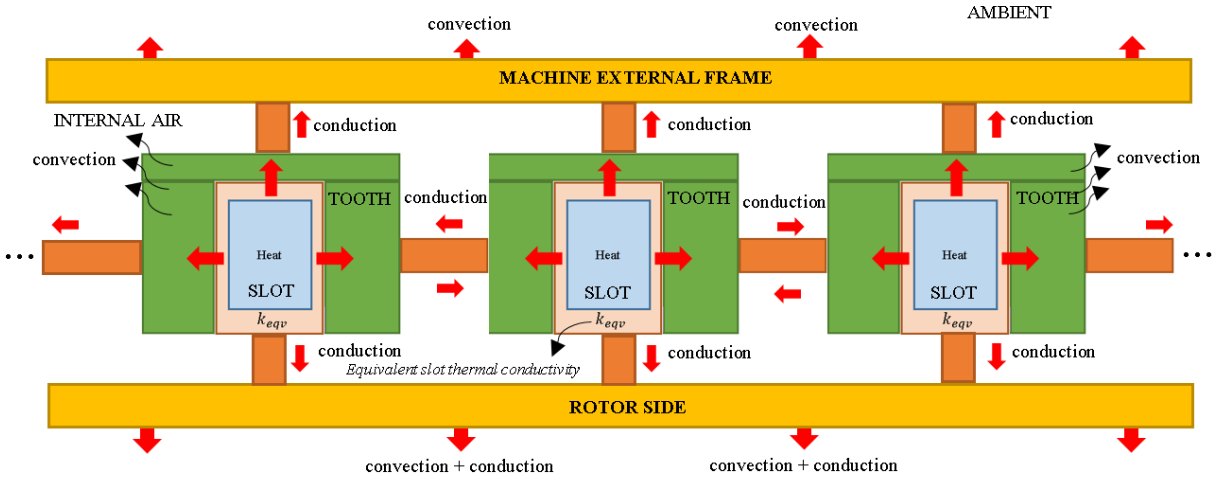

Figure 5.1 Heat flow inside an electrical machine due to winding heat generation

From the point of view of a thermal lumped model, the equivalent thermal resistance of the slot could be considered as a thermal barrier between bulk copper in the slot and stator teeth. In this case, first interference of heat flow occurs in a slot thermal barrier representing equivalent insulation material of stator windings. The equivalent slot thermal conductivity, k_{eqv} for an electrical machine with a number of stator slots, N_s is defined as:

$$k_{eqv} = \frac{l_{barrier}}{N_s \times R_{eqv} \times A} \tag{5.1}$$

where R_{eqv} stands for equivalent thermal resistance between the bulk copper and stator laminations and $l_{barrier}$ and A are equivalent insulation thickness and surface area of equivalent insulation material, respectively.

On the other hand, an electrical machine might be represented as a first order thermal lumped circuit consisting of global thermal resistance and global thermal capacitance. The equivalent slot thermal resistance could be linked to the global thermal resistance of an electrical machine. The overall machine thermal resistance might be written in the form:

$$R_{global} = R_{eqv} + R_{conduction+convection} \tag{5.2}$$

As represented in equation (5.2), R_{eqv} is simply in series to all other thermal resistances around the machine since R_{eqv} is the first compulsory path of heat flow inside the machine. Keeping R_{eqv} to be as small as possible is vital for electrical machines because the generated heat inside the stator slots should be removed quickly from the machine windings to keep copper losses low and to provide longer service life.

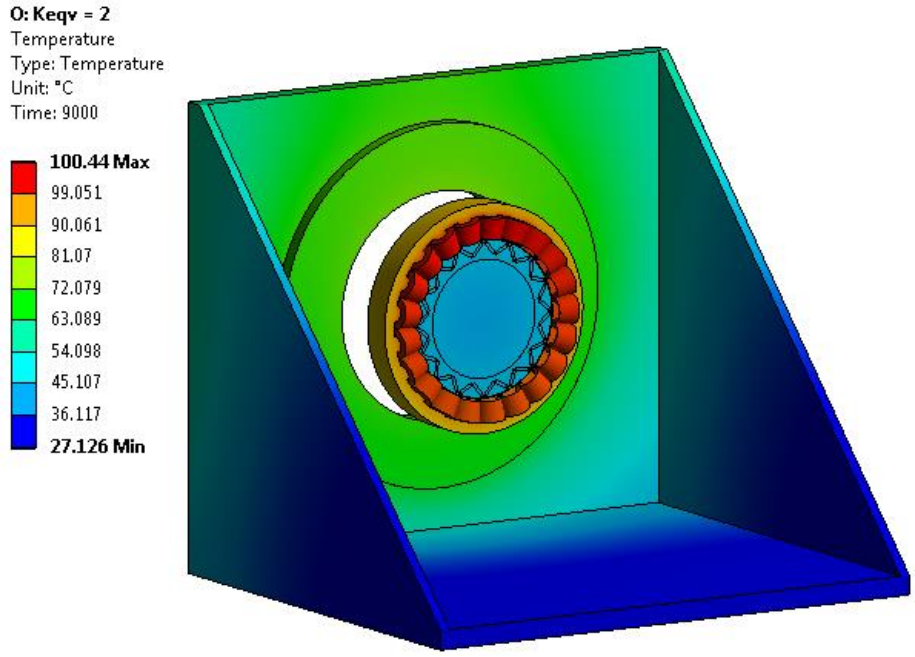

Figure 5.2 Thermal FEA model of 21 slot / 16 pole V-shape ISG with a slot thermal insulation of $k_{eqv} = 2\ W/(m°K)$ – (the ISG housing is not shown.)

The effect of equivalent slot thermal conductivity on machine thermal distribution has been investigated by carrying out transient thermal FEA (i.e. Ansys CAE) simulations of 21 slot/16

pole interior V-shape PM ISG as proposed in Chapter 3 (Figure 5.2[5]). A thermal insulation as a barrier between the bulk copper and stator teeth with 0.18 mm thickness is modelled as k_{eqv}, which is randomly varied to investigate the temperature distribution. Only natural convection from external surfaces is assumed in this case for the machine cooling.

As reported in Chapter 3[6], 470 Watts of copper losses are generated in the ISG stator windings at 2000 rpm generator mode when 91 turn, 1.25 mm conductors are utilised .The ISG copper losses are injected to each single tooth winding and temperature distribution is obtained by varying equivalent slot thermal conductivity. As a result, thermal conductivity versus temperature increase is plotted in Figure 5.3. From the point of view of thermal lumped parameter model, the variation of thermal resistance: $[R_{global} - R_{eqv}]$ as described in equation (5.2) is also given in Figure 5.3.

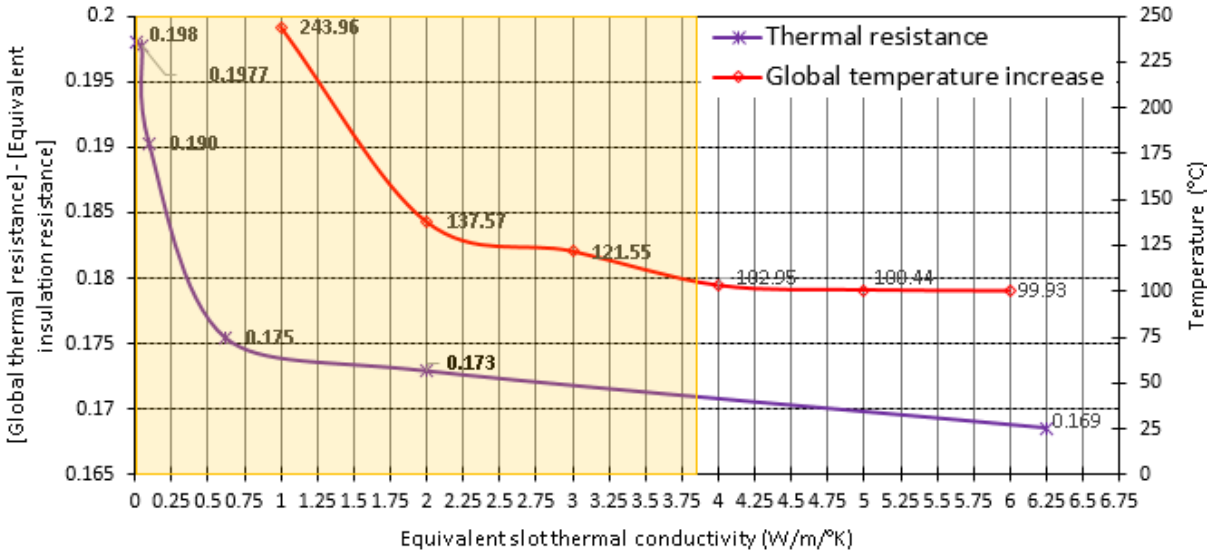

Figure 5.3 Slot thermal conductivity vs peak temperature in the ISG – no cooling instruments

In Figure 5.3, it can be noted that when k_{eqv} is very low (0.01-0.1), the winding temperature increases excessively. For values of k_{eqv} higher than 0.1, the winding temperature settles at around 100°C. Slot thermal conductivity is quite sensitive at smaller values as reducing k_{eqv} from 0.05 to 0.01 increases winding temperature to about 106°C. On the other hand, k_{eqv} is less sensitive at greater values, increasing k_{eqv} from 2 to 6.25 reduces the winding temperature by only 0.51°C. Therefore, R_{eqv} should be reduced by improving equivalent slot thermal conductivity to avoid high temperature increase, likely to destroy the machine due to magnet wire degradation. Lastly, the machine global thermal resistance is derived from the first order

[5] For 3-D thermal FEA modelling of the ISG machine given in Figure 5.2, natural convection heat transfer coefficients are computed using empirical formulations given in Appendix – B. The calculated parameters are given in Table B.4 in Appendix – B.

[6] In Chapter 4, Section 4.8.2, the detailed loss analysis of the 21 slot -16 pole V-shape ISG machine can be found.

RC thermal equivalent circuit although it is difficult to define the whole machine as a single thermal resistance and capacitance. This is still a fair theoretical approximation for this case.

5.3 Case Study: Slot Fill Factor versus Effective Thermal Conductivity

Slot fill factor affects phase resistance (end turn resistance and slot resistance), conductor peak current density, copper losses, slot heat density and power efficiency. For conventional electric machines, slot fill factors of 0.4 – 0.6 can be achieved. In a simple equation, slot fill factor is written:

$$Fill\ Factor = \frac{Conductor\ area}{Stator\ slot\ area} \tag{5.3}$$

In order to increase slot fill factor, effective conductor area should be maximized within stator slot. Electrical machine designers usually do not model random wound mush winding, as it is very difficult to model the position of each conductor. For this reason, they prefer to model solid copper bodies. However, this approach might cause inaccuracy due to neglecting of non-homogenous distribution of magnet wires inside the slot. Furthermore, machine designers sometimes use equivalent analytical lumped parameter model for thermal analysis of an electric machine. Since this method requires analytical calculation of thermal resistances between certain nodes, effective thermal conductivity of a stator winding will be crucial for higher precision. This demonstrates that it is useful to predict thermal conductivity of a stator winding by modelling individual turns so as to predict average thermal conductivity. Then, estimated thermal conductivities could be used in FEA models or equivalent lumped parameter models of an electrical machine.

5.3.1 FEA Modelling of Stator Winding

In a conventional stator winding, conductors are distributed as seen in Figure 5.4. Basic repeating unit of the whole geometry will create a single thermal resistance. Each of these thermal resistances might be in series or in parallel with respect to direction of one dimensional heat flow. As shown in Figure 5.4, every single unit has an effective thermal resistance and thermal conductivity. Thermal resistance values and thermal conductivities are the same for each unit of the whole geometry. Nevertheless, as the geometry of the single unit is not isotropic along an axis, it is difficult to estimate effective thermal resistance of any basic repeating unit using one dimensional Fourier law of heat since it assumes that the thickness of the certain material along the heat flow is exactly known. However, the material span along the heat flow varies as illustrated in Figure 5.4. Therefore, FEA results for steady state thermal conduction have been utilised to better estimate the value of equivalent thermal resistance of a repeating geometry.

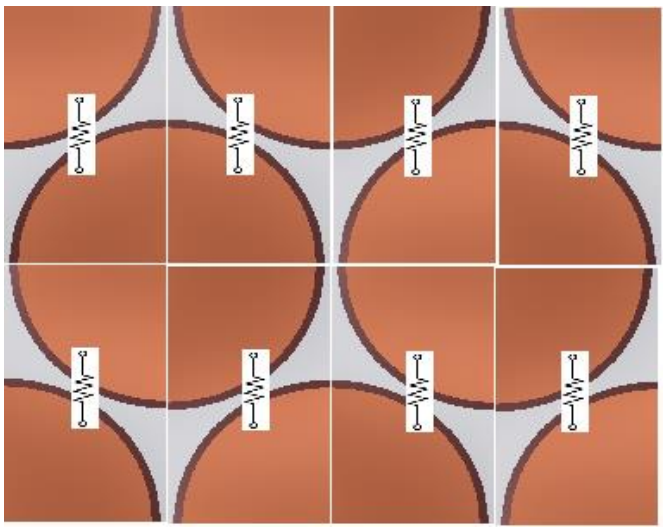

Figure 5.4 Uniform distribution of copper conductors in a bobbin

During the heat flow, heat flux will cross the different materials between the thermal boundary conditions. For this reason, thermal conductivity of each material used in the geometry should be known. Since copper conductors, magnet wire enamels and air constitutes the whole geometry in terms of thermal materials, Table 5.1 shows the thermal conductivity of these materials at room temperature.

Table 5.1 Thermal conductivities of materials in a stator slot

Material	Isotropic Thermal Conductivity	Unit
Air	0.026	$W\ m^{-1}\ °C^{-1}$
Polyimide (wire enamel)	0.25	$W\ m^{-1}\ °C^{-1}$
Copper	400	$W\ m^{-1}\ °C^{-1}$

To calculate the average thermal conductivity, the basic repeating part of a winding segment is taken into consideration. For boundary conditions, temperature on the upper surface is selected to be 150°C and for the lower surface is 130° C. This gives a ΔT = 20°C. Heat flux will flow from upper surface to lower surface by passing through copper conductor, polyimide coating and air region. The FEA heat flux density figure of the repeating part with original geometry is shown in Figure 5.5. Some air regions could be ignored due to very low heat flux density. If the amount of heat flux is less than 10% of the maximum heat flux inside air, then the corresponding air region between the conductors was neglected in the calculations.

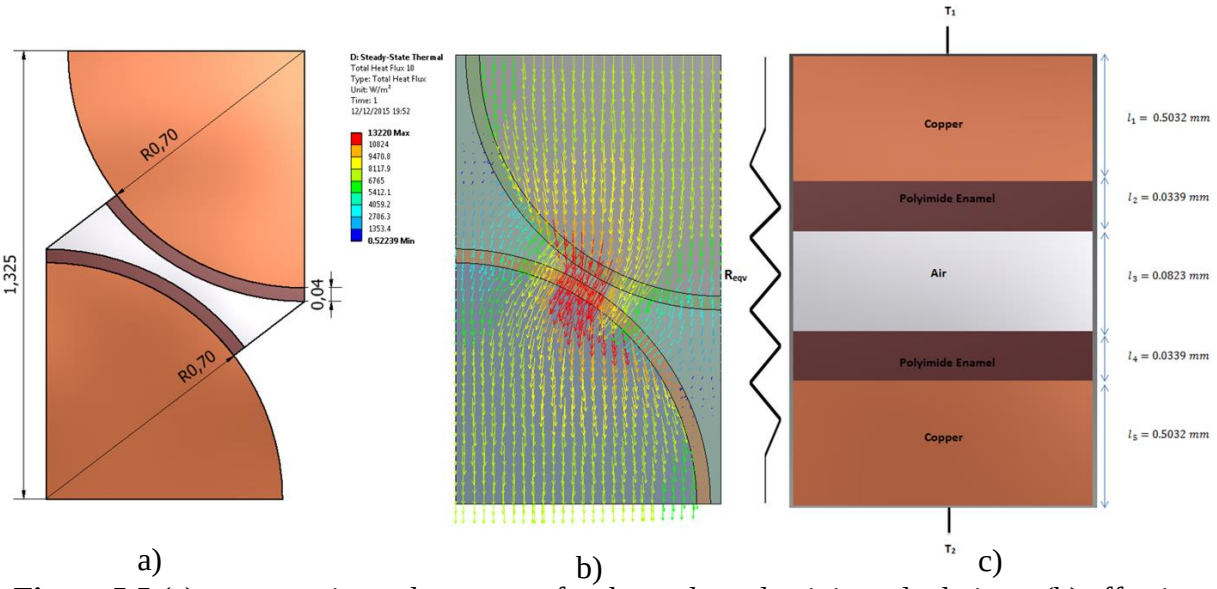

a) b) c)

Figure 5.5 (a) an approximated geometry for thermal conductivity calculations, (b) effective heat flux regions, (c) the equivalent plane wall approximation for 1-D heat conduction

In Figure 5.5a, the effective regions are demonstrated. Using the thermal resistance equation, thermal conductivity can be calculated. To do this, volume of the copper conductors, polyimide enamel and air region should be calculated. Considering a plane wall with a certain width, thickness of each material can be calculated by using the total volume of the materials. This gives a slab with different materials at different thickness along the heat flow between the boundary conditions.

5.3.1.1 Semi-Analytical Thermal Conductivity Estimation and Comparisons with FEA Results

Assuming that r_1, r_2, r_3, r_4 and r_5 represent thermal resistance of the materials from the top to bottom in Figure 5.5c, the equivalent thermal resistance is represented by r_6. Here,

$$r_1 + r_2 + r_3 + r_4 + r_5 = r_6 \tag{5.4}$$

and

$$r_1 = \frac{l_1}{k_1 A},\ r_2 = \frac{l_2}{k_2 A},\ r_3 = \frac{l_3}{k_3 A}, r_4 = \frac{l_4}{k_4 A},\ r_5 = \frac{l_5}{k_5 A},\ r_6 = \frac{l_{total}}{k_{eff} A}$$

$$\frac{l_1}{k_1 A} + \frac{l_2}{k_2 A} + \frac{l_3}{k_3 A} + \frac{l_4}{k_4 A} + \frac{l_5}{k_5 A} = \frac{l_{total}}{k_{eff} A} \tag{5.5}$$

$$k_1 = k_5$$

$$k_2 = k_4$$

$$l_{total} = l_1 + l_2 + l_3 + l_4 + l_5$$

where k_1, k_2, k_3 *and* k_{eff} are thermal conductivities of copper, polyimide, air and average conductivity respectively.

$$\frac{l_1 + l_5}{k_1} + \frac{l_2 + l_4}{k_2} + \frac{l_3}{k_3} = \frac{l_1 + l_2 + l_3 + l_4 + l_5}{k_{eff}}$$

$$k_{eff} = \frac{k_1 k_2 k_3 [l_1 + l_2 + l_3 + l_4 + l_5]}{k_2 k_3 (l_1 + l_5) + k_1 k_3 (l_2 + l_4) + k_1 k_2 (l_3)} \tag{5.6}$$

In equation 5.6, effective thermal conductivity can be calculated as all parameters are known from Figure 5.5c. This equation is valid only for steady state, one dimensional conduction across the plane wall with thermal boundary conditions.

Thermal conductivities of the actual materials are as follows:

$$k_1 = 400\ W\ m^{-1}\ °C^{-1}$$

$$k_2 = 0.25\ W\ m^{-1}\ °C^{-1}$$

$$k_3 = 0.026\ W\ m^{-1}\ °C^{-1}$$

where, k_1 is copper thermal conductivity, k_2 is polyimide insulation thermal conductivity and k_3 is air thermal conductivity. The length of copper, polyimide and air has been illustrated in Figure 5.5c. Using equation 5.6, the effective conductivity is calculated:

$$k_{eff} = \frac{k_1 k_2 k_3 [l_1 + l_2 + l_3 + l_4 + l_5]}{k_2 k_3 (l_1 + l_5) + k_1 k_3 (l_2 + l_4) + k_1 k_2 (l_3)}$$

$$= \frac{3.0069}{6.541x10^{-3} + 0.70512 + 8.23} = 0.3362\ Wm^{-1}\ °C^{-1}$$

In order to prove the thermal conductivity result, FEA simulation results can be compared with analytical results. Thermal conductivity can be also calculated using Fourier Law of thermal heat conduction. However, heat flux density should be known in addition to thermal boundary conditions and length of the plane wall, in this case. Heat flux can be estimated by taking samples in equal intervals across the basic repeating unit of the conventional stator coil. This is illustrated in Figure 5.6.

In Figure 5.6, each path has a different average heat flux density, because length of the material along *y*-axis varies. In other words, if average heat flux density (W/m^2) and thermal boundary conditions (i.e. assume ΔT=20°C) for upper and lower surface are known, then effective conductivity can be calculated as follows:

$$Q = -k\frac{\partial T}{\partial X} = -k\left[\frac{T_{x=1} - T_{x=0}}{l}\right] => k = \frac{Q \times l}{\Delta T} \tag{5.7}$$

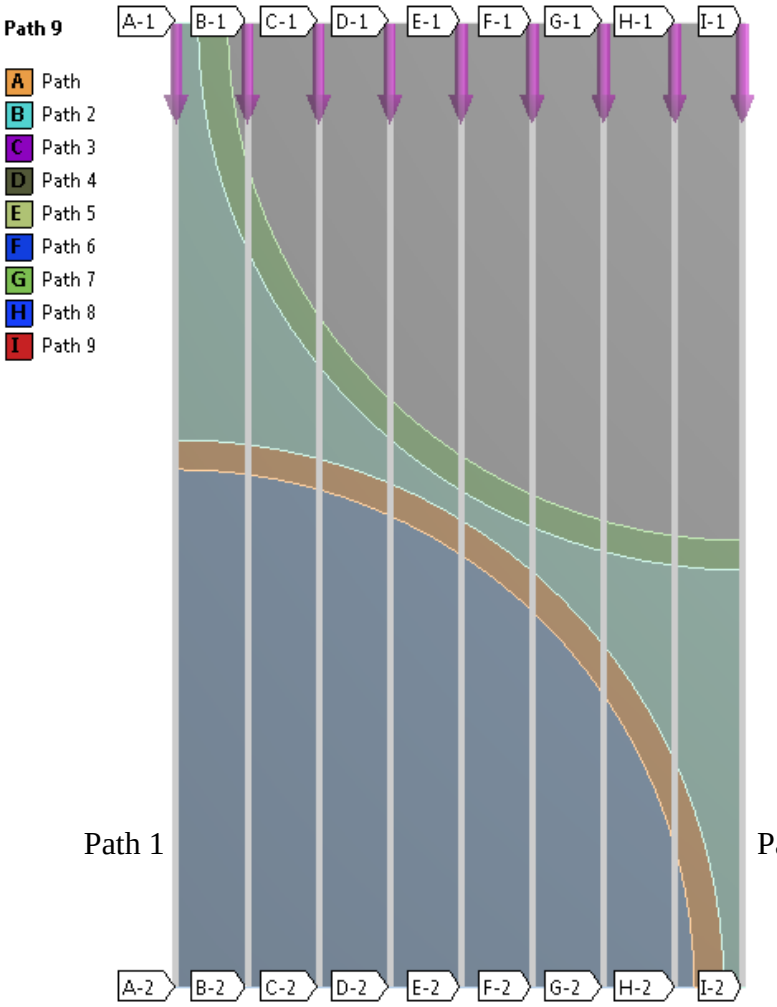

Figure 5.6 A winding segment to estimate average thermal conductivity

Using equation (5.7),

$$Path\ 1:\ k_{1,sim} = \frac{Q \times l}{\Delta T} = \frac{3464.2\ x\ 0.001325}{20} = 0.2295\ Wm^{-1}\ °C^{-1}$$

$$Path\ 2:\ k_{2,sim} = \frac{Q \times l}{\Delta T} = \frac{4461.82\ x\ 0.001325}{20} = 0.2955\ Wm^{-1}\ °C^{-1}$$

$$Path\ 3:\ k_{3,sim} = \frac{Q \times l}{\Delta T} = \frac{5794.604\ x\ 0.001325}{20} = 0.3838\ Wm^{-1}\ °C^{-1}$$

$$Path\ 4:\ k_{4,sim} = \frac{Q \times l}{\Delta T} = \frac{6798\ x\ 0.001325}{20} = 0.4503\ Wm^{-1}\ °C^{-1}$$

$$Path\ 5:\ k_{5,sim} = \frac{Q \times l}{\Delta T} = \frac{7262.03\ x\ 0.001325}{20} = 0.4811\ Wm^{-1}\ °C^{-1}$$

$$Path\ 6:\ k_{6,sim} = \frac{Q \times l}{\Delta T} = \frac{6802.667\ x\ 0.001325}{20} = 0.4506\ Wm^{-1}\ °C^{-1}$$

$$Path\ 7:\ k_{7,sim} = \frac{Q \times l}{\Delta T} = \frac{5795.52\ x\ 0.001325}{20} = 0.3839\ Wm^{-1}\ °C^{-1}$$

$$Path\ 8:\ k_{8,sim} = \frac{Q \times l}{\Delta T} = \frac{4460.98\ x\ 0.001325}{20} = 0.2955\ Wm^{-1}\ °C^{-1}$$

Path 9: $k_{9,sim} = \frac{Q \times l}{\Delta T} = \frac{3464.20\ x\ 0.001325}{20} = 0.2295\ Wm^{-1}\ °C^{-1}$

Average of $k_1$to k_9 gives effective thermal conductivity of Figure 5.6.

$$\therefore k_{eff,sim} = \frac{k_{1,sim} + k_{2,sim} + k_{3,sim} + k_{4,sim} + k_{5,sim} + k_{6,sim} + k_{7,sim} + k_{8,sim} + k_{9,sim}}{9} = 0.3555\ Wm^{-1}\ °C^{-1}$$

Now, analytical approach and FEA thermal simulation results can be compared at steady state for one dimensional thermal conduction.

$$Error_1\ (\%) \approx \left(1 - \frac{k_{\ eff}}{k_{eff,sim}}\right) \times\ 100 = \left(1 - \frac{0.3362}{0.3555}\right) \times\ 100 = 5.43\ \%$$

This error shows that simulation results and analytical approach are consistent to estimate the one dimensional steady state thermal conduction.

According to Pyrhonen et al, [120], the average conductivity can be also calculated as follows:

$$k_{av}\ \approx k_{air}\ \times \left(\frac{Bare\ Conductor\ diameter}{Distance\ between\ the\ bare\ Conductors} + \frac{Distance\ between\ the\ bare\ Conductors}{Overall\ Wire\ Diameter}\right) \quad (5.8)$$

Equation (5.8) is a pure analytical approach to predict average thermal conductivity of stator winding segment. If equation (5.8) is utilised to predict winding thermal conductivity:

$$k_{av} = 0.026\ \times\ \left(\frac{1.4\ mm}{0.13\ mm} + \frac{0.13\ mm}{1.48\ mm}\right) = 0.2822\ Wm^{-1}\ °C^{-1}$$

Then error is calculated considering FEA simulation results:

$$Error_2\ (\%) \approx \left(1 - \frac{k_{\ av}}{k_{eff,sim}}\right) \times\ 100 = \left(1 - \frac{0.2822}{0.3555}\right) \times\ 100 = 20.61\ \%$$

Although the error between FEA approach and equation (5.8) is around 20%, the accuracy of equation (5.8) is not exactly known and the estimated thermal conductivities are still acceptable range and would not lead to significant temperature distribution error inside machine windings.

5.3.1.2 Radial Heat Flow and Analytical Thermal Conductivity Calculations

Heat flow is not only in a certain plane axis between the thermal boundary conditions. Radial heat flow is also very important inside the stator winding. Therefore, the thermal conductivity in radial direction should be studied. In Figure 5.7, how the round conductors come together in conventional windings is illustrated.

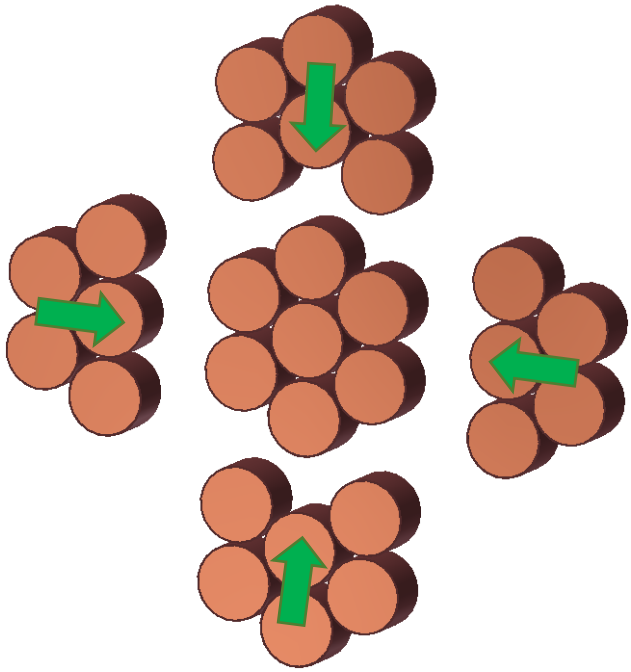

Figure 5.7 Round conductors when radial accumulation of conductors is considered

It is not easy to conduct an analytical approach for the thermal conductivity prediction when the radial heat flow is taken into account in a piece of winding segment. Nonetheless, the radial heat flow might be still represented if a conductor is centred in a plane and the heat flow paths are created from the centre conductor radially. This is depicted in Figure 5.8 with a centre magnet wire and surrounding conductors placed radially around the centre conductor.

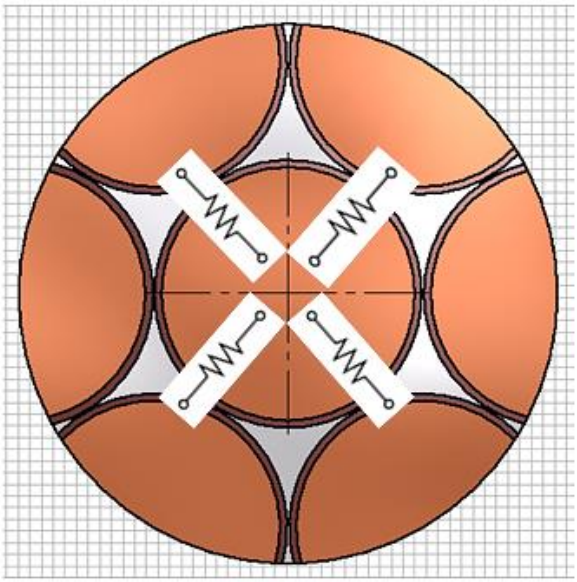

Figure 5.8 A thermal lumped model for a piece of winding segment with a centre conductor surrounded by other conductors radially

If a quarter of the Figure 5.8 is taken into account, simple resistive thermal circuit can be achieved. This is illustrated in Figure 5.9a.

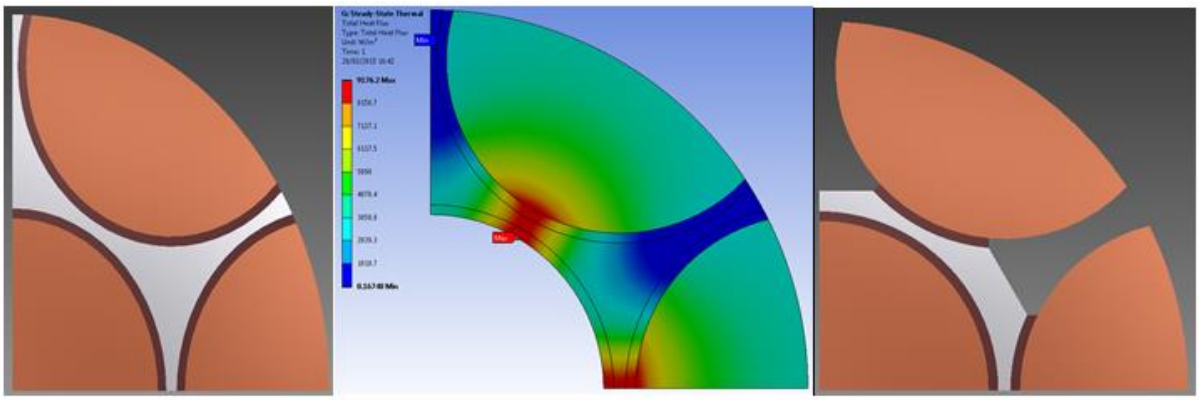

Figure 5.9 Effective heat flux regions and the approximated geometry for thermal conductivity estimations

Since the temperature gradients are in the radial direction, radial systems can be also considered as one dimensional heat flow systems. Boundary conditions are selected as: inner radius of the centred copper conductor and outer radius of the circular region. The effective heat flux regions are also considered when the thickness of each material is calculated along the radial direction. Radial conduction in a cylindrical wall can be written as follows [122]:

$$R_{t,cond} = \frac{\ln\left(\frac{R_2}{R_1}\right)}{2\pi L k} \tag{5.9}$$

where R_2, R_1 are outer and inner radiuses, respectively and L is the total axial length and k is isotropic thermal conductivity. Inner and outer radiuses of the materials along the radial direction were calculated. The required radiuses are illustrated in Figure 5.10.

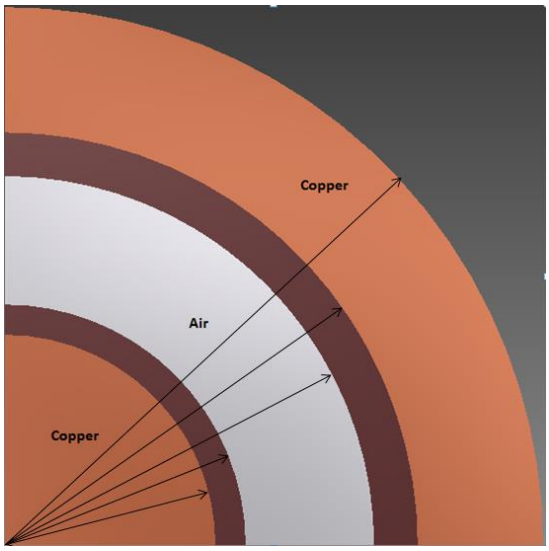

Figure 5.10 Representation of equivalent radial system estimation using effective heat flux regions

Assuming that r_1 , r_2, r_3 and r_4 represents thermal resistance of the materials from centre to top in Figure 5.10. The equivalent total thermal resistance is represented to be r_5.

$$r_1 + r_2 + r_3 + r_4 = r_5$$

$$r_1 = \frac{\ln(R_2/R_1)}{2\pi k_1 L},\ r_2 = \frac{\ln(R_3/R_2)}{2\pi k_2 L},\ r_3 = \frac{\ln(R_4/R_3)}{2\pi k_3 L}, r_4 = \frac{\ln(R_5/R_4)}{2\pi k_4 L},$$

$$r_5 = \frac{\ln(R_5/R_1)}{2\pi k_{eff} L}$$

$$k_1 = k_3$$

$$k_{eff} = \frac{k_1\, k_2\, k_4\, \ln\left(\frac{R_5}{R_1}\right)}{k_2\, k_4 \ln\left(\frac{R_2}{R_1}\right) + k_1\, k_4 \ln\left(\frac{R_3}{R_2}\right) + k_2\, k_4 \ln\left(\frac{R_4}{R_3}\right) + k_1 k_2 \ln\left(\frac{R_5}{R_4}\right)} \quad (5.10)$$

Using equation (5.10), the effective thermal conductivity can be theoretically calculated:

$$R_1 = 0.7\ mm\,, \qquad R_2 = 0.74\ mm\,, \qquad R_3 = 0.8444\ mm\,,$$
$$R_4 = 0.8696\ mm\,,\ R_5 = 1.4383\ mm$$

In equation (5.10), thermal conductivities of the actual materials are given as follows:

$$k_1 = k_3 = 0.25\ Wm^{-1}\,°C^{-1}$$

$$k_2 = 0.026\ Wm^{-1}\,°C^{-1}$$

$$k_4 = 400\ Wm^{-1}\,°C^{-1}$$

$$k_{eff} = \frac{k_1\, k_2\, k_4\, \ln\left(\frac{R_5}{R_1}\right)}{k_2\, k_4 \ln\left(\frac{R_2}{R_1}\right) + k_1\, k_4 \ln\left(\frac{R_3}{R_2}\right) + k_2\, k_4 \ln\left(\frac{R_4}{R_3}\right) + k_1 k_2 \ln\left(\frac{R_5}{R_4}\right)}$$

$$= \frac{1.87226}{0.88296 + 13.19 + 3.2701x10^{-3}} = 0.133\ Wm^{-1}\,°C^{-1}$$

This result can be compared to the FEA thermal simulation results. Using equation (5.7), average thermal conductivity for 19 different paths that radially spans the whole unit can be estimated. Sampled paths were demonstrated in Figure 5.11 below. The temperature boundary difference is chosen to be $\Delta T = 20°\,C$.

Path 1: $k_{1,sim} = \frac{Q \times l}{\Delta T} = \frac{5410.202\ x\ 0.000825}{20} = 0.2231\ Wm^{-1}\,°C^{-1}$

Path 2: $k_{2,sim} = \frac{Q \times l}{\Delta T} = \frac{5238.95\ x\ 0.000825}{20} = 0.2161\ Wm^{-1}\,°C^{-1}$

Path 3: $k_{3,sim} = \frac{Q \times l}{\Delta T} = \frac{5755.219\ x\ 0.000825}{20} = 0.1962\ Wm^{-1}\,°C^{-1}$

Path 4: $k_{4,sim} = \frac{Q \times l}{\Delta T} = \frac{4141.131\ x\ 0.000825}{20} = 0.1708\ Wm^{-1}\ °C^{-1}$

Path 5: $k_{5,sim} = \frac{Q \times l}{\Delta T} = \frac{3383.198\ x\ 0.000825}{20} = 0.1395\ Wm^{-1}\ °C^{-1}$

Path 6: $k_{6,sim} = \frac{Q \times l}{\Delta T} = \frac{2303.824\ x\ 0.000825}{20} = 0.0950\ Wm^{-1}\ °C^{-1}$

Path 7: $k_{7,sim} = \frac{Q \times l}{\Delta T} = \frac{743.1846\ x\ 0.000825}{20} = 0.0306\ Wm^{-1}\ °C^{-1}$

Path 8: $k_{8,sim} = \frac{Q \times l}{\Delta T} = \frac{2309.78\ x\ 0.000825}{20} = 0.0952\ Wm^{-1}\ °C^{-1}$

Path 9: $k_{9,sim} = \frac{Q \times l}{\Delta T} = \frac{3385.969\ x\ 0.000825}{20} = 0.1396\ Wm^{-1}\ °C^{-1}$

Path 10 $k_{10,sim} = \frac{Q \times l}{\Delta T} = \frac{4141.227\ x\ 0.000825}{20} = 0.1702\ Wm^{-1}\ °C^{-1}$

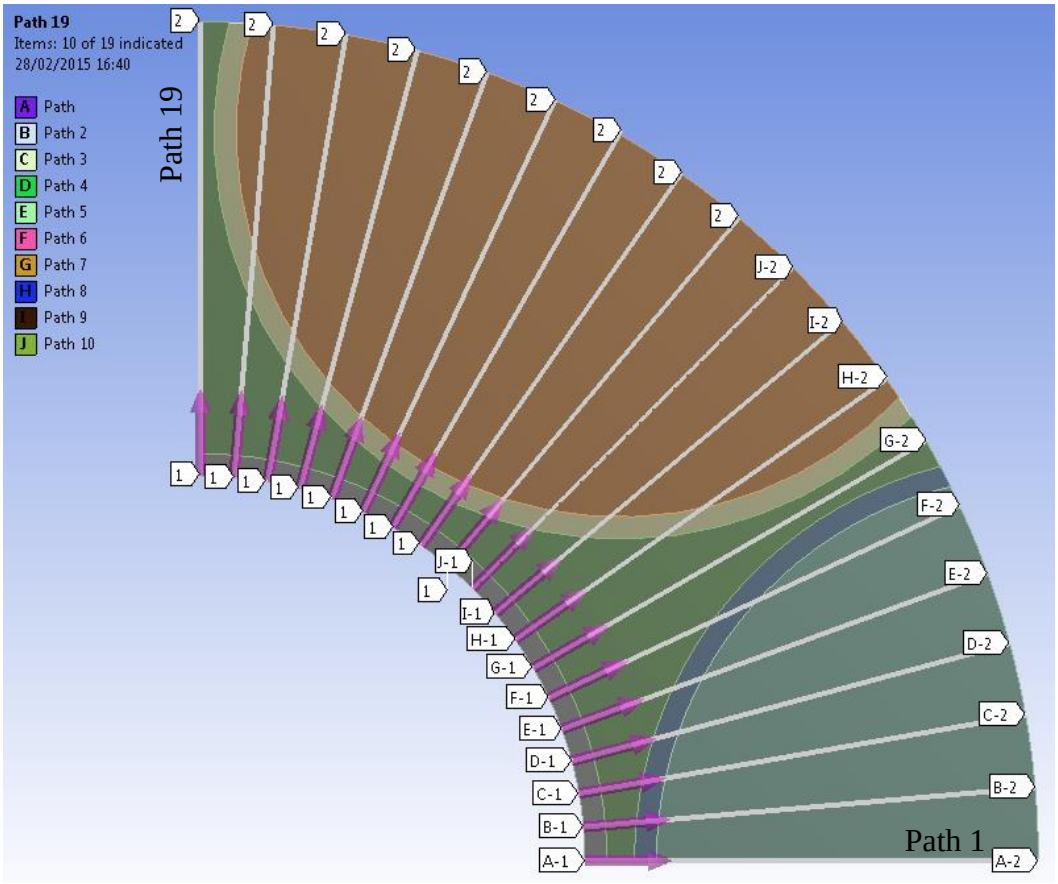

Figure 5.11 A winding segment sampled to estimate average thermal conductivity

Path 11: $k_{11,sim} = \frac{Q \times l}{\Delta T} = \frac{4756.531\ x\ 0.000825}{20} = 0.1961\ Wm^{-1}\ °C^{-1}$

Path 12: $k_{12,sim} = \frac{Q \times l}{\Delta T} = \frac{5236.167x\ 0.000825}{20} = 0.2160\ Wm^{-1}\ °C^{-1}$

Path 13: $k_{13,sim} = \frac{Q \times l}{\Delta T} = \frac{5445.481\ x\ 0.000825}{20} = 0.2260\ Wm^{-1}\ °C^{-1}$

Path 14: $k_{14,sim} = \frac{Q \times l}{\Delta T} = \frac{5235.392\ x\ 0.000825}{20} = 0.2160\ Wm^{-1}\ °C^{-1}$

Path 15: $k_{15,sim} = \frac{Q \times l}{\Delta T} = \frac{4749.996\ x\ 0.000825}{20} = 0.1959\ Wm^{-1}\ °C^{-1}$

Path 16: $k_{16,sim} = \frac{Q \times l}{\Delta T} = \frac{4141.19\ x\ 0.000825}{20} = 0.1708\ Wm^{-1}\ °C^{-1}$

Path 17: $k_{17,sim} = \frac{Q \times l}{\Delta T} = \frac{3387.598\ x\ 0.000825}{20} = 0.1398\ Wm^{-1}\ °C^{-1}$

Path 18: $k_{18,sim} = \frac{Q \times l}{\Delta T} = \frac{2307.261\ x\ 0.000825}{20} = 0.0951\ Wm^{-1}\ °C^{-1}$

Path 19: $k_{19,sim} = \frac{Q \times l}{\Delta T} = \frac{721.7905\ x\ 0.000825}{20} = 0.0300\ Wm^{-1}\ °C^{-1}$

$$\therefore\ k_{eff,sim} = \frac{Average\ [k_{1,sim} : k_{19,sim}]}{19} = 0.1559\ Wm^{-1}\ °C^{-1}$$

The error between the FEA thermal simulation results and analytical results can be compared and the error can be written as:

$$Error\ (\%) \approx \left(1 - \frac{k_{\ eff}}{k_{eff,sim}}\right) \times\ 100 = \left(1 - \frac{0.133}{0.1559}\right) \times\ 100 = 14.6\ \%$$

The effective conductivity for radial heat flow was calculated using the analytical approach and FEA steady state thermal simulations, the error between the simulation results and analytical approach is 14.6 %. This error is higher than what it has been calculated for the axial case, because in radial heat flow, equivalent thermal resistance approximation is quite difficult to estimate in comparison to plane wall calculation as performed in the previous section.

As a result, an analytical approach has been developed with the help of FEA simulation results. When simulation results and theoretical calculations are compared to each other, one dimensional heat flow for plane wall gives more accurate approximation with 5.41 % error. Nevertheless, radial heat flow calculations give more error which is 14.6 % when compared to simulation results. If the theoretical formula given in [120] is used to calculate effective conductivity for round copper coils, the error is almost 20%. This error will not lead to a significantly inaccurate temperature distribution since the effective thermal conductivity of windings is not a very sensitive parameter regarding temperature distribution if it is predicted usually within ±20% error as proved in [43]. This claims that the theoretical approach presented here predicts effective thermal conductivity of winding segment within acceptable accuracy.

5.3.2 A Detailed Investigation of Heat Flow through Windings

In order to understand how average thermal conductivity is calculated by taking samples on equal interval paths, the heat flow at each path can be investigated. Since the effective thermal conductivity is dependent on heat flux density, distance along the boundary conditions and the temperature difference, variation of heat flux density is very important parameter on the

determination of average thermal conductivity. Isotropic thermal conductivity of each material will directly affect the heat flux density in the material. In other words, if the thermal conductivity of the material is high, then the directional heat flux density across the temperature boundaries will be high or vice versa. For example, when heat flows into the copper and then into the magnet wire insulation, it is expected that the heat flux will gradually decrease because of huge thermal conductivity differences among the materials. The approach followed to calculate the average thermal conductivity of an anisotropic section of a bobbin is in fact based on the temperature change inside the coil. Temperature is usually the highest at the centre of the coil as it is the furthest from any cooling paths as illustrated in Figure 5.12.

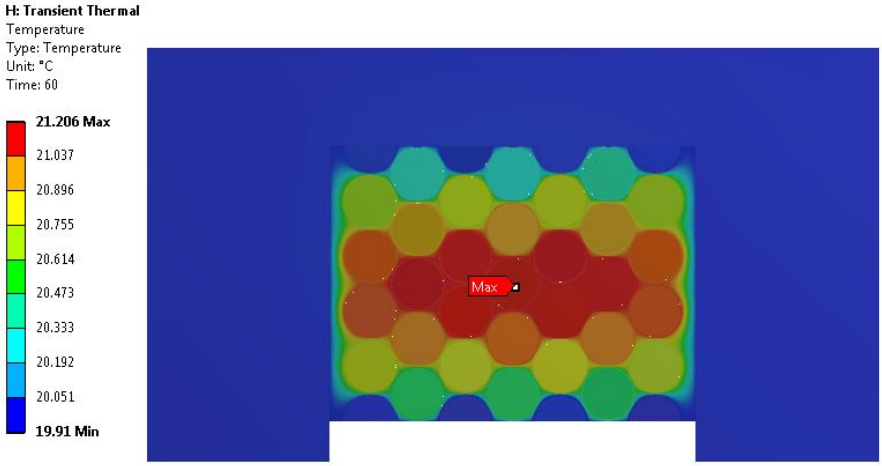

Figure 5.12 Temperature distribution inside a coil

When heat flux flows from the centre of the coil to an external surface, a temperature gradient occurs. This temperature difference could be used as a thermal boundary for the investigation of the effective thermal conductivity in one dimension. The variation of temperature for the example given in Figure 5.12 is plotted in Figure 5.13.

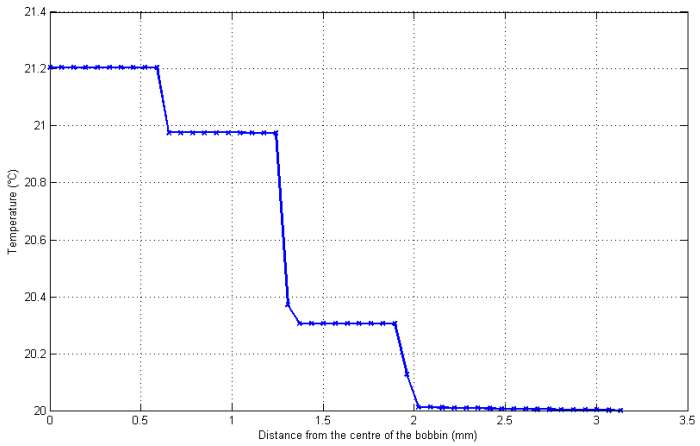

Figure 5.13 Temperature variation from the centre to a side (i.e. single path)

Normally, the temperature cannot change abruptly inside the coil, however, the plot given in Figure 5.13 was obtained on a single path. That is, temperature data is recorded without including effect of any temperature variation in multi-dimensional cases. This approach could help create a boundary condition for a tiny piece of stator winding. If the boundary conditions are set, then heat flux paths could be investigated for one dimensional case. Heat flux flow inside a piece of winding is demonstrated in Figure 5.14.

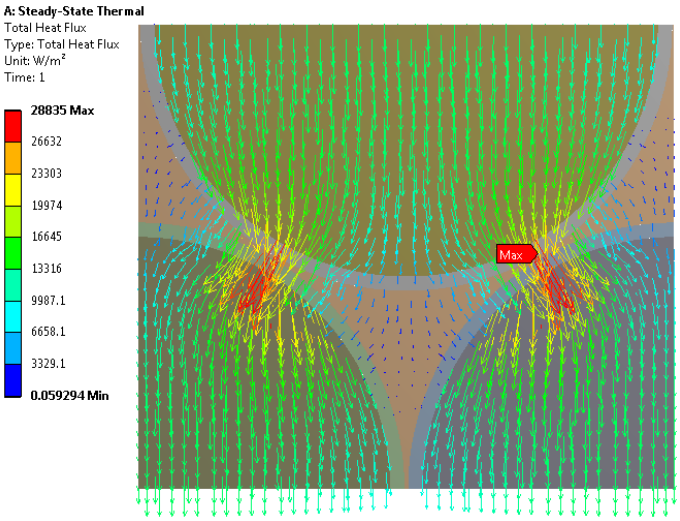

Figure 5.14 Heat flux flow across the conductors

In Figure 5.14, the distance between the copper conductors is 0.01 mm and heat flows from higher temperature to lower temperature boundary. Heat flux density is relatively higher inside the copper area compared to air region. Heat flux concentration increases in the region where conductors are close to each other. This is because heat flux vector tries to reach higher thermal conductivity region quickly.

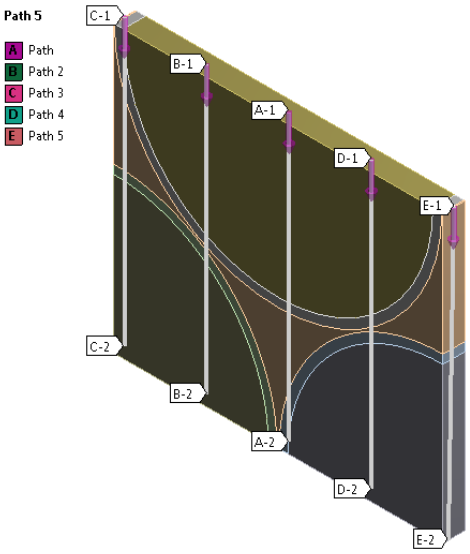

Figure 5.15 Selected paths in 3D model in a piece of winding segment

In Figure 5.15, five unique paths are illustrated in a piece of coil. The paths lay on along the temperature boundaries which are upper and lower faces in this case. Transition of heat flux from one region to another is not uniform due to varying thermal conductivity. Therefore, each path will have a unique heat flux plot. Since variation of heat flow directly affects the average thermal conductivity of each anisotropic path, the variation of heat flux density along different paths have been demonstrated in Figure 5.16.

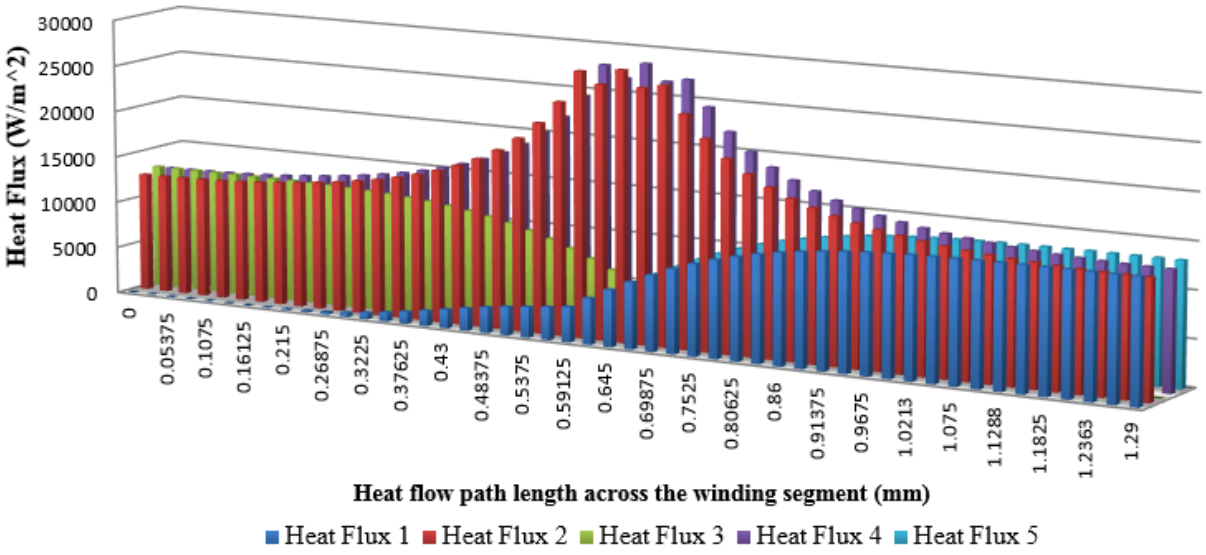

Figure 5.16 Variation of heat flux density for the selected paths

In Figure 5.16, the total distance across the thermal boundaries is 1.29 mm. Heat Flux 1 corresponds to Path C, Heat Flux 2 corresponds to Path B, and Heat Flux 3 corresponds to Path A. Heat Flux 4 and Heat Flux 5 are the same as Heat Flux 2 and Heat Flux 1, respectively because they correspond to the same paths in terms of order of heat flux transition between the materials. The important thing here is that heat flux density is too low in air region between the conductors. This severely reduces the average thermal conductivity of the winding. On the other hand, when conductors are close enough to each other, more regular heat flux density trend can be noticed. This demonstrates that the effect of air voids between the turns of any stator winding is negative with regard to effective thermal conductivity of an electrical machine slot.

5.3.3 Effect of Slot Fill Factor on Winding Thermal Conductivity

Varying the fill factor is possible by altering the distance between the turns uniformly, improvement of effective thermal conductivity is here studied in relation to variation of slot fill factor.

In Figure 5.5 in Section 5.3.1, if the average thermal flux density drops below 10% of the maximum value, the air region corresponding to that has been neglected and effective heat flux density fields have been represented in simple equivalent geometry. Using the first order

Fourier law of heat, the average thermal conductivities are calculated. In Figure 5.17, the semi-analytical method is repeated for different slot fill factors. The results show that FEA approach and semi-analytical thermal conductivity predictions are in a similar trend implying that the analytical method is sufficiently accurate.

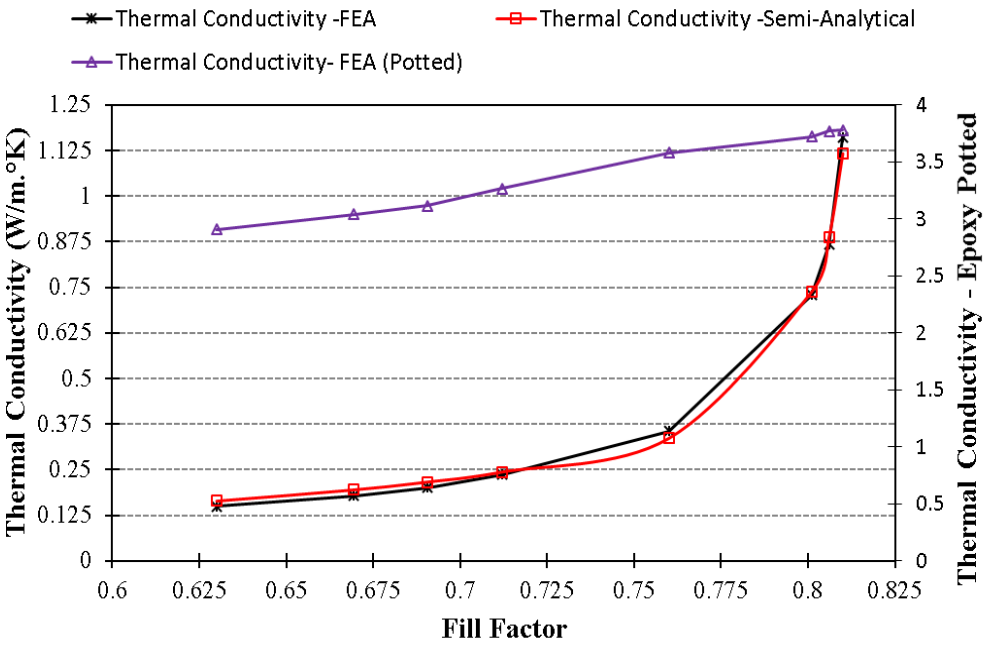

Figure 5.17 Slot fill factor vs. effective thermal conductivity of winding

According to Figure 5.17, the increase in slot fill factor improves the effective thermal conductivity of a winding segment. However, the main improvement is obtained after 0.75 slot fill factor as there is a significant reduction in air voids between the turns. Although average thermal conductivities vary between $0.149\,W/m.°K$ to $1.15\,W/m.°K$, this might not correspond to reality, because slot fill factor has been altered by varying the distance between the turns uniformly in this case. A manually wound electrical machine bobbin would be more random configuration and this will directly affect the anisotropy of the whole geometry. The effect of thermal potting material, which improving thermal conductivity significantly, with a thermal conductivity of 1.26 W/mK is also shown in Figure 5.17 by replacing the air region with a high thermal conductivity resin.

5.4 Case Study: Slot Fill Factor versus Temperature Increase

In this case study, the improvement of slot fill factor has been modelled by increasing the number of turns and by reducing the wire diameter rather than modelling a compressed coil. Reduction in a slot area mainly reduces air voids between the conductors. Since the thermal conductivity of air is very small in comparison to magnet wire enamel and copper conductor, reduction of the air region will improve the effective thermal conductivity of a coil.

When heat is transferred by conduction, interaction between the molecules at higher energy levels becomes predominant. This is achieved by increasing the contact area of solid bodies. Therefore, reduction in air between the coil turns will enhance heat transfer between conductors. Thus, generated I^2R losses that increase the temperature inside the coil will be removed quickly due to improved thermal conductivity.

5.4.1 FEA Modelling

From the point of view of FEA transient thermal simulations, it is very difficult to demonstrate this phenomenon for a compressed bobbin, because the cross sectional geometry of a bobbin pressed at very high pressures will not consist of uniformly distributed circular conductors. As the round copper wires are prone to come together in hexagonal geometry after compression, it is not possible to precisely represent the geometry in FEA.

The objective of this modelling is to investigate if improvement in slot fill factor by decreasing the slot width will enhance the bobbin thermally.

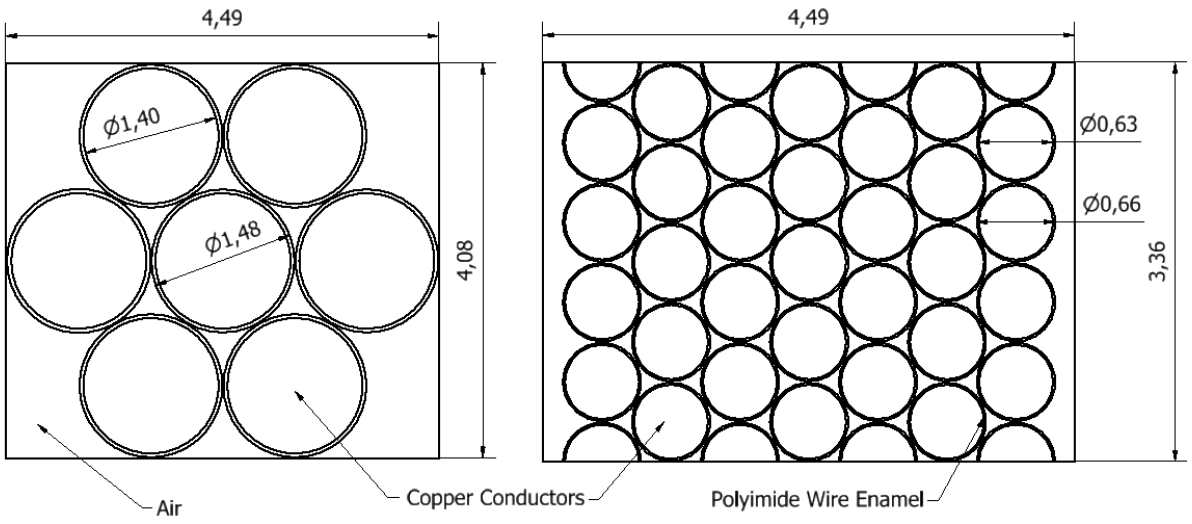

(a) 7-turn (b) 35-turn

Figure 5.18 Cross-sectional view of the FEA geometries

It is clear that copper magnet wires in smaller overall diameter will provide a higher slot fill factor when compared to thicker copper magnet wires. Even for the optimum case, thicker conductors will end up with larger gaps between the individual turns compared to thinner magnet wires. The effect of varying magnet wire diameter on the slot fill factor could be used to demonstrate how temperature varies inside a coil. In other words, a higher fill factor model is achieved by using thinner copper conductors with greater number of turns as it is illustrated in Figure 5.18.

In Figure 5.18 a), a 7-turn bobbin with 1.48 mm overall diameter has been modelled. In Figure 5.18 b), a 35-turn bobbin has been represented in the same slot width as 7-turn bobbin but slot depths are different. The principal common feature between these 3D geometries is that they contain the same copper volume and magnet wire insulation volume. In other words, the 7-turn magnet wire has been equivalently modelled in 35-turns in order to improve slot fill factor by reducing the conductor diameter. Geometrical features of the models given in Figure 5.18 are tabulated in Table 5.2 to realize the difference between the geometries.

Table 5.2 Main geometrical features of FEA models given in Figure 5.18

Geometry Feature	7-turn bobbin	35-turn bobbin
Slot width ($\boldsymbol{mm}$)	4.49	4.49
Slot depth ($\boldsymbol{mm}$)	4.08	3.36
Copper volume ($\boldsymbol{mm^3}$)	1.07177	1.07177
Polyimide coating volume ($\boldsymbol{mm^3}$)	0.126336	0.126336
Air volume ($\boldsymbol{mm^3}$)	0.63012	0.31602
Axial length ($\boldsymbol{mm}$)	0.1	0.1
Slot Fill Factor	0.58	0.71

5.4.2 Results and Discussion

A reference current density of $6\ A/mm^2$ has been chosen for the both models to show how improving the slot fill factor reduces temperature increase in the case of heat transfer by convection from top and bottom faces of the 3-D models.

Internal heat generation is achieved according to following equations:

$$I = J\ \times\ A\ where\ J = 6\frac{A}{mm^2}$$

$$P =\ I^2\ \times\ R\ where\ R =\ \rho\ \frac{l}{A} = 1.68\ \times 10^{-8}\ \Omega.m\ for\ copper$$

$$Heat\ Generation:\ \rho_V = \frac{Copper\ Loss\ (P)}{Conductor\ Volume\ (mm^3)}\ \left(\frac{W}{mm^3}\right) \qquad (5.11)$$

According to equation (5.11), heat generation has been provided and temperature variation for given boundary conditions given in Table 5.3 is plotted with respect to time. A steady state temperature variation has been obtained at the end of the transient simulation.

Table 5.3 Boundary conditions for transient thermal FEA simulations

Parameter	Value	Unit
Current Density	6	A/mm^2
Total copper loss	6.515e-4	$Watt$
Heat transfer coefficient for the top and bottom faces	30	$W/(m^2 .°C)$
Simulation transient time	1200	$seconds$
Ambient Temperature	22	$°C$

The simulation is performed using a transient analysis with 20 minutes of time. After obtaining a steady state temperature distribution inside the coil, temperature increase with respect to initial ambient temperature has been compared. Total heat flux and temperature distribution are shown in Figure 5.19.

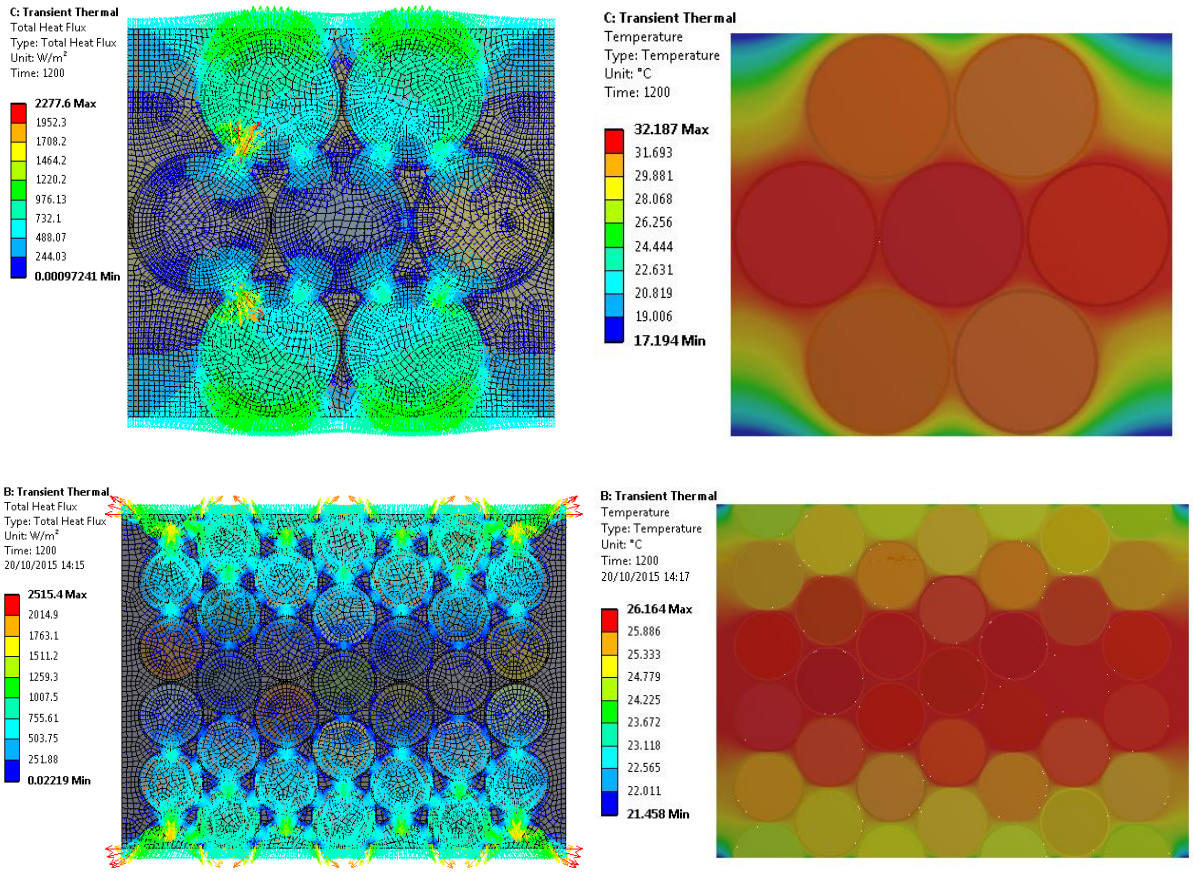

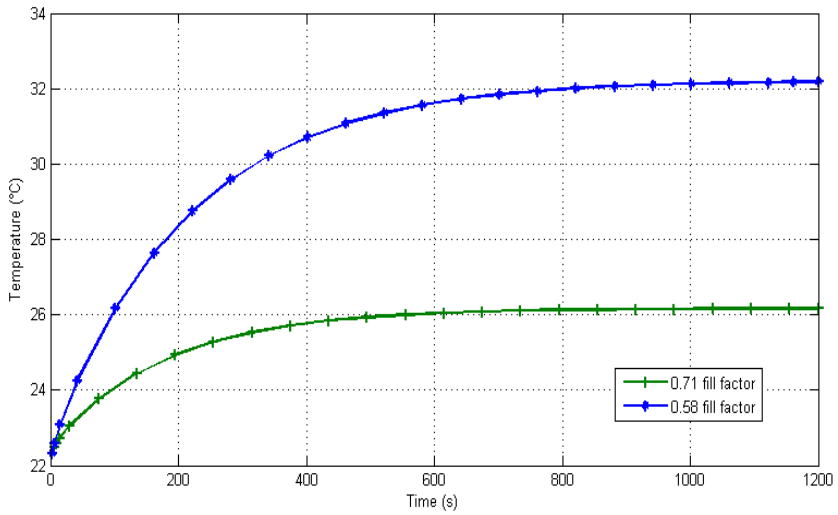

Figure 5.19 Heat flux and temperature distribution in the winding segments

As shown in Figure 5.19, the final temperature value of a high fill factor winding is lower than that of a low fill factor model at steady state. This demonstrates that densely packaging of copper conductors will help improve thermal conductivity of the coil. Thus, generated internal heat will be removed from the body quickly. If this is applied to rotating machine windings, the temperature will be kept lower compared to random wound low fill factor conventional windings. In addition to rapid copper loss removal in the windings, a high fill factor coil will enhance the overall average radial thermal conductivity of a rotating machine. Consequently, temperature increase will remain lower and the life expectancy of electrical machines will be improved.

5.5 Case Study: Epoxy Impregnated Winding Sample

A steady state thermal FEA investigation has been conducted on an epoxy impregnated winding sample to determine the effective thermal conductivity. The study is based on an experimental thermal parameter estimation technique previously reported by [34, 35, 123]. The winding sample consists of Class-H polyamide-imide copper wires with a dimeter of 1.6 mm and the sample was vacuum impregnated with epoxy ($k_{epoxy} = 0.85\ W/m.K$) to enhance average thermal conductivity. Approximately, 60% slot fill factor was achieved with round copper conductors. An effective thermal conductivity of 2.5-2.7 $W/m.K$ has been reported for the winding samples as given in [35].

In order to verify the thermal conductivity results reported previously in [35, 123], the steady state thermal FEA approach as described in Section 5.3.1 has been employed as depicted in Figure 5.20.

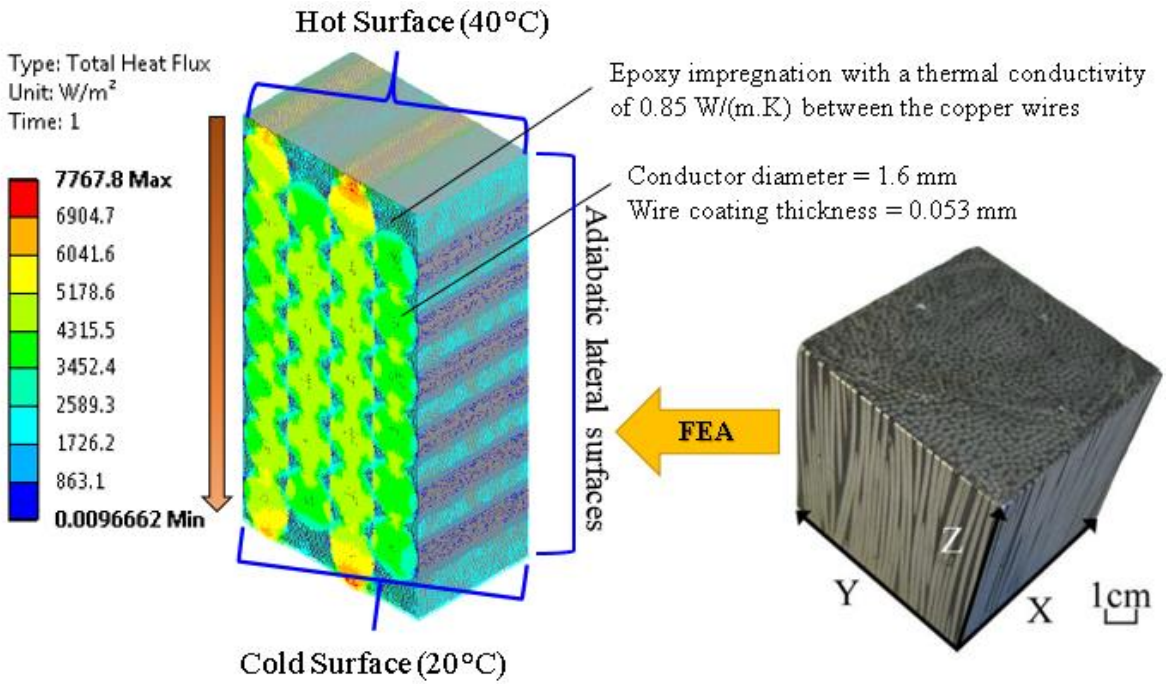

Figure 5.20 Winding sample previously reported in [35] and a developed FEA approach to estimate the thermal conductivity

The FEA results obtained from the geometry achieving about 0.6 fill factor, given in Figure 5.20, predict the effective thermal conductivity to be 2.47 W/m.K within 8.5% error in y-direction of the winding sample. This proves that the developed FEA method is promising for the accuracy of the thermal conductivity estimation and can be performed in much less amount of time to estimate the effective thermal conductivity of the winding samples. Moreover, the extensive thermal experiments might not be needed to measure the thermal conductivity of the stator windings.

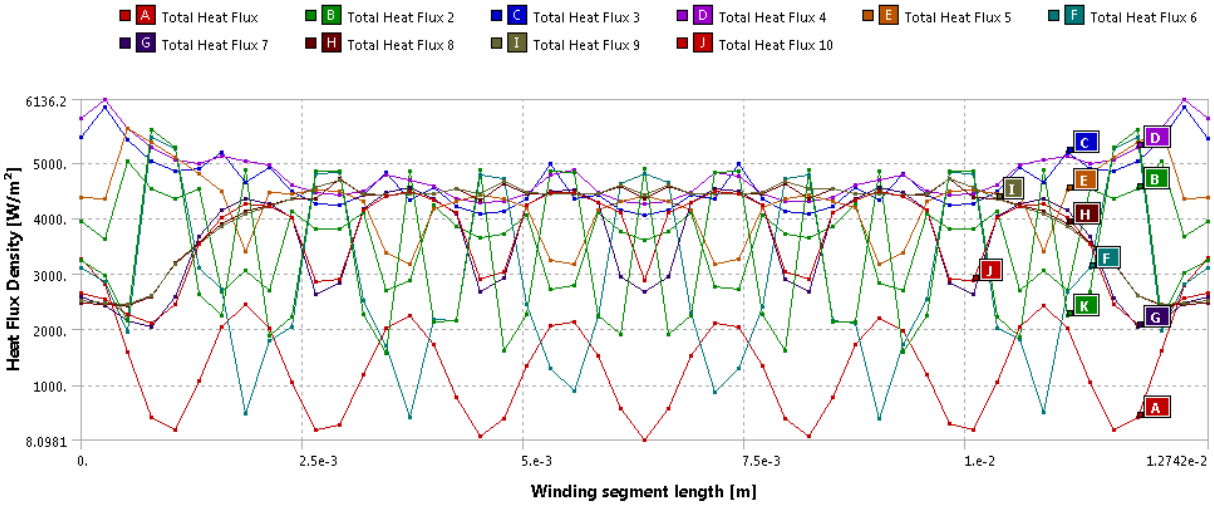

Figure 5.21 Heat flux density variations at different paths across the winding segment

The variation of heat flux across the temperature boundaries in the FEA winding sample given in Figure 5.20 is shown in Figure 5.21. It can be noted that each path has unique heat flux density that can be used to compute effective thermal conductivity by applying one dimensional Fourier's law of Heat as described in Section 5.3.1.1.

5.6 Conclusion: Key Findings

The outcome of winding thermal modelling using analytical and FEA methods and thermal conductivity improvement are summarised as follows:

- First of all, the importance of slot fill factor on the machine temperature distribution is described in Section 5.2. It is demonstrated that the effective thermal conductivity is one of the most important thermal parameters as it can affect the temperature distribution in an electrical machine significantly. Also, there is a certain value of the effective thermal conductivity where the temperature in windings settles. This must be estimated and achieved in real prototypes. Otherwise, elevated winding temperature would be observed in machine windings due to poor slot thermal conductivity.
- In order to show the effect of slot fill factor on the winding thermal conductivity, both FEA and analytical approaches have been conducted. The main purpose of the developed analytical approach was to claim that the FEA thermal model of a winding segment is accurate enough. By varying the distance between round copper conductors, slot fill factor vs. effective winding thermal conductivity is plotted. It should be noted that this type of plots are dependent on conductor diameter.
- FEA modelling of winding segments might be investigated in two forms. A uniform winding segment in xy–plane in which heat flows in $-y$ direction as illustrated in Figure 5.6 is the first one. The second form considers radial heat flow from the centre of a winding segment. In this case, one of the coil windings is considered to be centre conductor and heat flow occurs from the centre to outer diameters radially.
- The proposed analytical and FEA modelling techniques might be quite useful for initial approximation of the average winding thermal conductivity. For FEA thermal modelling of an electrical machine, calibration is usually required to match simulated results to experimental results. Since winding thermal conductivity is a very sensitive thermal parameter, the accurate prediction of it is crucial. Therefore, winding thermal conductivity can be first predicted using a piece of winding segment with or without a potting material, then the estimated values of thermal conductivity could be used as an initial estimation for a thermal calibration process.

- Slot fill factor versus temperature increase has also been studied in Section 5.4. One of the aims was to mimic a compressed coil by reducing conductor diameter. A higher slot fill factor case is represented with thinner and greater number of conductors, but the volume of copper and insulation material were kept the same for both cases. Temperature increase were observed by injecting the same amount of copper loss for the same amount of materials. At densely packed, high fill factor (0.71) case, hot spot temperature is about 18% less than that of low fill factor (0.58) case, showing that compressed windings might help reduce winding hot spot temperature.

Chapter 6. Thermal Investigation of Integrated Starter Generator with Compressed Stator Windings

6.1 Objectives

Thermal improvement of the optimum ISG model proposed in Chapter 3 is discussed here by employing on-tooth coil pressing method. The experimental methodology of coil pressing is also described in consideration of structural FEA of the ISG conductors. In order to estimate the average thermal conductivity of the compressed stator windings, short time transient thermal tests have been conducted and verified through the thermal FEA simulations. The principal objective of this work is to demonstrate that the thermal performance of the machine with compressed windings is better than that with random wound conventional windings.

6.2 Introduction

Higher torque/power density and better thermal performance can be provided in the 21 slot/16 pole V-shape PM ISG with pre-pressing stator coils. In regard to multi-objective optimisation function, efficiency and machine saliency, 21 slot-16 pole V-shape PM machine is the most appropriate choice for a crankshaft mounted ISG application as demonstrated in Chapter 3. The proposed 21 slot-16 pole ISG design is shown in Figure 6.1.

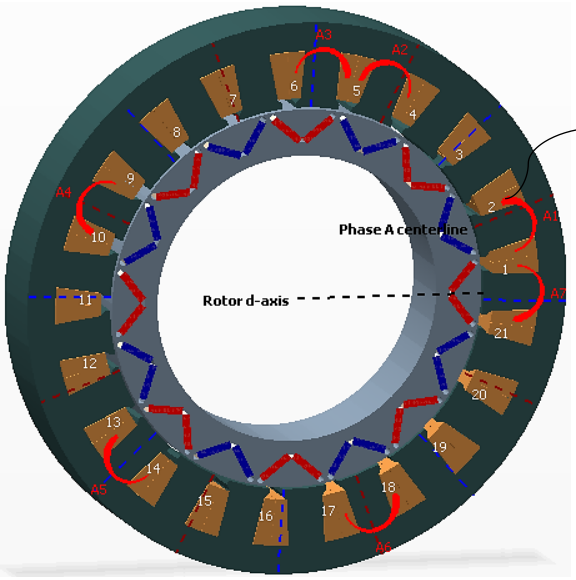

Asymmetrical winding configuration for phase-A, shown red. Number of parallel paths is chosen to be 7.

Figure 6.1 Proposed 21 slot /16 pole PM ISG configuration depicting winding configuration for a single phase – MotorSolve by Infolytica prototype geometry

On-tooth coil pressing in designs with a tooth tip necessitates stator segmentation. In the segmented machines, the stator consists of a multiple number of segmented pieces. Each piece is separately wound and the wound pieces are assembled together to form machine stator [119]. As the coils are wound separately before assembly, coil winding is simple in comparison to

conventional winding methods (i.e. insertion of windings into single piece stator). Another advantage is that copper usage might be reduced with single tooth windings. The main disadvantage of stator segmentation is that the segmented pieces might generate higher audible noise [119].

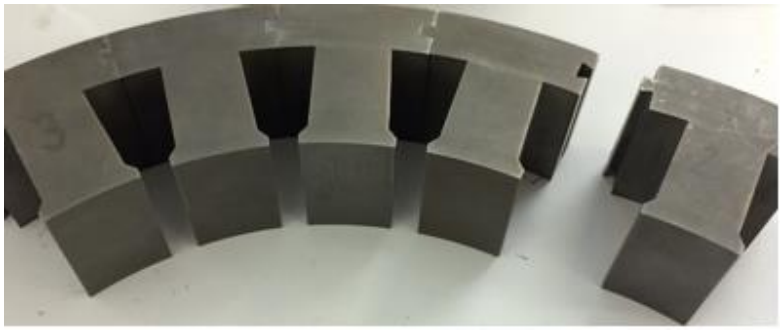

Figure 6.2 Modular stator teeth for the proposed 21 slot- 16 pole V-shape PM ISG

If the stator is segmented, a higher fill factor could be achieved due to modularity making it easier to wind. The modular stator segments for the proposed ISG are shown in Figure 6.2.

Analysis of the influence of coil pressing on machine thermal performance along with the reliability of the proposed method is investigated in this chapter by conducting mechanical and thermal FEA simulations and is experimentally validated. The following sections describe the work in detail.

6.3 Structural Analysis of Coil Pressing for the ISG Stator

1.25 mm and 1.4 mm conductor diameters have been identified as facilitating high fill factors for the proposed machine. 1.25 mm Grade-2 copper magnet wire was chosen for the ISG as compressibility of a greater number of turns and thinner conductor is much better than thicker conductors.

Quasi-static explicit dynamics simulations have been performed to investigate the maximum improvement in fill factor without damaging magnet wire insulation.

6.3.1 Structural FEA of Coil Pressing

The process of coil pressing is investigated by modelling a 5 layer, 15 turn polyimide enamelled magnet wire with conductor diameter 1.25 mm and 0.05 mm insulation thickness. When the coil pressing simulations are monitored to detect insulation failure, elongation and fracture strength of the insulation should be compared to simulation results as they imply material fracture at certain stress and strain values. Compression of the coil is achieved by applying a velocity load onto the steel punch to control the total displacement. As complex body-contact conditions, large deformations and material non-linearity are present, a mesh dominated by hexahedron elements is utilised.

Unbreakable bonded contact was provided between the copper wire and its enamel. Also, frictional turn to turn body interaction with a coefficient of 0.2 was applied to the model. Since increasing the loading rates might increase the contact interpenetration, velocity of the punch was optimised by performing several simulations. The software uses default pure-penalty method to solve body interactions. The simulation setup is shown in Figure 6.3.

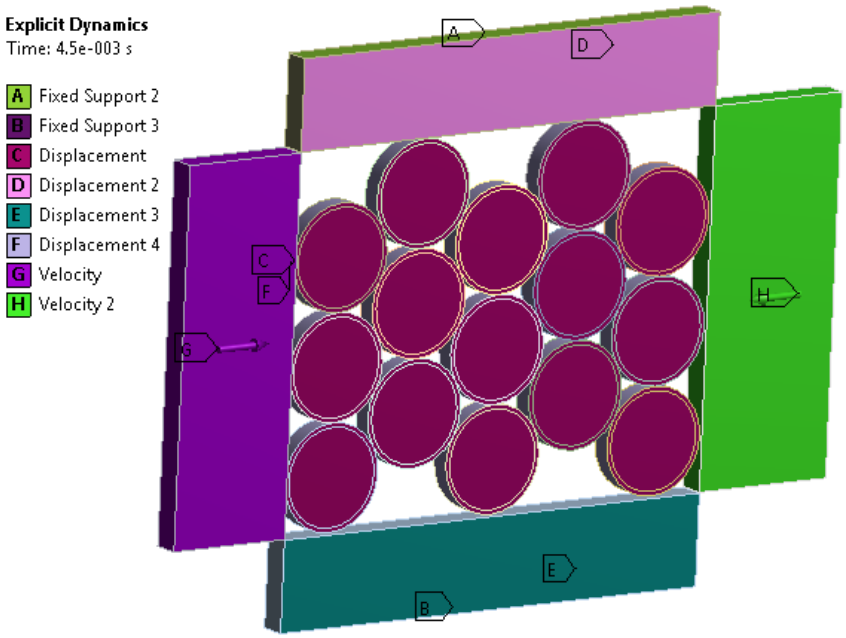

Figure 6.3 FEA boundary conditions for quasi-static pressing

The simulation is artificially accelerated to press the coil over a very small amount of time due to computational cost of the explicit dynamic systems. This model has been solved in about 40 hours with 4- core, 24 GB memory PC to see the total dynamic response of the system.

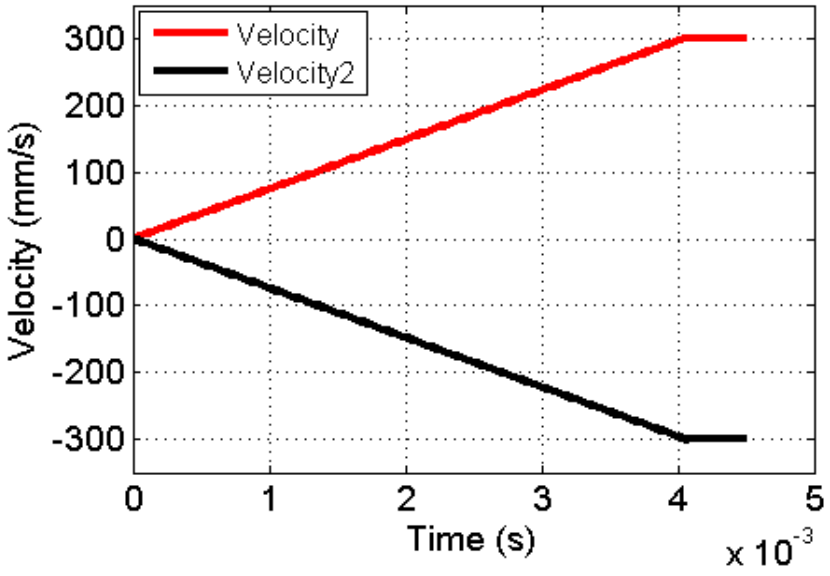

Figure 6.4 Applied velocity profile with respect to time

Note that if natural time of the coil pressing event was used for the models to obtain the original plastic strain results, converging to a solution would take about 4000 hours. The applied velocity functions with respect to time are shown in Figure 6.4. Time integration of the velocity profile gives the total displacement of the punch as 0.479 mm and the maximum speed of the punch is 300 mm/s, corresponding to a 30 cm displacement in one second. Clearly, the speed of punch does not reflect natural time of the event as coil pressing cannot be achieved in a few milliseconds in reality. The actual speed of the press is assumed to be at least 100 times slower than this. Therefore, simulated results of the compression process need to be scaled down a hundred times.

6.3.2 Quasi-Static FEA Results

Figure 6.5 shows the FEA results of a 15-turn coil pressed by applying horizontal load to permanently deform the coil. Results shown are for the final time instant before material fracture occurs on wire enamels.

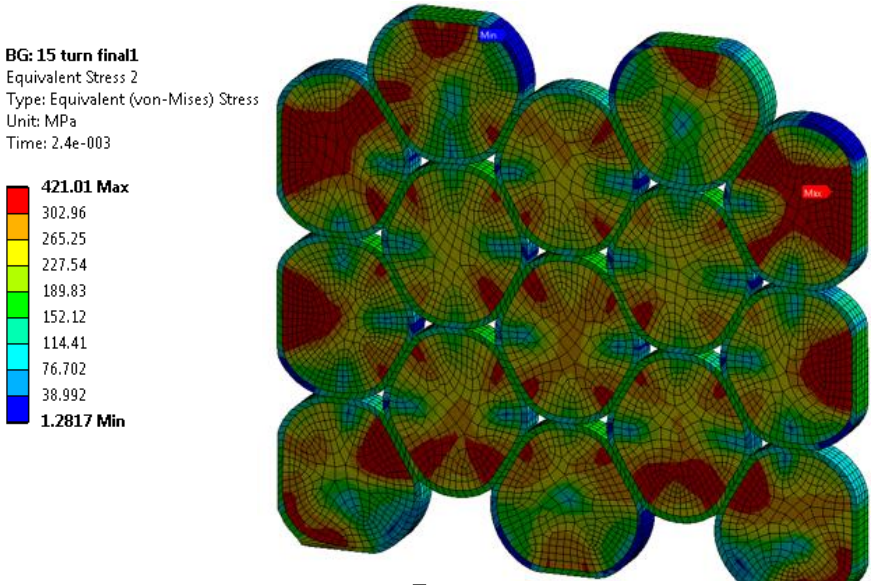

a)

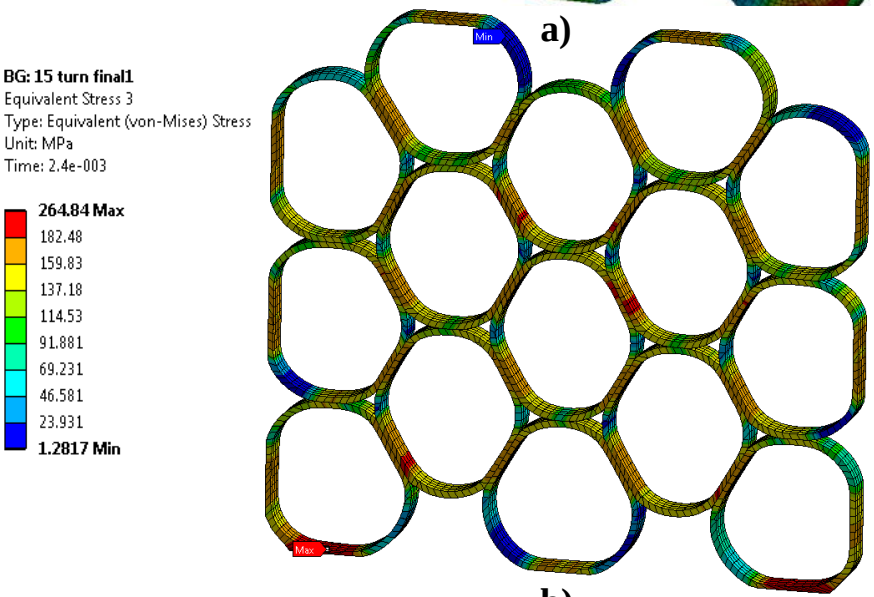

b)

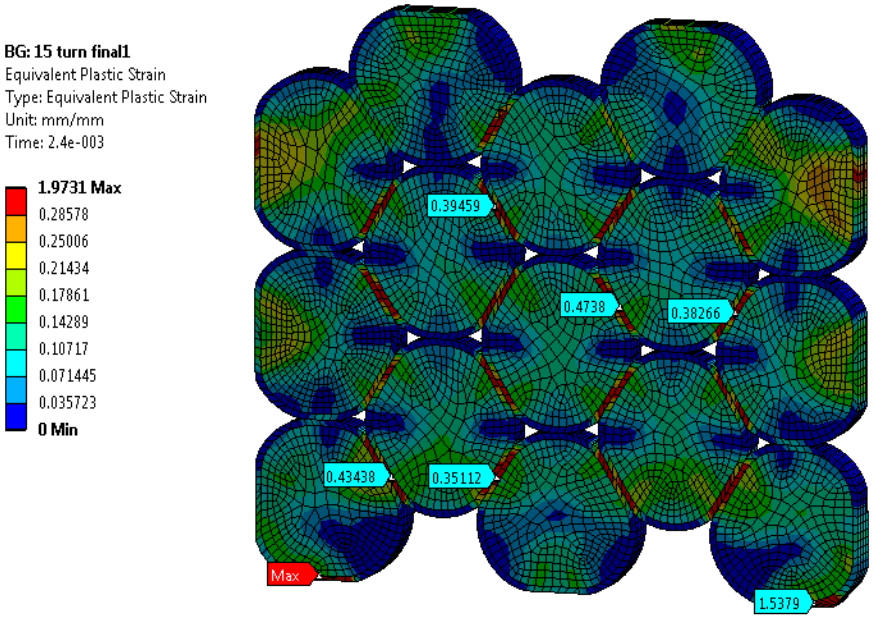

c)

Figure 6.5 (a) Equivalent von-Mises stress on magnet wires, (b) Equivalent von-Mises stress on wire insulations, (c) Plastic strain on wire insulation

Equivalent von-Mises stress and plastic strain results are monitored during the dynamic response of the compression to investigate insulation failure. In Figure 6.5a, the maximum equivalent von-Mises stress is 421 MPa. All magnet wires experience significant plastic deformation. Equivalent plastic strain rate on the magnet wire enamels is the most important indicator to detect material fracture. Since simulated material strain rates are increased by the same factor as the loading rate, plastic predicted strain rates are more than 100 times greater than reality. Corrected strain rates are 0.019 mm/mm on the magnet wire enamel and elongation of polyimide thermosets is 0.03 mm/mm. The insulation is still safe as the wire has not elongated more than the insulation. Moreover, equivalent von-Mises stress on the insulation is shown in Figure 6.5b to peak at 264.8 MPa, less than the fracture strength of polyimide of 345 MPa. Thus, magnet wires with 1.25 mm conductor diameter are predicted to be safely compressed to a 0.73 fill factor.

6.3.3 Magnet Wire Deformation: Experimental vs. FEA

Figure 6.6 shows that predicted deformation is mostly seen for the regions between steel cavity and magnet wire enamel since friction coefficient between steel and wire enamel is greater than that of inter-turn contact regions. This condition is sometimes encountered in experimental coil pressing (Figure 6.6). In order to prevent this, cavities of a die built for coil pressing must consider the bend radius of the end windings, as it expands while pressing the bobbin. End

winding deformation can be mitigated by proper design of die cavity used for compression of bobbins, it is not necessary to compress end windings to obtain higher slot fill factors.

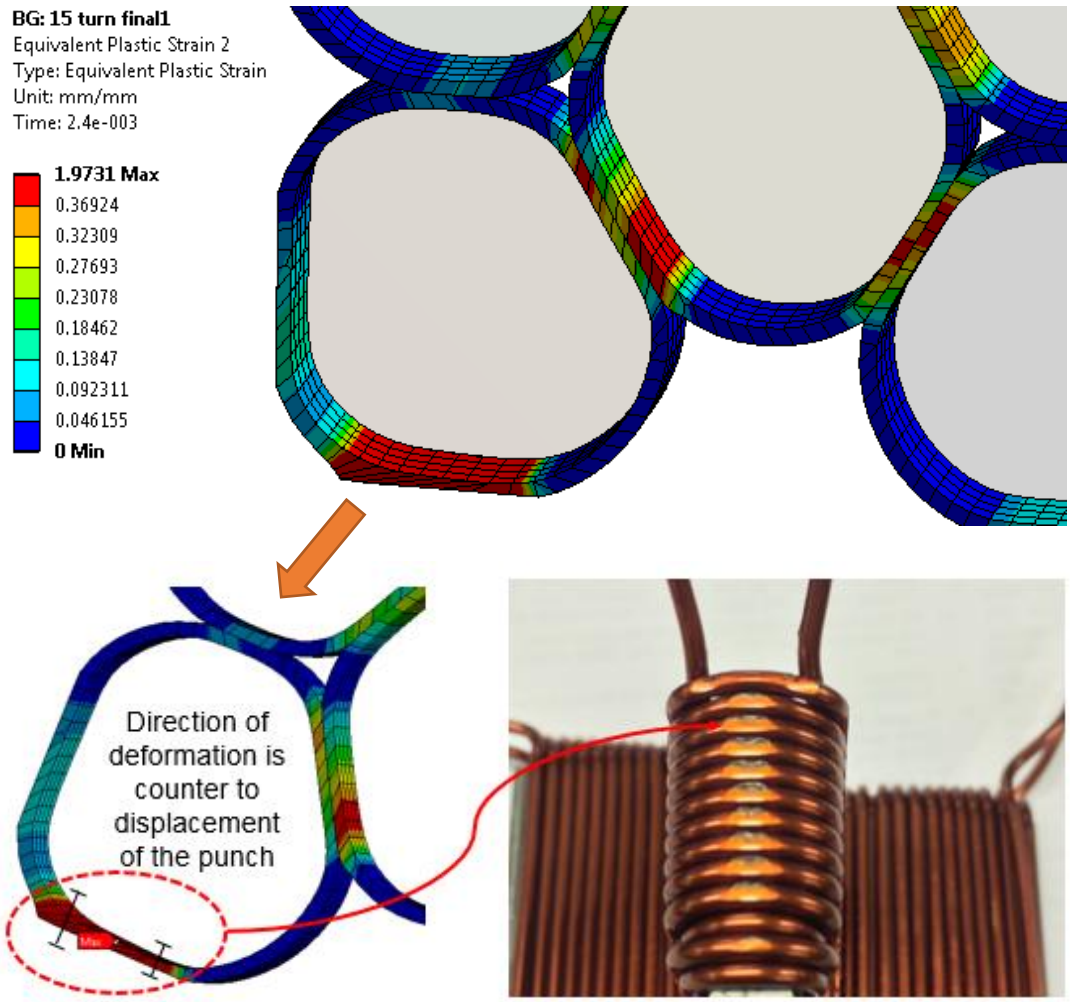

Figure 6.6 Deformation of end windings insulation during compression

In order to prevent the insulation deformation as illustrated in Figure 6.6, a method of on-tooth pressing has been applied to compress only lateral surfaces of a single tooth winding. As a result of quasi static FEA simulations, it was shown that a maximum of around 0.73 fill factor is achievable for Grade-2, 1.25 mm round copper wires. Further compression in this case results in material failure on wire enamels.

6.3.4 Experimental On-tooth Coil Pressing

Before compressing coils under hydraulic press, a pressing tool made of steel EN32B was built. Female steel pieces supporting the machine tooth from the yoke and tooth shoe was built and used for manual winding of segmented stator pieces as shown in Figure 6.7.

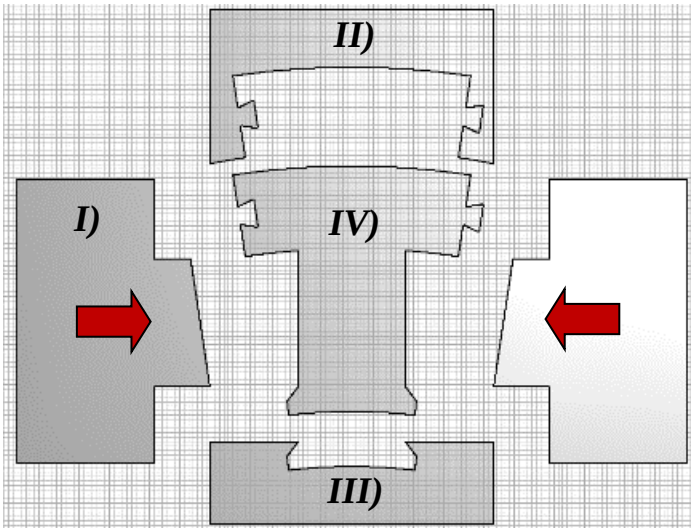

Figure 6.7 ***(I)*** Steel punch; ***(II)*** Tooth yoke support; ***(III)*** Tooth shoe support; ***(IV)*** Segmented ISG stator tooth

After inserting the segmented stator tooth into the female steel parts, both sides of the slot were covered by Nomex electrical insulation system of 0.25 mm thickness attached onto the tooth by polyimide tapes of 0.07 mm thickness. The manual winding process is shown in Figure 6.8 in which segmented tooth is attached to a manual winding machine including a winding counter tool. The winding machine can be run either manually or automatically via a small electric motor.

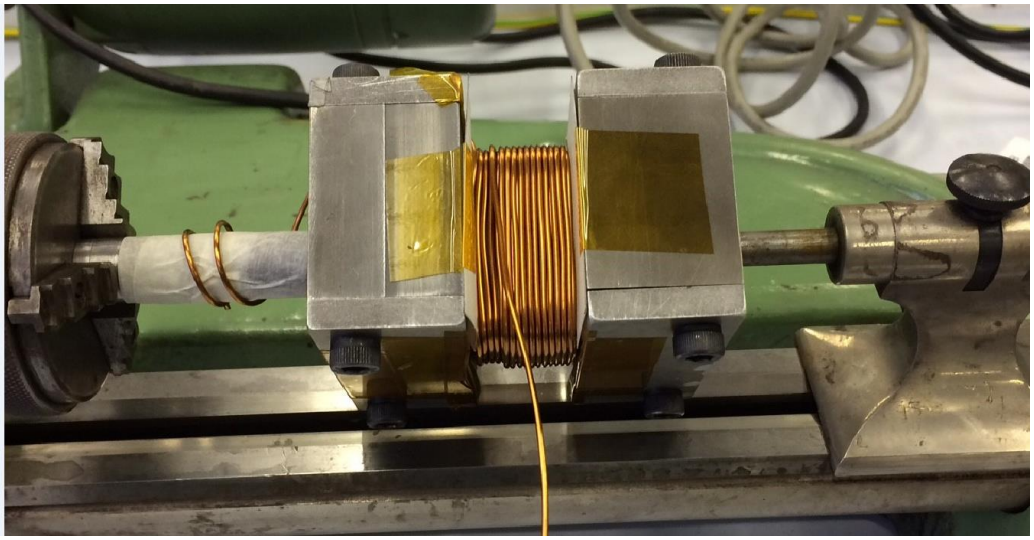

Figure 6.8 Manual winding of segmented stator tooth supported by both ends on a winding machine

After winding the coil (91 turns in this case), the external surfaces of the coil were wrapped with polyimide tape to prevent splitting of the most outer winding layers. It also helps minimize magnet wire deformation as high tensile strength polyimide tape directly in touch with steel punches providing extra strength on the coil external surfaces. The direct surface contact

between magnet wires and steel punch should be avoided as wire enamels are very weak regarding Young's modulus in comparison to EN32B steel parts. If any shear stress is present whilst compressing a coil, it might lead to deform winding insulation coating. A manually wound bobbin with 1.25 mm Grade-2 magnet wire is depicted in Figure 6.9 which looks safe for compression.

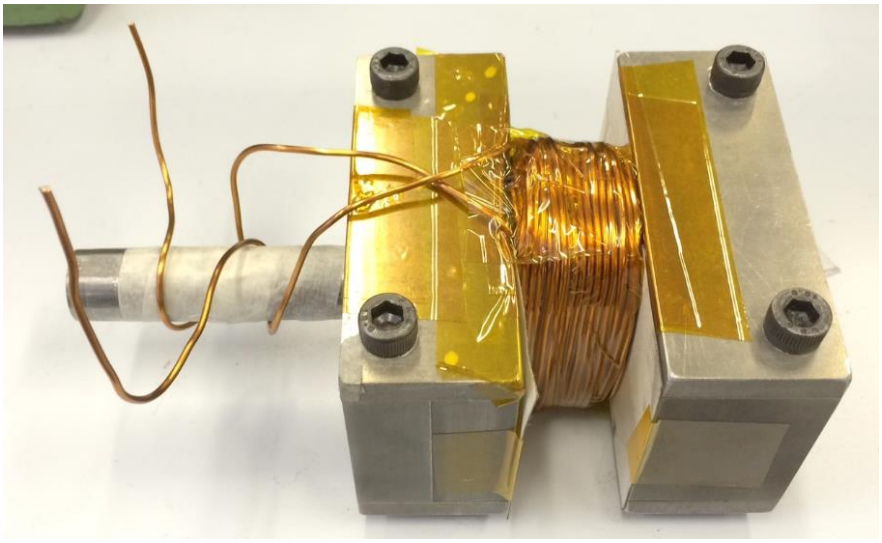

Figure 6.9 A manually wound ISG bobbin with a number of turns: 91

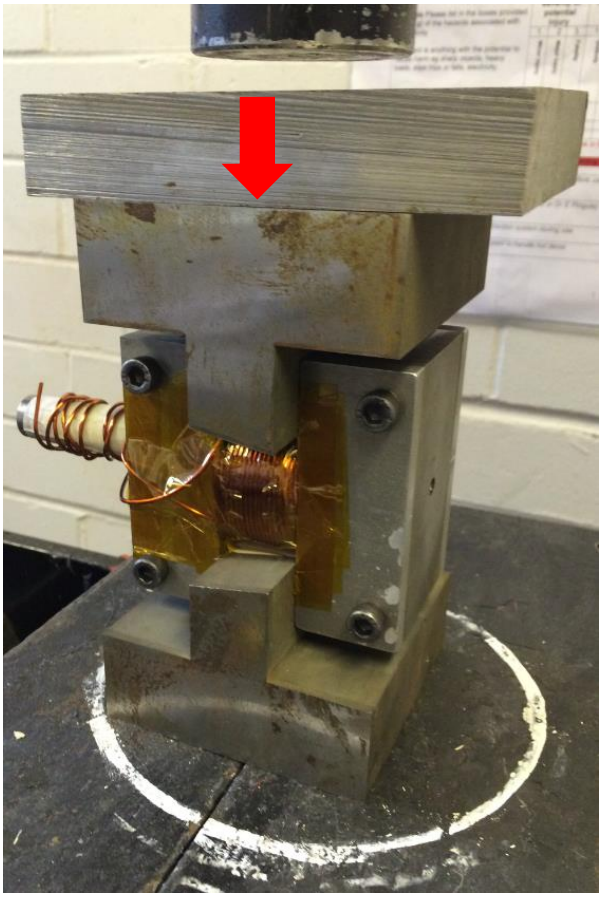

Figure 6.10 Compression of a coil under hydraulic press

The steel punches are placed on the cavity of the pressing tool. End windings are not pressed as experience showed they expand resulting in high localized stress regions. A manual press tool is utilised to compress segmented stator coils. Since end turns of the coil are prone to crushing, they are protected with polyimide tape providing temporarily an extra insulation layer. The compression process of a single tooth ISG winding is depicted in Figure 6.10, above.

A 0.72 slot fill factor has been achieved experimentally by compression of the windings. From a macroscopic point of view, there was not any insulation damage on the compressed windings. The lateral surfaces of the winding, however, flatten when a high pressure is applied onto the punches (10 to 14 tonnes). The flattened surfaces on the round wires were also observed in the deformed FEA results (Figure 6.5a). A compressed coil with deformed magnet wires and a comparison between conventional and compressed are illustrated in Figure 6.11.

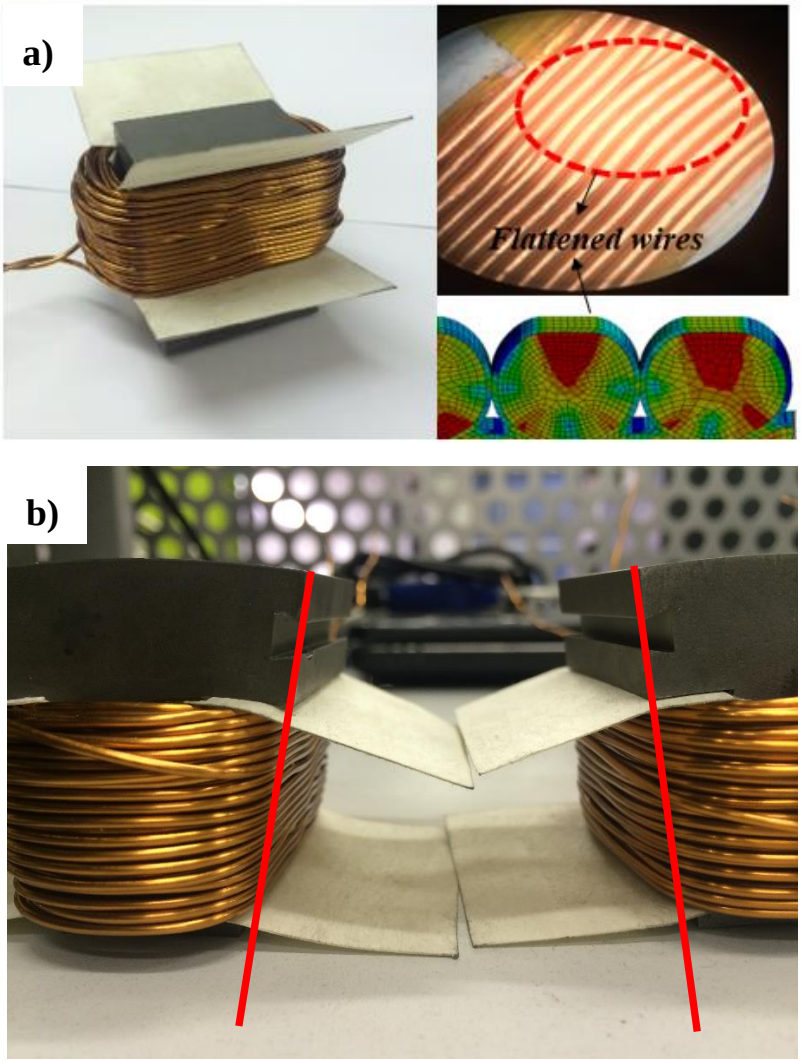

Figure 6.11 (a) Single tooth winding with deformed magnet wires, (b) comparison of on-tooth compressed coil (left) and conventional random wound coil (right)

IEEE 43 standard [124] states that random wound stator coils rated below 1 kV must have minimum 5 MΩ insulation resistance. Turn to ground high voltage tests were carried out on the pressed coils and no insulation failure has been observed as this standard was satisfied with measured insulation resistances varying around 2700 MΩ during electrical tests. Coil deformation and preservation of the insulation are therefore both in line with simulated results.

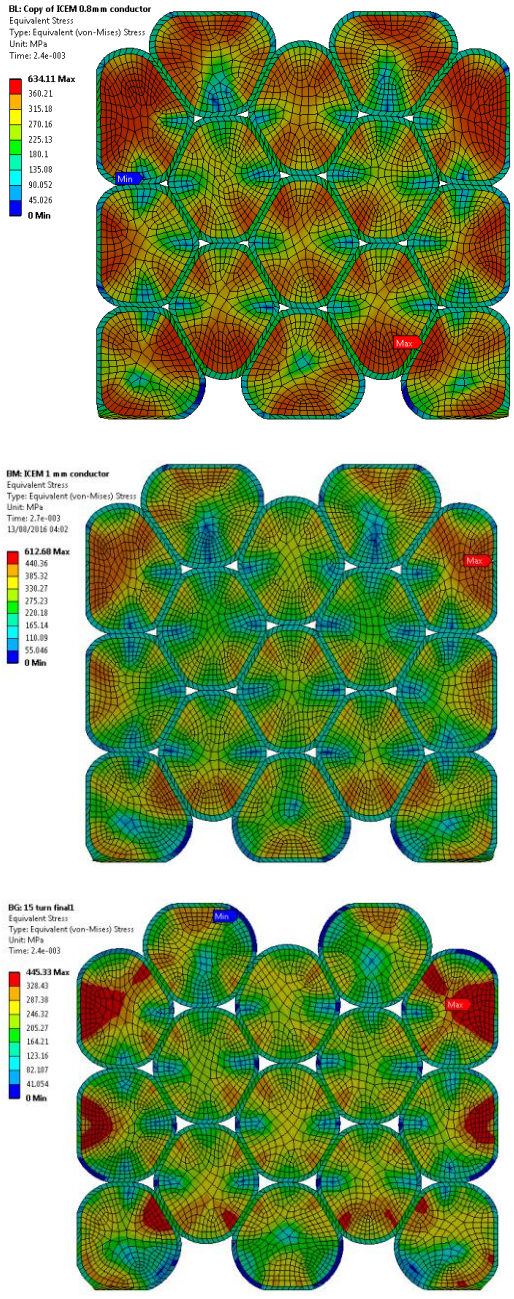

$$Ø_{max} = 0.8\ mm$$

$$Fill\ Factor_{max} = \ 0.77$$

$$Ø_{max} = 1\ mm$$

$$Fill\ Factor_{max} = \ 0.76$$

$$Ø_{max} = 1.25\ mm$$

$$Fill\ Factor_{max} = \ 0.72$$

Figure 6.12 Magnet wire diameter vs maximum achievable slot fill factor

Compressibility of round copper magnet wires is dependent on conductor diameter. Thinner conductors facilitates greater slot fill factor since initial slot fill factor of coils with thinner conductors is relatively greater than that of coils with thicker conductors. This is demonstrated by performing FEA simulations for three different conductor sizes as shown in Figure 6.12.

6.3.5 Macroscopic Deformation on the Compressed ISG Windings

A number of coils have been potted by black epoxy potting compound at room temperature for about 20 hours. The coil specimens were cut into two pieces to macroscopically investigate the deformation on the magnet wires as shown in Figure 6.13.

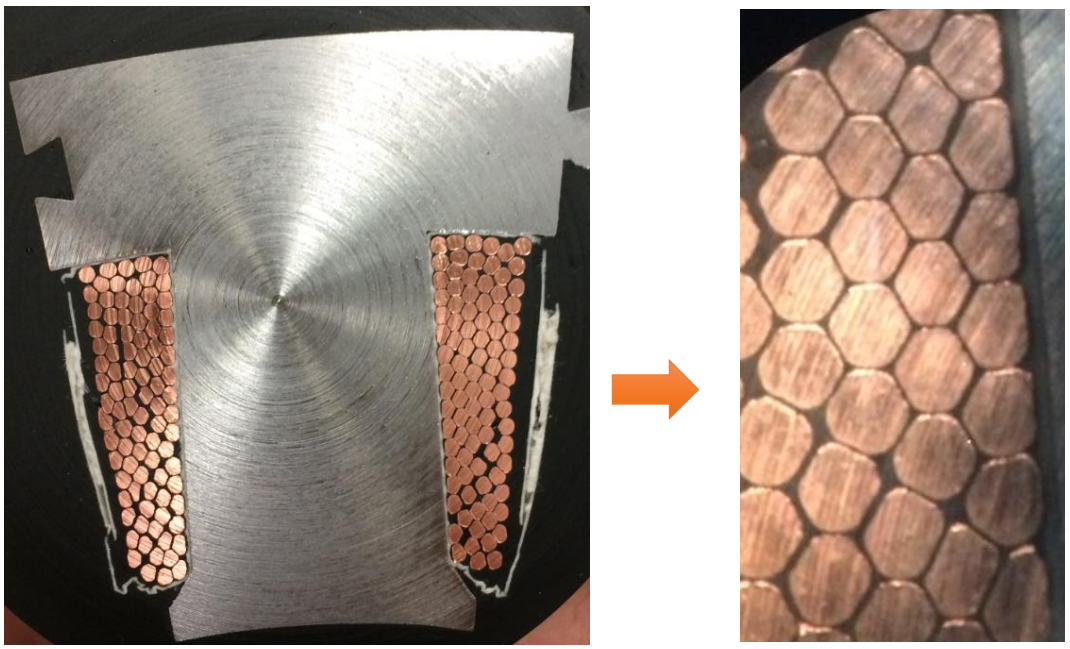

$\emptyset_{max} = 1.25\ mm$ $Fill\ Factor_{max} \cong 0.74$

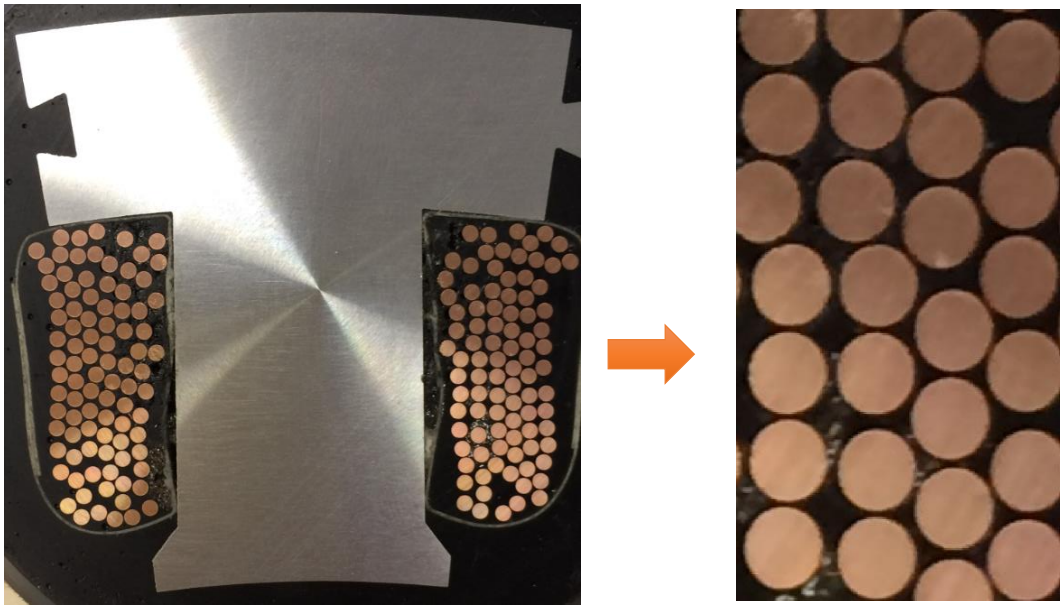

$\emptyset_{max} = 1.25\ mm$ $Fill\ Factor_{max} \cong 0.5$

Figure 6.13 Cross-sectional views of the potted, compressed (top) and random wound (bottom) ISG coils

In Figure 6.13, 20 tonnes of pressure was applied to compress an ISG coil to around 0.74 fill factor. The magnet wires were packed in a smaller volume in a quasi-hexagonal manner. The

experimental slot fill factor is higher than what the FEA results predict for 1.25 mm thick copper wires as previously depicted in Figure 6.12. However, it is worth mentioning that the magnet wires in FEA deform in a similar way yet fail at lower slot fill factors implying that FEA results are more pessimistic to estimate the maximum achievable slot fill factors. This is perhaps uncertainty of mechanical material properties and artificially increased loading rates in the performed structural simulations.

6.4 Thermal Analysis of Coil Pressing

In Section 6.3, on-tooth coil pressing for 21 slot-16 pole V-shape PM ISG machine is demonstrated. A 0.73 slot fill factor is achieved without deteriorating magnet wire insulation. The effect of high fill factor stator windings on machine thermal performance will be investigated in this section by performing steady state FEA thermal simulations and short time transient thermal tests.

6.4.1 Slot Thermal Conductivity Prediction for the Compressed ISG Stator Windings

Important thermal parameters of an electrical machine are dependent on manufacturing methods and on-tooth coil pressing will change the thermal parameters of the winding samples. It is known that thermal parameters are strongly influenced by critical thermal parameters [125] such as equivalent slot thermal conductivity, heat transfer coefficients (HTCs) for external surfaces and interface gaps between the machine parts. Thermal resistivity of the random wound coil is one of those parameters and it should be estimated accurately to model the machine thermally.

In the literature, a number of models have been proposed to obtain equivalent thermal model of round copper stator windings [35, 126]. One approach is based on extensive experimental tests to predict equivalent thermal conductivity [35]. For this reason, a thermal FEA simulation based approach has been developed to estimate equivalent slot thermal conductivity of the compressed ISG stator segments. The calculation method is based on the one–dimensional Fourier law of heat as recalled in equation (6.1).

$$Q = -k\frac{\partial T}{\partial X} = -k\left[\frac{T_{x=l} - T_{x=0}}{l}\right] => k = \frac{Q \times l}{\Delta T} \tag{6.1}$$

where $\partial T/\partial x$ is temperature gradient for a distance l (m) and k $(W/(mK)$ stands for thermal conductivity. Q (W/m^2) is heat flux density in one dimension. Whilst heat flows in a winding segment, heat flux passes through copper, wire insulation and air pockets inside the windings. Table 6.1 shows the isotropic thermal conductivity of the stator winding materials including slot liner at room temperature.

Table 6.1 Thermal conductivities for the materials in the slot

Material	Thermal Conductivity	Unit
Air	0.026	$W\ m^{-1}\ K^{-1}$
Polyimide	0.25	$W\ m^{-1}\ K^{-1}$
Copper	400	$W\ m^{-1}\ K^{-1}$
Nomex 410	0.14	$W\ m^{-1}\ K^{-1}$

In order to accurately estimate the thermal conductivity of a compressed winding segment, the deformed geometry, obtained in quasi static explicit dynamic simulations, should be constructed in a thermal FEA package with proper thermal boundary conditions. However, explicit dynamics package in Ansys Workbench does not allow the user to export a deformed mesh or CAD model. Although some structural analysis packages allow the user to export deformed mesh to reconstruct the deformed geometry in CAD software such as Autodesk Inventor or Solidworks, Explicit dynamic FEA modelling does not have this function.

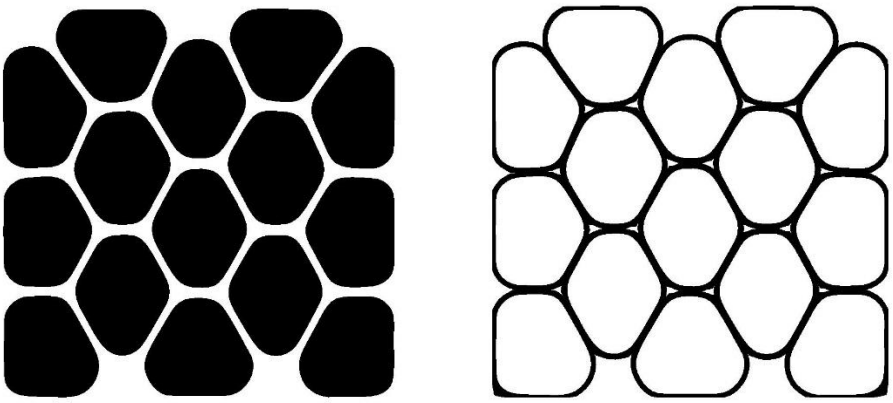

Figure 6.14 Binary images of a winding segment: copper bodies (left), wire insulation (right)

The deformed winding segment, however, can be reconstructed in a thermal FEA package by carrying out simple image processing and reverse engineering by utilising a number of software. The procedure for re-constructing a deformed geometry in a CAD used in this thesis was:

- A caption of deformed model is opened in Paint and saved as .PNG file format.
- .PNG image file is read in Matlab and converted to a binary image meaning that all pixels in the input image is either black or white depending on luminance of pixels. 0.5 is midway between black and white. By altering the black and white colour thresholds, the binary images are obtained as illustrated in Figure 6.14.

- The image is saved as .JPEG file format and subsequently converted to .STL (STereoLithography)[7]. During this conversion, the 2D binary image is swept to 3D by extrusion into an STL file known for 3D printing and usually defined in commercial 3D CAD software.
- .STL image must be converted to .SAT file as it is the primary 3D file format and can be opened any ACIS based CAD program such as Autodesk Inventor. Matlab has been used to convert .STL file to .SAT file.[8]
- .SAT file was converted to .IGES file in Autodesk Inventor. .IGES geometry is already defined 3D file format in Ansys Workbench. It is input to a steady state thermal FEA in Ansys Workbench.
- Finally, the deformed winding segment was simulated in thermal FEA with some temperature boundary conditions to achieve effective thermal conductivity of a compressed winding segment.

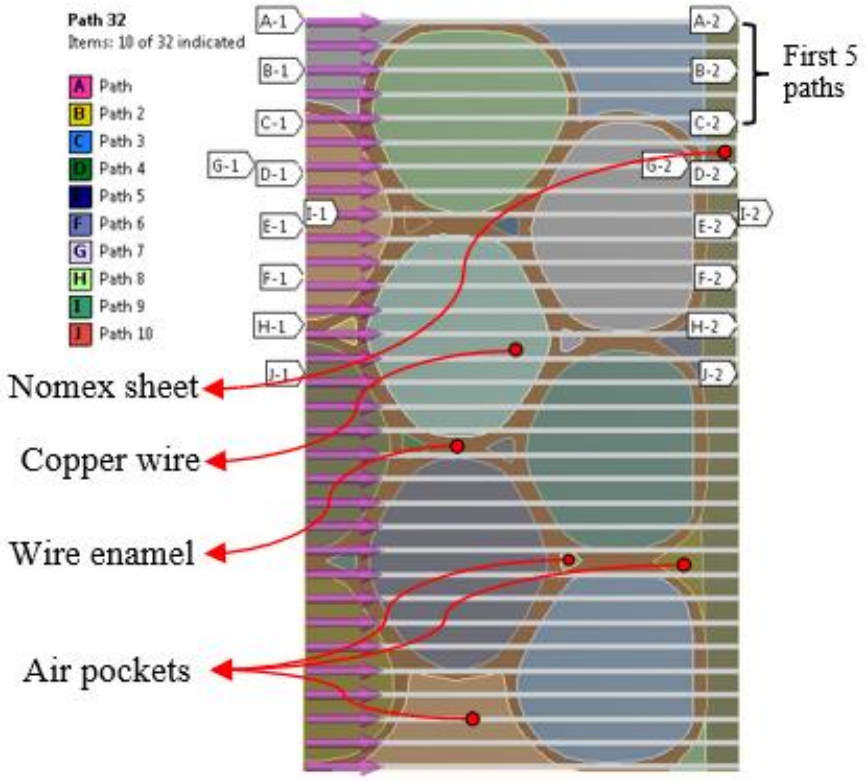

Figure 6.15 A compressed winding segment with heat flux sampled paths

In Figure 6.15, 1.25 mm Grade-2 magnet wires are illustrated at 0.73 slot fill factor for 21 slot -16 pole V-shape PM ISG application. The coil hottest point was assumed to be in the middle

[7] .JPEG file was converted to .STL by using a software: SELVA 3d available at https://www.selva3d.com/
[8] A code which is publicly accessible was used after importing .STL file into MATLAB workspace. This conversion might be also achievable by using some commercially available graphic software.

layer of the winding. By setting up temperature boundary conditions for top and bottom surfaces of the deformed winding segment, heat flow is obtained across the slab as shown in Figure 6.16.

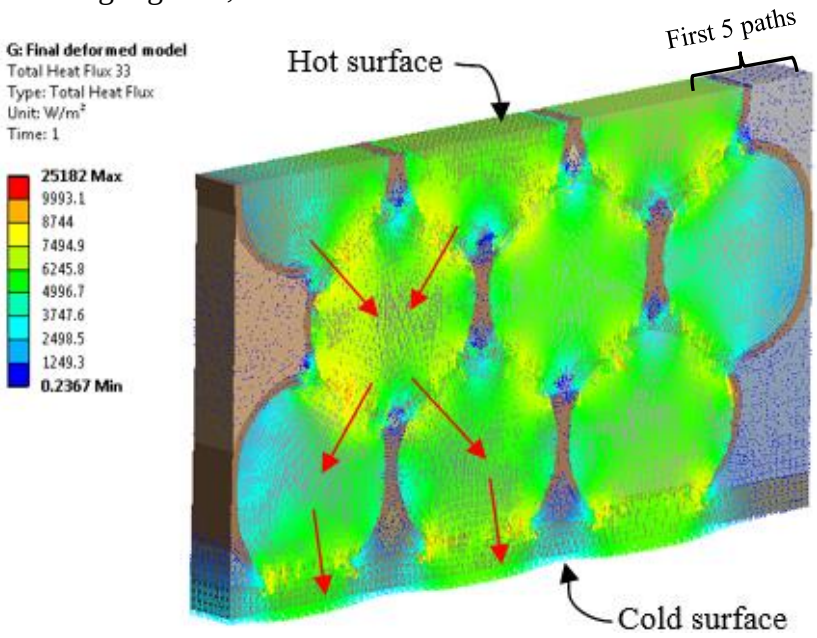

Figure 6.16 Heat flux flow through deformed winding segment

The deformed conductor shape, obtained from quasi-static explicit dynamic simulations in Section 6.3.2, was used to investigate heat flows through the winding after compression. Heat flux density samples are obtained along the paths shown in Figure 6.17 for only first five paths. Temperature gradient was provided with $\Delta T = 20°C$ for the top and bottom faces of the compressed winding segment. As thermal conductivity is a function of temperature gradient and heat flux density for the certain dimensions of the geometry, each path would have a different effective thermal conductivity due to varying heat flux densities along the paths. The average thermal conductivity is calculated by applying equation (6.1).

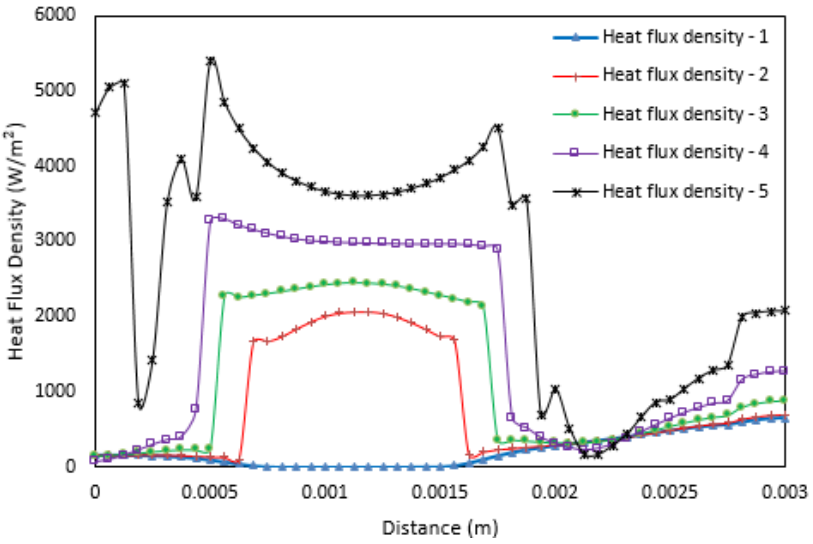

Figure 6.17 Variation of heat flux density along the sampled heat flow paths

The equivalent slot thermal conductivity using steady state FEA simulations is predicted to be $0.64\ W/(mK)$ in the main direction of heat flow. Heat flow in this case was considered in only one dimension, although the true nature of heat flow is three-dimensional. Axial heat flow inside the ISG coil was not taken into account as thermal conductivity is known to be significantly higher in this direction.

6.4.2 Short Time Transient Thermal Tests

The thermal resistance between the equivalent copper and laminations, R_{eq} is the most critical thermal parameter since inaccurate evaluation of this resistance results in wrong temperature prediction by thermal models such as thermal FEA and analytical lumped parameter models [126]. Also, R_{eq} is one of the most complex thermal parameters as it depends on many other factors such as winding insulation system, random wound wire disposition, the material and quality of the impregnation, residual air quantity after impregnation and manufacturing process [126]. All these factors make R_{eq} very difficult to define unless thermal tests and thermal calibration methods are carried out during the thermal modelling stage.

The traditional way of estimating R_{eq} thermal resistance is to perform a steady state thermal test through supplying the machine with a DC voltage when only stator Joule losses are active. This method requires a comprehensive calibration process, where temperature in the stator lamination, winding and the machine frame have to be measured.

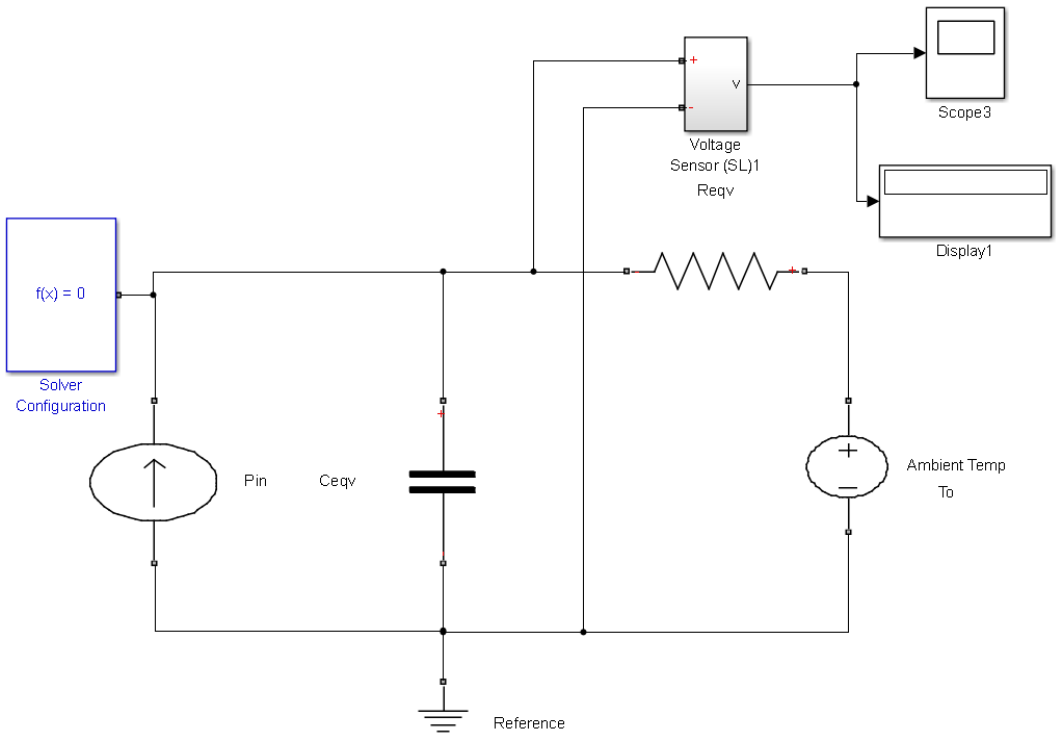

Figure 6.18 A first order thermal model in Simscape/Simulink

A simple and fast evaluation of determining equivalent thermal resistance of stator winding can be achieved by short time transient thermal tests. It is based on following hypothesis [125]:

- Over short time thermal transient, the stator lamination temperature can be considered constant.
- The thermal resistance of stator lamination is negligible in comparison to winding insulation system. (i.e. lamination thermal resistance is relatively very small)
- In very small amount of time (5-10 sec), the stator winding system can be considered as adiabatic system.

The test has to be finished when lamination temperature increases by about 1°C and stator winding temperature should be recorded during the test via a data acquisition unit. The length of test is hence mainly dictated by physical size of a component. Over this short time, the thermal time constant of the first order system (i.e. *RC* circuit in electrical analogy) will be dependent only on heat flow by conduction and temperature response of the model can thus be used to predict thermal conductivity. A first order thermal model is depicted in Figure 6.18.

In Figure 6.18, R_{eq} is the equivalent thermal resistance of winding insulation system and C_{eq} is the equivalent thermal capacitance of the winding and insulation system. Once R_{eq} is evaluated, the equivalent thermal conductivity of stator winding can be computed.

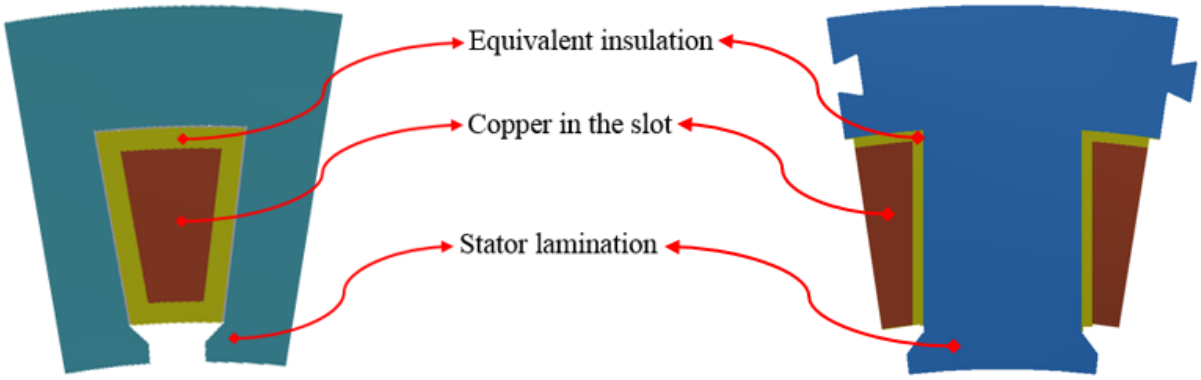

Figure 6.19 Sketch of the stator slot: distributed winding (left), single tooth winding (right)

In Figure 6.19, equivalent slot insulation and copper regions for both distributed windings and single tooth windings are shown. For distributed winding case, geometrical quantities including slot area (A_{sl}), slot fill factor (K_{wb}), peripheral length of the stator slot edge (l_{sl}), machine stack length (L_{stack}) and number of slots (N_s) are needed to compute equivalent thermal conductivity (k_{eq}) as given in equation (6.2) [126].

$$k_{eq} = \frac{A_{sl} \times (1 - K_{wb})}{N_s \, R_{eq} \, {l_{sl}}^2 L_{stack}} \tag{6.2}$$

where R_{eq} should be estimated using first order *RC* thermal lumped model. However, for fractional slot concentrated winding PM machines, equation (6.2) would not give accurate estimation of slot equivalent thermal conductivity. Therefore, the geometrical quantities for single tooth winding case should be analytically derived for each side of the tooth using slot dimensions and volume of the materials inside the slot. The main difference between distributed winding and single tooth winding is slot area and fill factor parameters since single tooth winding cannot utilise entire slot region between stator teeth meaning that there exists a space between winding regions.

6.4.2.1 Short Time Transient Thermal Tests for the ISG Single Tooth Windings

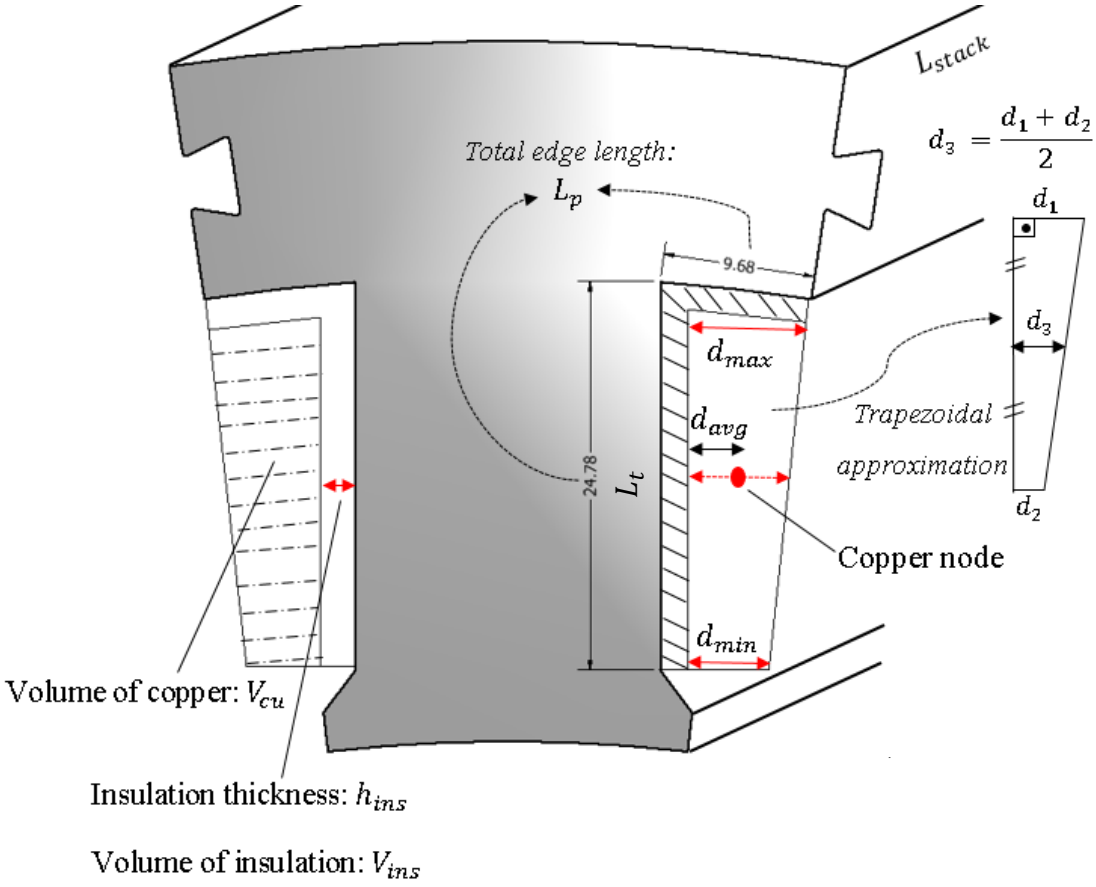

Figure 6.20 Geometrical quantities used for the equivalent thermal conductivity computation

In Figure 6.20, a stator segment of 21 slot -16 pole V-shape PM ISG is shown with some geometrical quantities required for the effective thermal conductivity calculation of the single tooth winding. An analytical approach has been developed to set a relationship between slot fill factor and thermal conductivity. It is described in the following equations:

$$R_{copper} = \frac{d_{avg}}{k_{cu} L_p L_{stack}} \tag{6.3}$$

where k_{cu} is copper thermal conductivity and $L_p L_{stack} = A_{cu}$ is lateral surface area of equivalent copper in the slot. d_{avg} represents the distance between the copper thermal node and equivalent insulation system as shown in Figure 6.20.

$$R_{ins\_eqv} = \frac{h_{ins}}{k_{eqv\_ins} L_p L_{stack}} \tag{6.4}$$

$$Copper\ cross-sectional\ area\ = K_{wb} \times \frac{A_{sl}}{2} = d_{avg} \times 2 \times L_t \tag{6.5}$$

$$d_{avg} = \frac{K_{wb} \times A_{sl}}{4 L_t} \tag{6.6}$$

where K_{wb} is slot fill factor and L_t is slot depth. The equivalent thermal resistance for a single side of the tooth is given

$$R_{slot\_left} = R_{slot\_right} = R_{copper} + R_{ins\_eqv} \tag{6.7}$$

By using equations (6.4), (6.5), (6.6) and (6.7), the equivalent thermal resistance for each side of the slot is in the form

$$R_{slot\_left} = \frac{K_{wb} A_{sl}}{4 L_t k_{cu} L_p L_{stack}} + \frac{h_{ins}}{k_{eqv\_ins} L_p L_{stack}} \tag{6.8}$$

Then, the equivalent thermal conductivity of the slot is written

$$k_{eqv\_ins} = \frac{h_{ins}}{\left(R_{slot\_left} - \frac{K_{wb} A_{sl}}{4 L_t k_{cu} L_p L_{stack}}\right) \times L_p L_{stack}} \tag{6.9}$$

In equation (6.9), it is explicit that increasing slot fill factor, K_{wb} boosts equivalent thermal conductivity of the slot insulation system.

In Figure 6.21, the equivalent slot thermal resistances: R_{slot_left} and R_{slot_right} are illustrated in each side of the ISG single tooth winding. These thermal resistances could be considered to be in parallel to each other as heat generated in windings reaches the lamination from both sides of the coil. It should be noted that R_{eqv} , where $R_{eqv} = R_{slot\_left} \,//\, R_{slot\_right}$, must be known to compute k_{eqv_ins} (i.e. equivalent thermal conductivity of the insulation system). R_{eqv} can be obtained from thermal time constant of short time transient tests, which is in the form:

$$\tau = R_{eqv} \times C_{eqv} \tag{6.10}$$

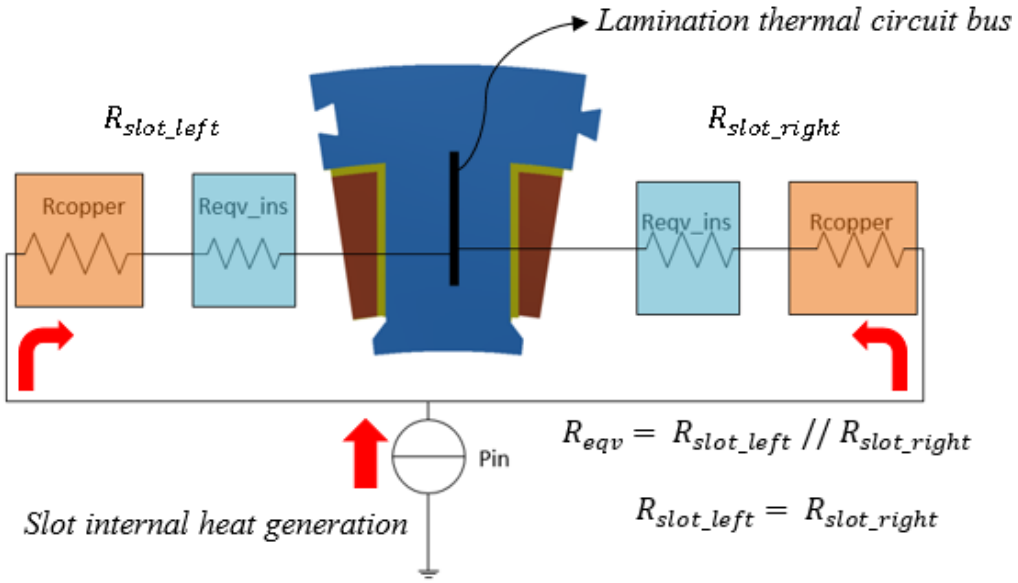

Figure 6.21 Representation of equivalent slot thermal resistance for single tooth winding

In equation (6.10), C_{eqv} is the equivalent thermal capacity of the winding and it includes thermal capacity of the winding due to copper weight, C_{wind} and the thermal capacity of insulation system C_{ins} as given in equation (6.11).

$$C_{eqv} = C_{wind} + C_{ins} \tag{6.11}$$

with

$$C_{wind} = V_{slot}\, K_{wb}\, d_{cu}\, c_{cu} \Rightarrow C_{wind} = m_{wind} \times c_{cu}$$

$$C_{ins} = V_{slot}\,(1 - K_{wb})\, d_{ins}\, c_{ins} \Rightarrow C_{ins} = m_{ins} \times c_{ins}$$

where V_{slot} is the slot volume, d_{cu} and d_{ins} are copper and insulation mass densities respectively and c_{cu} and c_{ins} stand for copper and insulation specific heat capacities. m_{wind} and m_{ins} are weights of stator copper and insulation system respectively.

C_{eqv} can be either calculated by using motor design data or can be measured by performing steady state thermal tests. Since material physical and thermal properties are known for the proposed ISG single tooth windings, C_{eq} was calculated using winding specific heat, mass density and volume, including both copper and insulation. Table 6.2 lists mass densities and specific heat capacities of the most used insulation materials and copper in machine windings.

Table 6.2 Specifications of the common insulation materials and copper

Material	*Mass density* kg/m^3	*Specific heat* $J/(kg°C)$
Copper	8933	385
Epoxy	1200	1500

Kapton	1420	1100
Polyester resin	1180	1400
Polyimide	1430	1130
Nylon	1100	1600
Nomex 410	1400	1300

For the proposed ISG PM machine, amount of materials have been calculated by using electrical resistance of single tooth winding, wire diameter, wire insulation grade and slot liner physical dimensions as illustrated in Figure 6.22.

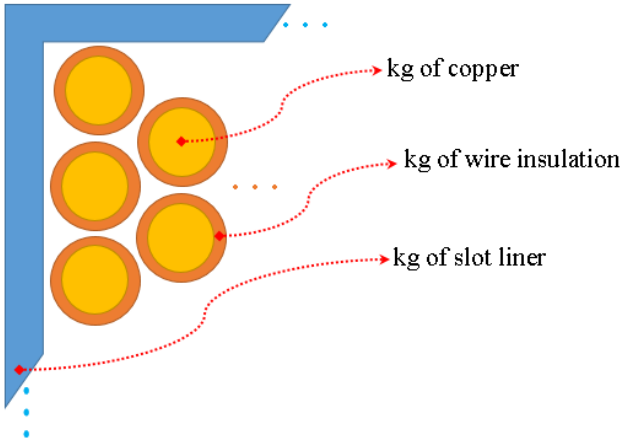

Figure 6.22 Estimation of amounts of materials in the slot

After obtaining the volume of copper and insulation materials, the total mass of copper and insulation materials have been computed, required for thermal capacity estimations. Table 6.3 gives estimated amount of materials for the single tooth ISG stator segment.

Table 6.3 Mass and volume of the materials in the ISG slot

Material in single ISG tooth	*Mass (kg)*	*Volume (mm^3)*	*Length (m)*	*Electrical resistance (**Ω**)*
Copper wire - 1.25 mm Grade 2	0.16074	17990.5	14.66	0.26
Wire insulation	4.2×10^{-3}	2994	n/a	n/a
Nomex slot liner – 0.25 mm thick	9.8×10^{-4}	700	n/a	n/a

The equivalent insulation system of the slot can be determined using equation (6.9). Thickness of the insulation system h_{ins} is estimated to be 0.788 mm when 1.25 mm Grade 2 magnet wire

with 0.25 mm Nomex slot liners is used. The only parameter left in equation (6.9) is equivalent slot thermal resistance, R_{eqv}. Therefore, short time thermal transient tests have been carried out for 91 turn single tooth winding ISG segments. Furthermore, the effect of slot fill factor K_{wb} on thermal performance of the ISG stator segments was investigated.

6.4.3 Experimental Results

6.4.3.1 Accuracy of the Thermal Tests

Supplied current: 4 A dc

Voltage variation: 0.9 V -1V

Measured resistance by applying a fixed current: 0.225 Ohm – 0.25 Ohm

Measured initial resistance by multi-meter: 0.25 Ohm – 0.26 Ohm

The winding temperature can be calculated using the well-known equation:

$$T = (234.5 + T_0)\frac{R_T}{R_0} - 234.5 \tag{6.12}$$

where 234.5 (ºC) is the copper temperature coefficient, T is actual temperature, T_0 is ambient temperature, R_T is actual electrical resistance and R_0 is electrical resistance at the reference temperature.

$$50.5°C = \left(\frac{0.25}{0.225}\right)(234.5°C + 22°C) - 234.5°C$$

The expected temperature value should be around $50°C$ due to the equation given in (6.12) specific to copper wires.

6.4.3.2 Thermal Test Results and Slot Thermal Conductivity Estimation

Figure 6.23 shows the short time transient tests being carried out in the laboratory by injecting 4A dc into a single tooth ISG winding with an initial resistance of 0.26 Ω. Thermocouples of K-type were used to monitor temperature variation every 500 ms in winding and tooth. The test was finished in 300 seconds by monitoring tooth temperature increase (≈ 1°C increase). The parameters of the first order system are given in Table 6.4.

Table 6.4 Parameters of first order model –compressed ISG coil

R_{eqv}	C_{eqv}	τ
3.5665	80.77	288.06

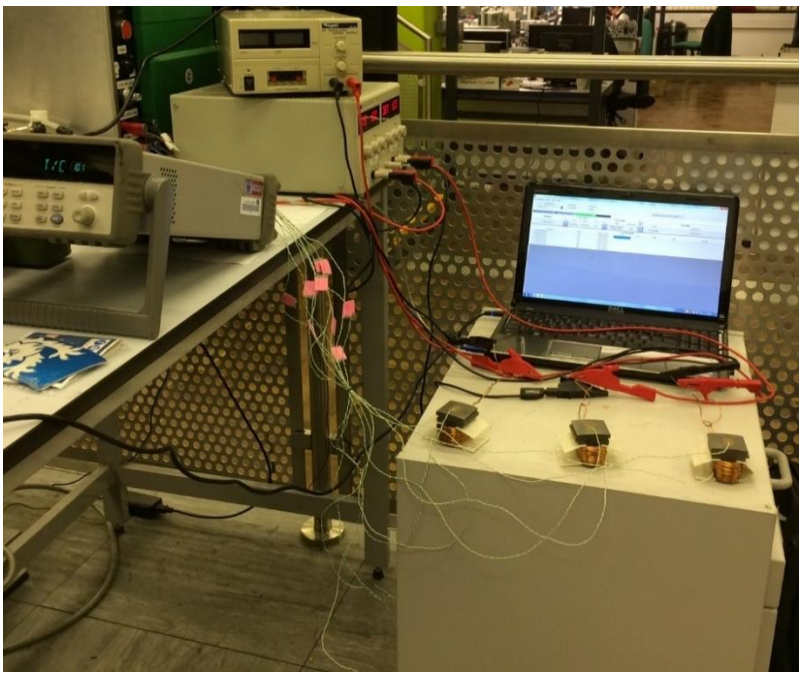

Figure 6.23 Experimental setup for testing single tooth ISG windings

Although C_{eqv} can be predicted from material data as tabulated in Table 6.5, C_{eqv} given in Table 6.6 was obtained by performing two variable minimisation which targets to minimise least square error between first order RC model and transient thermal tests. C_{eqv} was estimated to be 70.7 $J/°C$ theoretically. Nonetheless, C_{eqv} can be estimated more precisely using first order RC thermal lumped model given in Figure 6.18. It is clear that thermal capacities obtained from theoretical approach and *RC* model are not very different from each other showing that the estimation of R_{eqv} will become sufficiently accurate. Short time test results for random wound coil and pressed coils are compared to the temperature response of the first order model in Figure 6.24, showing the accuracy of the model.

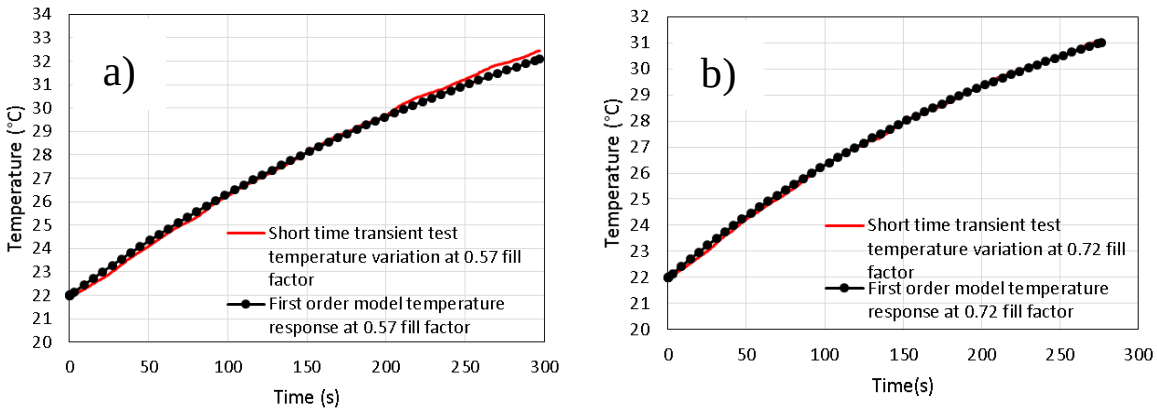

Figure 6.24 Short time transient thermal test results versus First order temperature response at (a) 0.57 slot fill factor; (b) 0.72 slot fill factor

Once R_{eqv} is determined, equivalent thermal conductivity of winding insulation system can be determined considering equivalent insulation system is a barrier between bulk copper in the slot and tooth. Using the approach given in equation (6.9), the slot equivalent thermal conductivity was estimated using short time thermal transient test results.

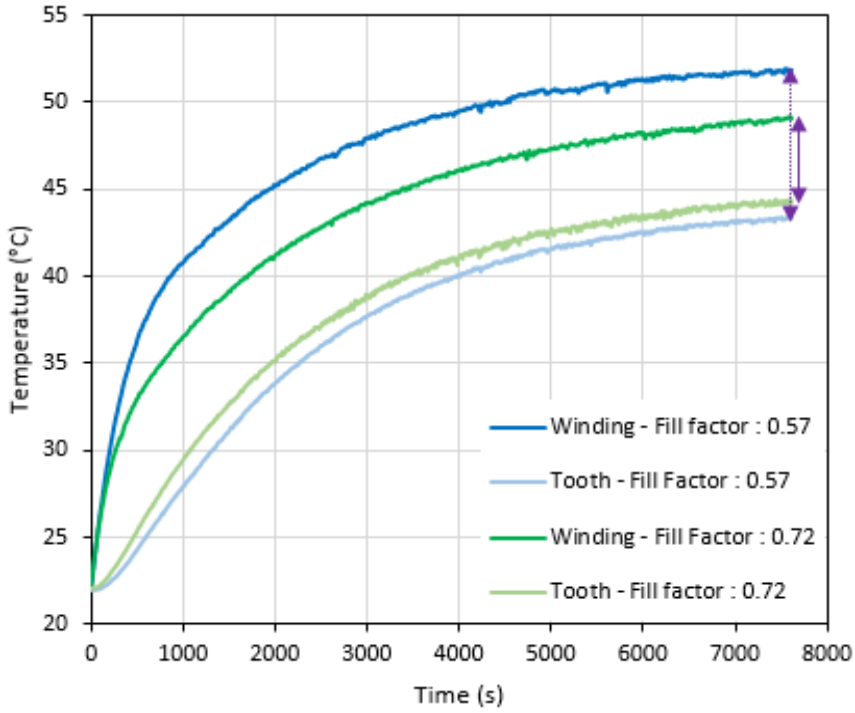

Figure 6.25 Measured temperature variations for pressed and not-pressed windings

Temperature differences at steady state between the tooth and winding in Figure 6.25 demonstrate that the average thermal conductivity is improved for the compressed winding as temperature difference is about 8.5°C for the conventional case and about 4.8°C for the compressed winding. The greater the temperature difference, the smaller winding thermal conductivity if the other thermal parameters such as natural convection and heat capacity are similar. To ensure this condition, transient thermal tests were performed simultaneously in the same environmental condition for the compressed and un-compressed ISG teeth.

The histogram chart given in Figure 6.26 shows equivalent thermal conductivity of the ISG stator slots at slot fill factors: 0.57 and 0.72, representing conventional random wound coil and compressed coil respectively.

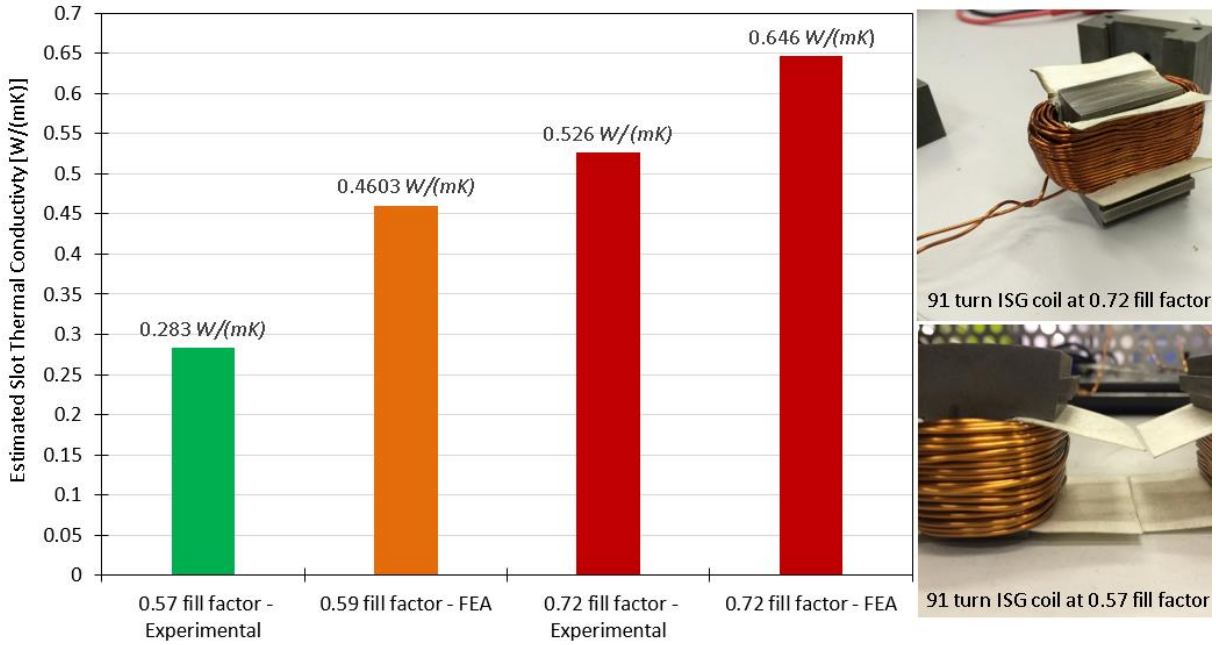

Figure 6.26 Slot thermal conductivity estimation for the ISG coils: random wound at 0.57 fill factor vs compressed coil at 0.72 fill factor

As depicted in Figure 6.26, the FEA simulations over predict the thermal conductivity as they are usually more optimistic in terms of thermal contact between different slot materials including slot liner, magnet wires and air voids etc. The percentage error between FEA and experimental estimations at 0.72 slot fill factor is about 18.5% which is still good approximation and will not cause a significant temperature error prediction in the machine windings. The thermal conductivity at 0.57 slot fill factor is being compared to 0.59 slot fill factor case, shown orange in the chart, because the rhombus arrangement of conductors in FEA geometry achieves 0.59 fill factor. This is the most ideal condition in conductor arrangements of stator windings. The measured slot fill factor is, however, about 0.57 which might be considered as conjugate of FEA model at 0.59 fill factor. The error between estimated thermal conductivities in this case becomes more significant as the FEA model is greatly ideal as shown in Figure 6.27.

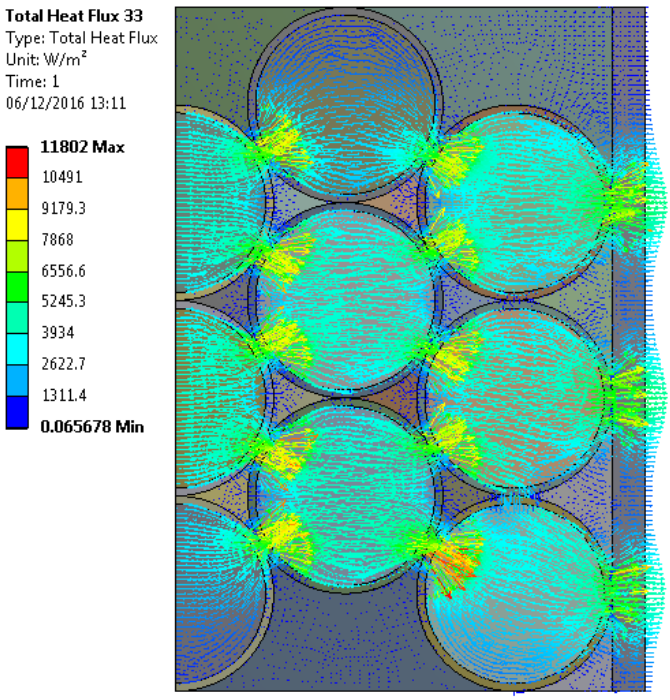

Figure 6.27 Rhombus arrangement of conductors at 0.59 slot fill factor showing the most ideal placement of magnet wires in machine slot

6.4.3.3 Comparisons of Transient Thermal FEA Models with Thermal Test Results

Transient thermal FEA modelling of the ISG tooth has also been performed with internal heat generation and natural convection boundary conditions to match long time transient thermal test results with simulations. The equivalent thermal conductivity results obtained from short time transient tests were inserted in the FEA to demonstrate that the thermal conductivity estimations are accurate enough for the machine thermal modelling.

Natural convection heat transfer coefficients will have significant influence on the temperature distribution of the ISG teeth. If heat flux sensors are not utilised to find out heat transfer coefficients on external surfaces of the tooth, the only way to determine the coefficients is through coarse prediction of thermal time constant when the tooth cools down after reaching steady state. This approach is based on the following hypothesis:

- Temperature variation with respect to time on external surfaces is recorded for both heating and cooling. → Long-time transient thermal testing
- Thermal time constant might be predicted using the equation given by:

$$\tau = \frac{\rho V c}{h A_s} = R \times C \tag{6.13}$$

where ρ is tooth lamination mass density, V is total volume of the tooth, c is specific heat and $1/hA_s$ stands for thermal resistance dependent upon tooth external surface

area. h (i.e. heat transfer coefficient) could be determined if all other parameters are estimated from long time thermal tests.

- It is well-known that the time constant represents the elapsed time required for the system response to decay to zero if the system had continued to decay at the initial rate [127]. The elapsed time in which the value of temperature decays to $1/e \approx 36.8\%$ when system response decays at initial rate will give time constant of the system.

The approach hypothesised above is illustrated in Figure 6.28.

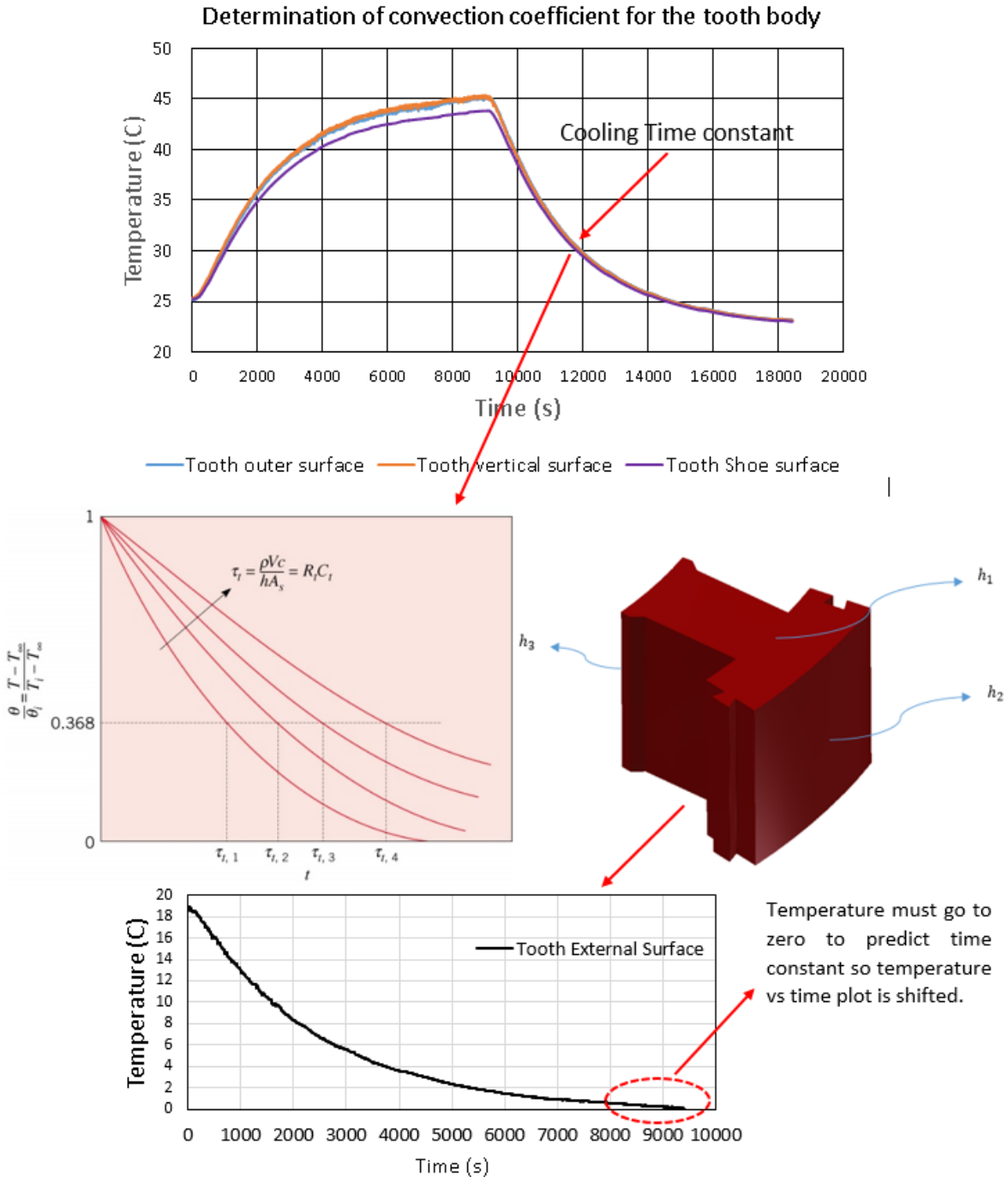

Figure 6.28 An experimental approach to predict heat transfer coefficients

In Figure 6.28, the cooling time constant which is almost the same for all external surfaces of the ISG tooth. Thermal time constant is a function of material heat capacity, heat transfer coefficient and surface area where cooling occurs. In Table 6.5, the required parameters are extracted.

Table 6.5 Rough heat transfer coefficient estimation for transient thermal FEA boundary condition

Thermal time constant (τ_t)	≈2270 sec
Specific heat ($kJ/(kg°C)$)	0.49
Tooth mass (kg)	0.381
Tooth surface area (mm^2)	9521
Estimated heat transfer coefficient ($W/(m^2K)$)	9.343

As tabulated in Table 6.5, the heat transfer coefficient is around 10 ($W/(m^2K)$), which is quite reasonable value for natural convection [128]. The estimated value of HTC is used for a thermal FEA modelling of ISG tooth after obtaining the equivalent thermal conductivity of winding insulation system. The FEA model is shown in Figure 6.29.

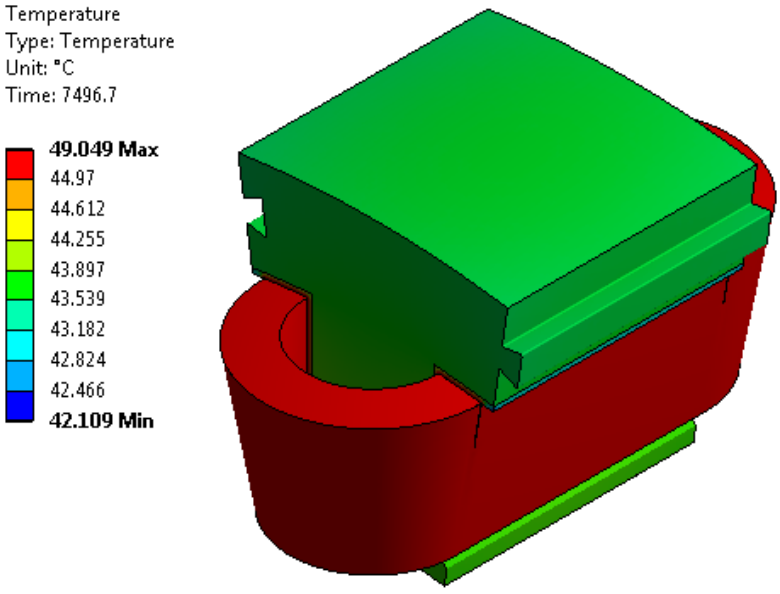

Figure 6.29 Thermal (transient) FEA model of ISG tooth at 0.72 slot fill factor

The transient temperature variation in the ISG tooth given in Figure 6.29 is compared to experimental results which is plotted in Figure 6.30. It is shown that there is a good agreement between the test results and FEA modelling demonstrating that the estimated thermal parameters as given in Table 6.5 are accurate enough for the ISG stator segments.

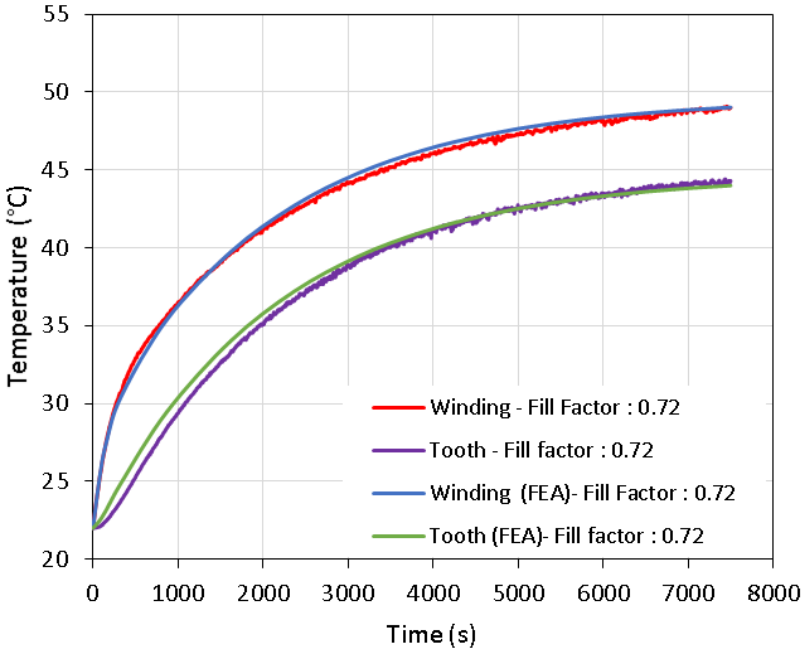

Figure 6.30 Temperature variation for the ISG tooth-slot at 0.72 fill factor: Experimental vs. FEA

Similarly, thermal FEA modelling has been achieved for the ISG stator segment at 0.57 slot fill factor. A comparison of temperature variation for a tooth – slot pair is given in Figure 6.31.

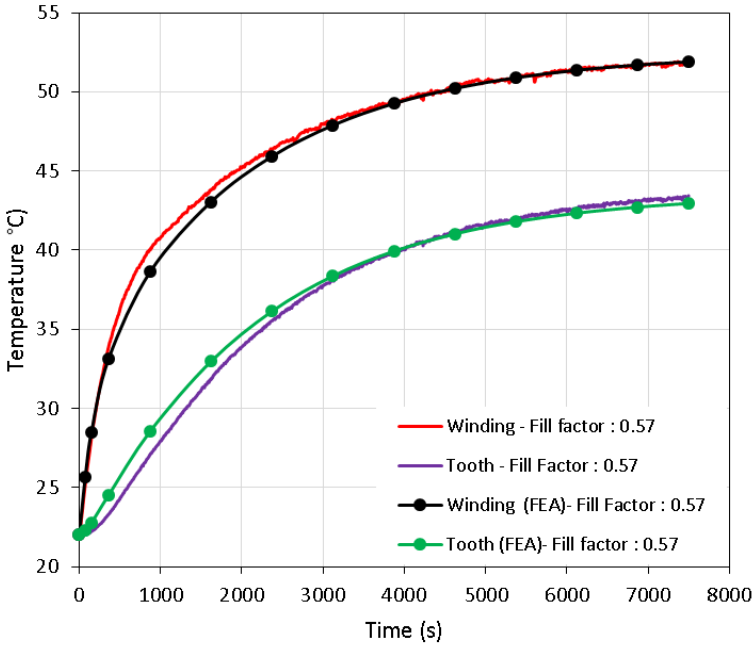

Figure 6.31 Temperature variation for the ISG tooth-slot at 0.57 fill factor: Experimental vs. FEA

6.4.3.4 Effect of Applied Pressure on the Equivalent Thermal Resistance of the Compressed Windings

The random wound ISG coils have been compressed at 14 and 20 tonnes. Both steady state thermal tests and short time transient thermal tests have been conducted. Slot thermal resistance of the ISG coils is determined by matching the experimental transient thermal results to first order *RC* thermal circuit. It is shown that the higher the applied pressure, the smaller the thermal resistance between the winding and tooth. This leads to a less temperature difference between the winding and tooth as illustrated in Figure 6.32.

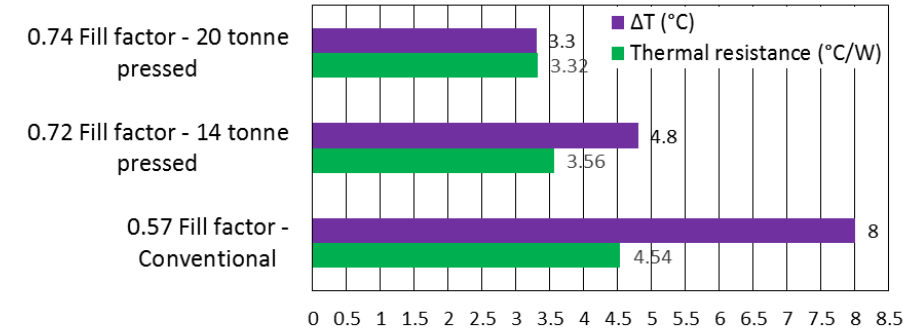

	0.57 Fill factor - Conventional	0.72 Fill factor - 14 tonne pressed	0.74 Fill factor - 20 tonne pressed
ΔT (°C)	8	4.8	3.3
Thermal resistance (°C/W)	4.54	3.56	3.32

Figure 6.32 Effect of applied pressure on the slot thermal resistance and temperature difference between the winding and tooth

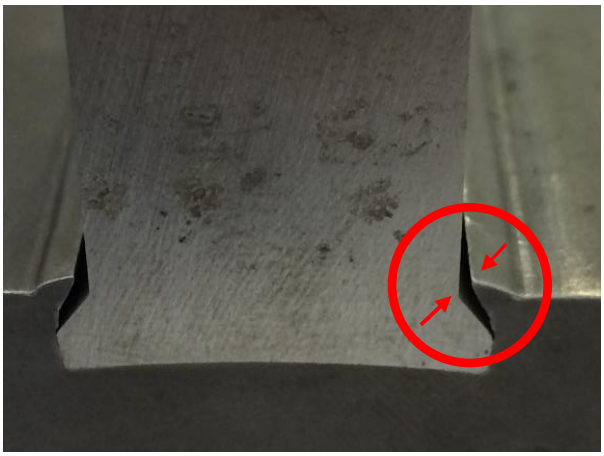

Figure 6.33 Damaged EN32B steel part due to stress concentration on the tooth tip

Although 20 tonne pressed coil is healthy regarding insulation dielectric strength ($\geq 100\ M\Omega$), the apparatus that is used to compress the coil was damaged during hydraulic pressing. This implies that 0.74 slot fill factor is the experimental limit of the ISG coils with 91 turn, 1.25 mm

conductors. The applied pressure concentrates on the sharp edges and make the coil support fail as depicted in Figure 6.33.

6.5 Thermal FEA Investigation of the Integrated Starter Generator with Compressed Windings

A 3-D geometry of the ISG has been thermally investigated at maximum power when the machine is a generator at 2000 rpm. Thermal improvement of the machine is investigated when the conventional coils are replaced with the pre-pressed coils.

6.5.1 Case Study: Determination of Thermal Contact Conductance between the Segmented ISG Teeth

Temperature distribution in the ISG stator might be affected from stator segmentation as it has the potential to decrease the heat flow through the segmented teeth resulting in less homogenous temperature distribution in the stator yoke. In this case study, a pair of segmented aluminium teeth is taken into account to investigate thermal contact conductance between the segments.

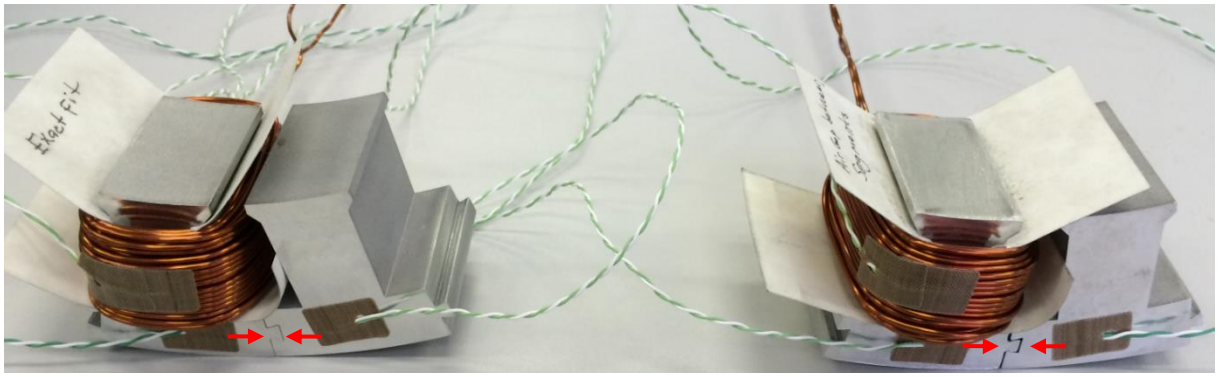

Figure 6.34 Thermal investigation of the ISG stator segmentation

As shown in Figure 6.34, I^2R losses ($I = 4A, R = 0.25\Omega$) are injected to coils at 0.57 fill factor identical in terms of coil electrical resistance. One of the segmented teeth pair has exact fit yet the other segmented teeth pair is loose due to interfacial gap between the teeth. Steady state thermal tests have been conducted and maximum temperature difference of 1.47°C (Figure 6.35) was obtained in the core backs of the teeth without coils. The temperature difference might be small but this is also dependent on injected power into the coils. The temperature difference can be significant at very high current loadings.

Thermal FEA simulations are performed to estimate thermal contact conductance between the segments. To do this, the FEA temperature distribution is calibrated to the experimental temperature variation. Temperature distribution and heat flux obtained from the FEA simulations are shown in Figure 6.36.

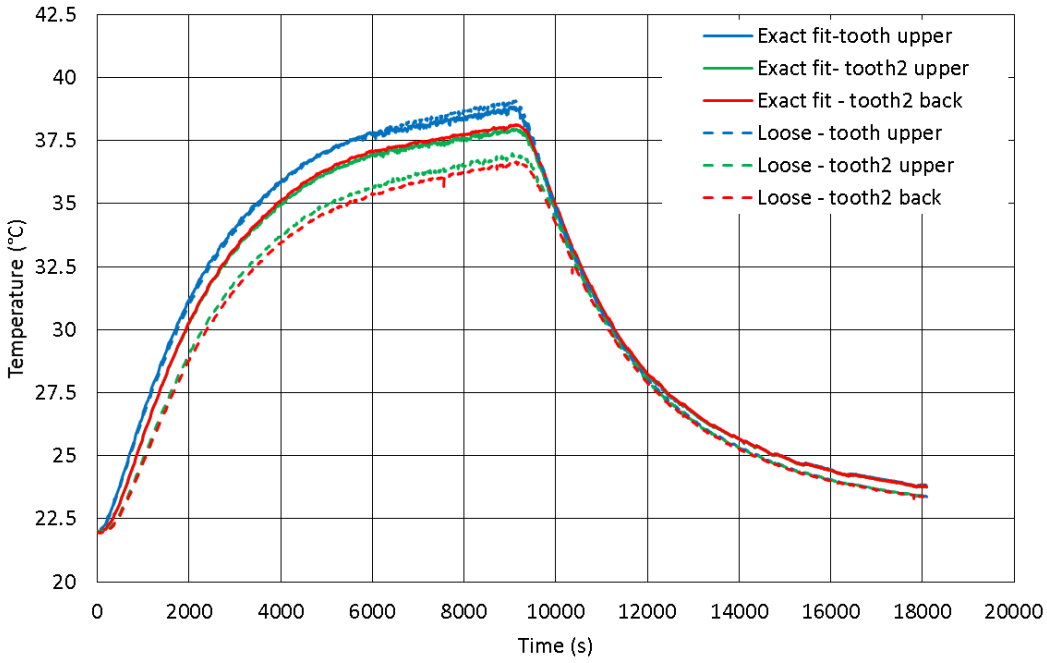

Figure 6.35 Temperature variations in steady state thermal test of segmented ISG teeth with exact and loose fittings - experimental

Exact Fit of Aluminium ISG Teeth Segments

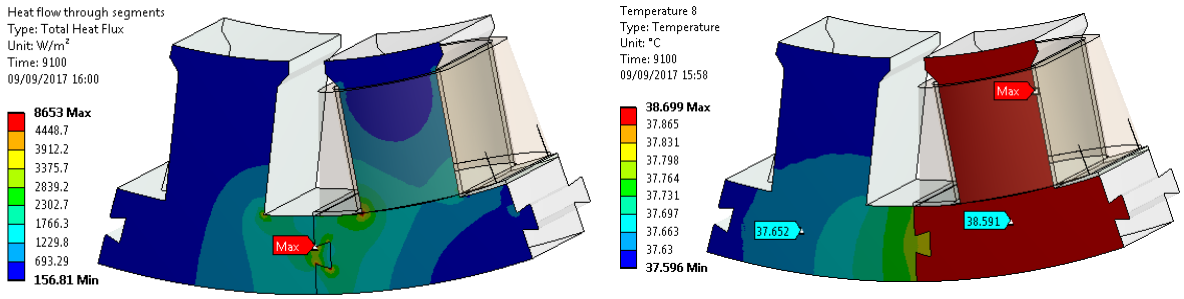

Loose Fit of Aluminium ISG Teeth Segments

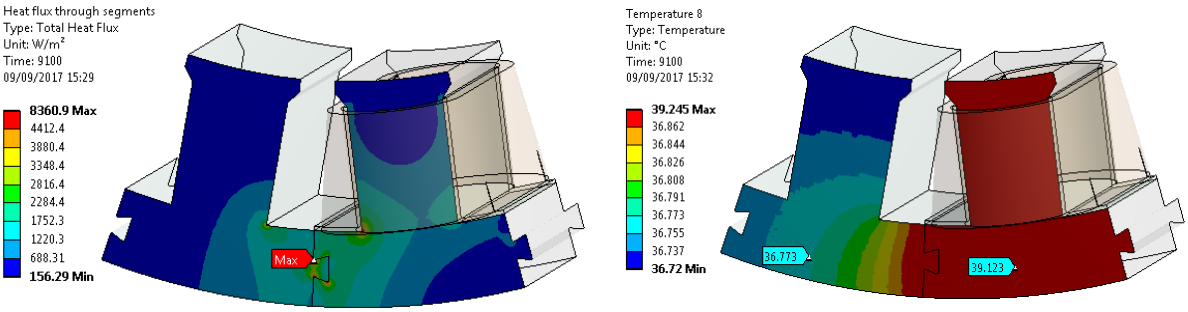

Figure 6.36 FEA temperature distributions (on right) and heat flux flows (on left) for the segmented ISG teeth with exact and loose fittings

Table 6.6 Comparison of Exact and Loose Fitting of the ISG teeth segments

	Exact Fit	***Loose Fit***	***Error, ΔT or difference***	
Heat flux through the segments	8653 W/m^2	8360 W/m^2	293 W/m^2	
Temperature (°C) in no coil tooth upper face (FEA-steady state)	37.652	36.773	0.879	15.8% error
Temperature (°C) in no coil tooth upper face (Experimental-steady state)	37.936	36.892	1.044	
Estimated thermal contact conductance between aluminium teeth	**1810 $W/m^2°C$**	**540 $W/m^2°C$**	1270 $W/m^2°C$	
Aluminium interfacial contact conductance in the literature	2200 $W/m^2°C$ – 12000 $W/m^2°C$			

As tabulated in Table 6.6, the estimated thermal contact conductance reduces if no exact fit is present in the ISG segments. Although there is a significant thermal contact conductance difference between the cases, the temperature difference between the segmented ISG teeth is not very affected by this parameter as heat density is very small in the coils. The higher the joule losses, the greater the difference between the temperatures as heat density of coils and area of the contact surface would make the thermal contact conductance more important parameter.

6.5.2 3-D Thermal FEA of the ISG and Effect of Coil Pressing on the Thermal Performance

In Figure 6.26 (Section 6.4.3.2), the effective thermal conductivities of the ISG slots at 0.57 and 0.72 slot fill factors are shown. Short time transient thermal tests are the key to predict thermal conductivity of the compressed windings. The calibrated thermal FEA models at 0.57 and 0.72 fill factors are also demonstrated in Figure 6.30 and Figure 6.31, respectively. The estimated thermal conductivities at 0.57 and 0.72 fill factors have been used in the full machine so as to investigate the influence of winding thermal conductivity on the ISG machine with liquid cooling system.

Table 6.7 gives thermal constraints of the machine when it is mounted on the HEV crankshaft.

Table 6.7 Thermal constraints for the crankshaft mounted ISG

Surrounding temperature	95°C
Coolant temperature	80°C
Inlet liquid flow rate	6 l/min
Total machine losses (excluding air windage, bearing and AC copper losses) at continuous generator mode	908.87 W

The machine has been investigated with heat transfer coefficients calculated by empirical formulations given in Appendix – B in detail. End windings, shaft, rotor surface, airgap convection coefficients are all based on empirical formulations as given in Appendix – B. Some of those heat transfer coefficients are dependent on the machine speed such as end windings, rotor surface etc. The important convection coefficients and heat transfer parameters are tabulated in Table 6.8 for the ISG machine at generator mode.

Table 6.8 Estimated heat transfer parameters for the ISG thermal model

Region	***HTCs when the ISG is spinning at 2000 rev/min***
ISG stator yoke	At 80°C due to liquid cooling
End windings	15.383 $W/m^2.°C$
Rotor cylindrical surface	44.478 $W/m^2.°C$
Air gap	58.253 $W/m^2.°C$
Modified Taylor No for rotor airgap	22086.18 (dimensionless)
Nusselt No for rotor airgap	4.481
ISG vertical plane surfaces dependent on film temperature	As shown in Figure B.3 in Appendix – B
ISG horizontal plane surfaces dependent on film temperature	As shown in Figure B.3 in Appendix – B

Since there is no experimental HTC measurements for the full ISG geometry, empirical formulations are the only option to be able to generate full thermal model of the ISG in FEA. The focus here is to examine the effect of slot thermal conductivity in the machine thermal characteristics with some assumptions as given in Table 6.8.

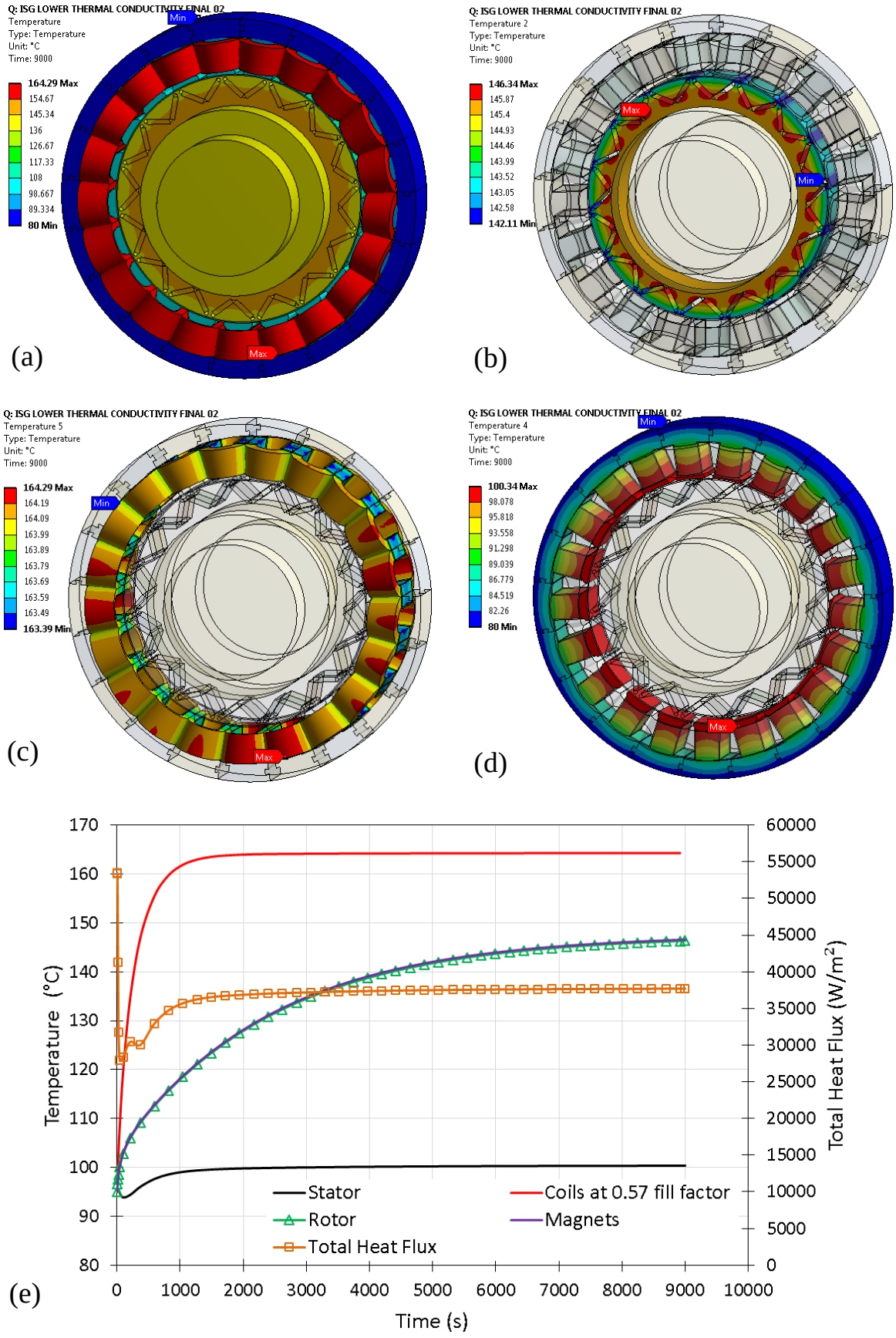

Figure 6.37 Temperature distributions: (a) Full machine; (b) Rotor; (c) Coils at 0.57 fill factor; (d) Stator; (e) Transient temperature variations around the ISG

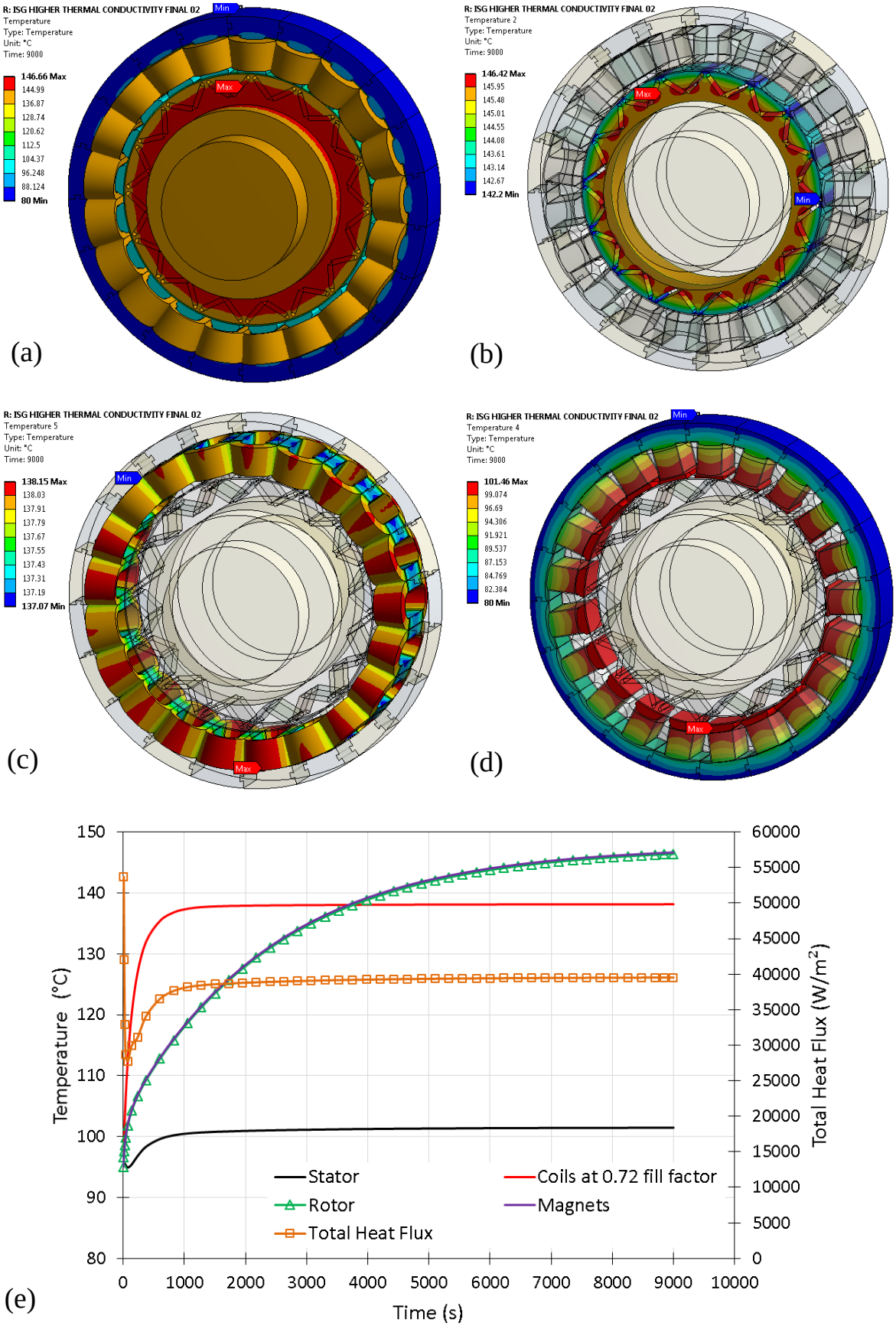

Figure 6.38 Temperature distributions: (a) Full machine; (b) Rotor; (c) Coils at 0.72 fill factor; (d) Stator; (e) Transient temperature variations around the ISG

In Figure 6.37 and Figure 6.38, temperature variations in the ISG are shown when the machine losses except to AC copper losses and friction losses, generate heat in the machine. The only sensitive parameter is the average thermal conductivity of the ISG slots. It is shown that there is a significant effect of slot fill factor on the machine thermal characteristic as winding temperature drops 26.1°C when the windings thermal conductivity increases from 0.283 W/mK to 0.526 W/mK as illustrated in Figure 6.39. If a 10°C temperature increase in windings temperature is assumed to reduce the machine life expectancy to one-half, as found in [3], 26.1°C temperature increase might be reducing the machine life more than one-quarter. Therefore, it is demonstrated that winding thermal conductivity is crucial parameter in terms of machine life expectancy.

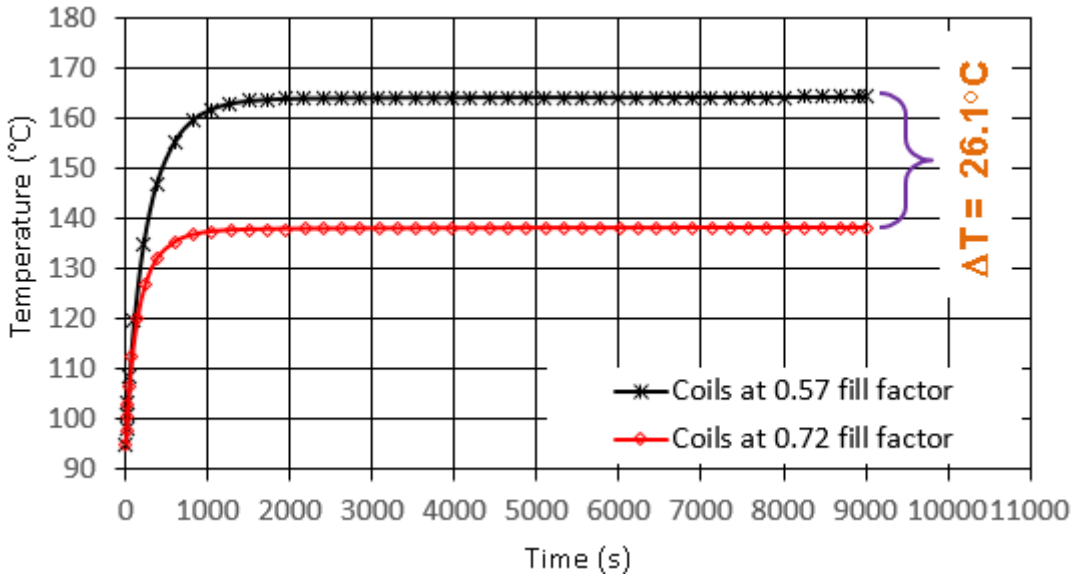

Figure 6.39 FEA temperature variations in the ISG coils at 0.57 and 0.72 slot fill factors

6.6 Conclusion

In this chapter, a number of methods including steady state thermal FEA and short time transient thermal tests have been employed to investigate the effective thermal conductivity of the ISG slots. After estimating the slot thermal conductivity, the influence of that parameter on the machine thermal performance has been demonstrated by performing transient thermal FEA simulations.

Steady state thermal FEA modelling of the compressed winding segment enables to estimate the thermal conductivity of the compressed windings. This is the only computational method to investigate the average thermal conductivity of compressed coils. The results obtained in the thermal simulations predict the thermal conductivity within about 18.5% error when compared to experimental approach. It was also reported that the thermal conductivity of the windings at 0.72 fill factor is about 85% higher than that at 0.57 fill factor.

Although increasing the slot fill factor by pressing coils is advantageous for the machine durability due to temperature drop in the windings (about 26 °C in this case), the influence of the coil pressing on the winding insulation resistance is not yet known. Turn to turn and turn to ground wall insulation resistances might be dropping in case of coil pressing. Coil insulation resistance should be also investigated as the compression of coils at high pressures (6 to 20 tonnes) might reduce insulation resistance significantly that can eliminate the potential advantages of coil pressing such as increase in machine durability due to hot spot temperature reduction.

Chapter 7. Thermal Aging Investigation of Random Wound Compressed Stator Windings

7.1 Objectives

Compression of the bobbins might cause insulation failure. The objective in this chapter is to investigate how stator winding insulation is influenced from on-tooth coil pressing. Therefore, the compressed stator windings have been aged by exposing them to high temperatures. Winding insulation resistance is monitored during this process to experimentally validate whether the compressed coils are healthy in terms of electrical insulation. In this case, a single stress (i.e. temperature) model is used to predict the reliability of the compressed coils. Accelerated life test results were also presented to inspect the life expectancy of compressed coils under thermal stress.

7.2 Introduction

The reliability of coil pressing is not clear in terms of stator winding electrical integrity. Mechanical deformation on the magnet wire enamel and slot insulation system might result in reduced life expectancy in the compressed stator windings. Therefore, the machine designers must ensure that the proposed technique does not deteriorate the electrical durability of stator windings and their insulation system.

There are two principal winding insulation system in rotating machines: turn to turn insulation and ground wall insulation. Mechanical and thermal stresses due to magnetically induced vibration and I^2R losses in windings might cause in-service failure because of turn to turn short and/or ground wall short between the conductors and the grounded stator core [81]. Since the compression of stator windings lead to a plastic deformation on magnet wires, the life expectancy of the compressed windings might be affected by the compression process. Therefore, thermal aging tests (i.e. single stress aging model) of the compressed windings have been carried out to investigate if there is a rapid insulation degradation in stator windings in comparison to conventional random wound coils.

The operating temperature of a winding causes thermal stress due to copper losses and core losses. The expected life of the insulation will be shorter when machine is run at over operating temperature. For this reason, the aging process can be sped up to obtain a life data a much shorter time if accelerated aging tests are performed [81].

The Arrhenius life–stress model is one of the most common life-stress relationship utilised in accelerated life testing when acceleration variable is temperature [81, 129]. By choosing at least

two over-operating temperature, a set of compressed coils which are almost identical in terms of applied pressure, number of turns and insulation system are aged in an environmental chamber operating up to 180°C. During the aging tests, off-line stator winding tests including insulation resistance (IR), high potential (HiPot) and high voltage surge tests have been conducted using 'Static Motor Analyser – Baker Instrument' to record failure time of each particular winding sample by testing coils periodically as depicted in Figure 7.1.

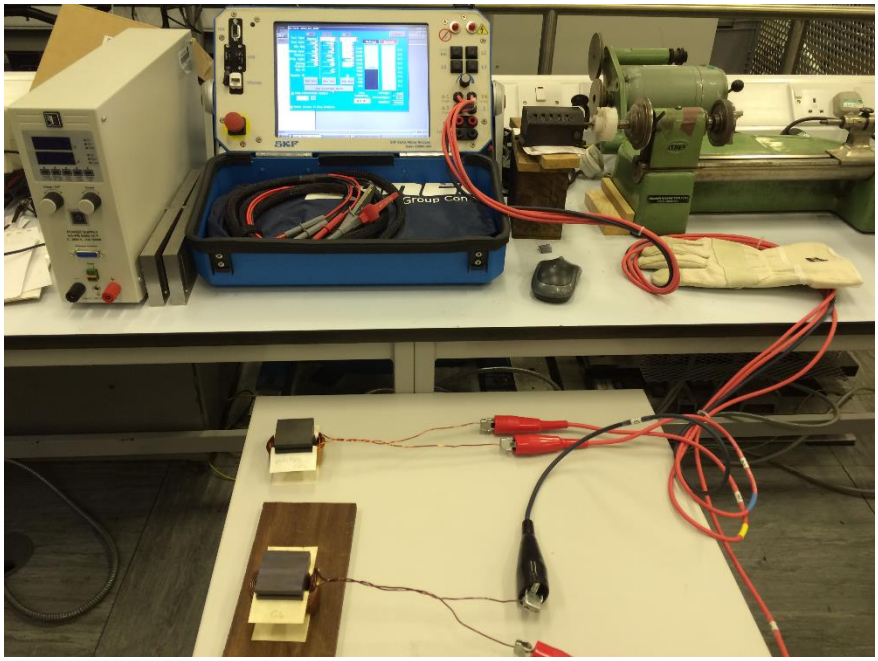

Figure 7.1 Static motor analyser

7.3 IEEE 43-2000 Standards

IEEE 43-2000 identifies minimum values for insulation resistance of rotating machines. This standard states that for most machines built after 1970 with random wound stator coils rated below one kV, the minimum insulation resistance is five mega-ohms [124]. All of these minimum values are based on a winding temperature of 40°C. If the insulation resistance is below the minimum levels, the machine should not be energized.

The most common instrument used for the insulation test for motors and generators is handheld 500 or 1000 colt dc mega-ohmmeter. According to IEEE 43 standard, the recommended test voltage for insulation resistance (IR) tests increases with machine voltage rating as tabulated in Table 7.1.

Table 7.1 IR test voltages versus rated voltages

Winding rated voltage (ac or dc)	**IR test voltage - dc**
<1000	500
1000-2500	500-1000
2501-5000	1000-2500
5001-12000	2500-5000
>12000	5000-10000

Mega-ohm, polarization index (PI) and HiPot tests are conventional insulation testing methods to identify leakage currents at high voltages. In order to prevent any coil to ground wall fault, the slot wall insulation dielectric strength must be high enough to limit leakage current. As shown in Figure 7.2, leakage current (I_L) is an important parameter of equivalent circuit of insulation resistance. A high leakage current means low insulation resistance. In Figure 7.2b, surface leakage resistance is also shown in an empirical model of insulation. A surface leakage current is usually caused by conductive contamination or moisture present in the machine. A static motor analyser can measure leakage current of slot wall insulation when Mega-ohm, HiPot or PI tests are conducted. Leakage current is usually in order of μA as it must be a very low amount for healthy coils.

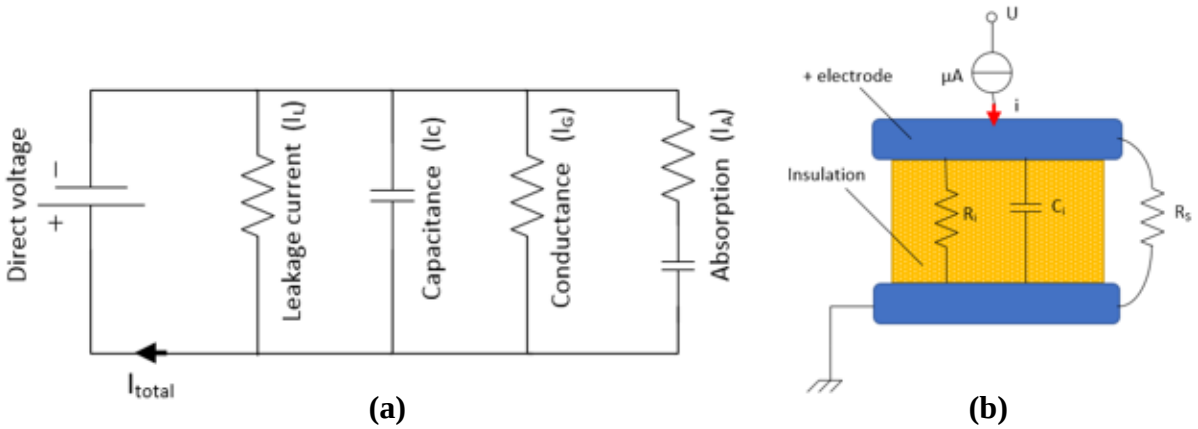

(a) **(b)**

Figure 7.2 (a) Equivalent circuit of IR test, (b) An empirical model of insulation

7.4 Static Motor Analyser Tests

Static motor analyser which is known as Baker Instrument (by SKF group company) is a coil testing equipment that can be used to conduct a series of tests to detect any electrical insulation weakness between turns of coil. It is also used to measure slot wall insulation resistance of coils. A number of insulation test methods have been described as follows:

7.4.1 Mega-ohm tests

Mega-ohm tests are carried out to detect insulation resistance between windings and ground wall. If any insulation weakness exists between the coil windings and ground, high leakage current is detected during the tests. According to IEEE 43, insulation resistance measurement is taken after the test direct voltage has been applied for 1 min [124].

For the 21 slot 16 pole V-shape PM ISG machine, the stator winding rated voltage ($\hat{V}_{phase} = 200\ volts$) is less than 1000 V meaning that Mega-ohm test voltage is 500 V. A static motor analyser has been used to carry out IR tests.

7.4.2 HiPot tests

HiPot tests are similar to Mega-ohm tests with higher test voltages. It is also known as dielectric withstand test. HiPot tests are helpful in finding crushed insulation and conductive contaminants [130]. The adequacy of creepage and clearance distances introduced during manufacturing process can be also detected.

HiPot tests have also been performed for random wound compressed ISG stator windings to detect if any coil to ground wall short occurs when the coils are compressed to higher fill factors at pressures varying between 6 tonnes to 14 tonnes. HiPot tests were conducted according to IEEE voltage standards stating that the test voltage is $2 \times (Operating\ voltage) + 1000V$ for 1 min [130]. The test direct voltage for the ISG coils has been determined: 1400 V.

7.4.3 Surge tests

A surge test is based on applying a high current impulse to a winding using a fast rise time that will induce a voltage difference between adjacent loops of wire within the winding [131]. If the voltage difference between the magnet wires is high enough, an arc occurs between the wires. The arc can be detected by observing a shift in the surge waveform. The surge waveform is directly related to coil's inductance as internal capacitance of the instrument and coil inductance form an LC type circuit with a resonant frequency (f_{res}) [131]:

$$f_{res} = \frac{1}{2\pi\sqrt{LC}} \tag{7.1}$$

The LC tank circuit responds to the surge pulse with a ringing or damped sinusoidal waveform pattern. The frequency of surge waveform is dependent on coil inductance. Any variation in the coil inductance will alter the frequency of the wave pattern which will cause a distinct shift on the waveform. A reduction in inductance occurs due to turn to turn faults in a coil because inductance is related to the number of turns in the winding as stated:

$$L \propto N^2 \tag{7.2}$$

A winding with a short between adjacent turns would have an inductance of:

$$L \propto (N-1)^2 \tag{7.3}$$

The percentage change in inductance can be written:

$$\Delta L = \frac{N^2 - (N-1)^2}{N^2} \times 100 \tag{7.4}$$

The response of surge waveform identifies a turn to turn short by

- A distinct surge waveform shift between healthy coil and faulty coil
- A voltage amplitude reduction on the waveform as it is a function of: $V = L\ (di/dt)$

As compression of the ISG stator windings might lead to turn to turn short, surge tests have also been performed using Static Motor Analyser. The test voltage based on IEEE 43 voltage standards is found to be 1400 V.

7.4.3.1 Surge test methodology for two terminal devices

Since only two terminal ISG bobbins have been tested using surge test, the following approach has been used to investigate turn to turn fault:

- Test lead 1 is connected to one side of the coil
- Test lead 2 is connected to opposite side of the coil
- Ground lead is connected to the metal core material
- Surge tests were run on lead 1 and lead 2. Left shift in *x*-axis and amplitude change in RLC tank circuit response were monitored.

7.5 Thermal Aging Tests of the ISG Stator Coils of Thermal Class: F

Since accelerated life tests can take a significant amount of time, it is recommended that a number of preliminary aging tests would be useful to make sure that the experimental methodology is sustainable for long time period aging tests. Before conducting the accelerated life tests, a set of coil were compressed at different amount of pressures (6 to14 tonnes). The compressed coils were identical in terms of number of turns (91) and insulation system. 0.25 mm thick Nomex 410 slot liner was used for ground wall insulation. The windings were compressed directly on the tooth using a hydraulic press tool.

1.25 mm - Grade 1 magnet wires in a temperature class of ‘F’ (155°C) have been utilised for the ISG stator windings. A preliminary thermal aging test with an acceleration factor of 1.12 at 175°C have been performed for 35 days to monitor insulation degradation in random wound

conventional windings and compressed windings. Offline electrical insulation tests including Mega-ohm test, HiPot test and surge test have been carried out to investigate thermal endurance of the coil insulation system. A set of experimental results are shown in Figure 7.3.

The tests were conducted according to IEEE 43 voltage standards for 6 tonne pressed, 8 tonne pressed, 14 tonne pressed and conventional windings. It is shown that on-tooth compression of windings leads to a rapid ground wall insulation deterioration as plotted in Figure 7.3 illustrating Mega-ohm test results at 500 volts during 35 day aging tests. The offline insulation tests have been repeated at every 168 hours to record insulation resistance data.

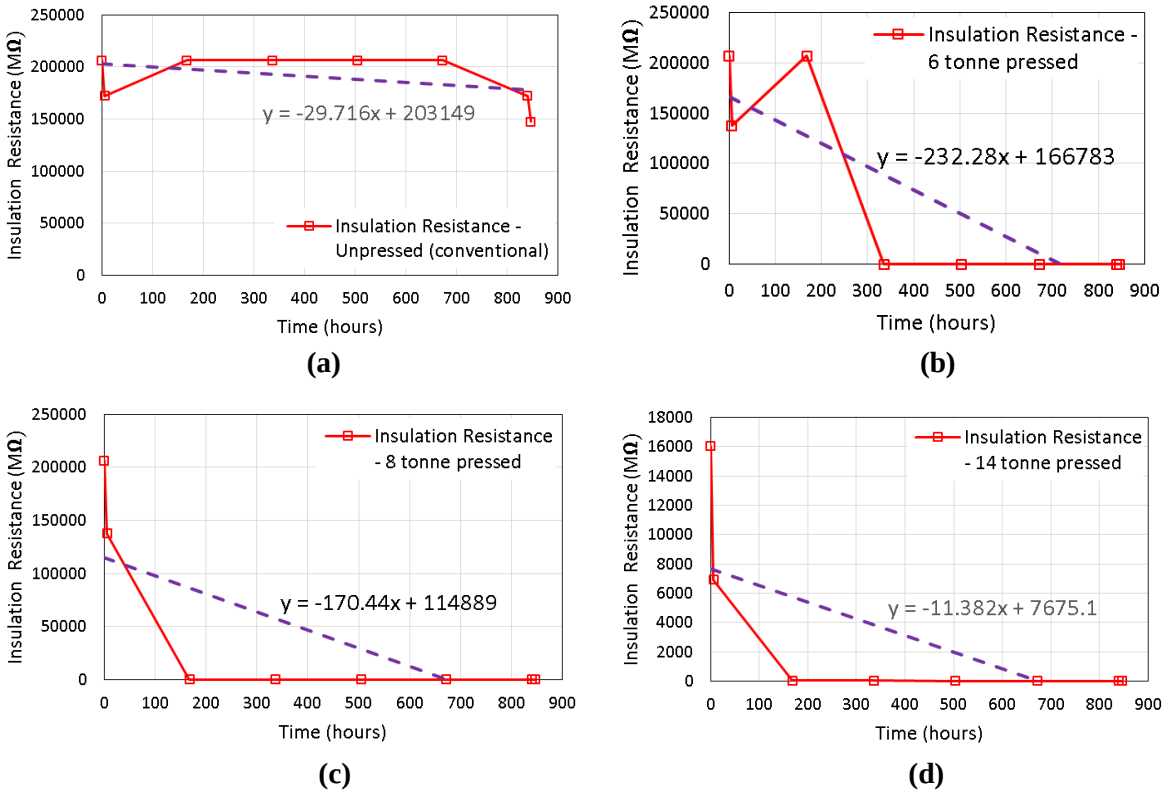

Figure 7.3 Thermal aging test results for the ISG stator windings at 175°C at different pressures

There is no conventional method to compare thermal endurance of the compressed coils but if linear regression lines are employed for insulation resistance versus time data as depicted in Figure 7.3, the area under trend lines would be useful to investigate magnet wire deterioration. It is shown in Figure 7.3a, an un-pressed ISG stator winding keeps its dielectric strength between winding to ground wall for significantly longer time during thermal aging tests. On the contrary, the dielectric strength of 14-tonne pressed ISG winding rapidly drops as illustrated in Figure 7.3d. These initial results state that the conventional windings have higher thermal endurance than the compressed windings regarding slot insulation system.

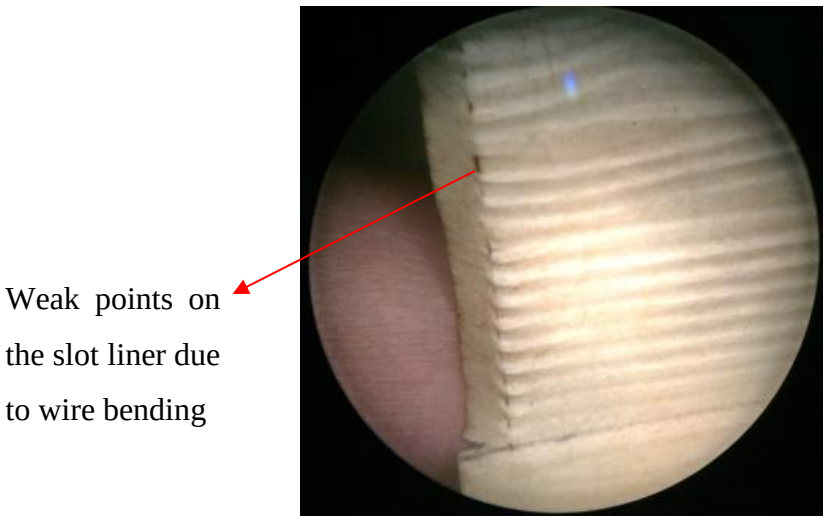

Figure 7.4 Plastic deformation in Nomex 410 slot liners during compression – aged 840 hours

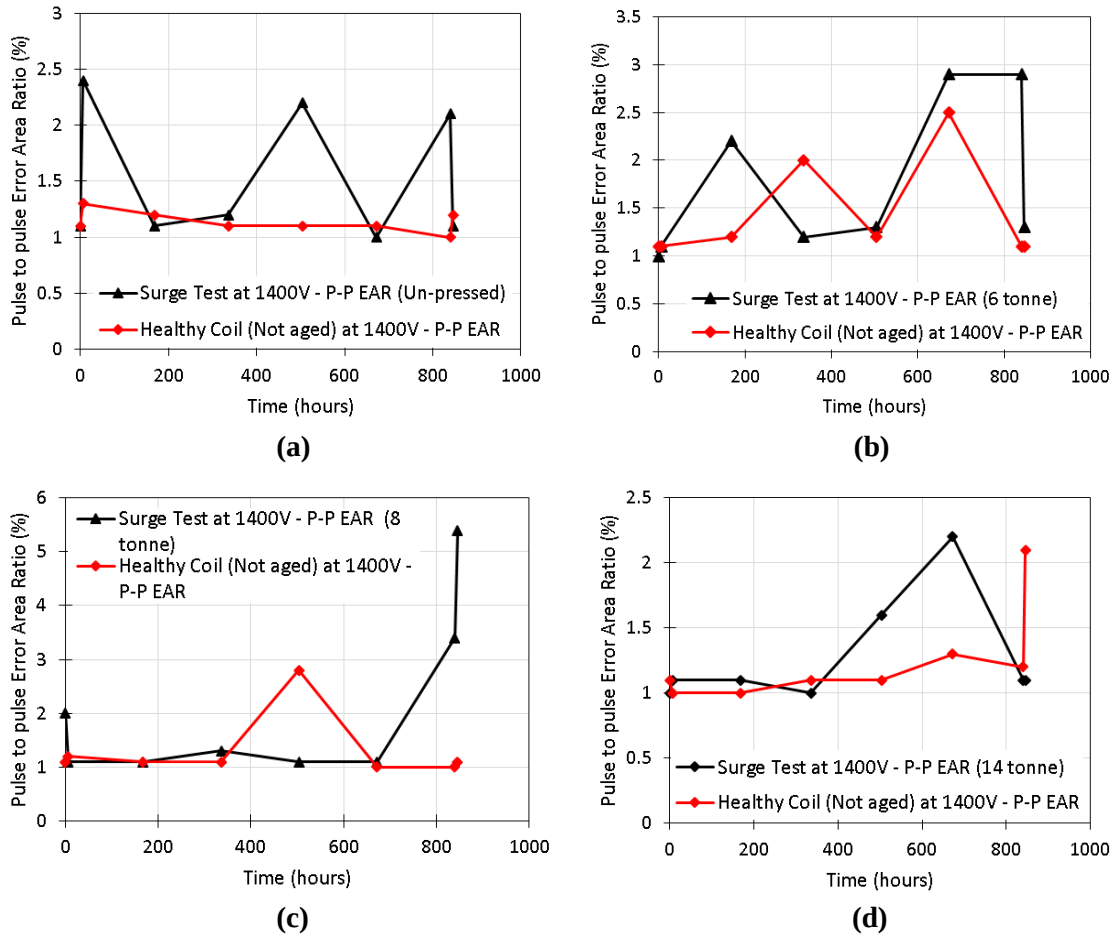

Figure 7.5 Pulse to pulse error area ratio (%) for detection of turn to turn short during thermal aging tests

On the other hand, a turn to turn short was not observed as given in Figure 7.5 for all the surge tested coils, implying that the reason behind the drop of insulation resistance is perhaps highly deformed slot liners as shown in Figure 7.4. This might be mitigated by replacing slot liners after compression.

Pulse to pulse error area ratio (ppEAR) compares successive pulses to each other when a surge test proceeds [131]. If there is a change in amplitude or shift in frequency due to inductance variation, the ppEAR number jumps up [131]. The allowed ppEAR was set to 10% that is also default in Static Motor Analyser. In Figure 7.5, the maximum ppEAR does not exceed 6% implying that turn to turn short was not observed in thermally aged compressed coils. This also demonstrates that on-tooth coil pressing damages slot liners contrary to magnet wire enamels.

An ISG coil with an already known turn to turn short has been surge tested to investigate the response of ppEAR in a fault condition which is shown in Figure 7.6.

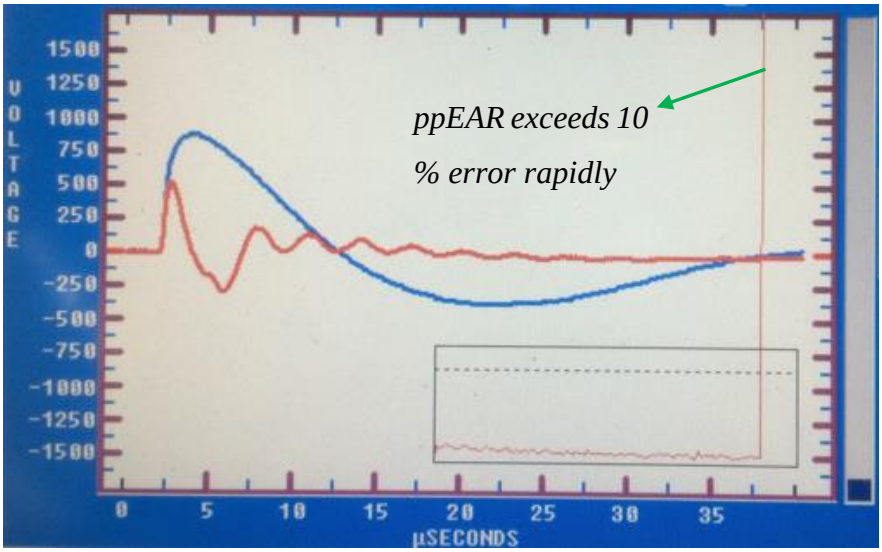

Figure 7.6 Faulty condition during 1400 V surge test due to turn to turn short

According to preliminary aging tests, on-tooth coil pressing is still a valid approach to improve the slot fill factor since magnet wire failure has not been observed even for Grade 1 coatings. Nonetheless, slot wall insulation has been negatively affected by the coil pressing. This would be alleviated by replacing the slot liners if a dummy tooth were used, enabling the winding to be removed from the tooth.

7.6 Reliability Analysis – Accelerated Life Tests

Under normal service conditions, it may take several years for the insulation to fail. However, accelerated test conditions are an alternative model to estimate the life time characteristics of the insulations under thermal, electrical or humidity stresses. This technique is useful due to its effectiveness, timeliness and cost effectiveness [132].

Accelerated life tests can be performed on a certain AWG wire gauge with a specific type of insulations such as polyimide, polyester-imide or polyester enamelled copper wires. An experimental process has been set up and statistical methods were employed to estimate the life time characteristics of the pressed coils under thermal stress.

7.6.1 Accelerated Life Test System

A model that predicts time-to-fail as a function of operating stresses is known as an acceleration model. A set of pressed ISG coils at similar slot fill factors can be considered to be samples for the experiment. Faulty specimens (coils) must be kept away from the experiment. All coils must be inspected if there are any faulty coils before the experiment commences. If all coils are healthy, then samples of pressed coils can enter the experiment.

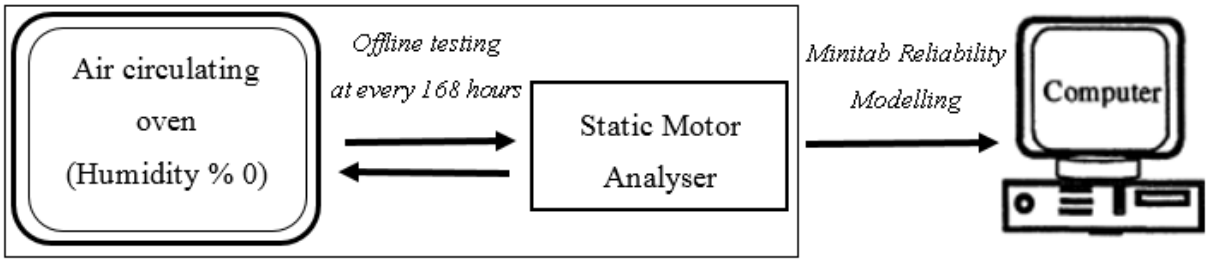

Figure 7.7 Schematic of accelerated life test system

In Figure 7.7, a schematic of accelerated life testing system is shown. There is an air circulating oven that provides temperature controlled testing at certain humidity value. Humidity was set to zero (in percent) since single stress (temperature) model was employed in the experiment.

7.6.2 Arrhenius – Weibull Life Model

There are different types of life models that can be used to estimate life characteristics of the pressed coils using statistical methods after collecting data from aging experiments. These life models are useful to calculate the life time at service level conditions.

Statistical distributions such as Log-normal distribution, Weibull distribution are also needed to analyse test results. If failure rate increases with time, there is an aging process. Weibull distribution, a continuous distribution, with a $\beta > 1$ as given in equation (7.6) is the most commonly used statistical distribution in aging tests [129]. The main purpose of statistical distributions is to quantify the normal amount of variation in an outcome [81]. Arrhenius-Weibull statistical method has been applied to find a relationship between failure time of compressed windings and unreliability at certain accelerated temperatures. Also, a regression model can be derived to estimate how long the insulation will last at machine operating temperature when coils are pre-pressed. Using the outcome of statistical data after performing thermal aging tests in an environmental chamber, the life expectancy of compressed windings can be revealed. As it is not realistic to maintain life test for a very long time period, some coil units after aging test need to be suspended implying that exact failure time could not be recorded as insulation failure has not been detected yet. In this case, advanced statistical methods, known as data censoring (i.e. suspension of data), are required to treat this condition.

7.6.2.1 Parameter Estimation for "Arrhenius – Weibull" Life Model

The Arrhenius life stress model is formulated by assuming life is proportional to the inverse reaction rate of the process as given [129]:

$$L(V) = C\, e^{\frac{B}{V}} \tag{7.5}$$

where L represents a quantifiable life measure (i.e. mean life), V is the level of stress (e.g. temperature in °K), C is one of the model parameters to be determined ($C > 0$). B is another model parameter to be determined.

The probability density function (pdf) for the *2*-parameter Weibull distribution is given by:

$$f(t) = \frac{\beta}{\eta}\left(\frac{t}{n}\right)^{\beta-1} e^{-\left(\frac{t}{\eta}\right)^{\beta}} \tag{7.6}$$

where β is shape parameter. By setting $\eta = L(V) = C\, e^{\frac{B}{V}}$ and substituting for η in the Weibull distribution equation, Arrhenius – Weibull model pdf can be obtained as given:

$$f(t,V) = \frac{\beta}{C\, e^{\frac{B}{V}}}\left(\frac{t}{C\, e^{\frac{B}{V}}}\right)^{\beta-1} e^{-\left(\frac{t}{C\, e^{\frac{B}{V}}}\right)^{\beta}} \tag{7.7}$$

Parameter estimation can be carried out by using Maximum Likelihood Estimation Method. The Arrhenius – Weibull log-likelihood function is as follows [129]:

$$\begin{aligned}\Lambda = \sum_{i=1}^{F_e} N_i ln\left[\frac{\beta}{C\, e^{\frac{B}{V_i}}}\left(\frac{T_i}{C\, e^{\frac{B}{V_i}}}\right)^{\beta-1} e^{-\left(\frac{T_i}{C\, e^{\frac{B}{V_i}}}\right)^{\beta}}\right] - \sum_{i=1}^{S} N'_i\left(\frac{T'_i}{C\, e^{\frac{B}{V_i}}}\right)^{\beta} \\ + \sum_{i=1}^{FI} N_i'' \, ln\left[e^{-\left(\frac{T''_{L_i}}{C\, e^{\frac{B}{V_i}}}\right)^{\beta}} - e^{-\left(\frac{T''_{R_i}}{C\, e^{\frac{B}{V_i}}}\right)^{\beta}}\right]\end{aligned} \tag{7.8}$$

with

$$R''_{L_i} = e^{-\left(\frac{T''_{L_i}}{C\, e^{\frac{B}{V_i}}}\right)^{\beta}}$$

$$R''_{R_i} = e^{-\left(\frac{T''_{R_i}}{C\, e^{\frac{B}{V_i}}}\right)^{\beta}}$$

where:

F_e is the number of groups of exact times-to-failure data points.

N_i is the number of times-to-failure data points in the i^{th} time-to-failure data group.

β is the Weibull shape parameter.

B is the Arrhenius parameter.

C is the second Arrhenius parameter.

V_i is the stress level of the i^{th} group.

T_i is the exact failure time of the i^{th} group.

S is the number of groups of suspension data points.

N'_i is the number of suspensions in the i^{th} group of suspension data points.

T'_i is the running time of the i^{th} suspension data group.

FI is the number of interval data groups.

N''_i is the number of intervals in the i^{th} group of data intervals.

T''_{L_i} is the beginning of the i^{th} interval.

T''_{R_i} is the ending of the i^{th} interval.

The solution is found by solving for $\hat{\beta}$, $\hat{B}$ and $\hat{C}$ so that $\frac{\partial \Lambda}{\partial \beta} = 0, \frac{\partial \Lambda}{\partial B} = 0, \frac{\partial \Lambda}{\partial C} = 0$, where:

$$\begin{aligned}
&\frac{\partial \Lambda}{\partial \beta} \\
&= \frac{1}{\beta}\sum_{i=1}^{F_e} N_i + \sum_{i=1}^{F_e} N_i \, ln\left(\frac{T_i}{C\, e^{\frac{B}{V_i}}}\right) - \sum_{i=1}^{F_e} N_i \left(\frac{T_i}{C\, e^{\frac{B}{V_i}}}\right)^{\beta} ln\left(\frac{T_i}{C\, e^{\frac{B}{V_i}}}\right) \\
&- \sum_{i=1}^{S} N'_i \left(\frac{T'_i}{C\, e^{\frac{B}{V_i}}}\right)^{\beta} ln\left(\frac{T'_i}{C\, e^{\frac{B}{V_i}}}\right) \\
&- \sum_{i=1}^{FI} N_i'' \, \frac{\left(\frac{T''_{L_i}}{C\, e^{\frac{B}{V_i}}}\right)^{\beta} \ln\left(\frac{T''_{L_i}}{C\, e^{\frac{B}{V_i}}}\right) R''_{L_i} - \left(\frac{T''_{R_i}}{C\, e^{\frac{B}{V_i}}}\right)^{\beta} \ln\left(\frac{T''_{R_i}}{C\, e^{\frac{B}{V_i}}}\right) R''_{R_i}}{R''_{L_i} - R''_{R_i}}
\end{aligned} \tag{7.9}$$

$$\frac{\partial \Lambda}{\partial B} = -\beta \sum_{i=1}^{F_e} N_i \frac{1}{V_i} + \beta \sum_{i=1}^{F_e} N_i \frac{1}{V_i} \left(\frac{T_i}{\hat{C}\, e^{\frac{\hat{B}}{V_i}}} \right)^{\beta} + \beta \sum_{i=1}^{S} N'_i \frac{1}{V_i} \left(\frac{T'_i}{\hat{C}\, e^{\frac{\hat{B}}{V_i}}} \right)^{\beta} + \sum_{i=1}^{FI} N_i'' \frac{\beta}{V_i} \frac{\left(T''_{L_i}\right)^{\beta} R''_{L_i} - \left(T''_{R_i}\right)^{\beta} R''_{R_i}}{\left(C\, e^{\frac{B}{V_i}} \right)^{\beta} \left(R''_{L_i} - R''_{R_i} \right)} \tag{7.10}$$

$$\frac{\partial \Lambda}{\partial C} = -\frac{\beta}{C} \sum_{i=1}^{F_e} N_i + \frac{\beta}{C} \sum_{i=1}^{F_e} N_i \left(\frac{T_i}{C\, e^{\frac{B}{V_i}}} \right)^{\beta} + \frac{\beta}{C} \sum_{i=1}^{S} N'_i \left(\frac{T'_i}{C\, e^{\frac{B}{V_i}}} \right)^{\beta} + \sum_{i=1}^{FI} N_i'' \frac{\beta}{C} \frac{\left(T''_{L_i}\right)^{\beta} R''_{L_i} - \left(T''_{R_i}\right)^{\beta} R''_{R_i}}{\left(C\, e^{\frac{B}{V_i}} \right)^{\beta} \left(R''_{L_i} - R''_{R_i} \right)} \tag{7.11}$$

7.6.3 Accelerated Life Test – Phase 1

In order to apply a regression model for Arrhenius – Weibull distribution, at least two accelerated stress (i.e. temperature) points are required. Abnormally high temperatures speed up deterioration of coils. With failure time information at accelerated temperatures, the temperature can be extrapolated to normal operating temperatures. Hence, life prediction of the compressed ISG coils can be achieved.

The logarithmic regression model can be attained using the relationship between temperature and failure time for the coil insulation system. Parameter estimation is crucial in accelerated life model. Maximum likelihood is one of the methods to estimate parameters in statistical models. By taking derivative of equation (7.8) with respect to Weibull shape parameter (β), Arrhenius parameter (B) and second Arrhenius parameter and solving the equations when they equal to zero, the parameter estimation can be done.

Instead of solving complex mathematical equations given in equations (7.9), (7.10) and (7.11) to estimate Arrhenius –Weibull parameters, a software package, Minitab has been used to numerically estimate the parameters. The software also provides Arrhenius-Weibull life modelling. Thus, probability plots with respect to failure time can be achieved in the software.

The most important part of accelerated life data analysis is to conduct reliable thermal aging tests of ISG coils at an accelerated temperature at 0% humidity. In Phase 1 of the accelerated life tests, 5 compressed (≈350 bar hydraulic pressure) coils at about 0.72 fill factor and 5 conventional coils at 0.57 fill factor have been simultaneously tested. The ISG coils comprised of 91 turn, 1.25 mm conductors are of thermal class 200 and thermal endurance graph for the chosen magnet wires is given in Figure 7.8 [133].

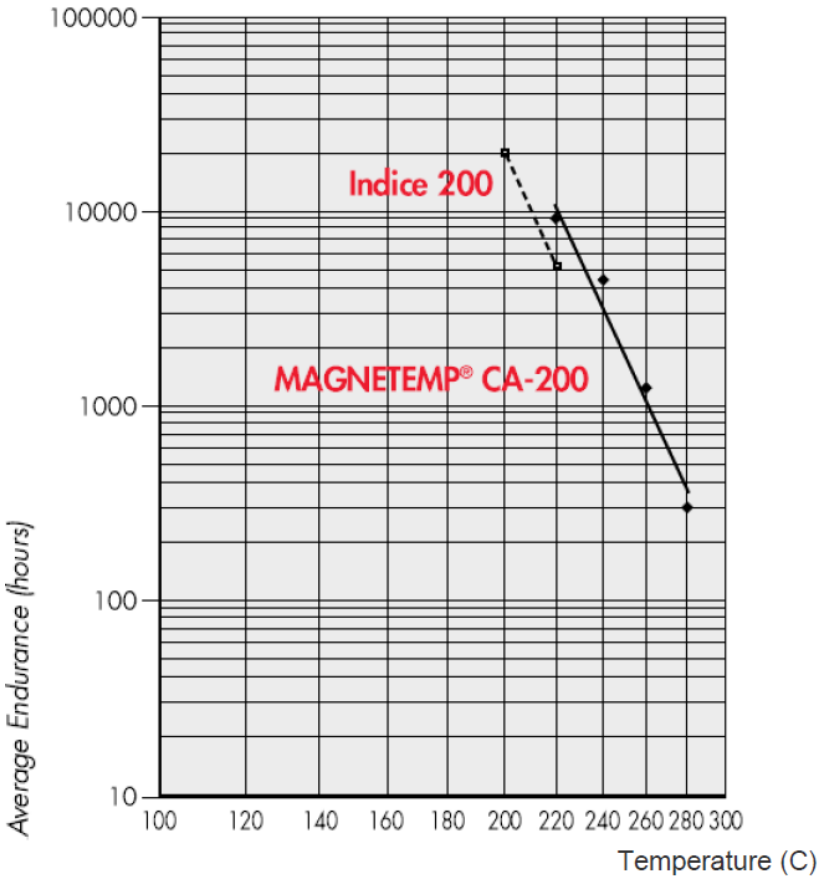

Figure 7.8 Log-linear life characteristics of commercial, Class N magnet wires [133]

As shown in Figure 7.8, Class 210 magnet wires have 5000 hour life at 220°C and 20,000 hour life at about 210°C. This can be read form the logarithmic plot. Although accelerated life tests should be conducted at temperatures higher than 210°C to speed up the process, 175°C was chosen for Phase 1 because preliminary aging test results shown in Figure 7.3 already demonstrates that coil pressing artificially changes (reduces) the thermal class of the coil insulation system.

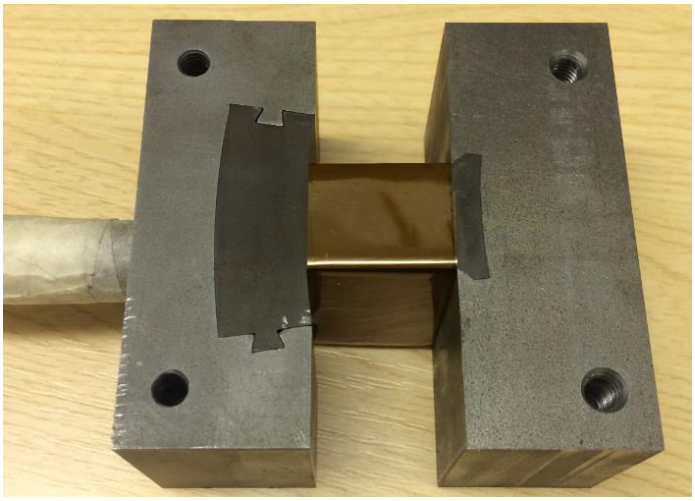

Figure 7.9 50µm Kapton Polyimide Film [134] – First insulation layer

In order to improve dielectric strength of the ISG coils, Kapton Polyimide film [134] of 50 μm thickness has been wrapped around the ISG teeth as depicted in Figure 7.9. The dielectric strength of the 2-mil (i.e. 0.0508 mm) film is 240 kV/mm [134]. The dielectric strength of air is approximately 3 kV/mm [135].

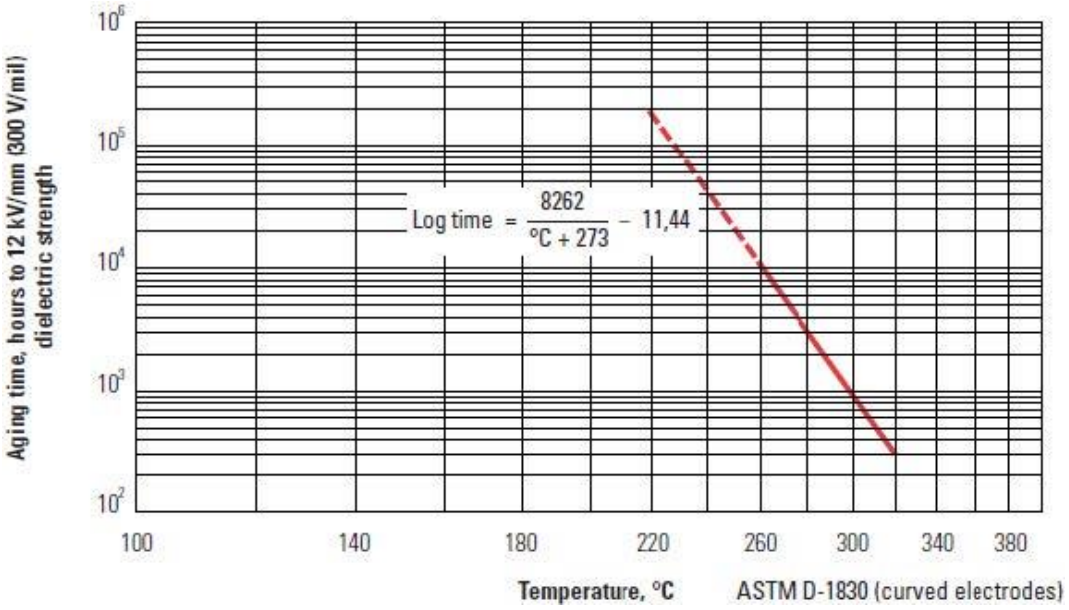

Figure 7.10 Nomex 410, 0.25 mm insulation: Life Vs Temperature [136]

In Figure 7.10, how Nomex 410 slot liner [136] maintains its dielectric strength of 12kV/mm is shown. At 175°C, the expected life for the slot liners is 10,045,330 hours. On-tooth coil pressing with Nomex 410 liners might be harshly affecting the dielectric strength of the insulation. The preliminary test results (Figure 7.3) indicate that the slot liners lose its dielectric strength significantly since all the compressed coils in 35 day aging test fail.

All the coils have been tested using Static Motor Analyser before commencing the aging tests to make sure that they all are healthy in terms of insulation resistance. The coils are shown in Figure 7.11. One of the entirely healthy conventional ISG coils was used for comparison purpose and not aged in the oven. When surge tests have been performed as described in Section 7.4.3.1, the healthy un-aged ISG coil is considered as a reference to investigate a turn to turn short by comparing pulse to pulse error area ratios in the coils that must be less than 10%.

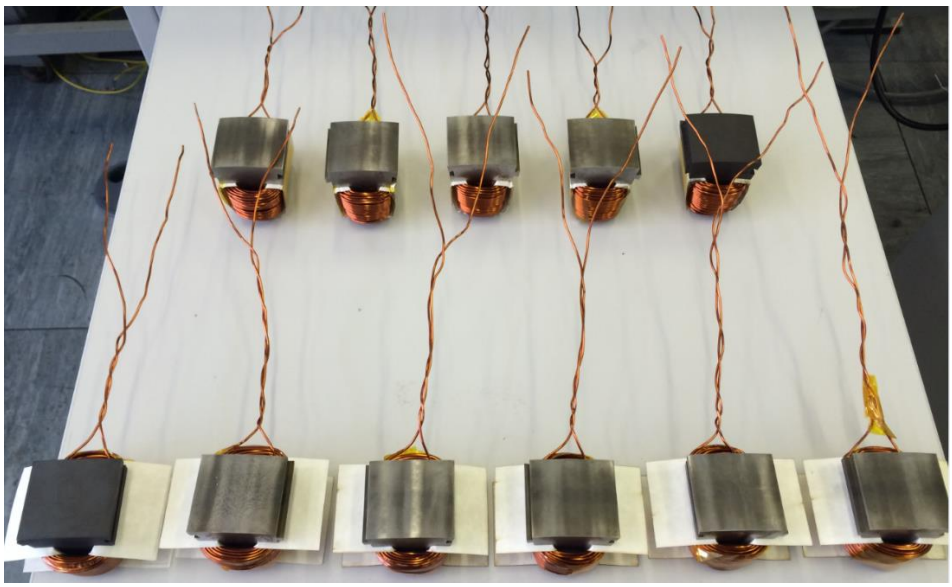

Figure 7.11 Compressed and conventional ISG coils before thermal aging

In Figure 7.13 a, b, c, d and e, variation of turn to ground wall insulation resistance of the random wound compressed ISG coils are given. In Figure 7.13 f, g, h, i and j, variation of turn to ground wall insulation resistance of the random wound un-compressed ISG coils are shown. Linear regression lines are employed to investigate the behaviour of the ISG coils in terms of insulation resistance varying with time. A rapid decrease in insulation resistance is observed in all the compressed windings. The coils shown in Figure 7.12 are in an environmental chamber operating at 175°C at 0% humidity and 100% fan speed.

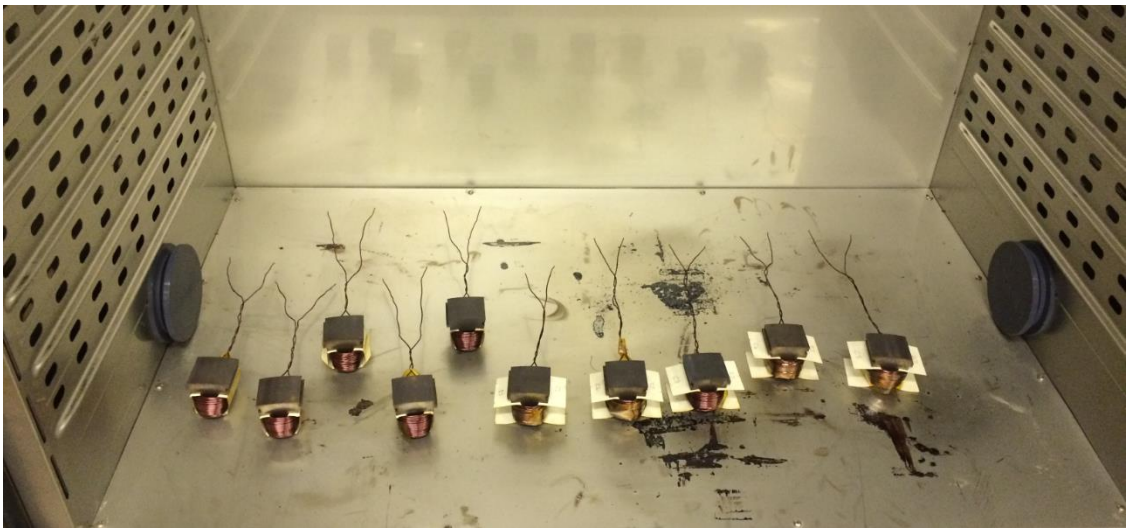

Figure 7.12 Conventional and compressed ISG coils in the environmental chamber

The ISG coils have been aged at 175°C for 49 days and off-line turn to turn and turn to ground wall insulation tests have been performed at every 168 hours to monitor the insulation resistance and to catch the failure time intervals.

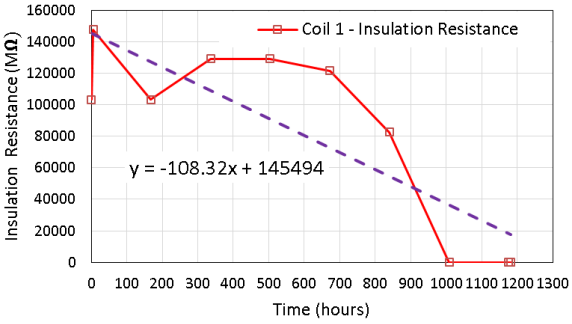
Coil 1 - Insulation Resistance
y = -108.32x + 145494
Insulation Resistance (MΩ)
Time (hours)

(a)

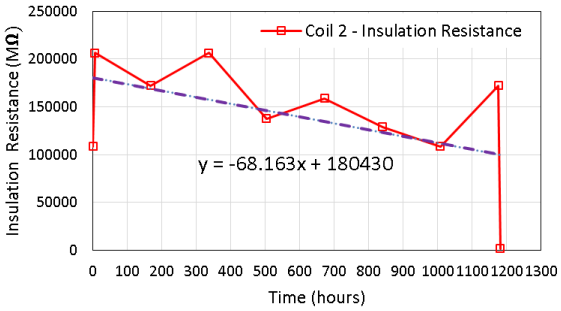
Coil 2 - Insulation Resistance
y = -68.163x + 180430
Insulation Resistance (MΩ)
Time (hours)

(b)

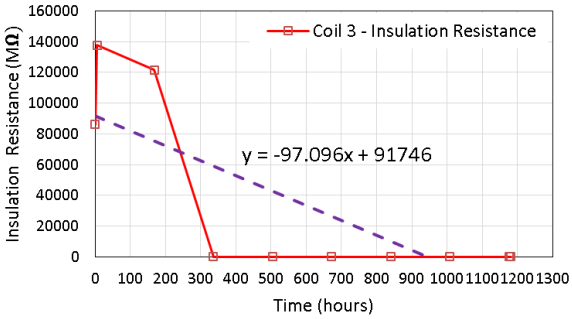
Coil 3 - Insulation Resistance
y = -97.096x + 91746
Insulation Resistance (MΩ)
Time (hours)

(c)

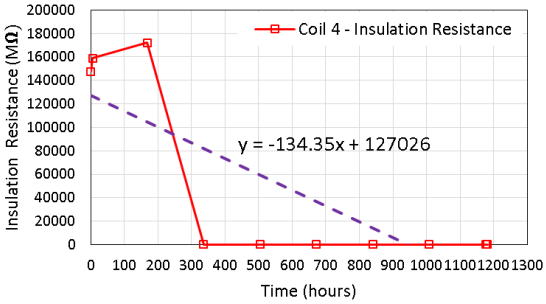
Coil 4 - Insulation Resistance
y = -134.35x + 127026
Insulation Resistance (MΩ)
Time (hours)

(d)

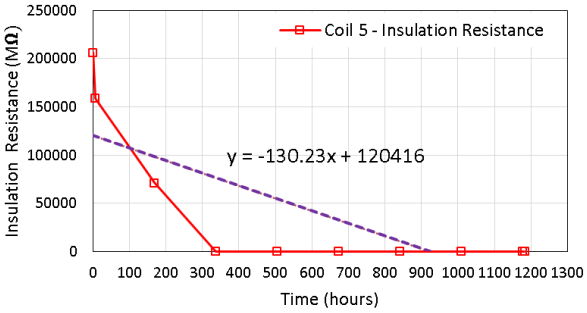
Coil 5 - Insulation Resistance
y = -130.23x + 120416
Insulation Resistance (MΩ)
Time (hours)

(e)

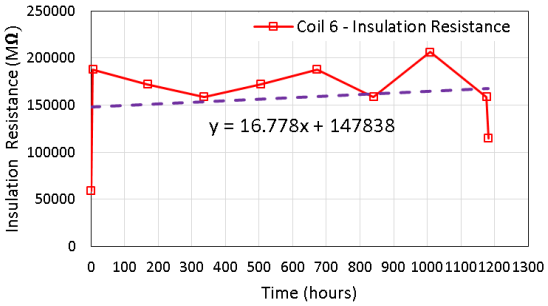
Coil 6 - Insulation Resistance
y = 16.778x + 147838
Insulation Resistance (MΩ)
Time (hours)

(f)

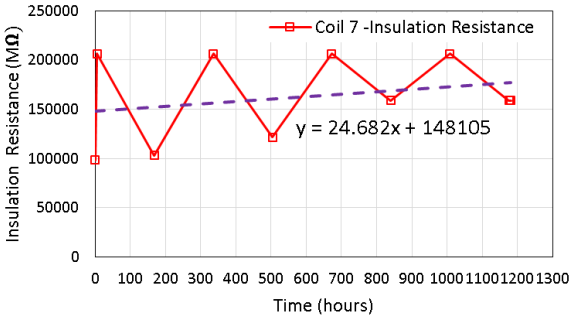
Coil 7 -Insulation Resistance
y = 24.682x + 148105
Insulation Resistance (MΩ)
Time (hours)

(g)

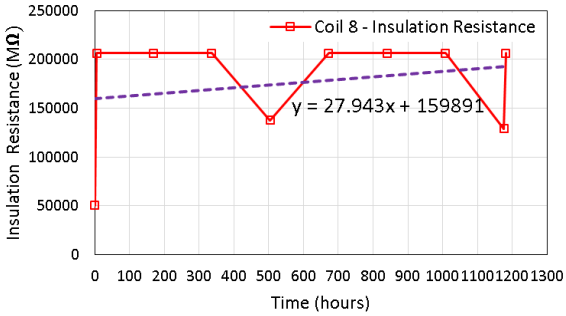
Coil 8 - Insulation Resistance
y = 27.943x + 159891
Insulation Resistance (MΩ)
Time (hours)

(h)

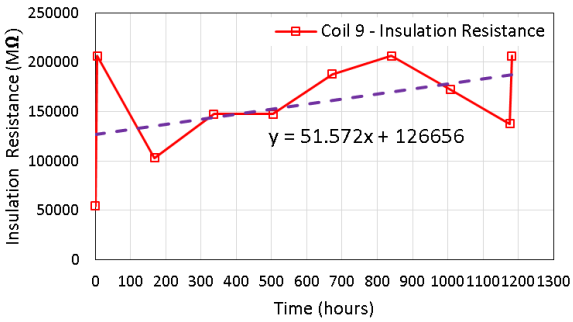
Coil 9 - Insulation Resistance
y = 51.572x + 126656
Insulation Resistance (MΩ)
Time (hours)

(i)

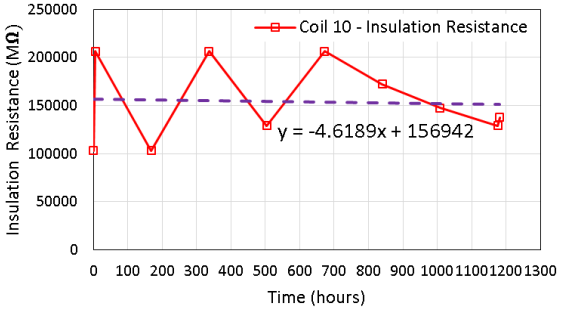
Coil 10 - Insulation Resistance
y = -4.6189x + 156942
Insulation Resistance (MΩ)
Time (hours)

(j)

Figure 7.13 Aging of pressed and conventional ISG coils at 175°C for 49 days

In Table 7.2, time to failure data of the aging test at 175°C is tabulated. The censored ('C') data implies no failure observed statistically throughout the experiment. The failure criterion is that turn to ground wall insulation resistance must be higher than 5MΩ as reported in IEEE standards. A turn to turn short has not been observed for any coil surge tested during the thermal aging experiment. Furthermore, time to failure intervals are recorded if a failure occurs in a coil. The exact failure time is not known as the coils have been inspected at every 168 hours.

Table 7.2 Accelerated Life Test Phase 1 – Time to Failure

Stress: Temperature	**175°C (448K)**	C: Censored – Failure not observed
		Criterion: $IR_{MIN} \geq 5M\Omega$
		$\mathbf{0h < t < 1182h}$
Compressed ISG coils – Time Failed (hrs)	Coil #1	'C'
	Coil #2	'C'
	Coil #3	$168h < t_{Fail} < 336h$
	Coil #4	$168h < t_{Fail} < 336h$
	Coil #5	$336h < t_{Fail} < 504h$
Conventional random wound ISG coils – Time Failed (hrs) No Failure Observed.	Coil #6	'C'
	Coil #7	'C'
	Coil #8	'C'
	Coil #9	'C'
	Coil #10	'C'

7.6.4 Accelerated Life Test – Phase 2

In Phase 2 of the aging tests, a set of coil (six compressed and one conventional) have been aged at 140°C for 70 days and off-line turn to turn and turn to ground wall insulation tests have been performed at every 168 hours to monitor the insulation resistance and catch failure time intervals.

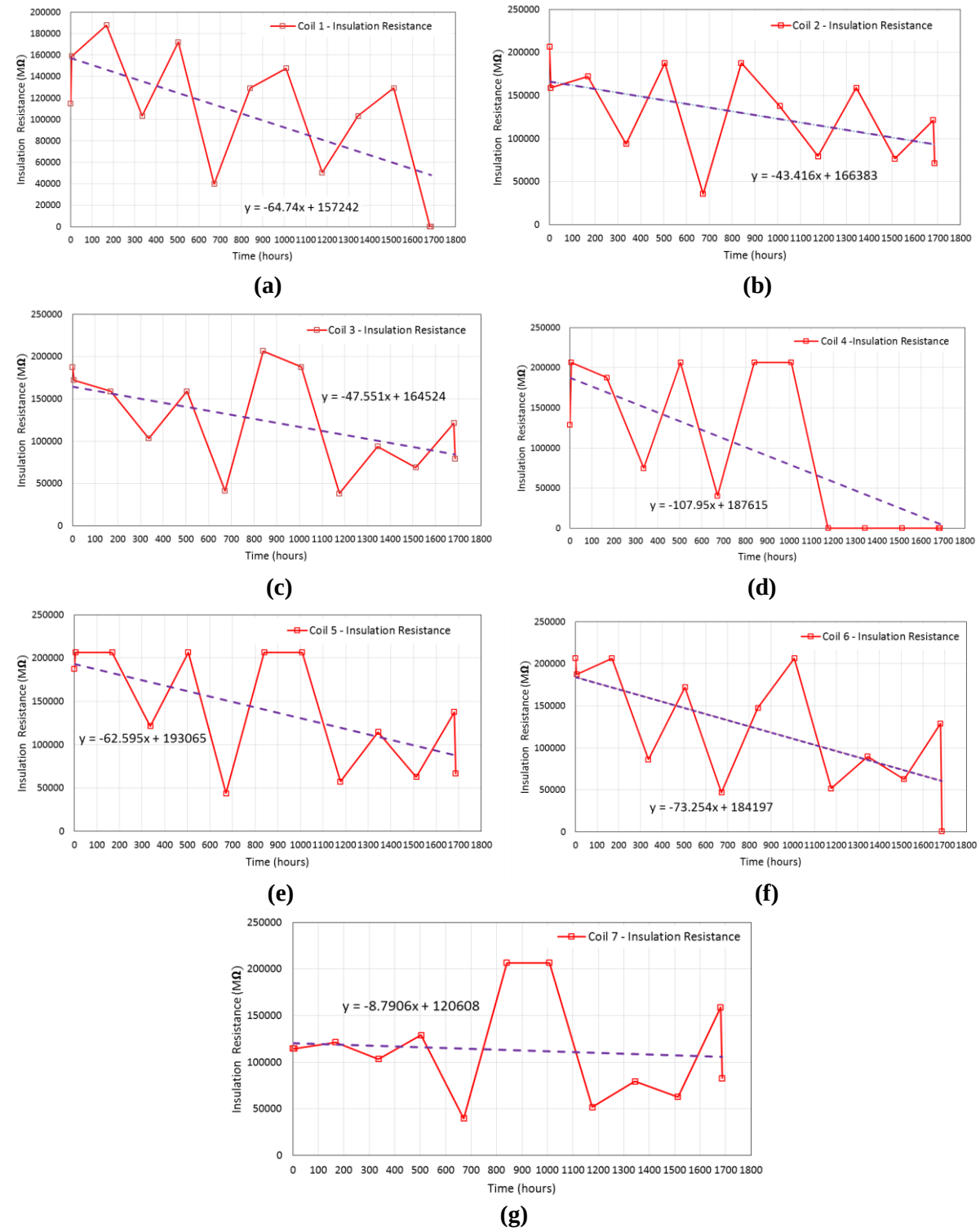

Figure 7.14 Aging of pressed and conventional ISG coils at 140°C for 70 days

In Figure 7.14 a, b, c, d, e and f, the variation of turn to ground wall insulation resistance of the random wound compressed ISG coils are given. Figure 7.14 g depicts the insulation resistance of the conventional ISG coil under thermal stress. In Table 7.3, time to failure summary of the aging test at 140°C is shown.

Table 7.3 Accelerated Life Test Phase 2 – Time to Failure

Stress: Temperature	**140°C (413K)**	C: Censored – Failure not observed
		Criterion: $IR_{MIN} \geq 5M\Omega$
		$\mathbf{0h < t < 1686h}$
Compressed ISG coils – Time Failed (hrs)	Coil #1	$1512h < t_{Fail} < 1686h$
	Coil #2	'C'
	Coil #3	'C'
	Coil #4	$1008h < t_{Fail} < 1176h$
	Coil #5	'C'
	Coil #6	'C'
Conventional random wound ISG coil – Time Failed (hrs) No Failure Observed.	Coil #7	'C'

7.6.5 Accelerated Life Test – Phase 3

In Phase 3, a set of coils (five compressed and one conventional) have been aged at 160°C for 49 days and off-line turn to turn and turn to ground wall insulation tests have been performed periodically.

In Figure 7.15 a, b, c, d and e, the variation of turn to ground wall insulation resistance of the random wound compressed ISG coils are given. Figure 7.15f shows insulation resistance of conventional random wound coil.

In Table 7.4, a summary of the Phase 3 including time to failure data is given. There are two coils failed during 49 day aging tests at 160°C. Failure data for the other coils are censored since an insulation failure was not observed during the experiment.

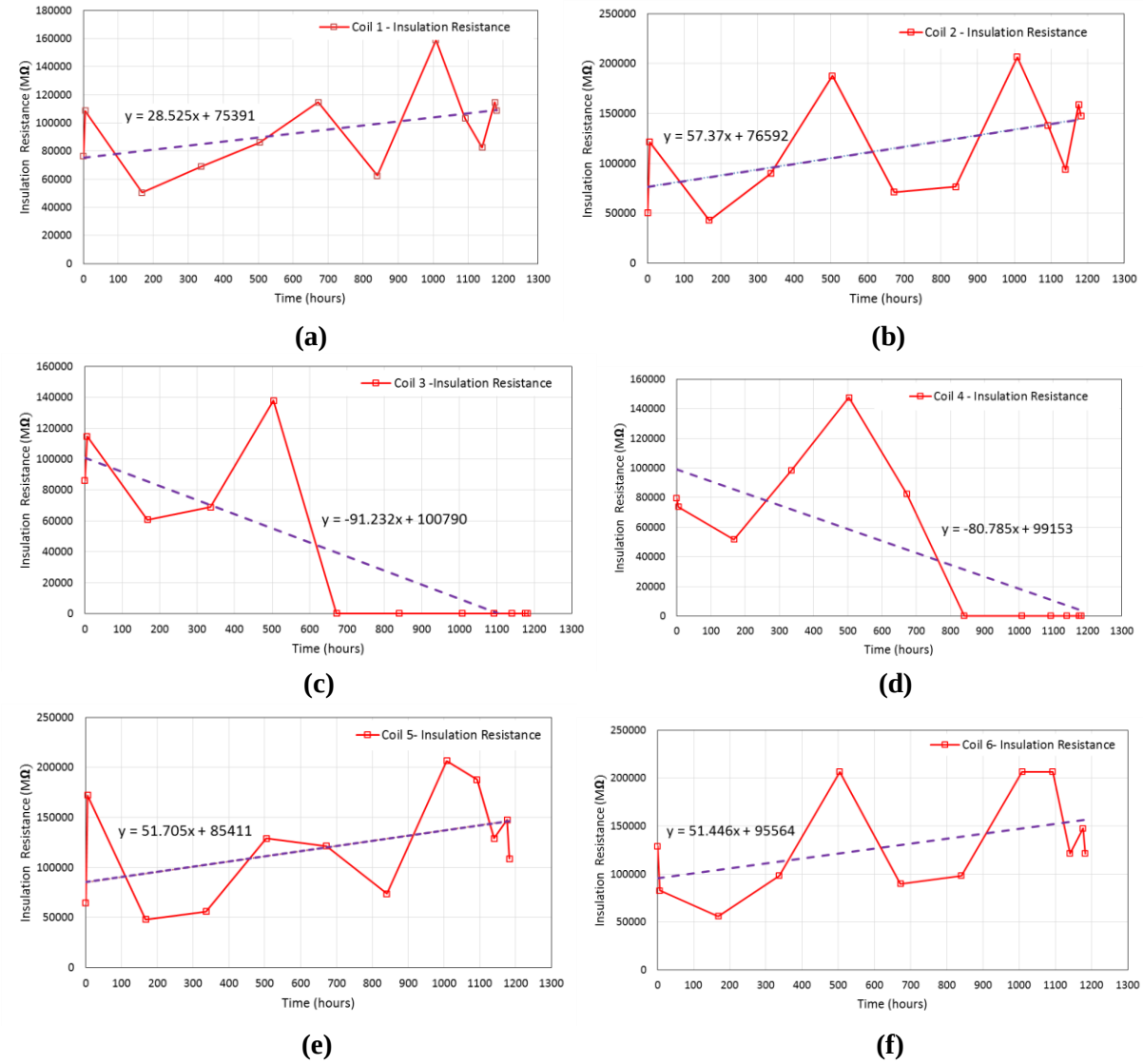

Figure 7.15 Aging of pressed and conventional ISG coils at 160°C for 49 days

Table 7.4 Accelerated Life Test Phase 3 – Time to Failure

Stress: Temperature	**160°C (433K)**	C: Censored – Failure not observed
		Criterion: $IR_{MIN} \geq 5M\Omega$
		$\mathbf{0h < t < 1182h}$
Compressed ISG coils – Time Failed (hrs)	Coil #1	'C'
	Coil #2	'C'
	Coil #3	$672h < t_{Fail} < 840h$
	Coil #4	$840h < t_{Fail} < 1008h$

	Coil #5	'C'
Conventional random wound ISG coil – Time Failed (hrs) No Failure Observed.	Coil #6	'C'

7.6.6 Life Estimation of the Compressed ISG Coils

The experimental time to failure data collected from '3 Phase' Accelerated Life Tests at 140°C, 160°C and 175°C have been used to predict life expectancy of the on-tooth compressed coils. All phases of the aging experiments are very similar in terms of the coils employed as they achieve very similar fill factors with the same number of turns and insulation systems. 3 different temperate point enables to extrapolate thermal life plot to estimate the life expectancy of the compressed ISG coils at operating temperature which is found to be 138°C from the 3D thermal FEA simulations as reported in Chapter 6.

It should be noted that exact time to failure data from the experiments were not obtained as the coils have been tested at every 168 hours. This requires interval censoring which means that "failure" occurred within some given time period. The statistical software such as Minitab is useful to perform reliability analysis with censored data. The software executes Maximum Likelihood Estimation method for the given data to estimate Arrhenius-Weibull life model parameters which are required to plot the probability graphs.

The overall summary of the accelerated life tests is tabulated in Table 7.5, below.

Table 7.5 Interval Censored and Right Censored time to failure data from the experiments

Temperature (°C)	Arrhenius Temperature	Failure Interval Start	Failure Interval End	Frequency
175	25.8943	168	336	2
175	25.8943	336	504	1
175	25.8943	1182	*	2
160	26.7910	672	840	1
160	26.7910	840	1008	1
160	26.7910	1182	*	3

140	28.0879	1008	1176	1
140	28.0879	1512	1686	1
140	28.0879	1686	*	3
* denotes that a number of coils are right censored (suspended) implying that no insulation failure recorded within the time period of the aging experiments.				

The frequency column in Table 7.5 indicates the number of failures recorded within given time interval. The pure experimental data given in Table 7.5 is sufficient to estimate life expectancy of the on-tooth compressed coil. The conventional random wound coils did not fail during the aging tests. Turn to ground wall insulation failures were observed only in the compressed windings.

Arrhenius-Weibull life model parameters for the conducted aging tests are tabulated in Table 7.6.

Table 7.6 Arrhenius-Weibull Life Data Analysis

Acceleration variable		Temperature		
Distribution :		Weibull		
Estimation:		Maximum Likelihood		
Relationship with accelerating variable:		Arrhenius		
Right censored data:		8		
Interval censored data:		7		
Number of data (coils):		15		
Regression Table				
Predictor	*Coefficient*	*Standard Error*	*95% Normal Confidence Interval -Lower*	*95% Normal Confidence Interval -Upper*
Intercept	-4.83446	7.63350	-19.7958	10.1269
Temperature	0.456644	0.286164	-0.104226	1.01751
Shape	1.59653	0.548019	0.814696	3.12865
Log-likelihood = -23.661				

From the regression table given in Table 7.6, the coefficients for the regression model are obtained. For a Weibull distribution, this model describes the relationship between temperature and failure time for the insulation as given by [137]:

$$log_e(failure\ time) = -4.83446 + 0.456644(Arrhenius\ Temp) + (\frac{1}{1.59653})\varepsilon_p \quad (7.12)$$

Where ε_p is the p[th] percentile of the standard extreme value distribution. Arrhenius temperature is calculated as given [137]:

$$Arrhenius\ Temp = \frac{11604.83}{Temperature\ in\ °C + 273.16} \quad (7.13)$$

The Goodness-of-Fit is an important parameter for the accuracy of the statistical approach. Minitab software provides Anderson-Darling statistic indicates the quality of the fit [137]. A smaller value of the Goodness of Fit means a better fit. At 140°C, the goodness level is 18.67, at 160°C, the goodness level is 18.73 and at 175°C the goodness level is 8.32. Since more coils fail at 175°C, this level of aging tests collect more information statistically in comparison to lower test temperatures.

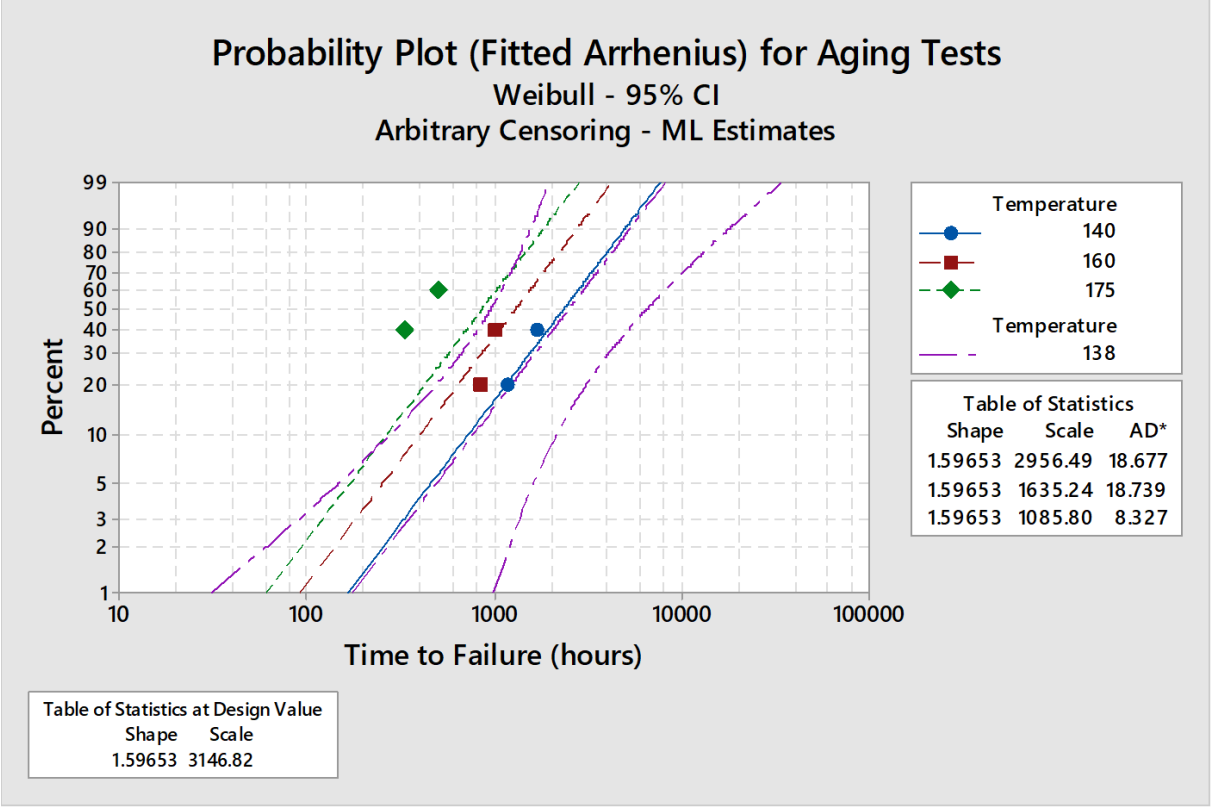

Figure 7.16 Arrhenius-Weibull probability plot – extrapolated to 138°C

The probability plot given in Figure 7.16 can help determine if the distribution at each level of accelerating variable (i.e. temperature) is appropriate or not. If the fitted lines are approximately parallel, the probability model becomes more accurate. According to Figure 7.16, 99% (probability) of the compressed ISG coils fail in 8190.35 hours (mean life) if they operate at 138 °C.

The 50th percentile is a good estimate of insulation life expectancy. Therefore, 2501.34 hours life in average is expected from the coils running at 138°C. This states that the dielectric strength of turn to ground wall insulation for the compressed ISG windings is significantly affected negatively by on-tooth compression method.

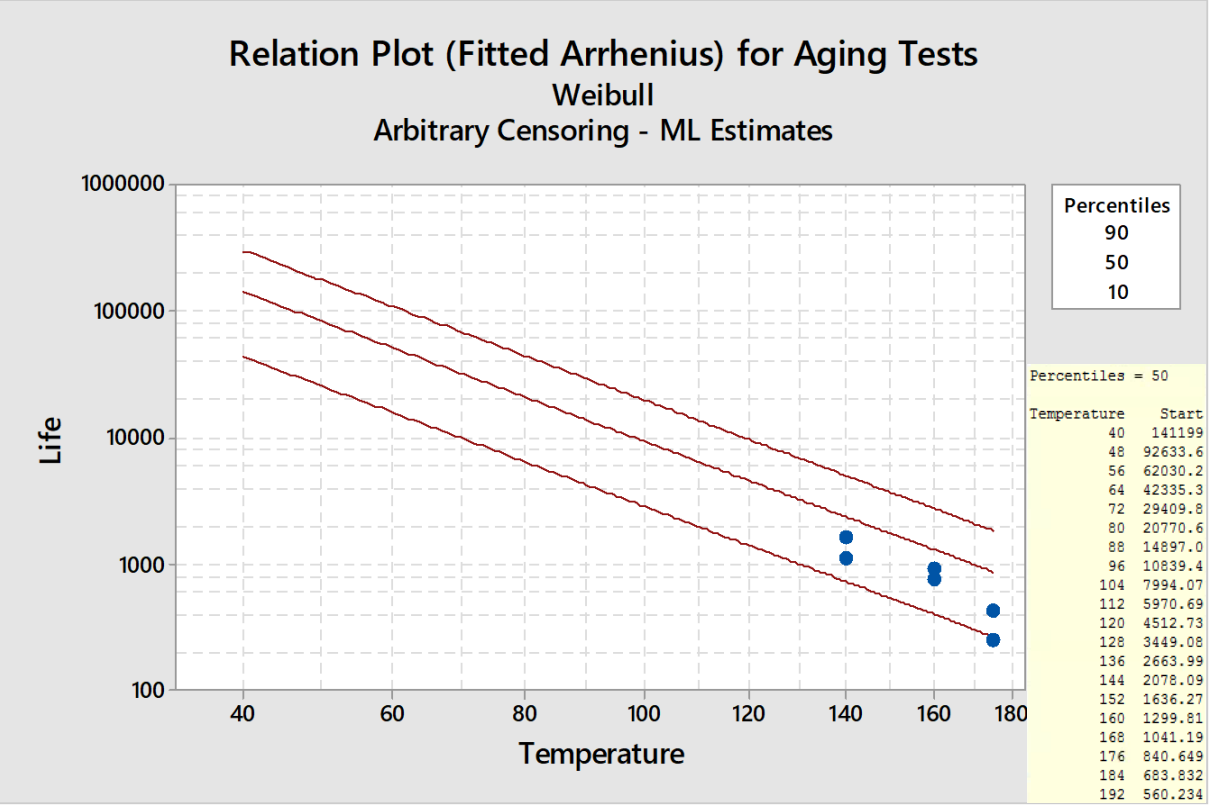

Figure 7.17 Arrhenius-Weibull probability plot – extrapolated to 138°C

In Figure 7.17, the expected mean life of the compressed coils within the range of 40°C and 190°C is shown. The mean life at 80°C is 20770.6 hours whereas it rapidly drops to 1299.81 hours at 160°C.

Furthermore, the accuracy of the chosen distribution which is 'Weibull' is depicted in Figure 7.18. In Weibull probability plot in Figure 7.18, the points fit the lines adequately verifying that the single stress (i.e. temperature) reliability modelling of the compressed ISG coils can be performed particularly using Weibull distribution which was an assumption before the aging tests. The shape of the probability density function (pdf) is also given in Figure 7.18.

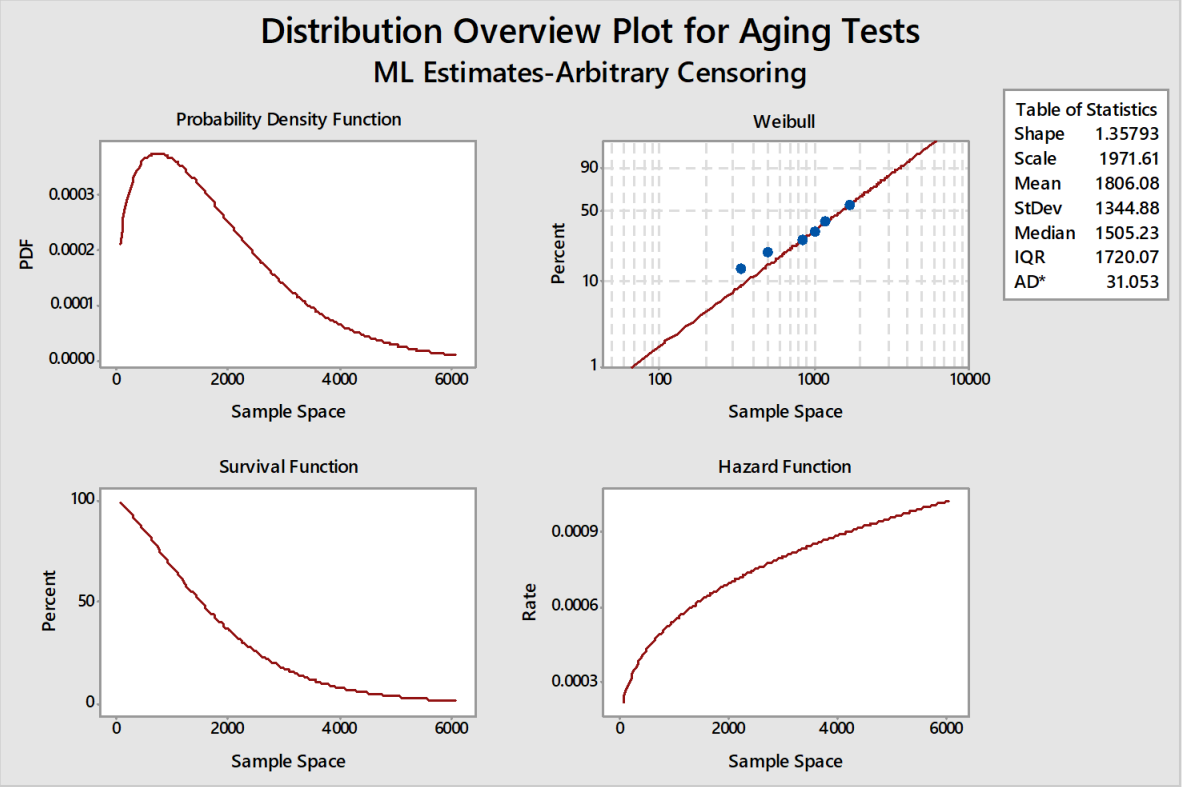

Figure 7.18 Weibull probability plot of the aging tests- an overview

7.7 ASTM Standard Test Method for Thermal Endurance of Round Magnet Wires

Commercial magnet wire companies rely upon the ASTM (American Section of the International Association for Testing Materials) standards when testing the round magnet wire specimens. ASTM D 2307 is a magnet wire standard that specifies the preparation of the specimens and the aging of the specimens at elevated temperatures [138]. Temperature index of the wire insulation is determined by extrapolation of the thermal life plot of the data crosses the 20,000 hour point [139].

The rules for the standard are given as follows [139]:

- Must have at least three temperature points plotted
- Minimum 95% correlation coefficient on data points – pretty straight lines
- No data points less than 100 hours will be valid
- Must have an end point with a minimum of 5000 log average hours of life that is at least 20°C above the thermal index of the wire

According to ASTM D 2307 standard, insulation deteriorate according to Arrhenius formula;

$$L = C\, e^{\frac{B}{V}} \tag{7.14}$$

Equation (7.5) is recalled in equation (7.14). This can be written in a linear form as given:

$$log_{10}L = log_{10}C + (log_{10}e).(\frac{B}{V}) \quad (7.15)$$

Assuming that;

$$N = number\ of\ test\ temperatures$$

$$Y = log_{10}L$$

$$a = log_{10}C$$

$X = 1/V$ – Reciprocal Of The Test Temperature in °K

$$b = log_{10}e\ .B$$

Then

$$Y = a + bX \quad (7.16)$$

The parameters a and b can be calculated from the method of least squares from the following:

$$a = \frac{(\sum_N Y - b\sum_N X)}{N} \quad (7.17)$$

$$b = \frac{(N\sum_N XY - \sum_N X\sum_N Y)}{(N\sum_N X^2 - (\sum_N X))^2} \quad (7.18)$$

If a and b are known, any required life can be calculated as given in equation (7.16).

This life estimation method is valid for only magnet wire 'enamels'. However, magnet wire enamel failure has never been detected via surge testing during accelerated life tests. The ASTM standard can be generalised to predict the life expectancy of the compressed ISG coils since Arrhenius model is still valid for the ground wall aging tests when the acceleration variable is solely temperature.

The calculation table given in Table 7.7 is useful to predict a and b to implement Arrhenius equation:

Table 7.7 Arrhenius equation parameter calculations using the method of least squares

Temp	$X = 1/V$	$X^2 = 1/V^2$	$L(V)^*$	$Y = log_{10}L$	$XY = (log_{10}L)/V$	Y^2
140°C	0.002420428	5.85847E-06	1345.5	3.128883702	0.007573239	9.789913221
160°C	0.002308669	5.32995E-06	840	2.924279286	0.006751193	8.551409343
175°C	0.002231396	4.97913E-06	308	2.488550717	0.005552941	6.192884669
Σ $N = 3$	0.006960493	1.61676E-05		8.541713705	0.019877374	24.53420723

* The average time to failure is computed by only considering the failed ISG coils – the censored data was not included in the calculations.

The values of a and $b - slope$ are calculated to be 3276.715 and -4.7552 from Table 7.7. After that log-linear life expectancy is plotted in Excel as a linear function as depicted in Figure 7.19.

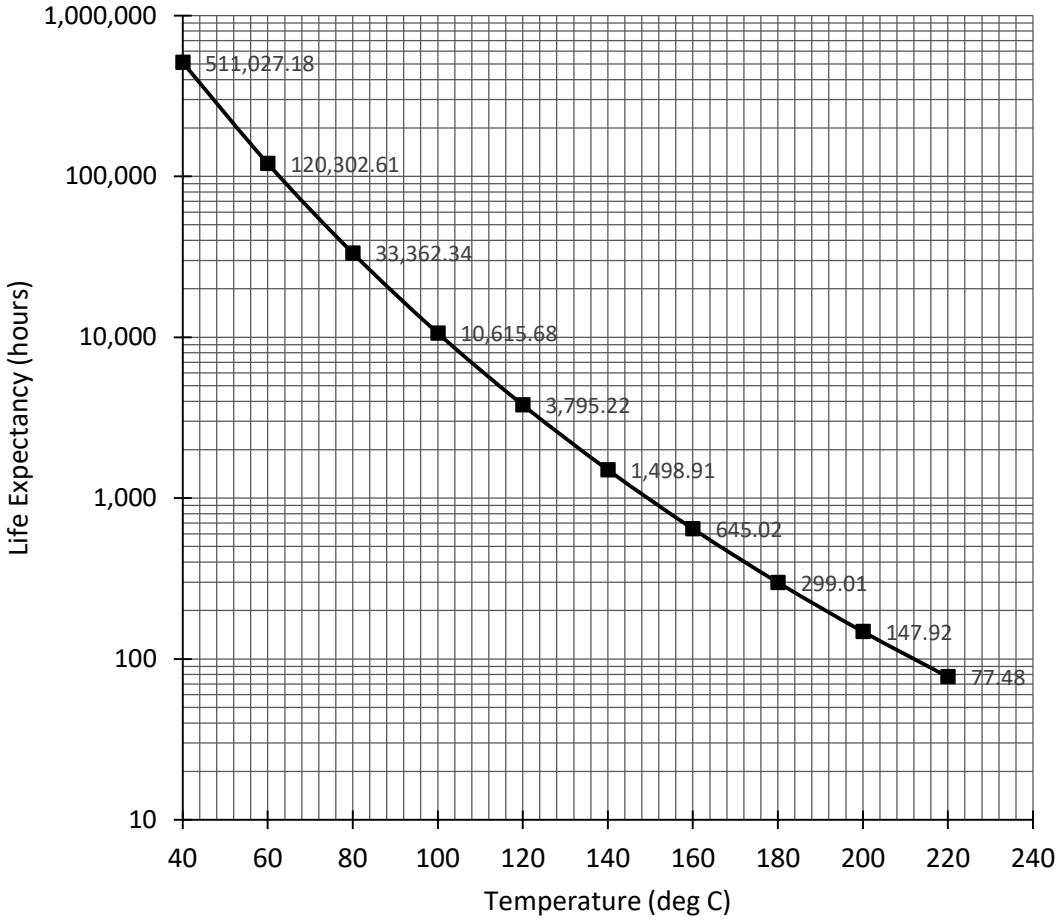

Figure 7.19 Life expectancy of the compressed ISG coils by neglecting censored data

At 138°C, the ISG machine will stay healthy for 1638.15 hours according to log - linear thermal endurance plot given in Figure 7.19. This estimation gives less life expectancy compared to accelerated life test results (2501.34 hours) since right censored-suspended data cannot be included in this mathematical model. In ASTM D 2307 standard, exact time to failure for all specimens must be known. Otherwise, the approach cannot compute the life expectancy without considering probabilistic distribution methods such as Weibull or Lognormal etc.

This method is based on Arrhenius equation with normal distribution and mean life of the ISG coils in each thermal aging experiment has been used to estimate the insulation life of the compressed windings.

7.8 Reliability of Commercial Round Magnet Wires

ASTM D 2307 standard determines the thermal index of magnet wires. The magnet wires used in the ISG stator windings are of temperature class 200°C. This means that it has 20,000 hour life at maximum 200°C. This information is based on ASTM D 2307 specimen testing methodology. The preparation of specimens are given in [138]. The specimens for aging tests usually consist of twisted pair of wires with film insulations and a holder. However, the magnet wires with a class of 200°C used in random wound un-pressed ISG windings fail at 175°C as shown in Figure 7.20. This was noticed when wires have been un-wound from the tooth. This shows that commercial magnet wires might not be operated at their temperature class and also emphasise that keeping the temperature low for stator windings is vital.

Figure 7.20 Damaged magnet wire after 49 day thermal aging at 175°C – not a pressed coil

7.9 Conclusion

In this chapter, accelerated life tests for the compressed and conventional stator windings with a thermal class of 200°C are described. A three stage (140°C, 160°C and 175°C) thermal aging tests of the ISG coils enable to perform Arrhenius –Weibull life model. The employed statistical model proves that on-tooth coil pressing reduce the life expectancy dramatically due to reduced turn to ground wall dielectric strength. This could not be prevented even with two layer of insulation system (Kapton HN film + Nomex 410). It is reported that if the windings are directly pressed on the tooth, the life expectancy will be about 2500 hours for the compressed ISG coils operating at 138°C as it is highlighted in Chapter 6 – Section 6.5.2. Therefore, this suggests that stator windings can be pressed off tooth (on a dummy tooth) and then they can be placed into the original stator with un-damaged slot liners. This observation is in line with the aging test results since turn to turn short in the ISG coils has never caught by static motor analyser during the experiments. In other words, the compression of coils usually damage external insulation layers rather than magnet wire coatings. Moreover, the accuracy of the statistical analysis given in this work might be improved by increasing the number of specimens entering the experiments.

Chapter 8. Development of a Thermal Equivalent Circuit to Quantify the Effect of Thermal Paste on Heat Flow through a Permanent Magnet Alternator

8.1 Objectives

This chapter describes the thermal modelling approach of a permanent magnet alternator (PMA). The principal focus is to investigate the quantitative effect of thermal paste added into the machine end region. A thermal lumped parameter network is proposed to investigate the principal heat flow paths for the flange mounted alternator. The thermal model is implemented in Simulink, which allows many different heat paths to be easily combined. Since the addition of a thermal paste introduces new axial heat flow by conduction paths between the stator windings and frame, the developed thermal network considers the detailed heat flow paths when thermal paste is present. The thermal network is extended to the machine frame and a part of the mounting plate. It is shown that axial heat flow has been improved 5.6% for the PMA with thermal paste. This in turn reduces winding temperature around 10.5%. The model accuracy has been validated by performing FEA thermal simulations.

8.2 Introduction

With the increasing requirements for fault tolerance and high performance electric machines in aerospace, thermal analysis is important to achieve higher life expectancy. A fault tolerant 28 slot -18 pole surface mounted PM alternator which will be thoroughly investigated in terms of thermal performance is depicted in Figure 8.1.

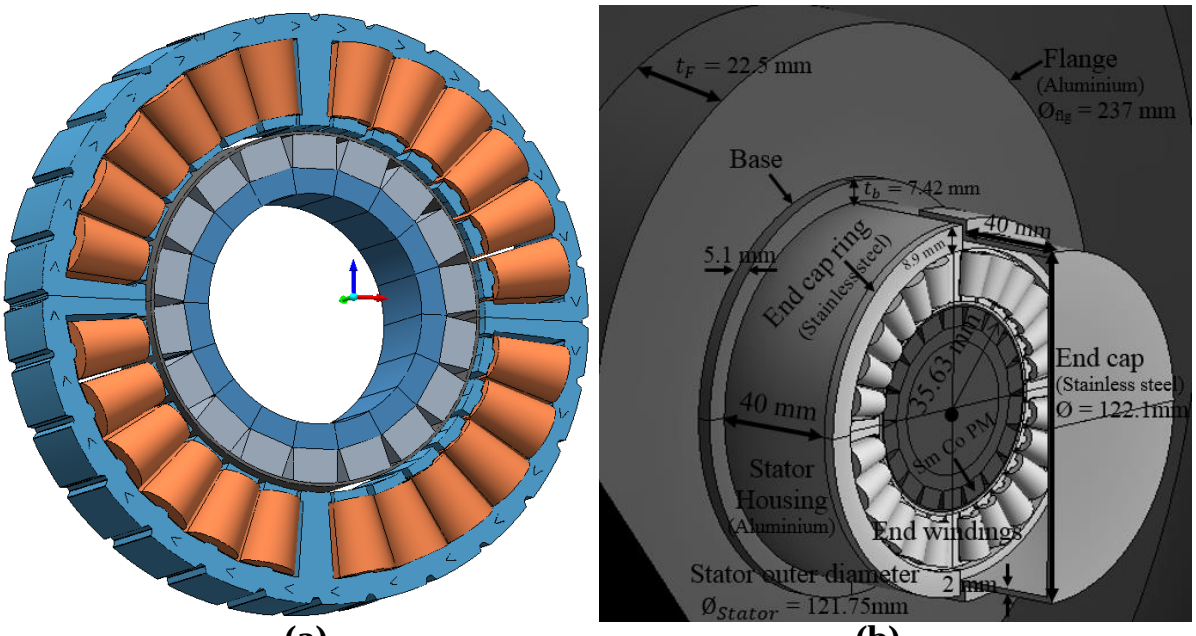

Figure 8.1 (a) Permanent magnet alternator, (b) Flange mounted PMA with the dimensions

Although numerical methods such as finite element analysis (FEA) and computational fluid dynamics (CFD) are more practical methods to analyse electric machines thermally, the analytical approach help designers calculate the temperature variation under certain boundary conditions more quickly [4]. More importantly, it would help designers understand heat transfer mechanisms and main heat flow paths. This could contribute to improvement of the machine under investigation by selecting or adding more appropriate materials to provide better thermal performance.

In the literature, majority of reported work on electric machine lumped parameter modelling has addressed traditional induction machines [37, 140]. The most important aspect of temperature distribution problem in the previous papers is to reduce the hot spot temperature in the machine with a certain distribution of losses [27, 79]. Thermal investigation would be more complicated when a test bench is present during the dynamic or static DC thermal tests as shown in Figure 8.2

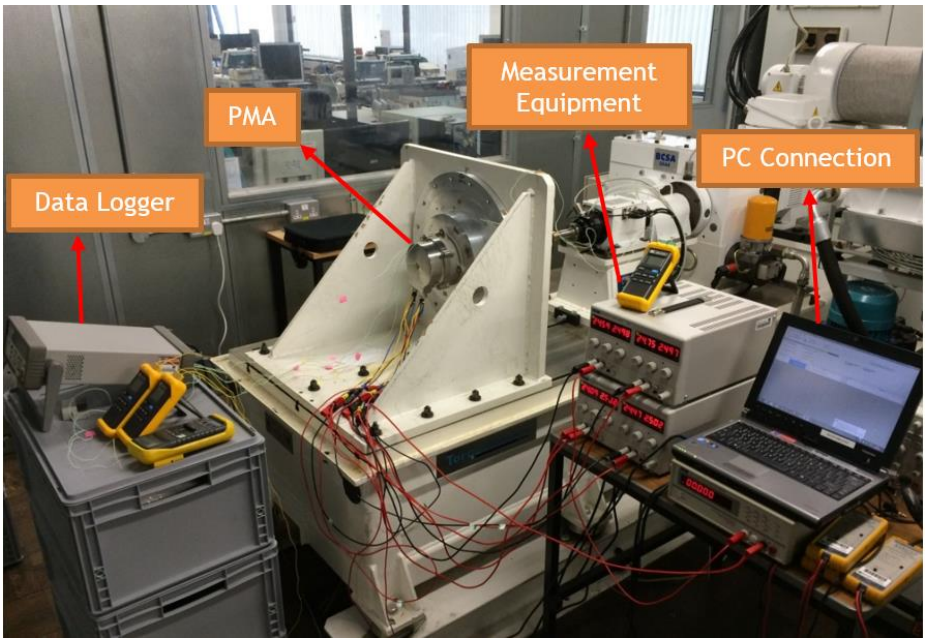

Figure 8.2 Thermal test setup with a large test bench

In [141], the presence of the test bench in the thermal model is included using a special software package enabling the user to include rectangular flange with certain dimensions to analyse the whole structure. When the size of the thermally conductive parts and convective surfaces on the test bench were considered during machine thermal testing, the total structure cannot be neglected in the thermal models. Moreover, modelling the machine using numerical methods such as transient thermal FEA method might not be achieved without modelling the whole test bench as steady state temperature cannot be reached in the absence of an active cooling system.

This chapter aims to quantify the effect of thermal paste on heat flow through the PMA, a convenient way of thermal modelling should be pursued to analytically extract principal heat flow paths. For this reason, this research addresses:

- A proper way of geometry simplification which is necessary to develop experimentally calibrated FEA steady state and transient thermal results.
- A computation of amount of heat flow through the thermal paste potted into the machine end region.
- A thermal performance comparison between PMAs with and without thermal paste when the machine is stationary and spinning with Y-connected, short circuited 3-phase lanes.

A lumped parameter (LP) thermal modelling approach including radial, axial and circumferential heat flows has been also developed to determine the important thermal parameters including equivalent slot thermal conductivity, thermal contact resistance between machine segments and some natural convection heat transfer coefficients, which are usually difficult to obtain with solely experimental methods.

8.3 Thermal Paste

High thermal conductivity materials such as epoxy resin are usually vacuum impregnated to enhance the thermal path between the winding and the casing [142]. Alternatively, average machine thermal conductivity can be improved by potting of thermal paste into the machine end region. This provides a thermal contact between the stator and machine housing – effectively opening up a new heat path in the machine.

To investigate this, two PMA machines: with and without thermal paste were considered. The machines are identical in terms of rotor, stator and housing structure. The only difference is that a thermal potting material ‘Silcotherm AS1420’ with 1.38 W/(mK) thermal conductivity was added to end region of the machine to improve the machine cooling, Figure 8.3.

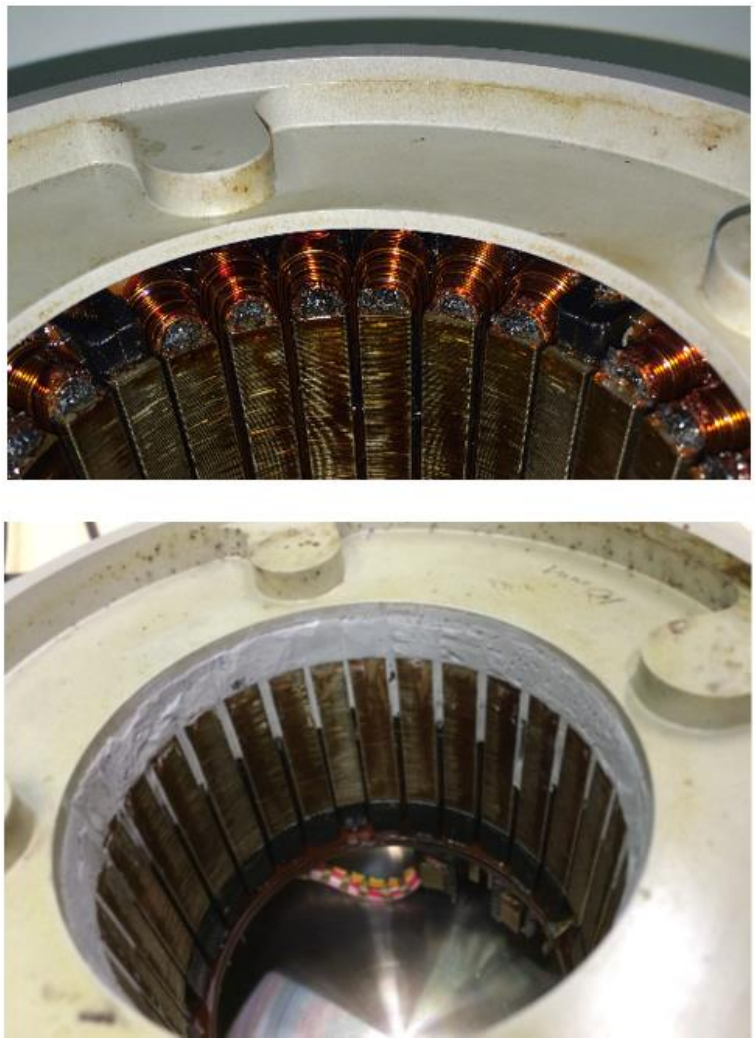

Figure 8.3 PMA with (below) and without (above) thermal paste

8.4 Steady State Thermal Tests

A steady state thermal test was performed by applying dc current to the stator windings to heat the machine without observing any air circulation effect inside the machine casing. 3.5 A dc current was injected to the Y-connected power lanes until steady state temperature distribution is obtained around the PMA casing.

The variation of electrical resistance in the windings due to temperature rise is monitored to indicate the accuracy of thermal modelling as there was no dedicated temperature sensors in the machine windings.

Voltage varies for a fixed current given by the well-known relationship between temperature increase and electrical resistance as stated in equation (6.12) [143]. This is recalled:

$$T = \left(234.5 + T_0\right)\frac{R_T}{R_0} - 234.5 \tag{8.1}$$

where T_0 and T are initial and actual temperatures respectively, R_T is actual electrical resistance and R_0 is electrical resistance at reference temperature. 234.5 (°C) is the temperature coefficient of copper.

Table 8.1 Variation of electrical resistance of the Y-connected winding lanes

Time (min)	Current (A)	Voltage (V) PMA without paste	Voltage (V) PMA with paste	Resistance (Ω) PMA without paste	Resistance (Ω) PMA with paste
0.	3.5	11.91	11.04	3.402	3.154
30.	3.5	15.15	13.51	4.328	3.86
60.	3.5	15.57	13.86	4.448	3.96
90.	3.5	15.82	14.08	4.52	4.022

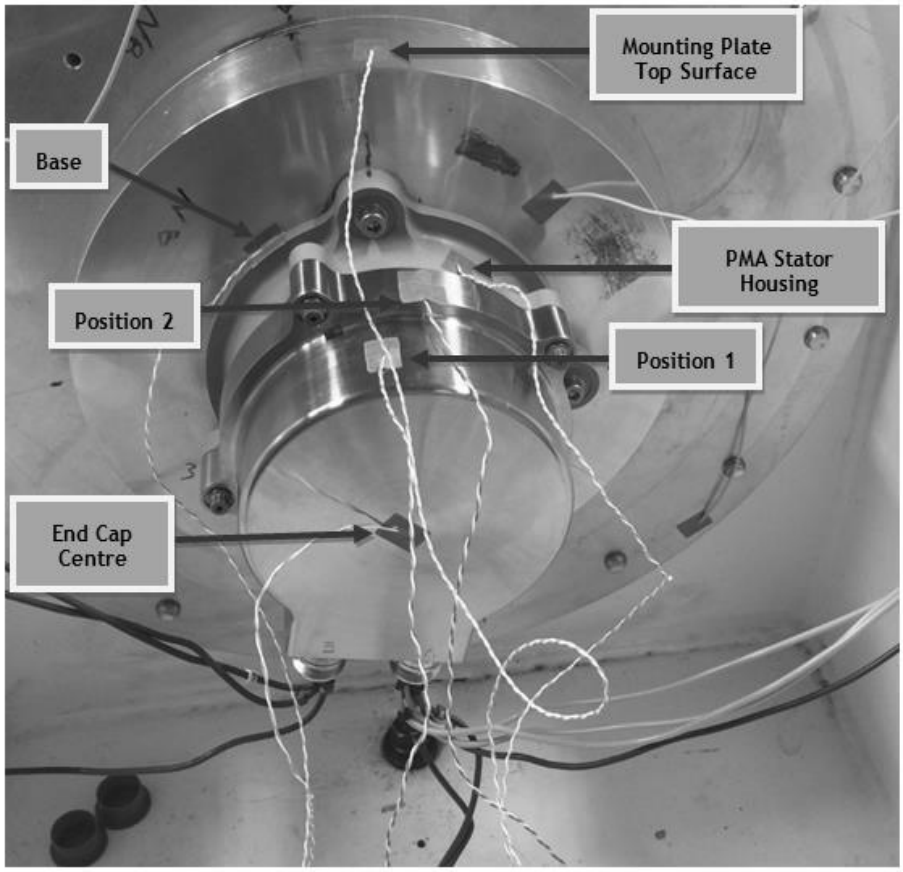

Figure 8.4 Labelled PMA external surfaces

In order to find copper losses precisely, a sufficient number of DC voltage and current data have been recorded at different time instants throughout steady state thermal tests as shown in Table 8.1.

The external surfaces of the PMA were labelled as shown in Figure 8.4. The machine was monitored by K-type thermocouples allowing to record temperature variation at every 5 seconds until reaching to the steady state. In Figure 8.5, several experimental temperature variation results are compared for the prototypes with and without thermal paste.

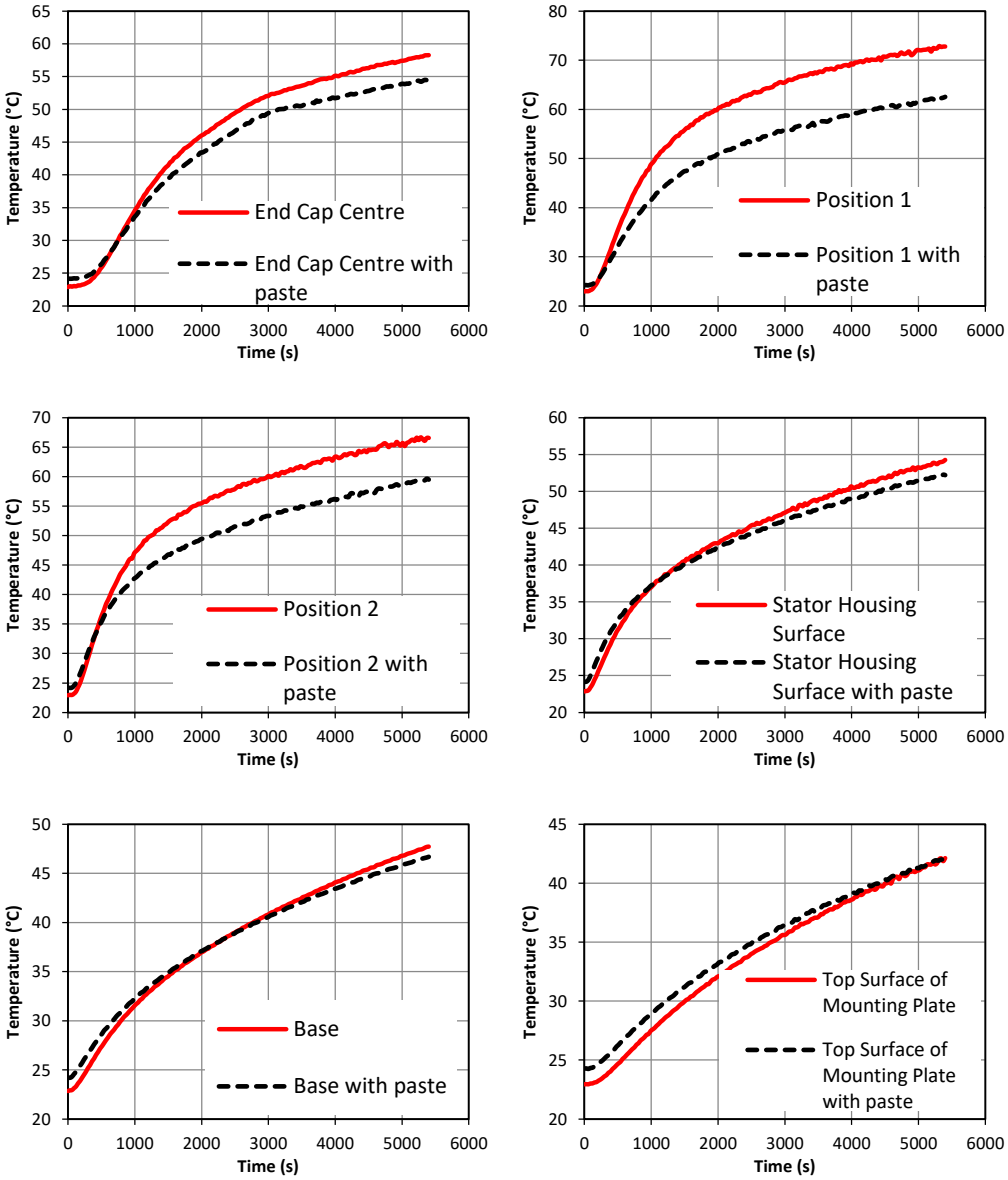

Figure 8.5 Experimental temperature rise with and without thermal paste

By comparing temperature difference (ΔT) in Table 8.2, the more explicit results are obtained as initial temperature values are not the same for the conducted static thermal tests of the PMA prototypes.

Table 8.2 Temperature difference (ΔT) comparison between the PMAs with and without thermal paste

Position	Initial Temperature (°C)	Final Temperature (°C)	ΔT	Cooler PMA
End cap centre – thermal paste	24.152	54.52	30.36	✓
End cap centre – without thermal paste	23.005	58.255	35.25	
Position 1- thermal paste	24.22	62.538	38.31	✓
Position 1 –without thermal paste	22.938	72.784	49.84	
Position 2 – thermal paste	24.192	59.654	35.46	✓
Position 2 –without thermal paste	22.908	66.553	43.64	
Stator housing – thermal paste	24.166	52.263	28.097	✓
Stator housing - without thermal paste	22.856	54.261	31.405	
Base –thermal paste	24.196	46.681	22.48	✓
Base - without thermal paste	22.915	47.718	24.80	
Top surface of the mounting plate – thermal paste	24.279	42.134	17.85	✓

Top surface of the mounting plate -without thermal paste	22.946	42.124	19.18	
Front face of the mounting plate- thermal paste	24.25	39.703	15.45	✓
Front face of the mounting plate- without thermal paste	22.885	39.696	16.81	
Horizontal face of the mounting plate – thermal paste	24.249	28.472	4.22	✓
Horizontal face of the mounting plate- without thermal paste	22.895	27.76	4.86	

The steady state tests clearly demonstrate that temperature rise for the PMA with thermal paste is lower than that for the PMA without thermal paste. Pure experimental results cannot be used to adequately compute the amount of heat flow through thermal potting material in the machine end region and quantify the paste's advantages. Therefore, an analytical lumped parameter modelling is developed to extract heat flow data in the machine components in the presence of thermally conductive paste.

8.5 FEA Modelling

8.5.1 Identification of Heat Transfer Coefficients (HTCs)

There are three types of external surface in the PMA: vertical plane, horizontal plane and horizontal cylinder for natural convection between the ambient surroundings and the PMA. Since there are no external instruments to cool the machine, only heat transfer by natural convection was considered for the PMA. Temperature dependent heat transfer coefficients are used for the external horizontal and cylindrical surfaces as plotted in Figure B.3 – Appendix-B.

Empirical formulations which have been detailed in Appendix – B are used to estimate heat transfer coefficients in end windings, rotor surface, and mounting plate when the machine is spinning at rated speed (14820 rpm) and is stationary. It should be noted that speed dependent heat transfer coefficients such as air gap HTC, rotor surface HTC and end windings HTC will

not be significant when machine is stationary in dc static thermal tests. The estimated HTCs are tabulated in Table 8.3.

Table 8.3 Heat transfer coefficients of the PMA internal and external surfaces

Region	***HTCs when the PMA is spinning at 14820 rev/min***	***HTCs when the PMA is stationary***
PMA casing external surfaces- horizontal cylinder	Film temperature dependent as plotted in Figure B.3[9]	Film temperature dependent as plotted in Figure B.3
End windings:	36.543 $W/m^2.°C$	6.5 $W/m^2.°C$
Rotor surface – horizontal cylinder	83.977 $W/m^2.°C$	Film temperature dependent as plotted in Figure B.3
Air gap	119.13 W/m^2°C	Heat transfer by conduction is considered through air
Horizontal plate upper surface:	6.96 $W/m^2.°C$	6.96 $W/m^2.°C$
Horizontal plate lower surface:	1.76 $W/m^2.°C$	1.76 $W/m^2.°C$
Flange external surface – vertical plate	Film temperature dependent as plotted in Figure B.3	Film temperature dependent as plotted in Figure B.3

8.5.2 Simplification of Thermal Model for FEA

The presence of relatively large test bench as shown in Figure 8.6 would cause significant finite element analysis (FEA) modelling problems since the geometry is too complex due to uncertainty of thermal parameters such as convection heat transfer coefficients of external surfaces and thermal contact conductance between test rig parts. Furthermore, thermal properties of the materials forming the whole test bench with rough dimensions of 3.15m × 0.795m × 0.712m might not be precisely known. Therefore, thermal investigation of the PMA requires further geometry simplification.

[9] Figure B.3 that gives film temperature dependent heat transfer coefficients, is shown in Appendix – B.

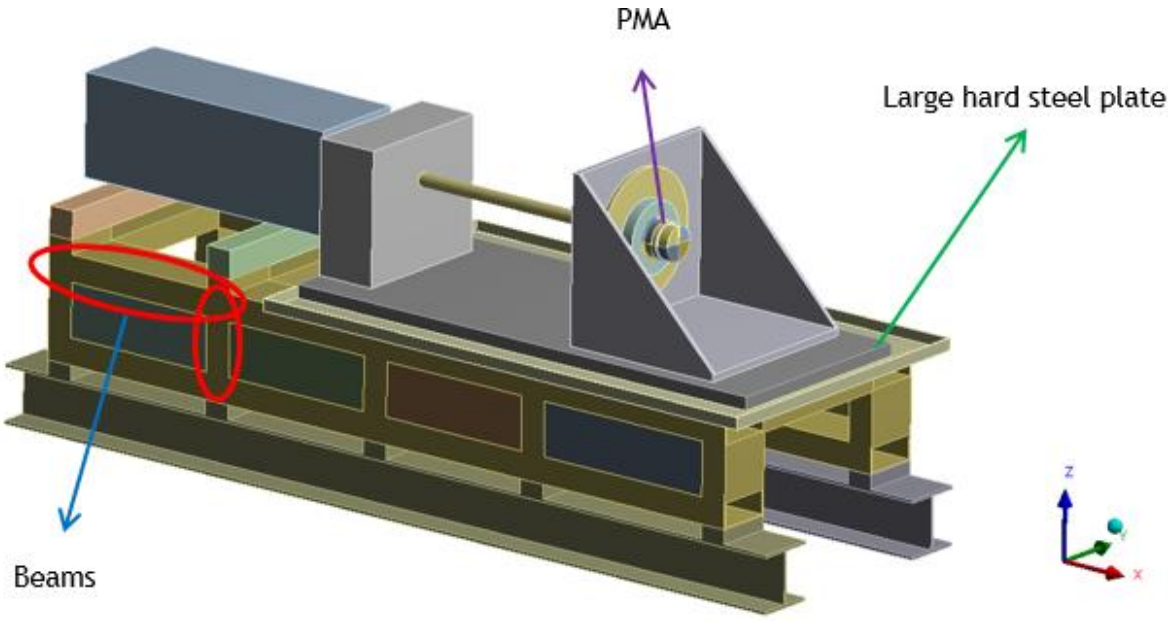

Figure 8.6 CAD model of the test bench

Challenges and model features:

- 128 solid parts in the whole test rig
- 892 thermal contact faces between the solid bodies
- 24 heat generation coils
- 321 heat transfer by convection surfaces
- Perfect insulation between ground and test rig as ground is a sort of wood with very low thermal conductivity compared to steel parts.

As presented above, FEA modelling of the PMA will not be very precise when the whole test rig is considered in a thermal model. Furthermore, transient thermal simulations will be very costly in terms of CPU time if whole test rig is considered.

If all these challenges are considered for the modelling of the PMA, it can be noted that precision of the temperature variation will be affected from too many thermal contact faces and estimation of heat transfer coefficients for the external surfaces of the test rig. For this reason, a model simplification for thermal simulations is necessary.

In order to reduce thermal complexity of the test rig consisting of too many solid parts, mounting plate of the test rig was isolated from the whole test rig as shown in Figure 8.7. Wood pieces in 60 mm height were utilised to isolate the mounting plate from the test rig. Thermal conductivity of wood is 0.17 $W/(mK)$ which is low enough to prevent thermal contact between the mounting plate and test rig. Thermal FEA modelling of the PMA has been investigated only for the machine and the mounting plate as this will reduce the physical and thermal

complexity dramatically. Figure 8.8 shows the isolated part of the test rig with PMA assembled onto an aluminium flange.

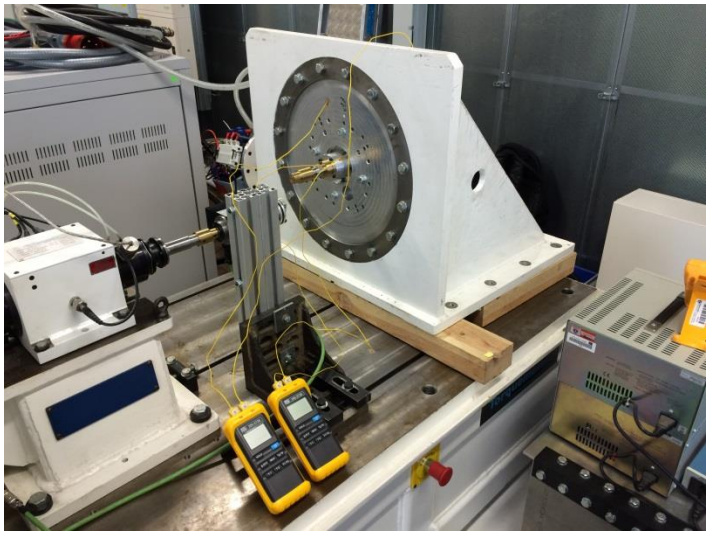

Figure 8.7 Mounting plate isolated from the test rig using wood pieces

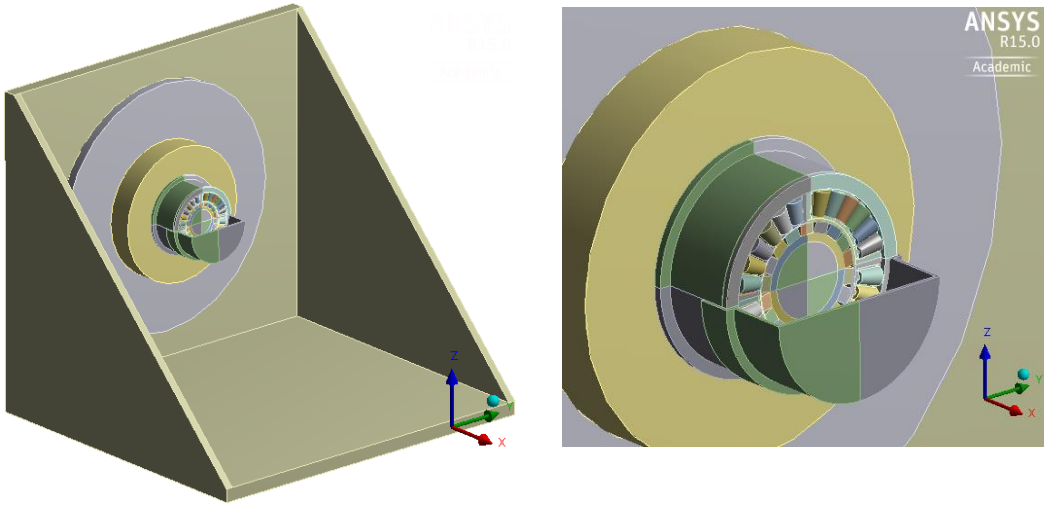

Figure 8.8 Simplified FEA geometry of the PMA

The machine can be further simplified by taking the symmetry into account. Therefore, a quarter of the PMA was used to investigate the machine thermal behaviour. The simplification procedure is described in Figure 8.9.

A time dependent temperature boundary condition was inserted to the top surface of the mounting plate that mimics the thermal behaviour of the isolated test rig without distorting the temperature distribution on the proposed FEA model as shown in Figure 8.9.

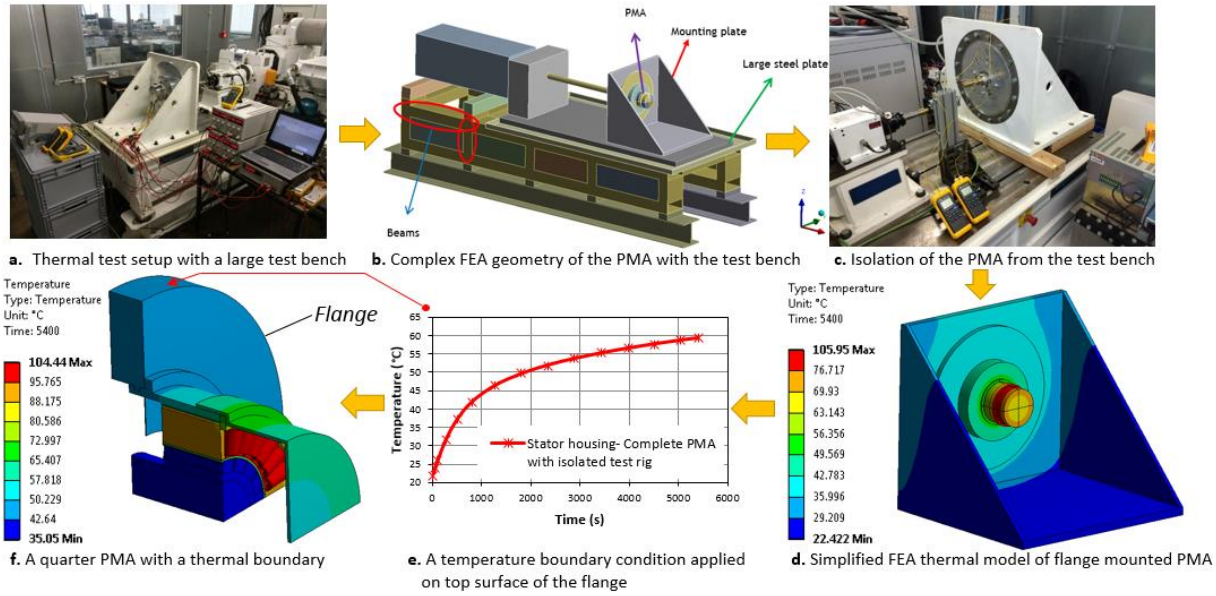

Figure 8.9 A modelling approach developed to simplify the thermal model of the PMA

The accuracy of the proposed geometry simplification is investigated by performing transient thermal FEA simulations. In Figure 8.10, temperature variations around the machine casing and stator for the full and one quarter models are very close, with less than 5% temperature error. This states that PMA can be simplified with proper boundary conditions, which will enable the designer to calculate amount of heat flow through the paste.

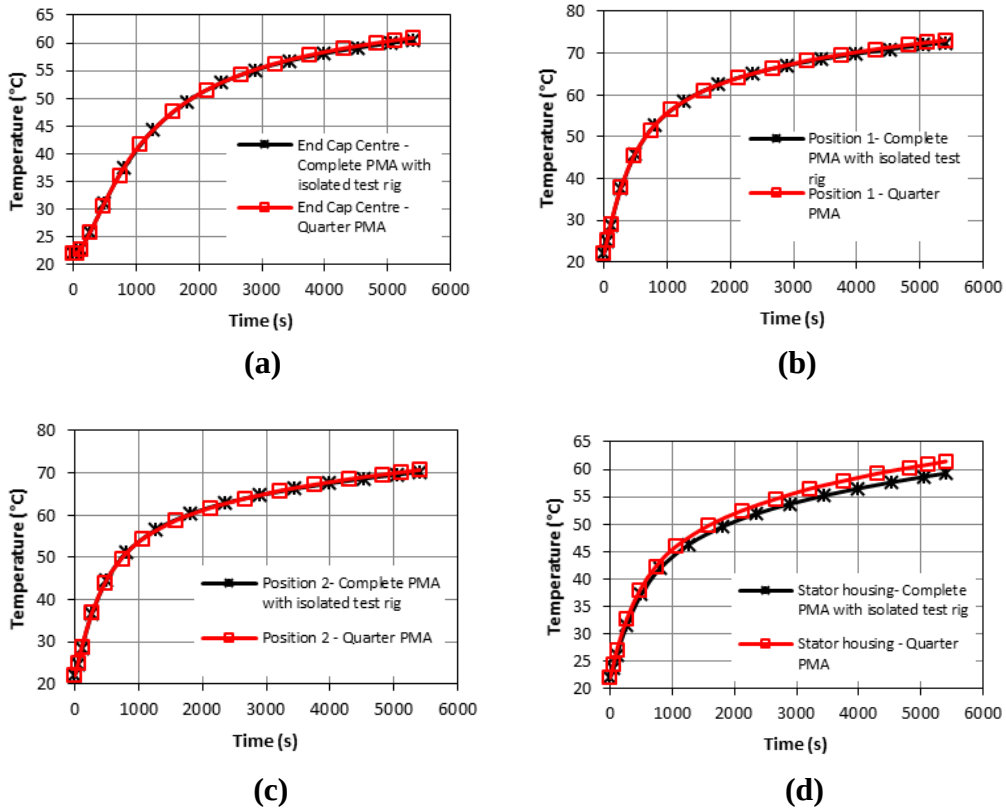

Figure 8.10 Comparison of temperature variations for the PMA external surfaces

This is demonstrated on transient temperature variation on the selected external surfaces of the PMA in Figure 8.10.

8.5.3 Thermal Parameters Determination

The thermal model was first calibrated to determine parameters such as thermal conductivity of the winding, frame to stator lamination contact resistance, thermal contact conductance between aluminium stator housing and stainless steel end cap. The calibration is performed by modifying the values within reasonable range until responses of transient thermal FEA results, thermal lumped parameter model and steady state DC thermal tests match. It is widely accepted that steady state thermal test is mandatory for the determination of the critical thermal parameters [144].

Some assumptions have been made for thermal modelling of the PMA as follows:

- Heat transfer by radiation was excluded.
- Stator windings were considered to be bulk copper with insulation around and effective thermal conductivity of the slot was predicted by FEA calibration to be $0.15\ W/(mK)$.
- Contact pressure which increases thermal contact conductance [43] between the solid bodies was not investigated.
- Since only steady state DC tests were referenced to predict the thermal performance improvement of the PMA with thermal paste, air flow inside the PMA casing and machine airgap was omitted.

Thermal properties of the materials are given in Table 8.4.

Table 8.4 Thermal Properties of the Materials

Material	**Thermal Conductivity (W/m.K)**	**Heat Capacity (kJ kg^{-1} K^{-1})**	**Density (kg/m^3)**	**Resistivity (Ω m.10^{-8})**
Air, stagnant	0.026	1	-	2.7
Aluminium	231	0.899	2700	2.8
Copper	400	0.385	8960	1.75
Magnifier 50 Lamination	13	0.48	8055	-
Stainless Steel	13.8	-	7900	-

Teflon	0.25	1.4	2250	-
Inconel Sleeve	230	0.435	8190	-
Sm Co (PM)	10	0.35	8300	-

In [145], interfacial conductance and interface gap of the metals were tabulated. Thermal contact conductance between stainless steel and aluminium varies between 3000 – 4500 $W/m^2.°C$. This is the case when effective gap is in the range 0.0058 – 0.0087 mm. During the thermal calibration process, it is noted that thermal contact conductance between stainless steel end casing and aluminium housing is around 1500 $W/m^2.°C$. This implies that there is not a perfect thermal contact between the machine housing parts. However, varying the thermal contact conductance between the stator housing and end casing in the range: 1000 $W/m^2.°C$ - 3000 $W/m^2.°C$ changes the temperature variation on the machine casing in the range 1°C - 3°C as this is not significant temperature difference to cause a substantial temperature distribution error.

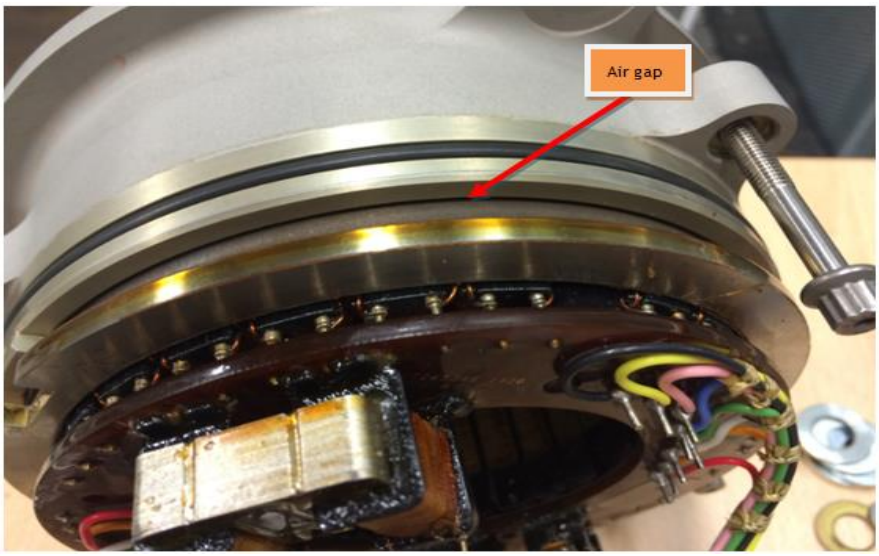

Figure 8.11 The interface gap between the stator and the stator housing

Another important thermal parameter is interface gap between the laminations and the external frame due to imperfections in the touching surfaces and it could be a function of material hardness, roughness and interface pressure [4]. Sensitivity analysis has been conducted and in Figure 8.11, it is shown that interface gap for the PMA is relatively large compared to values given in the literature [4, 146]. Typically, it varies around 0.01 – 0.08 mm whereas as in this machine, it is around 0.07- 0.09 mm which provides poor thermal contact between the stator and machine frame.

8.5.3.1 Experimental validation of poor thermal contact between the stator and stator housing

The effect of air gap between the stator and its housing can be also verified in static thermal tests. For this reason, the stator of the machine has been tested without its housing. Several thermocouples are positioned around the machine to see the temperature variation around the stator as shown in Figure 8.12.

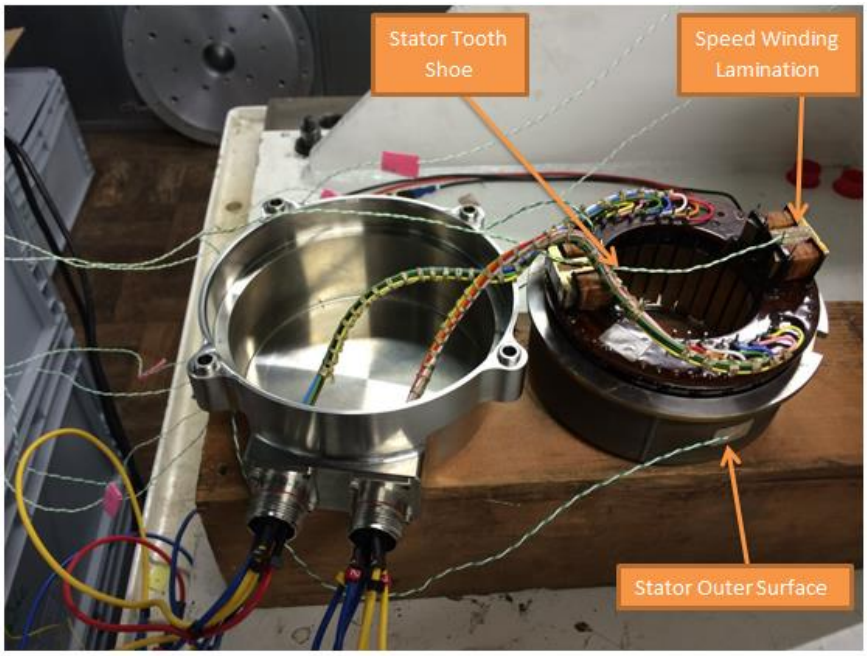

Figure 8.12 Bare stator thermal test setup

During the test, all power lanes were supplied with 2.5 A dc current. Temperature on the stator inner surface, outer surface and speed winding laminations were recorded for 45 minutes. The machine was tested for a short duration to prevent excessive heating in the windings.

In order to understand the effect of air gap between the stator and aluminium stator housing, the test has been repeated as depicted in Figure 8.13, after the stator was inserted into the aluminium stator housing.

It is hard to make a formal comparison between these two cases. However, the effect of air gap between the stator lamination and housing can be deduced from the temperature differences between the experiments. This is investigated in Table 8.5.

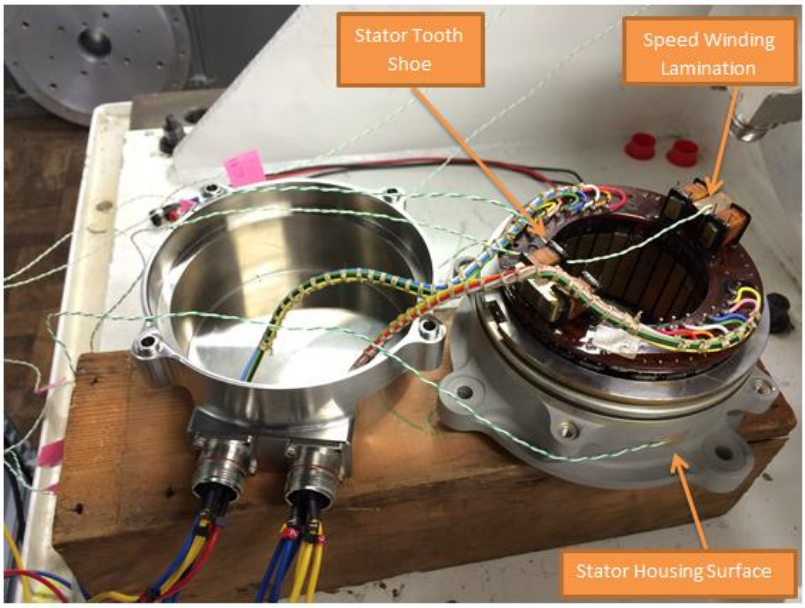

Figure 8.13 Stator thermal test with the stator housing

Table 8.5 The effect poor thermal contact between the stator and stator housing

Temperature Difference Investigation for 45 min DC Test at 2.5 A		
Part:	**Final Temperature (°C)**	**Temperature Difference (°C)**
Stator Surface	149.662	**49.319**
Stator Housing Surface	100.343	
Stator Tooth Shoe without housing	159.131	18.18
Stator Tooth Shoe with housing	140.951	
Speed Winding without housing	70.842	12.631
Speed Winding with housing	58.211	

In Table 8.5, the temperature difference between the stator surface and stator housing surface seems higher than expected when other temperature difference values for stator tooth and speed winding are considered. This demonstrates that heat flow by conduction is not perfect between the bodies: stator and stator housing. This leads to accumulation of the heat inside the machine due to lack of heat flow between the stator and its housing. In order to keep the machine cooler, perfect assembling for the stator and its housing is required with negligible air gap between the stator and stator housing.

By conducting several thermal FEA simulations, estimated thermal contact conductance is found to be 300 $W/m^2.°C$. The negative effect of the lower thermal contact conductance is that heat flow between the stator and machine frame is not perfect. The obtained thermal contact conductance values are also used for the determination of thermal resistances between the contact regions in lumped parameter model.

8.5.4 Thermal FEA Simulation Results

The calibrated thermal FEA results at steady state when only copper losses are injected, are given in Figure 8.14[10]. It can be noted that the prototype machine with thermal paste remains cooler. Thermal FEA simulation results show that winding hottest spot temperature is reduced by 10.59%. Samarium cobalt (SmCo) permanent magnet temperature is reduced around 2°C at standstill.

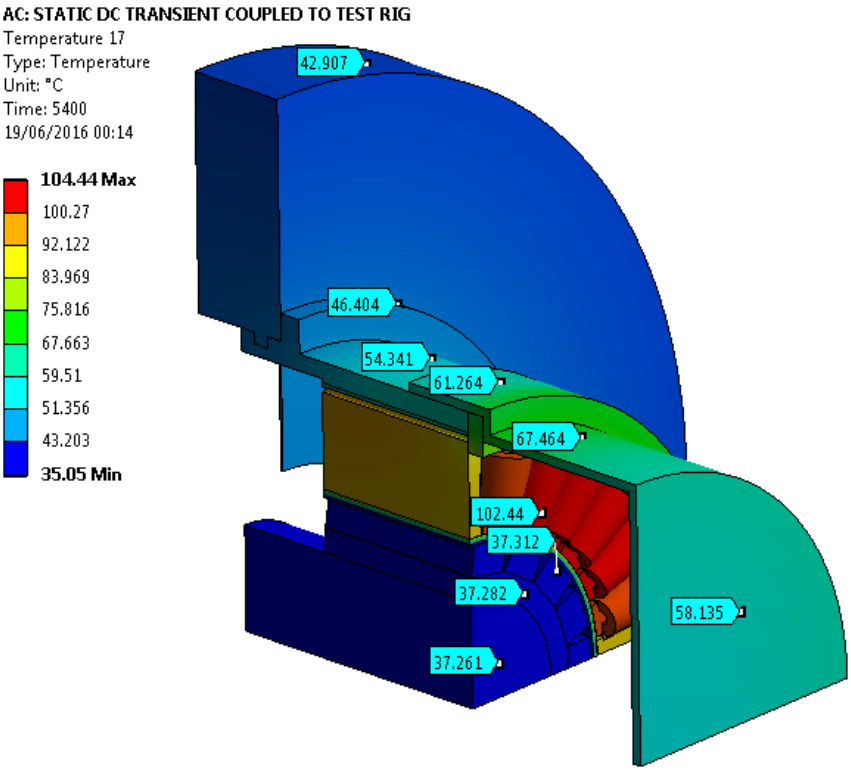

(a)

[10] Transient temperature variations for the PMAs with and without thermal paste as given in Figure 8.14 are plotted in Appendix – D.

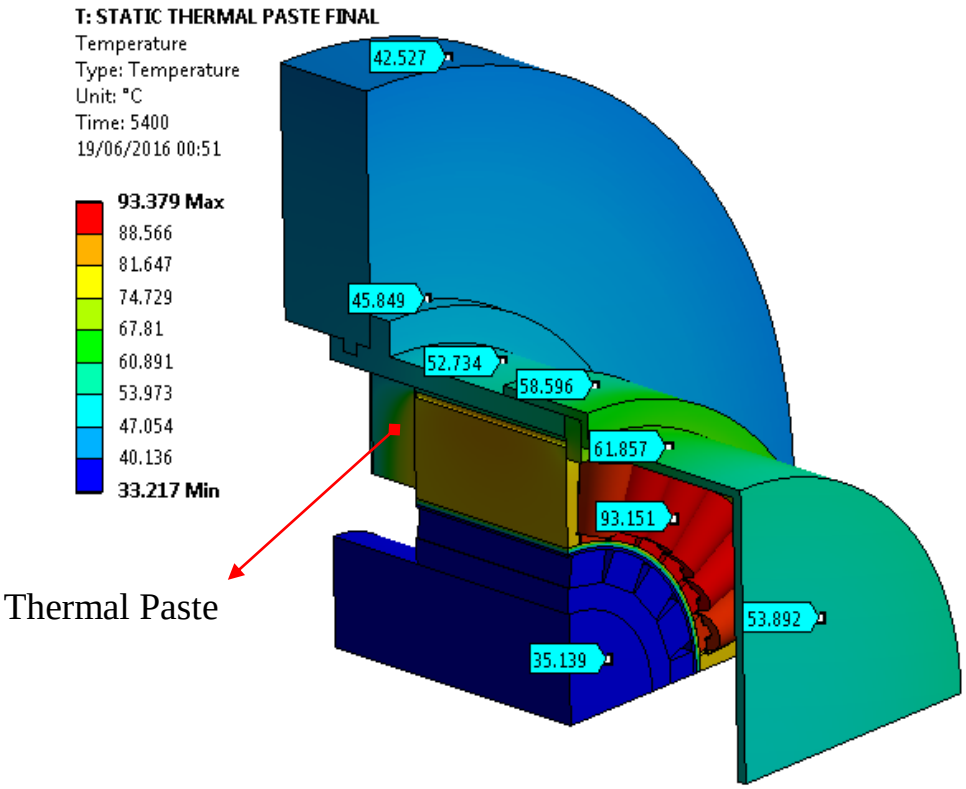

(b)

Figure 8.14 FEA results at steady state for the prototypes: PMA (a) without thermal paste; (b) with thermal paste

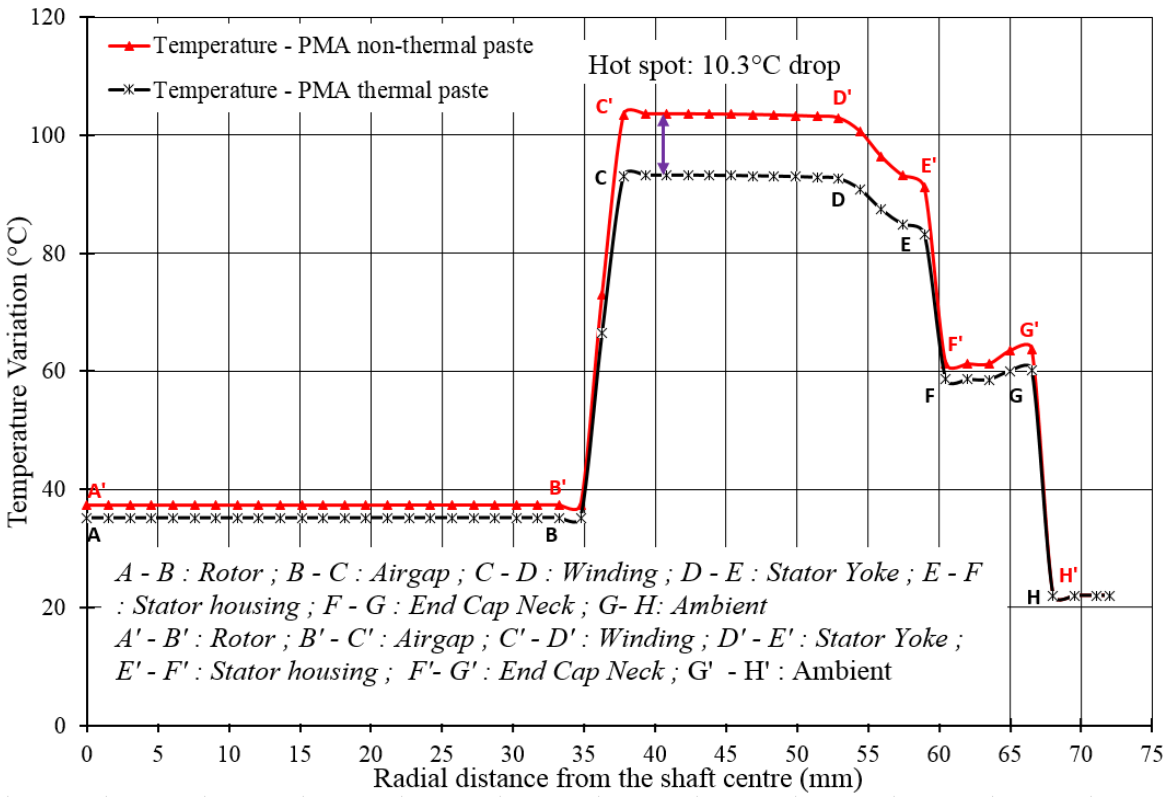

Figure 8.15 Radial temperature variation around the PMAs

Radial temperature variation starting from the shaft centre to ambient is plotted in Figure 8.15 using FEA results showing that temperature rise in the machine windings is significantly affected from the conductive thermal paste. Figure 8.16 compares transient thermal FEA results with steady state dc thermal tests when only copper losses are active in the machines.

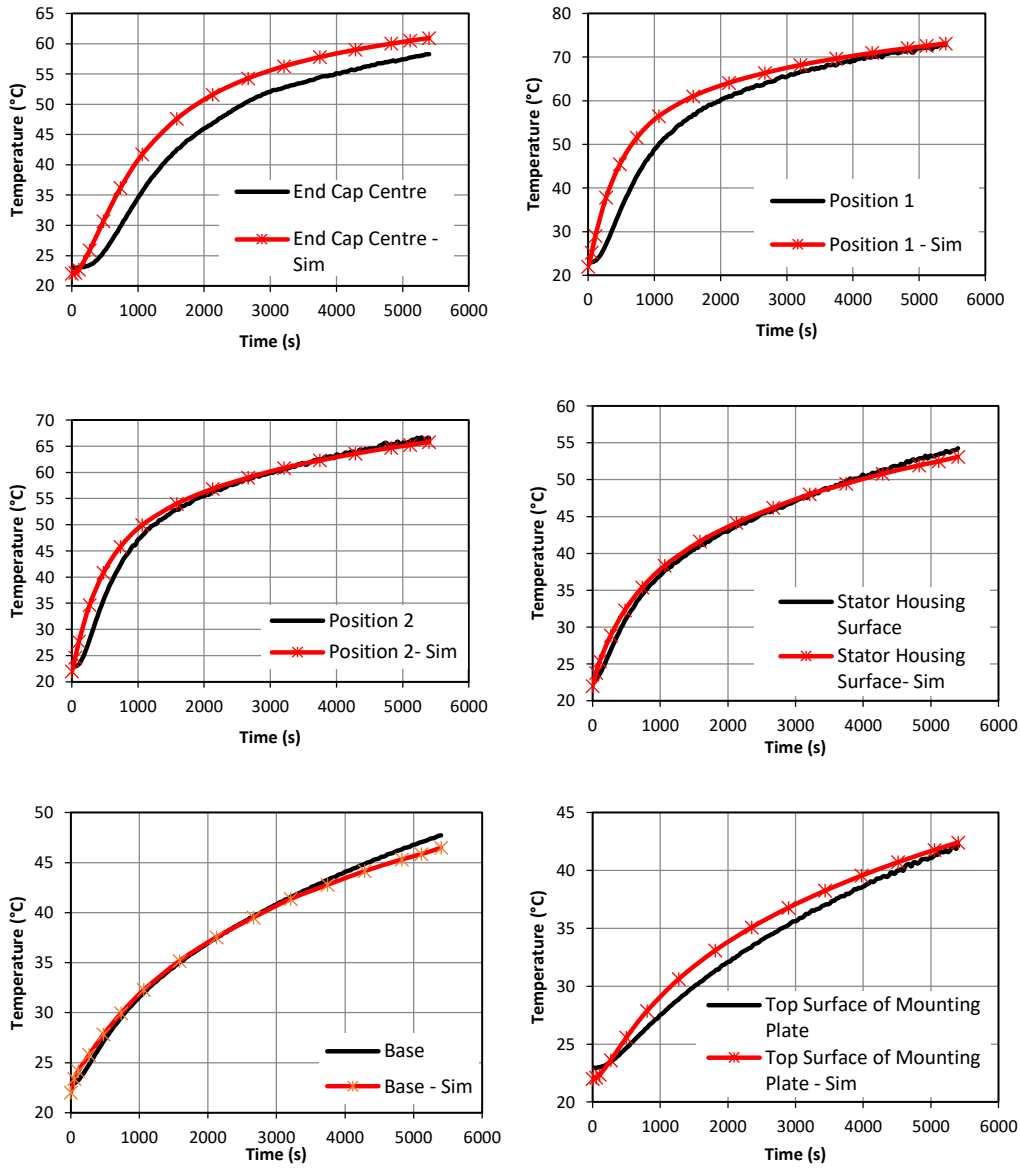

Figure 8.16 FEA vs experimental results comparison at selected external surfaces for the PMA without thermal paste

Similarly, thermal test results when thermal paste is present in the PMA have been compared to the FEA model of the PMA with thermal paste as demonstrated in Figure 8.17. Both FEA simulations and dc steady state thermal tests validates that the machine with conductive thermal paste gives less temperature rise and stays cooler.

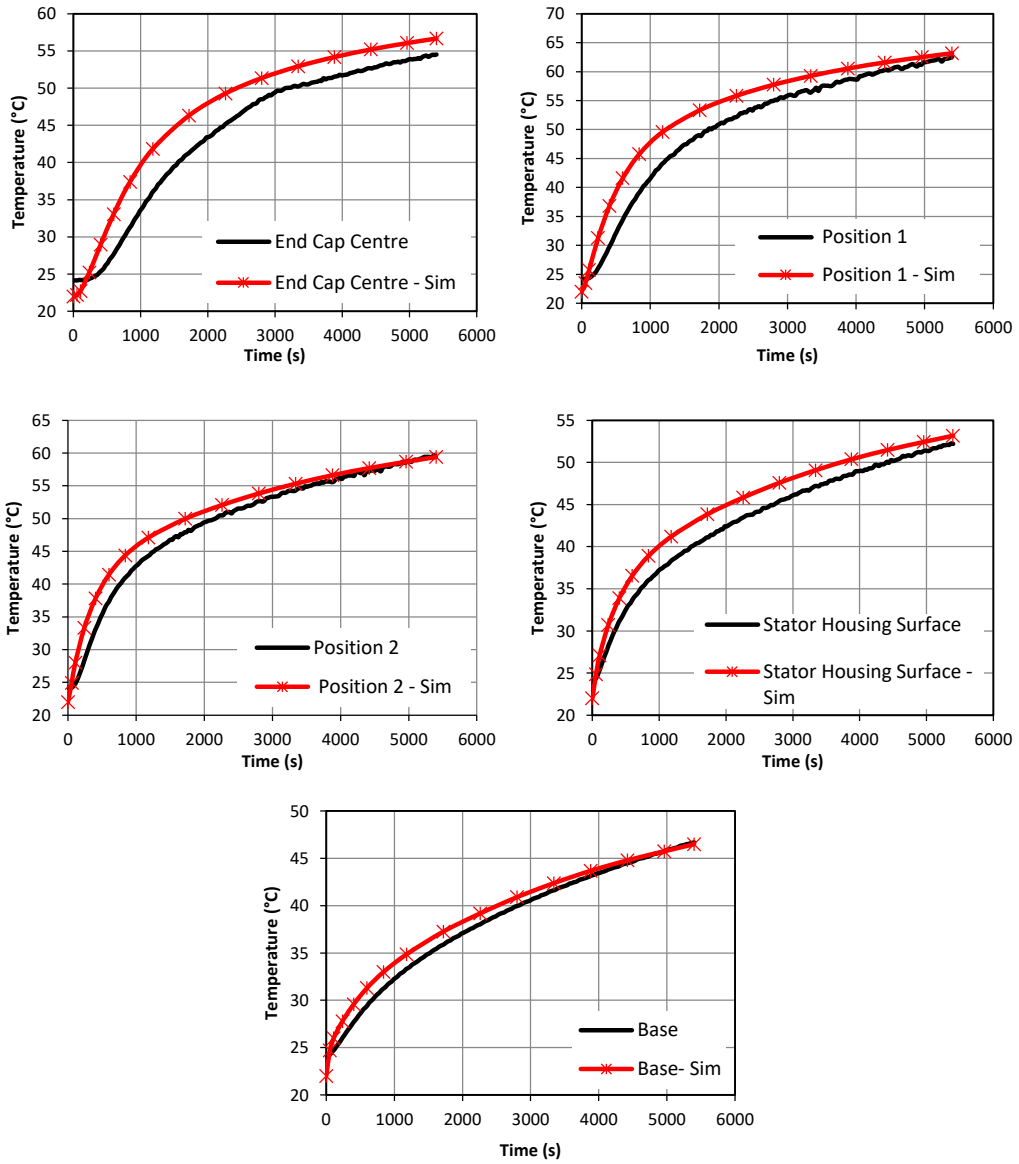

Figure 8.17 FEA vs experimental results comparison at selected external surfaces for the PMA with thermal paste

8.6 Thermal Lumped Parameter Modelling

The objective of the thermal network model is to divide the parts into basic thermal elements which are represented by a special node configuration. The thermal elements are linked together to form a network of a thermal elements. The heat flow is analogous to electric current flow. Resistive losses, iron losses, windage and friction losses are represented by individual heat flow sources. In Table 8.6, analogous between thermal and electrical quantities are shown.

Table 8.6 Analogy between thermal and electrical quantities

Thermal Flow	Symbol	Unit	Electric Flow	Symbol	Unit
Quantity of heat	Q'_{th}	J	Electric charge	Q	C
Heat flow rate	q_{th}	W	Electric current	I	A
Heat flow density	Q_{th}	W/m^2	Current density	J	A/m^2
Temperature	T	$°C$	Electric potential	V	V
Temperature rise	θ	$°C$	Voltage	U	V
Thermal conductivity	k	W/mK	Electric conductivity	σ	S/m
Thermal resistance	R_{th}	$°C/W$	Electric resistance	R	Ω
Thermal conductance	G_{th}	$W/°C$	Electric conductance	G	S
Heat capacity	C_{th}	J/K	Capacitance	C	F

Assume that there are n nodes; each of them is being linked to the others through thermal resistances $R_{i,j}$ where i and j are the indices for the linked nodes. Let $R_{i,i}$ be the thermal resistance between node i and the ambient. Then, steady state nodal temperature rise is in the form:

$$P_i = \frac{\theta_i}{R_{i,i}} + \sum_{j=1}^{n} \frac{\theta_i - \theta_j}{R_{i,j}} \qquad i = 1, 2, 3, \dots\dots, n \tag{8.2}$$

where θ_1 to θ_n are the temperature rises of each node and P_1 to P_n are the losses of each node. A conductance matrix is usually defined in a resistive electric circuit as:

$$G = \begin{bmatrix} \sum_{i=1}^{n} \frac{1}{R_{1,i}} & \frac{-1}{R_{1,2}} & \frac{-1}{R_{1,3}} & \cdots & \frac{-1}{R_{1,n}} \\ \frac{-1}{R_{2,1}} & \sum_{i=1}^{n} \frac{1}{R_{2,i}} & \frac{-1}{R_{2,3}} & \cdots & \frac{-1}{R_{2,n}} \\ \frac{-1}{R_{3,1}} & \frac{-1}{R_{3,2}} & \sum_{i=1}^{n} \frac{1}{R_{3,i}} & \cdots & \frac{-1}{R_{3,n}} \\ \vdots & \vdots & \vdots & \ddots & \vdots \\ \frac{-1}{R_{n,1}} & \frac{-1}{R_{n,2}} & \frac{-1}{R_{n,3}} & \cdots & \sum_{i=1}^{n} \frac{1}{R_{n,i}} \end{bmatrix} \tag{8.3}$$

The column vectors P and Θ are defined in the form:

$$P = \begin{bmatrix} P_1 \\ P_2 \\ P_3 \\ \vdots \\ P_n \end{bmatrix}, \quad \Theta = \begin{bmatrix} \theta_1 \\ \theta_2 \\ \theta_3 \\ \vdots \\ \theta_n \end{bmatrix} \qquad (8.4) – (8.5)$$

With the definition of conductance matrix and column vectors as given in equations (8.4) - (8.5), equation (8.2) can be generalised:

$$P = G\,\Theta \;\rightarrow\; \boldsymbol{\Theta = G^{-1}P} \qquad (8.6)$$

The steady state solution for a thermal problem is obtained directly from equation (8.6). Nonetheless, some parameters in P and G could be temperature dependent. If this is the case, iterative process should be pursued to update the value of parameter until error becomes sufficiently small.

8.6.1 Thermal Network Node Configurations

The machine is split into a series of heat paths, and each one is identified based on an annular ring. Since heat flow occurs in radial and axial directions, modelling of a thermal network includes radial and thermal heat flow networks, which should be considered separately. Two dimensional heat flows for an annular ring is shown in Figure 8.18 [43].

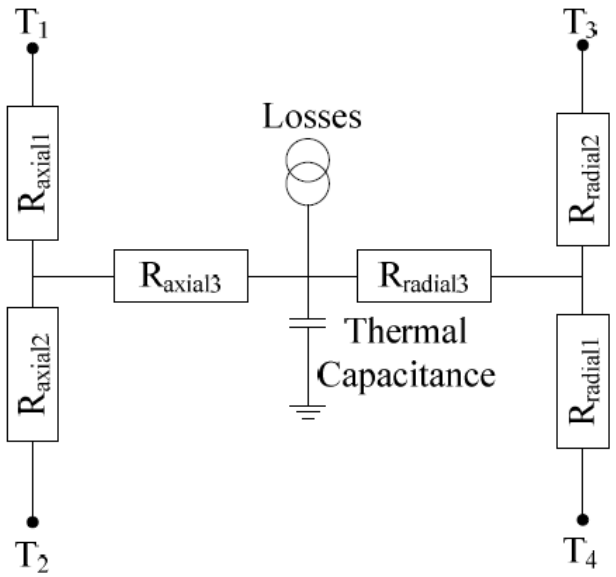

Figure 8.18 Two dimensional thermal network for an annular ring [43]

As shown in Figure 8.18, thermal circuit of an annular ring is represented by three radial and axial thermal resistors. Thermal joule losses such as copper loss or iron loss are injected in the node. The thermal conduction resistors are derived from heat transfer equations for a hollow cylinder.

Heat storage for an annulus is expressed as:

$$H_s = \rho\, V\, c_p T_{avg} \tag{8.7}$$

where

ρ = material density, kg/m^3

V = Total volume of the annulus, m^3

c_p = Specific heat capacity at constant pressure, J/kg K

T_{avg} = Average temperature of the annulus, K

The generic form of the annulus is given in Figure 8.19 [43]. The volume for the hollow cylinder is written:

$$V = \pi\,(r_2{}^2 - r_1{}^2).L \tag{8.8}$$

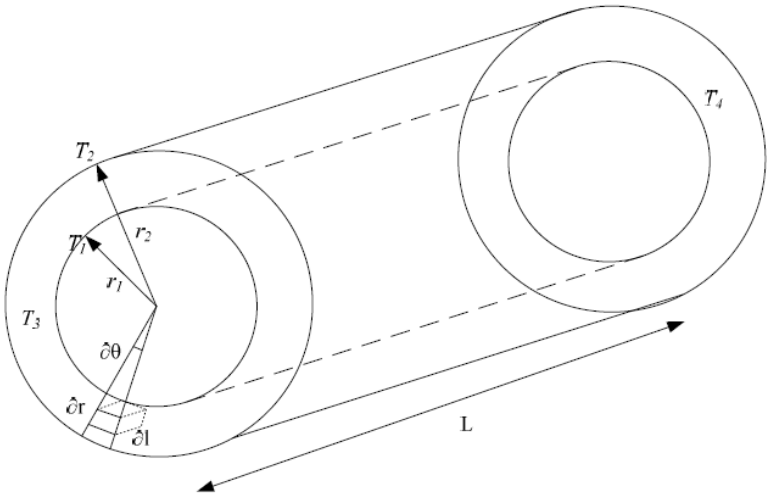

Figure 8.19 Annulus element for thermal resistor calculations [43]

The heat storage equation can be re-written as:

$$H_s = \rho.\pi.(r_2{}^2 - r_1{}^2).L.c_p.T_{avg} \tag{8.9}$$

For infinitesimal piece with the volume of v_e, elemental heat storage (H_{se}) is expressed as:

$$\begin{aligned} v_e &= r\, d\theta\, dr\, dl \\ H_{se} &= \rho\, c_p\, T\, r\, d\theta\, dr\, dl \end{aligned} \tag{8.10}$$

The volume integral for the hollow cylinder is in the form:

$$\rho.\pi.({r_2}^2 - {r_1}^2).L.c_p.T_{avg} = \int_0^r \int_0^l \int_0^{2\pi} \rho\, c_p\, T\, r\, d\theta\, dl\, dr \tag{8.11}$$

Then radial average temperature inside the annulus is written

$$T_{avg} = \frac{2}{({r_2}^2 - {r_1}^2)} \int_{r1}^{r2} T_r\ rdr \tag{8.12}$$

where, T_r is radial temperature profile. Similarly, axial temperature profile is expressed as:

$$T_{avg} = \frac{1}{L} \int_{l1}^{l2} T_l\ dl \tag{8.13}$$

The general form of one dimensional Fourier's law of heat in differential form is written

$$\frac{d^2T}{dr^2} + \frac{1}{r}\frac{dT}{dr} + \frac{g}{k_r} = 0 \tag{8.14}$$

where, g = Heat generated per unit volume (W/m^3)

k_r = Thermal conductivity in radial direction (W/mK)

The general solution for the second order differential equation given in equation (8.14) is in the form:

$$T_r = a \ln r + \frac{g\, r^2}{4k} + b \tag{8.15}$$

with constants a and b. By substituting boundary conditions into the solution, the constant a is evaluated to be:

$$a = \frac{1}{\ln\left(\frac{r_2}{r_1}\right)} \left[T_2 - T_1 + \frac{g\,({r_2}^2 - {r_1}^2)}{4k_r} \right]$$

Substituting equation 8.15 into equation 8.12 will result in:

$$\begin{aligned} T_{avg} = T_2 \left[\frac{{r_2}^2}{{r_2}^2 - {r_1}^2} - \frac{1}{2\ln\left(\frac{r_2}{r_1}\right)} \right] + T_1 \left[\frac{1}{2\ln\left(\frac{r_2}{r_1}\right)} - \frac{{r_1}^2}{{r_2}^2 - {r_1}^2} \right] \\ + \frac{g\,({r_1}^2 + {r_2}^2)}{8k_r} - \frac{g\,({r_2}^2 - {r_1}^2)}{8k_r \ln\left(\frac{r_2}{r_1}\right)} \end{aligned} \tag{8.16}$$

Assuming that internal heat generation g is zero and then the two resistor circuit has been obtained with an average temperature T_{avg}. Considering temperature to be voltage in an electrical circuit, node equations for two resistors circuit can be written in the form as follows:

$$T_{avg} = T_1 \frac{R_{radial2}}{R_{radial1} + R_{radial2}} + T_2 \frac{R_{radial1}}{R_{radial1} + R_{radial2}} \quad (8.17)$$

If the equations given in (8.16) and (8.17) are matched to find radial resistance values when internal heat generation is zero, then the thermal resistors in the radial direction will be in the form:

$$R_{radial1} = \frac{1}{4\pi k_r L}\left[\frac{2{r_2}^2 \ln\left(\frac{r_2}{r_1}\right)}{({r_2}^2 - {r_1}^2)} - 1\right] \quad (8.18)$$

$$R_{radial2} = \frac{1}{4\pi k_r L}\left[1 - \frac{2{r_1}^2 \ln\left(\frac{r_2}{r_1}\right)}{({r_2}^2 - {r_1}^2)}\right] \quad (8.19)$$

Since internal heat generation is likely due to copper and iron losses in a rotating machine, heat generated per unit volume should be considered. Therefore, for a non-zero g with an assumption $T_1$and T_2 equal to zero;

$$T_{avg} = g\left(R_{radial3} + \frac{R_{radial1}.R_{radial2}}{R_{radial1} + R_{radial2}}\right) \quad (8.20)$$

Applying the same boundary conditions into equation (8.16), T_{avg} can be expressed in the form:

$$T_{avg} = \frac{g\,({r_1}^2 + {r_2}^2)}{8k_r} - \frac{g\,({r_2}^2 - {r_1}^2)}{8k_r \ln\left(\frac{r_2}{r_1}\right)} \quad (8.21)$$

Comparing and equating equations (8.20) and (8.21), the additional thermal resistance value when the internal heat generation is not zero is expressed as:

$$R_{radial3} = \frac{-1}{8\pi k_r L({r_2}^2 - {r_1}^2)}\left[{r_2}^2 + {r_1}^2 - \frac{4{r_1}^2{r_2}^2 \ln\left(\frac{r_2}{r_1}\right)}{{r_2}^2 - {r_1}^2}\right] \quad (8.22)$$

Since $R_{radial3}$ is negative, the average temperature is lower than the original central temperature in the case that internal heat generation is non-zero. Using Fourier law of heat for axial direction will result in similar equations as derived for radial heat flow case. R_{axial1}, R_{axial2} and R_{axial3} are formulated in the equations given below.

$$R_{axial1} = \frac{L}{2\pi k_a({r_2}^2 - {r_1}^2)} \quad (8.23)$$

$$R_{axial2} = \frac{L}{2\pi k_a({r_2}^2 - {r_1}^2)} \tag{8.24}$$

$$R_{axial3} = \frac{-L}{6\pi k_a({r_2}^2 - {r_1}^2)} \tag{8.25}$$

As given in equations (8.23) and (8.24), thermal resistances in axial direction equal to each other. If internal heat generation is present, negative resistance will also be considered as given in equation (8.25). This might be modelled with a dependent source such as current controlled voltage source (CCVS) or voltage controlled voltage source (VCVS).

8.6.1.1 Current controlled voltage source (CCVS)

In an ideal CCVS, the source delivers the voltage as per the current of the dependent element [147]. General circuit configuration for CCVS is given in Figure 8.20.

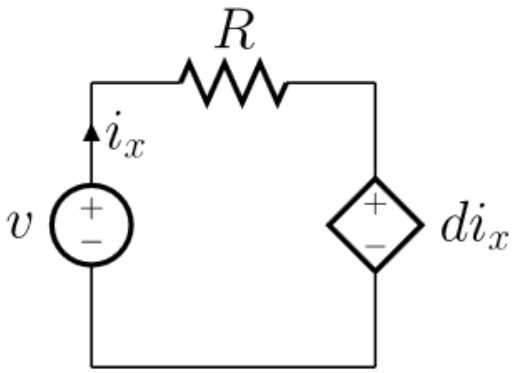

Figure 8.20 Current controlled voltage source (CCVS)

The voltage can be written as a function of current for a CCVS. It would be in the form:

$$V = f_d(i_x) \tag{8.26}$$

This type of circuit configurations are also known as trans-resistance amplifiers. A trans-resistance amplifier converts an input of current to an output of voltage. A generic form of trans-resistance amplifier is illustrated in Figure 8.21 [148].

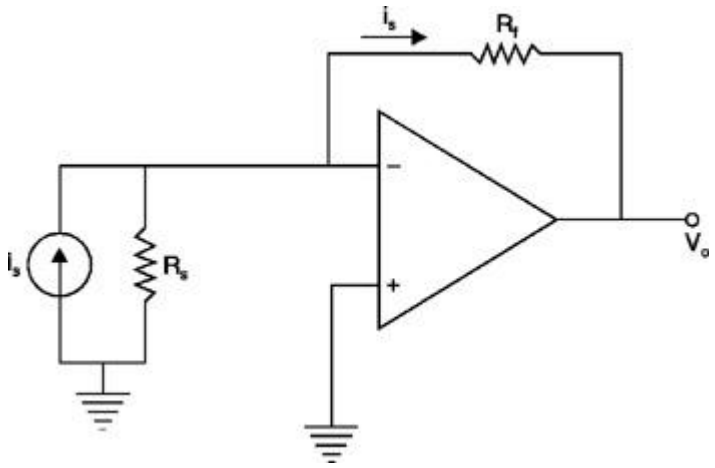

Figure 8.21 Trans-resistance amplifier [148]

Considering the current through R_f, the current i_s can be calculated. The following equations can be written to express the relationship between the source current and the output voltage.

$$i_s = \frac{Voltage\ difference}{R_f}$$

$$i_s = \left(\frac{0 - V_o}{R_f}\right)$$

$$-V_o = i_s R_f$$

$$V_o = -i_s R_f \tag{8.27}$$

Therefore, the output voltage is proportional to the input current. The principal use of this relationship between the voltage and current in current controlled voltage source will allow adjustment of the temperature drop due to negative thermal resistance in a thermal network. Thus, internal heat generation would be injected to any heat generating node in a thermal network.

8.6.2 PMA Thermal Lumped Parameter Model in Simulink/Simscape

Thermal lumped parameter modelling of the PMA is investigated for a quarter of the PMA due to symmetry. Top-down design approach for analytical thermal modelling of the quarter PMA without thermal paste is shown in Figure 8.22 Only copper losses due to 3.5 A dc static test are considered for thermal lumped parameter modelling of the PMA at steady state.

Using the design approach given in Figure 8.22, a thermal network has been created considering original dimensions of the PMA and thermal properties of the materials. Thermal network consists of sub-blocks which represent each particular part of the PMA and its housing. Since thermal network is designed for only steady state temperature values around the PMA, the thermal capacitance was not included in the model.

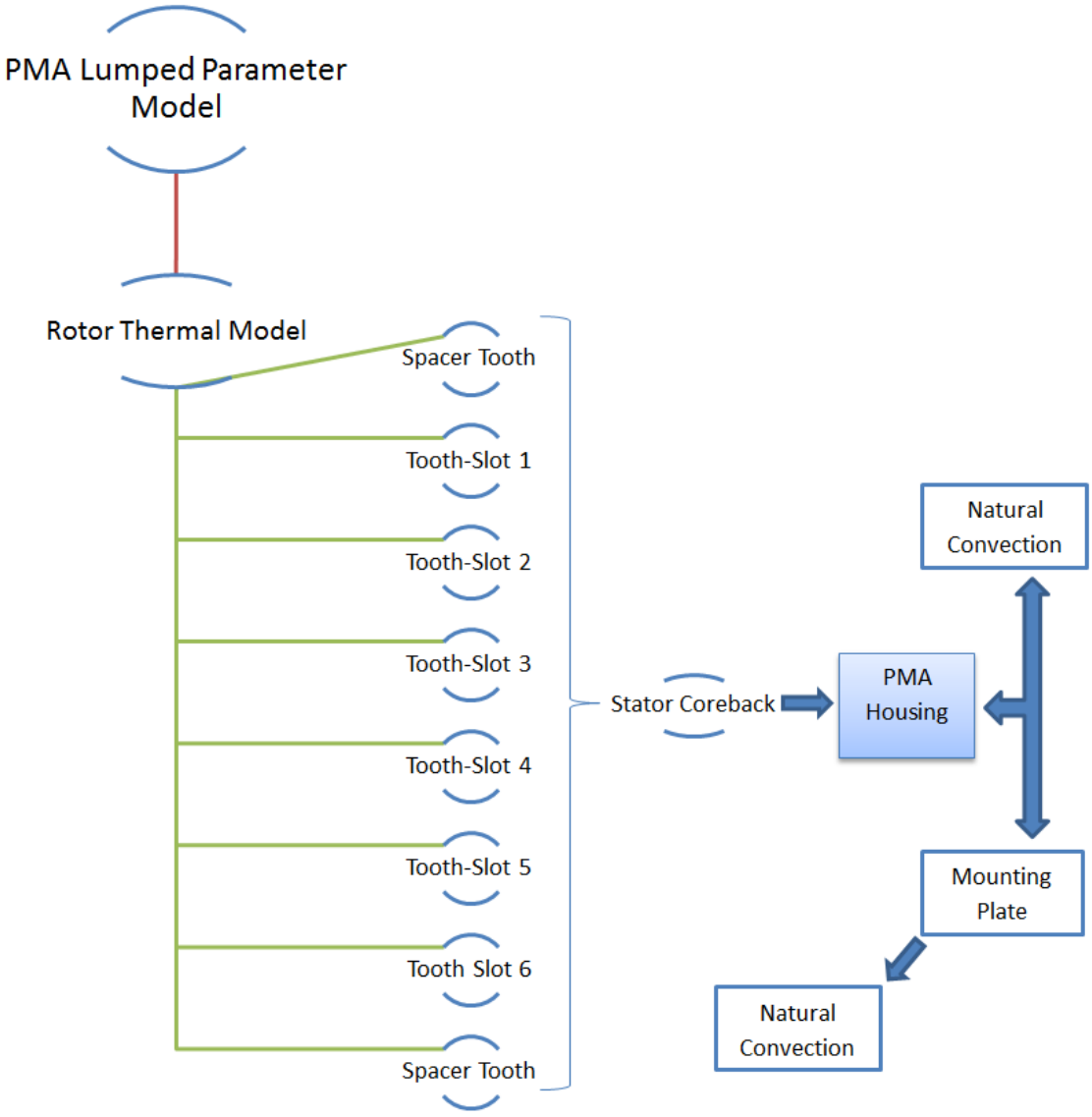

Figure 8.22 Top-Down design approach for theoretical thermal modelling of the PMA

8.6.2.1 Tooth-Slot Lumped Parameter Modelling

A thermal network was developed to identify the temperatures throughout the PMA including windings, laminations and external casing when only copper losses are injected to the coils at steady state. In much thermal network modelling, authors strive to reduce the number of nodes to simplify computation [39, 149]. Here, the thermal model is implemented in Simulink, which allows many different heat paths to be easily combined. The model incorporates negative compensation thermal resistance, which is represented in Simulink by current controlled voltage source (CCVS). It enables to take full advantage of Simulink software for this application. Thermal network sub-blocks were used for each significant part of the PMA.

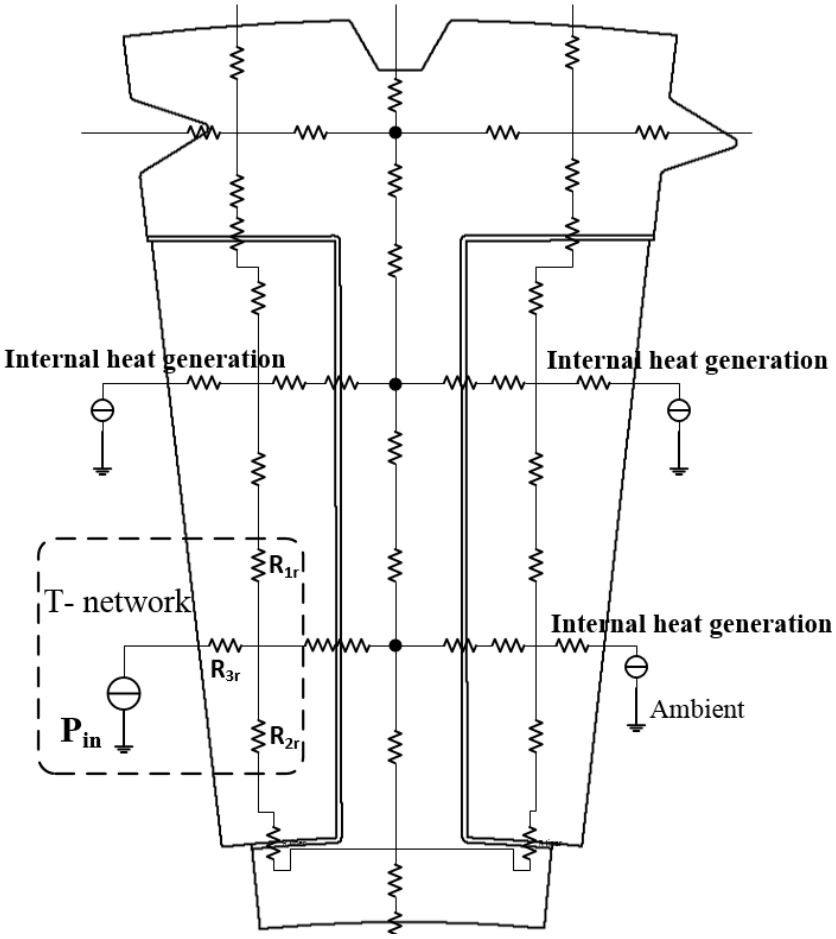

Figure 8.23 Tooth – slot equivalent LP model – only radial

For determination of thermal resistances, *T*-equivalent thermal model including radial and axial heat flow was developed. Figure 8.23 shows the radial heat flow on the PMA tooth-slot geometry. Since a radial flux machine consists of many heat generating 2D hollow cylinders with inner and outer radius r_1, r_2 , thermal conductivity k, and length L, *T*-equivalent thermal circuit is derived from the heat conduction equations given in (8.18), (8.19) and (8.22) for radial direction. For axial direction, equations to calculate *T*-equivalent thermal circuit parameters are given in (8.23), (8.24) and (8.25).

Note that $R_{radial3}$ and R_{axial3} in equations (8.22) and (8.25) are negative thermal resistances. They are modelled as a current controlled voltage source in the software to obtain a compensation resistance for thermal modelling of the slot. The thermal network sub-block for a single tooth-slot pair is depicted in Figure 8.24.

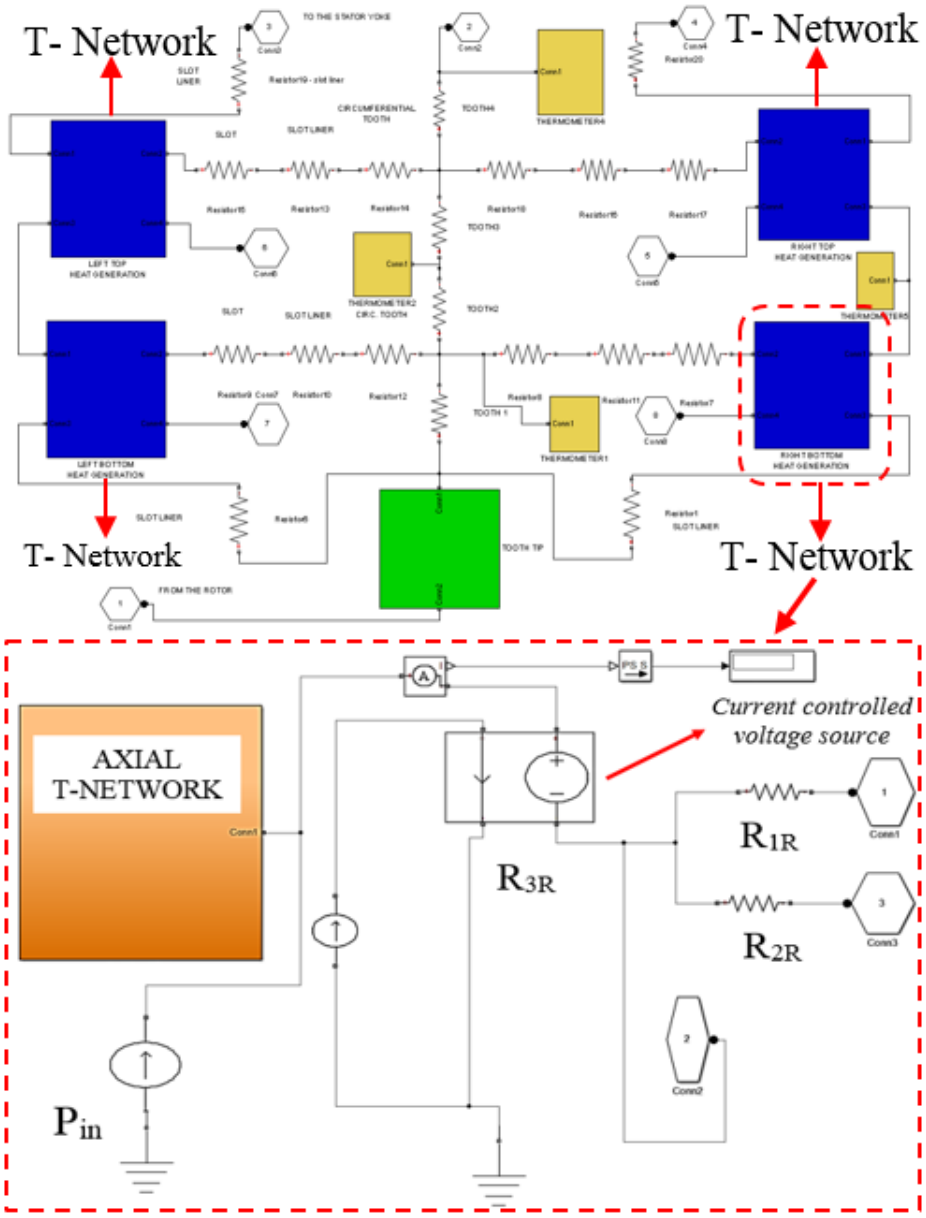

Figure 8.24 Simulink tooth-slot sub block

8.6.2.2 End windings Lumped Parameter Modelling

Stator end windings could be divided into discrete layers as trapezoidal shape of end windings forms a number of half hollow cylinders with a certain thickness. By assuming that heat flows into the paste through the top of the end windings as depicted in Figure 8.25, the half hollow cylinder shape winding segments can be divided into two parts. Each part forms a quarter hollow cylinder with a circumferential thermal resistance of R_{ew} and the heat is assumed to flow only θ direction and sets thermal boundary conditions: T_1 and T_2 at θ_1=0 and θ_2=π/2 respectively as shown in Figure 8.25

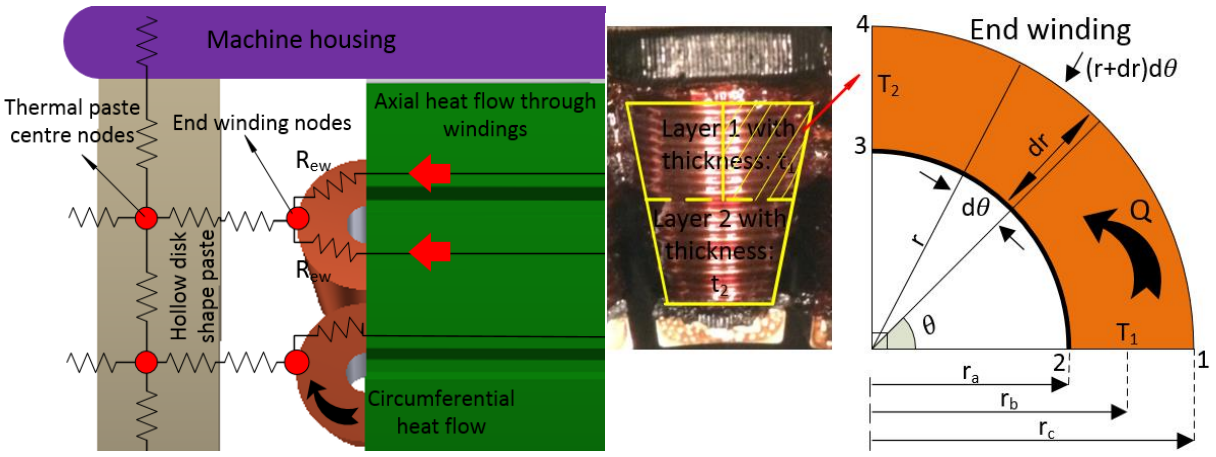

Figure 8.25 Discretization of stator end windings

The end windings are divided into two layers due to the relatively small end winding radiuses. Each layer consists of quarter hollow cylinders with a thermal resistance: R_{ew}

For steady conduction without heat generation in the end windings (i.e. assuming that all generated heat in the centre of the slot), the net conducted heat can be obtained by solving general heat equation in cylindrical coordinates [122] for a quarter hollow cylinder with temperature boundary conditions: T_1 and T_2. Heat flow (q) can be obtained for the upper quarter layer with a thickness of t_1 in Figure 8.25 as given in equation (8.28):

$$q = \frac{2k}{\pi} . ln \frac{r_b}{r_a} . [T_1 - T_2] t_1 \tag{8.28}$$

where k end winding axial thermal conductivity estimated at 10% less than copper isotropic thermal conductivity and the radiuses r_a and r_b are shown in Figure 8.25. By using the equation of thermal resistance for conduction, the thermal resistance, R_{ew} in θ direction can be written:

$$R_{ew} = \frac{\pi/2}{\ln\left(\frac{r_b}{r_a}\right) k t_1} \tag{8.29}$$

R_{ew} is only half of the end winding layers and each half of the winding layers would be considered to be in parallel to each other. Also, end winding layers are connected in parallel to each other. Each R_{ew} value can be computed using geometrical dimensions of the end windings. Thus, the equivalent thermal resistance of each PMA end windings, when only 2-layer system is considered, is found to be 0.654 °C/W using equation (8.29). The significance of end winding thermal resistance is usually dependent upon machine size.

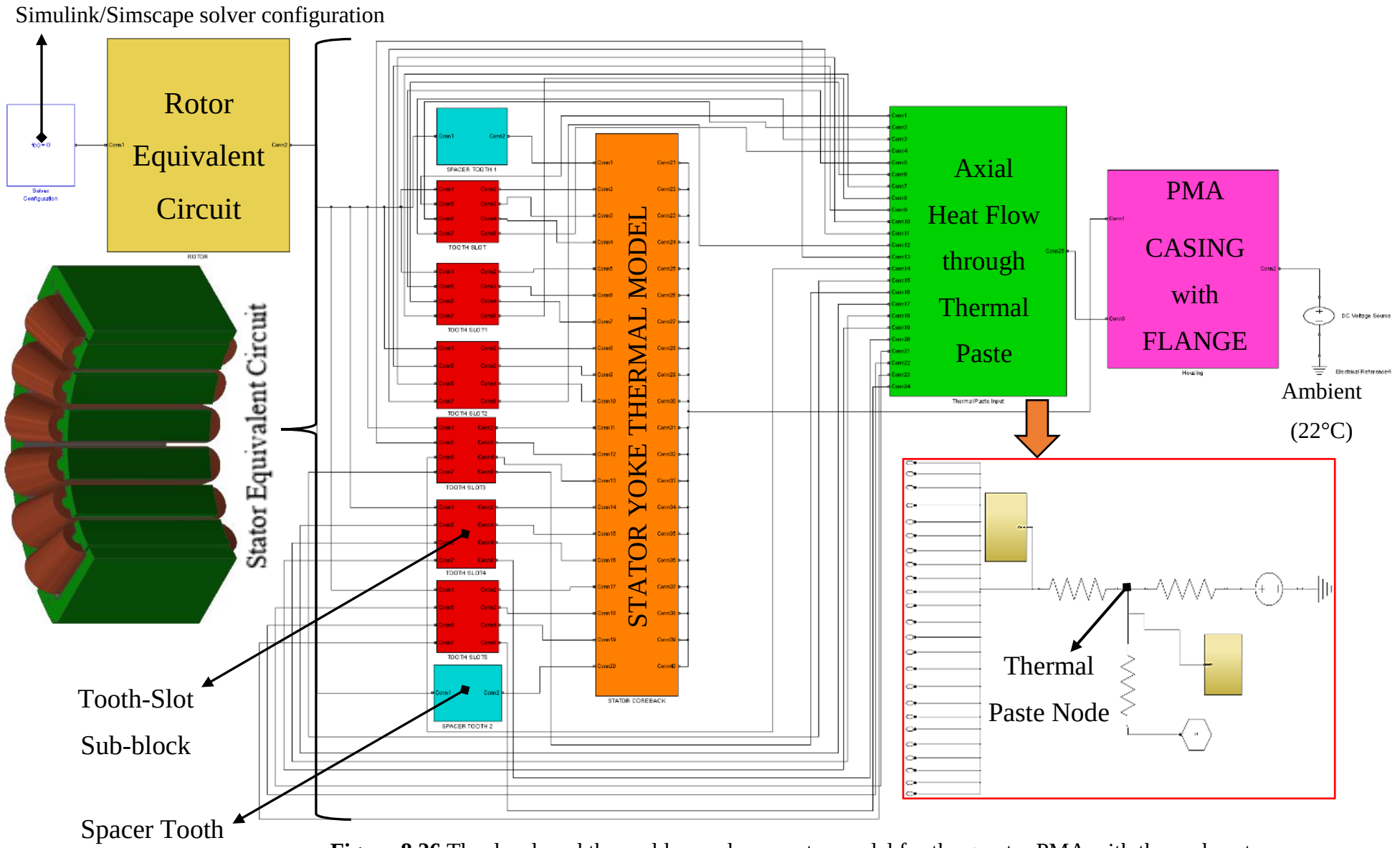

Figure 8.26 The developed thermal lumped parameter model for the quarter PMA with thermal paste

8.6.2.3 Simulink/Simscape Thermal Model of the PMA with Thermal Paste

In Figure 8.26, the overall thermal lumped parameter model consisting of the tooth-slot sub-blocks as depicted in Figure 8.24 is shown. As with the FEA model, the thermal network is developed for a quarter of the PMA with a part of the aluminium mounting plate, 6 single tooth windings and two spacer teeth. Each single tooth winding has radial, axial and circumferential heat flows. For the PMA without thermal paste, axial heat flow will not be significant as the machine is axially short (40 mm) and the end winding is not a significant part of the stator winding (End winding radius ≈ 4.62 mm). It is also noted that the machine does not have any dedicated cooling system so the main heat paths in the machine are on the radial direction rather than axial.

8.6.3 Experimental Validation of Models

In order to demonstrate the accuracy of analytical and FEA thermal models for the prototype machine with thermal paste[11], a comparison table with relative error between the modelling methods is shown in Table 8.7. Ambient temperature is assumed to be 22°C (i.e. 22Vdc as a voltage source in electrical analogy of the temperature) for the FEA and LP models.

As shown in Table 8.7, the relative error between the FEA simulations and the lumped parameter model is 4.9%. Also, the error between thermal lumped model and experimental results is 11.5%. It can be noted that no measurements were taken inside the prototype machine as there is no access to machine stator and windings. Nonetheless, measurements taken from the steady state thermal tests are adequate to quantify the amount of heat flow through the thermal paste by taking axial heat flow into account in thermal lumped model for the PMA with thermal paste.

[11] Relative error comparison for the original prototype without thermal paste is tabulated in Appendix – D.

Table 8.7 Temperature rise (ΔT) comparison for the PMA with thermal paste at steady state

Part	Thermal LP (°C)	Thermal FEA (°C)	Experiment (°C)	Error (%) FEA - LP	Error (%) Experiment- LP
Shaft	13.74	13.13	14.5	4.44	-5.531
Rotor core back	13.74	13.15	-	4.294	-
Magnets	13.74	13.17	-	4.148	-
Tooth tip	66.92	67.27	-	-0.523	-
Tooth centre	67.07	67.54	-	-0.701	-
Spacer tooth	62.13	59.04	-	4.973	-
Winding	68.05	69.68	-	-2.395	-
Stator core back	56.41	56.22	-	0.337	-
End cap centre	33.03	31.89	34.67	3.451	-4.965
Position 1	39.82	39.85	41.18	-0.075	-3.415
Position 2	33.6	35.03	37.49	-4.256	-11.577
Stator housing	32.89	31.59	30.2	3.953	8.179
Base	24.09	24.3	24.68	-0.872	-2.449

8.6.4 Investigation the Effect of Thermal Paste on the Machine Thermal Performance

8.6.4.1 Computation of Heat Flow through the Paste

When temperature change (ΔT) is compared for the test results, it is demonstrated that the prototype with thermal paste gives 14.86% less temperature rise on the external surfaces of the machine and mounting plate.

When a thermal paste is added to the single side of the stator end region, axial heat flow becomes a more significant part of the total heat flow inside the machine. In this case, the axial heat flow component is as important as the radial heat component. This should be considered for the thermal lumped parameter modelling of the PMA as a new conductive heat path around the stator housing. Therefore, heat flow by conduction occurs for the end windings when thermal paste is added to the PMA end region. Heat flow by conduction for the end windings was also modelled in the thermal lumped parameter network. The green sub-block given in Figure 8.26 shows that additional heat flow by conduction occurs through the thermal paste.

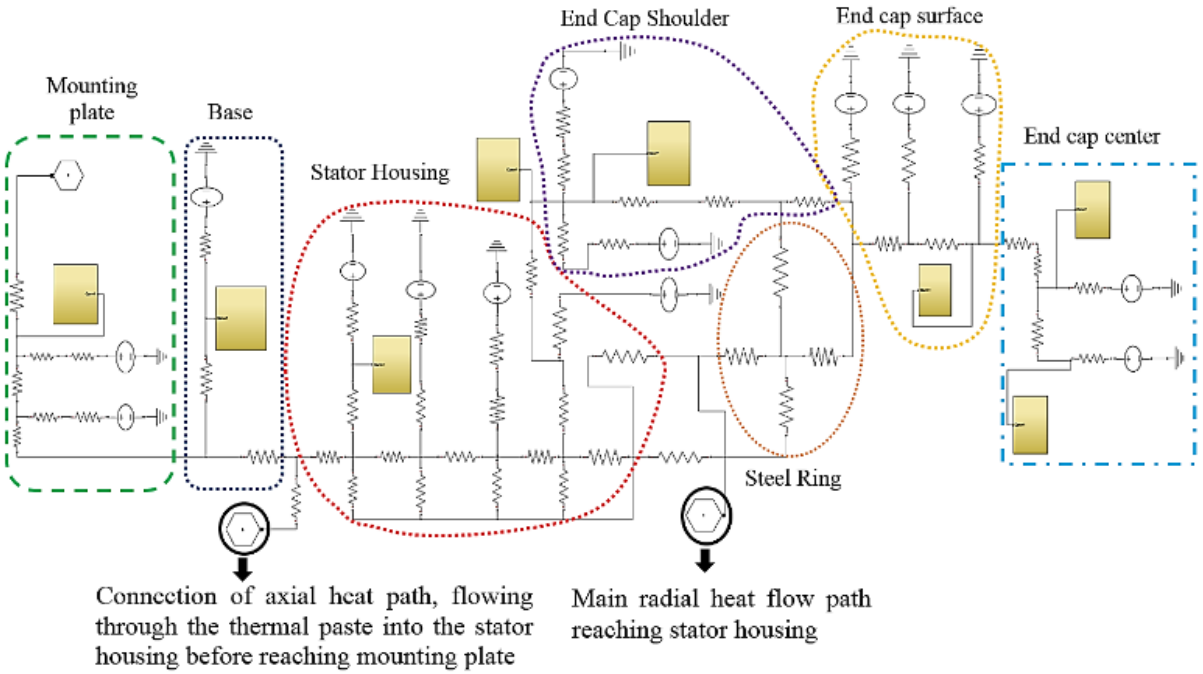

(a)

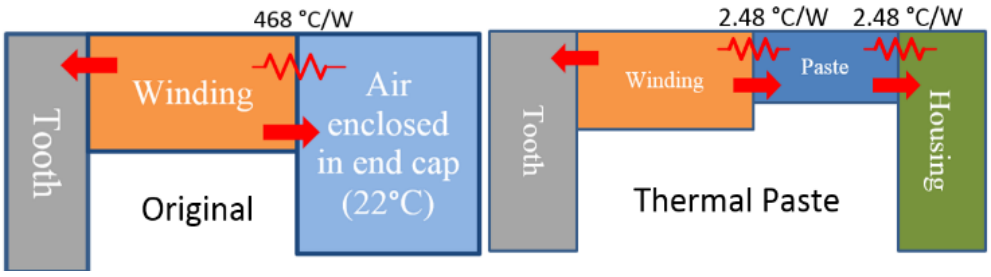

(b)

Figure 8.27 (a) Simplified thermal network for the PMA frame; (b) Equivalent thermal circuit representation of axial flow of end winding

The addition of thermal paste adds additional heat paths from the end winding of the coil to the base of the PMA. For the prototype without thermal paste, there is no physical contact between the coil end windings and the machine housing. As illustrated in Figure 8.27, replacing end winding convection with conduction through the thermal paste, the new thermal path reduces

thermal resistance by around one hundredth in that focused region. For a quarter of the machine with and without thermal paste, Table 8.8 shows significant heat flows when maximum copper loss is injected to the coils.

Table 8.8 Main heat paths around the PMA with thermal paste – LP Results

Rate of Heat Flow, watts (Joules per second)	***PMA with paste***	***PMA without paste***	***Unit***
Total	49.28	55.3	Watts
Radial	36.88	44.33	Watts
Axial	9.89	7.97	Watts
Rotor heat flow	2.36	3.02	Watts
Heat flow through thermal paste	6.847	-	Watts

As tabulated in Table 8.8, radial heat flow constitutes a significant part of the total heat flow (80.16%) for the PMA without thermal paste, as axial heat flow occurs only due to heat transfer by convection. Axial heat flow has been improved for the PMA with thermal paste. When 14.4% of the total generated heat flows axially for the prototype machine with paste, this has been increased to 20% by adding thermal paste. Therefore, it is clear that average thermal conductivity of the PMA machine has been improved by adding thermal paste since thermal resistance between the end windings and internal air is replaced by lower resistance value: 4.96 °C/W.

8.6.4.2 Dynamic Thermal Test Results – PMAs at rated speed

Thermal tests have also been performed when the machine was spinning with *Y*-connected, short circuited 3-phase lanes. The RMS phase current is 2 A and the machine rated speed is 14820 rpm. In this case, both iron losses and copper losses are active for the machine. As shown in Figure 8.28, temperature rise in the external surfaces of the PMA with thermal paste is slightly lower than that of the PMA without thermal paste. On average, the PMA with thermal paste is 2.35% cooler than the original machine when external surfaces are compared. When the PMAs are stationary, the effect of thermal paste on the thermal performance is more significant. This is perhaps due to the fan effect of rotating parts at very high speed in the machine end windings cooling, as thermal paste removes this effect at the flange side.

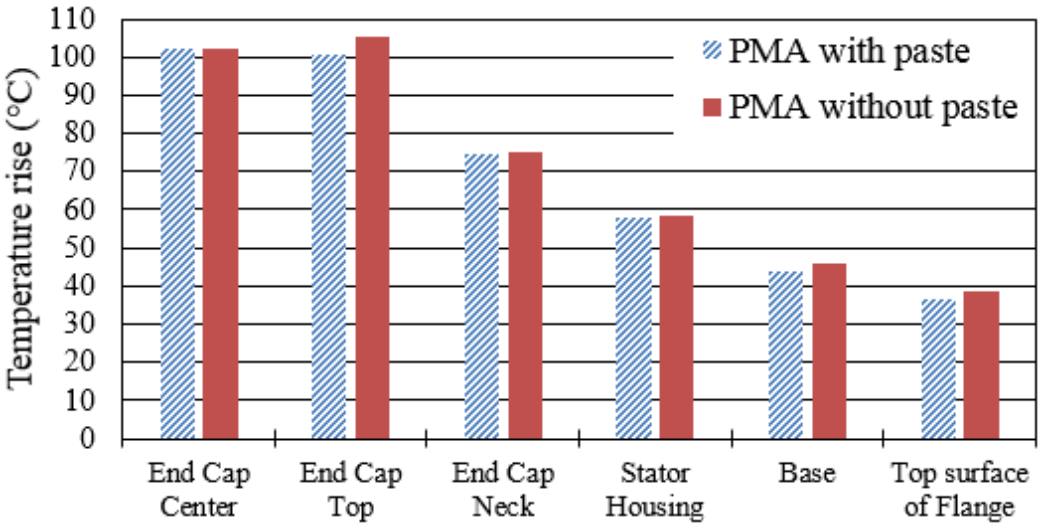

Figure 8.28 Temperature rise for the selected external surfaces when the PMAs at rated speed

Fault tolerance requires a low short circuit current in the PMA and therefore electrical loading is relatively small. Copper losses therefore constitute a very small portion (16%) of overall machine losses at short circuit rated speed (e.g. PMA iron loss ≈ 460 Watts). Therefore, the implementation of potted end windings for high electric loading and low speed machines would be more significant in terms of cooling.

8.7 Conclusion

In this work, a thermal test procedure has been presented for PMAs with and without thermal paste. Since the machines are mounted to a relatively large mounting plate, it is difficult to perform thermal FEA simulations as the majority of heat flows into the test rig when static thermal tests are conducted. Therefore, thermal design of the PMAs has been performed by introducing a thermal boundary condition at the machine flange side. This is required to simplify the model geometry for FEA simulations and thermal lumped parameter modelling.

The main focus of the thermal investigation is to quantify the effect of thermal paste added to the machine end region to improve thermal conductivity between the machine stator and housing. A thermal lumped parameter model for the static case of the PMA has been developed in Simulink, including radial and axial *T*-Network with thermal compensation resistances. Although simplification of a thermal network is usually preferred for the analytical lumped modelling, the proposed model aims to capture sufficient heat flow paths to be able quantify the effect of thermal paste. Key elements of the machine components were represented as sub-blocks. By introducing extra heat paths and thermal sub-blocks, thermal performance of the PMAs with and without thermal paste has been investigated analytically.

After sensitivity analysis of the PMAs with and without thermal paste, thermal performance of the prototypes have been compared by performing steady state dc tests, FEA simulations and

analytical lumped parameter modelling. It is shown that axial heat flow rate is increased 5.6% for the prototype with added thermal paste. This reduced the machine hot spot temperature around 10°C. Also, in average 14.86% temperature reduction was obtained on the external surfaces of the prototype machine with thermal paste. Both thermal FEA simulations and thermal lumped parameter satisfy experimental results with a low temperature estimation error.

Chapter 9. Conclusion

The influence of different manufacturing methods including on-tooth coil pressing and stator end windings encapsulation on the thermal performance of permanent magnet electrical machines has been studied in this thesis.

The proposed manufacturing techniques principally aim to increase the effective thermal conductivity of the machine windings leading to reduced winding temperature. Temperature rise in machine windings is not a significant parameter in terms of machine electromagnetic aspects, although it might drop machine torque slightly. Temperature rise in stator windings is critical regarding machine reliability and efficiency. Avoiding hot spots in electrical machine windings is crucial as the machine life expectancy will significantly depend on the homogeneity of temperature distribution in the machine structure. PM electrical machines for HEV and aerospace applications have been employed in this research to investigate how important thermal parameters are affected by the proposed manufacturing approaches.

The purpose of the work was achieved as important thermal parameters of the proposed manufacturing methods were estimated within acceptable accuracy. Furthermore, advantages and disadvantages of the proposed methods were explored regarding machine electro-thermal aspects and reliability.

9.1 Structural Analysis of Coil Pressing

Structural FEA modelling of coil pressing has been studied to investigate how deformation develops in the course of compression of magnet wires. In mechanical FEA simulations, the mechanical material properties are crucial in terms of accuracy of the stress and strain results. The more precise the material properties, the more accurate the simulation results. Commercial magnet wire companies do not provide some important material properties of polymer based wire coatings such as engineering stress-strain curve. However, thermoset materials used in magnet wires are known with general mechanical material properties which is still sufficient to perform a number FEA simulations.

In Chapter 3, structural analysis of coil pressing have been investigated with a proper selection of FEA modelling methodology. The non-linearity of the structure, high number of contact regions and material non-linearity are all challenging issues for the FEA modelling. They have been addressed in Chapter 3 by setting up proper boundary conditions in the FEA simulations.

Energy balance is crucial for the accuracy of coil pressing as it is the only way of monitoring the conservation of energy on the system. Any unrealistic deformation due to significant contact

and hourglass energy components can be observed on the deformed geometry. Therefore, all the simulated coil pressing results were ensured in terms of modelling accuracy. Maximum plastic strain was considered to be the failure criterion in the simulations. However, it is known that in material science, exceeding the yield stress of the material is usually accepted as failure. This criterion is not applicable for coil pressing since plastic deformation is present on the materials.

A certain amount of punch displacement results in material failure in the simulations which is usually dependent on magnet wire dimensions (i.e. conductor diameter, magnet wire grade etc.). The maximum achievable slot fill factors for several case studies have also been demonstrated without experiencing material fracture in magnet wire enamels.

9.2 Designing an Integrated Starter Generator

A number of permanent magnet machines with different pole slot combinations have been designed and optimised to meet the specifications of a crankshaft mounted integrated starter generator for a HEV application. In Chapter 4, 18 slot - 10 pole and 21 slot - 16 pole machine configurations employing surface and interior magnet topologies have been proposed. The advantages and disadvantages of the proposed machines in terms of efficiency, mass and torque ripple were discussed. It is shown that 21 slot – 16 pole interior PM (V-shape) ISG is the best candidate for the application with an efficiency merit of about 96%. By altering the winding connection from series to parallel and artificially varying the slot fill factor, the potential of the coil pressing on machine electrical performance improvement has been described theoretically. Moving from the traditional stator to segmented stator with on-tooth compressed coils, the machine torque is increased by about 17% for the same amount of copper loss implying that torque density has been significantly improved. This is achievable when more copper is utilised in the same slot volume by increasing the slot fill factor. This is an important result since machine can be overloaded without degrading the life expectancy. The design of an ISG machine with single tooth windings enabled further investigation of coil pressing regarding slot thermal conductivity and magnet wire life expectancy.

9.3 Thermal FEA Modelling of Stator Windings

In the literature, there are several theoretical approaches to estimate average thermal conductivity of the stator windings. They are usually dependent on homogenisation of round magnet wires by carrying out a proper mathematical approach. A steady state thermal FEA modelling method of winding segments have been proposed in Chapter 5. The developed method relies on sampling of a winding segment across the temperature boundaries. By employing one dimensional Fourier Law of Heat, effective thermal conductivity of the

anisotropic winding segments is predicted. This method also enables to extract variation of heat flux flow through the winding segments in one dimension. The accuracy of the proposed method has been validated by carrying out an analytical approach.

Furthermore, in order to demonstrate the effect of slot fill factor on winding temperature rise, a case study was proposed. Improvement of slot fill factor has been modelled by increasing the number of turns and by reducing the wire diameter rather than modelling a compressed coil. It was shown that maximum temperature in the winding at 0.71 fill factor is about 18% less than that obtained at 0.58 slot fill factor.

The proposed analytical and FEA modelling techniques might be quite useful for initial quick approximation of average winding thermal conductivity since the designer can take thermal parameters into account at an early stage in the optimisation process. However, it should be noted that the estimation of slot thermal conductivity of random wound, round copper stator windings is more complex in reality as multi point contact between the winding and its insulation system and contact pressure might change theoretical estimations significantly.

9.4 Thermal Analysis of the Compressed ISG Windings

The thermal parameters of stator windings will be affected by winding compression. Therefore, a number of methods such as steady state thermal FEA modelling and short time transient thermal tests have been employed to investigate how effective thermal conductivity changes when the ISG coils are compressed.

In Chapter 6, the experimental methodology of coil pressing was described and it is noted that the principal cause of insulation damage in FEA model of the winding segment is dynamic friction between magnet wire coatings and steel supports in contact with each other during compression. Inter-turn contact regions also experience severe plastic deformation which is relatively lower (i.e. about 20% of the peak plastic strain obtained in external surfaces of the winding) compared to external winding surfaces.

Due to the reduction in air voids between the turns, the compressed ISG windings exhibit better thermal performance and temperature difference between the winding and the segmented tooth decreases at higher fill factors. This indicates that the slot thermal conductivity becomes higher in the compressed coils. Short time transient thermal tests and first order RC circuit thermal representation of the windings enables to predict slot thermal resistance accurately. About 85% slot thermal conductivity improvement was shown in ISG windings at 0.72 fill factor in comparison to those at 0.57 fill factor.

A full thermal model of the ISG at rated operating condition is also included in Chapter 6. It is shown that temperature rise in the compressed ISG windings is 26.1°C less than those not pressed when the machine losses (i.e. DC copper, magnet and iron losses) actively generate heat in the machine components. This an important result in terms of stator winding reliability as a 10°C temperature rise in windings reduce the life expectancy of the machine dramatically according to Hendershot et al [3].

9.5 Thermal Aging Tests of the ISG Windings

Coil pressing might lead to electrical insulation deterioration in the coil insulation system: turn to turn and turn to ground wall. Rapid insulation resistance tests such as Mega-ohm test of compressed coils are not adequate to determine if the coils are electrically durable and maintain their thermal endurance whilst running in an electrical machine. In addition, the life expectancy of the compressed windings has not been studied in the literature. Therefore, the life expectancy of the on-tooth compressed windings have been studied to quantitatively estimate the thermal endurance of the compressed coils for an integrated starter generator.

Accelerated life tests at elevated temperatures with respect to the machine operating temperature have been carried out to investigate how the compressed ISG coils maintain their dielectric strength in long term operation. Three stage aging tests have been conducted to collect sufficient experimental data for further statistical analysis: Arrhenius – Weibull life model. According to the life model given in Chapter 7, the thermal endurance of the compressed ISG windings is around 2500 hours at the operating temperature (138ºC) of the integrated starter generator. The accuracy of the statistical analysis is also dependent upon the number of compressed winding samples used in the experiments, yet it is explicit that durability of the on-tooth compressed coils are low.

9.6 Encapsulation of Stator End Windings of a PM Alternator for Aerospace

The design of electric machines in aerospace applications target minimum mass with improved thermal performance. Natural convection is usually offered in aerospace as external cooling instruments might not be as reliable as natural convection. Therefore, the average thermal conductivity of a PM alternator used in aerospace can be improved by encapsulating machine end windings which adds axial heat flow paths between the stator windings and machine housing.

The machine was separated from the test rig by insulating it with some wood pieces to reduce thermal modelling complexity. A quarter of the PMA has been considered in the FEA that includes a temperature boundary mimicking the full machine with a flange. According to the

FEA results, the proposed geometry simplification is convenient approach since the temperature distribution error between the full PMA and quarter PMA is less than 5%.

Static DC thermal tests have been carried out to determine important thermal parameters of the machine such as effective thermal conductivity of the slot, stator to housing thermal resistance and the machine base to flange thermal contact conductance etc. The important feature of dc tests is that internal heat generation can be determined more accurately due to I^2R loss injection. This enables the development of a thermal lumped model of the machine when only copper losses are active and uncertainty of some thermal resistances around the machine can be quickly removed by thermal calibration.

Although the convection coefficient is a function of temperature rise, surface area and heat generation for the whole structure, local heat transfer coefficients around the machine is of importance. Thermal experiments are not conducted for the determination of local convection coefficients using heat flux sensors. The empirical heat transfer coefficient predictions for different types of surfaces such as horizontal cylinder, vertical plates etc. becomes sufficiently accurate after thermal calibration process.

A thermal lumped network was developed in Simulink to investigate 3-dimensional heat flow through the flange mounted machine when thermal paste with a thermal conductivity of 1.38 $W/(mK)$ is present. *T*-equivalent thermal sub-circuits derived from the heat conduction equations are used in the LP model. From the solution of one dimensional Fourier's law of heat in differential form, when the internal heat generation is not zero an additional compensation resistance exists which is negative. There are some commercial software such as Portunus to do some thermal LP calculations. However, Simscape in Matlab/Simulink is an alternative to such design environments. Negative thermal resistances are modelled to be CCVS in the software. Therefore, thermal LP modelling can be easily adapted to more common software such as Matlab.

The main target is to identify the amount of heat flow through the paste when it is present in the PMA housing. It is reported that about 14.8% temperature reduction is obtained on the external surfaces of the PMA with thermal paste. The encapsulation of the end windings also drops winding temperature of the PMA almost 10°C. This is a significant improvement for the copper loss removal through conduction in the PMA and lifetime.

9.7 Future Work

The analysis of the influence of coil pressing and end winding potting on electrical machine thermal performance is conducted in this thesis. Reliability of the on-tooth compressed coils is

also studied in terms of insulation life expectancy. However, a set of further investigation can be arisen from the work presented:

- Structural analysis of coil pressing, given in Chapter 3 can be further studied since the simulations given in this thesis do not consider the natural time of the event. More accurate deformation results can be obtained by running the simulations in parallel processors since non-linear explicit dynamic simulations are computationally costly.
- The proposed 21 slot / 16 pole crankshaft mounted ISG is asymmetrical in terms of winding configuration. Although it achieves high performance, acoustic noise, vibration and rotor eccentricity should be further investigated. Natural frequency analysis and mode shapes might be of interest when the machine is at rated operating condition. This might require radial pressure computations around the machine air gap.

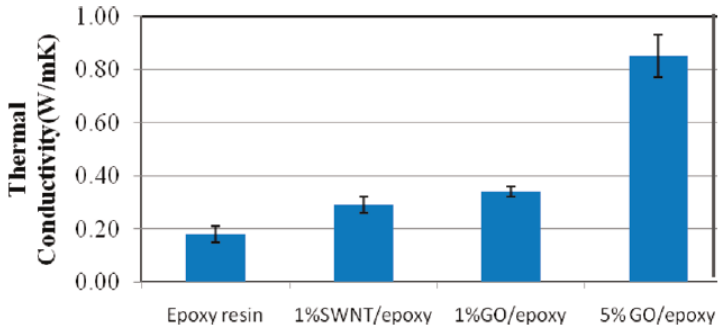

Figure 9.1 Thermal conductivity of the graphene composites reported by Wang et al [150]

- As electrical and electronic products continue to move toward miniaturisation, the most important challenge is increasing power dissipations. New materials can resolve the problem. The use of graphene based epoxy resins might be of interest in electrical machines.

  The thermal conductivity of a graphene layer is in the range of 3080 - 5150 $W/(mK)$ [150]. Although graphene is a both electrically and thermally conductive material, the graphene oxide (GO) is not highly conductive electrically due to the oxidised graphene layer edges. Therefore, graphene oxide based composites might be used to boost average thermal conductivity of machine windings. The thermal performance of the graphene based epoxy is given in Figure 9.1. The graphene based epoxy has almost four times higher thermal conductivity than pure epoxy resin. The potential of GO based insulation materials such as resins, adhesives etc. can be further investigated in terms of thermal performance of the electrical machines.
- The effective thermal conductivity of winding samples can be computed via reverse engineering. The original cross-sectional images of the machine windings can be image

processed and converted into 3-d geometries. This enables us to precisely compute effective thermal conductivity of the original windings using commercial FEA software. This is exemplified in Figure 9.2.

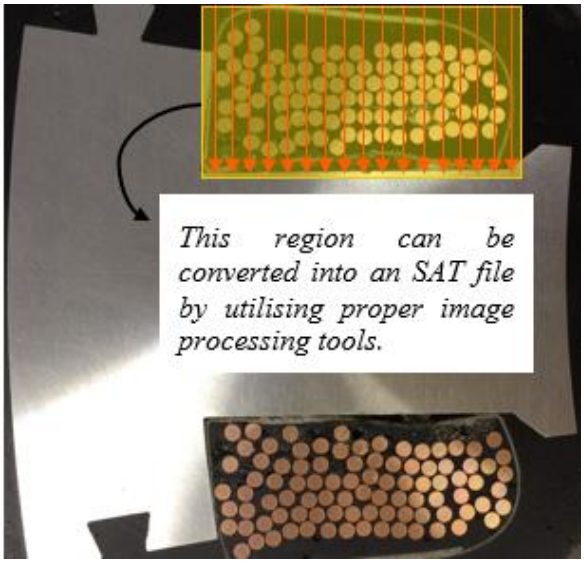

Figure 9.2 Slot thermal conductivity estimation via reverse engineering

- The on-tooth compressed ISG windings lose its dielectric strength rapidly as described in Chapter 7, implying that turn to ground wall insulation system of the windings deforms significantly during the compression. This can be overcome by implementing off-tooth coil pressing with a dummy tooth that enables to extract the winding off from the metal. Hence, winding insulation system can be kept healthy in the original machine stator. This might require a set of accelerated life tests of off-tooth compressed coils with healthy Nomex 410 slot liners and so thermal endurance of the compressed windings with un-deformed external insulation system can be investigated thoroughly.
- Thermal paste potting into the PMA stator housing effectively reduces the winding temperature, as reported in Chapter 8, but this might not be generalised for all electric machines as internal air HTC and end windings HTC might be affected by the shaft speed or external cooling instruments. There should be an optimum condition where end winding encapsulation is more effective than fan effect of the rotor depending upon speed, current rating and stator housing geometry. Therefore, the machine frame CFD analysis is further required to make appropriate comparison for the machines with and without thermal paste.

REFERENCES

[1] J. F. Gieras, *Advancements in Electric Machines*: Springer, 2008.

[2] J. Z. Gang Lei, Youguang Guo *Multidisciplinary Design Optimization Methods for Electrical Machines and Drive Systems*: Springer Berlin Heidelberg, 2016.

[3] J. R. Hendershot, Miller, T.J.E., *Design of Brushless Permanent-Magnet Motors*: Magna Physics & Oxford Science Publications, 1994.

[4] A. Boglietti, A. Cavagnino, D. Staton, M. Shanel, M. Mueller, and C. Mejuto, "Evolution and Modern Approaches for Thermal Analysis of Electrical Machines," *IEEE Transactions on Industrial Electronics,* vol. 56, pp. 871-882, 2009.

[5] J. Legranger, G. Friedrich, S. Vivier, and J. C. Mipo, "Combination of Finite-Element and Analytical Models in the Optimal Multidomain Design of Machines: Application to an Interior Permanent-Magnet Starter Generator," *IEEE Transactions on Industry Applications,* vol. 46, pp. 232-239, 2010.

[6] J. R. Hendershot, "MotorSolve analysis of the 2010 Toyota Prius Traction Motor," ed. Chicago: Hendershot 2015 Copyright, 2015.

[7] Z. Huang, F. J. Márquez-Fernández, Y. Loayza, A. Reinap, and M. Alaküla, "Dynamic thermal modeling and application of electrical machine in hybrid drives," in *2014 International Conference on Electrical Machines (ICEM)*, 2014, pp. 2158-2164.

[8] R. Wrobel, P. H. Mellor, M. Popescu, and D. A. Staton, "Power Loss Analysis in Thermal Design of Permanent-Magnet Machines—A Review," *IEEE Transactions on Industry Applications,* vol. 52, pp. 1359-1368, 2016.

[9] M. Amrhein, T. C. O. Connell, and J. R. Wells, "An integrated design process for optimized high-performance electrical machines," in *2013 International Electric Machines & Drives Conference*, 2013, pp. 847-854.

[10] A. H. Isfahani and B. Fahimi, "Multi-physics analysis of double stator switched reluctance machines," in *2013 IEEE Energy Conversion Congress and Exposition*, 2013, pp. 2827-2833.

[11] A. Sarikhani and O. Mohammed, "A multi-physics multi-objective optimal design approach of PM synchronous machines," in *2014 International Conference on Electrical Machines (ICEM)*, 2014, pp. 968-974.

[12] S. Schulte and K. Hameyer, "Multi-physics simulation of a synchronous claw-pole alternator for automotive applications," in *IEEE International Conference on Electric Machines and Drives, 2005.*, 2005, pp. 896-901.

[13] J. Alexandrova, H. Jussila, J. Nerg, and J. Pyrhönen, "Comparison between models for eddy-current loss calculations in rotor surface-mounted permanent magnets," in *The XIX International Conference on Electrical Machines - ICEM 2010*, 2010, pp. 1-6.

[14] N. Bianchi, S. Bolognani, and E. Fornasiero, "An Overview of Rotor Losses Determination in Three-Phase Fractional-Slot PM Machines," *IEEE Transactions on Industry Applications,* vol. 46, pp. 2338-2345, 2010.

[15] A. Boglietti, A. Cavagnino, L. Ferraris, and M. Lazzari, "Impact of the Supply Voltage on the Stray-Load Losses in Induction Motors," *IEEE Transactions on Industry Applications,* vol. 46, pp. 1374-1380, 2010.

[16] A. M. El-Refaie, J. P. Alexander, S. Galioto, P. Reddy, K. K. Huh, P. d. Bock, *et al.*, "Advanced high power-density interior permanent magnet motor for traction applications," in *2013 IEEE Energy Conversion Congress and Exposition*, 2013, pp. 581-590.

[17] Z. X. Fang, Z. Q. Zhu, L. J. Wu, and Z. P. Xia, "Simple and accurate analytical estimation of slotting effect on magnet loss in fractional-slot surface-mounted PM machines," in *2012 XXth International Conference on Electrical Machines*, 2012, pp. 464-470.

[18] D. A. Howey, P. R. N. Childs, and A. S. Holmes, "Air-Gap Convection in Rotating Electrical Machines," *IEEE Transactions on Industrial Electronics*, vol. 59, pp. 1367-1375, 2012.

[19] D. M. Ionel, M. Popescu, M. McGilp, T. Miller, S. Dellinger, and R. J. Heideman, "Computation of Core Losses in Electrical Machines Using Improved Models for Laminated Steel," in *Conference Record of the 2006 IEEE Industry Applications Conference Forty-First IAS Annual Meeting*, 2006, pp. 827-835.

[20] D. Ishak, Z. Q. Zhu, and D. Howe, "Eddy-current loss in the rotor magnets of permanent-magnet brushless machines having a fractional number of slots per pole," *IEEE Transactions on Magnetics*, vol. 41, pp. 2462-2469, 2005.

[21] M. Mirzaei, A. Binder, B. Funieru, and M. Susic, "Analytical Calculations of Induced Eddy Currents Losses in the Magnets of Surface Mounted PM Machines With Consideration of Circumferential and Axial Segmentation Effects," *IEEE Transactions on Magnetics*, vol. 48, pp. 4831-4841, 2012.

[22] M. Popescu, D. M. Ionel, A. Boglietti, A. Cavagnino, C. Cossar, and M. I. McGilp, "A General Model for Estimating the Laminated Steel Losses Under PWM Voltage Supply," *IEEE Transactions on Industry Applications*, vol. 46, pp. 1389-1396, 2010.

[23] J. Pyrhönen, S. Ruoho, J. Nerg, M. Paju, S. Tuominen, H. Kankaanpää, *et al.*, "Hysteresis Losses in Sintered NdFeB Permanent Magnets in Rotating Electrical Machines," *IEEE Transactions on Industrial Electronics*, vol. 62, pp. 857-865, 2015.

[24] A. M. E.-. Refaie, M. R. Shah, R. Qu, and J. M. Kern, "Effect of Number of Phases on Losses in Conducting Sleeves of Surface PM Machine Rotors Equipped With Fractional-Slot Concentrated Windings," *IEEE Transactions on Industry Applications*, vol. 44, pp. 1522-1532, 2008.

[25] R. Wrobel, D. Staton, R. Lock, J. Booker, and D. Drury, "Winding Design for Minimum Power Loss and Low-Cost Manufacture in Application to Fixed-Speed PM Generator," *IEEE Transactions on Industry Applications*, vol. 51, pp. 3773-3782, 2015.

[26] G. M. Gilson, T. Raminosoa, S. J. Pickering, C. Gerada, and D. B. Hann, "A combined electromagnetic and thermal optimisation of an aerospace electric motor," in *The XIX International Conference on Electrical Machines - ICEM 2010*, 2010, pp. 1-7.

[27] M. Galea, C. Gerada, T. Raminosoa, and P. Wheeler, "A Thermal Improvement Technique for the Phase Windings of Electrical Machines," *IEEE Transactions on Industry Applications*, vol. 48, pp. 79-87, 2012.

[28] M. Schiefer and M. Doppelbauer, "Indirect slot cooling for high-power-density machines with concentrated winding," in *2015 IEEE International Electric Machines & Drives Conference (IEMDC)*, 2015, pp. 1820-1825.

[29] A. Reinap, F. J. Márquez-Fernández, R. Andersson, C. Högmark, M. Alaküla, and A. Göransson, "Heat transfer analysis of a traction machine with directly cooled laminated

windings," in *2014 4th International Electric Drives Production Conference (EDPC)*, 2014, pp. 1-7.

[30] G. Karimi-Moghaddam, R. D. Gould, S. Bhattacharya, and D. D. Tremelling, "Thermomagnetic liquid cooling: A novel electric machine thermal management solution," in *2014 IEEE Energy Conversion Congress and Exposition (ECCE)*, 2014, pp. 1482-1489.

[31] M. Festa, H. D. Eberhardt, and W. Hofmann, "Advances in power density and efficiency — Circumferentially vs. conventionally cooled electric motors," in *2010 International Conference on Electrical Machines and Systems*, 2010, pp. 1307-1312.

[32] M. Popescu, D. Staton, A. Boglietti, A. Cavagnino, D. Hawkins, and J. Goss, "Modern heat extraction systems for electrical machines - A review," in *2015 IEEE Workshop on Electrical Machines Design, Control and Diagnosis (WEMDCD)*, 2015, pp. 289-296.

[33] Insulation System [Online]. Available: https://en.wikipedia.org/wiki/Insulation_system

[34] S. Ayat, R. Wrobel, J. Goss, and D. Drury, "Estimation of equivalent thermal conductivity for impregnated electrical windings formed from profiled rectangular conductors," in *8th IET International Conference on Power Electronics, Machines and Drives (PEMD 2016)*, 2016, pp. 1-6.

[35] N. Simpson, R. Wrobel, and P. H. Mellor, "Estimation of Equivalent Thermal Parameters of Impregnated Electrical Windings," *IEEE Transactions on Industry Applications*, vol. 49, pp. 2505-2515, 2013.

[36] A. Boglietti, A. Cavagnino, M. Lazzari, and M. Pastorelli, "A simplified thermal model for variable-speed self-cooled industrial induction motor," *IEEE Transactions on Industry Applications*, vol. 39, pp. 945-952, 2003.

[37] P. H. Mellor, D. Roberts, and D. R. Turner, "Lumped parameter thermal model for electrical machines of TEFC design," *IEE Proceedings B - Electric Power Applications*, vol. 138, pp. 205-218, 1991.

[38] D. Kuehbacher, A. Kelleter, and D. Gerling, "An improved approach for transient thermal modeling using lumped parameter networks," in *2013 International Electric Machines & Drives Conference*, 2013, pp. 824-831.

[39] A. M. E.-. Refaie, N. C. Harris, T. M. Jahns, and K. M. Rahman, "Thermal analysis of multibarrier interior PM synchronous Machine using lumped parameter model," *IEEE Transactions on Energy Conversion*, vol. 19, pp. 303-309, 2004.

[40] X. Ding, M. Bhattacharya, and C. Mi, "Simplified thermal model of PM motors in hybrid vehicle applications taking into account eddy current loss in magnets," *Journal of Asian Electric Vehicles*, vol. 8, pp. 1337-1343, 2010.

[41] D. A. Staton and A. Cavagnino, "Convection Heat Transfer and Flow Calculations Suitable for Analytical Modelling of Electric Machines," in *IECON 2006 - 32nd Annual Conference on IEEE Industrial Electronics*, 2006, pp. 4841-4846.

[42] D. J. Powell, "Modelling of high power density electrical machines for aerospace," PhD Thesis, Sheffield University, UK, 2003.

[43] L. C. Hong, "Thermal Modelling of the Ventilation and Cooling inside Axial Flux Permanent Magnet Generators," PhD Thesis, School of Engineering and Computer Science, Durham University, Durham, UK, 2010.

[44] E. H. M. R.C. Martinelli, L.M.K. Boelter, "An ivestigation of aircraft heaters, V- theory and use of heat meters for the measurement of rates of heat transfer which are

independent of time," NACA, National Advisory Committee for Aeronautics Reports 1942.

[45] L. Siesing, A. Reinap, and M. Andersson, "Thermal properties on high fill factor electrical windings: Infiltrated vs non infiltrated," in *2014 International Conference on Electrical Machines (ICEM)*, 2014, pp. 2218-2223.

[46] (2016, January, 2017). *Thin Film Heat Flux Sensor*. Available: http://www.omega.co.uk/pptst/HFS-3_HFS-4.html

[47] N. S. Flanders, "Heat flow sensors on walls – What can we learn? In Building Applications of heat flux transducers," *ASTM Selected Technical Papers 885*, pp. 140-159, 1985.

[48] M. G. Dunn, J. Kim, and W. J. Rae, "Investigation of the heat-island effect for heat-flux measurements in short-duration facilities," *Journal of turbomachinery*, vol. 119, pp. 753-760, 1997.

[49] U. Danielsson, "Convective heat transfer measured directly with a heat flux sensor," *Journal of applied physiology*, vol. 68, pp. 1275-1281, 1990.

[50] A. S. f. T. a. Materials., "Standard test method for E457-96 measuring heat transfer rate using thermal capacitance calorimeter," ed: ASTM, 1997.

[51] D. R. H. Gillespie, Z. Wang, P. T. Ireland, and S. T. Kohler, "Full surface local heat transfer coefficient measurements in a model of an integrally cast impingement cooling geometry," in *ASME 1996 International Gas Turbine and Aeroengine Congress and Exhibition*, 1996, pp. V004T09A019-V004T09A019.

[52] F. F. J. Schrijer, "Transient heat transfer measurements in a short duration hypersonic facility on a blunted cone-flare using QIRT," M. Sc. Thesis. Netherlands: TU Delft, 2003.

[53] Z. Wang, P. T. Ireland, T. V. Jones, and R. Davenport, "A color image processing system for transient liquid crystal heat transfer experiments," *Journal of turbomachinery*, vol. 118, pp. 421-427, 1996.

[54] S. Harmand, B. Watel, and B. Desmet, "Local convective heat exchanges from a rotor facing a stator," *International journal of thermal sciences*, vol. 39, pp. 404-413, 2000.

[55] M. Mori, L. Novak, and M. Sekavčnik, "Measurements on rotating blades using IR thermography," *Experimental Thermal and Fluid Science*, vol. 32, pp. 387-396, 2007.

[56] H. Akita, Y. Nakahara, N. Miyake, and T. Oikawa, "A new core," *IEEE Industry Applications Magazine*, vol. 11, pp. 38-43, 2005.

[57] S. Jianxin, W. Canfei, M. Dongmin, J. Mengjia, S. Dan, and W. Yunchong, "Analysis and optimization of a modular stator core with segmental teeth and solid back iron for pm electric machines," in *2011 IEEE International Electric Machines & Drives Conference (IEMDC)*, 2011, pp. 1270-1275.

[58] A. M. E.-. Refaie, "Fractional-Slot Concentrated-Windings Synchronous Permanent Magnet Machines: Opportunities and Challenges," *IEEE Transactions on Industrial Electronics*, vol. 57, pp. 107-121, 2010.

[59] (2017). *Concentrated winding*. Available: http://www.emetor.org/glossary/concentrated-winding/

[60] W. Chengyu, L. Chuang, J. Renhua, Z. Jie, and N. Yinhang, "Effect of slot-and-pole combination on the flux-weakening properties of fractional-slot concentrated

windings," in *2014 17th International Conference on Electrical Machines and Systems (ICEMS)*, 2014, pp. 344-348.

[61] L. Chong, R. Dutta, and M. F. Rahman, "Parameter analysis of an IPM machine with fractional-slot concentrated windings, part I: Open-circuit analysis," in *2008 Australasian Universities Power Engineering Conference*, 2008, pp. 1-5.

[62] L. Chong, R. Dutta, and M. F. Rahman, "Parameter analysis of an IPM machine with fractional-slot concentrated windings, part II: Including armature-reaction," in *2008 Australasian Universities Power Engineering Conference*, 2008, pp. 1-6.

[63] L. Yue, P. Yulong, Y. Yanjun, S. Yanwen, and C. Feng, "Increasing the saliency ratio of fractional slot concentrated winding interior permanent magnet synchronous motors," *IET Electric Power Applications*, vol. 9, pp. 439-448, 2015.

[64] F. Libert and J. Soulard, "Manufacturing Methods of Stator Cores with Concentrated Windings," in *Power Electronics, Machines and Drives, 2006. The 3rd IET International Conference on*, 2006, pp. 676-680.

[65] J. Hallberg, "Conceptual Evaluation and Design of a Direct-Driven Mixer," Master thesis, Department of Mechanical Engineering, University of Linkoping, 2005.

[66] T. Mitsuhiro, "Manufacturing Device for Spiral Laminated Core," *Patent JP1148046*, 1989.

[67] S.-W. Lee, "Laminated body of motor and manufacturing method thereof," ed: Google Patents, 2007.

[68] (2010). Available: www.zfsachs.com/dynastart-pc

[69] M. Gröninger, F. Horch, A. Kock, M. Jakob, and B. Ponick, "Cast coils for electrical machines and their application in automotive and industrial drive systems," in *2014 4th International Electric Drives Production Conference (EDPC)*, 2014, pp. 1-7.

[70] M. Gröninger, F. Horch, A. Kock, H. Pleteit, B. Ponick, D. Schmidt, *et al.*, "Casting production of coils for electrical machines," in *2011 1st International Electric Drives Production Conference*, 2011, pp. 159-161.

[71] R. Andersson, C. Högmark, A. Reinap, and M. Alaküla, "Modular three-phase machines with laminated winding for hybrid vehicle applications," in *2012 2nd International Electric Drives Production Conference (EDPC)*, 2012, pp. 1-7.

[72] D. S. Jung, Y. H. Kim, U. H. Lee, and H. D. Lee, "Optimum Design of the Electric Vehicle Traction Motor Using the Hairpin Winding," in *2012 IEEE 75th Vehicular Technology Conference (VTC Spring)*, 2012, pp. 1-4.

[73] J. H. Choi, Y. D. Chun, P. W. Han, M. J. Kim, D. H. Koo, J. Lee, *et al.*, "Design of High Power Permanent Magnet Motor With Segment Rectangular Copper Wire and Closed Slot Opening on Electric Vehicles," *IEEE Transactions on Magnetics*, vol. 46, pp. 2070-2073, 2010.

[74] H. Hayashi, K. Nakamura, A. Chiba, T. Fukao, K. Tungpimolrut, and D. G. Dorrell, "Efficiency Improvements of Switched Reluctance Motors With High-Quality Iron Steel and Enhanced Conductor Slot Fill," *IEEE Transactions on Energy Conversion*, vol. 24, pp. 819-825, 2009.

[75] A. G. Jack, B. C. Mecrow, P. G. Dickinson, D. Stephenson, J. S. Burdess, J. N. Fawcett, *et al.*, "Permanent magnet machines with powdered iron cores and pre-pressed windings," in *Conference Record of the 1999 IEEE Industry Applications Conference. Thirty-Forth IAS Annual Meeting (Cat. No.99CH36370)*, 1999, pp. 97-103 vol.1.

[76] P. G. Dickinson, "Application of Soft Magnetic Composites in Electrical Machines," PhD Thesis, Newcastle University, United Kingdom, 2002.

[77] J. Widmer, "Segmental rotor switched reluctance machines for use in automotive traction," Ph.D. Thesis, School of Electrical and Electronic Engineering, Newcastle University, 2014.

[78] J. D. Widmer, R. Martin, and B. C. Mecrow, "Pre-compressed and stranded aluminium motor windings for traction motors," in *2015 IEEE International Electric Machines & Drives Conference (IEMDC)*, 2015, pp. 1851-1857.

[79] J. D. Widmer, C. M. Spargo, G. J. Atkinson, and B. C. Mecrow, "Solar Plane Propulsion Motors With Precompressed Aluminum Stator Windings," *IEEE Transactions on Energy Conversion*, vol. 29, pp. 681-688, 2014.

[80] M. C. W. T., *Transformer and Inductor Design Handbook*, Third Edition ed.: Marcel Dekker Inc., 2004.

[81] G. C. Stone, E. A. Boulter, I. Culbert, and H. Dhirani, *Electrical insulation for rotating machines: design, evaluation, aging, testing, and repair* vol. 21: John Wiley & Sons, 2004.

[82] (2016, 06 February). *Magnet Wire Insulation Guide*. Available: http://www.mwswire.com/pdf_files/mws_tech_book/page2_3.pdf

[83] Q. Guo, *Thermosets: Structure, properties and applications*: Elsevier, 2012.

[84] (July 24). *Stress Strain Ductile Materials*. Available: commons.wikimedia.org/wiki/File:Stress_Strain_Ductile_Material.pdf

[85] W. D. Callister and D. G. Rethwisch, *Materials science and engineering* vol. 5: John Wiley & Sons NY, 2011.

[86] (2002, July 24). *Young's Modulus and Specific Stiffness*. Available: www-materials.eng.cam.ac.uk /mpsite/properties/units_pics/stiffness.jpg

[87] X. Chen and Y. Liu, *Finite element modeling and simulation with ANSYS Workbench*: CRC Press, 2014.

[88] H.-H. Lee, *Finite element simulations with ANSYS workbench 16*: SDC publications, 2015.

[89] (August 06). *Abaqus/Explicit: Advanced Topics: Quasi-Static Analysis Lecture 5*. Available: http://imechanica.org/files/l5-quasi-static.pdf

[90] L. Gabor. (2016, 06 August 2015). *Seismic Design Principles*. Available: www.wbdg.org/resources/seismic_design.php

[91] (2015, 13 February). *LS-DYNA Support page*. Available: http://www.dynasupport.com/howtos/element/hourglass

[92] "ANSYS® Academic Research, Release 15.0, Help System, Hourglassing," 2015.

[93] "ANSYS Customer Training Material Release 13.0, Mechanical Structural Nonlinearities, Lecture 3: Introduction to Contact," ed, 2010.

[94] "CAE Associates CFD Meshing with Ansys Workbench," ed, 2013.

[95] (2015). *Summary of Properties for Kapton Polyimide Films*. Available: www.dupont.com/content/dam/assets/products-and-services/membranes-films/assets/DEC-Kapton-summary-of-properties.pdf

[96] (2014, 25 October). *High Tensile Steels*. Available: www.interlloy.com.au/our-products/high-tensile-steels/4340-high-tensile-steel/?output=pdf

[97] C. J. Ifedi, "A high torque density, direct drive in-wheel motor for electric vehicles," 2014.

[98] H. Ouyang. (2014, 12 May). *What's the different between quasi-static and dynamic analyse?* [Online Forum]. Available: https://www.researchgate.net/post/Whats_the_different_between_quasi-static_and_dynamic_analyse

[99] J. Higgins, "Obtaining and Optimizing Structural Analysis Convergence," ed: Ansys, 2012.

[100] P. Barrett. (2014, 12 May). *Stress Analysis Convergence Tips for Dummies*. Available: https://caeai.com/blog/stress-analysis-convergence-tips-dummies

[101] L. Alberti, M. Barcaro, M. Dai Pre, A. Faggion, L. Sgarbossa, N. Bianchi, *et al.*, "IPM machine drive design and tests for an integrated starter–alternator application," *IEEE Transactions on Industry Applications,* vol. 46, pp. 993-1001, 2010.

[102] K. T. Chau, "Integrated-Starter-Generator Systems," *Electric Vehicle Machines and Drives: Design, Analysis and Application*, pp. 291-314, 2015.

[103] W. Cai, "Comparison and review of electric machines for integrated starter alternator applications," in *Industry Applications Conference, 2004. 39th IAS Annual Meeting. Conference Record of the 2004 IEEE*, 2004.

[104] W. Ding and D. Liang, "A fast analytical model for an integrated switched reluctance starter/generator," *IEEE Transactions on Energy conversion,* vol. 25, pp. 948-956, 2010.

[105] J. F. Bangura, "Directly coupled electromagnetic field-electric circuit model for analysis of a vector-controlled wound field brushless starter generator," *IEEE Transactions on Energy Conversion*, vol. 26, pp. 1033-1040, 2011.

[106] K. T. Chau and C. C. Chan, "Emerging energy-efficient technologies for hybrid electric vehicles," *Proceedings of the IEEE,* vol. 95, pp. 821-835, 2007.

[107] C.-F. Wang, M.-J. Jin, J.-X. Shen, and C. Yuan, "A permanent magnet integrated starter generator for electric vehicle onboard range extender application," *IEEE Transactions on Magnetics,* vol. 48, pp. 1625-1628, 2012.

[108] N. J. Baker, G. J. Atkinson, J. G. Washington, B. C. Mecrow, G. Nord, and L. Sjoberg, "Design of high torque traction motors for automotive applications using modulated pole SMC machines," in *Power Electronics, Machines and Drives (PEMD 2012), 6th IET International Conference on*, 2012, pp. 1-6.

[109] A. El-Refaie, "Fractional-slot concentrated-windings: A paradigm shift in electrical machines," in *Electrical Machines Design Control and Diagnosis (WEMDCD), 2013 IEEE Workshop on*, 2013, pp. 24-32.

[110] D. C. Hanselman, *Brushless motors: magnetic design, performance, and control of brushless dc and permanent magnet synchronous motors*: E-Man Press LLC, 2012.

[111] I. Petrov, P. Ponomarev, Y. Alexandrova, and J. Pyrhönen, "Unequal Teeth Widths for Torque Ripple Reduction in Permanent Magnet Synchronous Machines With Fractional-Slot Non-Overlapping Windings," *IEEE Transactions on Magnetics,* vol. 51, pp. 1-9, 2015.

[112] F. Rong and D. Manfeng, "Optimization design and analysis of a 30kW interior permanent magnet synchronous motor used in electric vehicles," in *Electrical Machines and Systems (ICEMS), 2012 15th International Conference on*, 2012, pp. 1-5.

[113] Z. Azar, L. J. Wu, D. Evans, and Z. Q. Zhu, "Influence of rotor configuration on iron and magnet losses of fractional-slot IPM machines," in *Power Electronics, Machines and Drives (PEMD 2010), 5th IET International Conference on*, 2010, pp. 1-6.

[114] J. Blum, J. Merwerth, and H. G. Herzog, "Magnet eddy-current losses in interior permanent magnet machines with concentrated windings-analysis and reduction of the major source," 2014.

[115] K. C. Kim, J. Lee, H. J. Kim, and D. H. Koo, "Multiobjective Optimal Design for Interior Permanent Magnet Synchronous Motor," *IEEE Transactions on Magnetics*, vol. 45, pp. 1780-1783, 2009.

[116] X. Liu, H. Chen, J. Zhao, and A. Belahcen, "Research on the performances and parameters of interior PMSM used for electric vehicles," *IEEE Transactions on Industrial Electronics*, vol. 63, pp. 3533-3545, 2016.

[117] S. Duan, L. Zhou, and J. Wang, "Flux weakening mechanism of interior permanent magnet synchronous machines with segmented permanent magnets," *IEEE Transactions on Applied Superconductivity*, vol. 24, pp. 1-5, 2014.

[118] H. Feng, X. Wang, X. Xu, and Y. Liu, "Optimization of asymmetric permanent magnetic synchronous motor for cogging torque minimization using finite element method," in *Electrical Machines and Systems, 2008. ICEMS 2008. International Conference on*, 2008, pp. 3559-3563.

[119] K. H. Nam, *AC motor control and electrical vehicle applications*: CRC press, 2010.

[120] J. Pyrhonen, T. Jokinen, and V. Hrabovcova, *Design of rotating electrical machines*: John Wiley & Sons, 2009.

[121] D. J. B. Smith, "High Speed High Power Electrical Machines," Ph.D. Thesis, School of Electrical and Electronic Engineering, Newcastle University, 2014.

[122] F. P. Incropera and F. P. Incropera, *Foundations of heat transfer*: Wiley, 2013.

[123] N. Simpson, P. H. Mellor, and R. Wrobel, "Estimation of equivalent thermal parameters of electrical windings," in *Electrical Machines (ICEM), 2012 XXth International Conference on*, 2012, pp. 1294-1300.

[124] "IEEE Recommended Practice for Testing Insulation Resistance of Electric Machinery - Redline," *IEEE Std 43-2013 (Revision of IEEE Std 43-2000) - Redline*, pp. 1-75, 2014.

[125] A. Boglietti, E. Carpaneto, M. Cossale, A. L. Borlera, D. Staton, and M. Popescu, "Electrical machine first order short-time thermal transients model: Measurements and parameters evaluation," in *Industrial Electronics Society, IECON 2014-40th Annual Conference of the IEEE*, 2014, pp. 555-561.

[126] A. Boglietti, E. Carpaneto, M. Cossale, M. Popescu, D. Staton, and S. Vaschetto, "Equivalent thermal conductivity determination of winding insulation system by fast experimental approach," in *Electric Machines & Drives Conference (IEMDC), 2015 IEEE International*, 2015, pp. 1215-1220.

[127] (2017, 25th of June). *Time Constant* [Online]. Available: https://en.wikipedia.org/wiki/Time_constant

[128] O. Keysan. (2017, 25th April). *EE564 Design of Electrical Machines* [Online]. Available: http://keysan.me/ee564/

[129] (2015, 02/07/2017). *Accelerated Life Testing Reference* [E-book]. Available: http://www.synthesisplatform.net/references/Accelerated_Life_Testing_Reference.pdf

[130] (2011, 08 August). *What is HIPOT Testing (Dielectric Strength Test)?* [Online]. Available: http://electrical-engineering-portal.com/what-is-hipot-testing-dielectric-strength-test

[131] (2013). *SKF Static Motor Analyzer User Manual* [Online].

[132] S. Grzybowski, S. Bandaru, N. Kota, and C. F. King, "Lifetime characteristics of magnet wires under pulse voltage [wire insulation multistress effects]," in *Electrical Insulation and Dielectric Phenomena, 2004. CEIDP'04. 2004 Annual Report Conference on*, 2004, pp. 145-148.

[133] "Magnetemp® CA-200," ed: Superior Essec Inc., 2010.

[134] "DuPont™ Kapton® Polyimide Films -Summary of Properties," ed: DuPont, 2017.

[135] G. Elert. (2016, 28/09/2017). *Dielectric Strength of Air* [Online]. Available: https://hypertextbook.com/facts/2000/AliceHong.shtml

[136] "DuPont™ Nomex® Paper Type 410 - Technical Data Sheet," ed. U.S.A.: DuPont, 2008.

[137] (2017, 05/12/2017). Minitab 17.0 Support. Available: https://support.minitab.com/en-us/minitab/18/help-and-how-to/modeling-statistics/reliability/how-to/accelerated-life-testing/before-you-start/overview/

[138] A. International, "Standard Test Method for Thermal Endurance of Film-Insulated Round Magnet Wire D2307," ed. West Conshohocken, PA, United States: ASTM International, 2013.

[139] R. Beeckman. 04/11/2017). NEMA Magnet Wire Thermal Class Ratings. [Manual].

[140] A. Boglietti, A. Cavagnino, and D. A. Staton, "TEFC induction motors thermal models: A parameter sensitivity analysis," *IEEE Transactions on Industry Applications*, vol. 41, pp. 756-763, 2005.

[141] A. Boglietti, A. Cavagnino, M. Pastorelli, D. Staton, and A. Vagati, "Thermal analysis of induction and synchronous reluctance motors," *IEEE Transactions on Industry Applications*, vol. 42, pp. 675-680, 2006.

[142] R. Wrobel, P. Mellor, and D. Holliday, "Thermal analysis of a segmented stator winding design," in *Energy Conversion Congress and Exposition (ECCE), 2010 IEEE*, 2010, pp. 1290-1297.

[143] A. Boglietti, M. Cossale, S. Vaschetto, and T. Dutra, "Experimental validation in operative conditions of winding thermal model for short-time transient," in *Energy Conversion Congress and Exposition (ECCE), 2016 IEEE*, 2016, pp. 1-6.

[144] A. Boglietti, E. Carpaneto, M. Cossale, and A. L. Borlera, "Stator thermal model for short-time thermal transients," in *Electrical Machines (ICEM), 2014 International Conference on*, 2014, pp. 1415-1421.

[145] D. Staton, A. Boglietti, and A. Cavagnino, "Solving the more difficult aspects of electric motor thermal analysis in small and medium size industrial induction motors," *IEEE Transactions on Energy Conversion*, vol. 20, pp. 620-628, 2005.

[146] W. L. Soong, "Thermal analysis of electrical machines: Lumped-circuit," *FE Analysis and Testing, Power Engineering Briefing Note Series, PEBN 6*, pp. 21-22, 2008.

[147] G. O. S. Ross. (2003, October 28). *Dependent Voltage and Current Sources, Lecture Notes by S. Ross and G. Oldham*. Available: inst.eecs.berkeley.edu/~ee40/sp03/lectures/student7_2003.pdf

[148] A. Sudhakar. (2015, October 27). *Trans-resistance amplifier and trans-conductance amplifier* Available: www.globalspec.com/reference/67831/203279/4-6-transresistance-amplifier-and-transconductance-amplifier

[149] F. Qi, A. Stippich, M. Guettler, M. Neubert, and R. W. De Doncker, "Methodical considerations for setting up space-resolved lumped-parameter thermal models for electrical machines," in *Electrical Machines and Systems (ICEMS), 2014 17th International Conference on*, 2014, pp. 651-657.

[150] S. Wang, M. Tambraparni, J. Qiu, J. Tipton, and D. Dean, "Thermal expansion of graphene composites," *Macromolecules,* vol. 42, pp. 5251-5255, 2009.

[151] (2017, 22th April). *Steady State Conduction - The Plane Wall*. Available: http://www.cdeep.iitb.ac.in/webpage_data/nptel/Mechanical/Heat%20and%20Mass%20Transfer/Conduction/Module%202/main/2.6.1.html

[152] P. Ravi. (2017, 22th April). *Heat transfer across Plane wall*. Available: https://mathtab.com/app_id=3746

[153] M. Bahrami, "Natural Convection Heat Transfer," ed. Canada: Simon Fraser University, 2011.

[154] S. W. Churchill and H. H. S. Chu, "Correlating equations for laminar and turbulent free convection from a vertical plate," *International journal of heat and mass transfer,* vol. 18, pp. 1323-1329, 1975.

[155] S. W. Churchill and H. H. S. Chu, "Correlating equations for laminar and turbulent free convection from a horizontal cylinder," *International journal of heat and mass transfer,* vol. 18, pp. 1049-1053, 1975.

[156] E. Radziemska and W. M. Lewandowski, "Heat transfer by natural convection from an isothermal downward-facing round plate in unlimited space," *Applied Energy,* vol. 68, pp. 347-366, 2001.

[157] J. R. Lloyd and W. R. Moran, "Natural Convection Adjacent to Horizontal Surface of Various Planforms," *Journal of Heat Transfer,* vol. 96, pp. 443-447, 1974.

[158] G. D. Demetriades, H. Z. De La Parra, E. Andersson, and H. Olsson, "A real-time thermal model of a permanent-magnet synchronous motor," *IEEE Transactions on Power Electronics,* vol. 25, pp. 463-474, 2010.

[159] J. Lindstom, "Thermal model of a permanent magnet motor for a hybrid electric vehicle," Ph.D. Thesis, Dept. Power Eng., Chalmers Univ. Technol., Goteborg-Sweden, 1999.

[160] G. Kylander, "Thermal modelling of small cage induction motors," Ph.D. dissertation, School of Electr. Comput. Eng., Chalmers Univ. Technol., Goteborg, Sweden, 1995.

[161] "Ansys Thermal Analysis Training Manual," ed, 2005.

[162] M. Markovic, L. Saunders, and Y. Perriard, "Determination of the thermal convection coefficient for a small electric motor," in *Industry Applications Conference, 2006. 41st IAS Annual Meeting. Conference Record of the 2006 IEEE,* 2006, pp. 58-61.

[163] (2017, 26th of April). *Emissivity values for common materials*. Available: http://www.infrared-thermography.com/material-1.htm

[164] M. A. Bramson, "Infrared radiation," 1968.

APPENDIX A: Integrated Starter Generator Performance Parameters

A.1 18 Slot / 10 Pole SPM ISG Machine Parameters

Table A.1 Main parameters of the optimized 18 slot / 10 pole SPM ISG

Shaft diameter	150 mm
Stator outer diameter	290 mm
Stator inner diameter	196.122 mm
Active stack length	40 mm
Rotor outer diameter	194.122 mm
Rotor inner diameter	150 mm
Air gap length	1 mm
Magnet pole pitch	0.819
Magnet thickness	4.104 mm
Tooth width	23.2 mm
Tooth tip thickness	4.551 mm
Slot opening	5.869 mm
Stator yoke thickness	16.6 mm
Slot area	426 mm^2
ISG mass without shaft	14.33 kg

A.2 18 Slot / 10 Pole SPM ISG Performance Parameters

Table A.2 18 slot-10 pole SPM ISG Performance Parameters

1500 rpm Generator Mode ($Efficiency_{min}$ = 93%)		
Winding:		
Number of phase	3	–
Slot fill factor	0.45	–
Number of turns	19	–
Number of parallel paths	1	–
Conductor diameter	2.53	mm
Current density	6.38	A_{rms}/mm^2
Phase current (rms)	32.17	A_{rms}
Electrical frequency	125	Hz
3-phase winding resistance	0.221	Ω
Torque:		

Mean torque	50.84	$N.m$
Torque ripple	5.056	% (in per cent)
Cogging torque (peak to peak)	1.8	$N.m$
Loss:		
Copper loss (DC) including end windings	229.01	$Watt$
Magnet ohmic loss	135.2	$Watt$
Stator hysteresis + eddy current loss	69.44	$Watt$
Rotor hysteresis + eddy current loss	0.35	$Watt$
Efficiency (windage + friction omitted)	94.56	%
2000 rpm Generator Mode		
Phase current (rms)	69.3	A_{rms}
Current density	13.7	A_{rms}/mm^2
Mean Torque	105.6	$N.m$
Torque ripple	3.26	%
Electrical frequency	166.667	Hz
Maximum continuous output power	22202.14	$Watt$
Peak phase voltage at load	202.8	$Volt$
DC Bus Voltage	350	$Volt$
200 rpm Motor Mode 180 Nm for 10 sec		
Phase current (rms)	128.69	A_{rms}
Current density	25.5	A_{rms}/mm^2
Average torque	181.1	$N.m$
Electrical frequency	16.6667	Hz
Multi-objective Optimization Function		
Magnet mass ($\lambda_1 = 0.3$)	0.893	kg
Torque ripple ($\lambda_2 = 0.3$)	5.05	%
Active length machine loss ($\lambda_3 = 0.4$)	331.48	$Watt$
$F(z)_{obj} \mid \ 0 < \{F_{obj}\} \leq 1$	0.3583	$p.u$

A.3 18 Slot / 10 Pole I-SHAPE PM ISG Machine Parameters

Table A.3 Main machine parameters for 18 slot -10 pole I-shape buried PM ISG

Shaft diameter	150 mm
Stator outer diameter	290 mm
Stator inner diameter	194 mm
Active stack length	40 mm
Rotor outer diameter	192 mm
Rotor inner diameter	150 mm
Air gap length	1 mm
Magnet pole pitch	0.77
Magnet thickness	4.802 mm

Tooth width	23.2 mm
Tooth tip thickness	4.5 mm
Slot opening	5.86 mm
Stator yoke thickness	16.6 mm
Slot area	440 mm^2
ISG mass without shaft	14.48 kg

A.4 18 Slot / 10 Pole I-SHAPE PM ISG Performance Parameters

Table A.4 18 slot-10 pole buried I-shape PM ISG Performance Parameters

1500 rpm Generator Mode ($Efficiency_{min}$ = 93%)		
Winding:		
Number of phase	3	–
Slot fill factor	0.45	–
Number of turns	20	–
Number of parallel paths	1	–
Conductor diameter	2.51	mm
Current density	6.81	A_{rms}/mm^2
Phase current (rms)	33.72	A_{rms}
Electrical frequency	125	Hz
3-phase winding resistance	0.237	Ω
Torque:		
Mean torque	50.02	$N.m$
Torque ripple	4.94	% (in per cent)
Cogging torque (peak to peak)	0.51	$N.m$
Loss:		
Copper loss (DC) including end windings	270	$Watt$
Magnet ohmic loss	65.48	$Watt$
Stator hysteresis + eddy current loss	67.75	$Watt$
Rotor hysteresis + eddy current loss	7.6	$Watt$
Efficiency (windage + friction omitted)	94.77	%
2000 rpm Generator Mode		
Phase current (rms)	73.18	A_{rms}
Current density	14.78	A_{rms}/mm^2
Mean Torque	105.33	$N.m$
Torque ripple	3.54	%
Electrical frequency	166.667	Hz
Maximum continuous output power	22300	$Watt$
Peak phase voltage at load	208.8	$Volt$
DC Bus Voltage	350	$Volt$
200 rpm Motor Mode 180 Nm for 10 sec		
Phase current (rms)	149.9	A_{rms}
Current density	30.28	A_{rms}/mm^2

Average torque	180	$N.m$
Electrical frequency	16.667	Hz
Multi-objective Optimization Function		
Magnet mass ($\lambda_1 = 0.3$)	0.641	kg
Torque ripple ($\lambda_2 = 0.3$)	4.94	%
Active length machine loss ($\lambda_3 = 0.4$)	289.97	$Watt$
$F(z)_{obj} \mid \ 0 < \{F_{obj}\} \leq 1$	0.3044	$p.u$

A.5 18 Slot / 10 Pole V-SHAPE PM ISG Machine Parameters

Table A.5 Main machine parameters for 18 slot -10 pole V-shape PM ISG

Stator outer diameter	290 mm
Stator inner diameter	194 mm
Active stack length	40 mm
Rotor outer diameter	192 mm
Rotor inner diameter	150 mm
Distance of V angle from the centre	84.34 mm
V angle	145.76°
Magnetic bridge thickness	1.15 mm
Magnet thickness	4.42 mm
Tooth width	23.2 mm
Tooth tip thickness	4 mm
Slot opening	7 mm
Stator yoke thickness	16.2 mm
Slot area	462 mm^2
ISG mass without shaft	14.53 kg

A.6 18 Slot / 10 Pole V-SHAPE PM ISG Performance Parameters

Table A.6 18 slot-10 pole interior V-shape PM ISG Performance Parameters

1500 rpm Generator Mode ($Efficiency_{min} = 93\%$)
Winding:

Number of phase	3	–
Slot fill factor	0.45	–
Number of turns	19	–
Number of parallel paths	1	–
Conductor diameter	2.63	mm
Current density	6.6	A_{rms}/mm^2
Phase current (rms)	36.18	A_{rms}
Electrical frequency	125	Hz
3-phase winding resistance	0.204	Ω
Torque:		
Mean torque	50.3	$N.m$
Torque ripple	3.35	% (in per cent)
Cogging torque (peak to peak)	0.86	$N.m$
Loss:		
Copper loss (DC) including end windings	266.8	$Watt$
Magnet ohmic loss	24.16	$Watt$
Stator hysteresis + eddy current loss	71.34	$Watt$
Rotor hysteresis + eddy current loss	10.23	$Watt$
Efficiency (windage + friction omitted)	95.29	%
2000 rpm Generator Mode		
Phase current (rms)	72.24	A_{rms}
Current density	13.57	A_{rms}/mm^2
Mean Torque	105.5	$N.m$
Torque ripple	5.6	%
Electrical frequency	166.667	Hz
Maximum continuous output power	23200	$Watt$
Peak phase voltage at load	201.8	$Volt$
DC Bus Voltage	350	$Volt$
200 rpm Motor Mode 180 Nm for 10 sec		
Phase current (rms)	148.4	A_{rms}
Current density	27.1	A_{rms}/mm^2
Average torque	180.5	$N.m$
Electrical frequency	16.667	Hz
Multi-objective Optimization Function		
Magnet mass ($\lambda_1 = 0.3$)	0.643	kg
Torque ripple ($\lambda_2 = 0.3$)	3.35	%
Active length machine loss ($\lambda_3 = 0.4$)	253.14	$Watt$
$F(z)_{obj} \mid \ 0 < \{F_{obj}\} \leq 1$	0.2535	$p.u$

A.7 21 Slot / 16 Pole SPM ISG Machine Parameters

Table A.7 The main machine parameters for 21 slot -16 pole SPM ISG

Shaft diameter	150 mm
Stator outer diameter	290 mm

Stator inner diameter	200.7 mm
Active stack length	40 mm
Rotor outer diameter	198.7 mm
Rotor inner diameter	150 mm
Air gap length	1 mm
Magnet pole pitch	0.8
Magnet thickness	3.35 mm
Tooth width	20 mm
Tooth shoe thickness	5 mm
Slot opening	5 mm
Stator yoke thickness	15 mm
Slot area	388 mm^2
ISG mass without shaft	14.23 kg

A.8 21 Slot / 16 Pole SPM ISG Performance Parameters

Table A.8 21 slot-16 pole SPM ISG Performance Parameters

1500 rpm Generator Mode ($Efficiency_{min}$ = 93%)		
Winding:		
Number of phase	3	–
Slot fill factor	0.45	–
Number of turns	13	–
Number of parallel paths	1	–
Conductor diameter	2.85	mm
Current density	5.4	A_{rms}/mm^2
Phase current (rms)	34.5	A_{rms}
Electrical frequency	200	Hz
3-phase winding resistance	0.133	Ω
Torque:		
Mean torque	50.6	$N.m$
Torque ripple	1.24	% (in per cent)
Cogging torque (peak to peak)	0.2	$N.m$
Loss:		
Copper loss (DC) including end windings	158.9	$Watt$
Magnet ohmic loss	150.3	$Watt$
Stator hysteresis + eddy current loss	79	$Watt$
Rotor hysteresis + eddy current loss	0.66	$Watt$

Efficiency (windage + friction omitted)	95.11	%
2000 rpm Generator Mode		
Phase current (rms)	72.24	A_{rms}
Current density	11.6	A_{rms}/mm^2
Mean Torque	105.4	$N.m$
Torque ripple	1.77	%
Electrical frequency	266.667	Hz
Maximum continuous output power (time averaged)	23300	$Watt$
Peak phase voltage at load	207.4	$Volt$
DC Bus Voltage	350	$Volt$
200 rpm Motor Mode 180 Nm for 10 sec		
Phase current (rms)	196.5	A_{rms}
Current density	21.7	A_{rms}/mm^2
Average torque	179.9	$N.m$
Electrical frequency	26.667	Hz
Multi-objective Optimization Function		
Magnet mass ($\lambda_1 = 0.3$)	0.607	kg
Torque ripple ($\lambda_2 = 0.3$)	1.242	%
Active length machine loss ($\lambda_3 = 0.4$)	321.89	$Watt$
$F(z)_{obj} \mid \ 0 < \{F_{obj}\} \leq 1$	0.2131	$p.u$

A.9 21 Slot / 16 Pole I-SHAPE PM ISG Performance Parameters

Table A.9 21 slot-16 pole interior I-shape PM ISG Performance Parameters

1500 rpm Generator Mode ($Efficiency_{min} = 93\%$)		
Winding:		
Number of phase	3	–
Slot fill factor	0.45	–
Number of turns	13	–
Number of parallel paths	1	–
Conductor diameter	2.85	mm
Current density	6	A_{rms}/mm^2
Phase current (rms)	39	A_{rms}
Electrical frequency	200	Hz
3-phase winding resistance	0.132	Ω
Torque:		
Mean torque	50.4	$N.m$
Torque ripple	2.94	% (in per cent)
Cogging torque (peak to peak)	0.065	$N.m$
Loss:		
Copper loss (DC) including end windings	202.5	$Watt$
Magnet ohmic loss	70.99	$Watt$
Stator hysteresis + eddy current loss	74.88	$Watt$
Rotor hysteresis + eddy current loss	9.47	$Watt$
Efficiency (windage + friction omitted)	95.48	%

2000 rpm Generator Mode		
Phase current (rms)	81.31	A_{rms}
Current density	12.7	A_{rms}/mm^2
Mean Torque	105.9	$N.m$
Torque ripple	2.97	%
Electrical frequency	266.667	Hz
Maximum continuous output power (time averaged)	21900	$Watt$
Peak phase voltage at load	197	$Volt$
DC Bus Voltage	350	$Volt$
200 rpm Motor Mode 180 Nm for 10 sec		
Phase current (rms)	160	A_{rms}
Current density	24.9	A_{rms}/mm^2
Average torque	180.1	$N.m$
Electrical frequency	26.667	Hz
Multi-objective Optimization Function		
Magnet mass ($\lambda_1 = 0.3$)	0.697	kg
Torque ripple ($\lambda_2 = 0.3$)	2.944	%
Active length machine loss ($\lambda_3 = 0.4$)	272.42	$Watt$
$F(z)_{obj} \mid \ 0 < \{F_{obj}\} \leq 1$	0.2585	$p.u$

A.10 21 Slot / 16 Pole V-SHAPE PM ISG Machine Parameters

Table A.10 The main machine parameters for 21 slot -16 pole V-shape PM ISG

Stator outer diameter	290 mm
Stator inner diameter	200.7 mm
Active stack length	40 mm
Rotor outer diameter	198.7 mm
Rotor inner diameter	150 mm
Distance of V angle from the centre	84.25 mm
V angle	130°
Magnetic bridge thickness	1.127 mm
Magnet thickness	4 mm
Tooth width	19.5 mm
Tooth tip thickness	2.5 mm
Slot opening	7 mm

Stator yoke thickness	15 mm
Slot area	388 mm^2
ISG mass without shaft	14.16 kg

A.11 21 Slot / 16 Pole V-SHAPE PM ISG Performance Parameters

Table A.11 21 slot-16 pole interior V-shape PM ISG Performance Parameters

1500 rpm Generator Mode ($Efficiency_{min}$ = 93%)		
Winding:		
Number of phase	3	–
Slot fill factor	0.45	–
Number of turns	13	–
Number of parallel paths	1	–
Conductor diameter	2.92	mm
Current density	5	A_{rms}/mm^2
Phase current (rms)	33.9	A_{rms}
Electrical frequency	200	Hz
3-phase winding resistance	0.125	Ω
Torque:		
Mean torque	50.5	$N.m$
Torque ripple	2.3	% (in per cent)
Cogging torque (peak to peak)	0.066	$N.m$
Loss:		
Copper loss (DC) including end windings	151.3	$Watt$
Magnet ohmic loss	23.38	$Watt$
Stator hysteresis + eddy current loss	82	$Watt$
Rotor hysteresis + eddy current loss	10.46	$Watt$
Efficiency (windage + friction omitted)	96.71	%
2000 rpm Generator Mode		
Phase current (rms)	70.49	A_{rms}
Current density	10.5	A_{rms}/mm^2
Mean Torque	105.4	$N.m$
Torque ripple	3.83	%
Electrical frequency	266.667	Hz
Maximum continuous output power (time averaged)	22900	$Watt$
Peak phase voltage at load	210.4	$Volt$
DC Bus Voltage	350	$Volt$
200 rpm Motor Mode 180 Nm for 10 sec		
Phase current (rms)	135.7	A_{rms}
Current density	20.2	A_{rms}/mm^2
Average torque	180	$N.m$
Electrical frequency	26.667	Hz
Multi-objective Optimization Function		

Magnet mass ($\lambda_1 = 0.3$)	0.710	kg
Torque ripple ($\lambda_2 = 0.3$)	2.309	%
Active length machine loss ($\lambda_3 = 0.4$)	211.074	$Watt$
$F(z)_{obj} \mid \ 0 < \{F_{obj}\} \leq 1$	0.2293	$p.u$

A.12 Mechanical Properties of Thin Non-Oriented NO18 Electrical Steel

Table A.12 Mechanical properties of NO18 for FEA Stress Analysis

Nominal thickness	0.178	mm
Density	7.65	g/cm^3
Yield Strength	370	N/mm^2
Tensile Strength	450	N/mm^2
Young's Modulus	185,000	N/mm^2
Hardness	180	HV5

APPENDIX B: Heat Transfer in Electrical Machines

B.1 Introduction

Heat transfer by natural convection is significant when there is no dedicated cooling instruments such as totally enclosed fan cooling or liquid cooling for electrical machines. Natural convection heat transfer coefficients can be calculated by using empirical formulations which are usually dependent upon fluid (i.e. air) characteristics and the dimensions of the physical object.

Heat transfer basics and estimation of heat transfer coefficients are discussed here.

B.2 Heat Transfer in Electric Machines

There are two major thermal aspects of any electrical machines: heat removal and temperature distribution within the motor. Temperature distribution around a machine is basically a heat transfer problem and it is often difficult to analyse precisely because of three dimensional effect of heat transfer, uncertainty of thermal contact resistance between separate bodies and uncertainty of material thermal behaviour etc. Accuracy of a thermal analysis based on accuracy of thermal resistance calculations and determination of heat transfer coefficients. Therefore, heat transfer coefficients and crucial thermal parameters of electrical machines should be chosen as accurately as possible.

B.3 Heat Removal

The heat is removed by conduction, convection and radiation in electrical machines. Fundamental mechanisms of heat removal are discussed in this section.

B.3.1 Heat removal by Conduction

Heat transfer by conduction can be achieved by molecular interaction at a higher energy level or free electrons which is the case for metals as they have a higher number of free electrons [120]. Heat transfer by conduction is possible between solids, liquids and gases. Since pure metals are the best heat conductors, heat is usually transferred by conduction in metals.

As shown in Figure B.1, one-dimensional, steady state conduction in a plane wall with no heat generation and constant thermal conductivity, the temperature varies linearly with x [151]. However, constant thermal conductivity is not the case for anisotropic plane wall in which conductivity varies due to material anisotropy. Thermal conductivity also depends on the temperature. Typically, thermal conductivity decreases as the temperature increases for metals. On the other hand, heat transfer rate increases for the insulation materials such as thermosetting insulation films, magnet wire coatings etc. when the temperature rises [120].

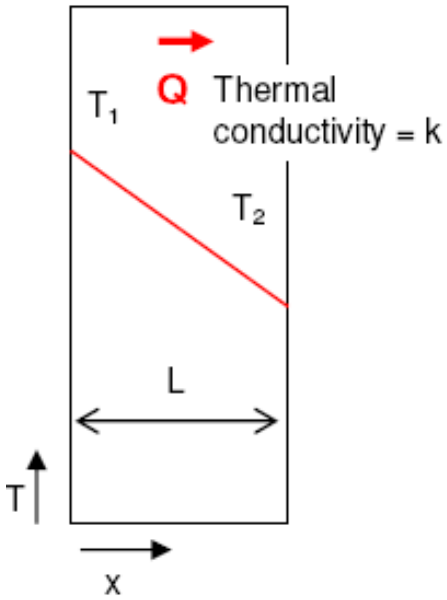

Figure B.1 Heat transfer through a plane wall with constant thermal conductivity [152]

$$Q = -k\frac{\partial T}{\partial X} = -k\left[\frac{T_{x=l} - T_{x=0}}{l}\right] \tag{B.1}$$

In equation (B.1), one dimensional steady state Fourier law of heat conduction is given. This equation demonstrates that thermal conductivity is dependent on heat flux density, Q (W/m^2) and gradient of the temperature $(\partial T/\partial X)$ between the boundary conditions along the direction of heat flow. In (B.1), k stands for thermal conductivity, $Wm^{-1}{}^{\circ}C^{-1}$. By using the analogy between the electrical circuit and thermal circuit, equivalent thermal resistance network can be obtained using the thermal resistance equation as given in equation (B.2).

$$R_{th,cond} = \frac{T_1 - T_2}{q_x} = \frac{L}{kA} \tag{B.2}$$

Composite walls can be characterized by series-parallel thermal resistance configurations. For example, if heat flows only in x-axis, thermal resistances along the x-axis should be connected in series. On the other hand, if there is more than one thermal paths along the direction of heat flow, they will be connected in parallel on the direction of heat flow. This states that different composite material configurations can be modelled using series and parallel thermal resistance network which in turn helps find temperature on pre-determined nodes. Hence, effective thermal conductivity of any anisotropic geometry can be theoretically predicted.

B.3.2 Mechanism of Heat Transfer By Convection

Convection is a heat transfer process due to fluid motion. In natural convection, the fluid motion occurs by natural means such as buoyancy [153]. As the velocity of fluid is low in natural convection, the associated heat transfer coefficients with natural convection is also low.

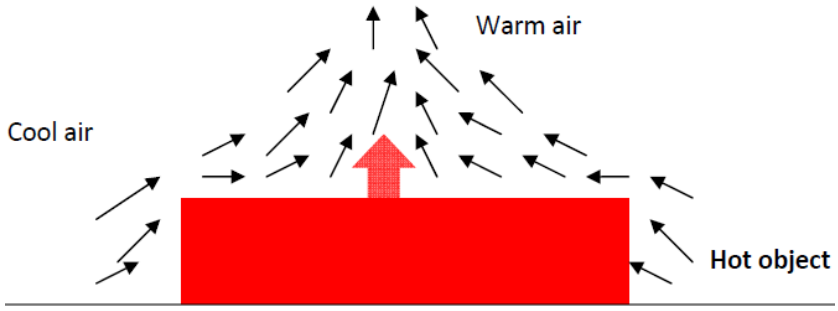

Figure B.2 Natural convection from a hot body [153]

The mechanism of heat transfer by convection is explained using Figure B.2 above. The hot object is surrounded with thin layer of warm air and heat will be transferred from this layer to outer layers of air. Thus, temperature of the object will drop as a result of heat transfer with cold air surrounded by the object. Since the hot air has lower density than the cold air, heated air with lower density around the object rises. In a gravitational field, there is a buoyancy force that pushes a light fluid upwards in a heavier fluid. The magnitude of the buoyancy force is the weight of fluid displaced by a body or heavier fluid. The net force, F_{net} in this case is written:

$$F_{net} = W - F_{buoyancy}$$
$$F_{net} = (\rho_{body} - \rho_{fluid})\, g\, V_{body} \quad \text{(B.3)}$$

where ρ, g and V_{body} stand for mass density, gravity of Earth and volume of body respectively. The net force is dependent on difference in densities of the fluid and body. This equation in fact represents Archimedes' principle. The important thing in equation (B.3), buoyancy force always needs the gravity field. For this reason, the buoyancy effects does not exist in space demonstrating that heat transfer by convection cannot occur in electrical machines in aerospace (i.e deep space) applications. In this case, heat transfer by radiation is an important heat transfer process for cooling.

Since density is a function of temperature and the buoyancy force is proportional to mass density difference between the fluid and the body, the larger buoyancy forces will occur at larger temperature differences between the solid and fluid [153].

A frictional force due to contact between the solid object and fluid is developed at steady state. This is called viscous forces on the fluid. The ratio between the buoyancy forces to the viscous

forces acting on the fluid is defined as dimensionless Grashof (Gr) number as expressed in equation (B.4) [122].

$$Gr = \frac{buoyancy\ forces}{viscous\ forces} = \frac{g\beta\Delta TV}{\rho v} = \frac{g\beta(T_s - T_\infty)\delta^3}{v^2} \quad (B.4)$$

where

g = $gravitational\ acceleration\ , m/s^2$

β = $coefficient\ of\ volume\ expansion, 1/K$

δ = $characteristic\ length\ of\ the\ geometry\ , m$

v = $kinematic\ viscosity\ of\ the\ fluid, m^2/s$

ΔT = $temperature\ difference\ between\ surface\ and\ stream - air, °C$

ρ = $mass\ density\ of\ the\ fluid, kg/m^3$

Natural convection is usually based on experimental correlations. The Rayleigh number is defined as product of Grashof and Prandtl numbers. Prandtl number is defined as ratio of momentum diffusivity and thermal diffusivity as given in equation (B.5) [122].

$$Pr = \frac{viscous\ diffusion\ rate}{thermal\ diffusion\ rate} = \frac{C_p\mu}{k} \quad (B.5)$$

where C_p $(J/kg - °K)$, μ $(N\ s/m^2)$ and k $(Wm^{-1}°K^{-1})$ are specific heat, dynamic viscosity and thermal conductivity, respectively. Hence, Rayleigh number is in the form as given in equation (B.6):

$$Ra\ =\ GrPr = \frac{g\beta(T_s - T_\infty)\delta^3}{v^2} \times \frac{c_p\mu}{k} \quad (B.6)$$

The typical form of natural convection correlation is described by Nusselt number which is in the form [145]:

$$Nu = a(GrPr)^b = a\ (Ra)^b \quad (B.7)$$

The Nusselt number describes the relationship between convective heat transfer and conductive heat transfer. Therefore, Nusselt number might be also in the form [5, 122]:

$$Nu = \frac{h \times D_h}{k_{air}} \quad (B.8)$$

where h is the convection heat transfer coefficient, k_{air} is the thermal conductivity of air and D_h is the hydraulic diameter of the geometry or characteristic length of the surface.

Although the Nusselt number is a function of Rayleigh and Prandtl numbers for free convection, it is a function of Reynold (Re) and Prandtl numbers for forced convections. Thus, empirical correlations for Nu number are always written, if f denotes a function:

$$Nu = f(Ra, \Pr) \text{ ; natural convection}$$
$$Nu = f(Re, \Pr) \text{ ; forced convection} \quad \text{(B.9)}$$

Since natural convection is dependent on geometry of the surface and its orientation, convectional heat transfer estimations of a number of surfaces at different orientations in space have been conducted using empirical formulations. These empirical formulations are required for predicting heat transfer coefficients on machine external surfaces between the solid parts and stagnant air. They are presented as follows:

B.3.2.1 Natural convection on a Vertical Surface

A correlation might be applied over the entire range of Ra has been recommended by Churchill and Chu [154] and is of the form:

$$Nu = \frac{h\,L}{k} \;, \qquad \Pr = \frac{\mu\, C_p}{k} \quad \text{(B.10-B.11)}$$

Rayleigh number $$Ra = Gr\,Pr \quad \text{(B.12)}$$

Grashof number: $$Gr = \left[\frac{L^3 \rho^2 g \Delta T \beta}{\mu^2}\right] \quad \text{(B.13)}$$

Nusselt number: *(For all values of Rayleigh No)*

$$Nu = \left\{0.825 + \frac{0.387\, Ra^{\frac{1}{6}}}{\left[1 + \left(\frac{0.492}{Pr}\right)^{\frac{9}{16}}\right]^{\frac{8}{27}}}\right\}^2 \quad \text{(B.14)}$$

For laminar flow:

$$Nu = \left\{0.68 + \frac{0.670\, Ra^{\frac{1}{4}}}{\left[1 + \left(\frac{0.492}{Pr}\right)^{\frac{9}{16}}\right]^{\frac{4}{9}}}\right\} \quad \text{(B.15)}$$

Film Temperature: $$T_f = (T_\infty + T_w)/2 \quad \text{(B.16)}$$

Equation (B.15) gives slightly better accuracy if the flow is laminar on the surface. Nevertheless, equation (B.14) is suitable for most of engineering calculations when convectional heat transfer coefficient is estimated for a vertical plate. Air properties if the fluid

is assumed to be air is also given in Table B.1 required for the estimation of Nu and Ra numbers.

Table B.1 Air properties

Temperature difference:	ΔT	$°C$	
Height of surface:	L	m	
Fluid density:	ρ	1.1	kg/m^3
Fluid viscosity:	μ	1.87×10^{-5}	Ns/m^2
Fluid specific heat:	C_p	1	$J/g°K$
Fluid thermal conductivity:	k	0.026	W/mK
Fluid Thermal Expansion coefficient:	β	0.003143	$°K^{-1}$
Fluid:	Air		

B.3.2.2 Natural convection on a Horizontal Cylinder

Ra and Nu numbers for isothermal horizontal cylinder is dependent on cylinder diameter. Churchill and Chu [155] have recommended a single correlation for a wide range of Ra number as given in equation (B.21). Note that D, (m) stands for cylinder diameter in equations (B.17) and (B.20).

$$Nu = \frac{h\,D}{k}\ , \qquad \Pr = \frac{\mu\,C_p}{k} \tag{B.17-B.18}$$

$$Ra = Gr\ Pr \tag{B.19}$$

Grashof Number:

$$Gr = \left[\frac{D^3\rho^2 g\Delta T\beta}{\mu^2}\right] \tag{B.20}$$

Nusselt Number:
(For all values of Rayleigh No)

$$Nu = \left\{0.6 + \frac{0.387\ Ra^{\frac{1}{6}}}{\left[1 + \left(\frac{0.559}{Pr}\right)^{\frac{9}{16}}\right]^{\frac{8}{27}}}\right\}^2 \tag{B.21}$$

For $Ra \leq 10^{12} => Ra = GrPr$

B.3.2.3 Natural convection on a Horizontal Plate

Nu and Ra numbers for horizontal plate might be estimated using equations (B.26) and (B.27) as proposed by [156, 157].

$$Nu = \frac{h\,L}{k}\ , \qquad \Pr = \frac{\mu\,C_p}{k} \tag{B.22-B.23}$$

$$Ra = Gr\ Pr \tag{B.24}$$

Grashof Number:

$$Gr = \left[\frac{L^3 \rho^2 g \Delta T \beta}{\mu^2}\right] \tag{B.25}$$

Upper surface of hot plate

$$Nu = 0.54\ Ra^{1/4} \quad (10^4 \leq Ra \leq 10^7)$$
$$Nu = 0.15\ Ra^{1/3} \quad (10^7 \leq Ra \leq 10^{11}) \tag{B.26}$$

Lower surface of hot plate

$$Nu = 0.27\ Ra^{1/4} \quad (10^5 \leq Ra \leq 10^{10}) \tag{B.27}$$

B.3.3 Heat Transfer Coefficients with respect to Film Temperature

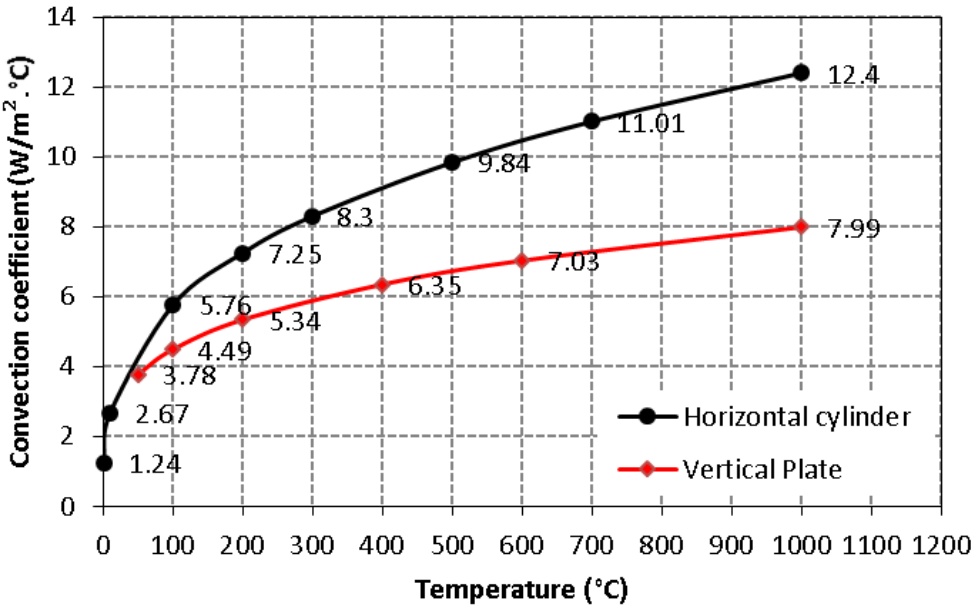

Figure B.3 Heat transfer coefficients as a function of film temperature

Natural convection heat transfer coefficients varying with respect to average film temperature for relatively small diameter cylinders and vertical plates is plotted in Figure B.3 which might

be used in transient thermal FEA simulations for horizontally placed relatively small electric machines.

B.3.4 Convection Heat Transfer Coefficients

The heat transfer rate, q $(Watt)$ when convection occurs is described by:

$$q = h\,A\,(T_s - T_\infty) \tag{B.28}$$

Where T_s is the temperature of the object and T_∞ is the temperature of the fluid. A is the surface area and h $(W/m^2.°C)$ is convection heat transfer coefficient. The thermal resistance for convection is defined as:

$$R_{th} = \frac{1}{Ah} \tag{B.29}$$

Equation (B.29) is an important when electrical analogy of thermal lumped parameter modelling is considered. In the absence of external cooling, natural convection from external surfaces of electrical machines occurs and estimation of heat transfer coefficients becomes important for the accuracy of thermal modelling. Therefore, in the literature, convection heat transfer coefficients for machine end windings, airgap, rotor and internal air are proposed, based on empirical formulations, obtained after conducting thermal experiments. They are described as follows:

B.3.4.1 Machine airgap convection heat transfer coefficient

The convection heat transfer coefficient in the machine air gap depends on the characteristics of the flow. There are two types of fluid flow: laminar flow and turbulence flow. A turbulent air flow gives a higher heat transfer coefficient in comparison to laminar flow [158]. The modified Taylor number is used to calculate the value of Nu number which is written as:

$$\alpha_m = \frac{\omega^2 d_{stator\ bore}\delta^3}{2\vartheta^2} \tag{B.30}$$

where ω is the angular velocity, δ is the air gap length, ϑ is the kinematic viscosity of the air. Nu is given in the form:

$$Nu = \begin{cases} 2, & T\alpha_m < 1740 \\ 0.409\,T\alpha_m{}^{0.241} - 137\,T\alpha_m{}^{-0.75}, & T\alpha_m > 1740 \end{cases} \tag{B.31}$$

Using the equations (B.30) and (B.31), heat transfer coefficient, h_{airgap} is written:

$$h_{airgap} = \frac{Nu \times k_{air}}{2\delta} \tag{B.32}$$

B.3.4.2 End windings convection heat transfer coefficient

In the literature, a number of heat transfer coefficients for machine end windings have been proposed. However, the most popular equation for estimation of end windings heat transfer coefficient is given in equation (B.33) [159, 160].

$$h_{ew} = 6.5 + 5.25^{0.6} u_r{}^{0.6} \tag{B.33}$$

where u_r is rotor peripheral velocity. If the machine is stationary, the equation (B.33) simply gives 6.5 $W/m^2.°C$ heat transfer coefficient for machine end windings.

In addition to equation (B.33), Boglietti et al [36] proposes an equation for end winding convection coefficient as given in equation (B.34).

$$\begin{aligned} h_{ew} &= 15.5\ (0.29 v_i + 1) \\ v_i &= R_{ro} \omega \eta \end{aligned} \tag{B.34}$$

where R_{ro} rotor outer radius, ω is rotor angular speed and η stands for fan efficiency and usually assumed to be 0.5.

B.3.4.3 Rotor surface and internal air heat transfer coefficients

Rotor surface heat transfer coefficient and internal air convection coefficient in machine frame are given in equations (B.35) and (B.36), respectively. These equations are proposed in [158-160].

$$h_{rotor} = 16.5^{0.65} u_r{}^{0.65} \tag{B.35}$$

$$h_{internal} = 15.5 + 6.75^{0.65} u_r{}^{0.65} \tag{B.36}$$

B.3.5 Thermal contact and Interface gaps between components

The accuracy of motor temperature distribution is dependent on the estimate of many thermal resistances within the machine. A contact resistance is due to imperfections in the touching surfaces and is a complex function of material hardness, roughness, contact pressure and air pressure [145]. In Table B.2, interfacial thermal contact conductance between various materials are given.

Table B.2 Interfacial conductance and interface gaps of various materials [145]

Contact Interface	*Interfacial Conductance (W/m²/°C)*	*Effective Interface Gap(mm)*
Stainless Steel – Stainless Steel	1700-3700	0.0070-0.0153

Aluminium – Aluminium	2200-12000	0.0022-0.0012
Stainless Steel - Aluminium	3000-4500	0.0058-0.0087
Iron - Aluminium	4000-40000	0.00006-0.0060
Copper - Copper	10000-25000	0.0010-0.0026

As tabulated in Table B.2, interfacial thermal contact conductance values might be within a large range. As an example, thermal contact conductance between aluminium blocks might vary between 2200 -12000 W/m^2/°C showing that a thermal calibration process in thermal FEA modelling is required as thermal contact resistance between separate parts is crucial for the accuracy of temperature distribution around an electrical machine. The imperfect contact is illustrated in Figure B.4.

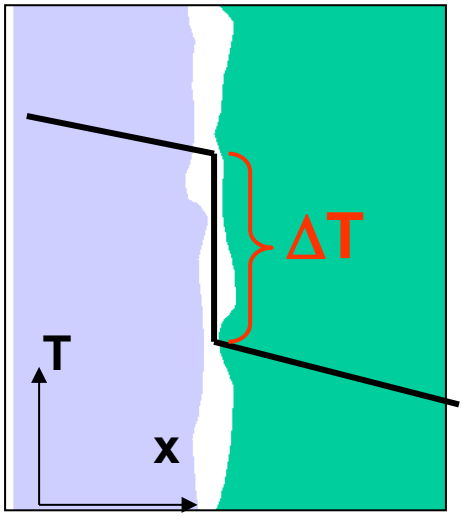

Figure B.4 Temperature drop due to imperfect contact interface [161]

In Ansys thermal packages, the software uses perfect thermal contact between parts, which means that no temperature drop is assumed at the contact interface. However, a finite thermal conductance value can be included during the thermal calibration process for better thermal accuracy. This is explained using the heat flow, q (W/m^2) equation in the thermal contact interface as given:

$$q = TCC\ (T_{Target} - T_{Contact}) \tag{B.37}$$

Where TCC stands for thermal contact conductance $W/m^2.K$, and T_{Target} is target surface temperature and $T_{Contact}$ is contact surface temperature in FEA. By default, TCC represents perfect conductance between parts but it can be manually altered for thermal calibration. Table B.2 gives an insight what could be the thermal contact conductance between the common metals

when thermal parameter estimation is required during thermal modelling of an electrical machine.

B.3.6 Heat removal by Radiation

Radiation from the external surfaces of electrical motors comprises a part of heat transfer or cooling. It can be theoretically incorporated with the natural convection on external surfaces. The surface heat density, q_r evacuated from a body surface when radiation occurs, is of the form [162]:

$$q_r = \varepsilon_c \sigma_c \left({T_s}^4 - {T_a}^4\right) \tag{B.38}$$

where, σ_c is Stefan-Boltzman constant $(5.67 \times 10^{-8} W/m^2/K^4)$ and ε_c is the emissivity coefficient which always takes values between 0 and 1, depending on the material and its colour. The emissivity coefficients, ε_c of various materials are given in Table B.3 [163, 164].

Table B.3 Emissivity of various materials [163, 164]

Material	Surface/Type/Colour	Emissivity, ε_c
Copper	Commercial	0.07
Aluminium	Polished	0.04-0.06
	Rough	0.06-0.07
Steel	Alloy (8%Ni, 18%Cr)	0.35
	Stainless, rolled	0.45
Cast iron	casting	0.81
Paper	black	0.90
Plastic	black	0.95
Thermoset polymer	dark	0.97

Heat removal by radiation has been excluded in thermal FEA investigations in later chapters as it is assumed to be not significant compared to natural convection. However, heat transfer by radiation has been used to measure temperature using an infrared camera (IR). IR imaging is useful to detect temperature on machine external surfaces and its operation principle is based on thermal radiation. The IR camera measures the passive infrared radiation emitted by the target surface and converts this radiation into two dimensional thermal image. In electrical machines external surfaces do not have to be of the same material. Machine housing and endcaps might be composed of different materials (i.e. metals in different colour/type or

roughness) and this makes thermal imaging difficult due to varying emissivity values. IR camera must be calibrated to a surface of unique material for which the emissivity is known.

B.4 Overview of Theoretical Estimation of Thermal Parameters

Obtaining accurate values of thermal resistances, natural convection heat transfer coefficients and thermal contact conductance between different bodies is challenging but they must be estimated as accurately as possible to predict temperature distribution around electrical machines. In the literature, there are many proposed analytical and empirical heat transfer coefficient formulations as described in Sections B.3.2, B.3.3 and B.3.4. Heat transfer coefficients might be predicted using the proposed Nusselt numbers for horizontal cylinder, vertical and horizontal plates. Nonetheless, air properties surrounding an electrical machine might be changing and heat transfer coefficients therefore are dependent on film temperatures. In other words, heat transfer coefficients cannot be a constant number and usually vary during thermal experiments. Uncertainty in thermal experiments is a challenge that should be mitigated by accurate calibration of an experiment to a thermal model.

To sum up, some important thermal parameters of electrical machines have been described below:

a) ***Stator end windings thermal resistance***

   Both convection to internal air and conduction to laminations or frame might occur. It is a complex but can be approximated.

b) ***Stator coils thermal resistance***

   This is difficult to estimate due to mixture of copper, wire enamel, impregnation and slot liner. An additional airgap exists between the slot liner and stator tooth sides. It is a function of slot fill factor and materials used for winding. It is one of the most important thermal parameter that should be estimated accurately as machine hot spot which is not desired regarding magnet wires life expectancy, usually occurs in the coils.

c) ***Laminations thermal resistance***

   Thermal conductivity of the lamination material must be known but material processing and punching might affect radial and axial thermal conductivity. The axial thermal conductivity usually 20 to 40 times larger than radial conductivity [146]. It might be also complex function of lamination stacking factor.

d) ***Stator yoke to frame thermal resistance***

   The effective interfacial gap between the stator yoke and frame can be significant and should be estimated via thermal calibration. The quality of contact and contact pressure can influence the thermal parameter in this case.

e) Machine airgap thermal resistance

The heat transfer depends on airflow between the stator and rotor. When the machine is stationary, air might be modelled as solid material with a certain thermal conductivity. Heat transfer by convection also occurs when the machine is running or stationary.

f) Frame to ambient thermal resistance

This is complex due to a mixture of natural and forced convection. Radiation might also be significant at some applications such as aerospace. The air properties surrounding the machine might affect thermal parameters significantly.

B.5 Natural Convection in Small Electrical Machines

Using the Nu numbers for a horizontal cylinder and vertical plate, the equivalent convection coefficient for a horizontally placed motor can be determined. The motor dimensions are shown in Figure B.5.

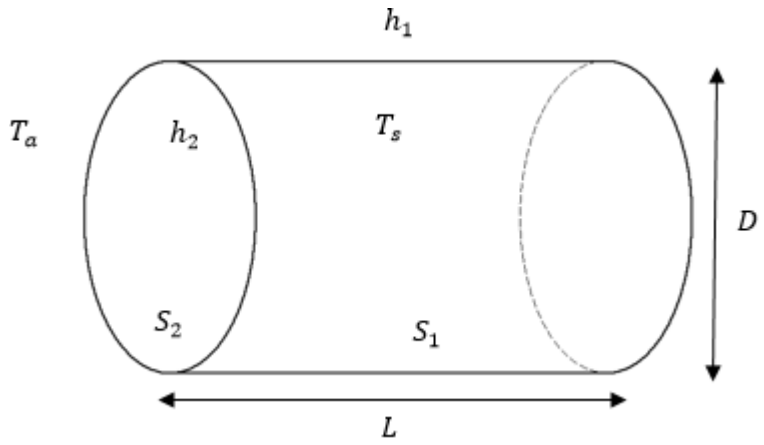

Figure B.5 Motor configuration

Convection from the surface S_1 is given:

$$h_1 = \frac{Nu_1 \times k}{D} \tag{B.39}$$

where k is fluid thermal conductivity and Nu_1 is equal to equation (B.21). Convection from surface S_2 is given:

$$h_2 = \frac{Nu_2 \times k}{H} \tag{B.40}$$

Where H is vertical plate height and it can be approximated from circular vertical surfaces as

$$H^2 = \frac{D^2\pi}{4} => H = 0.886D \tag{B.41}$$

Thermal resistances for surfaces S_1 and S_2 can be written:

$$R_1 = \frac{1}{h_1 S_1} = \frac{T_s - T_a}{P_1}, R_2 = \frac{1}{h_2 S_2} = \frac{T_s - T_a}{P_2} \quad and \; P = P_1 + 2P_2 \qquad \text{(B.42) - (B.43)}$$

where P is the total power evacuated from the external surfaces. The equivalent convection resistance is also written if equations (B.42), (B.43) and (B.44) are combined:

$$R_c = \frac{T_s - T_a}{P} => R_c = \frac{R_1 R_2}{2R_1 + R_2} \qquad \text{(B.44)}$$

Therefore, the equivalent convection coefficient for the motor surfaces, S given in Figure B.5 is of the form:

$$h_c = \frac{h_1 S_1 + 2h_2 S_2}{S} = \frac{2h_1 L + h_2 D}{2L + D} \qquad \text{(B.45)}$$

B.6 ISG Natural Convection Coefficients

Table B.4 Estimated heat transfer coefficients for the stationary ISG

Region	***HTCs when the ISG is stationary***
End windings	6.5 $W/m^2.°C$
Rotor cylindrical surface	As shown in Figure B.3
ISG vertical plane surfaces dependent on film temperature	As shown in Figure B.3
ISG horizontal plane surfaces dependent on film temperature	As shown in Figure B.3

APPENDIX C: Drawings

C.1 Pressing Tools Exploded View

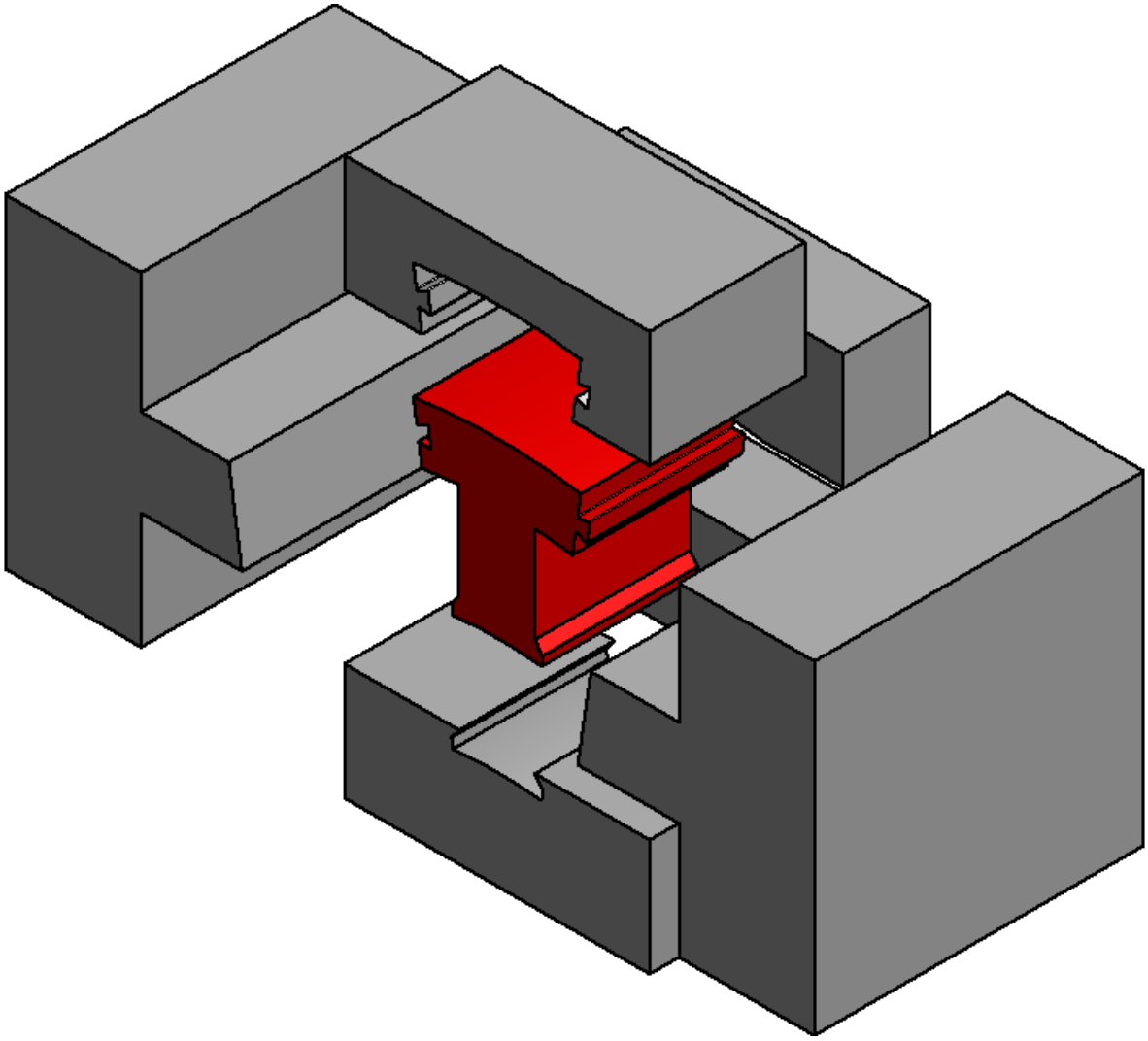

Figure C.1 Overview of the pressing tool for the ISG teeth

C.2 Segmented ISG Tooth Drawing

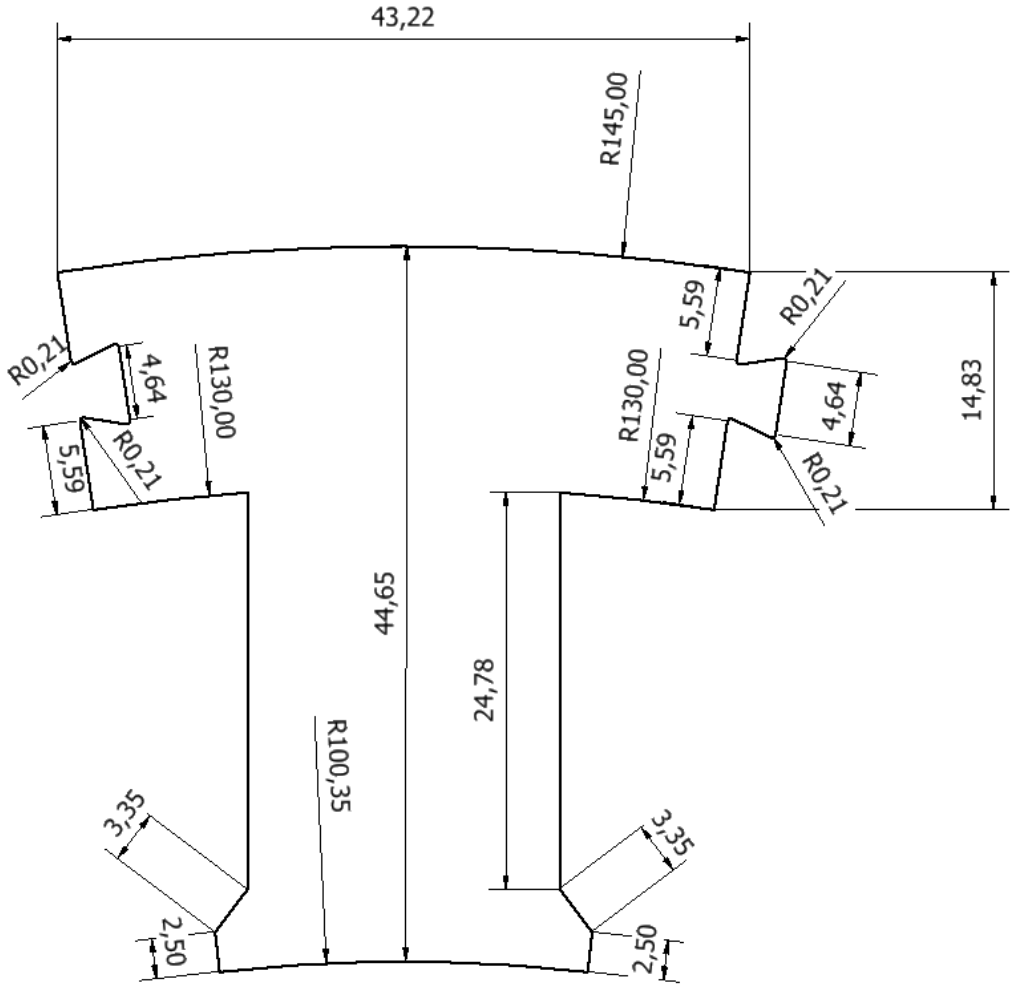

Figure C.2 Integrator starter generator segmented tooth dimensions

C.3 Female Tooth Fixing Drawings

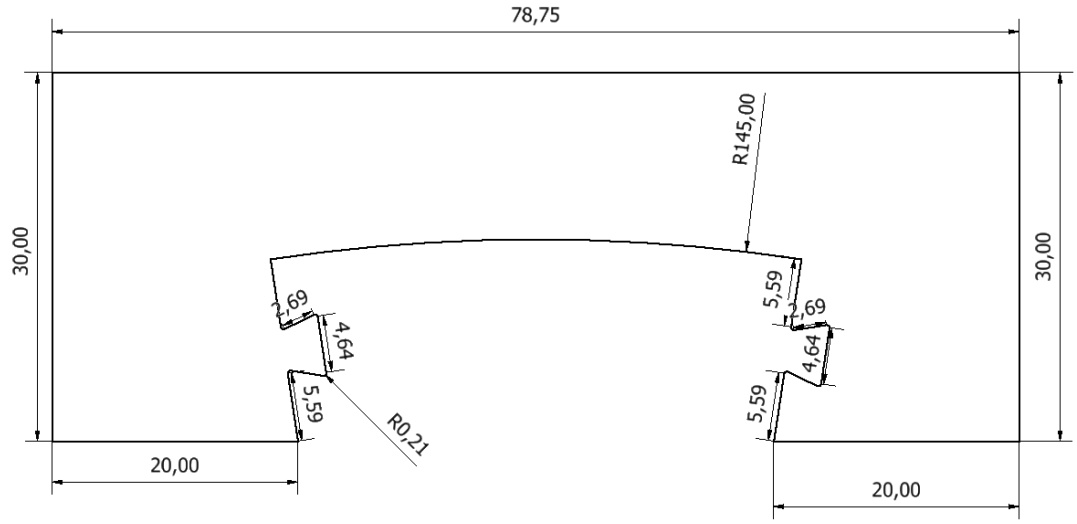

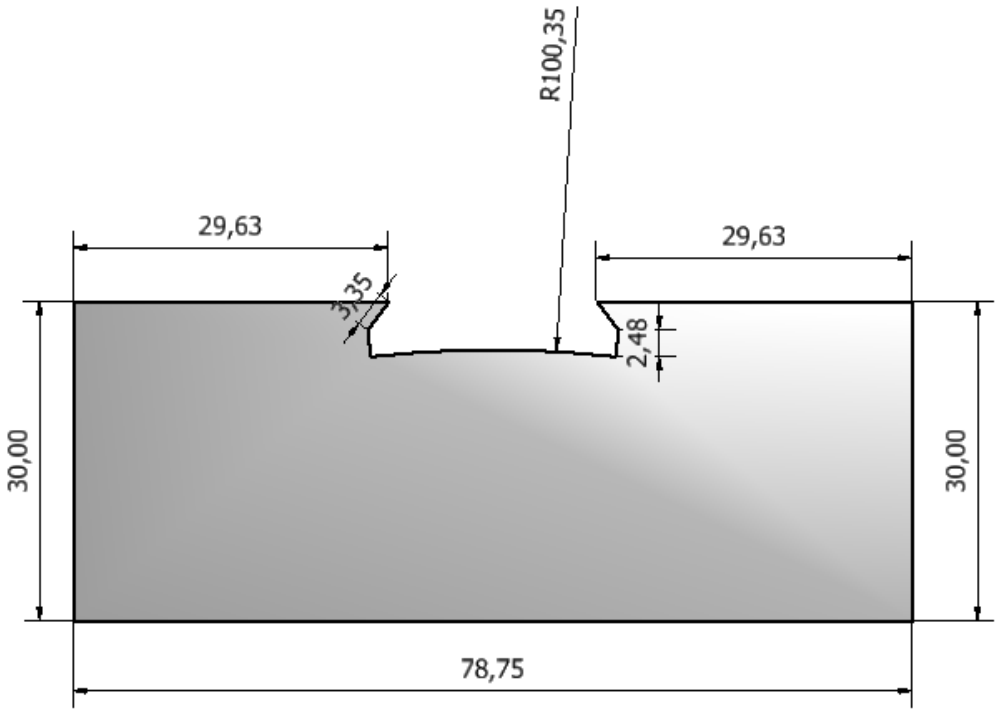

Figure C.3 Female supports of the ISG segmented tooth

C.4 Drawings of Top and Bottom Sides Fixing Plates

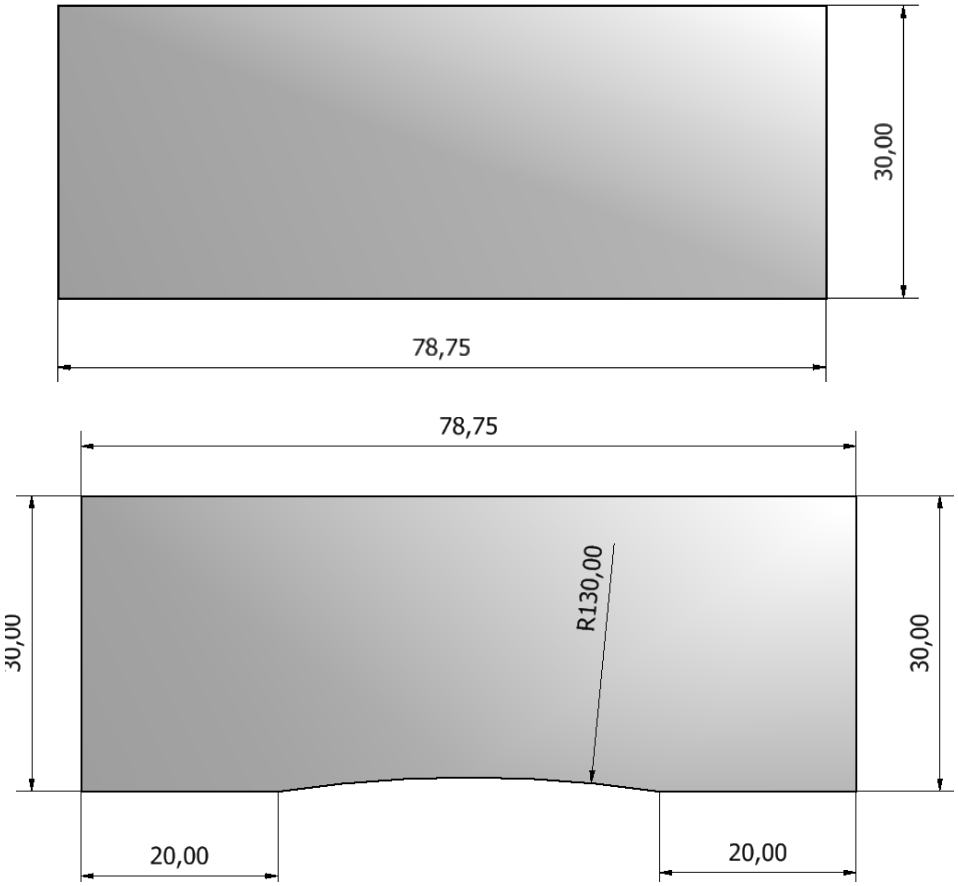

Figure C.4 Pressing tool end fixing plates

C.5 Punch Drawing

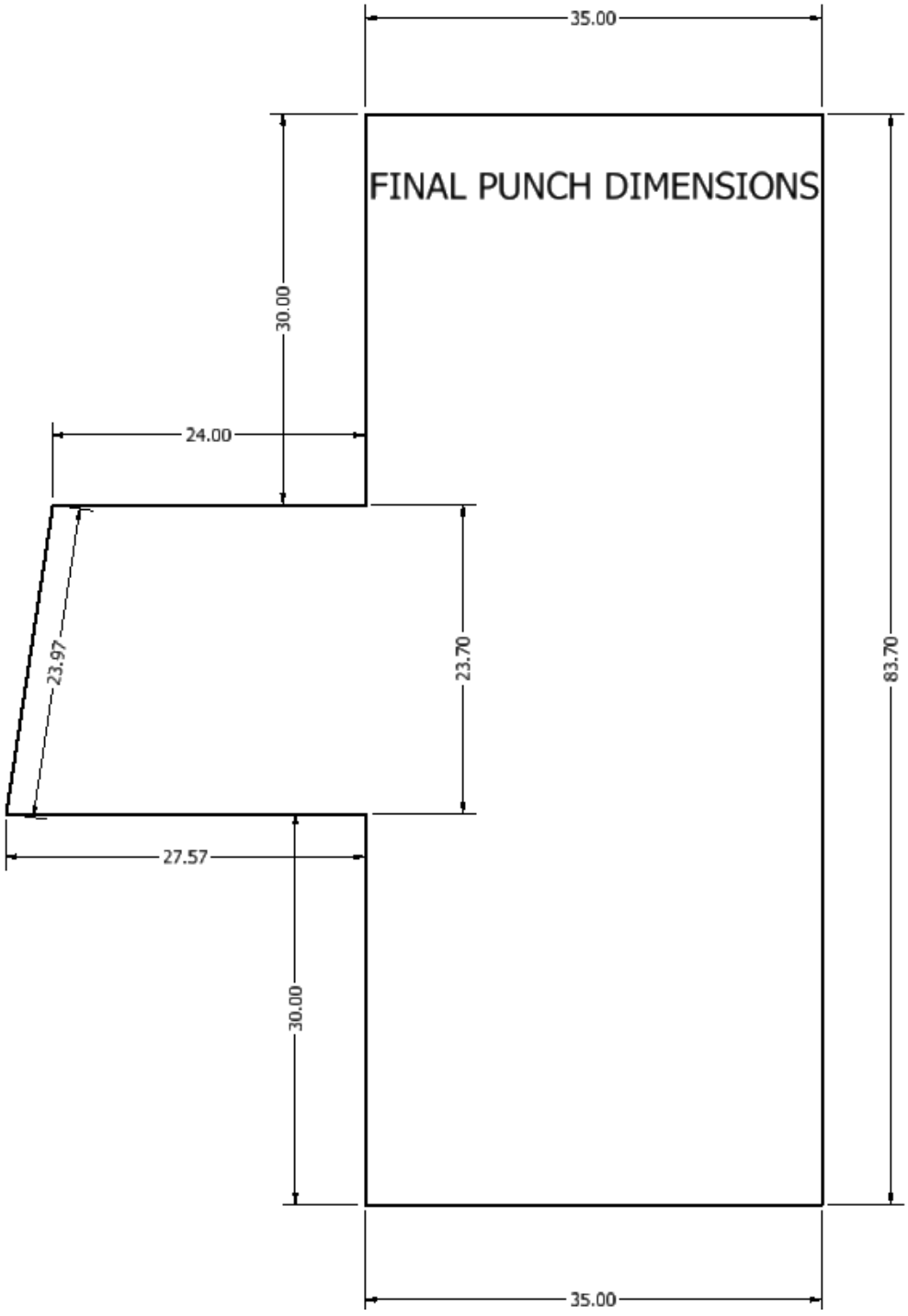

Figure C.5 Punch dimensions

APPENDIX D: Permanent Magnet Alternator Thermal Analysis Details

D.1 Transient Thermal FEA Simulation Results for the PMAs with and without Thermal Paste

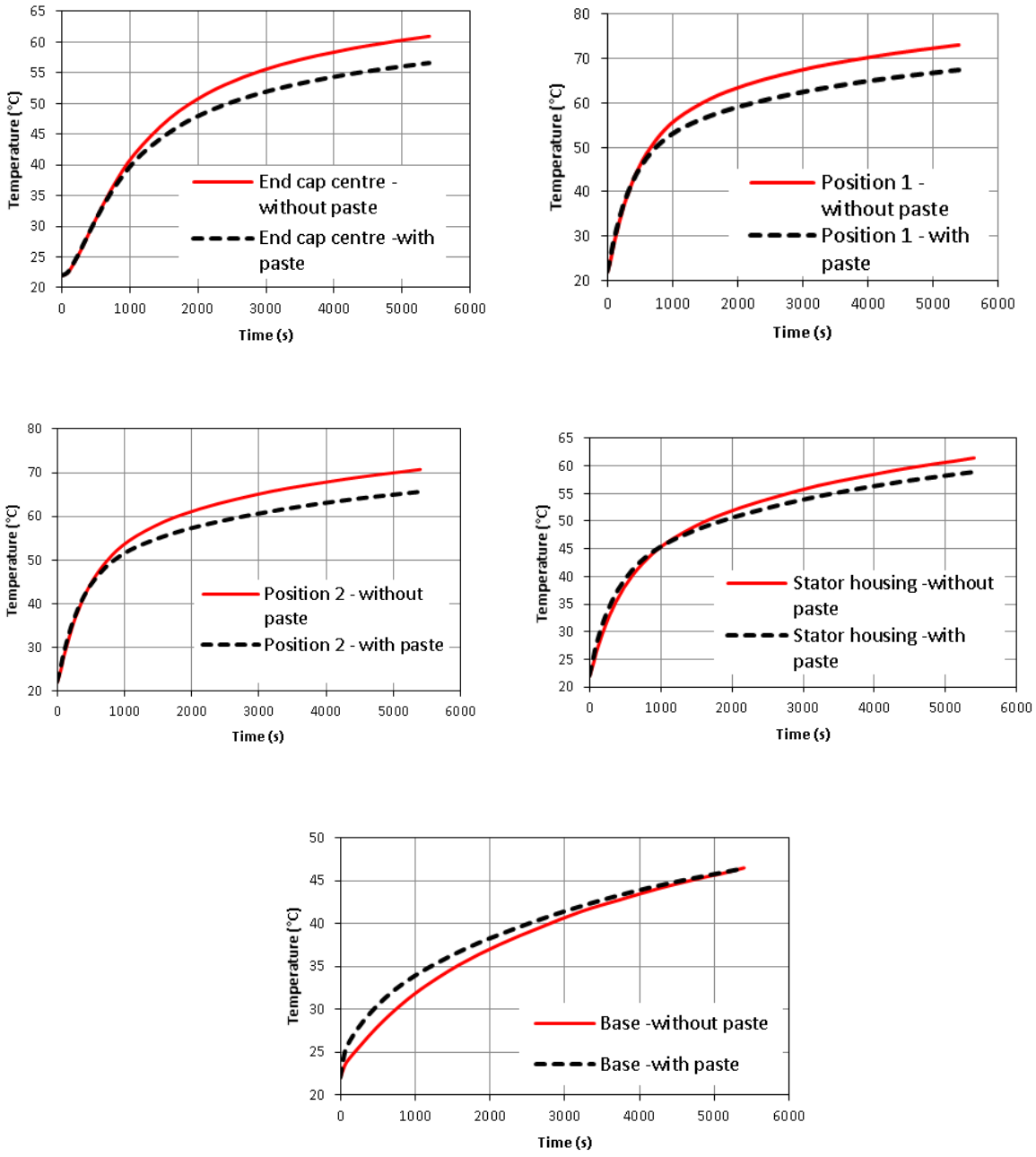

Figure D.1 Comparisons of thermal FEA results for the PMAs with and without thermal paste

D.2 Rotor Equivalent Circuit

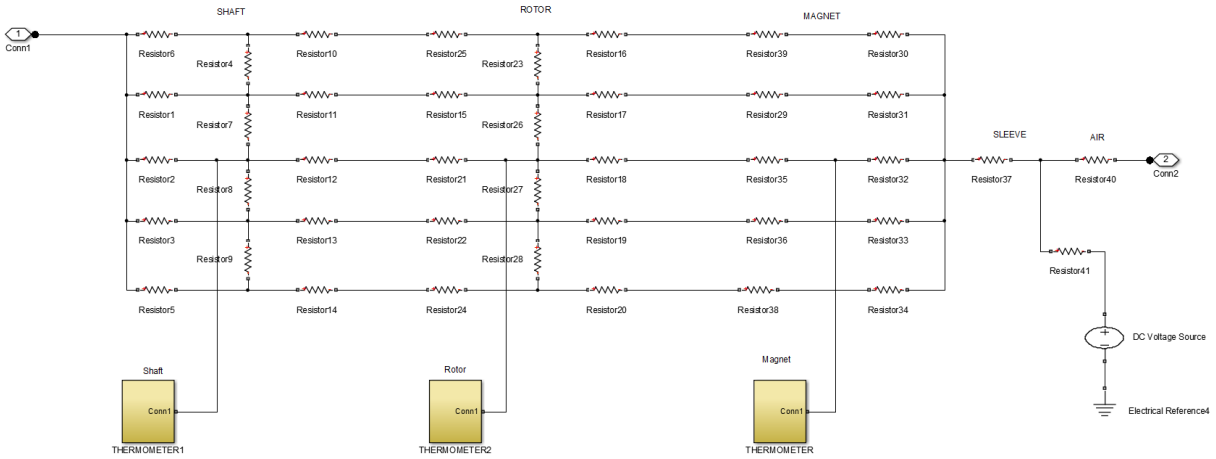

Figure D.2 Rotor thermal lumped model

D.3 Spacer Tooth Equivalent Thermal Circuit

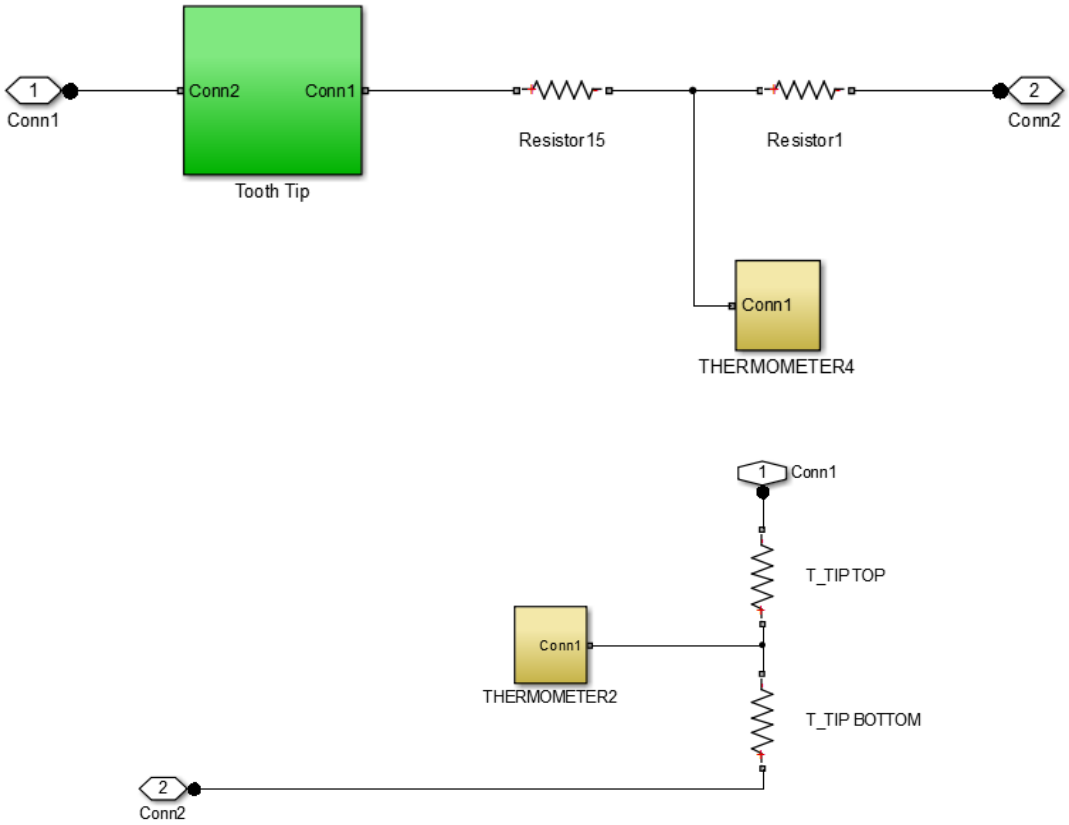

Figure D.3 Spacer tooth thermal lumped model

D.4 Tooth- Slot Equivalent Circuit for the PMA without Thermal Paste

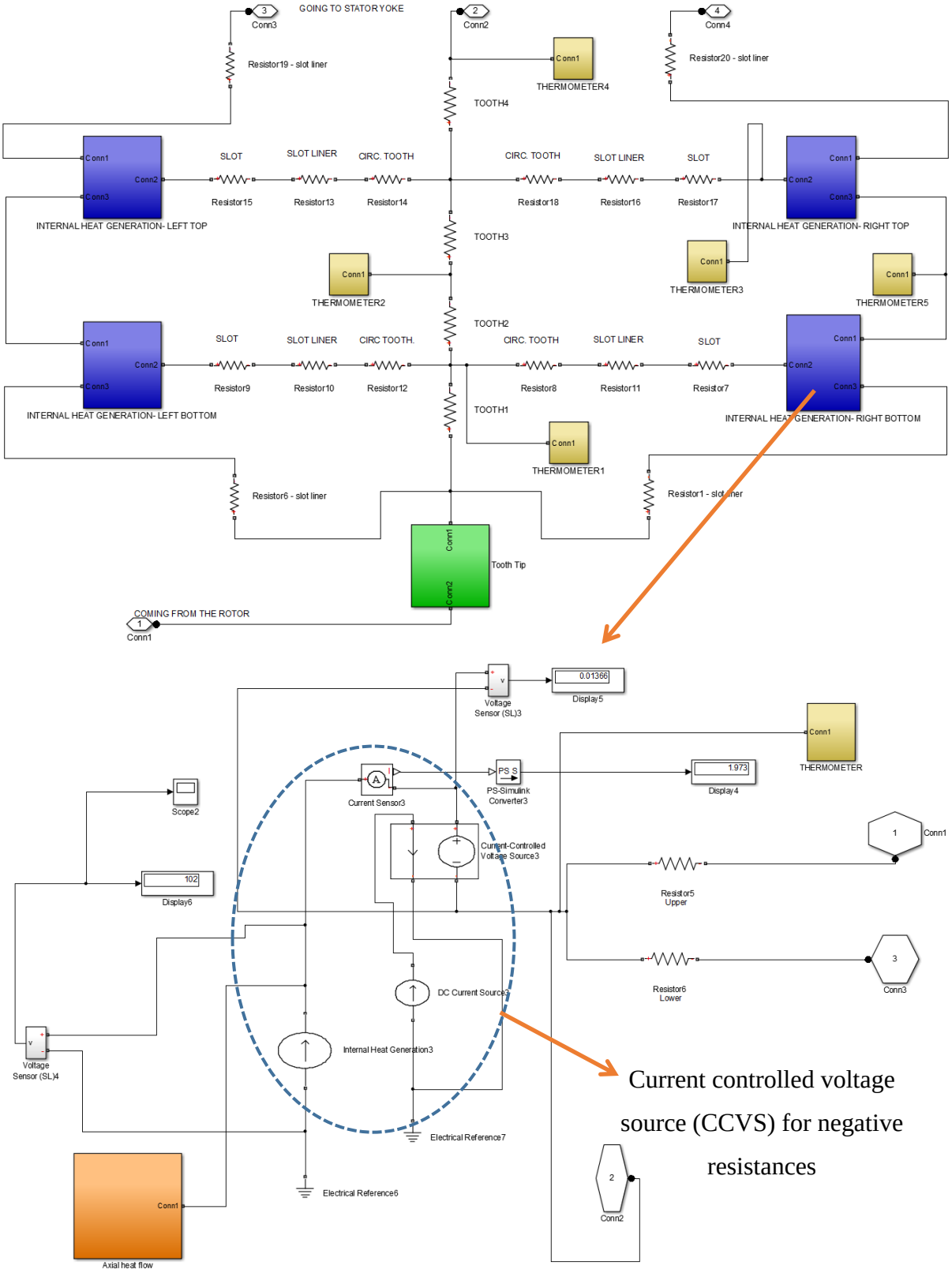

Figure D.4 Tooth - Slot thermal lumped parameter model for the PMA without thermal paste

D.4.1 Axial Heat Flow through the PMA Slots

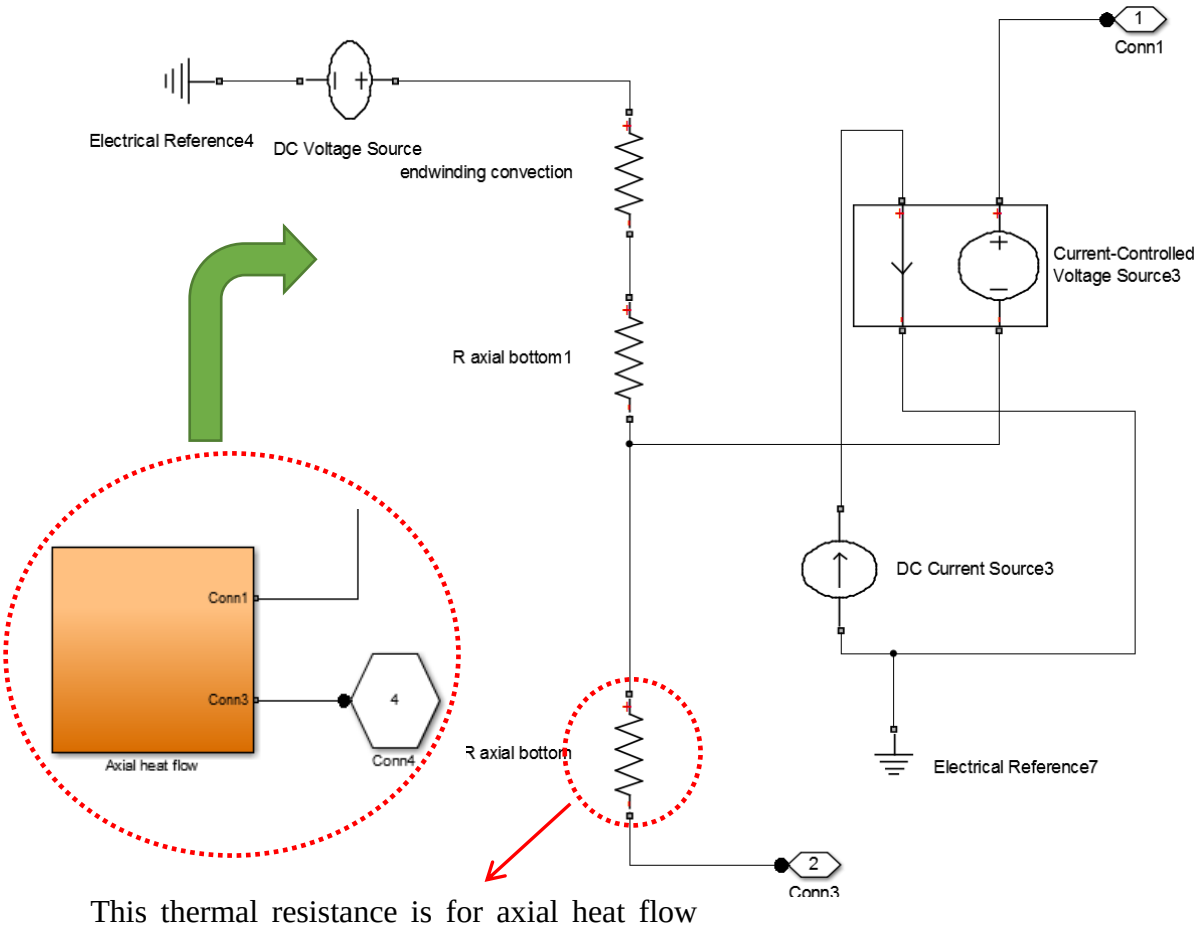

This thermal resistance is for axial heat flow from the centre of the coil to the end windings.

Figure D.5 Axial heat flow thermal lumped parameter model

D.5 PMA Stator Yoke Equivalent Thermal Circuit

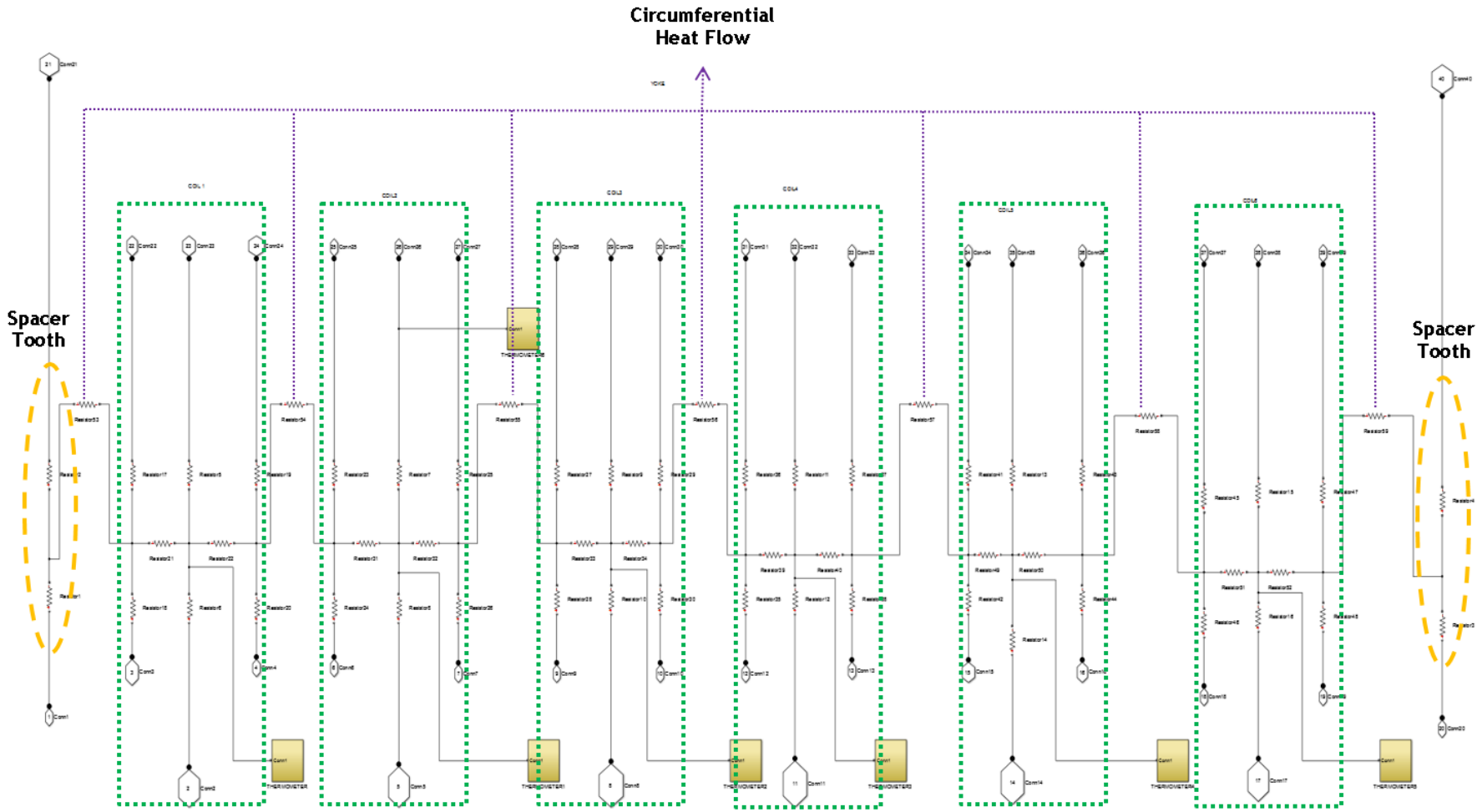

Figure D.6 PMA stator yoke thermal lumped parameter model

D.6 Experimental Validation of Thermal Models for the PMA without thermal paste

Table D.1 Temperature rise (ΔT) comparison for the PMA without thermal paste at steady state

Part	Thermal LP (°C)	Thermal FEA (°C)	Experiment (°C)	Error between FEA and Thermal LP (%)	Error between Experiment and Thermal LP (%)
Shaft	16.131	15.26	12.5	5.40	22.5
Rotor core back	16.131	15.28	n/a	5.276	n/a
Magnets	16.131	15.31	n/a	5.090	n/a
Tooth tip	78.55	80.23	n/a	-2.139	n/a
Tooth	78.83	81.59	n/a	-3.501	n/a
Spacer tooth	73.47	70.36	n/a	4.233	n/a
Winding	80.08	81.35	n/a	-1.586	n/a
Stator core back	67.44	66.01	n/a	2.120	n/a
End cap centre	38.56	36.13	38.94	6.302	-0.985
Position 1	46.5	45.46	51.12	2.237	-9.935
Position 2	39.66	39.26	43.8	1.009	-10.439
Stator housing	32.6	32.34	31.1	0.798	4.601
Base	23.72	24.4	24.48	-2.867	-3.204
Ambient	22	22	22-23	n/a	n/a

D.6.1 Temperature Distribution in PMA Stators

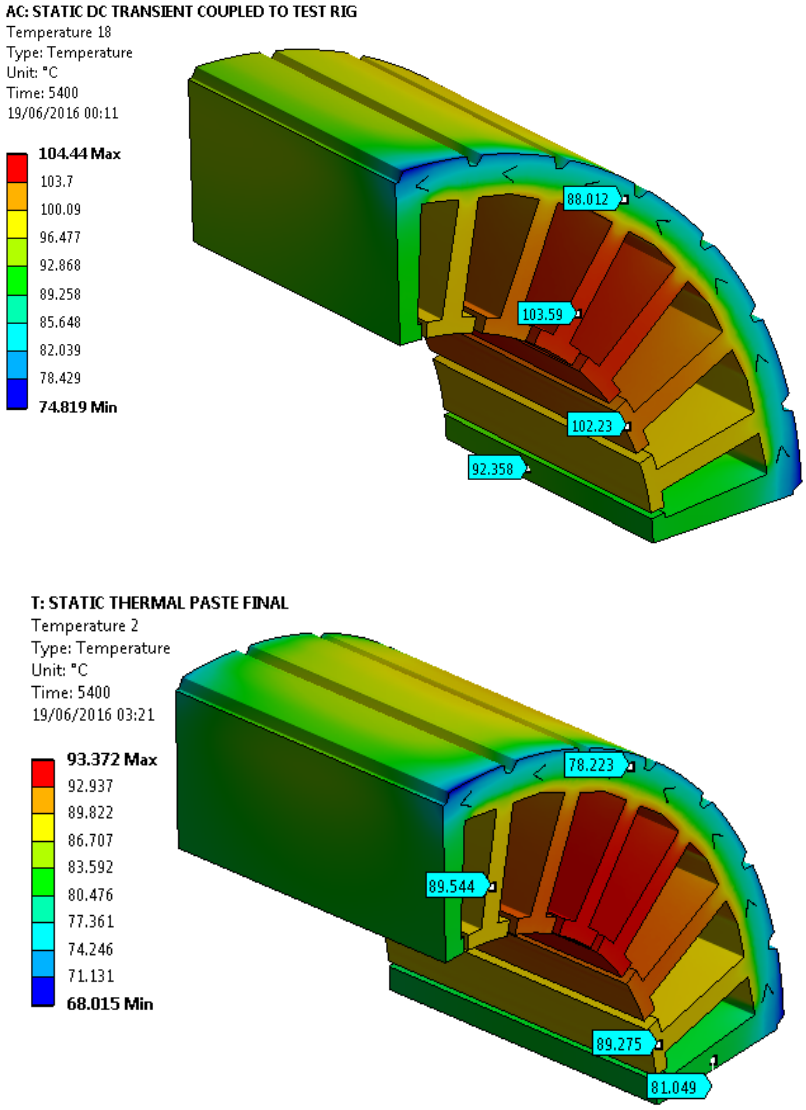

Figure D.7 Temperature distributions in the stators: PMA without thermal paste (top), with thermal paste (bottom)

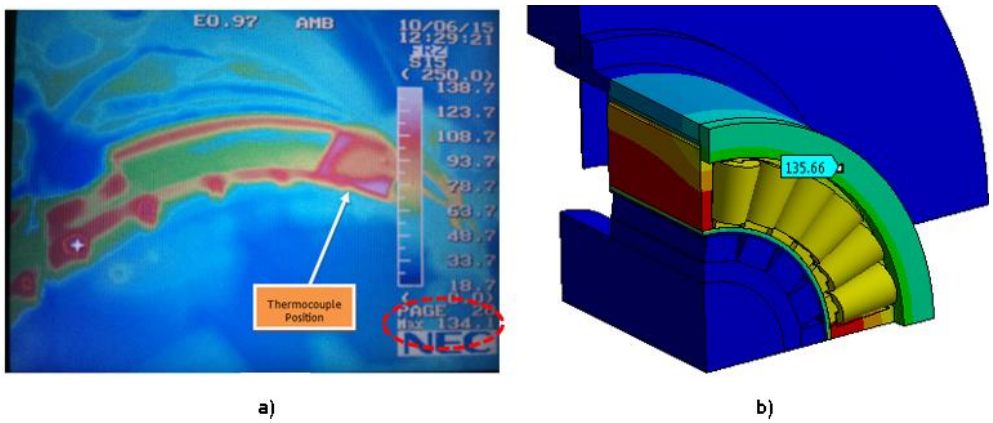

Figure D.8 Temperature distribution in the PMA casing at 100% speed (FEA) and validation through infrared (IR) image

D.7 Iron Loss Prediction of the PMA at 100% speed

Iron loss can be predicted by extrapolation of the thermal data obtained from static dc tests. Total copper loss is calculated for the PMA without thermal paste. The reference point for temperature increase is chosen to be "Base".

Table D.2 Copper loss vs final temperature at the position "Base"

Total copper loss @ 2.5 A dc test	Corresponding steady state final temperature at position "Base" for 2.5 A dc test
89.407 watt	35.416 °C
Total copper loss @ 3.5 A dc test	Corresponding steady state final temperature at position "Base" for 3.5 A dc test
221.986 watt	48.145 °C

In addition to temperature increase for copper losses, temperature increase for iron loss is required to extrapolate loss data by taking final temperature data as reference at the base of the PMA without thermal paste. Therefore, 100% speed open circuit transient thermal test results for the PMA without thermal paste is given in Figure D.9.

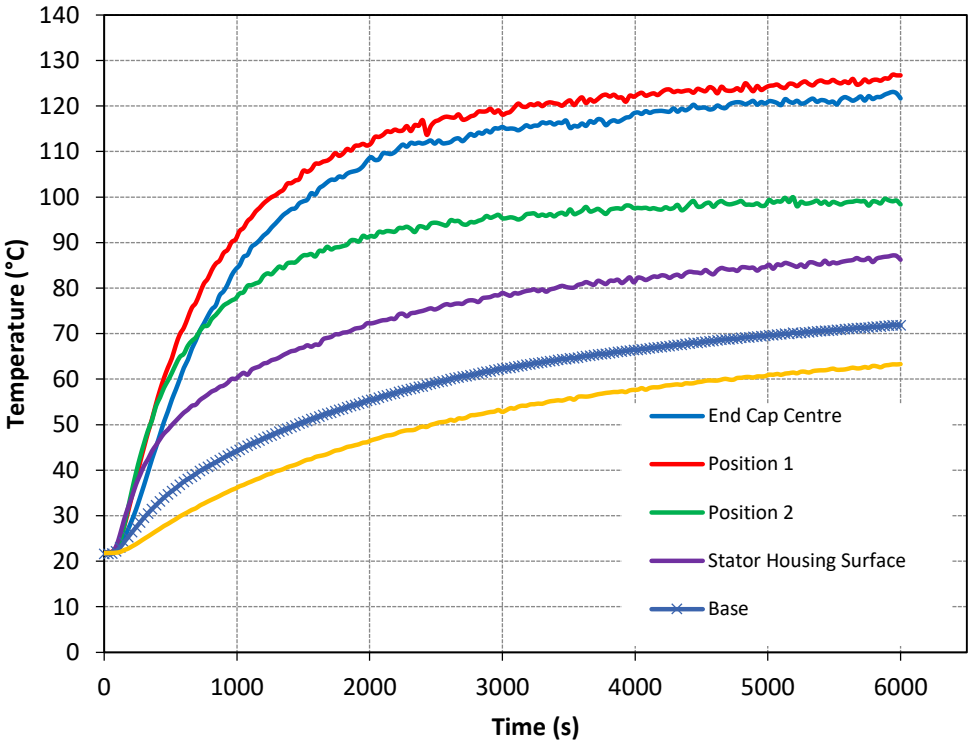

Figure D.9 Transient temperature variation for the PMA without thermal paste at rated speed

In Figure D.9, final temperature at "Base" after 90 min reaches 70.552°C. In Figure D.10, temperature increase at base versus corresponding loss data is plotted.

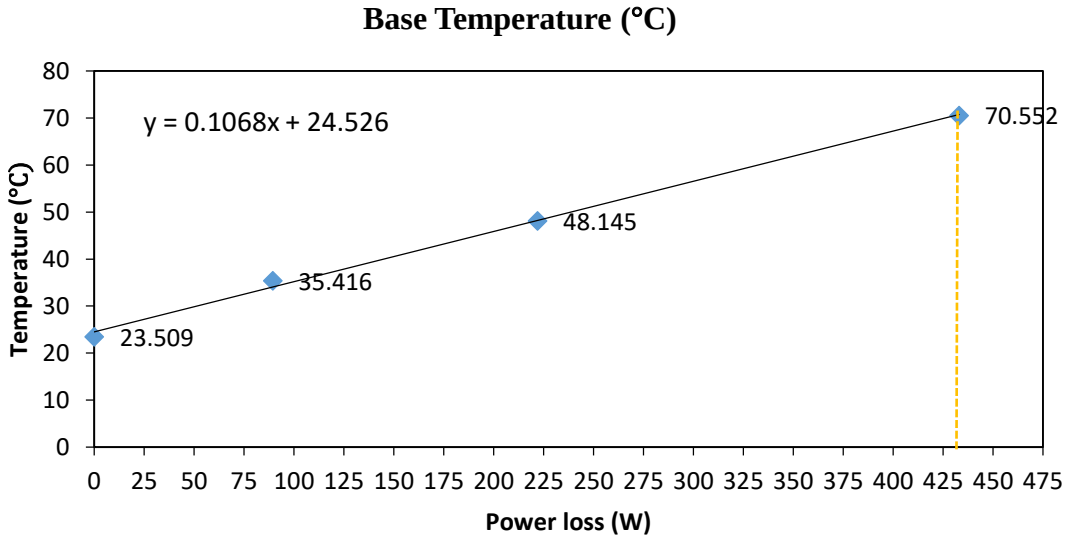

Figure D.10 Iron loss prediction by extrapolation of dc loss data

As shown in Figure D.10, iron loss corresponding to 70.55°C temperature is 431 watts for the PMA without thermal paste. This prediction is based on variation of temperature for different amounts of internal heat generations inside the machine stator.